

Topics in Current Chemistry Collections

Yan Li
Shigeo Maruyama *Editors*

Single-Walled Carbon Nanotubes

Preparation, Properties and
Applications



Topics in Current Chemistry Collections

Journal Editors

Massimo Olivucci, Siena, Italy and Bowling Green, USA
Wai-Yeung Wong, Hong Kong, China

Series Editors

Hagan Bayley, Oxford, UK
Greg Hughes, Codexis Inc, USA
Christopher A. Hunter, Cambridge, UK
Seong-Ju Hwang, Seoul, South Korea
Kazuaki Ishihara, Nagoya, Japan
Barbara Kirchner, Bonn, Germany
Michael J. Krische, Austin, USA
Delmar Larsen, Davis, USA
Jean-Marie Lehn, Strasbourg, France
Rafael Luque, Córdoba, Spain
Jay S. Siegel, Tianjin, China
Joachim Thiem, Hamburg, Germany
Margherita Venturi, Bologna, Italy
Chi-Huey Wong, Taipei, Taiwan
Henry N.C. Wong, Hong Kong, China
Vivian Wing-Wah Yam, Hong Kong, China
Chunhua Yan, Beijing, China
Shu-Li You, Shanghai, China

Aims and Scope

The series *Topics in Current Chemistry Collections* presents critical reviews from the journal *Topics in Current Chemistry* organized in topical volumes. The scope of coverage is all areas of chemical science including the interfaces with related disciplines such as biology, medicine and materials science.

The goal of each thematic volume is to give the non-specialist reader, whether in academia or industry, a comprehensive insight into an area where new research is emerging which is of interest to a larger scientific audience.

Each review within the volume critically surveys one aspect of that topic and places it within the context of the volume as a whole. The most significant developments of the last 5 to 10 years are presented using selected examples to illustrate the principles discussed. The coverage is not intended to be an exhaustive summary of the field or include large quantities of data, but should rather be conceptual, concentrating on the methodological thinking that will allow the non-specialist reader to understand the information presented.

Contributions also offer an outlook on potential future developments in the field.

More information about this series at <http://www.springer.com/series/14181>

Yan Li • Shigeo Maruyama

Editors

Single-Walled Carbon Nanotubes

Preparation, Properties and Applications

With contributions from

Hakim Amara • Moh. R. Amer • Christophe Bichara • Xuan Cao
Yu Cao • Sen Cong • Guodong Dong • E. H. Hasdeo • Jun Hirotani
N. T. Hung • W. Izumida • Il Jeon • Xilai Jia • Esko I. Kauppinen
Patrik Laiho • Meihui Li • Pan Li • Yan Li • Xuelei Liang
Qingzhou Liu • Xiyan Liu • Shigeo Maruyama • Yutaka Matsuo
A. R. T. Nugraha • Yutaka Ohno • lianmao Peng • R. Saito
Boyuan Tian • Xiao Wang • Fei Wei • Nan Wei • Fanqi Wu • Jiye Xia
Feng Yang • Jin Zhang • Qiang Zhang • Xiulan Zhao • Ming Zheng
Chongwu Zhou



Editors

Yan Li
Peking University
Beijing, China

Shigeo Maruyama
The University of Tokyo
Tokyo, Japan

Partly previously published in Top Curr Chem (Z) Volume 374 (2016); Top Curr Chem (Z) Volume 375 (2017); Top Curr Chem (Z) Volume 376 (2018); Topics in Current Chemistry Volume 377 (2019).

ISSN 2367-4067

Topics in Current Chemistry Collections

ISBN 978-3-030-12699-5

© Springer Nature Switzerland AG 2019

This work is subject to copyright. All rights are reserved by the Publisher, whether the whole or part of the material is concerned, specifically the rights of translation, reprinting, reuse of illustrations, recitation, broadcasting, reproduction on microfilms or in any other physical way, and transmission or information storage and retrieval, electronic adaptation, computer software, or by similar or dissimilar methodology now known or hereafter developed.

The use of general descriptive names, registered names, trademarks, service marks, etc. in this publication does not imply, even in the absence of a specific statement, that such names are exempt from the relevant protective laws and regulations and therefore free for general use.

The publisher, the authors and the editors are safe to assume that the advice and information in this book are believed to be true and accurate at the date of publication. Neither the publisher nor the authors or the editors give a warranty, expressed or implied, with respect to the material contained herein or for any errors or omissions that may have been made. The publisher remains neutral with regard to jurisdictional claims in published maps and institutional affiliations.

This Springer imprint is published by the registered company Springer Nature Switzerland AG
The registered company address is: Gewerbestrasse 11, 6330 Cham, Switzerland

Contents

Preface.....	vii
Modeling the Growth of Single-Wall Carbon Nanotubes.....	1
Hakim Amara and Christophe Bichara: Top Curr Chem (Z) 2017, 2019:55 (8, May 2017) DOI 10.1007/s41061-017-0141-8	
Metallic Catalysts for Structure-Controlled Growth of Single-Walled Carbon Nanotubes	25
Meihui Li, Xiyan Liu, Xiulan Zhao, Feng Yang, Xiao Wang and Yan Li: Top Curr Chem (Z) 2017, 2019:29 (1, March 2017) DOI 10.1007/s41061-017-0116-9	
Preparation of Horizontal Single-Walled Carbon Nanotubes Arrays.....	69
Pan Li and Jin Zhang: Top Curr Chem (Z) 2016, 2019:85 (30, November 2016) DOI 10.1007/s41061-016-0085-4	
Recent Developments in Single-Walled Carbon Nanotube Thin Films Fabricated by Dry Floating Catalyst Chemical Vapor Deposition	99
Qiang Zhang, Nan Wei, Patrik Laiho and Esko I. Kauppinen: Top Curr Chem (Z) 2017, 2019:90 (27, November 2017) https://doi.org/10.1007/s41061-017-0178-8	
Sorting Carbon Nanotubes.....	129
Ming Zheng: Top Curr Chem (Z) 2017, 2019:13 (12, January 2017) DOI 10.1007/s41061-016-0098-z	
Electronic and Optical Properties of Single Wall Carbon Nanotubes	165
R. Saito, A. R. T. Nugraha, E. H. Hasdeo, N. T. Hung and W. Izumida: Top Curr Chem (Z) 2017, 2019:7 (28, December 2016) DOI 10.1007/s41061-016-0095-2	

Review of Electronics Based on Single-Walled Carbon Nanotubes.....	189
Yu Cao, Sen Cong, Xuan Cao, Fanqi Wu, Qingzhou Liu, Moh. R. Amer and Chongwu Zhou: Top Curr Chem (Z) 2017, 2019:75 (14, August 2017) DOI 10.1007/s41061-017-0160-5	
 Carbon Nanotube Thin Film Transistors for Flat Panel Display	
Application	225
Xuelei Liang, Jiye Xia, Guodong Dong, Boyuan Tian and lianmao Peng: Top Curr Chem (Z) 2016, 2019:80 (21, November 2016) DOI 10.1007/s41061-016-0083-6	
 Carbon Nanotube Thin Films for High-Performance Flexible	
Electronics Applications	257
Jun Hirotani and Yutaka Ohno: Topics in Current Chemistry 2019, 2019:3 (2, January 2019) https://doi.org/10.1007/s41061-018-0227-y	
 Single-Walled Carbon Nanotubes in Solar Cells.....	271
Il Jeon, Yutaka Matsuo and Shigeo Maruyama: Top Curr Chem 2018, 2019:4 (22, January 2018) https://doi.org/10.1007/s41061-017-0181-0	
 Advances in Production and Applications of Carbon Nanotubes	299
Xilai Jia and Fei Wei: Top Curr Chem (Z) 2017, 2019:18 (30, January 2017) DOI 10.1007/s41061-017-0102-2	

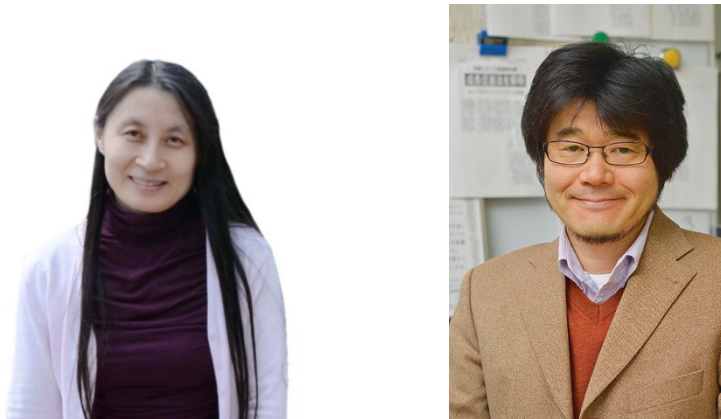
Preface

Carbon nanotubes (CNTs) have been standing among the most important materials in both scientific research and technical applications since 1990s. CNTs are composed of hexagonal sp^2 carbon networks rolled up into cylinders. This unique structure endows them outstanding physical, mechanical, and chemical properties. For instance, CNTs are on the top list of superior materials in mechanical strength, electrical and thermal conductivity, as well as stability. In addition, the structure-dependent electronic and optical properties of single-walled CNTs (SWCNTs) bring great potentials in electronic and optoelectronic applications.

After 27 years (since 1991) of both research and application, now is the right time to summarize the existing knowledge, discuss the present challenges, and look forward to the future of CNTs. Therefore, we edit this collection on these purposes. The collection contains 11 contributions, covering topics on preparation, property and devices, application and industrialization. All the contributions are authored by active researchers in the field. Since preparation is always the basis of materials research and application, we therefore begin the collection with the preparation. It starts from the theoretical study on the growth mechanism, then introduces catalysts for controlled growth, further extends to the growth of horizontally aligned SWCNT arrays and SWCNT films, and finishes with the sorting of SWCNTs. Subsequently, the optical and electronic properties are discussed. The application and industrialization part involves the applications in panel display, flexible electronics, and solar cells as well as the macro production and commercialization of CNTs.

CNTs have shown to be materials with great scientific importance and remarkable potentials in advanced applications. We believe this collection can bring you comprehensive information on the progress and deep insight into the emerging future in this field.

Finally, we would like to thank all authors of every contribution. Without their enormous efforts, we would not have this collection.



Yan Li (left) and Shigeo Maruyama (right)
Peking University and The University of Tokyo



Modeling the Growth of Single-Wall Carbon Nanotubes

Hakim Amara¹ · Christophe Bichara²

Received: 7 November 2016/Accepted: 16 April 2017/Published online: 8 May 2017
© Springer International Publishing Switzerland 2017

Abstract More than 20 years after their discovery, our understanding of the growth mechanisms of single-wall carbon nanotubes is still incomplete, in spite of a large number of investigations motivated by potential rewards in many possible applications. Among the many techniques used to solve this challenging puzzle, computer simulations can directly address an atomic scale that is hardly accessible by other experiments, and thereby support or invalidate different ideas, assumptions, or models. In this paper, we review some aspects of the computer simulation and theoretical approaches dedicated to the study of single-wall carbon nanotube growth, and suggest some ways towards a better control of the synthesis processes by chemical vapor deposition.

Keywords SWNT · Growth mechanisms · Modeling · CVD

1 Introduction

Almost 25 years after their first identification, carbon nanotubes [1] (CNTs), among which the single-wall ones (SWNTs) [2] are most promising for applications related to their electronic properties, still face very difficult challenges regarding their controlled and selective synthesis. Selectivity may concern the tube's electronic

Chapter 1 was originally published as Amara, A. & Bichara C. Top Curr Chem (Z) (2017) 375: 55.
DOI 10.1007/s41061-017-0141-8.

✉ Christophe Bichara
bichara@cinam.univ-mrs.fr

¹ Laboratoire d'Etude des Microstructures, ONERA-CNRS, BP 72, 92322 Châtillon Cedex, France

² Aix Marseille University, CNRS, CINAM, Campus de Luminy, Marseille, France

properties (semiconducting or metallic), or, even more challenging, its structure, characterized by its chiral indexes (n, m). Quite amazingly after hundreds of papers devoted to the subject, a very recent review [3] still stresses the lack of complete understanding of the SWNT growth mechanisms and ways towards controlled selectivity. Because its ability to be upscaled to industry requirements, catalytic chemical vapor deposition (CCVD, or CVD here, in short) is the method of choice that is most widely used and investigated. Very briefly, it consists of the decomposition of carbon-bearing molecules on a nanosized catalyst particle, typically a metallic one, which eventually gives rise to a tube that keeps growing until some event causes the growth to stop. All this takes place at high temperature (600–1100 °C), in a complex ambient, with catalyst nanoparticles either bound to a substrate, or floating at the tip of the growing tube. This complex synthesis has been studied by a very large number of techniques. Among these, theoretical modeling and computer simulation stand in a particular position, since they directly address the atomic scale that is relevant to the problem, with a number of approximations, though. An extended review by leading experts has been published recently [4] and we refer the interested reader to it. Our goal here is to give a more personal viewpoint, focusing on some recent results, some of which still in the process of being published, that have been obtained in close collaboration with experimental groups. In fact, we do believe that this is the most fruitful, though not the fastest, way to progress in this difficult field.

While some models [5] discuss kinetic aspects of SWNT growth, neglecting the role of the catalyst nanoparticle, we focus here on catalyst nanoparticles, their interaction with carbon under CVD growth conditions, and their interface with the tube, that are critical to understand nucleation and growth mechanisms. In doing so, we pay attention to thermodynamic aspects of the growth, and, to start with, we can remember that carbon science has a long history. Growing a tube indeed displays some similarities with the growth of carbon fibers, except that the very small nanoparticle and tube diameters induce some peculiarities that are discussed later. As explained in [6], the growth of filamentous carbon on a Ni catalyst results from a gradient of carbon chemical potential between the carbon atoms delivered at the surface of the catalyst by the precursor decomposition, and the carbon sp^2 walls that act as a sink for carbon since they are at a lower Gibbs energy. In this process, the chemical potential of carbon at the nanoparticle surface is fixed by the thermochemical conditions of the precursor decomposition reaction. It can hence be tuned by playing with CVD parameters: temperature, pressure, and composition of the gas feed.

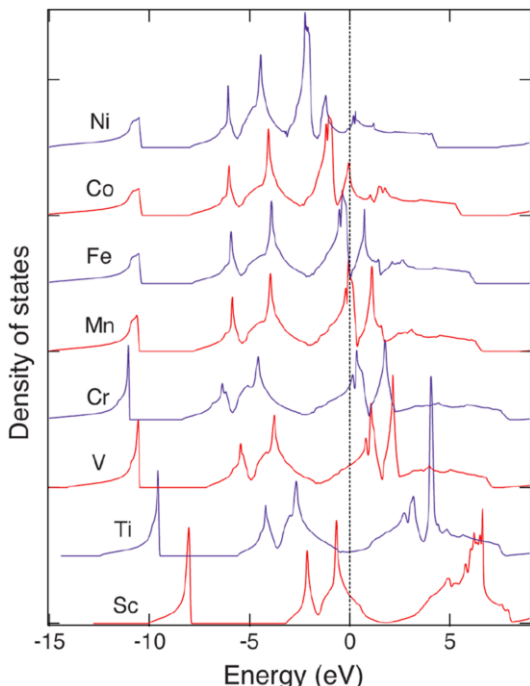
The approach we develop explicitly takes this carbon chemical potential into account, while it is somewhat by-passed in other contributions that are also presented in this paper. Starting from some general considerations on the carbon–metal catalyst interaction, we discuss the atomistic models and computer simulation techniques. Their possibilities and limitations are discussed and we then briefly summarize some peculiarities of the interface between nickel, cobalt, and iron catalysts, and the sp^2 carbon layer forming graphene or nanotube wall. A critical analysis of the different ways to address the nucleation and growth of SWNTs is then proposed, followed by a discussion of our viewpoint on the ways to control the SWNTs' diameter by tuning their “growth mode”. Carbon dissolution in subsurface

or bulk of the nanoparticles and the physical, solid, or molten, state of the nanoparticles are shown to be important since they contribute to modify their surface and interface properties.

2 Metal–Carbon Interactions

Until now, most CCVD experiments offering a reasonable yield and a possible upscaling to industrial dimensions use nanoparticles of late transition metals, or alloys, as catalysts. Fe, Co, and Ni, the lightest elements of these columns 8, 9, 10 of the periodic table have been extensively used. These elements are sometimes used alloyed [7, 8], or in conjunction with other metals such as Mo [9], Cu [10], or, more recently W [11]. The reason why Fe, Co, and Ni have been so popular catalysts is that they display a large enough affinity for carbon, to adsorb carbon precursor molecules and possibly dissolve some carbon, while keeping it in the surface layers. This is sometimes illustrated in the form of a “volcano” plot [12, 13]. Looking at the electronic densities of states of carbides of transition metals of the first row in a (sometimes fictitious) NaCl structures, displayed in Fig. 1, one immediately realizes that a rigid-band model is valid to describe the density of states of carbides. Indeed, at low energy, a narrow band derived from the 2s states of carbon can be identified. At higher energy, a fairly broad band of strongly hybridized states between the p states of carbon and the metallic d states appears, with a pseudogap, exactly separating bonding states from antibonding states in the case of Ti, that is known to

Fig. 1 Density of states of carbides with transition element of the 3d series, in a rocksalt structure, calculated with DFT-GGA. The Fermi level is set to zero. Ref. [14]



form a very stable carbide. For Fe, Co, and Ni, this hybridization effect is weaker, and the Fermi level shifted to higher energies, explaining why carbides of these elements are less stable. The outstanding ability of transition metals to combine strongly with carbon stems from the major role played by covalent bonds formed between the p states of carbon atoms and the valence d states of the metal ones, leading to an hybridized pd band [14, 15].

For Fe, Co, and Ni, this carbon–metal interaction also directly translates into specific features of their phase diagrams that display limited carbon solubility. Solubility limits of carbon in bulk Ni and Co are quite similar, around 4% atomic carbon fraction at their respective eutectic temperatures, with no stable bulk carbide structure reported. Carbon solubility is larger in Fe with (meta-)stable carbide phases observed. Deck and Vecchio [16], who led a systematic study of metals with various carbon solubilities, point out that efficient catalysts have a limited, though non-zero carbon solubility, while metals with vanishing C-solubility or forming stable carbide compounds do not promote SWNT growth. If one considers the possibility to open the parameter space by including alloyed nanoparticles, this conclusion leaves space for discovering other, more efficient and selective catalysts.

Considering bulk thermodynamic properties and phase diagrams is a first step, but does not tell much about the details of carbon–metal interactions. CCVD synthesis of SWNTs is a surface process involving catalyst particles in the 1–5 nm diameter range, where strong nanometric size effects should be expected. Although *in situ* XPS experiments have been performed during SWNT growth [17–19] or Pd-based catalysis [20], emphasizing the role of subsurface carbon, a real insight in carbon metal interaction is typically provided by ab initio calculations. Such calculations, generally performed within the framework of the density functional theory (DFT), provide accurate estimates of the interaction energy between carbon in various forms, and different metals, considering different configurations: adsorbed on surfaces, at step edges, or in interstitial sites [21, 22]. As shown in Fig. 2, Ni and Pd display [21] rather similar energetics with respect to carbon, with subsurface sites more prone to accept carbon incorporation.

DFT calculations appear as the reference tool to study the relative stability of nanotubes in contact with the nanoparticle from which they grow [23, 24], thus emphasizing the need for adequate tube/catalyst interaction strength, or searching for efficient catalysts, beyond the well-established Fe, Co, and Ni. Such calculations have been used to study the interaction energy of carbon flakes [25, 26] and nanotube caps with catalyst nanoparticles or flat surfaces, searching for preferential lattice matching of the cap [27], and hence tube chiralities. Quite recently, calculations searching for an optimal matching of some tube's chirality with an appropriate lattice plane of crystalline W₆Co₇ [11] or WC [28] have been proposed to support the interpretation of chiral selective CVD experiments, assuming a vapor–solid–solid model [29] of SWNT growth. Whether such perfect crystalline facets actually exist during CVD synthesis of SWNTs is still to be proven, illustrating a classical dilemma of computer simulations in materials science: use highly accurate methods on ideal, though possibly non-relevant

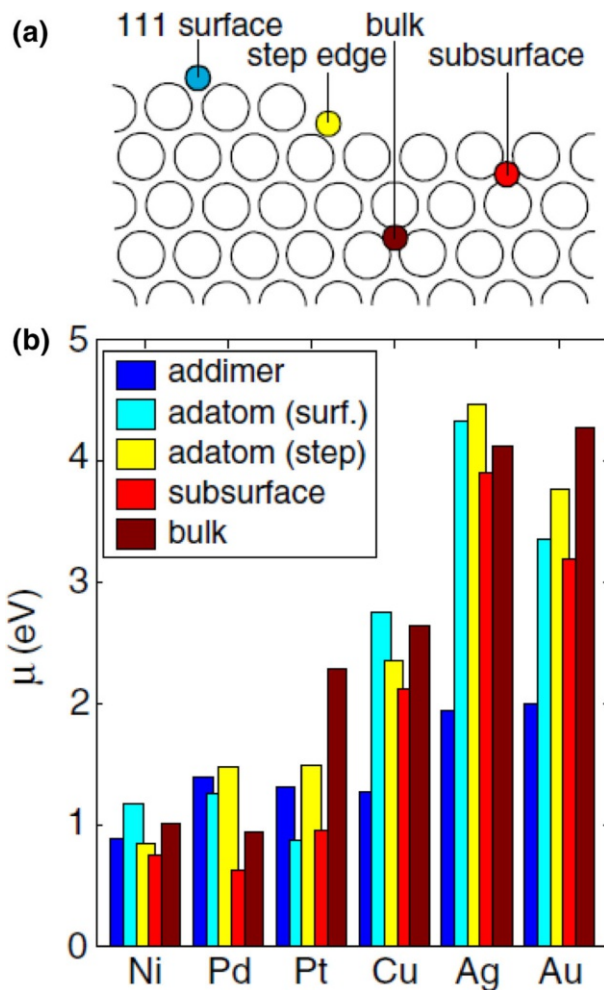


Fig. 2 **a** Schematic representation of carbon positions at metal surfaces. **b** Binding energies of monoatomic and diatomic carbon on different late-transition (Ni, Pd, Pt) and coinage (Cu, Ag, Au) metals. Ref. [21]

structures, or approximate ones, able to directly deal with the complexity of the problem (here: high temperature, presence of active carbon, and ambient,...) at the expense of accuracy. Beyond these calculations, interesting new approaches tackle the decomposition of molecular carbon precursors, such as methane [30] or ethanol [31] on the catalyst surface. These results show that CCVD process is indeed more complex than the interaction of atomic carbon with a bare catalyst surface, as often described in computer simulations of SWNT growth. Before returning to our main topic, let us mention that non-metallic catalysts [32–34] have been successfully used to grow nanotubes, though not always with a high enough yield.

3 Interatomic Interaction Models and Computer Simulation Techniques

Cohesion energies of graphene and diamond, respectively, displaying sp^2 and sp^3 hybridized carbon–carbon bonds, are large, on the order of 7.2 eV/atom. Typical first row transition metals display cohesive energies in the 4–5 eV/atom range. This means that the energies involved breaking molecules, form intermediate carbon–metal, and reform carbon–carbon bonds are large. On the other hand, tiny energy differences exist between the possible carbon adsorption sites, and also between the possible tube/catalyst bonding interactions. Assuming pure metal nanoparticles, the interaction between tubes with different chiralities and metals of different kinds [23, 24], has been evaluated using DFT calculations. Figure 3 indicates that efficient catalysts display intermediate interactions with tubes, somewhat corresponding to a “Goldilocks” principle. Accurately describing these various energy ranges within the same framework is a first requirement that has to be met by interatomic energy model to be used in Monte Carlo or molecular dynamics simulations of carbon nanotubes growth. A second, not less demanding aspect, concerns the time scales and complexity of the CVD process. This implies that a trade-off has to be found between contradictory requirements. The only source of relief is the nanometric size of the systems under consideration: nanoparticles relevant to CVD growth of single-wall carbon nanotubes are typically in the 1–5 nm diameter range,—a hundred to a few thousands atoms, and the issues associated to SWNT structure do not require more than a few hundred carbon atoms to be included in the computed system. These are easily handled in relatively simple order N models. However, direct DFT calculations of systems consisting of a tube in contact with a catalyst have to be limited to smaller samples and time scales of 10–100 ps, using standard plane wave DFT codes.

Empirical force fields have been specifically developed for Fe–C [35] and Ni–C [36], while so-called “reactive force field” (ReaxFF) modeling has been used by Neyts et al. [37] who incorporated this in a sophisticated hybrid molecular

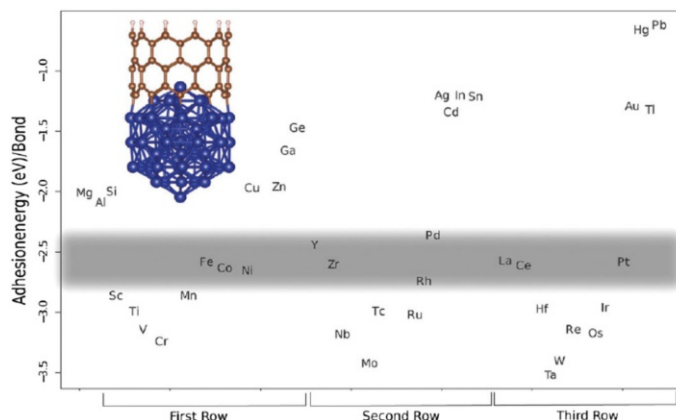


Fig. 3 DFT calculations of the adhesion energies per bond of a (10, 0) nanotube on a nanoparticle of various metals in icosahedral structure, with 55 atoms. Ref. [24]

dynamics-force biased Monte Carlo computer simulation algorithm, leading to less defective carbon structures. Choosing an alternative at the opposite end of the complexity scale for the description of the interatomic interactions, but still manageable for decent molecular dynamics simulations, Irle et al. [38] used density functional tight binding (DFTB) to simulate the early stages of the nucleation of tubes on various catalysts, such as Fe or Ni [39, 40], or more exotic catalysts, such as alumina [41]. Although lighter than plain DFT calculations, such models still suffer from a non-linear scaling with system sizes, and hence are limited in size- and time-scales. Retaining the physically grounded assumptions of the tight binding approximation, but in a lighter, order N way, the present authors developed a tight binding model for Ni–C alloys, approximated at the fourth moment of the local electronic density of states, and incorporated in a Monte Carlo code working in either canonical or grand canonical ensemble [14].

Beyond these carbon–metal interaction models, additional degrees of complexity should be considered. Among the important factors that are generally overlooked in computer simulations, the ambient and the presence of molecular fragments, in particular hydrogen, oxygen, hydroxyls etc., adsorbed on the nanoparticle surface certainly represent major issues. Except for the recent work of Shibuta et al. [30], and Khalikov et al. [42], the decomposition of the carbon precursor at the catalyst surface is generally not taken into account. Also, in real supported CVD processes, the substrate, quite often an oxide (SiO_2 , Al_2O_3 ...) plays an important role to stabilize the catalyst nanoparticle along the growth. A strong interaction between the nanoparticle and its support will change its shape and thermodynamic properties. This has been studied [43, 44], in relation with *in situ* TEM observation of SWNT growth [45].

Once an interatomic energy model has been selected, one has to choose a computer simulation technique to simulate some aspects of the CVD synthesis, since, quite obviously, a full atomistic description of the process is not possible, and approximations have to be made. The most straightforward idea is to use molecular dynamics simulations to “throw” carbon atoms onto the cluster surface, and to regularly feed new carbon atoms in the gas phase to keep its density almost constant. This approach suffers from many drawbacks. The first is the short computed time scale, leading to observed growth rates that are often orders of magnitude faster than the experimental one. The most recent and longest simulations [46], though, growing nanometer long tubes over a few 100-ns MD trajectories, are closer to, but still higher than experimental growth rates. The second is that the key quantity to address the reactivity of carbon at the surface of a catalyst is its chemical potential, which is fixed by the thermochemistry of the precursor decomposition reaction, and not simply by a gas phase pressure. An interesting discussion of this thermodynamic aspect in the case of the growth of filamentous carbon is given by Snoeck et al. [6]. The statistical mechanical framework to deal with this carbon chemical potential is the grand canonical ensemble that can be conveniently sampled by Monte Carlo simulations. However, these computer simulation techniques are designed to deal with thermodynamic equilibrium situations, and not with growth. In the present instance, its use can be justified assuming a local thermodynamic equilibrium at the tube nanoparticle interface, because growth is slow as compared to the high atomic mobility at typical

CVD temperatures [47]. Clearly, choices have to be made, which will emphasize different aspects of the growth process.

These challenging requirements explain why only a few groups actively worked on the understanding of the SWNT growth mechanisms, using various computer simulation approaches, and focusing on different aspects of the problem.

4 Properties of the sp^2 Carbon Wall–Metal Catalyst Interface

At the heart of the SWNT synthesis mechanism lies the close contact between the growing tube and the metal nanoparticle that enables the molecular feedstock to decompose, yielding atomic carbon that is then incorporated in the tube wall. Apart from the nanometric scale of the process in the case of SWNTs, similar behaviors have been observed and discussed in the context of carbon nanowires and graphene growth, and valuable insight has been gained in these somewhat easier cases.

The burst of experimental and theoretical work devoted to the mechanisms of graphene growth on different substrates, reviewed by Batzill [48], brings useful and sometimes surprising information. Different experimental and theoretical studies [21, 49] have shown that, in the case of graphene growth on face-centered cubic (111) nickel surfaces, the most favorable place to incorporate individual carbon atoms or dimers is in octahedral subsurface interstitial sites. On a free Ni surface, upon increasing carbon feed and at high temperature, carbon atoms would diffuse towards the bulk, and a carbon concentration gradient, with a carbon enrichment close to the surface would be observed. Quite surprisingly though, once a graphene layer is formed on the surface of Ni, a depletion of carbon close to the interface is observed. This has been evidenced experimentally [50], using *in situ*, depth-resolved X-ray photoemission spectroscopy (XPS) during graphene growth, a technique that is quite efficient to address this surface science problem. As illustrated in Fig. 4, this has also been independently observed [51], using both tight binding and DFT calculations, and similar experimental *in situ* XPS technique.

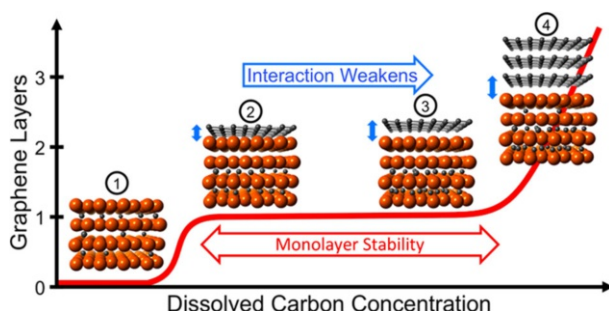


Fig. 4 Different steps illustrating the presence of a carbon-depleted zone during the growth of graphene on Ni(111) slab. 1 Some C atoms are incorporated in subsurface positions. 2, 3 When increasing C concentration, epitaxial graphene is formed on Ni(111) leading to the subsurface carbon depletion preventing additional layer formation. 4 Additional layers are formed at large concentration of carbon. Ref. [51]

This latter reference also shows that the adhesion energy of a graphene layer on a Ni surface becomes weaker when carbon atoms are present in Ni subsurface. Empirically tuning the work of adhesion between the tube and the metal nanoparticle, Ribas et al. [52] have shown the importance of this parameter to enable the nucleation and growth of a tube, and avoid catalyst encapsulation. In this respect, the role of dissolved carbon in the nanoparticle is fundamental, since it will affect the interfacial and wetting properties of Ni (and also Co and Fe), as shown in the early 1970s for bulk metal drops on graphite [53]: for these elements, the contact angle of a bulk metal drop on a graphite surface increases from 50° to 120°, when the fraction of carbon dissolved in the metal increases from 0 to about 2.7 wt%. Remembering Young–Dupré's equation:

$$1 + \cos \theta = \frac{W_{\text{adh}}(x_C)}{\gamma_{M(x_C)}},$$

where θ is the contact angle, W_{adh} is the work of adhesion, and $\gamma_{M(x_C)}$ is the surface energy of the metal nanoparticle, at a carbon concentration x_C , one can see that a vanishing work of adhesion and a lower but finite surface energy, both resulting from the increase of x_C , lead to an increase of the contact angle θ . According to our calculations [54], displayed in Fig. 5, this effect is particularly marked for small nanoparticles that can incorporate larger carbon fractions (up to about $x_C = 0.20$ –0.25) than macroscopic ones. Both carbon depletion close to Ni surface, and change of wetting and interfacial properties induced by carbon dissolution in the nanoparticles, will have a significantly stronger effect in the case of SWNT growth than for larger, macroscopic systems. These calculations, performed for Ni, are probably qualitatively valid for Co and Fe. Indeed, DFT-based calculation of surface energies of Fe [55] show a dependence on the surface coverage by carbon atoms, which remains limited because only crystalline structures are considered.

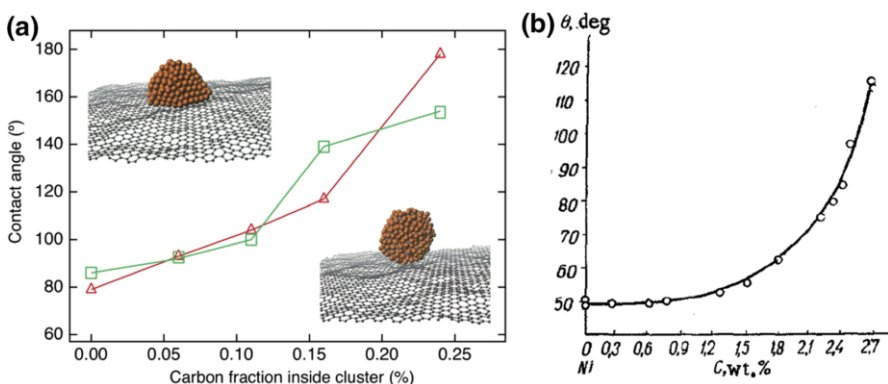


Fig. 5 Wetting properties of Ni on sp^2 carbon. **a** Contact angles of a Ni nanoparticle on graphene after performing Monte Carlo simulations at 1000 K (red triangles) and 1400 K (green squares) for different carbon concentration. Ref [54]. **b** Experimental contact angle of an Ni droplet containing carbon deposited on graphite at 1550 °C. Ref. [53]

5 Nucleation of Carbon Caps

From a fundamental point of view, nucleation is a stochastic and rare event, the frequency of which is related to the magnitude of its driving force. In the present instance, this driving force is the excess of carbon chemical potential, relative to that of C atoms dissolved in the NP, at the saturation limit. Quite generally, most direct computer simulations of nucleation rely on exceedingly large driving forces to observe nucleation [56] in the short time of the simulation. Sophisticated biased methods [57] have been proposed to address this problem. In spite of this, most computer simulation studies devoted to SWNT synthesis are in fact dealing with nucleation mechanisms, because they involve smaller numbers of atoms, while the total number of atoms in the computer simulation box remains an issue for reasonably accurate carbon–metal interaction models. There is also a widespread belief that the SWNT structure can be controlled at the nucleation step. This might seem reasonable since C–C bonds are quite strong, and difficult to break and reform in order to heal or form a defect (non-hexagonal ring) that could modify the tube chirality. However, a number of *in situ* TEM investigations [17, 58] of SWNT growth tend to indicate that very short nanotube nuclei, say below 3 nm, as typically considered in computer simulations, are not stable. Along the same line, post-mortem statistical investigations of SWNT length distribution suggested [59] that a critical length threshold (around 5 nm) exists, beyond which stable and sustainable growth would take place. In addition, this study exhibits some nanoparticles giving birth to two tube nuclei. Since no such configuration is observed for longer, stable tubes, one has to conclude that one of the nuclei disappeared or both merged, a possibility that has been nicely illustrated numerically (see Fig. 6) in the computer simulations of Neyts et al. [60], and post-mortem TEM observations.

In spite of this possible limitation, studying the SWNT nucleation mechanisms is still quite relevant since it can provide guidance in the quest for better, more selective catalysts. As early as 2004, using an empirical atomic interaction model, Ding et al. [35] demonstrated that small Fe catalyst nanoparticles should be carbon-saturated in order to nucleate a (very defective) tube cap. This is illustrated in Fig. 7. Almost simultaneously, an impressive attempt to directly simulate the nucleation of

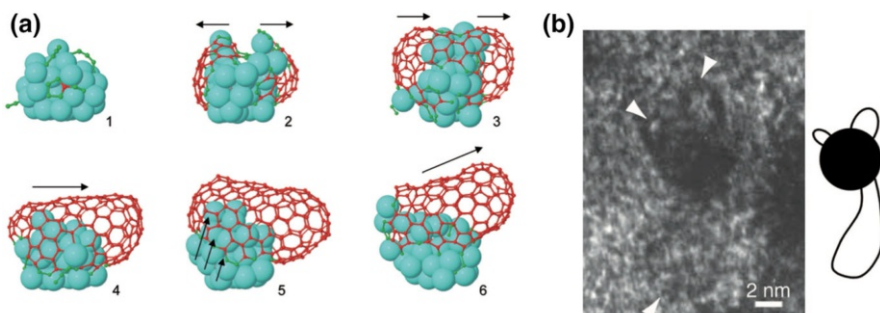


Fig. 6 Formation of two small caps during the first steps of the nucleation process from: **a** atomic scale modelization. Ref. [60]; **b** post-mortem TEM observations. Ref. [59]

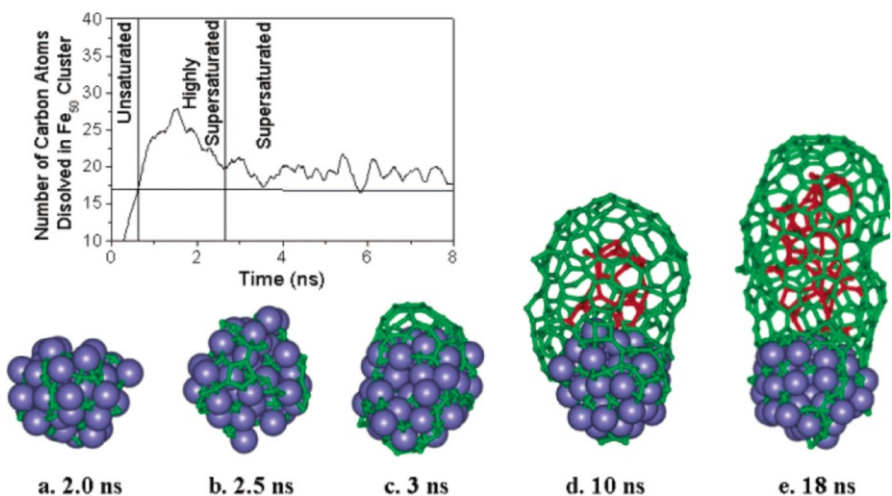


Fig. 7 Top evolution of the carbon concentration inside the nanoparticle during the formation of the tube. Bottom simulation growth evolution of a carbon nanotube from a cluster containing 50 Fe atoms at 900 K. Carbon atoms inside the tubular structure are represented in red. Ref. [35]

a tube cap on a small Fe nanoparticle using DFT-based molecular dynamics has been proposed by Raty et al. [61]. However, it was soon realized that such a calculation was too far from real experimental conditions, because of a too high C incorporation rate and a too short total simulated time. An intermediate route was then proposed by the Irle/Morokuma group [62], using their DFTB Molecular Dynamics modeling, which is a somewhat more efficient trade-off between chemical accuracy and computing efficiency. Page et al. [63] compared SWNT nucleation on Ni and Fe small nanoparticles of less than 100 atoms, pointing out differences between these two metal catalysts that could be attributed to differences in the strength of metal–carbon interactions. In the case of Ni, a study [64] taking into account carbon chemical potential as the control variable to calculate carbon sorption isotherms using grand canonical Monte Carlo simulations, enabled to investigate the energetics and the role of carbon atoms, either dissolved inside the nanoparticle, in sub-surface, or segregated outside. Cap nucleation was shown to take place in a well-defined chemical potential range, when a critical concentration of surface carbon atom is reached. In both studies, this cap formation follows the same process, described in Fig. 8: saturation of sub-surface with carbon atom, formation of polyyne chains weakly bound to the surface that ultimately connect each other to form Y-shaped junctions and then 5- and 6-membered rings.

The caps structures observed in these simulations are far from being perfect, with an excess of 5- and 7-membered rings as compared to ideal ones formed with six pentagons, the rest being hexagons. Whether this is due to the too short time scales spanned by the computer simulation or a genuine effect, characteristic of the early stages of tube nucleation is indeed an interesting question that would influence the way one can envision strategies towards a controlled and selective SWNT synthesis. If the cap formation takes place at random, selectivity should be searched

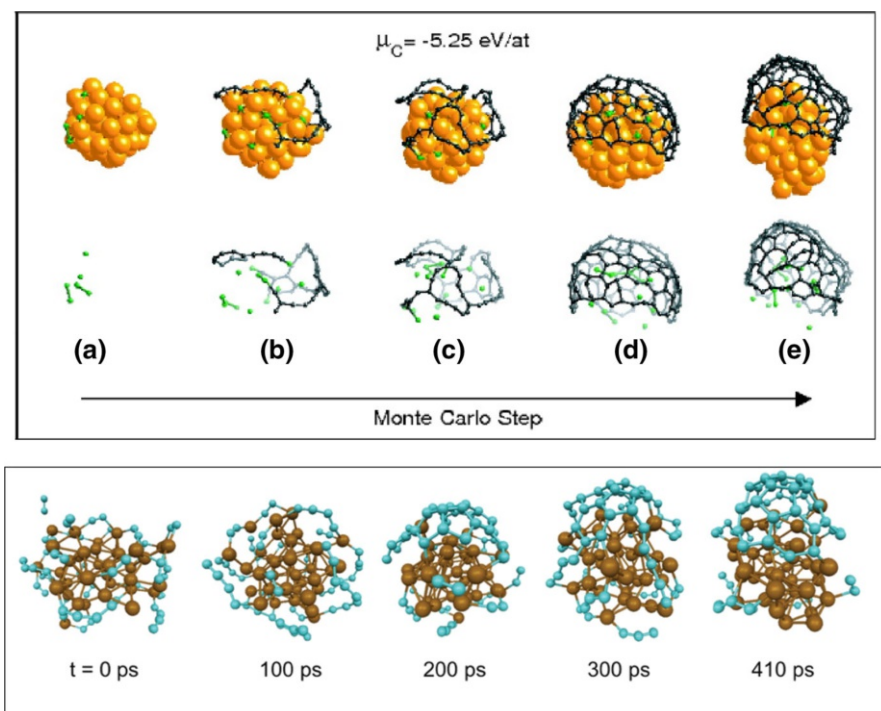


Fig. 8 *Upper panel* grand Canonical Monte Carlo simulations on a Ni cluster at 1000 K and $\mu_C = -5.25 \text{ eV/at}$. Different stages of the nucleation of a C cap are presented, where linear chains act as precursors to grow a graphene network on the Ni surface. Ni atoms are orange, outer C atoms are black, surface or bulk C atoms are green. Ref. [64]. *Lower panel* nucleation of a tube cap on an Fe₃₈ nanoparticle simulated by DFTB-based molecular dynamics. Polyyne chains are formed first, then cross forming Y-junctions and ring are formed, starting with pentagons. Obvious similarities exist between MC and MD approaches. Ref. [38]

elsewhere, either during growth itself, or by removing (etching) undesirable tubes during the synthesis or after it. If the cap structure is fixed at the very early stages of the nucleation, a smart engineering of the catalyst and growth conditions could lead to selectivity. This issue is quite complex, not yet solved up to now, and different groups have followed different approaches [3].

Focusing here on theoretical contributions, we first note that, according to Penev et al. [65], no significant energy differences were observed among the large number (4548!) of cap structures studied, thus precluding a selectivity based on the energetics of the cap alone. One might then consider possible energy differences between cap structures, originating from the interaction of the cap with the catalyst, in the spirit of the early work of Reich et al. [27], followed by Gomez-Gualdrón and Balbuena [66], and Wang et al. [67]. These calculations shed useful light on the electronic structure of the metal/carbon cap junction, which plays a major role for incorporating carbon atoms at the rim of the tube, but do not provide strong evidence for preferential chiralities. In addition, they are performed on idealized pure metal structures, —flat Ni layer, Co or Ni clusters, while there is little doubt

that carbon is dissolved close to the surface for such metals under growth conditions [68]. Quantum chemistry or DFT-based calculations investigated in detail the electronic structure of the cap/catalyst interface [67].

Summarizing theoretical studies of tube nucleation and cap formation mechanisms, it seems that they provide no strong support of the idea that the tube structure can be controlled at the nucleation step. What has been proposed, however, is that a matching could exist between a given tube structure and the solid-state particle from which it grew [11]. In this paper, DFT-based calculations were performed at 0 K, to study the matching of tubes with different chiralities on a (0, 0, 12) plane of a W₆Co₇ nanoparticle, in order to explain CVD experiments performed at 1030 °C, implicitly assuming a crystal structure and neglecting the temperature-induced disorder.

This raises the question of the catalyst nanoparticle's state under reaction conditions at high temperature, in the presence of a complex gaseous ambient, and usually interacting with a substrate. This very complex problem cannot be treated in full, and a number of approximations have to be made. Apart from the work of Jiang et al. [69], who calculated Fe–C phase diagrams of nanoparticles in the 1.1–1.6 nm range, with and without alumina substrate, the latter is generally neglected. Ding et al. [70] and Engelmann et al. [71] studied the melting behavior of Fe–C and Ni–C clusters, respectively. A full phase diagram calculation for Ni–C clusters, including F.C.C. and icosahedral Ni structures between 55 and 807 Ni atoms, has recently been proposed by Magnin et al. [72]. This phase diagram is simply a translation in the concentration–temperature space of the carbon sorption isotherms, calculated in a chemical potential–temperature space [73], but it enables one to understand directly the differences brought about by the nanometric size of the nanoparticles, as compared to a bulk system. Both are displayed in Figs. 9 and 10. The most striking ones, as far as nucleation and growth of SWNTs are concerned, are the important downshift of the eutectic temperature, and the existence of a crystalline core–molten shell domain, instead of the solid–liquid two-phase domain of the bulk phase diagram. These calculations also indicate that, on Ni nanoparticles below 3 nm, nucleation will take place on a non-crystalline surface for temperatures above ~800 K, meaning that for Ni or similar metals, no epitaxial control of the tube structure during the nucleation and growth can be expected.

6 Modeling the Growth of Carbon Nanotubes

Apart from the work of Gavillet et al. [74], investigating how C atoms can diffuse and attach to the tube rim, thus supporting a root growth mechanism, papers reporting simulations where tubes are grown up to a decent length usually rely on simplified carbon–metal interaction models. For many of these, a model validation is not always available, leaving the reader with unanswered questions about their range of applicability. However, similar SWNT growth mechanisms on Ni nanoparticles, involving the formation and coalescence of polyynes chains that forms the carbon rings, have been evidenced using approximate TB-based GCMC calculations and more accurate DFTB-based molecular dynamics [75], thus

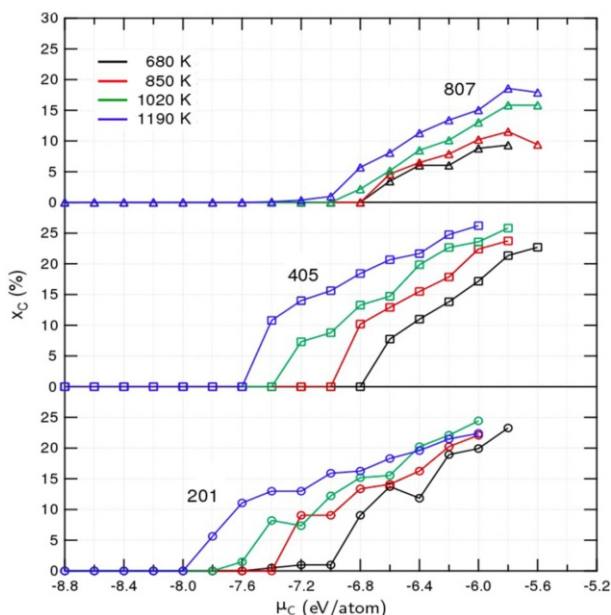


Fig. 9 Carbon sorption isotherms on face-centered cubic, Wulff-shaped, nanoparticles, with 201, 405, and 807 Ni atoms. Carbon fraction (x_C) inside the nanoparticle is plotted as a function of temperature and C chemical potential (μ_C). Four different temperatures are considered. Ref. [73]

mutually supporting the robustness of these findings. In both cases, though, and in other similar calculations [52, 63] as well, the poor quality of the structures generated is a major problem: most direct computer simulations of nanotube growth are impaired by an excess of defects created probably because of the too short time range spanned. Very recently, MD simulations of a few 100 ns have been performed [46] and seem to overcome this hurdle. Beyond a certain fraction of defects, we are more dealing with amorphous sp^2 bonded carbon, than real tubes. On the opposite, some perfect tubes have been grown [76], but make use of a questionable modified Monte Carlo algorithm. Simply growing a tube on the computer is not very interesting, if grown tubes are too defective to enable defining their chirality. Trying to understand how defects can be healed [77], is more relevant. The role of the metal catalyst in the healing process has been underlined [78–80], suggesting that once a defect survives the early stages of the growth, close to the catalyst nanoparticle, it has a lower probability to get healed.

Beyond these important though somewhat neglected issues, two highly debated questions concerning growth mechanisms and a possible control of the tubes' chirality during their synthesis have been addressed from a theory and modeling point of view. The first one concerns the respective role of thermodynamic and kinetic contributions to the chiral selectivity. The screw dislocation model of nanotube growth, proposed by Yakobson et al. [5], predicts that the growth rate should be proportional to the tube's chiral angle. It has been validated by some experiments, among which in situ Raman spectroscopy on individual growing tubes

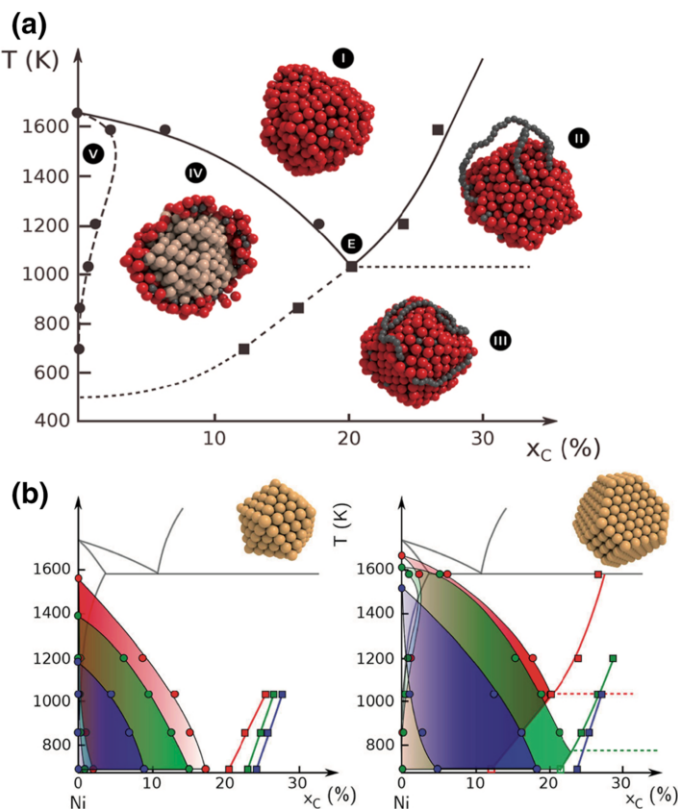


Fig. 10 **a** Ni–C phase diagram for a Ni nanoparticle with 807 Ni atoms, as calculated from grand Canonical Monte Carlo simulations. Different phases can be identified: *I* homogeneous liquid solution; *II* C segregation at the surface of liquid NP; *III* C segregation at the surface of mostly solid NP; *IV* solid core (*beige*)/liquid shell (*red*) nanoparticle, with upper liquid cap removed to visualize the crystalline core; *V* solid solution. **b** Size-dependent Ni–C phase diagrams for icosahedral (left 55, 147, and 309 Ni atoms) and face-centered cubic (right 201, 405, and 807 Ni atoms) nanoparticles compared to the bulk one (full black line). Ref. [72]

[81]. In this kinetic approach, the main point of controversy is the neglect of the catalyst nanoparticle and CVD conditions, while many reports [82–84] underline the role of the catalyst, substrate, pressure, and temperature on the resulting (n, m) distribution of nanotubes formed. The second one concerns the structure of the catalyst nanoparticle under growth conditions. Assuming a crystalline structure of the catalyst, Artyukhov et al. [85] developed a model showing that chiral distribution results from antagonistic trends. Thermodynamic stability criterion favors a flat contact between the tube and the nanoparticle crystalline surface, hence the zig-zag or armchair edges, while the above-mentioned kinetic factor would favor chiral tubes. As a result, shown in Fig. 11, a strong preference towards (n, n–1) chiralities is predicted. Interestingly, somewhat similar lattice-matching arguments have been used to explain recent findings of favored (12, 6) [11] and (8, 4) [28] chiralities. Quite obviously, some clarification is needed, and we now focus

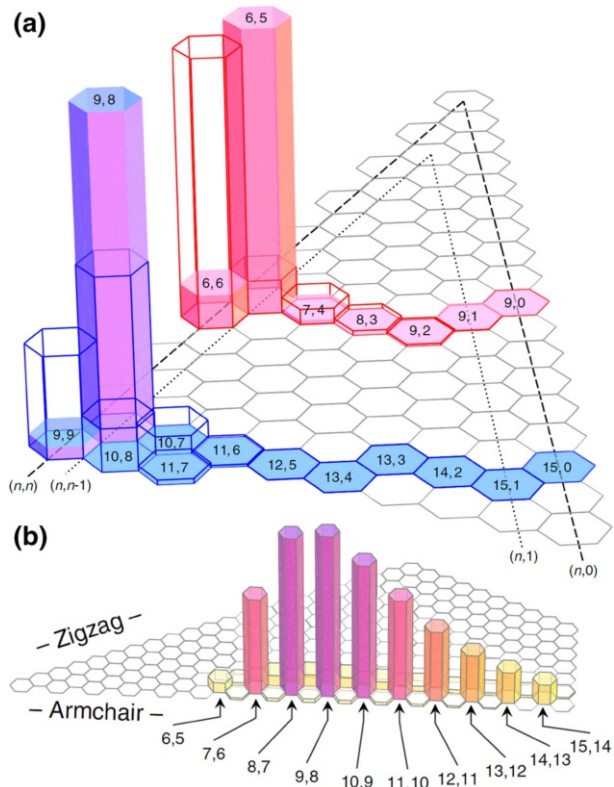


Fig. 11 **a** Chiral distributions resulting from the models proposed by Ding et al. [5] (empty bars), further refined by Artyukhov et al. [85] (full bars) in the case of a solid-state catalyst. **b** In the latter model, interfacial energies calculated by molecular dynamics lead to very sharp (n , $n-1$) probability distributions, even though the temperature considered is significantly higher than experimental ones

on less controversial situations where the nanoparticle is soft enough—fully liquid or with a solid core—disordered shell structure—to adapt itself to the tube structure.

7 Controlling Growth Modes

If a full control of the tube's chirality is a highly desirable, yet very difficult goal, establishing a relationship between the diameter of the tube and that of the nanoparticle from which it grows is already quite useful. A systematic TEM analysis of this relation has been performed by Fiawoo et al. [59], who proposed to discriminate between so-called “perpendicular” and “tangential” growth modes (see Figs. 12, 13). The former corresponds to situations where the tube diameter is significantly smaller than that of the particle from which it grew, the latter, sometimes called “octopus” in reference to the carbon chains crawling around the nanoparticles, to the case where both diameters are almost equal. Quite recently, significant progress has been achieved in this direction, based on the understanding

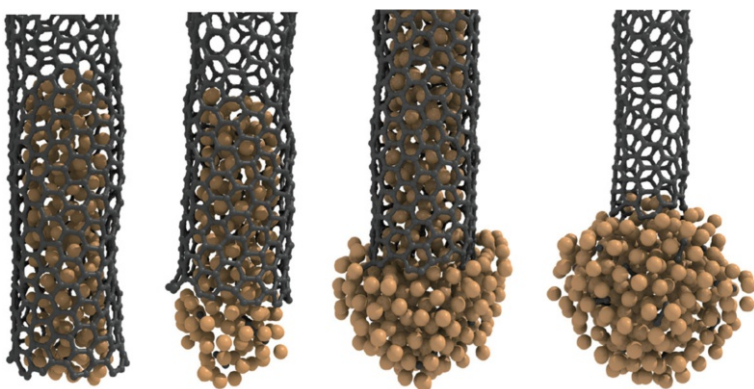


Fig. 12 Sketch of nanotube/nanoparticle geometries resulting from our Monte Carlo relaxations at 1200 K, ranging from tangential (*left*) to perpendicular (*right*), when C content inside the NP increases. Courtesy Y. Magnin

[54] of the interplay between carbon solubility in typical catalysts such as Fe, Co, and Ni, and their wetting properties with respect to the sp^2 carbon wall of the tube. Since the following results are still in the process of being published, we give some more details on the consequences of the carbon concentration dependence of these interfacial properties on the control of the growth mode. It is characterized by the tube/nanoparticle diameter ratio, and finding a way to tune them is indeed essential, because many important properties depend on the tube diameter. Small-diameter tubes display a smaller number of (n, m) types, making a (n, m) selective growth in principle easier. Selective etching of metallic tubes has been shown [86] to be more efficient for smaller diameter tubes, probably because larger curvature makes small diameter tubes more reactive.

To control tube diameter, a first step is to start with a narrow size distribution of catalyst nanoparticles, which is now well under control experimentally. The second step is then to play with the growth mode, and here the input from joint experimental, essentially TEM [59], and computer simulations studies, proves essential. Turning back to the carbon solubility issue, the following computer simulation results provide direct visual evidence: we start by putting nanoparticles with 219 Ni atoms and variable fractions of carbon inside, in contact with SWNTs with different chiralities, and diameters around 0.9–1.2 nm. After relaxation at 1400 K with our TBMC code, we notice that the pure Ni nanoparticle is almost completely “sucked” in the SWNT and that the fully saturated one (with about 25% carbon dissolved in) remains outside. Between these two extreme cases, a partial wetting of the inner part of the tube is observed to increase with decreasing carbon fraction dissolved in the nanoparticle. This is displayed in Fig. 12. Visual inspection reveals that the metal inside the tube has a very small or vanishing fraction of carbon dissolved in, while the outer part of the nanoparticle retains most of the carbon atoms that were initially put in the Ni nanoparticle. This reminds us of the carbon depletion effect in Ni layers close to a Ni/graphene interface observed in [50, 51]. This splitting of the Ni nanoparticle into two parts, an almost pure one

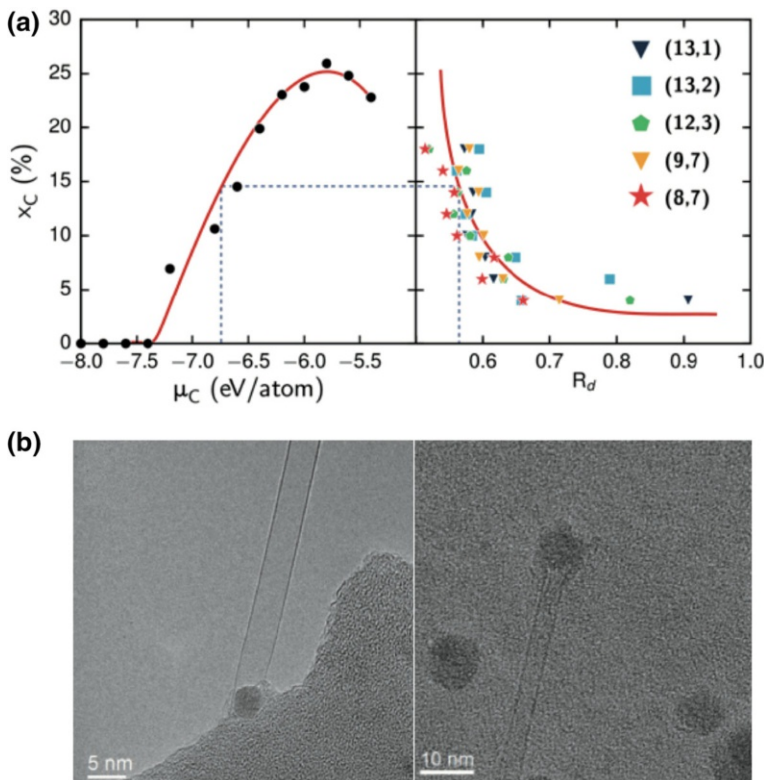


Fig. 13 **a** *Left* typical carbon sorption isotherm showing the relation between the carbon chemical potential (μ_C) and the mole fraction x_C of carbon dissolved in the catalyst nanoparticle. *Right* diameter ratios $R_d = D_{SWNT}/D_{NP}$ (x -axis), plotted for different carbon concentrations (y -axis), and different tube chiralities, displayed with *different colors*. As indicated by the *dashed lines*, the growth mode depends on the driving force for carbon incorporation: small μ_C favors large R_d , while larger μ_C leads to smaller R_d . Courtesy Y. Magnin. **b** TEM images of SWCNTs grown by tangential mode (*left*) and perpendicular mode (*right*) from Fe NP. Courtesy M. He

inside the tube, and another one containing the remaining or totality of dissolved carbon outside the tube, is observed only for tubes with a diameter larger than ~ 0.8 nm. No metal can penetrate inside tubes with a smaller diameter. Alternatively, when tubes and nanoparticles are very large, in particular in the case of thicker multi wall carbon nanotubes, we can reasonably expect that the carbon depletion effect close to the sp^2 wall has a more limited influence. However, this tendency to form inhomogeneous nanoparticles with respect to their carbon content is relevant for the growth of high-quality SWNTs to be used in electronic applications, grown at high temperatures and in a 1–3 nm diameter range.

From these simulations, we can define an aspect ratio $R_d = \frac{d_{SWNT}}{d_{NP}}$, and calculate it by assuming a spherical shape of the outer part of the nanoparticle. This aspect ratio, plotted in Fig. 13, depends strongly on the carbon fraction dissolved in the nanoparticle (x_C), and seems to depend slightly on the tube chirality. This figure also

presents two TEM images of tubes grown on Fe nanoparticles displaying two different growth modes. The “perpendicular” one, with $R_d < 1$, has been obtained with CO as a feedstock, while CH₄ has been used for the “tangential” one, with $R_d \approx 1$. In the former, the tube/nanoparticle contact is reduced to a line, and in the latter, a much larger contact area between the tube and the nanoparticle is formed by the tube rim and the inner part of the tube that is wetted by the metal catalyst. This suggests (at least) two ways to control the growth mode, and hence the tube diameter distribution.

The first one is to play with the carbon chemical potential resulting from the catalytic decomposition of the feedstock on the nanoparticle surface. The carbon fraction inside the nanoparticle is indeed related to it via carbon sorption isotherms, such as those calculated in [73]. This is illustrated in Fig. 9. This provides a possible explanation to the experiments by Yao et al. [87] who used a temperature modulation to modify the tube diameter during its growth. At higher temperature, carbon solubility in the catalyst (Co or Fe) nanoparticle increases, hence the growth tends to be more “perpendicular”. Lowering temperature reversibly gives larger diameter tubes. Another straightforward way to achieve this experimentally is to change the feedstock. This has been done by He [88] who demonstrated that tube diameter could be reversibly modified by alternating CO and CH₄ feedstocks to create tube junctions with large diameter differences. In both cases, the observed reversibility indicates that the nanoparticle size is unaffected, leaving a change in carbon fraction dissolved in the nanoparticle as the only option to explain the observed modulation. Beyond these two proven techniques, one can imagine that shifting the equilibrium of the feedstock decomposition reaction by modulating the ambient, or the pressure of one of the reactants or products, might be an alternative.

The second one is to modify carbon solubility of the catalyst nanoparticle. We have tested numerically [89] the effect of changing it in our tight-binding model for nickel. Thanks to its physically grounded roots, it is quite easy to change the heat of solution of carbon inside Ni by simply shifting the relative positions of the nickel d- and carbon p-bands, keeping all other parameters constant. In doing so, we see in Fig. 14 that chemical potential thresholds to start incorporating carbon in the nanoparticles are shifted, as well as the solubility limits. Quite interestingly, we also note that lower carbon solubility enhances the differences between face-centered cubic and icosahedral nanoparticles. This might provide an explanation to the experimental observation [90] that, under the same CVD conditions, tubes would grow from fcc gold nanoparticles and not from icosahedral ones. How these growth modes can influence the SWNT structure is the next important question that is not yet fully understood.

8 Conclusions

In this paper, we show that computer simulation provides useful insight into the mechanisms of SWNT growth by CCVD. Highly accurate DFT-based calculations are used to investigate fundamentals of metal–carbon interactions, and give quantitative estimates of binding energies between tubes and metal surfaces or

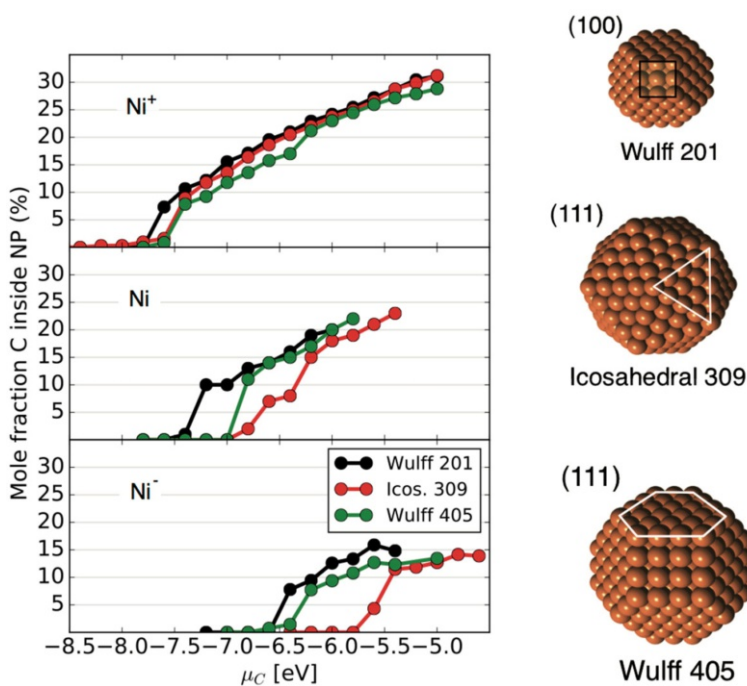


Fig. 14 *Left* carbon sorption isotherms calculated at 1000 K, using grand Canonical Monte Carlo simulations for nanoparticles with 201, 309, and 405 Ni atoms. Different Ni–C models have been used, corresponding to different carbon solubilities. *Right* schematic representation of icosahedral and face-centered cubic nanoparticles, with different facets are presented. Ref.: Aguiar-Hualde et al. [89]

nanoparticles in different situations. Interatomic interaction potentials with various levels of complexity and accuracy are used to drive molecular dynamics or Monte Carlo simulations, which enables simulating different aspects of the SWNT synthesis, such as nucleation, growth, or defect healing. Apart from the paper by Ding et al. [23], growth termination mechanisms that are of great practical importance, have not been extensively investigated yet by atomistic models, and are not discussed.

A central point in this review is to stress the importance of considering the mutual interaction between the growing tube and the catalyst nanoparticle from which it grows. In most computer simulations, under growth conditions, the surface of the nanoparticle in contact with the tube appears to be disordered, even if its core sometimes remains crystalline [72]. Wetting properties of the metallic nanoparticle, with respect to the sp^2 carbon wall of the tube are shown to play an important role by controlling the growth modes. For Ni, taken as a typical and simple example, these interfacial properties, and hence the growth modes, depend on the carbon fraction dissolved in the nanoparticle. So do the growth modes, and hence the tube diameter.

From a more general point of view, if modeling and computer simulations significantly contributed to a better atomic scale understanding of SWNT growth

mechanisms over the last 10 years, a lot remains to be done to uncover the mechanisms underlying the experiments that have recently reported a (n, m) selective growth [11]. Apart from some stability calculations performed under conditions that might be far from the real experimental ones, and a kinetic model [5], based on a spiral growth hypothesis, that is not strongly supported by experimental evidence, no general and predictive model concerning the tube (n, m) structure is currently available. This leaves open challenges for future work.

Acknowledgements The research leading to these results has received funding from the European Union Seventh Framework Programme (FP7/2007-2013) under Grant Agreement No. 604472 (IRENA project) and French Research Funding Agency under Grant No. ANR-13-BS10-0015-01 (SYNAPSE project). Drs. M. He, Y. Magnin and J.-M. Aguiar-Hualde are gratefully acknowledged for making some of their results available prior to publication.

References

- Iijima S (1991) Nature 354:56–58
- Iijima S, Ichihashi T (1993) Nature 363:603–605
- Liu C, Cheng HM (2016) J Am Chem Soc 138:6690–6698
- Page AJ, Ding F, Irle S, Morokuma K (2015) Rep Prog Phys 78:36501
- Ding F, Harutyunyan AR, Yakobson BI (2009) Proc Natl Acad Sci 106:2506–2509
- Snoeck J, Froment GF, Fowles M (1997) J Catal 169:240–249
- Chiang W, Sankaran RM (2009) Nat Mater 8:882–886
- Chiang W-H, Sankaran RM (2012) Carbon NY. 50:1044–1050
- Bachilo SM, Balzano L, Herrera JE, Pompeo F, Resasco DE, Weisman RB (2003) J Am Chem Soc 125:11186–11187
- He M, Chernov AI, Fedotov PV, Obraztsova ED, Sainio J, Rikkinen E, Jiang H, Zhu Z, Tian Y, Kauppinen EI, Niemelä M, Krause AOI (2010) J Am Chem Soc 132:13994–13996
- Yang F, Wang X, Zhang D, Yang J, Luo D, Xu Z, Wei J, Wang J-Q, Xu Z, Peng F, Li X, Li R, Li Y, Li M, Bai X, Ding F, Li Y (2014) Nature 510:522–524
- Nørskov JK, Bligaard T, Logadottir A, Bahn S, Hansen LB, Bollinger M, Bengaard H, Hammer B, Sljivancanin Z, Mavrikakis M, Xu Y, Dahl S, Jacobsen CJH (2002) J Catal 209:275–278
- Robertson J (2012) J Mater Chem 22:19858
- Amara H, Roussel J-M, Bichara C, Gaspard J-P, Ducastelle F (2009) Phys Rev B 79:14109
- Schwarz KJ (1977) Phys C Solid State Phys 10:195–210
- Deck C, Vecchio K (2006) Carbon NY 44:267–275
- Hofmann S, Sharma R, Ducati C, Du G, Mattevi C, Cepek C, Cantoro M, Pisana S, Parvez A, Cervantes-Sodi F, Ferrari AC, Dunin-Borkowski R, Lizzit S, Petaccia L, Goldoni A, Robertson J (2007) Nano Lett 7:602–608
- Hofmann S, Blume R, Wirth CT, Cantoro M, Sharma R, Ducati C, Hävecker M, Zafeiratos S, Schnoerch P, Oestereich A, Teschner D, Albrecht M, Knop-Gericke A, Schlägl R, Robertson J (2009) J Phys Chem C 113:1648–1656
- Rinaldi A, Tessonniere J-P, Schuster ME, Blume R, Girgsdies F, Zhang Q, Jacob T, Abd Hamid SB, Su DS, Schlägl R (2011) Angew Chem Int Ed Engl 50:3313–3317
- Teschner D, Borsodi J, Woitsch A, Révay Z, Hävecker M, Knop-Gericke A, Jackson SD, Schlägl R (2008) Science 320:86–89
- Yazyev OV, Pasquarello A (2008) Phys Rev Lett 100:1–4
- Hu X, Björkman T, Lipsanen H, Sun L, Krasheninnikov AV (2015) J Phys Chem Lett 6:3263–3268
- Ding F, Larsson P, Larsson JA, Ahuja R, Duan H, Rosén A, Bolton K (2008) Nano Lett 8:463–468
- Silveary F, Larsson P, Jones SLT, Ahuja R, Larsson JA (2015) Mater Chem C 3:3422–3427
- Fan X, Buczko R, Puretzky A, Geohegan DB, Howe J, Pantelides S, Pennycook S (2003) Phys Rev Lett 90
- Yuan Q, Gao J, Shu H, Zhao J, Chen X, Ding F (2012) J Am Chem Soc 134:2970–2975
- Reich S, Li L, Robertson J (2006) Chem Phys Lett 421:469–472

28. Zhang S, Kang L, Wang X, Tong L, Yang L, Wang Z, Qi K, Deng S, Li Q, Bai X, Ding F, Zhang J (2017) *Nature* 543:234–238
29. Li M, Liu X, Zhao X, Yang F, Wang X, Li Y (2017) *Top Curr Chem* 375:29
30. Shibuta Y, Arifin R, Shimamura K, Oguri T, Shimojo F, Yamaguchi S (2013) *Chem Phys Lett* 565:92–97
31. Oguri T, Shimamura K, Shibuta Y, Shimojo F, Yamaguchi S (2014) *Chem Phys Lett* 595–596:185–191
32. Takagi D, Hibino H, Suzuki S, Kobayashi Y, Homma Y (2007) *Nano Lett* 7:2272–2275
33. Liu B, Ren W, Gao L, Li S, Pei S, Liu C, Jiang C, Cheng H-M (2009) *J Am Chem Soc* 131:2082–2083
34. Takagi D, Kobayashi Y, Homma Y (2009) *J Am Chem Soc* 131:6922–6923
35. Ding F, Bolton K, Rosén A (2004) *J Phys Chem B* 108:17369–17377
36. Martinez-Limia A, Zhao J, Balbuena PB (2007) *J Mol Model* 13:595–600
37. Neyts EC, Shibuta Y, van Duin ACT, Bogaerts A (2010) *ACS Nano* 4:6665–6672
38. Page AJ, Ohta Y, Irle S, Morokuma K (2010) *Acc Chem Res* 43:1375–1385
39. Ohta Y, Okamoto Y, Irle S, Morokuma K (2008) *ACS Nano* 2:1437–1444
40. Page AJ, Minami S, Ohta Y, Irle S, Morokuma K (2010) *Carbon NY* 48:3014–3026
41. Page AJ, Saha S, Li H-B, Irle S, Morokuma K (2015) *J Am Chem Soc* 137:9281–9288
42. Khalilov U, Bogaerts A, Neyts EC (2015) *Nat Commun* 6:10306
43. Burgos JC, Jones E, Balbuena PB (2011) *J Phys Chem C* 115:7668–7675
44. Growth SCN, Diego AG, Gómez-Gualdrón DA, McKenzie G, Alvarado JF, Balbuena PB (2012) *ACS Nano* 6:720–735
45. Gomez-Ballesteros JL, Burgos JC, Lin PA, Sharma R, Balbuena PB (2015) *RSC Adv* 5:106377–106386
46. Yoshikawa R, Maruyama S (**private communication**)
47. Lin M, Ying Tan JP, Boothroyd C, Loh KP, Tok ES, Foo Y-L (2006) *Nano Lett* 6:449–452
48. Batzill M (2012) *Surf Sci Rep* 67:83–115
49. Moors M, Amara H, Visart De Bocarmé T, Bichara C, Ducastelle F, Kruse N, Charlier J-C (2009) *ACS Nano* 3:511–516
50. Benayad A, Li X (2013) *J Phys Chem C* 117:4727–4733
51. Weatherup RS, Amara H, Blume R, Dlubak B, Bayer BC, Diarra M, Bahri M, Cabrero-Vilatela A, Caneva S, Kidambi PR, Martin M, Deranlot C, Seneor P, Schlägl R, Ducastelle F, Bichara C, Hofmann S (2014) *J Am Chem Soc* 136:13698–13708
52. Ribas MA, Ding F, Balbuena PB, Yakobson BI (2009) *J Chem Phys* 131:224501
53. Naidich YV, Perevertailo VM, Nevodnik GM (1971) *Powder Met Met Ceram* 10:45–47
54. Diarra M, Zappelli A, Amara H, Ducastelle F, Bichara C (2012) *Phys Rev Lett* 109:185501
55. Riikonen S, Krasheninnikov AV, Nieminen R (2010) *Phys Rev B* 82:1–13
56. Honeycutt JD, Andersen HC (1984) *Chem Phys Lett* 108:535–538
57. van Duijneveldt JS, Frenkel D (1992) *J Chem Phys* 96:4655
58. Picher M, Lin PA, Gomez-Ballesteros JL, Balbuena PB, Sharma R (2014) *Nano Lett* 14:6104–6108
59. Fiawoo M-FC, Bonnot A-M, Amara H, Bichara C, Thibault-Pénisson J, Loiseau A (2012) *Phys Rev Lett* 108:195503
60. Neyts EC, van Duin ACT, Bogaerts A (2011) *J Am Chem Soc* 133:17225–17231
61. Raty J-Y, Gygi F, Galli G (2005) *Phys Rev Lett* 95:96103
62. Ohta Y, Okamoto Y, Irle S, Morokuma K, Page AJ, Wang Y (2009) *Nano Res* 2:755–767
63. Page AJ, Yamane H, Ohta Y, Irle S, Morokuma K (2010) *J Am Chem Soc* 132:15699–15707
64. Amara H, Bichara C, Ducastelle F (2008) *Phys Rev Lett* 100:56105
65. Penev ES, Artyukhov VI, Yakobson BI (2014) *ACS Nano* 8:1899–1906
66. Gomez-gualdrón DA, Balbuena PB (2009) *J Phys Chem C* 113:698–709
67. Wang Q, Yang S-W, Yang Y, Chan-Park MB, Chen Y (2011) *J Phys Chem Lett* 2:1009–1014
68. Wirth CT, Hofmann S, Robertson J (2009) *Diam Relat Mater* 18:940–945
69. Jiang A, Awasthi N, Kolmogorov A, Setyawan W, Börjesson A, Bolton K, Harutyunyan AR, Curtarolo S (2007) *Phys Rev B* 75:1–12
70. Ding F, Bolton K, Rosén A (2004) *J Vac Sci Technol A Vac Surf Film* 22:1471
71. Engelmann Y, Bogaerts A, Neyts EC (2014) *Nanoscale* 6:11981–11987
72. Magnin Y, Zappelli A, Amara H, Ducastelle F, Bichara C (2015) *Phys Rev Lett* 205502:1–5
73. Diarra M, Amara H, Ducastelle F, Bichara C (2012) *Phys Status Solidi* 249:2629–2634

74. Gavillet J, Loiseau A, Journet C, Willaime F, Ducastelle F, Charlier J-C (2001) Phys Rev Lett 87:275504
75. Page AJ, Irle S, Morokuma K (2010) J Phys Chem C 114:8206–8211
76. Xu Z, Yan T, Ding F (2015) Chem Sci 6:4704–4711
77. Page AJ, Ohta Y, Okamoto Y, Irle S, Morokuma K (2009) J Phys Chem C 113:20198–20207
78. Karoui S, Amara H, Bichara C, Ducastelle F (2010) ACS Nano 4:6114–6120
79. Diarra M, Amara H, Bichara C, Ducastelle F (2012) Phys Rev B 85:245446
80. Yuan Q, Xu Z, Yakobson BI, Ding F (2012) Phys Rev Lett 108:245505
81. Rao R, Liptak D, Cherukuri T, Yakobson BI, Maruyama B (2012) Nat Mater 11:1–4
82. Lolli G, Zhang L, Balzano L, Sakulchaicharoen N, Tan Y, Resasco DE (2006) J Phys Chem B 110:2108–2115
83. Wang B, Poa CHP, Wei L, Yang Y, Chen Y (2007) J Am Chem Soc 129:9014–9019
84. He M, Jiang H, Kauppinen EI, Lehtonen J (2012) Nanoscale 4:7394
85. Artyukhov VI, Penev ES, Yakobson BI (2014) Nat Commun 5:4892
86. Li J, Ke CT, Liu K, Li P, Liang S, Finkelstein G, Wang F, Liu J (2014) ACS Nano 8:8564–8572
87. Yao Y, Li Q, Zhang J, Liu R, Jiao L, Zhu YT, Liu Z (2007) Nat Mater 6:293–296
88. He M, Magnin Y, Amara H, Jiang H, Cui H, Fossard F, Castan A, Kauppinen E, Loiseau A, Bichara C (2017) Carbon 113:231–236
89. Aguiar-Hualde J-M, Magnin Y, Amara H, Bichara C, submitted to Carbon. <http://arxiv.org/abs/1702.06742>
90. He M, Amara H, Jiang H, Hassinen J, Bichara C, Ras RHA, Lehtonen J, Kauppinen EI, Loiseau A (2015) Nanoscale 7:20284–20289



REVIEW

Metallic Catalysts for Structure-Controlled Growth of Single-Walled Carbon Nanotubes

Meihui Li^{1,2} · Xiyuan Liu¹ · Xiulan Zhao¹ ·
Feng Yang¹ · Xiao Wang¹ · Yan Li^{1,2}

Received: 30 November 2016/Accepted: 28 January 2017/Published online: 1 March 2017
© Springer International Publishing Switzerland 2017

Abstract Single-walled carbon nanotubes (SWNTs) have shown great potential in various applications attributed to their unique structures and outstanding structure-dependent properties. The structure-controlled growth of SWNTs is a crucial issue for their advanced applications and has been a great challenge in this field for two decades. Metal catalyst-mediated SWNT growth is believed to be very efficient. In this review, progresses in diameter and chirality controlled growth of SWNTs with metal catalysts is summarized from several aspects, including growth mechanism and theory, effects of catalysts, and the chemical vapor deposition conditions. The design, preparation, handling and dispersion, and the size evolution of metal catalysts are all discussed. The influences of growth environment including the type, composition, and pressure/concentration of the carbon source as well as the temperature on the selectivity toward the nanotube structure are analyzed. We also discuss some of the challenges and trends in this field.

Keywords Single-walled carbon nanotubes · Metallic catalyst · Chemical vapor deposition · Controlled growth · Diameter · Chirality

M. Li, X. Liu and X. Zhao contributed equally to this work.

Chapter 2 was originally published as Li, M., Liu, X., Zhao, X., Yang, F., Wang, X. & Li, Y. Top Curr Chem (Z) 375: 29. DOI 10.1007/s41061-017-0116-9.

- ✉ Feng Yang
fengyang@pku.edu.cn
- ✉ Yan Li
yanli@pku.edu.cn

¹ Beijing National Laboratory of Molecular Sciences, Key Laboratory for the Physics and Chemistry of Nanodevices, State Key Laboratory of Rare Earth Materials Chemistry and Applications, College of Chemistry and Molecular Engineering, Beijing 100871, China

² Academy for Advanced Interdisciplinary Studies, Peking University, Beijing 100871, China

Abbreviations

AFI	Zeolite AlPO ₄ -5
AFM	Atomic force microscope
APTES	3-Aminopropyltriethoxysilane
CVD	Chemical vapor deposition
DFT	Density functional theory
Dps	DNA-binding proteins
E ₁₁	First van Hove optical transition energy
E-TEM	Environmental transmission electron microscopy
EDS	Energy-dispersive X-ray spectroscopy
FCCVD	Floating catalyst CVD
FFT	Fast Fourier transform
FTIR	Fourier transform infrared spectroscopy
G6OH	Sixgeneration polyamidoamine dendrimers with 100% hydroxyl termination
HAADF	High angle annular dark field
HMDS	1,1,1,3,3,3-Hexamethylidisilazane
PAMAM	Polyamidoamine
POM	Polyoxometalate
PS- <i>b</i> -PFEMS	Polystyrene- <i>block</i> -polyferrocenylethylmethyilsilane
PS- <i>b</i> -PVP	Polystyrene- <i>block</i> -polyvinylpyridine
ptz	Pyrazine
RBM	Radial breathing mode
SDBS	Sodium dodecyl benzene sulfonate
SOG	Spin-on-glass
STEM	Scanning transmission electron microscope
SWNTs	Single-walled carbon nanotubes
TEM	Transmission electron microscope
UHV	Ultrahigh vacuum
UV-Vis-	Ultraviolet/visible/near-infrared
NIR	
VLS	Vapor–liquid–solid
VSS	Vapor–solid–solid

1 Introduction

Single-walled carbon nanotubes (SWNTs) are one of the most widely studied materials in the past two decades. Their outstanding properties endowed by their unique structure have shown great potential in various applications such as nanoelectronics [1–4], sensors [5, 6], energy conversation and storage [7–10], biomedicine [11, 12], and functional composites [13–15]. A SWNT can be seen as a cylinder formed by rolling up a piece of graphene sheet along the chiral vector $C_h = na_1 + ma_2$ (where a_1 and a_2 are lattice unit vectors of the graphene sheet) from the origin point (0, 0) toward the point (n, m) on the graphene sheet, as shown

in Fig. 1. Not only the structure of each SWNT but also its band structure is uniquely defined by its chiral index (n, m) [16, 17]. Therefore, the structure-controlled synthesis of SWNTs has been one of the most important topics in the field.

Chemical vapor deposition (CVD) synthesis method has become the most promising method for structure-controlled growth of SWNTs because it offers more parameters to achieve better control of the catalysts, substrates, and growth conditions [18]. It is also easier to be scaled up. In a CVD process, carbon precursors convert into SWNTs through interacting with the catalyst, which means SWNTs nucleate and grow from active catalyst nanoparticles. Therefore, the structure of catalyst nanoparticles, including size, composition, morphology, and their evolution during the CVD process plays a critical role in the selective synthesis of SWNTs.

In this review, we start from the introduction on the growth mechanism of SWNTs, then describe the structure-controlled growth of SWNTs through catalytic nanoparticles engineering and the evolution of catalyst nanoparticles during SWNTs process. The effect of the CVD conditions is also included. We also discuss the challenges and opportunities toward the structure controlled growth of SWNTs.

2 Growth Mechanism of SWNTs

In order to control the structure of SWNTs, such as diameter and chirality, it is very important to understand the growth mechanism. Catalytic nanoparticles are usually used to initiate the growth of SWNTs, though there are a few reports about non-metallic catalysts such as SiC, Ge, Si [19], and BN [20], oxide nanoparticles such as

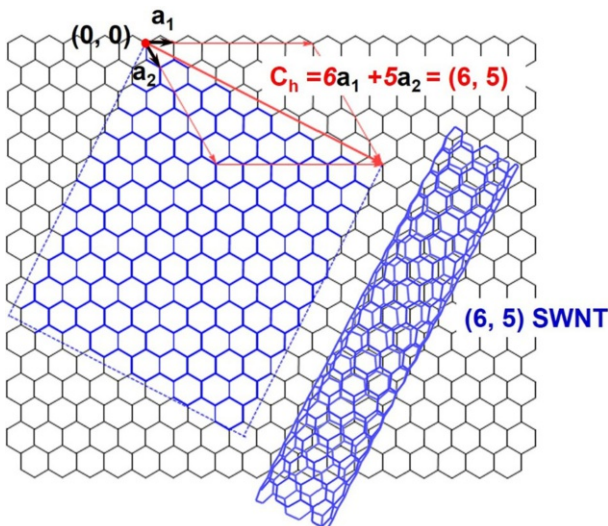


Fig. 1 Schematic illustration of a (6, 5) SWNT rolled up from a graphene sheet. The chiral indices (n, m) uniquely define the structure of a SWNT

SiO_2 [21–24], Al_2O_3 [24], and TiO_2 [25], and crystalline diamond particles [26]. Metallic nanoparticles, including Fe, Cu, Co, Ni, Pt, Pd, Mn, Mo, Cr, Sn, Au, Mg, Al, and Rh, have been intensively used for SWNT growth [27–30] because they are believed to be generally more efficient than non-metal catalysts. Various metallic catalysts have different activities in catalyzing the decomposition of the carbon precursors, which always affect the properties of the as-grown SWNTs [27, 31]. For instance, cleaner SWNTs with smaller diameters and narrower size distributions were obtained from Cu catalyst when compared with Fe [32]. It is believed that the metal catalyst-driven growth of SWNTs is generally via a vapor–liquid–solid (VLS) mechanism (Fig. 2a), which was originally used to explain the growth of silicon whiskers from liquid Au droplets on silicon substrate [33]. In this process, carbon species diffuses on the surface of metal nanoparticles and then decompose into carbon species, which are dissolved to form a liquid alloy between metal and carbon. When the liquid catalyst particles are saturated with carbon, the carbon atoms begin to precipitate from the surface of a particle to form the cap of a SWNT [34–37]. Jourdain and Bichara summarized the four roles of the catalysts in SWNT growth [38]. Similar to the case of normal heterogeneous catalytic reactions, the catalysts catalyze the decomposition of carbon source and manage the reaction and diffusion of carbon intermediates on the surface and within the catalyst particles. These are the first two roles of metallic catalysts. The other two roles are serving as the nucleation sites for carbon caps and keeping the sites active to grow nanotubes.

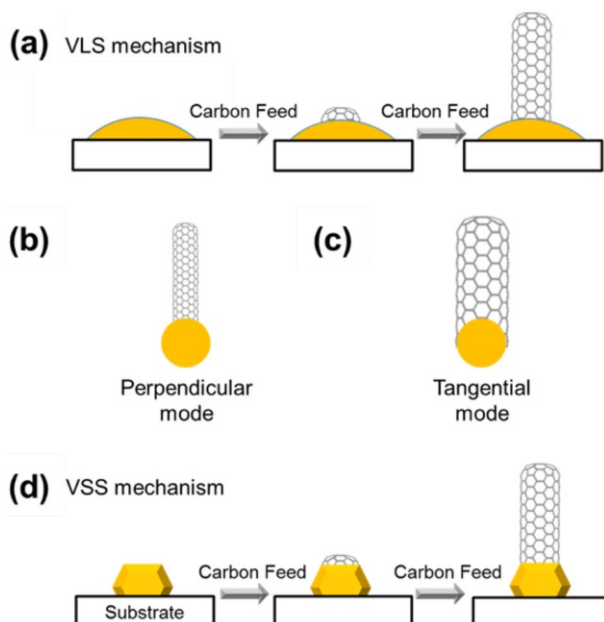


Fig. 2 Schemes of different SWNT growth mechanisms. **a** VLS mechanism. **b** Perpendicular mode. **c** Tangential mode. **d** VSS mechanism. VLS mechanism and tangential nucleation mode give the possibility of controlling the diameter of SWNTs via control the properties of catalytic nanoparticles (Corresponding figure is reproduced with permission [44], Copyright 2016, American Chemical Society)

Therefore, it is reasonable to conclude that catalysts are extremely important for the structure-controlled growth of SWNTs [27].

Loiseau et al. found that there are two nucleation modes describing the contact between the graphitic wall of the tubes and the particle, i.e. tangential mode and perpendicular mode [39]. In the case of tangential mode, the graphitic wall of the tube grows tangentially with respect to the nanoparticle surface (Fig. 2c), while in the perpendicular mode, the graphitic wall stands perpendicularly on the surface of the nanoparticle (Fig. 2b). The diameter of the resulting SWNT is similar to the size of the catalytic nanoparticle when growing via the tangential mode, while in perpendicular mode, the diameter of a SWNT will be smaller and independent from the size of the catalytic nanoparticle. There is a competition between the two nucleation modes. According to the simulation study, the perpendicular growth mode often happens when the growth condition is far from the local thermodynamic equilibrium [39]. It is proposed that the presence of nitrogen [40–42] or sulfur [43] in carbon feeding stock also leads to the growth in perpendicular mode because the heteroatoms can interact with the surface of catalytic nanoparticles.

Statics on the structure distribution of SWNTs grown by different processes shows that components with larger chiral angle (θ) normally have higher contents in the samples [45]. According to theoretical studies including molecular dynamics (MD) simulations and static density functional theory (DFT) calculations [45–47], there is a strong dependence of SWNT growth rate on chiral angle θ , and the growth of SWNTs with larger chiral angle is favorable. This rule was further proved experimentally [48, 49]. Yakobson et al. combined the thermodynamics of tube-catalyst interface and the kinetic growth theory to discuss the chirality selectivity in SWNT growth [50]. Catalyst particles in liquid state have irregular and highly mobile structures; therefore, the kinetic route of selection becomes dominant, resulting in the selective growth of $(2m, m)$ tubes with the fastest growth. The energetic preference towards achiral tubes and the faster growth kinetics of chiral nanotubes work together leading to the enriched growth of near-armchair SWNTs such as $(6, 5)$, $(7, 5)$, and $(9, 8)$ tubes. By using metal catalysts with uniform size, SWNTs enriched with a specified chirality in $(n, n - 1)$ or $(2m, m)$ regime may be synthesized. However, it is very difficult to reach a high selectivity in any chirality other than $(n, n - 1)$ or $(2m, m)$ types with ordinary metal catalysts.

Beyond the normal VLS growth of SWNTs with metal catalysts, there is another possibility of growing SWNTs via the vapor-solid-solid (VSS) mechanism (Fig. 2d), in which the catalyst nanoparticles do not melt and remain solid state during the CVD process. Robertson et al. proposed an epitaxial nucleation model of SWNTs [51, 52]. Through ab initio calculations, they showed that the formation of some specific types of caps is favored by their epitaxial relationship to the surface structure of solid-state catalyst and subsequently the tubes with corresponding chiralities grow preferentially. Based on the VSS mechanism, they proposed an idea for the chirality-selective growth of nanotubes by controlling the type of caps that form on the catalyst at the nucleation stage [51]. However, Yakobson et al. showed later that the energy variability associated with the carbon nanotube caps is tiny compared to that of the interfaces between nanotubes and catalyst nanoparticles [53]. As a result, the differentiation between the formation energy of caps cannot be

a dominant factor determining the chiral distribution. The chirality selective growth may be realized by tuning the interaction between nanotube edges and catalysts through the selection of different metals and manipulating the structures. Balbuena et al. [54] suggested that a sufficiently strong metal-substrate interaction keep the crystallinity of the metal catalyst at high temperature and subsequently limits the diffusion of carbon atoms into the body of the nanoparticle. This leads to the favorable growth of carbon structures templated by the metal surface. The nucleation normally occurs on metal atoms at the steps with lowest coordination.

It seems VSS mechanism offers better opportunities for realizing chirality selective growth. If the “contact” epitaxial matching between the metal atoms of the catalyst nanocrystal and the edge structure of a SWNT is specific enough, a cap with determined structure will be formed epitaxially and subsequently a SWNT with specified chirality will be produced [44].

3 Catalysts for Diameter-Controlled Growth of SWNTs

Diameter control is a basic part of SWNTs structure control. Many of SWNT properties are related to their diameter. For instance, the bandgap of a semiconducting SWNT is approximately inversely proportional to its diameter [17]. Therefore, it is of great interest to produce SWNTs with desired diameter and narrow diameter distribution. According to the growth mechanism, there is a positive correlation between the size of catalytic nanoparticles and the diameters of SWNTs. The size control of catalyst nanoparticles at the very first step of the growth is the most significant part in diameter control of SWNTs. In this part, we will discuss the methodology in the size control of catalyst nanoparticles, the dispersion and evolution of nanocatalysts in CVD process, and the diameter-controlled growth of SWNTs.

3.1 Size-Controlled Preparation of Metallic Nanocatalysts

3.1.1 Capping Agent-Assisted Preparation of Nanoparticles with Narrow Size Distribution

Capping agents have been widely used to control the size of nanoparticles in solution-based preparations. Capping agents can adsorb on the surface of nanoparticles by coordination or static charge interactions to prevent the un-desired growth of particles and obtain nanoparticles with smaller size and narrower size distribution. Liu et al. used a mixture of long-chain carboxylic acid and long-chain amine as protective and dispersive agent and prepared uniform iron-molybdenum nanoparticles with the diameters varied from 3 to 14 nm and standard deviation as small as ~7–8% (Fig. 3) [55]. The ratio of metal precursor to capping agents and the ratio of acid to amine both affect the size of synthesized nanoparticles. Lieber’s group obtained nearly monodispersed iron nanoparticles with average diameters of 3, 9, and 13 nm by changing the carbon chain length of the carboxylic acid surfactant, and the carbon nanotubes produced were with the average diameters of 3, 7, and 12 nm, respectively [56].

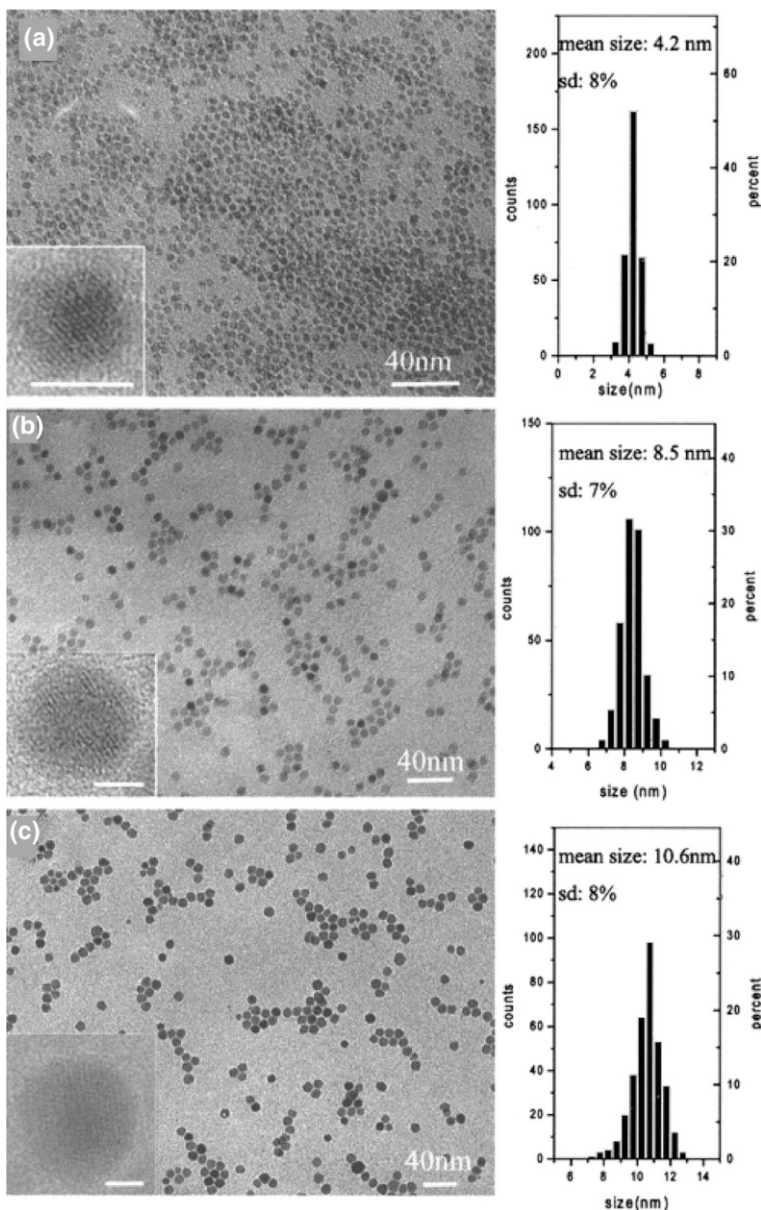


Fig. 3 Transmission electron microscope (TEM) images of Fe–Mo nanoparticles synthesized under typical conditions (with a 1:1 mixture of bis-2-ethylhexylamine and octanoic acid at a concentration of 0.100 mmol) (a) and 2.50 mmol (b) or 5.00 mmol (c) of protective agent was used. The scale bars in the inserts are all 4 nm (Corresponding figure is reproduced with permission [55], Copyright 2001, American Chemical Society)

3.1.2 Using Precursors with Uniform Size to Prepare Mono-Dispersed Nanoparticles

Metal-Loaded Protein Precursors Dai's group used ferritin, an iron-storage protein, to synthesize discrete iron oxide nanoparticles with controllable diameters and grew SWNTs from these nanoparticles on substrate by CVD (Fig. 4) [57]. The apoferritin protein is made of 24 polypeptide subunits, with a central core ~8 nm in diameter and can store up to 4500 iron atoms. They synthesized two types of catalytic nanoparticles with different diameters by changing the Fe loading in apoferritin precursor. The diameters of catalytic Fe_2O_3 nanoparticles produced by loading ~200 and ~1100 Fe atoms were 1.5 ± 0.4 and 3.0 ± 0.9 nm, respectively, while the diameters of as-grown SWNTs were 1.9 ± 0.3 and 3.7 ± 1.1 nm,

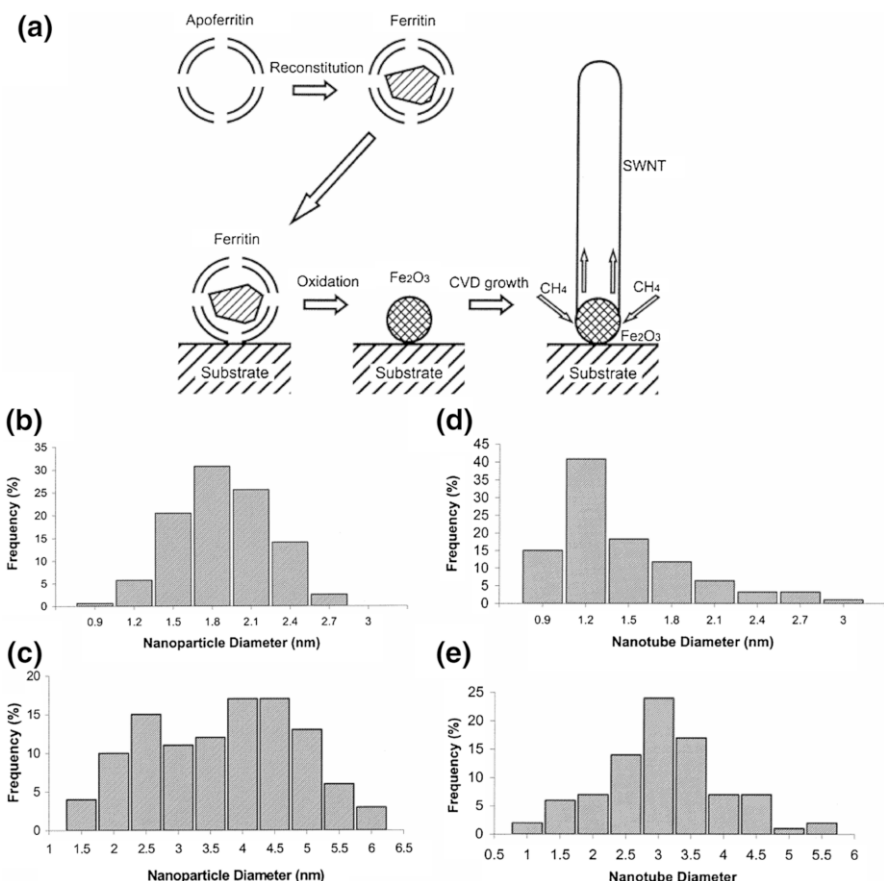


Fig. 4 **a** Schematic image of process for SWNT synthesis from discrete nanoparticles by CVD. Diameter distribution for Fe_2O_3 nanoparticles and nanotubes grown from nanoparticles produced by loading different numbers of Fe atoms: **b** ~200 Fe atoms loading; **c** 1100 Fe atoms loading; Diameter distribution of nanotubes grown from nanoparticles produced by loading different numbers of Fe atoms: **d** 200 Fe atoms loading; **e** 1100 Fe atoms loading (Corresponding figure is reproduced with permission [57], Copyright 2001, American Chemical Society)

respectively. Researchers also filled cobalt [58] and gold [59] atoms into apo-ferritin shells and obtained uniform catalytic nanoparticles to grow SWNTs. Ferritin with narrower size distribution, which is favorable for producing catalyst nanoparticles with uniform size, can be obtained by sedimentation velocity centrifugation [60].

In addition to ferritin [61, 62], Jeong et al. also used DNA-binding proteins (Dps) [63] to load Fe. There is an iron compound with the size of ~ 4 nm in the hollow space of Dps [64]. The SWNTs (diameter 1.1 ± 0.3 nm) were grown by using iron nanoparticles (size 2.4 ± 0.5 nm) derived from Dps on silicon wafer or suspended on pillars. In addition, polymerized hemoglobin containing 11 Hb molecules was also used as the catalyst precursor of SWNTs synthesis. SWNTs with very narrow diameter distribution of 1.08 ± 0.26 nm were obtained from the iron oxide nanoparticles with an average diameter of 1.30 ± 0.36 nm [65].

Dendrimers and Copolymer Mediated Preparation Polymers such as dendrimers [66–69] and block copolymers [70–76] can be used to control the size of catalytic nanoparticles. Dai's group first used six generation polyamidoamine dendrimers with 100% hydroxyl termination (G6OH), which is a kind of dendrimer of polyamidoamine (PAMAM), to transfer Fe(III) ions onto the SiO₂ substrate with good dispersion [69]. The G6OH molecules have ion complexation capability from the tertiary amines of the outmost shells and each molecule can seize a maximum of 64 Fe(III) ions. The Fe(III) loaded G6OH molecules were dispersed on the substrate and transformed into iron oxide nanoparticles by annealing. These iron oxide nanoparticles were reduced to form uniform Fe nanoparticles with the size of 1–2 nm, which further catalyzed the growth of SWNTs with a narrow diameter distribution of 1–2 nm. The size of the eventually formed Fe nanoparticles can be adjusted by the size of the dendrimers, the density of the functional groups on the shells of the dendrimers, and the loading of Fe(III), hence the diameter of the resultant nanotubes can also be manipulated [66–68].

Block copolymer molecules are composed of fragments with different properties. The phase separation of block copolymers occurs at a certain temperature and forms periodic nanostructures [75, 76]. This property makes it possible for them to serve as a template for the preparation and deposition of metal catalyst nanoparticles on substrates (Fig. 5).

Polystyrene-*block*-polyvinylpyridine (PS-*b*-PVP) block copolymers have pyridine sites to coordinate with transition metal ions and the complexes can form spherical micelles in toluene, in which metal-PVP complex present at the core and PS chain at the outer shell, shown in Fig. 5. By further annealing and reduction, well-dispersed uniform metal nanoparticles were obtained to grow SWNTs [70–73]. Liu et al. applied PS-PVP micelles loaded with different amount of FeCl₃ as catalyst precursors for SWNT growth [70]. They tried the Fe/PVP ratios of 0.6, 0.2, and 0.06. The as-formed nanoparticles after O₂ plasma treatment were well-dispersed with uniform size according to the atomic force microscope (AFM) measurements (Fig. 6). The average sizes of the nanoparticles are 6.6, 3.0, and 1.9 nm, respectively, while the diameters of the SWNTs produced are 2.7 ± 0.3 , 1.2 ± 0.1 , and 0.9 ± 0.1 nm, respectively. Lu et al. and Belcher et al. used PS-PVP block copolymer micelles to produce a series of transition metal nanoparticles such as iron, cobalt, nickel [72], molybdenum [71], and bimetallic Fe–Mo [71] with

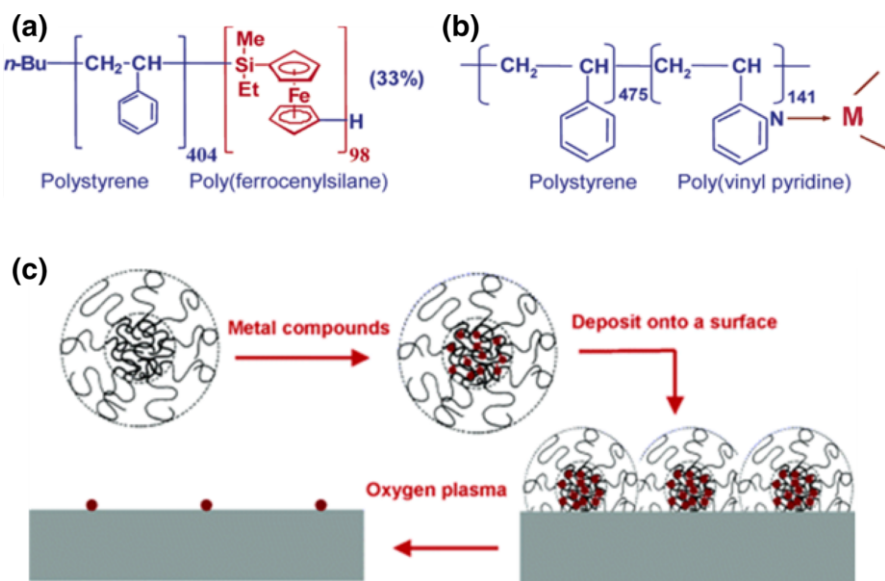


Fig. 5 **a** The structure of polystyrene-*b*-block-polyferrocenylethylmethylsilane (PS-*b*-PFEMS) (Corresponding figure is reproduced with permission [73], Copyright 2006, American Chemical Society). **b** The structure of PS-*b*-PVP (Corresponding figure is reproduced with permission [73], Copyright 2006, American Chemical Society). **c** Schematic of the preparation of nanoparticles by using block copolymer micelles (Corresponding figure is reproduced with permission [72], Copyright 2006, American Chemical Society)

controlled size and then to produce high quality SWNTs with narrow size distribution. Similar to the Fe/PVP system, by changing the ratio of metal/PVP, both the sizes of nanoparticles and SWNTs were tuned [71].

Different from the pristine PS-*b*-PVP block copolymers, PS-*b*-PFEMS already holds iron atoms in the structure and, therefore, can be directly used to prepare Fe nanoparticles for SWNT growth [74]. Using Fe nanoparticles produced by this method, SWNTs with diameters of 1 nm or less were prepared.

Nanocluster Precursors Polyoxometalate (POM) clusters are a family of polyatomic oxyanions of several transition metals (such as Mo, W, V, Nb, and Ta). There are enormous numbers of polyoxometalate clusters. Most of them have discrete cluster structures of definite sizes and shapes formed by metallic oxide polyhedrals (such as octahedral and tetrahedral) with exact numbers linking to each other by sharing corners and edges [77]. Attributed to the well-defined composition and size, the nano-scaled clusters are superior precursors for preparing metallic nanoparticles. Monometallic Mo clusters [78, 79] and bimetallic Fe–Mo clusters [78, 80–83] and Fe–W clusters [84] have been used as catalyst precursors for diameter-controlled growth of SWNTs.

Liu's group reported the growth of SWNTs using nanoclusters (denoted as FeMoC), originally synthesized by Müller et al. [85, 86], as catalyst precursors to produce small and uniform Fe–Mo nanocatalysts [80] (Fig. 7). The SWNTs grown have an average diameter of 1.0 nm with the standard deviation of 0.18 nm (17%).

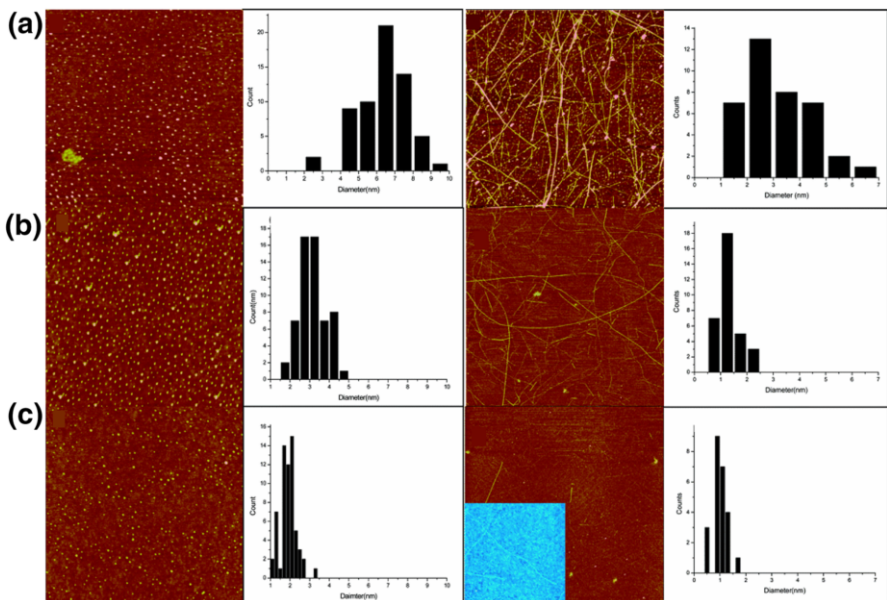


Fig. 6 AFM image and diameter distributions of nanoclusters formed and nanotubes grown on the surface with different ratios between FeCl₃ and the PVP block: **a** FeCl₃: PVP = 0.6; **b** FeCl₃: PVP = 0.2; **c** FeCl₃: PVP = 0.06. All images are $3 \times 3 \mu\text{m}^2$ (Corresponding figure is reproduced with permission [70], Copyright 2004, American Chemical Society)

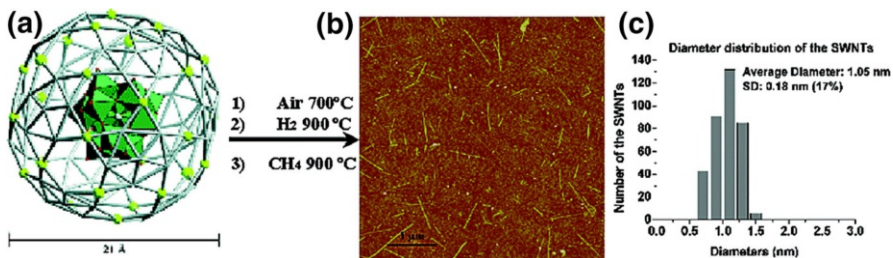


Fig. 7 **a** The single-crystal "cluster-within-a-cage" structure of FeMoC cluster; **b** AFM images of the SWNTs grown from FeMoC nanoclusters; **c** diameter distribution of the SWNTs grown from FeMoC nanoclusters (Corresponding figure is reproduced with permission [80], Copyright 2002, American Chemical Society)

Barron et al. systematically studied the FeMoC system [81]. They found that pure FeMoC is inactive as a pre-catalyst for the growth of SWNTs because an individual FeMoC molecule may not contain sufficient metal atoms to make an active catalyst. SWNTs can only grow when FeMoC clusters form small aggregations with the size of around ~4 nm or excess iron is added. The diameters of the SWNTs grown from the cluster precursors with well-controlled aggregation are very uniform and can also be adjusted as shown in Table 1.

Table 1 Comparison of lengths and diameters for SWNTs grown from FeMoC catalyst system

Growth method	Substrate	Average length ^a (μm)	Average diameter (nm)	References
FeMoC	Si	>1	1.3 (± 0.50)	[80]
FeMoC-ethanol ^b	Si	>1	1.1 (± 0.1)	[81]
FeMoC-ethanol ^b	SOG	0.3	2.1 (± 0.1)	[81]
FeMoC-ptz (1:25) ^b	SOG	>1	1.25 (± 0.25)	[81]
FeMoC-ptz-Fe(NO ₃) ₃ (1:25:25) ^b	SOG	>1	1.6 (± 0.2)	[81]

Corresponding table is reproduced with permission [81], Copyright 2006, Royal Society of Chemistry
SOG spin-on-glass, ptz pyrazine

^a The length of the as grown SWNT will depend on the reaction time

^b Reaction time 15 min

Li et al. also used FeMoC clusters as the catalyst precursors. But instead of silicon wafers, they grew horizontally aligned SWNTs on ST-cut quartz substrates [83]. Because MoO₃ is easy to be vaporized at the temperature above 600 °C, the annealing process in air is unfavorable for obtaining uniform catalyst nanoparticles. It was also found that the size of the catalyst nanoparticles as well as the diameter of the produced SWNTs is remarkably dependent on the growth temperatures. The diameter of the SWNTs was adjusted from 0.76 to 1.53 nm when the growth temperature was changed from 900 to 970 °C.

3.1.3 Catalyst Nanoparticles Confined in Porous Materials

Mesoporous materials such as MCM-41 [87] present nanometer-scaled channels which can serve as templates to confine the size of the catalytic nanoparticles. Various types of metals including Co [88–95], Fe [96, 97], Ni [95], Mo [98], Nb [98], and Fe-Zn [97] have been incorporated into MCM-41.

Haller et al. used Co and Ni incorporated MCM-41 to grow SWNTs [95]. All the procedures including annealing, reduction, and growth were performed at 700 °C. The MCM-41 template maintained its structure after successive reaction cycles. This result shows that mesoporous materials have enough thermal stability to act as the templates confining the size of catalyst nanoparticles for tube growth.

The pore sizes of MCM-41 also can be tuned. Haller et al. used alkyl templates with different carbon chain lengths of 10–18 carbon atoms to prepare Co incorporated MCM-41. The pore sizes changes from 1.8 to 3.5 nm according to the nitrogen physisorption measurements [88]. In another work, they prepared Co-MCM-41 with C12 and C16 alkyl chains and resulted in pore diameters of 2.6 and 3.3 nm, respectively [90]. The diameter of the SWNTs grown by such confined catalysts was normally smaller than the pore size of the mesoporous materials. The average diameters of the SWNTs produced from the Co-MCM-41 with pore sizes of 2.6 and 3.3 nm were determined to be ~0.67 and ~0.85 nm, respectively.

The loading of metals can be adjusted. Pfefferle et al. [91] found that Co-MCM-41 samples with different cobalt loadings have different stability against reduction.

It could lead to producing tubes with a narrow distribution of diameters until the co-loading of ~4 wt%. In the case of an Fe–MCM-41 system, the diameter of SWNTs produced from a 2 wt% Fe-loaded sample is well controlled to 0.67–1.28 nm, but the multi-walled carbon nanotubes became predominant when the Fe-loading was increased to 3 wt% [96].

The type and composition of the metal also affect the diameters of produced SWNTs. The diameters of SWNTs produced from Mo–MCM-41 and Nb–MCM-41 are 1.06–2.9 and 1.08–2.3 nm, respectively [98]. The Fe–Zn–MCM-41 can produce SWNTs with a narrow diameter distribution in the range of 1.5–2.5 nm when the Fe:Zn ratio is 3:1.

Other than the silica-based mesoporous materials, Ago et al. also used porous MgO as the catalyst support to perform the diameter-controlled growth of SWNTs [99]. The produced tubes show a narrow diameter distribution with a mean diameter of 0.93 nm, while the crystalline MgO-supported catalysts resulted in a very broad distribution in the nanotube diameters under the same conditions.

In addition to the metal-loaded mesoporous materials, SWNTs can also be synthesized within the channels of microporous zeolite. In the latter case, no metallic catalysts are needed. For example, ultrathin SWNTs with a diameter of 0.42 ± 0.02 nm were prepared by the pyrolysis of tripropylamine molecules in the channels of zeolite AlPO₄-5 (AFI) single crystals [100–104].

3.2 Dispersion of Catalytic Nanoparticles

In addition to the size of the catalytic nanoparticles, the dispersion and deposition of catalysts on substrates are also important in the controlled growth of SWNTs. This procedure should be well designed to avoid the aggregation of catalysts or catalyst precursors.

There are different approaches to disperse catalysts onto substrate to control the diameter of SWNTs. Sputtering a thin film of catalytic metal thin film on the surface with a defined thickness is a simple method to prepare catalysts and to grow carbon nanotubes with narrow diameter distribution [105, 106]. Arc plasma deposition can also deposit catalyst thin film with controlled thickness and composition. All these approaches have different control range on the nanotube diameters [107].

Solution-mediated process is another route. Modifying the catalyst surface with capping agents, increase of surface charge, and the presence of surfactants can all improve the solubility of catalyst nanoparticles or catalyst precursors [108–110]. The good dispersibility of nanoparticles is one of the important issues for preparing the uniform catalysts on substrates. The other important issues are the surface property of substrates and the interaction between the nanoparticles and substrates.

The nanoparticles can be deposited onto the substrates relying on electrostatic interactions [80], hydrophobic interactions [111], and coordination interactions [112]. For example, if simply dropping the aqueous solution of nanoclusters onto a substrate, the nanoclusters will aggregate along with the evaporation. Liu et al. [80] used 3-aminopropyltriethoxysilane (APTES) to modify the silicon dioxide surface. Upon the self-assembly of APTES on silicon dioxide surface, an amine group terminated surface was obtained and the surface becomes positively charged. Through the

Coulombic attraction, the negatively charged nanoclusters were bonded strongly with the positively charged $-NH_2$ groups on the substrate to obtain well-dispersed nanoclusters, which benefits the formation of uniform catalyst nanoparticles. Surface modification have also be done taking advantage of hydrophobic interaction [111]. The self-assembly of 1,1,1,3,3-hexamethyldisilazane (HMDS) can make the surface of Si/SiO₂ substrate hydrophobic, as shown in Fig. 8. Then the Fe/Mo nanoparticles capped with alkyl amine and alkyl carboxylic acid, which show a hydrophobic surface property, can be uniformly distributed on the substrates [55] (Fig. 8).

3.3 Evolution of Catalytic Nanoparticles

It is generally accepted that metal nanoparticles tend to aggregate during the calcination and reduction processes. The nanoparticles may also undergo Ostwald ripening [113] during the reduction and CVD processes. The smaller particles evaporate and the larger particles continue to grow. All the above processes lead to larger nanoparticles with broader size distribution, which is definitely unfavorable for controlling the diameter distribution of as-grown SWNTs and should be avoided as much as possible.

3.3.1 Evolution of Fe Nanoparticles During Calcination and Reduction

Before introducing the carbon source into the CVD system, the precursors normally need to undergo calcination and reduction processes to from catalytic metal nanoparticles. During these processes, the size and morphology of the catalysts change and affect the SWNT growth. We will use the iron nanoparticle as a model to understand how the nanoparticles change in these processes and how to control them.

The evolution of nanoparticles was generally studied by systematic nanoparticle-size analysis at each step before and during CVD process under typical growth conditions without any carbon feeding using AFM and transmission electron microscope (TEM). The different processes involved during reduction are sketched in Fig. 9.

At the first stage, the average size decreases after calcination because of the removal of the organic components in the precursor [61], the evaporation also lead to the size decrease of the nanoparticles [114, 115]. Then two competing processes, Ostwald ripening and subsurface diffusion, govern the morphological change of the catalyst particles at annealing process [114, 116]. After a few minutes of annealing, Ostwald ripening begins, larger particles appear, and the density of particles decreases, which leads to broadening particle diameter distributions [117, 118]. When elongating the annealing time, the catalytic nanoparticles embed into the substrate [62], especially in the system of Fe nanoparticles/Al₂O₃ substrates [118]. The cross-sectional TEM observation confirmed that Fe nanoparticles indeed diffused into the alumina layer (Fig. 10). Spectroscopic investigations developed by Colaianni et al. revealed that the surface diffusion of Fe into Al₂O₃ can be initiated at temperatures as low as 600 °C [119]. If Fe was deposited between two layers of Al₂O₃, Fe nanoparticles with a narrow distribution can be obtained to grow SWNTs

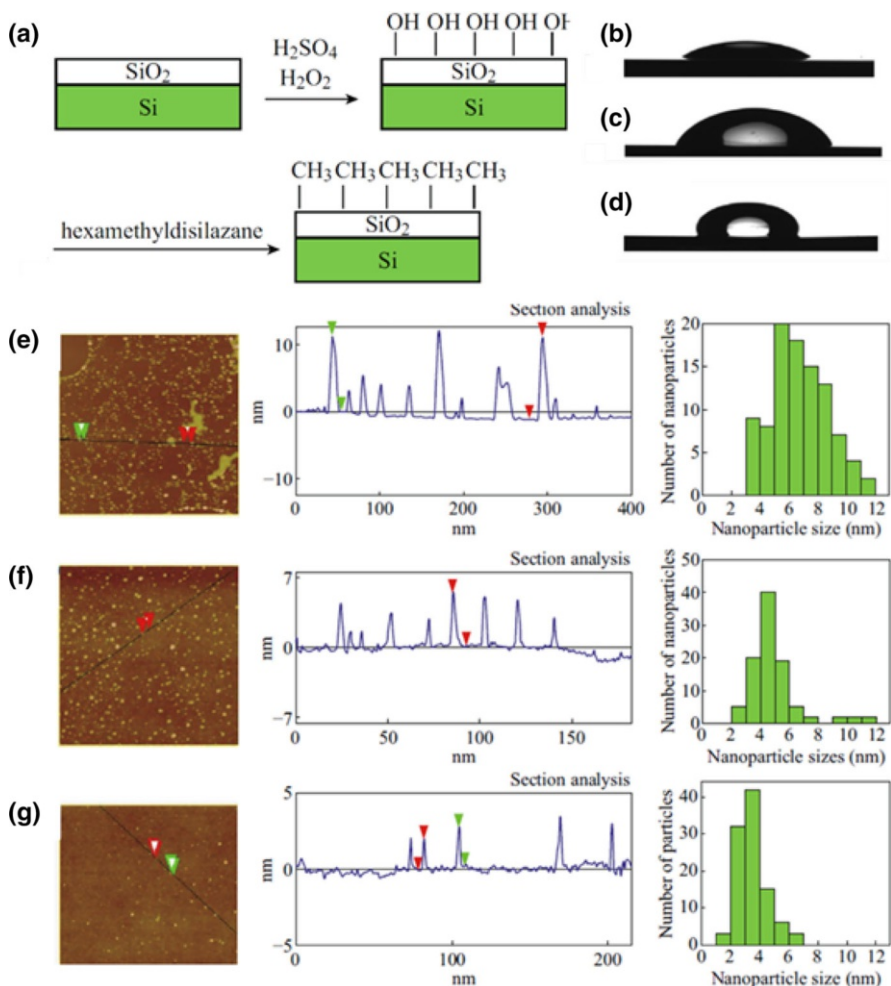


Fig. 8 **a** Schematic representation of the chemical modification on substrate surface. Photo of a water droplet on different substrates: **b** bare substrate; **c** modified with HMDS at room temperature for 1 min, **d** 150 °C for 30 min; AFM images, height measurement, and diameter distribution of the Fe/Mo NPs on different substrate surfaces: **e** bare substrate; **f** modified by HMDS for 1 min at room temperature; **g** annealed 150 °C for 30 min (Corresponding figure is reproduced with permission [111], Copyright 2015, Huang S)

with uniform diameter via moderating the annealing time to control the state of the diffusion [120].

While continuing to prolong the annealing time, there is another process: the Fe atoms precipitate from the sapphire subsurface and the particles start Ostwald ripening at the high temperature again [121].

In the reduction process, hydrogen is crucial to form the nanoparticles with proper size especially when the catalyst precursor is a metal thin film [116]. Hydrogen helps to break down the metal thin film to form small particles. A

Fig. 9 Illustration of catalyst particle evolution model during reduction

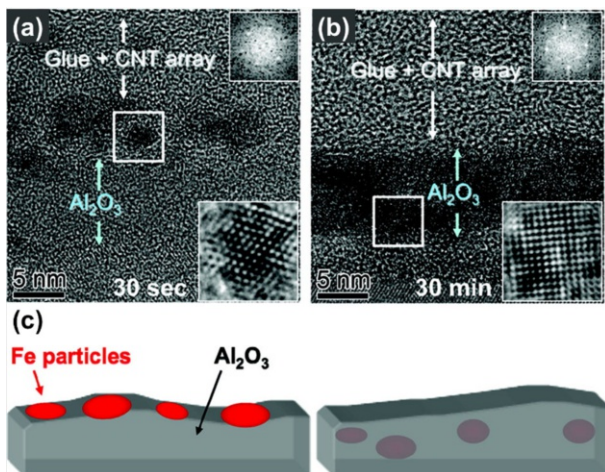
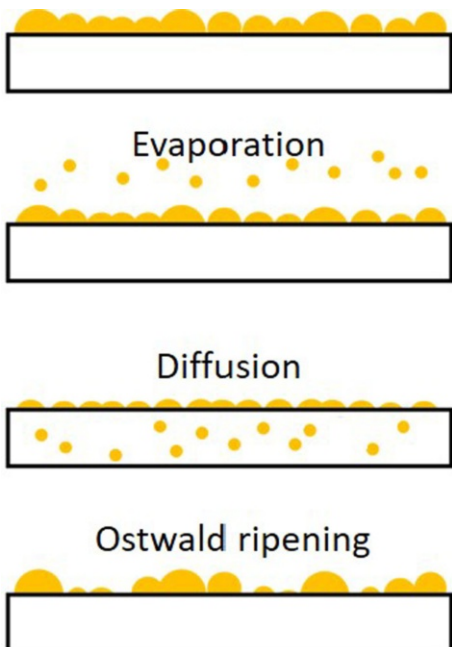


Fig. 10 Cross-sectional TEM images of the Fe catalyst and Al_2O_3 support after growth for **a** 30 s and **b** 30 min. Insets in the top corner are the fast Fourier transform (FFT) from the areas outlined in rectangles and insets in the bottom corner are the inverse FFTs using only the primary diffraction points from the FFTs. **c** Scheme illustrating the cross-sectional TEM images shown in **a**, **b** emphasizing the location of the Fe particles with respect to the Al_2O_3 layer (Corresponding figure is reproduced with permission [118], Copyright 2010, American Chemical Society)

sufficient amount of hydrogen can fully guarantee the reduction of metal oxide nanoparticles and produce small metal nanoparticles. Hata et al. found that under the same conditions, when the concentration of hydrogen was 90%, the average size

of as-formed catalyst particles was 2–3 nm, but when using 10% hydrogen, the particle size was larger than 5 nm.

3.3.2 Prevent Aggregation and Ripening of Catalytic Nanoparticles

It is always helpful to prevent the aggregation of catalyst nanoparticles by lowering the particle density. Jeong et al. found that when the density of catalytic nanoparticles decreased, diameter distribution of the nanotubes became narrower [75]. At the lowest catalyst density, only a single peak of radial breathing mode (RBM) corresponded to the tube diameter of 1.08 nm was observed from Raman spectra, suggesting the growth of homogeneous SWNTs.

The conditions for preparing catalytic nanoparticles, such as the time and temperature of annealing and reduction and the amount of reduction gas exposed, are also important. By manipulating the catalyst formation temperature and H₂ exposure condition, Hata et al. adjusted the size distribution of Fe nanoparticles originated from Fe thin film, and eventually produced SWNT forest with the controlled diameters ranging from 1.9 to 3.2 nm at a suitable growth condition [116]. They investigated the relationship between the particle sizes of the catalyst and their surface energies and found that the increase in decreasing the size of particle. They used high concentration of H₂ to increase the surface energy of Fe nanoparticles, thus reducing the SWNT diameters. While the tube diameter showed a direct proportionality with catalyst formation temperature, the lower temperature reduced the aggregation and Ostwald ripening efficiently, shown in Fig. 11. Park et al. [122] also reported lower temperature can suppress catalyst agglomeration and Ostwald ripening. Moderating the reduction time is also helpful to maintain the size of catalytic nanoparticles and consequently the diameter of as-produced SWNTs [114] (Fig. 11).

By using the competition relationship between Ostwald ripening, substrate diffusion and atom evaporation, the aggregation and ripening can also be suppressed. Ago et al. controlled the size of Fe nanoparticles by annealing in ultrahigh vacuum (UHV) [121]. They found that the thermal annealing in UHV for 1 h combined with H₂ reduction reduced the size of Fe nanoparticles and narrowed its distribution, which resulted in the growth of horizontally aligned SWNTs with uniform-diameter. 76% of the nanotubes have diameters between 1.3 and 1.4 nm. The UHV in the high temperature improved the evaporation of Fe atoms, which is the main reason for the decreasing of the Fe nanoparticle size. Substrate diffusion still exists in the UHV-assisted CVD process, which results in size increase of Fe nanoparticles when prolonging the annealing time.

Last, bimetallic or trimetallic catalysts have frequently been used to prevent the aggregation of the catalytic nanoparticles, in which one of the components can serve as active part while the others serve as dispersant or protector [97, 107, 123, 124]. These kinds of multi-component metallic catalysts can achieve a good selectivity of both diameter and chirality of SWNTs, which will be discussed in details in next part of the review.

In summary, the diameter of the carbon nanotubes is closely related to the size of the catalysts. To achieve diameter-controlled growth of SWNTs, the size of the

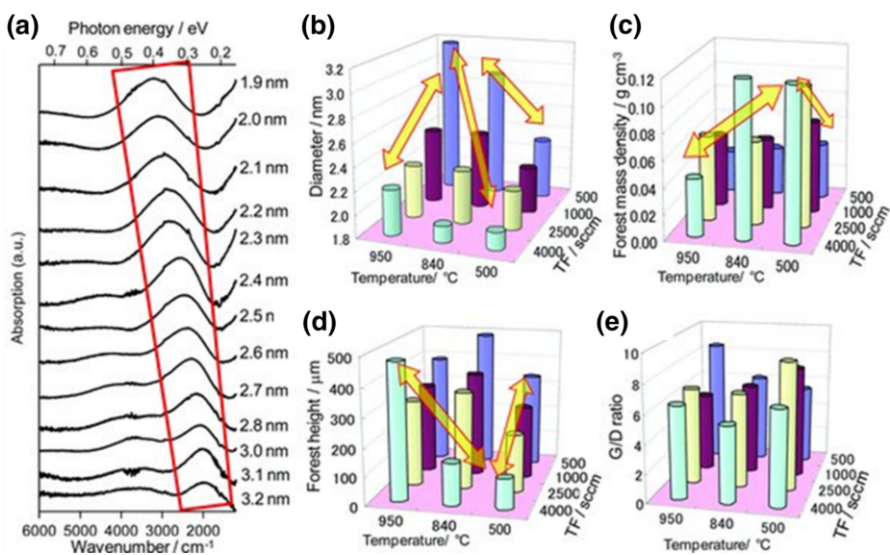


Fig. 11 **a** Fourier transform infrared spectroscopy (FTIR) spectra of SWNT forests synthesized from various catalyst formation conditions. The red trapezia indicates the region of first van Hove optical transition energy (E_{11}) of SWNT. SWNT diameters converted from E_{11} positions are shown at the right side of each spectrum. Plots of diameters obtained from FTIR **(b)**, forest mass densities **(c)**, forest heights **(d)**, and G/D-band ratios measured from Raman spectroscopy **(e)** as a function of the catalyst formation conditions (temperature and total flow rate) for SWNT forests synthesized with fixed hydrogen concentration of 90% (Corresponding figure is reproduced with permission [116], Copyright 2013, WILEY-VCH Verlag GmbH & Co. KGaA, Weinheim)

catalyst nanoparticles should be well-controlled and maintained via the following procedures: first, synthesize the catalytic particles with designed size and narrow size distribution by using catalyst precursors with uniform size such as nanoclusters, iron-loaded ferritin or confined by mesoporous materials and block copolymers; second, make the catalyst particles well-dispersed on substrates with the help of surfactants and/or surface-modification of substrates; third, maintain the size of catalyst nanoparticles by preventing aggregation and Ostwald ripening.

4 Chirality-Selective Growth of SWNTs

As stated above, the property of SWNTs is fully determined by their structures, which are described by their chiral index. A SWNT sample composed of nanotubes with a single chirality and identical band structure presents homogenous property, which is desired in many high-end applications such as nanoelectronics [125, 126], photovoltaic process [127, 128], and bioimaging [129, 130]. Therefore, to control the chirality distribution of SWNTs in catalytic CVD synthesis and produce SWNTs with uniform properties is essential to explore and achieve their potential applications [40, 131]. Catalyst design plays a key role in the efforts toward chirality-controlled synthesis of SWNTs.

4.1 Bimetallic Catalysts

Resasco et al. used CoMo bimetallic catalyst with an initial Co:Mo molar ratio of 1:3 to grow SWNTs. After a CO CVD synthesis at 750 °C, the (6, 5) and (7, 5) tubes represented 38% of all species as shown in Fig. 12a [132]. Then they optimized the CVD process by varying the temperature, the carbon feed composition, and the supporting materials for catalysts. A (*n*, *m*) population distribution of 54% (6, 5) SWNTs characterized by optical absorption was obtained using CoMo catalyst under the reaction condition of growth temperate at 700 °C, CO as the carbon feed composition, and SiO₂ as the catalyst support [133]. They suggested that the bimetallic CoMo catalyst precursor contains highly dispersed molybdenum oxide covered by a CoMoO₄ layer. Upon exposure to CO, the molybdenum oxide is partially converted into molybdenum carbide. Co is reduced by CO from the CoMoO₄ layer and the metallic Co migrates to the surface of catalyst, nucleating into small catalytic nanoparticles. The molybdenum oxide/carbide stabilizes the Co nanoparticles against aggregation in high-temperature sintering. Such Co nanoparticles with uniform size can therefore grow SWNTs with narrow (*n*, *m*) distribution.

Kauppinen et al. developed a FeCu bimetallic catalyst that provides a predominant growth of (6, 5) SWNTs with a CO CVD process at 600 °C [134, 135]. The formation of Fe particles in the FeCu bimetallic catalyst can be realized at 600 °C, which is lower than the reduction temperature of monometallic Fe catalyst (>700 °C). The XPS characterizations show a higher binding energy of Fe 2p_{3/2} in FeCu catalyst, suggesting that Cu plays an important role in the Fe reduction process. They further observed the formation of catalyst nanocrystals and the growth of SWNTs using in situ environmental transmission electron microscopy (E-TEM) (Fig. 12b) [136]. They found that Fe only exists and is anchored on the surface of the reduced Cu in the form of small particles. The Cu-stabilized Fe nanoparticles then grow SWNTs with narrow chirality distribution.

Maruyama et al. studied bimetallic the CoCu catalysts supported on SiO₂ film on a scanning transmission electron microscope (STEM) by using energy-dispersive X-ray spectroscopy (EDS) and high-angle annular dark field (HAADF) imaging [137] (Fig. 12c). It was observed that Co catalysts were anchored on Cu nanoparticles. Furthermore, the presence of SiO₂ is also necessary because it can stabilize Cu which has a low melting point. They conclude that in the CoCu bimetallic catalyst system, Cu anchors the Co catalysts to inhibit the formation of larger nanoparticles, protecting small Co particles from being overloaded by carbon precursors and assisting the thorough reduction of Co nanoparticles. The threefold effect of Cu makes the structure selective growth of high-quality SWNT forests with a possible sub-nanometer-diameter.

The enrichment of (6, 5) SWNTs were also obtained with CoMn [92] and CoCr [93] catalysts. In some other bimetallic catalysts, such as FeCo [138, 139], FeCr [140], and FeMn [79], the preferential growth of (6, 5) and (7, 5) SWNTs were observed. It seems there is a positive correlation between the temperature and the tube diameter of enriched chirality. It was found that lower temperature benefits the formation of (6, 5) tubes and higher temperature enhances the growth of (7, 5) tubes [79, 141–143]. Similarly, it was observed in CoPt catalysts that the population of (6,

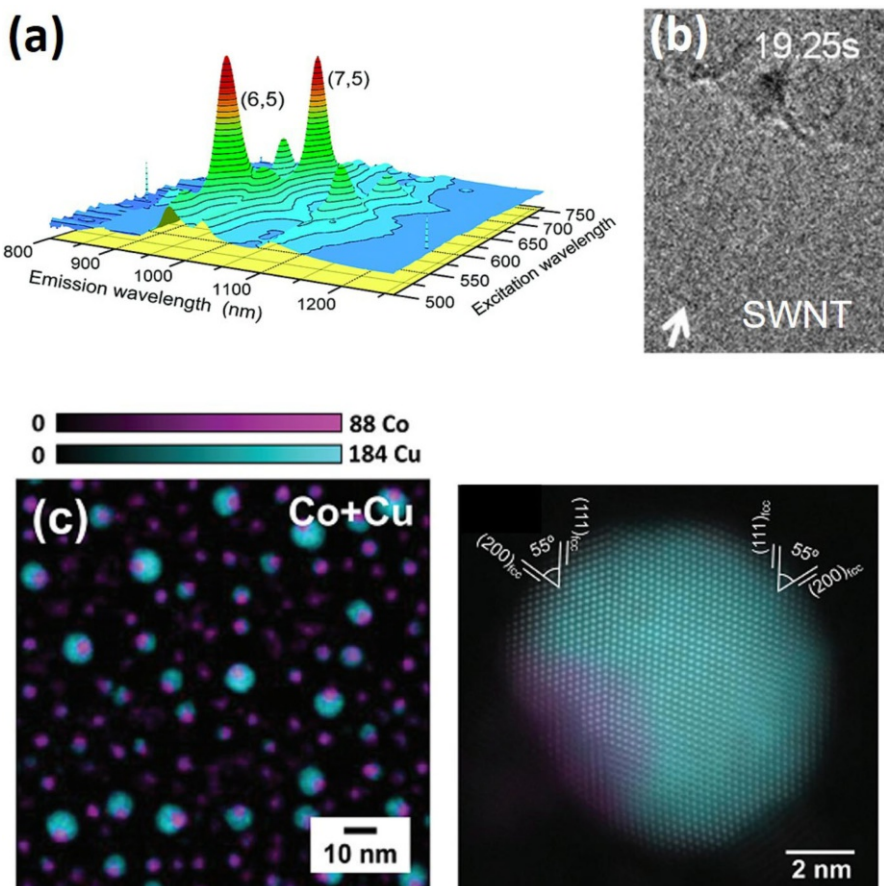


Fig. 12 Characterization of bimetallic catalysts and SWNTs grown. **a** Photoluminescence emission intensities under various excitation energies for the SWNTs grown from CoMo catalyst (Corresponding figure is reproduced with permission [132], Copyright 2003, American Chemical Society). **b** Bright field E-TEM image of a SWNT grown from Cu-supported metallic Fe nanoparticles (Corresponding figure is reproduced with permission [136], Copyright 2012, American Chemical Society). **c** Elemental mapping image by EDS showing Co nanoparticles are anchored by Cu in the bimetallic CoCu catalyst. EDS-STEM mapping of Co and Cu overlapped on high-resolution HAADF-STEM (Corresponding figure is reproduced with permission [137], Copyright 2015, Royal Society of Chemistry)

5) SWNTs is the highest among all species in the product grown at 800 °C, but (7, 6) becomes dominant at 850 °C [142].

4.2 Supported Catalysts

He and Kauppinen et al. achieved the selective growth of (6, 5) SWNTs on partially reduced Co–SiO₂ catalyst at a low growth temperature of 600 °C (Fig. 13a) [144]. Co₂SiO₄ possibly forms on the surface of SiO₂. They suggested that because of the modest reduction temperature, the catalyst precursor Co²⁺ is partially reduced to metallic Co by CO and anchors on the surface by unreduced Co²⁺ and Co⁺ as the

anchoring sites, which constrain the mobility of the reduced metallic Co and thus facilitate the formation of sub-nanometer nanoparticles. As-formed sub-nanometer Co nanoparticles can then catalyze the growth of a small diameter of SWNTs with a narrow chirality distribution.

They further realized the preferential growth of semiconducting SWNTs (~90%) with an exceptionally large population of 53% (6, 5) tubes with Co–MgO catalyst [145]. They carefully observed the structure of catalyst and the growth of SWNTs *in situ* using a high-resolution E-TEM. The Co cations in the $\text{Co}_x\text{Mg}_{1-x}\text{O}$ solid solution catalyst precursor were reduced in the solid phase by CO and then quickly migrated to the surface and finally crystallized into metal nanoparticles. The nanoparticles showed a narrow size distribution with a mean value of 1.8 nm. Well defined (0 1 1) patterns for both fcc MgO ($a = 0.422$ nm) and fcc Co ($a = 0.354$ nm) demonstrates unambiguously an epitaxial relationship between Co nanoparticles and the MgO matrix as shown in Fig. 13b. Because the mismatch in the lattice constants between the two materials is as large as ~16%, the Co nanocrystal is severely strained to match the lattice of the MgO matrix. The misfit strain causes the deformation of the Co lattice and leads to the formation of smaller Co nanoparticles to decrease the interface area between MgO and Co. Therefore, SWNTs with small diameter and narrow chirality distribution were produced.

Ago et al. used CoMo-based catalyst to grow aligned SWNTs on the A-plane, R-plane, and C-plane sapphire substrates, respectively. The preferential growth of near-zigzag (16, 2) tubes at 900 °C and (15, 1) tubes at 800 °C was observed on the A-plane, while the preferential growth of near-armchair (9, 8) tubes at 750 °C on the R-plane was observed. They suggested that the dissimilar atomic structures of the A- and R-plane sapphire surfaces may induce differences in the particle morphology, thereby affects the chirality distribution of the produced SWNTs [146].

4.3 Preparing Catalysts via Intermediates with Uniform Size

With CoSO_4 as the precursor of Co, Chen et al. developed a series of supported monometallic Co catalyst, namely Co-TUD-1 [147] and Co– SiO_2 [148–150], and grew SWNTs with the enrichment of (9, 8) species. They proposed that the formation of Co_9S_8 nanoparticles with a narrow size distribution is crucial in this process [151]. Co_9S_8 nanoparticles, as an intermediary compound, is reduced to metallic Co nanoparticles with uniform size and further grow (9, 8)-enriched SWNTs (Fig. 14b). Photoluminescence results showed the chirality selectivity toward (9, 8) nanotubes is 37.9% among semiconducting nanotubes.

4.4 Solid-State Catalysts

In the VSS process, the solid state catalyst nanoparticles keep their morphology while the tubes are growing. This offers the opportunity to control the structure of SWNTs by epitaxial growth from the solid state catalyst [152] with well-defined structures [44].

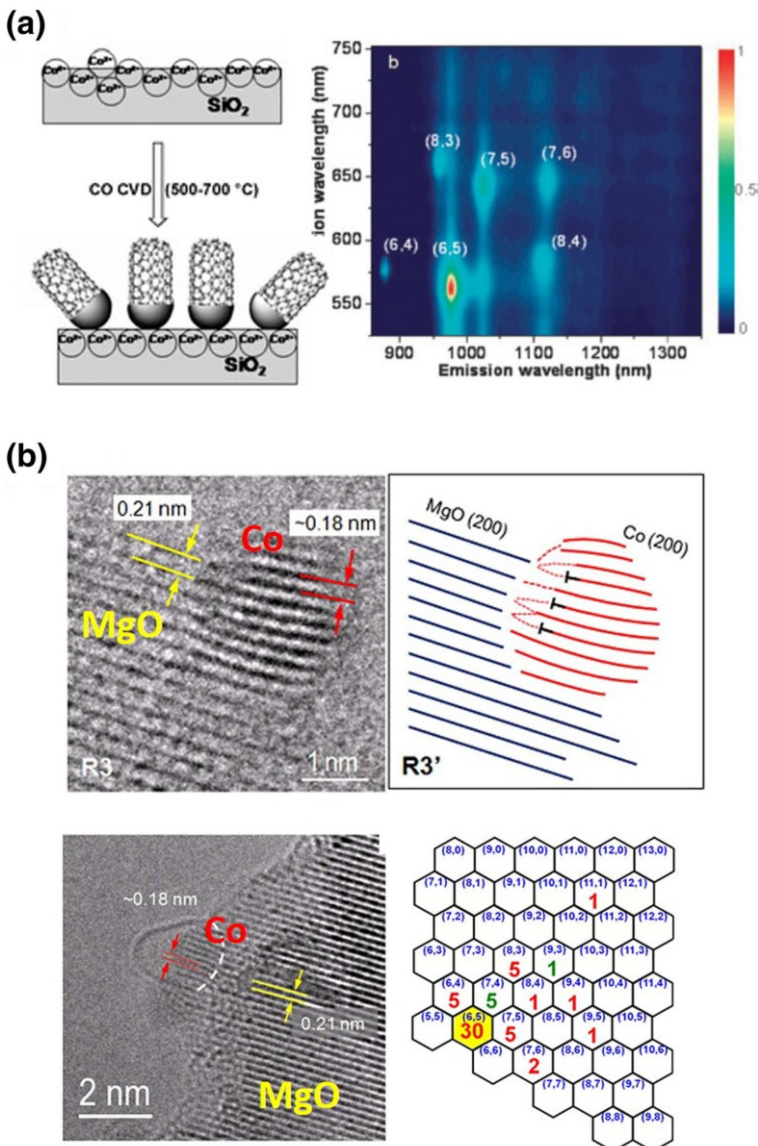


Fig. 13 Characterization of supported catalysts and grown SWNTs. **a** Schematic illustration of SWNT growth on a partially reduced Co–SiO₂ supported catalyst and contour plot of normalized photoluminescence emission intensities under the various excitation energies for SWNTs with Co–SiO₂ catalyst (Corresponding figure is reproduced with permission [144], Copyright 2010, Royal Society of Chemistry). **b** In situ E-TEM studies of the epitaxially formed Co nanoparticles in Co–MgO catalyst, and a schematic representation of the Co–MgO lattice configurations. In situ HRTEM lattice images showing carbon cap formation on epitaxial Co nanoparticles formed from the Co_xMg_{1-x}O solid solution and chirality map measured from electron diffraction analysis (Corresponding figure is reproduced with permission [145], Copyright 2013, Nature Publishing Group)

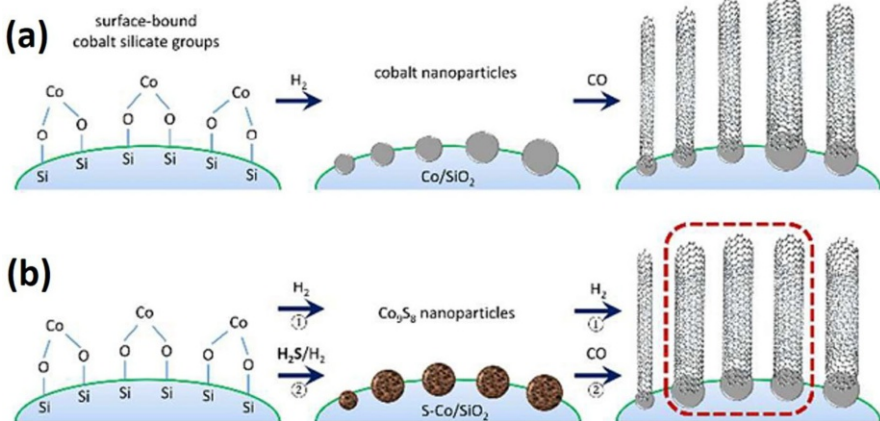


Fig. 14 Schematic illustration of Co–SiO₂ transformation under sulfidation and SWNT synthesis (Corresponding figure is reproduced with permission [151], Copyright 2016, Royal Society of Chemistry)

Sankaran et al. observed shifts of chirality distributions of as-grown SWNTs by tuning the composition of Ni_xFe_{1-x} nanoparticles. An enrichment of (8, 4) SWNTs was observed when the composition of the catalyst was Ni_{0.27}Fe_{0.73} (Fig. 15a) [153]. Since Fe was incorporated into the Ni lattice, an expansion of the Ni fcc phase was observed in X-ray diffraction (XRD) characterization. They believe that these perturbations to the crystal structure affect the lattice match of the catalyst with certain chiralities. They further investigated the mechanism by DFT calculations based on the epitaxial nucleation model. They found that (8, 4) SWNT is more stably bound to a surface that resembles a Ni_{0.27}Fe_{0.73} catalyst [154]. The stable bound of (8, 4) tube end on a plane of the catalyst might be the reason of selective growth of (8, 4) tubes.

Zhang et al. also realized the selective growth of (8, 4) SWNTs. By using solid Mo₂C catalysts, a population of 46.6% (8, 4) SWNTs was obtained via a hydrogen-free CVD synthesis under very short growth time and low carbon feeding conditions

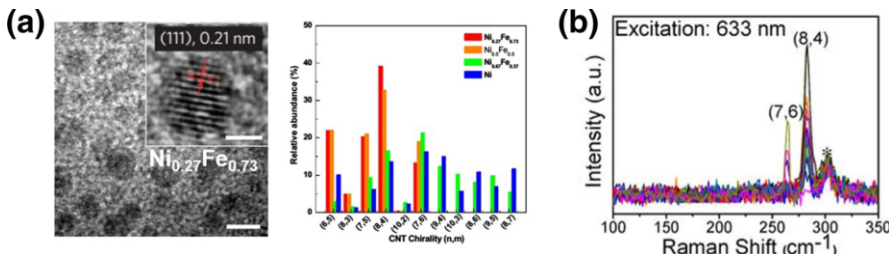


Fig. 15 Characterization of solid-state catalysts and SWNTs grown. **a** TEM images of Ni_{0.27}Fe_{0.73} particles and chirality distributions of SWNTs grown with compositionally tuned Ni_xFe_{1-x} nanocatalysts measured by optical absorbance measurements (Corresponding figure is reproduced with permission [153], Copyright 2009, Nature Publishing Group). **b** Raman spectra in the RBM region of the Mo₂C catalyzed SWNTs measured with 633 nm laser (Corresponding figure is reproduced with permission [155], Copyright 2016, American Chemical Society)

(Fig. 15b) [155]. Only small Mo nanoparticles are carbonized into stable Mo₂C and act as the catalyst. This might be one of the reasons that (8, 4) SWNTs with a small diameter were produced.

The presence of catalyst support is often helpful for maintaining the solid state of catalysts and may influence the morphology and structure of the particles. FePt nanoparticles were fabricated on a single-crystal MgO substrate by sputtering deposition. These FePt nanoparticles were partially (1 1 1)-faceted and the as-grown tubes show higher content of metallic SWNTs [156]. Similar results were obtained with FePtAu–MgO catalyst [157]. A pre-treatment of Co on SiO₂/Si substrate with NH₃ brought about an obvious enrichment of (6, 5) SWNTs, which may be caused by the change of facet distribution of the Fe catalyst nanoparticles [42].

4.5 Intermetallic Compound Catalysts

Inspired by the high selectivity of enzyme-catalyzed reactions, Li et al. consider that catalysts with lower crystalline symmetry and unique atomic arrangements are more suitable for chirality-selective growth of SWNTs because such catalysts can offer more specific structural recognition of SWNTs with different (*n*, *m*). Tungsten-based intermetallic compounds were used as catalysts. The high melting point originating from the presence of W, endows them the ability to maintain the crystal structure during the CVD process, while satisfying catalytic activity for SWNT growth is enabled by another component (Fe, Co, Ni, etc.). More importantly, such intermetallic compounds have unique structures, which is crucial for ensuring high selectivity of produced SWNTs. A heteropoly acid containing W and Co is used to prepare intermetallic catalyst nanoparticles under moderate conditions. They achieved highly preferential growth of (12, 6) SWNTs with an exceptionally large population well above 92% (94.4% from micro-Raman spectra, 92.5% from ultraviolet/visible/near-infrared [UV–Vis–NIR] absorption spectra, and 94.9% from AFM-Raman combined method) with W₆Co₇ catalyst based on the epitaxial nucleation [158] (Fig. 16b). Through *in situ* HRTEM measurements at 1100 °C, W₆Co₇ nanoparticles clearly exhibited lattice fringes during the whole heating process. HRTEM images of the SWNT-catalyst interfaces show that the (12, 6) tubes are always perpendicular to the (0 0 12) plane of the W₆Co₇ catalyst. DFT simulations revealed a perfect geometric match between the (12, 6) tube and (0 0 12) plane and a poor match for all of the other tubes examined. The above results suggest that the lower structural symmetry and the inhomogeneity of different planes in W₆Co₇ critically favor the specific structural matching between the catalyst nanoparticles and SWNTs, thus resulting in chirality-selective SWNT growth.

Similarly, as the DFT simulations showed that the (16, 0) SWNT exhibits a good structural match to the (1 1 6) plane of the W₆Co₇ catalyst (Fig. 16a). Then the dominant growth of zigzag (16, 0) tubes at a content of 79.2 ± 2.2% under the optimized growth conditions was realized by using catalysts with higher abundance of (1 1 6) planes [159] (Fig. 16c). They also achieved highly preferential growth of

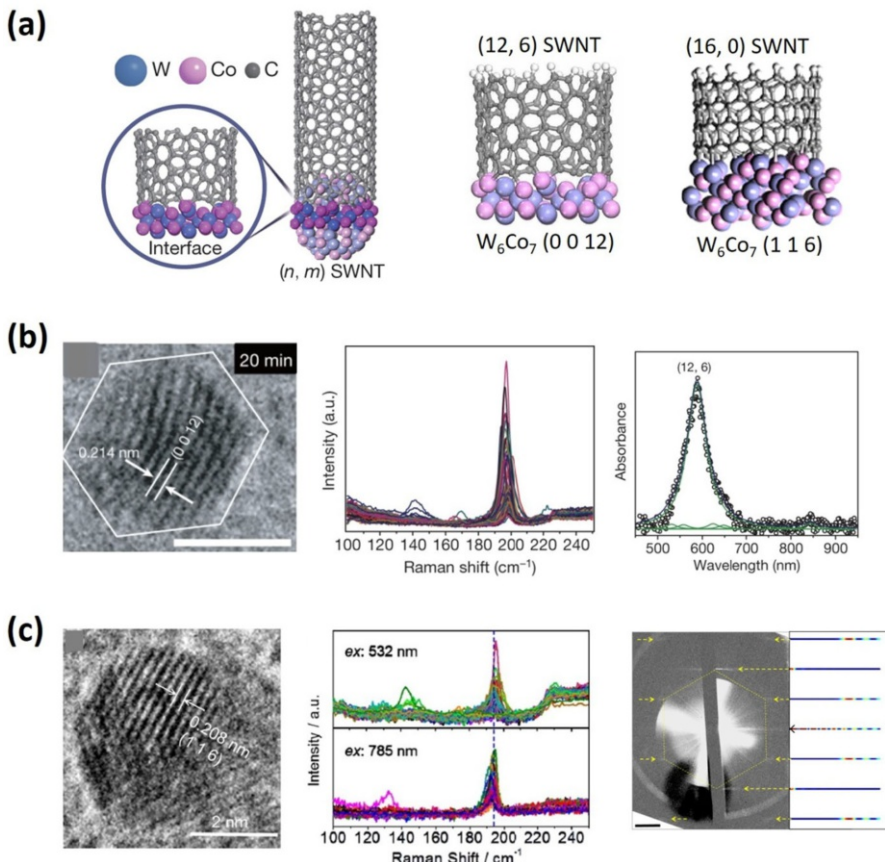


Fig. 16 **a** Templated growth of a SWNT with specified (n, m) from W_6Co_7 intermetallic compound catalyst (Corresponding figure is reproduced with permission [158, 159], Copyright 2015, Nature Publishing Group and Copyright 2015, American Chemical Society). DFT simulations of $(12, 6)$ tubes on the $\text{W}_6\text{Co}_7 (0\ 0\ 12)$ plane, and $(16, 0)$ tubes on the $\text{W}_6\text{Co}_7 (1\ 1\ 6)$ plane. **b** Characterizations of catalyst structure with *in situ* HRTEM images of W_6Co_7 catalyst particles in vacuum, showing a clear $(0\ 0\ 12)$ plane. Raman spectra and UV–Vis–NIR absorption characterizations of SWNTs using W_6Co_7 catalyst grown at 1030 °C, showing highly preferential growth of $(12, 6)$ SWNTs (Corresponding figure is reproduced with permission [158], Copyright 2014, Nature Publishing Group). **c** Characterizations of catalyst structure with HRTEM images of W_6Co_7 catalyst particles prepared at 1050 °C, showing a clear $(1\ 1\ 6)$ plane. Raman spectra and electron beam diffraction characterizations of SWNTs using W_6Co_7 catalyst grown at 1050 °C with a higher flow rate of H_2 , showing highly preferential growth of $(16, 0)$ SWNTs (Corresponding figure is reproduced with permission [159], Copyright 2015, American Chemical Society)

above 97% $(14, 4)$ SWNTs, which exhibits a good structural match to the enriched $(1\ 0\ 10)$ plane of the W_6Co_7 catalyst prepared by $\text{H}_2/\text{H}_2\text{O}$ [160].

Maruyama et al. used in-plane TEM to reveal morphology differences after reducing CoW catalyst at different temperature. An intermediate structure of $\text{Co}_6\text{W}_6\text{C}$ is unambiguously identified and associated with the selective growth of $(12, 6)$ SWNTs at 50–70% [161].

4.6 Summary of Chirality-Specific Growth

Two factors, thermodynamic preference to tubes with lower formation energy, or kinetic preference of tubes with higher growth speed, play competitive roles in defining the distribution of SWNT chirality [50]. SWNTs with structural selectivity produced with various metal catalysts were concluded in Fig. 17. Epitaxial growth of SWNTs using intermetallic compound catalysts with well-defined structure may be a key solution to the challenge of chirality-specific growth.

It is worthy to point out that the detection methods are also shown in Fig. 17. This information is necessary for us reasonably to analyze and compare the results. Indeed, many techniques, including electron diffraction, optical absorption, Raman spectroscopy, Rayleigh scattering, and photoluminescence, have been used for quantitative analysis of the SWNT abundance [162]. However, the applicability of these methods to the tube samples should be taken into account. For instance, photoluminescence can only be used for semiconducting SWNTs [163]. Raman spectroscopy works for all types of SWNTs, although it suffers from the limitation of resonance windows [164]. Nevertheless, this limitation can be largely overcome by using multiple wavelengths and tunable lasers [165, 166]. Electron diffraction is normally applied for suspended SWNTs [167]. Thus, it is possible to lose information of the short tubes because it is difficult to put them across a gap for detection. Optical absorption is applicable for SWNTs well-dispersed in solutions, but hindered by the low resolution or weak differentiation between certain chiralities [133]. A new optical absorption method was developed by Wang et al. to realize the detection of individual tubes on substrates [168]. A new Rayleigh scattering based method was also developed by Jiang et al., which can easily show the structural uniformity of the tubes by the color of the tube images [169]. These two methods are both applicable to SWNTs on substrates; however, the substrates must be very clean and the SWNTs should be well aligned and sufficiently long. From the above, the selection of suitable techniques is important for obtaining

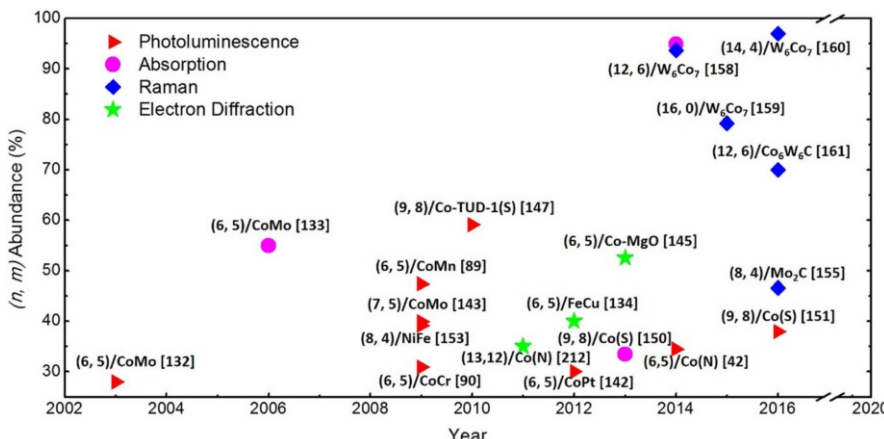


Fig. 17 Reports on selective SWNT growth using metal catalysts

reliable quantification of SWNTs. Normally, a combination of several techniques [158, 170] is needed to acquire a reasonable result.

5 Effect of the CVD Conditions on the Selective Growth of SWNTs

Catalysts play a very important role in the controlled preparation of SWNTs. However, the influence of growth conditions cannot be ignored. The change of growth conditions will directly affect the carbon supply and the catalyst activity, thus affect the growth of SWNTs. At present, there is no universal criteria guiding researchers to get the best growth conditions, but people have accumulated a lot of experience after years of research.

Many carbon-containing molecules can be used as carbon source to grow SWNTs in CVD, such as alcohols [138], hydrocarbons [171, 172], and carbonic oxide [132]. At present, the most commonly used carbon sources in CVD processes are ethanol, carbon monoxide, methane, ethylene, and acetylene. The thermodynamic stability of the carbon source is very different. The decomposition of methane requires higher temperatures, while the pyrolysis of acetylene, ethylene, and ethanol is easier since they decompose exothermally at atmospheric pressure [173]. The main reaction path is disproportionation of CO into carbon and CO₂, when there are no other reactants (e.g. H₂ [174]) in the system. As the reaction is highly exothermic, the reaction equilibrium shifts toward the reverse reaction direction when increasing the temperature. Obviously, this difference in decomposition of the carbon source will directly affect the SWNT growth. On the other hand, the carbon precursors not only present carbon, but also other elements such as hydrogen or oxygen. When the carbon source is decomposed, many hydrogen- and oxygen-containing by-products such as hydrogen and hydroxyl radicals will be produced. These by-products may significantly affect the growth of carbon nanotubes according to many studies on SWNT synthesis [175–180]. Therefore, the carbon source is an important factor in the controlled growth of SWNTs [181, 182].

5.1 Effect of Carbon Precursor Species

Resasco et al. used CO and CH₄ as the carbon sources to grow SWNTs and found only CO resulted a narrow (*n*, *m*) distribution with a single dominating (6, 5) chirality of 54% (Fig. 18a) [133]. As stated above, the disproportionation of CO is exothermic, while the dehydrogenative decomposition of CH₄ is endothermic. Furthermore, the by-products of CH₄ pyrolysis are reductive hydrogen-containing species, while those from CO disproportionation are the oxidative oxygen-containing species. The larger diameter and broader chirality distribution of CH₄-generated tubes may be attributed to the hydrogen produced by the CH₄ decomposition. Hydrogen can accelerate the reduction and sintering of the catalysts, meanwhile, it also decreases the surface fugacity of carbon atoms then hinders the nucleation of carbon on the catalyst surface [183, 184]. Therefore, carbon nanotubes with large-diameter and broader distribution are obtained.

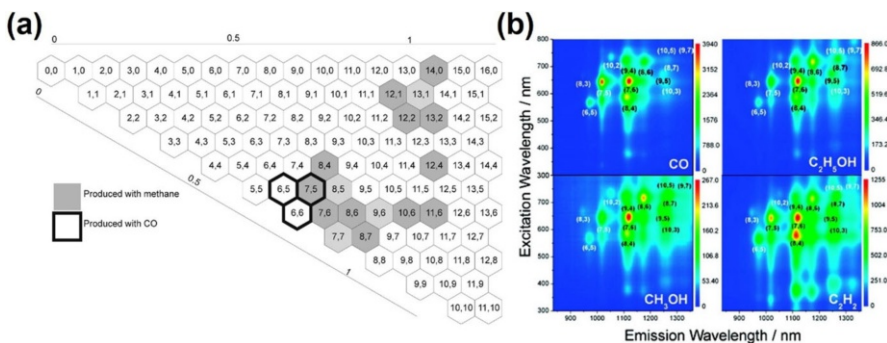


Fig. 18 Effect of carbon species on chirality of SWNTs: **a** chirality maps of SWNT samples produced from two different carbon precursors: CH₄ and CO (Corresponding figure is reproduced with permission [133], Copyright 2006, American Chemical Society). **b** Photoluminescence excitation intensity maps of sodium dodecyl benzene sulfonate (SDBS)-dispersed SWNTs produced from four different carbon precursors on CoMo catalysts (Corresponding figure is reproduced with permission [185], Copyright 2007, American Chemical Society)

Chen et al. [185] used four types of carbon precursors including CO, C₂H₅OH, CH₃OH, and C₂H₂ to grow SWNTs with CoMo catalysts. The chirality distribution of the SWNTs produced by CO was the narrowest and dominated by (7, 6), (7, 5), and (8, 4) tubes, while C₂H₅OH and CH₃OH produced more tubes with larger diameters, namely (8, 6), (9, 5), and (8, 7), and the chirality distribution was also much wider (Fig. 18b). C₂H₂ decomposes much faster than CO. The carbon feeding rate to cobalt surface is also different, leading to different (*n*, *m*) selectivity. He et al. found that SWNTs with narrow diameter distribution of 0.7–1.6 nm were produced by using CO as the carbon source, while large diameter SWNTs ranging from 1.0 to 4.7 nm were produced by using CH₄ as the carbon source [186].

In addition to the decomposition rate of carbon stocks, the decomposition products also affect the selectivity in the growth of SWNTs [176, 179]. Liu et al. selectively grew aligned semiconducting nanotubes by introducing methanol in the growth process [175]. The selectivity was caused by the ·OH radical produced from methanol, which can selectively etch metallic SWNTs because of their smaller ionization potential compared to semiconducting ones.

5.2 Effect of Carbon Feeding

In addition to the carbon source species, the carbon feeding rate (concentration of carbon source) also directly affects the growth of the carbon nanotubes [187–190]. Liu's group synthesized uniform small-diameter SWNTs at a low flow rate of ethane [188]. The average diameter and the diameter distribution of SWNTs increased with the increase of ethane concentration. The diameter of the SWNTs increased with the increasing ethane feeding rates (Fig. 19b). Based on these results, a hypothesis on conditioned activation was proposed. At a given carbon feeding condition, catalysts have an optimal size to nucleate SWNTs. The greater degree of the catalyst's diameter deviation from the optimum size, the less likely it can catalyze the growth of the carbon nanotubes. Smaller nanoparticles are poisoned due to “overfeeding” and larger

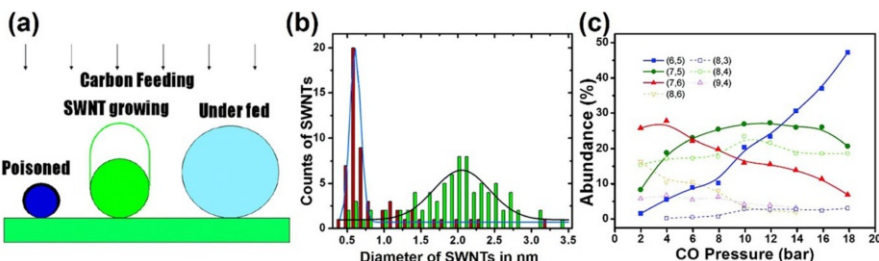


Fig. 19 Effect of source feeding on diameter and chirality of SWNTs: **a** under a given carbon feeding rate, only particles with a moderate and suitable size can nucleate growth (Corresponding figure is reproduced with permission [188], Copyright 2006, American Chemical Society). **b** Diameter distributions of SWNTs grown at different ethane concentrations at 800 °C by AFM measurement: red, 4200 ppm; green, 14,400 ppm (Corresponding figure is reproduced with permission [188], Copyright 2006, American Chemical Society). **c** Abundances of dominant (*n*, *m*) chiral tubes identified by photoluminescence analysis systematically altered with changing CO pressure (Corresponding figure is reproduced with permission [193], Copyright 2007, American Chemical Society)

nanoparticles are inactive due to “underfeeding”. Thus, it is necessary to adjust the carbon source supply rate for the catalyst of given size.

The pressure of the carbon source also directly influences the supply of carbon, which in turn affects the growth of the carbon nanotubes [191–194]. Chen et al. selectively produced bulk SWNT samples with different dominant chiralities enriched by adjusting the pressure of CO on CoMo catalysts from 2 to 18 bar (Fig. 19c) [193]. The higher CO pressure may increase the concentration of the active carbon interacting with Co clusters. Maruyama [195] and Resasco et al. [196] had proposed that carbon caps are formed when carbon in the catalyst particles is saturated. Under higher CO pressure, SWNT growth may be initiated faster and produce thinner tubes, for example (6, 5) and (8, 3). Under lower CO pressure, it should take a longer period for the catalyst nanoparticles to be saturated and form a stable carbon cap. At this period, Co clusters may continuously aggregate due to high-temperature sintering and grow larger to produce larger diameter SWNTs such as (7, 6) and (9, 4). Maruyama group also systematically studied the optimum ethanol pressure for vertically aligned single-walled carbon nanotubes at different CVD temperatures and found that the optimized pressure increases with CVD temperature [191]. SWNT arrays with diameters of 1.47 ± 0.39 and 1.76 ± 0.53 nm were obtained at 60 and 1300 Pa of ethanol pressure, respectively. In addition, higher density of horizontally aligned SWNTs were achieved at lower carbon pressure [194].

5.3 Effect of Growth Temperature

Obviously, growth temperature can influence the growth of SWNTs by changing decomposition of the carbon source or the size of the catalysts [89, 133, 134, 139, 141, 188, 197]. Pfefferle’s group synthesized SWNTs with different diameter distributions through changing reaction temperatures [197]. The diameter of SWNTs shifted systematically from 0.6–0.8 to 1.8–2.0 nm by increasing the reaction temperature from 550 to 950 °C. They speculated that the

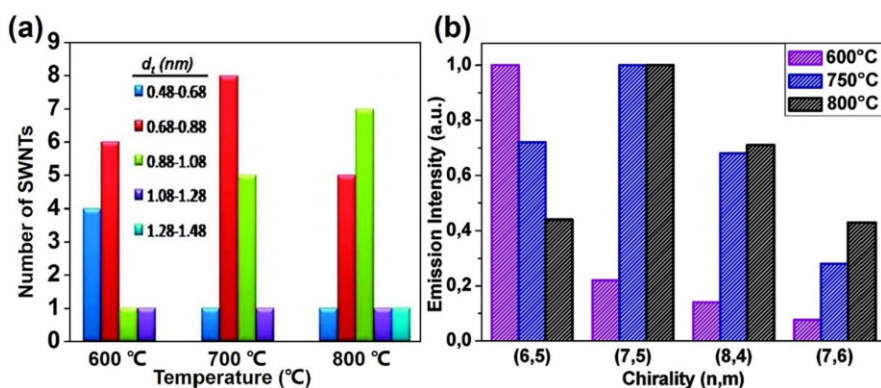


Fig. 20 Effect of growth temperature on diameter and chirality of SWNTs: **a** Diameter distribution of SWNTs synthesized at 600, 700, and 800 °C using CoMn–MCM-41 bimetallic catalyst (Corresponding figure is reproduced with permission [198], Copyright 2010, American Chemical Society). **b** Normalized photoluminescence emission intensities of SWNTs grown at temperatures of 600, 750, and 800 °C using MgO supported FeCu catalyst (Corresponding figure is reproduced with permission [134], Copyright 2010, American Chemical Society)

increase in the diameter of SWNTs was related to the change of the Co catalyst diameters. At low temperature, the average particle diameter of the catalysts was small because the catalyst migrated slowly and the degree of agglomeration was low. Small size catalysts nucleated smaller diameter carbon nanotubes, while large size catalysts sintered at high temperature and grew large diameter carbon nanotubes. A similar phenomenon was found when they used bimetallic CoMn supported on MCM-41 silica templates as catalysts (Fig. 20a) [198].

Fouquet [141] and Chen [89] also found a similar tendency with Co catalyst on Si/SiO₂ substrate. The dominating chirality of the SWNTs grown with CoMo–SiO₂ catalysts changes with temperature and higher chiral enrichment was obtained at lower temperature [133]. The SWNT distribution shifted from a dominant (6, 5) at 700–800 °C to (7, 6) and (8, 7) at 850 °C. Using FeCo [139] and FeCu [134] as the catalysts, the chirality distribution was also changed at different growth temperature (Fig. 20b). Zhang et al. found that when increasing the temperature in the carbon nanotube growth process, the diameter of the carbon nanotubes becomes smaller, and vice versa [199]. Temperature may affect the morphology and the interfacial energy between the catalyst and the SWNT. By periodically changing the growth temperatures, they realized the production of SWNTs with narrow distribution of small chiral angles [200].

5.4 Effect of Additive Species

In addition to carbon source, other additive species may also be used to modulate the growth of SWNTs by regulating the decomposition of carbon stocks [201–204], adjusting the activity and surface property of catalysts [41, 204–207], and selectively etching the more reactive tubes [189, 208–210].

Sulfur has been widely used as an additive species in the growth of SWNTs. It is believed that sulfur can act as the initiator of carbon nanotubes to increase the yield [201]. Generally, sulfur as the growth promoter yielded SWNTs with larger diameters by facilitating the localized nucleation of SWNTs. Cheng [203] and Liu [202] respectively produced large diameter semiconducting SWNTs and metallic SWNTs using sulfur as the growth promoter combined with the appropriate CVD conditions. Chen et al. selectively grew large-diameter (9, 8) nanotubes with 51.7% abundance among semiconducting tubes and 33.5% over all tube species [150]. Sulfur could limit the aggregation of Co atoms [148] to make the catalyst size suitable for the chiral selectivity toward (9, 8) tubes. They proved the formation of Co_9S_8 nanoparticles with narrow size distribution acting as the intermediates made the final Co catalyst uniform [151].

In addition to sulfur, nitrogen is also used as an additive in the growth of SWNTs. Maruyama et al. modulated the mean diameter of the vertically aligned SWNTs from approximately 2–1 nm through adding 5 vol% acetonitrile to ethanol as the carbon feedstock during the growth [41]. When the growth condition was near the thermodynamic equilibrium, SWNT was nucleated through the tangential mode [39]. When acetonitrile was introduced to the system, the decomposed nitrogen atoms absorbed on the surface of the catalyst particles. Compared with carbon, nitrogen interacts more strongly with the Co nanoparticles, thus the nitrogen on the Co nanoparticle surface hinders the formation of the carbon sp^2 network, and hence the tangential growth mode can hardly be maintained. Therefore, the SWNTs grow via the perpendicular growth mode and the diameter of SWNTs is much smaller than the size of the catalysts. Through this method, the diameter of SWNTs can be controlled independent of catalyst preparation [207].

However, the types of nitrogen-containing compounds will directly affect the growth of carbon nanotubes [211, 212]. Kauppinen et al. produced (*n, m*)-selective SWNTs with over 90% SWNTs having large chiral angles in the range of 20°–30° and about 50% in the range of 27°–29° by introducing NH_3 into the floating catalyst CVD (FCCVD) process. The average diameter increased from 1.60 to 1.67 nm rather than decreasing when NH_3 increased from 0 to 500 ppm [212]. The abundances of the three main chiralities (13, 12), (12, 11), and (13, 11) is 13, 8, and 8%, respectively. NH_3 , as a strong etchant, selectively etched off more reactive SWNTs with smaller chiral angles [213] and smaller diameters [214], resulting in selective growth.

There are still many other additives used as etchants to control the growth of carbon nanotubes, for example, H_2O [84, 189, 215], O_2 [203, 216], CO_2 [210], and H_2 [208, 209]. Many reports have shown that the selective elimination of SWNTs is diameter-dependent (Fig. 21) [84, 175]. The smaller SWNTs are more active because the larger strain associated with greater curvature [217]. At the same time, metallic-SWNTs are preferentially etched and removed by oxidation of the etchant due to their smaller ionization potential [218]. Liu [84] and Cheng [203] et al. synthesized semiconducting SWNTs by controlling the diameter of the SWNTs and introducing the etchant at the same time. Liu controlled the diameter of the SWNTs by using uniform stable FeW nanoclusters as the catalyst precursors and improved semiconducting selectivity by adding H_2O etchant (Fig. 21). The introduction of the

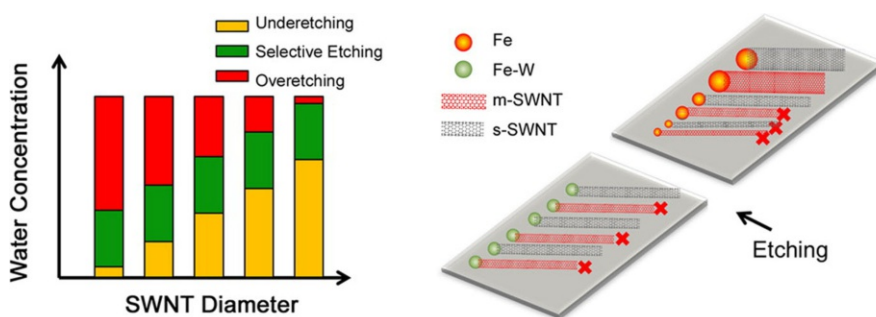


Fig. 21 Schematic illustration of the tube diameter-dependent and electronic-type-dependent etching mechanisms (Corresponding figure is reproduced with permission [84], Copyright 2014, American Chemical Society)

etchant will usually produce larger diameter semiconducting SWNTs. Kauppinen et al. [210] found that the mean diameters of the SWNTs was efficiently altered from 1.2 to 1.9 nm by the addition of appropriate amounts of CO₂ to the carbon source (CO) in FCCVD.

5.5 Effect of the Growth Environment

From above discussion, we know the specific structure of catalyst plays an important role in the synthesis of single-chirality carbon nanotubes. Furthermore, the growth environment also directly affects the chirality of the SWNTs. We found that the selective growth of SWNTs with W₆Co₇ catalysts changed following the CVD conditions [44, 159]. All of the W₆Co₇ catalysts were prepared at 1030 °C and then different ratios of Ar-carried ethanol and hydrogen were used to grow SWNTs at 1030 °C. Higher ethanol/H₂ ratios resulted in better selectivity toward (12, 6) tubes, and smaller ethanol/H₂ ratios resulted in SWNTs of larger diameter (Fig. 22) [44]. We also found that the selective growth of (16, 0) tubes can only achieved at the high H₂ concentration (Table 2) [159]. As discussed previously, hydrogen may lower the carbon fugacity on the catalyst surface and consequently delay the nucleation of caps. We propose that the higher H₂ ratio in the feed gas suppresses

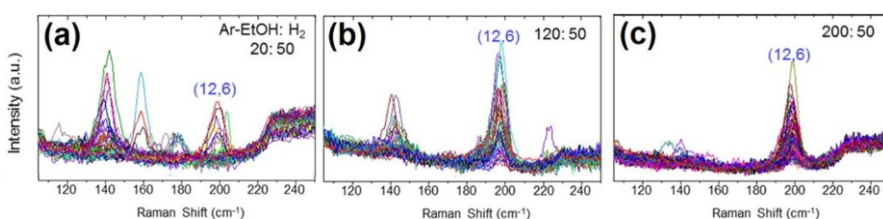


Fig. 22 Effect of the ethanol/H₂ ratios on the chirality distribution of SWNTs. (a-c) Raman spectra (excitation at 633 nm) of SWNT samples grown at 1030 °C under Ar fluxes of **a** 20, **b** 120, and **c** 200 cm³ min⁻¹ through the ethanol bubbler (ice-water bath). The H₂ feed rate was fixed at 50 cm³ min⁻¹ (Corresponding figure is reproduced with permission [44], Copyright 2016, American Chemical Society)

Table 2 Statistics on the RBM peaks and the corresponding (n, m) for the sample grown at 1050 °C by introducing different flow rates of H₂ and constant Ar flow

H ₂ flow (cm ³ ·min ⁻¹)					
120		70		30	
(n, m)	%	(n, m)	%	(n, m)	%
(16, 0)	39.5	(16, 0)	14.6	(16, 0)	0.9
(12, 6)	15.5	(12, 6)	27.1	(12, 6)	61.4
(11, 10)	9.7	(14, 4)	12.5	(12, 8)	5.2
(10, 6)	9.0	(12, 8)	7.8	(13, 6)	4.7
(13, 6)	7.2	(17, 6)	7.2	(14, 4)	3.9
(10, 5)	5.8	(13, 6)	6.2	(11, 8)	3.4
(14, 4)	3.2	(11, 10)	5.6		
(12, 8)	3.0	(16, 8)	5.6		

Corresponding table is reproduced with permission [159], Copyright 2015, American Chemical Society
Each analysis was based on more than 200 RBM peaks collected with Raman 532, 633, and 785 nm excitations

the growth kinetics of all types of tubes and the kinetically unfavorable growth of zigzag tubes are effectively improved.

It can be seen the regulation of growth conditions is very important in the controlled preparation of carbon nanotubes. Only under the suitable growth conditions, the catalyst with controlled structure will be able to catalyze the selective growth of SWNTs with designed chirality. However, the regulation of growth conditions is very complex. There is no very effective way to guide us to find the optimal conditions quickly yet. Therefore, more studies are needed for us to eventually generalize some common rules.

6 Summary

It is obvious that the catalysts play a critical role in the selective growth of SWNTs. We can control the diameter of SWNTs by controlling the catalyst size and the SWNT chirality through further controlling the structure of the catalyst. However, since the growth temperature is high, to constrain the size and structure of catalyst particles is not easy. The catalysts need to have high melting points to maintain a fixed structure and the structure of the catalyst should be unique to improve the selectivity. Tungsten-based intermetallic compounds with unique atomic arrangements and high melting points are the suitable candidates of catalysts for structure-specified growth of SWNTs. Besides the catalysts, the CVD conditions are also very important. The CVD conditions not only affect the nucleation and growth of the SWNTs, but also affect the property of catalysts. Therefore, the highly chirality-selective growth of SWNTs can be realized only by the cooperation of the structural template effect of the catalyst and the optimized CVD conditions.

Acknowledgements This research is financially supported by Ministry of Science and Technology of the People's Republic China (2016YFA0201904), National Natural Science Foundation of China (21631002, U1632119, and 91333105).

References

- Kharlamova MV (2016) Advances in tailoring the electronic properties of single-walled carbon nanotubes. *Prog Mater Sci* 77:125–211
- Chen K, Gao W, Emaminejad S, Kiriya D, Ota H, Nyien HYY, Takei K, Javey A (2016) Printed carbon nanotube electronics and sensor systems. *Adv Mater* 28(22):4397–4414
- Islam AE, Rogers JA, Alam MA (2015) Recent progress in obtaining semiconducting single-walled carbon nanotubes for transistor applications. *Adv Mater* 27(48):7908–7937
- Nanot S, Haroz EH, Kim JH, Hauge RH, Kono J (2012) Optoelectronic properties of single-wall carbon nanotubes. *Adv Mater* 24(36):4977–4994
- Meyyappan M (2016) Carbon nanotube-based chemical sensors. *Small* 12(16):2118–2129
- Cao Q, Rogers JA (2009) Ultrathin films of single-walled carbon nanotubes for electronics and sensors: a review of fundamental and applied aspects. *Adv Mater* 21(1):29–53
- Wen L, Li F, Cheng HM (2016) Carbon nanotubes and graphene for flexible electrochemical energy storage: from materials to devices. *Adv Mater* 28(22):4306–4337
- Ni JF, Li Y (2016) Carbon nanomaterials in different dimensions for electrochemical energy storage. *Adv Energy Mater* 6(17):1600278
- Liu Y, Wang S, Peng LM (2016) Toward high-performance carbon nanotube photovoltaic devices. *Adv Energy Mater* 6(17):1600522
- Zhang Z, Wei L, Qin X, Li Y (2015) Carbon nanomaterials for photovoltaic process. *Nano Energy* 15:490–522
- Mehra NK, Jain NK (2016) Multifunctional hybrid-carbon nanotubes: new horizon in drug delivery and targeting. *J Drug Target* 24(4):294–308
- Liang F, Chen B (2010) A review on biomedical applications of single-walled carbon nanotubes. *Curr Med Chem* 17(1):10–24
- Banerjee S, Hemraj-Benny T, Wong SS (2005) Covalent surface chemistry of single-walled carbon nanotubes. *Adv Mater* 17(1):17–29
- Niyogi S, Hamon MA, Hu H, Zhao B, Bhowmik P, Sen R, Itkis ME, Haddon RC (2002) Chemistry of single-walled carbon nanotubes. *Acc Chem Res* 35(12):1105–1113
- Hirsch A (2002) Functionalization of single-walled carbon nanotubes. *Angew Chem Int Ed* 41(11):1853–1859
- Saito R, Dresselhaus G, Dresselhaus MS (1998) Physical properties of carbon nanotubes. Imperial College Press, London
- Saito R, Fujita M, Dresselhaus G, Dresselhaus MS (1992) Electronic structure of chiral graphene tubules. *Appl Phys Lett* 60(18):2204–2206
- Zhang Q, Huang JQ, Zhao MQ, Qian WZ, Wei F (2011) Carbon nanotube mass production: principles and processes. *ChemSusChem* 4(7):864–889
- Takagi D, Hibino H, Suzuki S, Kobayashi Y, Homma Y (2007) Carbon nanotube growth from semiconductor nanoparticles. *Nano Lett* 7(8):2272–2275
- Tang DM, Zhang LL, Liu C, Yin LC, Hou PX, Jiang H, Zhu Z, Li F, Liu B, Kauppinen EI, Cheng H (2012) Heteroepitaxial growth of single-walled carbon nanotubes from boron nitride. *Sci Rep* 2:971
- Chen Y, Zhang J (2011) Diameter controlled growth of single-walled carbon nanotubes from SiO₂ nanoparticles. *Carbon* 49(10):3316–3324
- Yu D, Zhang Q, Dai L (2010) Highly efficient metal-free growth of nitrogen-doped single-walled carbon nanotubes on plasma-etched substrates for oxygen reduction. *J Am Chem Soc* 132(43):15127–15129
- Liu B, Ren W, Gao L, Li S, Pei S, Liu C, Jiang C, Cheng H-M (2009) Metal-catalyst-free growth of single-walled carbon nanotubes. *J Am Chem Soc* 131(6):2082–2083
- Huang S, Cai Q, Chen J, Qian Y, Zhang L (2009) Metal-catalyst-free growth of single-walled carbon nanotubes on substrates. *J Am Chem Soc* 131(6):2094–2095
- Kang L, Hu Y, Liu L, Wu J, Zhang S, Zhao Q, Ding F, Li Q, Zhang J (2015) Growth of close packed semiconducting single-walled carbon nanotube arrays using oxygen-deficient TiO₂ nanoparticles as catalysts. *Nano Lett* 15(1):403–409
- Takagi D, Kobayashi Y, Homma Y (2009) Carbon nanotube growth from diamond. *J Am Chem Soc* 131(20):6922–6923
- Li Y, Cui R, Ding L, Liu Y, Zhou W, Zhang Y, Jin Z, Peng F, Liu J (2010) How catalysts affect the growth of single-walled carbon nanotubes on substrates. *Adv Mater* 22(13):1508–1515

28. Li P, Zhang X, Liu J (2016) Aligned single-walled carbon nanotube arrays from rhodium catalysts with unexpected diameter uniformity independent of the catalyst size and growth temperature. *Chem Mater* 28(3):870–875
29. Takagi D, Homma Y, Hibino H, Suzuki S, Kobayashi Y (2006) Single-walled carbon nanotube growth from highly activated metal nanoparticles. *Nano Lett* 6(12):2642–2645
30. Yuan D, Ding L, Chu H, Feng Y, McNicholas TP, Liu J (2008) Horizontally aligned single-walled carbon nanotube on quartz from a large variety of metal catalysts. *Nano Lett* 8(8):2576–2579
31. Peng F, Liu Y, Cui RL, Gao DL, Yang F, Li Y (2012) Direct growth of single-walled carbon nanotubes on substrates. *Chin Sci Bull* 57(2–3):225–233
32. Cui R, Zhang Y, Wang J, Zhou W, Li Y (2010) Comparison between copper and iron as catalyst for chemical vapor deposition of horizontally aligned ultralong single-walled carbon nanotubes on silicon substrates. *J Phys Chem C* 114(37):15547–15552
33. Wagner RS, Ellis WC (1964) Vapor–liquid–solid mechanism of single crystal growth. *Appl Phys Lett* 4(5):89–90
34. Saito Y (1995) Nanoparticles and filled nanocapsules. *Carbon* 33(7):979–988
35. Gavillet J, Loiseau A, Journet C, Willaime F, Ducastelle F, Charlier JC (2001) Root-growth mechanism for single-wall carbon nanotubes. *Phys Rev Lett* 87(27):275504
36. Gavillet J, Thibault J, Stephan O, Amara H, Loiseau A, Bichara C, Gaspard J-P, Ducastelle F (2004) Nucleation and growth of single-walled nanotubes: the role of metallic catalysts. *J Nanosci Nanotechnol* 4(4):346–359
37. Harris PJF (2007) Solid state growth mechanisms for carbon nanotubes. *Carbon* 45(2):229–239
38. Jourdain V, Bichara C (2013) Current understanding of the growth of carbon nanotubes in catalytic chemical vapour deposition. *Carbon* 58:2–39
39. Fiawoo MF, Bonnot AM, Amara H, Bichara C, Thibault-Pénisson J, Loiseau A (2012) Evidence of correlation between catalyst particles and the single-wall carbon nanotube diameter: a first step towards chirality control. *Phys Rev Lett* 108(19):195503
40. Shulaker MM, Hills G, Patil N, Wei H, Chen H-Y, Wong H-SP, Mitra S (2013) Carbon nanotube computer. *Nature* 501(7468):526–530
41. Thurakitseree T, Kramberger C, Kumamoto A, Chiashi S, Einarsson E, Maruyama S (2013) Reversible diameter modulation of single-walled carbon nanotubes by acetonitrile-containing feedstock. *ACS Nano* 7(3):2205–2211
42. Fouquet M, Bayer BC, Esconjauregui S, Thomsen C, Hofmann S, Robertson J (2014) Effect of catalyst pretreatment on chirality-selective growth of single-walled carbon nanotubes. *J Phys Chem C* 118(11):5773–5781
43. Yu F, Yang M, Li F, Su C, Ma B, Yuan Z, Chen J, Ma J (2012) The growth mechanism of single-walled carbon nanotubes with a controlled diameter. *Physica E* 44(10):2032–2040
44. Yang F, Wang X, Li M, Liu X, Zhao X, Zhang D, Zhang Y, Yang J, Li Y (2016) Templated synthesis of single-walled carbon nanotubes with specific structure. *Acc Chem Res* 49(4):606–615
45. Ding F, Harutyunyan AR, Yakobson BI (2009) Dislocation theory of chirality-controlled nanotube growth. *Proc Natl Acad Sci* 106(8):2506–2509
46. Gomez-Gualdrón DA, Balbuena PB (2008) The role of cap chirality in the mechanism of growth of single-wall carbon nanotubes. *Nanotechnology* 19:485604
47. Li H-B, Page AJ, Irle S, Morokuma K (2012) Single-walled carbon nanotube growth from chiral carbon nanorings: prediction of chirality and diameter influence on growth rates. *J Am Chem Soc* 134(38):15887–15896
48. Rao R, Liptak D, Cherukuri T, Yakobson BI, Maruyama B (2012) *In situ* evidence for chirality-dependent growth rates of individual carbon nanotubes. *Nat Mater* 11(3):213–216
49. Liu B, Liu J, Tu X, Zhang J, Zheng M, Zhou C (2013) Chirality-dependent vapour-phase epitaxial growth and termination of single-wall carbon nanotubes. *Nano Lett* 13(9):4416–4421
50. Artyukhov VI, Penev ES, Yakobson BI (2014) Why nanotubes grow chiral. *Nat Commun* 5:4892
51. Reich S, Li L, Robertson J (2006) Control the chirality of carbon nanotubes by epitaxial growth. *Chem Phys Lett* 421(4–6):469–472
52. Reich S, Li L, Robertson J (2006) Epitaxial growth of carbon caps on Ni for chiral selectivity. *Phys Status Solidi (b)* 243(13):3494–3499
53. Penev ES, Artyukhov VI, Yakobson BI (2014) Extensive energy landscape sampling of nanotube end-caps reveals no chiral-angle bias for their nucleation. *ACS Nano* 8(2):1899–1906
54. Gómez-Gualdrón DA, Zhao J, Balbuena PB (2011) Nanocatalyst structure as a template to define chirality of nascent single-walled carbon nanotubes. *J Chem Phys* 134(1):014705

55. Li Y, Liu J, Wang Y, Wang ZL (2001) Preparation of monodispersed Fe–Mo nanoparticles as the catalyst for CVD synthesis of carbon nanotubes. *Chem Mater* 13(3):1008–1014
56. Cheung CL, Kurtz A, Park H, Lieber CM (2002) Diameter-controlled synthesis of carbon nanotubes. *J Phys Chem B* 106(10):2429–2433
57. Li YM, Kim W, Zhang YG, Rolandi M, Wang DW, Dai HJ (2001) Growth of single-walled carbon nanotubes from discrete catalytic nanoparticles of various sizes. *J Phys Chem B* 105(46):11424–11431
58. Jeong GH, Yamazaki A, Suzuki S, Yoshimura H, Kobayashi Y, Homma Y (2005) Cobalt-filled apoferritin for suspended single-walled carbon nanotube growth with narrow diameter distribution. *J Am Chem Soc* 127(23):8238–8239
59. Takagi D, Yamazaki A, Otsuka Y, Yoshimura H, Kobayashi Y, Homma Y (2007) Gold-filled apoferritin for investigation of single-walled carbon nanotube growth on substrate. *Chem Phys Lett* 445(4–6):213–216
60. Lukas D, Jason G, Thomas H, Matthias M, Roland R, Christofer H (2009) Narrowing SWNT diameter distribution using size-separated ferritin-based Fe catalysts. *Nanotechnology* 20(35):355601
61. Jeong G-H, Suzuki S, Kobayashi Y, Yamazaki A, Yoshimura H, Homma Y (2005) Effect of nanoparticle density on narrow diameter distribution of carbon nanotubes and particle evolution during chemical vapor deposition growth. *J Appl Phys* 98(12):124311
62. Jeong G-H, Yamazaki A, Suzuki S, Kobayashi Y, Homma Y (2006) Behavior of catalytic nanoparticles during chemical vapor deposition for carbon nanotube growth. *Chem Phys Lett* 422(1–3):83–88
63. Grant R, Filman D, Finkel S, Kolter R, Hogle J (1998) The crystal structure of DPS, a ferritin homolog that binds and protects DNA. *Nat Struct Mol Biol* 5(4):294–303
64. Jeong G-H, Yamazaki A, Suzuki S, Yoshimura H, Kobayashi Y, Homma Y (2007) Production of single-walled carbon nanotubes with narrow diameter distribution using iron nanoparticles derived from DNA-binding proteins from starved cells. *Carbon* 45(5):978–983
65. Kim H-J, Seo SW, Lee J, Jung G, Lee K-H (2014) The synthesis of single-walled carbon nanotubes with narrow diameter distribution using polymerized hemoglobin. *Carbon* 69:588–594
66. Alvarez NT, Orbaek A, Barron AR, Tour JM, Haug RH (2010) Dendrimer-assisted self-assembled monolayer of iron nanoparticles for vertical array carbon nanotube growth. *ACS Appl Mater Inter* 2(1):15–18
67. Placidus BA, Baratunde AC, Timothy DS, Xianfan X, Timothy SF (2007) Dendrimer-assisted controlled growth of carbon nanotubes for enhanced thermal interface conductance. *Nanotechnology* 18(38):385303
68. Hirano I, Imaoka T, Yamamoto K (2013) Preparation of carbon nanotubes using iron oxide(III) nanoparticles size-controlled by phenylazomethine dendrimers. *J Inorg Organomet Poly Mater* 23(1):223–226
69. Choi HC, Kim W, Wang D, Dai H (2002) Delivery of catalytic metal species onto surfaces with dendrimer carriers for the synthesis of carbon nanotubes with narrow diameter distribution. *J Phys Chem B* 106(48):12361–12365
70. Fu Q, Huang S, Liu J (2004) Chemical vapor depositions of single-walled carbon nanotubes catalyzed by uniform Fe_2O_3 nanoclusters synthesized using diblock copolymer micelles. *J Phys Chem B* 108(20):6124–6129
71. Sreekar B, Alfonso R, Jifa Q, Jing K, Angela MB (2006) Block-copolymer assisted synthesis of arrays of metal nanoparticles and their catalytic activities for the growth of SWNTS. *Nanotechnology* 17(20):5080
72. Lu J, Yi SS, Kopley T, Qian C, Liu J, Gulari E (2006) Fabrication of ordered catalytically active nanoparticles derived from block copolymer micelle templates for controllable synthesis of single-walled carbon nanotubes. *J Phys Chem B* 110(13):6655–6660
73. Lu J, Kopley T, Dutton D, Liu J, Qian C, Son H, Dresselhaus M, Kong J (2006) Generating suspended single-walled carbon nanotubes across a large surface area via patterning self-assembled catalyst-containing block copolymer thin films. *J Phys Chem B* 110(22):10585–10589
74. Lu JQ, Kopley TE, Moll N, Roitman D, Chamberlin D, Fu Q, Liu J, Russell TP, Rider DA, Manners I (2005) High-quality single-walled carbon nanotubes with small diameter, controlled density, and ordered locations using a polyferrocenylsilane block copolymer catalyst precursor. *Chem Mater* 17(9):2227–2231

75. Hashimoto T, Kimishima K, Hasegawa H (1991) Self-assembly and patterns in binary mixtures of Si block copolymer and PPO. *Macromolecules* 24(20):5704–5712
76. Winey KI, Thomas EL, Fetter LJ (1991) Ordered morphologies in binary blends of diblock copolymer and homopolymer and characterization of their intermaterial dividing surfaces. *J Chem Phys* 95(12):9367–9375
77. Coronado E, Gómez-garcía CJ (1995) Polycxometalates: from magnetic clusters to molecular materials. *Comments Inorg Chem* 17(5):255–281
78. Edgar K, Spencer JL (2006) The synthesis of carbon nanotubes from müller clusters. *Curr Appl Phys* 6(3):419–421
79. He M, Fedotov PV, Chernov A, Obraztsova ED, Jiang H, Wei N, Cui H, Sainio J, Zhang W, Jin H, Karppinen M, Kauppinen EI, Loiseau A (2016) Chiral-selective growth of single-walled carbon nanotubes on Fe-based catalysts using CO as carbon source. *Carbon* 108:521–528
80. An L, Owens JM, McNeil LE, Liu J (2002) Synthesis of nearly uniform single-walled carbon nanotubes using identical metal-containing molecular nanoclusters as catalysts. *J Am Chem Soc* 124(46):13688–13689
81. Anderson RE, Colorado JR, Crouse C, Ogrin D, Maruyama B, Pender MJ, Edwards CL, Whitsitt E, Moore VC, Koveal D, Lupu C, Stewart MP, Smalley RE, Tour JM, Barron AR (2006) A study of the formation, purification and application as a SWNT growth catalyst of the nanocluster $[H_xPMo_{12}O_{40} \subset H_4Mo_{72}Fe_{30}(O_2CMe)_{15}O_{254}(H_2O)_{98}]$. *Dalton Trans* 25(25):3097–3107
82. Goss K, Kamra A, Spudat C, Meyer C, Kögerler P, Schneider CM (2009) CVD growth of carbon nanotubes using molecular nanoclusters as catalyst. *Phys Status Solidi (b)* 246(11–12):2494–2497
83. Peng F, Luo D, Sun H, Wang J, Yang F, Li R, Yang J, Li Y (2013) Diameter-controlled growth of aligned single-walled carbon nanotubes on quartz using molecular nanoclusters as catalyst precursors. *Chin Sci Bull* 58(4–5):433–439
84. Li J, Ke C-T, Liu K, Li P, Liang S, Finkelstein G, Wang F, Liu J (2014) Importance of diameter control on selective synthesis of semiconducting single-walled carbon nanotubes. *ACS Nano* 8(8):8564–8572
85. Müller A, Das SK, Kögerler P, Bögge H, Schmidtmann M, Trautwein AX, Schünemann V, Krickemeyer E, Preetz W (2000) A new type of supramolecular compound: molybdenum-oxide-based composites consisting of magnetic nanocapsules with encapsulated Keggin-ion electron reservoirs cross-linked to a two-dimensional network. *Angew Chem* 112(19):3555–3559
86. Müller A, Das SK, Bogge H, Schmidtmann M, Botar A, Patrut A (2001) Generation of cluster capsules (I_h) from decomposition products of a smaller cluster (Keggin- T_d) while surviving ones get encapsulated: species with core-shell topology formed by a fundamental symmetry-driven reaction. *Chem Commun* 7(7):657–658
87. Beck JS, Vartuli JC, Roth WJ, Leonowicz ME, Kresge CT, Schmitt KD, Chu CTW, Olson DH, Sheppard EW, McCullen SB, Higgins JB, Schlenker JL (1992) A new family of mesoporous molecular sieves prepared with liquid crystal templates. *J Am Chem Soc* 114(27):10834–10843
88. Lim S, Ciuparu D, Pak C, Dobek F, Chen Y, Harding D, Pfefferle L, Haller G (2003) Synthesis and characterization of highly ordered Co-MCM-41 for production of aligned single walled carbon nanotubes (swnt). *J Phys Chem B* 107(40):11048–11056
89. Chen Y, Ciuparu D, Lim S, Yang Y, Haller GL, Pfefferle L (2004) Synthesis of uniform diameter single-wall carbon nanotubes in Co-MCM-41: effects of the catalyst prereduction and nanotube growth temperatures. *J Catal* 225(2):453–465
90. Ciuparu D, Chen Y, Lim S, Haller GL, Pfefferle L (2004) Uniform-diameter single-walled carbon nanotubes catalytically grown in cobalt-incorporated MCM-41. *J Phys Chem B* 108(2):503–507
91. Chen Y, Ciuparu D, Lim S, Haller GL, Pfefferle LD (2006) The effect of the cobalt loading on the growth of single wall carbon nanotubes by Co disproportionation on Co-MCM-41 catalysts. *Carbon* 44(1):67–78
92. Loebick CZ, Derrouiche S, Marinkovic N, Wang C, Henrich F, Kappes MM, Haller GL, Pfefferle LD (2009) Effect of manganese addition to the Co-MCM-41 catalyst in the selective synthesis of single wall carbon nanotubes. *J Phys Chem C* 113(52):21611–21620
93. Zoican Loebick C, Derrouiche S, Fang F, Li N, Haller GL, Pfefferle LD (2009) Effect of chromium addition to the Co-MCM-41 catalyst in the synthesis of single wall carbon nanotubes. *Appl Catal A* 368(1–2):40–49
94. Wei L, Bai S, Peng W, Yuan Y, Si R, Goh K, Jiang R, Chen Y (2014) Narrow-chirality distributed single-walled carbon nanotube synthesis by remote plasma enhanced ethanol deposition on cobalt incorporated MCM-41 catalyst. *Carbon* 66:134–143

95. Lim S, Wang C, Yang Y, Ciuparu D, Pfefferle L, Haller GL (2007) Evidence for anchoring and partial occlusion of metallic clusters on the pore walls of MCM-41 and effect on the stability of the metallic clusters. *Catal Today* 123(1–4):122–132
96. Amama PB, Lim S, Ciuparu D, Yang Y, Pfefferle L, Haller GL (2005) Synthesis, characterization, and stability of Fe–MCM-41 for production of carbon nanotubes by acetylene pyrolysis. *J Phys Chem B* 109(7):2645–2656
97. Atchudan R, Pandurangan A, Somanathan T (2009) Bimetallic mesoporous materials for high yield synthesis of carbon nanotubes by chemical vapour deposition techniques. *J Mol Catal A: Chem* 309(1–2):146–152
98. Subashini D, Pandurangan A (2007) Synthesis of mesoporous molecular sieves as catalytic template for the growth of single walled carbon nanotubes. *Catal Commun* 8(11):1665–1670
99. Ago H, Imamura S, Okazaki T, Saito T, Yumura M, Tsuji M (2005) CVD growth of single-walled carbon nanotubes with narrow diameter distribution over Fe/MgO catalyst and their fluorescence spectroscopy. *J Phys Chem B* 109(20):10035–10041
100. Tang ZK, Sun HD, Wang J, Chen J, Li G (1998) Mono-sized single-wall carbon nanotubes formed in channels of AlPO₄-5 single crystal. *Appl Phys Lett* 73(16):2287–2289
101. Wang N, Tang ZK, Li GD, Chen JS (2000) Materials science: single-walled 4 Å carbon nanotube arrays. *Nature* 408(6808):50–51
102. Tang ZK, Zhang L, Wang N, Zhang XX, Wen GH, Li GD, Wang JN, Chan CT, Sheng P (2001) Superconductivity in 4 angstrom single-walled carbon nanotubes. *Science* 292(5526):2462–2465
103. Wang N, Li GD, Tang ZK (2001) Mono-sized and single-walled 4 Å carbon nanotubes. *Chem Phys Lett* 339(1–2):47–52
104. Li ZM, Tang ZK, Liu HJ, Wang N, Chan CT, Saito R, Okada S, Li GD, Chen JS, Nagasawa N, Tsuda S (2001) Polarized absorption spectra of single-walled 4 angstrom carbon nanotubes aligned in channels of an AlPO₄-5 single crystal. *Phys Rev Lett* 87(12):127401
105. Yamada T, Namai T, Hata K, Futaba DN, Mizuno K, Fan J, Yudasaka M, Yumura M, Iijima S (2006) Size-selective growth of double-walled carbon nanotube forests from engineered iron catalysts. *Nat Nanotechnol* 1(2):131–136
106. Zhong G, Warner JH, Fouquet M, Robertson AW, Chen B, Robertson J (2012) Growth of ultrahigh density single-walled carbon nanotube forests by improved catalyst design. *ACS Nano* 6(4):2893–2903
107. Chen G, Seki Y, Kimura H, Sakurai S, Yumura M, Hata K, Futaba DN (2014) Diameter control of single-walled carbon nanotube forests from 1.3–3.0 nm by arc plasma deposition. *Sci Rep* 4:3804
108. Kim C, Lee H (2009) Change in the catalytic reactivity of Pt nanocubes in the presence of different surface-capping agents. *Catal Commun* 10(9):1305–1309
109. Chandrasekaran P, Viruthagiri G, Srinivasan N (2012) The effect of various capping agents on the surface modifications of sol–gel synthesised ZnO nanoparticles. *J Alloys Compd* 540:89–93
110. Liu W, Wang H (2016) Influence of surface capping on oxygen reduction catalysis: a case study of 1.7 nm Pt nanoparticles. *Surf Sci* 648:120–125
111. Chen J, Xu X, Zhang L, Huang S (2015) Controlling the diameter of single-walled carbon nanotubes by improving the dispersion of the uniform catalyst nanoparticles on substrate. *Nano-Micro Lett* 7(4):353–359
112. Balyan A, Fukuda T, Uchida T, Nakajima Y, Hanajiri T, Maekawa T (2012) Synthesis of diameter controlled carbon nanotubes using self-assembled catalyst nanoparticles. *Chem Phys Lett* 519–520:78–82
113. Voorhees PW (1985) The theory of Ostwald ripening. *J Stat Phys* 38(1–2):231–252
114. Schweiger M, Schaudig M, Gannott F, Killian MS, Bitzek E, Schmuki P, Zaumseil J (2015) Controlling the diameter of aligned single-walled carbon nanotubes on quartz via catalyst reduction time. *Carbon* 95:452–459
115. He M, Duan X, Wang X, Zhang J, Liu Z, Robinson C (2004) Iron catalysts reactivation for efficient CVD growth of SWNT with base-growth mode on surface. *J Phys Chem B* 108(34):12665–12668
116. Sakurai S, Inaguma M, Futaba DN, Yumura M, Hata K (2013) Diameter and density control of single-walled carbon nanotube forests by modulating ostwald ripening through decoupling the catalyst formation and growth processes. *Small* 9(21):3584–3592
117. Amama PB, Pint CL, McJilton L, Kim SM, Stach EA, Murray PT, Hauge RH, Maruyama B (2009) Role of water in super growth of single-walled carbon nanotube carpets. *Nano Lett* 9(1):44–49

118. Kim SM, Pint CL, Amama PB, Zakharov DN, Hauge RH, Maruyama B, Stach EA (2010) Evolution in catalyst morphology leads to carbon nanotube growth termination. *J Phys Chem Lett* 1(6):918–922
119. Colaianni ML, Chen PJ, Yates JT (1990) Spectroscopic studies of the thermal modification of the Fe/Al₂O₃ interface. *Surf Sci* 238(1):13–24
120. Song W, Jeon C, Kim YS, Kwon YT, Jung DS, Jang SW, Choi WC, Park JS, Saito R, Park C-Y (2010) Synthesis of bandgap-controlled semiconducting single-walled carbon nanotubes. *ACS Nano* 4(2):1012–1018
121. Ago H, Ayagaki T, Ogawa Y, Tsuji M (2011) Ultrahigh-vacuum-assisted control of metal nanoparticles for horizontally aligned single-walled carbon nanotubes with extraordinary uniform diameters. *J Phys Chem C* 115(27):13247–13253
122. Youn SK, Yazdani N, Patscheider J, Park HG (2013) Facile diameter control of vertically aligned, narrow single-walled carbon nanotubes. *RSC Adv* 3(5):1434–1441
123. Wang X, Yue WB, He MS, Liu MH, Zhang J, Liu ZF (2004) Bimetallic catalysts for the efficient growth of SWNTs on surfaces. *Chem Mater* 16(5):799–805
124. Xiang R, Einarsson E, Murakami Y, Shiomi J, Chiashi S, Tang Z, Maruyama S (2012) Diameter modulation of vertically aligned single-walled carbon nanotubes. *ACS Nano* 6(8):7472–7479
125. Wei L, Liu BL, Wang XT, Gui H, Yuan Y, Zhai SL, Ng AK, Zhou CW, Chen Y (2015) (9, 8) single-walled carbon nanotube enrichment via aqueous two-phase separation and their thin-film transistor applications. *Adv Elec Mater* 1(1):1500151
126. He XW, Gao WL, Xie LJ, Li B, Zhang Q, Lei SD, Robinson JM, Haroz EH, Doorn SK, Wang WP, Vajtai R, Ajayan PM, Adams WW, Hauge RH, Kono J (2016) Wafer-scale monodomain films of spontaneously aligned single-walled carbon nanotubes. *Nat Nanotechnol* 11(7):633–639
127. Jain RM, Howden R, Tvrdy K, Shimizu S, Hilmer AJ, McNicholas TP, Gleason KK, Strano MS (2012) Polymer-free near-infrared photovoltaics with single chirality (6, 5) semiconducting carbon nanotube active layers. *Adv Mater* 24(32):4436–4439
128. Isborn CM, Tang C, Martini A, Johnson ER, Otero-de-la-Roza A, Tung VC (2013) Carbon nanotube chirality determines efficiency of electron transfer to fullerene in all-carbon photovoltaics. *J Phys Chem Lett* 4(17):2914–2918
129. Diao S, Hong GS, Robinson JT, Jiao LY, Antaris AL, Wu JZ, Choi CL, Dai HJ (2012) Chirality enriched (12, 1) and (11, 3) single-walled carbon nanotubes for biological imaging. *J Am Chem Soc* 134(41):16971–16974
130. Yomogida Y, Tanaka T, Zhang M, Yudasaka M, Wei X, Kataura H (2016) Industrial-scale separation of high-purity single-chirality single-wall carbon nanotubes for biological imaging. *Nat Commun* 7:12056
131. De Volder MF, Tawfick SH, Baughman RH, Hart AJ (2013) Carbon nanotubes: present and future commercial applications. *Science* 339(6119):535–539
132. Bachilo SM, Balzano L, Herrera JE, Pompeo F, Resasco DE, Weisman RB (2003) Narrow (*n, m*) distribution of single-walled carbon nanotubes grown using a solid supported catalyst. *J Am Chem Soc* 125(37):11186–11187
133. Lolli G, Zhang L, Balzano L, Sakulchaicharoen N, Tan Y, Resasco DE (2006) Tailoring (*n, m*) structure of single-walled carbon nanotubes by modifying reaction conditions and the nature of the support of CoMo catalysts. *J Phys Chem B* 110(5):2108–2115
134. He M, Chernov AI, Fedotov PV, Obraztsova ED, Sainio J, Rikkilä E, Jiang H, Zhu Z, Tian Y, Kauppinen EI (2010) Predominant (6, 5) single-walled carbon nanotube growth on a copper-promoted iron catalyst. *J Am Chem Soc* 132(40):13994–13996
135. He M, Chernov AI, Obraztsova ED, Jiang H, Kauppinen EI, Lehtonen J (2012) Synergistic effects in FeCu bimetallic catalyst for low temperature growth of single-walled carbon nanotubes. *Carbon* 52:590–594
136. He M, Liu B, Chernov AI, Obraztsova ED, Kauppi I, Jiang H, Anoshkin I, Cavalca F, Hansen TW, Wagner JB, Nasibulin AG, Kauppinen EI, Linnekoski J, Niemelä M, Lehtonen J (2012) Growth mechanism of single-walled carbon nanotubes on iron–copper catalyst and chirality studies by electron diffraction. *Chem Mater* 24(10):1796–1801
137. Cui K, Kumamoto A, Xiang R, An H, Wang B, Inoue T, Chiashi S, Ikuhara Y, Maruyama S (2016) Synthesis of subnanometer-diameter vertically aligned single-walled carbon nanotubes with copper-anchored cobalt catalysts. *Nanoscale* 8(3):1608–1617
138. Maruyama S, Kojima R, Miyauchi Y, Chiashi S, Kohno M (2002) Low-temperature synthesis of high-purity single-walled carbon nanotubes from alcohol. *Chem Phys Lett* 360(3):229–234

139. Miyauchi Y, Chiashi S, Murakami Y, Hayashida Y, Maruyama S (2004) Fluorescence spectroscopy of single-walled carbon nanotubes synthesized from alcohol. *Chem Phys Lett* 387(1–3):198–203
140. He M, Fedotov PV, Obraztsova ED, Viitanen V, Sainio J, Jiang H, Kauppinen EI, Niemelä M, Lehtonen J (2012) Chiral-selective growth of single-walled carbon nanotubes on stainless steel wires. *Carbon* 50(11):4294–4297
141. Fouquet M, Bayer B, Esconjauregui S, Blume R, Warner J, Hofmann S, Schlögl R, Thomsen C, Robertson J (2012) Highly chiral-selective growth of single-walled carbon nanotubes with a simple monometallic Co catalyst. *Phys Rev B* 85(23):235411
142. Liu B, Ren W, Li S, Liu C, Cheng H-M (2012) High temperature selective growth of single-walled carbon nanotubes with a narrow chirality distribution from a CoPt bimetallic catalyst. *Chem Commun* 48(18):2409–2411
143. Wang B, Yang Y, Li L-J, Chen Y (2009) Effect of different catalyst supports on the (*n, m*) selective growth of single-walled carbon nanotube from Co–Mo catalyst. *J Mater Sci* 44(12):3285–3295
144. He M, Chernov AI, Fedotov PV, Obraztsova ED, Rikkinen E, Zhu Z, Sainio J, Jiang H, Nasibulin AG, Kauppinen EI, Niemelä M, Krause AOI (2011) Selective growth of SWNTs on partially reduced monometallic cobalt catalyst. *Chem Commun* 47(4):1219–1221
145. He M, Jiang H, Liu B, Fedotov PV, Chernov AI, Obraztsova ED, Cavalca F, Wagner JB, Hansen TW, Anoshkin IV, Obraztsova EA, Belkin AV, Sairanen E, Nasibulin AG, Lehtonen J, Kauppinen EI (2013) Chiral-selective growth of single-walled carbon nanotubes on lattice-mismatched epitaxial cobalt nanoparticles. *Sci Rep* 3:1460
146. Ishigami N, Ago H, Imamoto K, Tsuji M, Iakoubovskii K, Minami N (2008) Crystal plane dependent growth of aligned single-walled carbon nanotubes on sapphire. *J Am Chem Soc* 130(30):9918–9924
147. Wang H, Wang B, Quek XY, Wei L, Zhao J, Li LJ, Chan-Park MB, Yang Y, Chen Y (2010) Selective synthesis of (9, 8) single walled carbon nanotubes on cobalt incorporated TUD-1 catalysts. *J Am Chem Soc* 132(47):16747–16749
148. Wang H, Goh K, Xue R, Yu D, Jiang W, Lau R, Chen Y (2013) Sulfur doped Co/SiO₂ catalysts for chirally selective synthesis of single walled carbon nanotubes. *Chem Commun* 49(20):2031–2033
149. Wang H, Ren F, Liu C, Si R, Yu D, Pfefferle LD, Haller GL, Chen Y (2013) CoSO₄/SiO₂ catalyst for selective synthesis of (9, 8) single-walled carbon nanotubes: effect of catalyst calcination. *J Catal* 300:91–101
150. Wang H, Wei L, Ren F, Wang Q, Pfefferle LD, Haller GL, Chen Y (2013) Chiral-selective CoSO₄/SiO₂ catalyst for (9, 8) single-walled carbon nanotube growth. *ACS Nano* 7(1):614–626
151. Yuan Y, Karahan HE, Yıldırım C, Wei L, Birer O, Zhai S, Lau R, Chen Y (2016) “Smart poisoning” of Co/SiO₂ catalysts by sulfidation for chirality selective synthesis of (9, 8) single-walled carbon nanotubes. *Nanoscale* 8(40):17705–17713
152. Zhu H, Suenaga K, Wei J, Wang K, Wu D (2008) A strategy to control the chirality of single-walled carbon nanotubes. *J Cryst Growth* 310(24):5473–5476
153. Chiang WH, Sankaran RM (2009) Linking catalyst composition to chirality distributions of as-grown single-walled carbon nanotubes by tuning Ni_xFe_{1-x} nanoparticles. *Nat Mater* 8(11):882–886
154. Dutta D, Chiang W-H, Sankaran RM, Bhethanabotla VR (2012) Epitaxial nucleation model for chiral-selective growth of single-walled carbon nanotubes on bimetallic catalyst surfaces. *Carbon* 50(10):3766–3773
155. Kang L, Deng S, Zhang S, Li Q, Zhang J (2016) Selective growth of subnanometer diameter single-walled carbon nanotube arrays in hydrogen-free CVD. *J Am Chem Soc* 138(39):12723–12726
156. Ohashi T, Shima T (2015) Synthesis of vertically aligned single-walled carbon nanotubes with metallic chirality through facet control of catalysts. *Carbon* 87:453–461
157. Ohashi T, Iwama H, Shima T (2016) Growth of vertically aligned single-walled carbon nanotubes with metallic chirality through faceted FePt–Au catalysts. *J Appl Phys* 119(8):084303
158. Yang F, Wang X, Zhang D, Yang J, Luo D, Xu Z, Wei J, Wang J-Q, Xu Z, Peng F, Li X, Li R, Li Y, Li M, Bai X, Ding F, Li Y (2014) Chirality-specific growth of single-walled carbon nanotubes on solid alloy catalysts. *Nature* 510(7506):522–524
159. Yang F, Wang X, Zhang D, Qi K, Yang J, Xu Z, Li M, Zhao X, Bai X, Li Y (2015) Growing zigzag (16, 0) carbon nanotubes with structure-defined catalysts. *J Am Chem Soc* 137(27):8688–8691
160. Yang F, Wang X, Si J, Zhao X, Qi K, Jin C, Zhang Z, Li M, Zhang D, Yang J, Zhang Z, Xu Z, Peng L-M, Bai X, Li Y (2016) Water-assisted preparation of high-purity semiconducting (14, 4) carbon nanotubes. *ACS Nano* 11(1):186–193

161. An H, Kumamoto A, Takezaki H, Ohyama S, Qian Y, Inoue T, Ikuhara Y, Chiashi S, Xiang R, Maruyama S (2016) Chirality specific and spatially uniform synthesis of single-walled carbon nanotubes from sputtered Co–W bimetallic catalyst. *Nanoscale* 8(30):14523–14529
162. Zhang D, Yang J, Li Y (2013) Spectroscopic characterization of the chiral structure of individual single-walled carbon nanotubes and the edge structure of isolated graphene nanoribbons. *Small* 9(8):1284–1304
163. Bachilo SM (2002) Structure-assigned optical spectra of single-walled carbon nanotubes. *Science* 298(5602):2361–2366
164. Dresselhaus MS, Dresselhaus G, Saito R, Jorio A (2005) Raman spectroscopy of carbon nanotubes. *Phys Rep* 409(2):47–99
165. Maultzsch J, Telg H, Reich S, Thomsen C (2005) Radial breathing mode of single-walled carbon nanotubes: optical transition energies and chiral-index assignment. *Phys Rev B* 72(20):205438
166. Araujo PT, Pesce PBC, Dresselhaus MS, Sato K, Saito R, Jorio A (2010) Resonance Raman spectroscopy of the radial breathing modes in carbon nanotubes. *Physica E* 42(5):1251–1261
167. Qin L-C (2006) Electron diffraction from carbon nanotubes. *Rep Prog Phys* 69(10):2761–2821
168. Liu K, Hong X, Zhou Q, Jin C, Li J, Zhou W, Liu J, Wang E, Zettl A, Wang F (2013) High-throughput optical imaging and spectroscopy of individual carbon nanotubes in devices. *Nat Nanotechnol* 8(12):917–922
169. Wu W, Yue J, Lin X, Li D, Zhu F, Yin X, Zhu J, Wang J, Zhang J, Chen Y (2015) True-color real-time imaging and spectroscopy of carbon nanotubes on substrates by enhanced Rayleigh scattering. *Nano Res* 8(8):2721–2732
170. Naumov AV, Kuznetsov OA, Harutyunyan AR, Green AA, Hersam MC, Resasco DE, Nikolaev PN, Weisman RB (2009) Quantifying the semiconducting fraction in single-walled carbon nanotube samples through comparative atomic force and photoluminescence microscopies. *Nano Lett* 9(9):3203–3208
171. Kong J, Soh HT, Cassell AM, Quate CF, Dai H (1998) Synthesis of individual single-walled carbon nanotubes on patterned silicon wafers. *Nature* 395(6705):878–881
172. Pattinson SW, Ranganathan V, Murakami HK, Koziol KKK, Windle AH (2012) Nitrogen-induced catalyst restructuring for epitaxial growth of multiwalled carbon nanotubes. *ACS Nano* 6(9):7723–7730
173. Haynes WM (2015–2016) CRC handbook of chemistry and physics. CRC Press, Hammond
174. Geurts FWAH, Sacco A (1992) The relative rates of the boudouard reaction and hydrogenation of CO over Fe and Co foils. *Carbon* 30(3):415–418
175. Ding L, Tselev A, Wang J, Yuan D, Chu H, McNicholas TP, Li Y, Liu J (2009) Selective growth of well-aligned semiconducting single-walled carbon nanotubes. *Nano Lett* 9(2):800–805
176. Che Y, Wang C, Liu J, Liu B, Lin X, Parker J, Beasley C, Wong HSP, Zhou C (2012) Selective synthesis and device applications of semiconducting single-walled carbon nanotubes using isopropanol as feedstock. *ACS Nano* 6(8):7454–7462
177. Li W-S, Hou P-X, Liu C, Sun D-M, Yuan J, Zhao S-Y, Yin L-C, Cong H, Cheng H-M (2013) High quality, highly concentrated semiconducting single-wall carbon nanotubes for use in field effect transistors and biosensors. *ACS Nano* 7(8):6831–6839
178. Hou P-X, Li W-S, Zhao S-Y, Li G-X, Shi C, Liu C, Cheng H-M (2014) Preparation of metallic single-wall carbon nanotubes by selective etching. *ACS Nano* 8(7):7156–7162
179. Ibrahim I, Kalbacova J, Engemaier V, Pang J, Rodriguez RD, Grimm D, Gemming T, Zahn DRT, Schmidt OG, Eckert J, Rümmeli MH (2015) Confirming the dual role of etchants during the enrichment of semiconducting single wall carbon nanotubes by chemical vapor deposition. *Chem Mater* 27(17):5964–5973
180. Futaba DN, Goto J, Yasuda S, Yamada T, Yumura M, Hata K (2009) General rules governing the highly efficient growth of carbon nanotubes. *Adv Mater* 21(47):4811–4815
181. Resasco DE, Herrera JE, Balzano L (2004) Decomposition of carbon-containing compounds on solid catalysts for single-walled nanotube production. *J Nanosci Nanotechnol* 4(4):398–407
182. Barnard JS, Paukner C, Koziol KK (2016) The role of carbon precursor on carbon nanotube chirality in floating catalytic chemical vapour deposition. *Nanoscale* 8(39):17262–17270
183. Boudart M (1989) Virtual pressure and virtual fugacity in catalysis and electrocatalysis. *Catal Lett* 3(2):111–115
184. Iglesia E, Baumgartner JE, Price GL (1992) Kinetic coupling and hydrogen surface fugacities in heterogeneous catalysis: I. Alkane reactions on Te/NaX, H-ZSM5, and Ga/H-ZSM5. *J Catal* 134(2):549–571

185. Wang B, Poa CHP, Wei L, Li LJ, Yang Y, Chen Y (2007) (n, m) selectivity of single-walled carbon nanotubes by different carbon precursors on Co–Mo catalysts. *J Am Chem Soc* 129(29):9014–9019
186. He M, Jiang H, Kauppinen EI, Lehtonen J (2012) Diameter and chiral angle distribution dependencies on the carbon precursors in surface-grown single-walled carbon nanotubes. *Nanoscale* 4(23):7394–7398
187. Qi H, Yuan DN, Liu J (2007) Two-stage growth of single-walled carbon nanotubes. *J Phys Chem C* 111(17):6158–6160
188. Lu C, Liu J (2006) Controlling the diameter of carbon nanotubes in chemical vapor deposition method by carbon feeding. *J Phys Chem B* 110(41):20254–20257
189. Zhou W, Zhan S, Ding L, Liu J (2012) General rules for selective growth of enriched semiconducting single walled carbon nanotubes with water vapor as *in situ* etchant. *J Am Chem Soc* 134(34):14019–14026
190. Wang Y, Liu Y, Li X, Cao L, Wei D, Zhang H, Shi D, Yu G, Kajiura H, Li Y (2007) Direct enrichment of metallic single-walled carbon nanotubes induced by the different molecular composition of monohydroxy alcohol homologues. *Small* 3(9):1486–1490
191. Einarsson E, Murakami Y, Kadokawa M, Maruyama S (2008) Growth dynamics of vertically aligned single-walled carbon nanotubes from *in situ* measurements. *Carbon* 46(6):923–930
192. Navas H, Maruyama B, Weaver K, Paillet M, Zahab A-A, Fossard F, Loiseau A, Quesnel E, Anglaret E, Jourdain V (2014) Interplay of interfacial compounds, catalyst thickness and carbon precursor supply in the selectivity of single-walled carbon nanotube growth. *Carbon* 80:599–609
193. Wang B, Wei L, Yao L, Li LJ, Yang Y, Chen Y (2007) Pressure-induced single-walled carbon nanotube (n, m) selectivity on Co–Mo catalysts. *J Phys Chem C* 111(40):14612–14616
194. Inoue T, Hasegawa D, Badar S, Aikawa S, Chiashi S, Maruyama S (2013) Effect of gas pressure on the density of horizontally aligned single-walled carbon nanotubes grown on quartz substrates. *J Phys Chem C* 117(22):11804–11810
195. Shibuta Y, Maruyama S (2003) Molecular dynamics simulation of formation process of single-walled carbon nanotubes by CCVD method. *Chem Phys Lett* 382(3–4):381–386
196. Balbuena PB, Zhao J, Huang S, Wang Y, Sakulchaicharoen N, Resasco DE (2006) Role of the catalyst in the growth of single-wall carbon nanotubes. *J Nanosci Nanotechnol* 6(5):1247–1258
197. Li N, Wang X, Ren F, Haller GL, Pfefferle LD (2009) Diameter tuning of single-walled carbon nanotubes with reaction temperature using a Co monometallic catalyst. *J Phys Chem C* 113(23):10070–10078
198. Zoican Loebick C, Podila R, Reppert J, Chudow J, Ren F, Haller GL, Rao AM, Pfefferle LD (2010) Selective synthesis of subnanometer diameter semiconducting single-walled carbon nanotubes. *J Am Chem Soc* 132(32):11125–11131
199. Yao Y, Li Q, Zhang J, Liu R, Jiao L, Zhu YT, Liu Z (2007) Temperature-mediated growth of single-walled carbon-nanotube intramolecular junctions. *Nat Mater* 6(4):293–296
200. Zhao Q, Xu Z, Hu Y, Ding F, Zhang J (2016) Chemical vapor deposition synthesis of near-zigzag single-walled carbon nanotubes with stable tube-catalyst interface. *Sci Adv* 2(5):1501729
201. Cheng HM, Li F, Su G, Pan HY, He LL, Sun X, Dresselhaus MS (1998) Large-scale and low-cost synthesis of single-walled carbon nanotubes by the catalytic pyrolysis of hydrocarbons. *Appl Phys Lett* 72(25):3282–3284
202. Li J, Otsuka K, Zhang X, Maruyama S, Liu J (2016) Selective synthesis of large diameter, highly conductive and high density single-walled carbon nanotubes by thiophene-assisted chemical vapor deposition method on transparent substrates. *Nanoscale* 8(29):14156–14162
203. Yu B, Liu C, Hou P-X, Tian Y, Li S, Liu B, Li F, Kauppinen EI, Cheng H-M (2011) Bulk synthesis of large diameter semiconducting single-walled carbon nanotubes by oxygen-assisted floating catalyst chemical vapor deposition. *J Am Chem Soc* 133(14):5232–5235
204. Zhang L, Hou P-X, Li S, Shi C, Cong H-T, Liu C, Cheng H-M (2014) *In situ* TEM observations on the sulfur-assisted catalytic growth of single-wall carbon nanotubes. *J Phys Chem Lett* 5(8):1427–1432
205. Koziol KKK, Ducati C, Windle AH (2010) Carbon nanotubes with catalyst controlled chiral angle. *Chem Mater* 22(17):4904–4911
206. Yuan Y, Wei L, Jiang W, Goh K, Jiang R, Lau R, Chen Y (2015) Sulfur-induced chirality changes in single-walled carbon nanotube synthesis by ethanol chemical vapor deposition on a Co/SiO₂ catalyst. *J Mater Chem A* 3(7):3310–3319

207. Thurakitsee T, Kramberger C, Zhao P, Aikawa S, Harish S, Chiashi S, Einarsson E, Maruyama S (2012) Diameter-controlled and nitrogen-doped vertically aligned single-walled carbon nanotubes. *Carbon* 50(7):2635–2640
208. Zhang G, Qi P, Wang X, Lu Y, Mann D, Li X, Dai H (2006) Hydrogenation and hydrocarbonation and etching of single-walled carbon nanotubes. *J Am Chem Soc* 128(18):6026–6027
209. Liu Q, Ren W, Chen Z-G, Wang D-W, Liu B, Yu B, Li F, Cong H, Cheng H-M (2008) Diameter-selective growth of single-walled carbon nanotubes with high quality by floating catalyst method. *ACS Nano* 2(8):1722–1728
210. Tian Y, Timmermans MY, Kivistö S, Nasibulin AG, Zhu Z, Jiang H, Okhotnikov OG, Kauppinen EI (2011) Tailoring the diameter of single-walled carbon nanotubes for optical applications. *Nano Res* 4(8):807–815
211. Susi T, Nasibulin AG, Ayala P, Tian Y, Zhu Z, Jiang H, Roquelet C, Garrot D, Lauret J-S, Kauppinen EI (2009) High quality SWCNT synthesis in the presence of NH₃ using a vertical flow aerosol reactor. *Phys Status Solidi (b)* 246(11–12):2507–2510
212. Zhu Z, Jiang H, Susi T, Nasibulin AG, Kauppinen EI (2011) The use of NH₃ to promote the production of large-diameter single-walled carbon nanotubes with a narrow (*n*, *m*) distribution. *J Am Chem Soc* 133(5):1224–1227
213. Boršník U, Hodošček M, Janežič D, Lukovits I (2005) Electronic structure properties of carbon nanotubes obtained by density functional calculations. *Chem Phys Lett* 411(4–6):384–388
214. Gülsen O, Yıldırım T, Ciraci S (2002) Systematic ab initio study of curvature effects in carbon nanotubes. *Phys Rev B* 65(15):153405
215. Li J, Liu K, Liang S, Zhou W, Pierce M, Wang F, Peng L, Liu J (2014) Growth of high-density-aligned and semiconducting-enriched single-walled carbon nanotubes: decoupling the conflict between density and selectivity. *ACS Nano* 8(1):554–562
216. Yu B, Hou P-X, Li F, Liu B, Liu C, Cheng H-M (2010) Selective removal of metallic single-walled carbon nanotubes by combined *in situ* and post-synthesis oxidation. *Carbon* 48(10):2941–2947
217. Zhou W, Ooi YH, Russo R, Papanek P, Luzzi DE, Fischer JE, Bronikowski MJ, Willis PA, Smalley RE (2001) Structural characterization and diameter-dependent oxidative stability of single wall carbon nanotubes synthesized by the catalytic decomposition of Co. *Chem Phys Lett* 350(1–2):6–14
218. Lu J, Nagase S, Zhang X, Wang D, Ni M, Maeda Y, Wakahara T, Nakahodo T, Tsuchiya T, Akasaka T, Gao Z, Yu D, Ye H, Mei WN, Zhou Y (2006) Selective interaction of large or charge-transfer aromatic molecules with metallic single-wall carbon nanotubes: critical role of the molecular size and orientation. *J Am Chem Soc* 128(15):5114–5118



REVIEW

Preparation of Horizontal Single-Walled Carbon Nanotubes Arrays

Pan Li^{1,2} · Jin Zhang¹

Received: 31 July 2016 / Accepted: 16 November 2016 / Published online: 30 November 2016
© Springer International Publishing Switzerland 2016

Abstract The synthesis of SWNTs has achieved great success with the development of synthetic methodologies. From the viewpoint of exploiting the exceptional electrical properties of single-walled carbon nanotubes (SWNTs) in advanced applications, one of the most difficult challenges is how to assemble the SWNTs with high degrees of alignment and purity in electronic conducting (mainly semiconducting) behavior into functional nanodevices. Numerous approaches have been developed to reach this goal, which could be divided into two categories. One is direct preparation of SWNT arrays on the substrate, and the other is self-assembly of pre-sorted SWNTs from solution. The former one obtains SWNT arrays via chemical vapor deposition (CVD) growth, with the sorting realized by either selective growth or post-growth treatment; the latter one assembles SWNT into arrays from solution, with the sorting process occurring before the aligning process in most cases. This review will highlight both in situ and post-synthetic approaches for preparing samples of aligned arrays of SWNTs with well-defined electronic properties—including the working mechanism for directional growth of SWNTs, growth/sorting methods like catalyst engineering, cloning/cap engineering, in situ etching, and ex situ selective removal/etching for surface-grown SWNT sample, and assembling technologies from SWNT solution such as dielectrophoresis, adsorption

Chapter 3 was originally published as Li, P. & Zhang, J. Top Curr Chem (Z) (2016) 374: 85.
DOI 10.1007/s41061-016-0085-4.

✉ Jin Zhang
jinzhang@pku.edu.cn

¹ Center for Nanochemistry, Beijing Science and Engineering Technology Research Center for Low Dimensional Carbon Materials, College of Chemistry and Molecular Engineering, Peking University, Beijing 100871, People's Republic of China

² Key Laboratory for Organic Electronics and Information Displays and Institute of Advanced Materials, Nanjing University of Posts and Telecommunications, Nanjing 210046, People's Republic of China

on lithographically patterned and/or chemically functionalized substrates, Langmuir–Blodgett and Langmuir–Schaefer techniques, and evaporation-driven self-assembly—and research efforts towards direct growth of arrays of complex SWNT structures.

Keywords SWNT array · Semiconducting · Selective growth · Self-assembly

1 Introduction

The superb charge transport properties of single-walled carbon nanotubes (SWNTs) make them excellent candidates for various applications in electronics, including but not limited to radio frequency (RF) analog devices, flexible circuits, and heterogeneous integration of such systems onto complementary oxide semiconductor (CMOS) chips [1–3]. The structure of SWNTs is typically discussed in terms of graphene, where a SWNT can be made by rolling up graphene to form a seamless cylinder [4]. Many properties of a SWNT, such as the electronic properties and diameter, depend on the direction in which the graphene is rolled up to form the nanotube [5]. Normally, approximately 67% of SWNTs are semiconducting (s-SWNT) and 33% of SWNTs are metallic (m-SWNT) at room temperature [5]. However, to achieve uniform performance of electrical devices, SWNTs need to be monodisperse in their electronic type. For example, an important consideration for high-performance digital logic is the degree to which metallic nanotubes can be eliminated [3]. The SWNTs are normally produced by exposing a carbonaceous feedstock to a metal catalyst at high temperatures. The common means of synthesizing SWNTs including arc discharge, laser ablation, and chemical vapor deposition (CVD) produce SWNT samples that lack uniformity in their properties [6]. Progress has been made in controlling the electronic properties of SWNTs both during and after growth, aimed at producing identical populations of SWNTs [7, 8]. Although great efficiency for enriching surface-grown and bulk-phase semiconducting nanotubes have both been demonstrated, currently sorting with the aid of solution processing has been considered the more effective technique for better reproducibility and higher throughput [9, 10]. Furthermore, compared with random SWNT networks, large-scale and horizontally aligned SWNT arrays can effectively preclude both the mis-oriented ones and tube–tube connections, with the demonstrated ability to yield device performance approaching expectations based on the intrinsic properties of pristine SWNTs [11, 12]. In order to get SWNT samples with a high degree of alignment, researchers have invested substantial effort towards the development of post-synthetic assembly schemes and direct growth methods on crystal substrates. Another challenge facing carbon nanotube (CNT)-based electronic devices is low CNT growth densities. For example, to maximize device packing density and provide sufficient drive current (or power output) for each CNFET, dense, aligned arrays of electronically pure nanotubes will be required in practical integrated circuits (ICs) [13, 14]. In 2013, the IBM researchers stated that in order to realize SWNT-based ICs applications, the close-packed SWNT arrays should have $\geq 99.9999\%$ s-SWNT purity with a density higher than 125 tubes/ μm

[3]. Typically, the precise placement of carbon nanotubes with desired morphology and density on a substrate involves one of the following three techniques: direct growth of SWNT array on a substrate, transfer of grown nanotubes onto a target substrate via nanotube-captured solid mediate or solution dispersion, or self-assembly of nanotubes on a device substrate during deposition.

To achieve widespread use of the resulting SWNT arrays in commercial applications, beyond having the highest possible purity and array density, an ideal preparation strategy should also be: (1) scalable (that is, it should be possible to ramp up the process to produce more material to meet the anticipated increases in demand); (2) universal (which yielding similar results between different systems when the same procedure is used for a selective growth method, or compatible with a wide range of as-synthesized SWNT samples with different SWNT lengths and diameters for post-growth sorting method); (3) nondestructive (that is, the remarkable properties of SWNTs should not be degraded during selective growth or sorting); (4) free from additional contamination or unwanted structures like bundles that affect the device performance in most applications. This review highlights progress towards these goals with an emphasis on recent developments.

We will highlight both *in situ* and post-synthetic approaches for preparing samples of aligned arrays of SWNTs with well-defined electronic properties. Figure 1 shows an overview of the main content of this review. We will first present the main working mechanisms for directional growth of SWNT arrays on surfaces via CVD. The efforts on improving the tube density in the array and direct growth of arrays of complex SWNT structures will be introduced as well. Then, the preparation strategies will be covered and discussed by referring to two main categories: one category covers *in situ* or *ex situ* sorting for CVD-grown aligned arrays of SWNTs on substrates, with growth/sorting methods such like catalyst engineering, cloning/cap engineering, *in situ* etching, and *ex situ* selective removal/etching methods, as well as strategies for density improvement including particular catalyst design, multiple-cycle growth and multiple transfer. The other is about assembling separated SWNTs from solution into aligned arrays under directional guidance such as an external electric field and a shear force, with specific assembling technologies that include dielectrophoresis, adsorption on lithographically patterned and/or chemically functionalized substrates, Langmuir–Blodgett and Langmuir–Schaefer techniques, and evaporation driven self-assembly.

2 Orientational Growth of SWNTs

To obtain horizontally aligned arrays of SWNTs with desired properties, many different methods have been developed. Among various technologies, CVD growth of SWNTs on substrates has attracted lots of research interest because it can offer the levels of perfection in quality, lengths, arrangements, alignment, and linearity required for most applications in electronics [27]. Additionally, the CVD growth method is compatible with the standard fabrication procedure of silicon-based devices [28, 29]. In this section, synthesis of SWNT arrays via CVD method will be discussed beginning with an introduction to the alignment modes during the growth

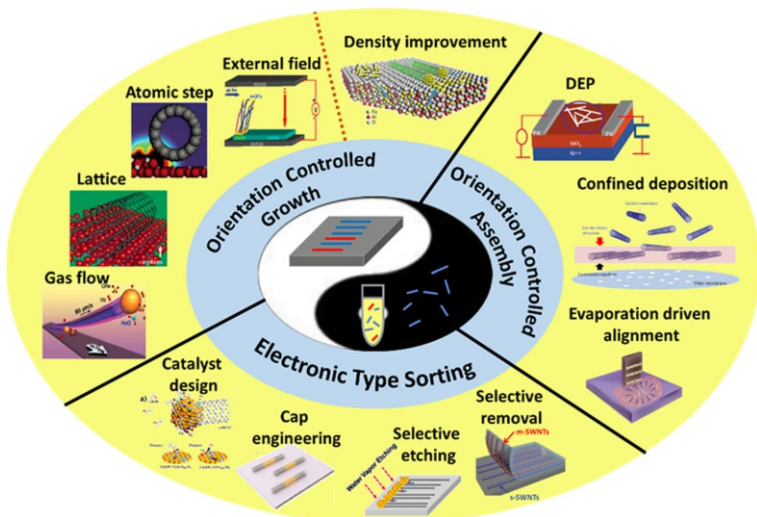


Fig. 1 Recent developments in preparation strategies for horizontally aligned SWNT arrays. The orientation controlled growth of SWNT arrays on substrate by different guiding modes, with representative works shown in the figure: gas flow-directed mode (corresponding figure is reproduced with permission [15], Copyright 2010, American Chemical Society), crystallographic lattice-guided mode (corresponding figure is reproduced with permission [16], Copyright 2005, American Chemical Society), atomic step-guided mode (corresponding figure is reproduced with permission [17], Copyright 2004, Wiley–VCH), and external field-directed mode (corresponding figure is reproduced with permission [18], Copyright 2011, Elsevier), and methods for improving the array density (corresponding figure is reproduced with permission, [19] Copyright 2015, Nature Publishing Group), are covered. Then both in situ and ex situ sorting technologies for the surface-grown SWNTs are also introduced, with representative strategies described in following references: catalyst design (corresponding figure is reproduced with permission [20], Copyright 2015, American Chemical Society), cap engineering (corresponding figure is reproduced with permission [21], Copyright 2012, Nature Publishing Group), selective etching (corresponding figure is reproduced with permission [22], Copyright 2014, American Chemical Society) and selective removal (corresponding figure is reproduced with permission [23], Copyright 2011, Wiley–VCH). Afterwards, arranging of SWNT into aligned arrays from pre-sorted SWNT solution via self-assembly techniques are presented, with typical methods described in following reference: dielectrophoresis (DEP) (corresponding figure is reproduced with permission [24], Copyright 2011, American Chemical Society), confined deposition (corresponding figure is reproduced with permission, [25] Copyright 2016, Nature Publishing Group), and evaporation driven alignment (corresponding figure is reproduced with permission [26], Copyright 2014, American Chemical Society)

process. Based on the guiding force for nanotube alignment, current guided growth methods can be classified into three categories: gas flow-directed growth [30], surface-guided growth [17, 31], and external field-assisted growth [32]. Figure 2 gives an illustration on these guiding modes and their corresponding typical growth results.

2.1 Gas Flow-Directed Growth

As shown in Fig. 2a, the gas flow-directed growth of nanotubes is realized through lifting the catalyst nanoparticle away from the substrate surface and maintaining the floating state of the nanoparticle and the attached nanotube. Thus, the aligned orientation of CNTs is entirely controlled by gas flow [15]. Catalyst–substrate

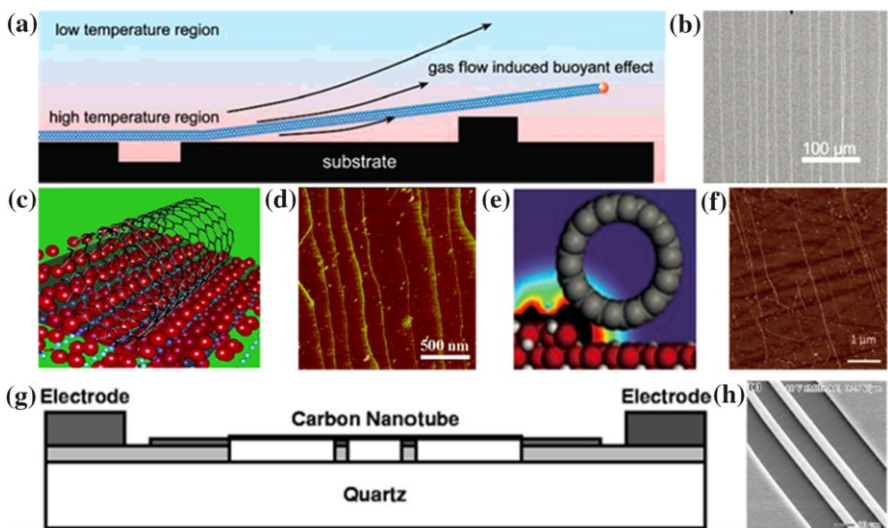


Fig. 2 Orientation controlled growth of SWNTs with different guiding modes. **a, b** Gas flow-directed growth mode and the SWNT arrays grown by ultra-low feeding gas (reproduced with permission, [37] Copyright 2007, American Chemical Society). **c, d** Lattice-directed growth mode and the SWNT array grown on sapphire substrate (reproduced with permission [16], Copyright 2005, American Chemical Society). **e, f** Nano-step-guided growth mode and the obtained SWNTs (reproduced with permission [41], Copyright 2005, American Chemical Society). **g, h** Electric field-directed growth mode and the aligned SWNTs (reproduced with permission [32], Copyright 2005, AIP Publishing LLC)

interaction and flow stability are the key factors to optimize both the lift-up process and the floating process. For the lift-up stage, a sufficiently high temperature is required because the interactions between catalyst/SWNT and the substrate can be significantly weakened with increasing temperature, as proved in the “fast-heating” CVD method [33]. The temperature difference resulting from rapid heating causes a convection flow, which can lift up some nanotubes with the catalyst. To realize the purpose of decreasing the catalyst–substrate interaction, the catalyst system was also specially designed. For example, silica nanoparticles were dispersed on the substrate surface to hinder the catalyst–substrate interaction [34], and Cu was preferred as the catalyst to promote the growth of aligned SWNTs because this metal possesses weaker interactions with SiO_2 than Fe does [35, 36]. Besides the fast heating, ultra-low feeding speed of the gases is considered as another factor that is important for guiding aligned ultra-long SWNT arrays [37]. The ultra-low gas speed helps generate steady laminar flow, which allows the catalyst/SWNT to remain floating above the substrate surface (Fig. 2a). The floating catalyst has substantially improved lifetime and activity because it is free from the interaction with the substrate. The synthesis of ultra-long SWNTs by the gas flow directed mode (Fig. 2b) is believed to benefit from a superior growth rate [37]. In this way, Zhu et al. reported the synthesis of a 4 cm-long individual SWNT at a rate of 11 $\mu\text{m}/\text{s}$ in 2004 [38]. Although the gas flow-directed growth method produced ultra-long SWNTs, bottlenecks still exist for requirements such as increasing the extremely low tube density, and improvement of the alignment and linearity [34, 39].

2.2 Surface Structure-Guided Growth

Surface guided growth of SWNTs by CVD on crystalline substrates such as sapphire and quartz can produce arrays of SWNTs with nearly ideal arrangements. Both theoretical and experimental studies of the alignment process of SWNTs have been conducted to understand the underlying mechanisms in depth. Overall, the surface-directed growth mode is essentially governed by anisotropic van der Waals interactions between SWNT and substrate. Depending on the specific surface structure that provide the guiding force, the SWNTs can form in epitaxy along a lattice direction [16, 40], or in graphoepitaxy along faceted nanosteps [17, 41] and/or etched trenches [42], which are defined as lattice-directed (Fig. 2c, d) and nanostep-directed mode (Fig. 2e, f) respectively.

The first report on oriented growth of SWNTs by crystallographic lattices was on Si (100) and (110) substrates [31]. Subsequently, this kind of substrate were extended to sapphire (A- and R-plane of α -Al₂O₃), and mis-cut quartz (Y-, ST-, R-, and Z-cut) for growing SWNT aligned in only one direction [29]. Additionally, MgO, mica, and graphene have been explored to prepare other ordered structures with special morphologies following the lattice directions [43, 44]. Theoretical simulations with quartz as the substrate revealed the existence of an energetically favorable direction, predicting that SWNTs would orient along molecular-scale topological grooves that exist in that direction on the surface of the substrate [27]. On the other hand, by varying the miscut orientation and annealing conditions of the sapphire substrate, it was observed that graphoepitaxy led to the formation of either well-aligned straight SWNTs, or to wavy nanotubes loosely conforming to sawtooth-shaped faceted nanosteps. Specific nanotube geometries were as shown in Fig. 2f. [41]. Furthermore, a specially fabricated sapphire surface with numerous faceted nano-steps was also proven able to regularly induce a particular orientation and conformation of SWNTs. The SWNTs obtained completely reflected the atomic features on the surface, such as crystalline facets, defects, and kinks [45].

It is noteworthy that clear competition between lattice-directed and nanostep-directed modes presented during SWNT growth have been observed on both sapphire and quartz substrates. Ago et al. found these two modes can cooperate to build curved networks of SWNTs, on A-plane sapphire with a large mis-cut angle [46], while Li et al. synthesized arrays of kinked SWNTs on ST-cut quartz by utilizing the cooperation and competition between the two modes [47].

2.3 External Field-Directed Growth

Besides gas flow and surface nano-structure, external fields, such as the electric and magnetic fields [32, 48], have also been introduced to align SWNTs during growth. Electrical polarizability along a nanotube axis is much higher than that along its radial direction, so that SWNTs tend to align parallel to an applied electric field. In this way, a force can be applied to rotate and align the SWNTs, as shown in Fig. 2g, h. Dai's group first used electric fields (EF) to guide the growth of SWNTs and found that the SWNTs could be well aligned even when the electric field was perpendicular to gas flow [32]. Interestingly, Peng et al. discovered that when an EF

was introduced during gas flow-guided growth of SWNT array, the proportion of m-SWNTs was increased [18]. The nanotubes were polarized and the electric field force helped lift them into the laminar flow. The greater polarizability of m-CNTs compared to s-CNTs resulted in more m-CNTs lifted and an increased m- to s-CNT ratio in the array. The peak percentage of m-CNTs could reach 80% under EF-assisted CVD. This is the first time that the role of electric field was fully investigated for *in situ* sorting of m-/s-SWNTs. Magnetic fields had already been utilized to direct the growth orientation of SWNTs with the SWNTs aligned parallel to the applied magnetic field [48].

Comparing these three exploited-growth modes, it is obvious that CVD growth of large-scale, well-aligned SWNT arrays via surface-directed mode produced the best results. On both quartz and sapphire, the levels of nanotube alignment can be controlled to better than 0.01° , with linear shapes to within a few nanometers over lengths of many micrometers, and average tube lengths reach hundreds of micrometers (up to \sim millimeters) [16, 28, 49]. The highest density ever reported was ~ 160 SWNTs/ μm [50]. Sorting strategies could be applied at any stage starting from the nucleation of nanotubes, to early/whole growth stage and after growth.

2.4 Density Improvement Method

As has been mentioned, the outstanding performance of the CNT-based transistors can be fully explored only with high-density integration of nanotubes, a high degree of alignment, and the high-purity enrichment of s-SWNTs. SWNT arrays with high density would afford a nanotube-based device higher current, more robust performance, and thus guarantee smaller device-to-device variation, which represents ideal formats for integration. Great progress on preparing horizontally aligned arrays of SWNT with high density has been made by using highly efficient catalyst, multi-growth/transfer technique, and comprehensive optimization of the basic growth parameters, as summarized in Fig. 3a. These research efforts are believed to provide a desirable platform for the electronic-type controlled preparation of SWNTs.

2.4.1 Trojan Catalyst Technique

The essence of growing high-density SWNT array is considered to be maintaining a high density of active catalysts during growth, thus giving catalyst nanoparticles more opportunity to nucleate SWNTs, and providing new catalysts during SWNT growth. A clever method proposed by Hu et al. is continuously and gradually releasing iron catalysts that have been pre-embedded in a sapphire substrate (Fig. 3b) [19]. Horizontally aligned SWNT arrays with a density of 130 SWNTs/ μm were synthesized through the use of these so-called Trojan catalysts. Researchers from the same group introduced Mo catalyst particles to help suppress agglomeration of Fe nanoparticles in the Trojan catalyst [51]. Mo was reported as being able to help suppress agglomeration of Fe nanoparticles on sapphire substrates, thus improving the SWNT yield as well as reproducibility [52]. This design successfully

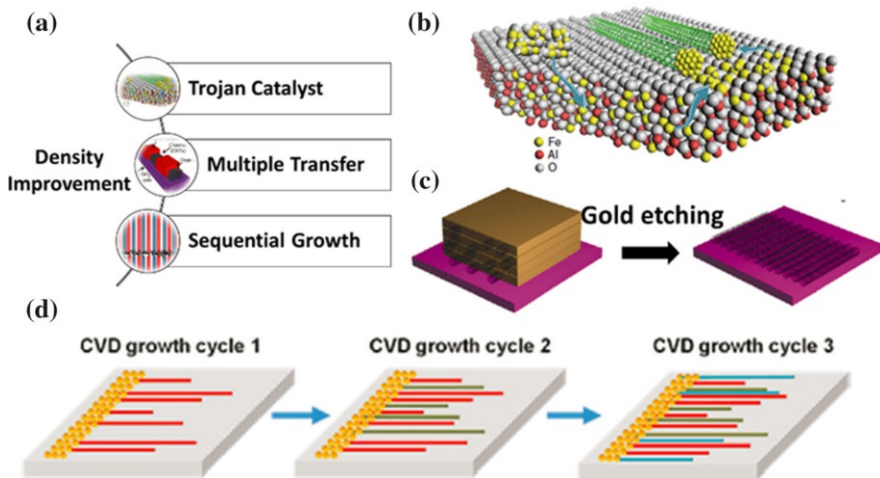


Fig. 3 Preparation of high-density SWNT arrays on substrate surface. **a** Scheme on strategies for increasing the nanotube density in the SWNT arrays by improving the growth efficiency or multiple transfer technique; **b** Growth of ultra-high density SWNT array by using “Trojan catalyst” (reproduced with permission [19], Copyright 2015, Nature Publishing Group). **c** Preparation of high-density aligned SWNTs by stacked multiple transfer method (reproduced with permission [55], Copyright 2011, American Chemical Society). **d** Multiple-cycle CVD method for synthesis of horizontally aligned arrays of SWNTs with high density (reproduced with permission [56], Copyright 2011, American Chemical Society)

expanded the growth area of SWNT arrays and increased the array density to as high as 160 tubes/ μm .

2.4.2 Multiple Growth/Transfer Technique

Multiple growth or transfer represents simple routes to improve the density of SWNT arrays [22, 53–56]. Preparation of high-density aligned SWNTs has been reported by a stacked multiple transfer method, which transferred nanotubes through multiple sacrificial layers, as illustrated in Fig. 3c [55]. A linear increase in drain-source currents of CNT-based FETs was realized by the linear increase of nanotube density. The multiple growth approach relies on multiple, separate CVD growth cycles on a single substrate. A typical multi-cycle growth process is shown in Fig. 3d. In principle, this process can be extended to triple, quadruple, and quintuple growths and beyond. However, most works have found that the percentage increase in density diminished with multiple cycles [53]. As to the multiple transfer techniques, they can, in principle, linearly increase CNT density on the target substrate without limits. Nonetheless, the alignment of SWNTs gets harder to maintain as the number of transfers increases [54]. One interesting example for obtaining SWNT arrays based on the transfer method is that of transforming random SWNT films grown on SiO_2 substrates onto a receiving surface by sliding the growth substrate during the transfer process [57].

Other than the technology mentioned above, optimization of basic approach was also tried and demonstrated effective in producing high-density SWNT arrays. The effects of basic synthetic parameters such as metal catalyst and gas composition on nanotube density have been systematically studied [58]. There are many reports on comprehensively optimizing the basic growth conditions such as the catalyst material, substrate annealing, and the catalyst patterning for density improvement of the SWNT arrays [28, 59–61].

2.5 Growth of Arrays of Complex SWNT Structures

With SWNT arrays having perfect alignment representing the most promising building block for future electronic devices, the preparation of arrays of SWNTs with special morphologies such as bends, loops, kinks, intramolecular junctions, and crossbars is believed to bring many new important properties for different functional nanosystems [36, 62]. Compared with the special structures produced by post-growth assembly methods, direct growth can retain the intrinsic properties of nanotubes. Zhang's group has reported preparation of intramolecular junctions, which was realized by altering the diameter of a SWNT during its elongation by changing the growth temperature rapidly (Fig. 4a) [62]. Serpentine/kinked SWNTs have all been synthesized by combining the lattice-guided growth mode with other forces, with remarkable device performance observed for serpentine nanotubes [47, 63, 64]. Moreover, synthesis of SWNT serpentines with controlled length, density, and number of parallel tube segments was realized by a controlled landing process, as shown in Fig. 4b. The synthesis of cross bar structures has been realized by several approaches, mainly involving combinations of guiding forces from the gas flow, the lattice, and the electric field [36, 65, 66]. As illustrated in Fig. 4c and 4d, SWNT cross-bar with node density up to $10^7/\text{cm}^2$ were prepared by a “one-batch” approach, which was based on a combination of gas flow-directed growth mode and lattice-orientated growth mode [36]. During the CVD process, the direction of gas flow and the direction of lattice of the substrate were perpendicular to each other.

3 Selective Preparation of s/m-SWNT Arrays

3.1 Catalyst Design

For the controlled growth of SWNTs in a CVD system, either the generally accepted vapor–liquid–solid (VLS) mechanism [67, 68] or the newly developed vapor–solid–solid (VSS) mechanism [69–71] points to the importance of engineering the catalyst nanoparticle appropriately. Basically, the catalyst nanoparticles have two essential functions during the formation of SWNTs, which are (1) catalyzing the decomposition of carbon resource gases and (2) serving as centers for SWNT nucleation and growth. Hence, composition, morphology and surface lattice of the catalyst nanoparticles may all be tuned to affect the structure and growth efficiency of the SWNTs that are grown. For example, the catalysts with the desired atomic

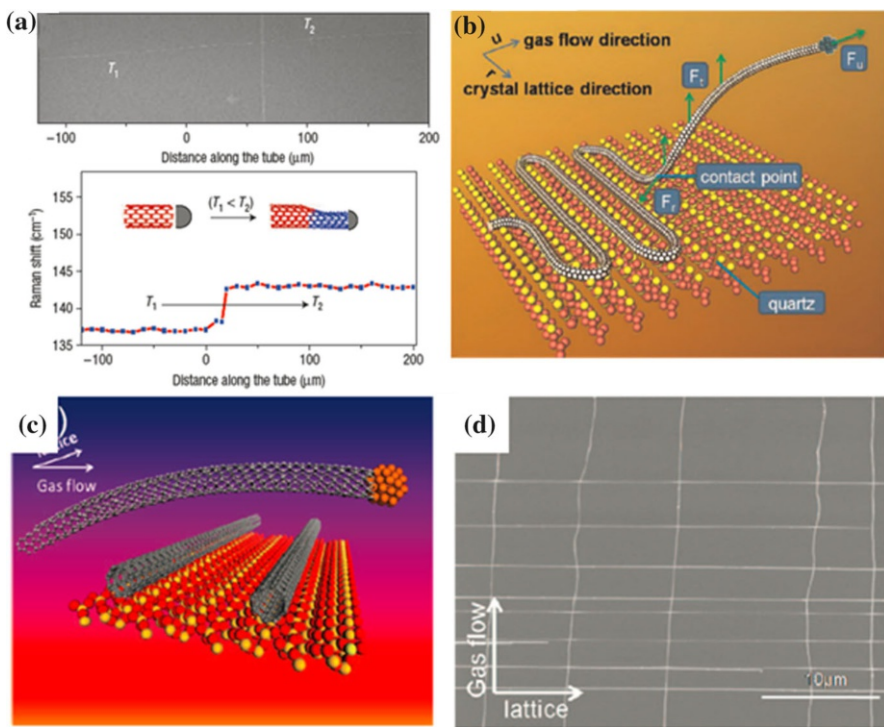


Fig. 4 Growth of arrays of special SWNT structures. **a** Temperature-mediated growth of SWNT intramolecular junctions (reproduced with permission [62], Copyright 2007, Nature Publishing Group). **b** Crinkling SWNT into serpentine by a controlled landing process (reproduced with permission [64]. Copyright 2009, Wiley–VCH). **c, d** One-batch growth of SWNT cross-bar (reproduced with permission [36]. Copyright 2009, American Chemical Society)

arrangements in their crystal planes were successfully used as structural templates for chirality-specific growth of SWNTs [72]. Yang et al. developed a new family of catalysts, tungsten-based intermetallic compounds, to facilitate the growth of SWNTs with designed chirality [73]. By the use of W_6Co_7 catalysts, (12, 6) SWNTs were grown with purity higher than 92%, which is considered due to a good structural match between the carbon atom arrangement around the nanotube circumference and the metal atom arrangement of (0 0 12) planes in the catalyst. Although more efforts are still needed, the production of structure-pure SWNT arrays based on such a catalyst design is considered quite promising.

Generally speaking, the structure-controlled growth of SWNTs via catalyst design is realized by two pathways: one is the structural match between SWNTs and the catalysts makes the growth of SWNTs with specific structure thermodynamically favorable, and the other is manipulation of growth kinetics for SWNTs to suppress the growth of the unwanted SWNT species. As indicated in Fig. 5a, based on the chemical composition of the catalyst, the catalyst used for controlled growth of SWNT array is categorized into three kinds, which are monometal (mainly Fe),

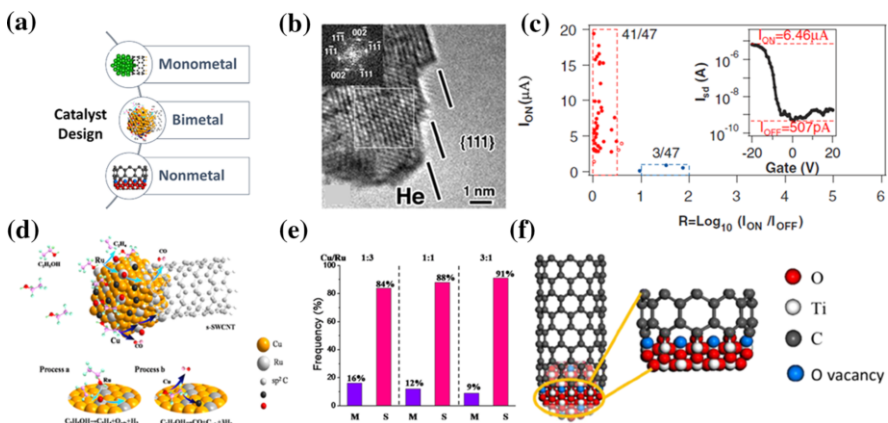


Fig. 5 Catalyst design strategy for preferential growth of s-/m-SWNT arrays on substrate surface. **a** Scheme on typical catalysts used for realizing growth of arrays of SWNT with specific electronic type. **b, c** Growth of SWNT arrays with enriched m-SWNTs (reproduced with permission [74], Copyright 2009, the American Association for the Advancement of Science). **d, e** Preferential growth of s-SWNTs by bimetal catalysts consisting of Ru or Pd metal (reproduced with permission [20], Copyright 2015, American Chemical Society). **f** Selective growth of s-SWNTs by oxygen-deficient TiO₂ nanoparticles (reproduced with permission [50], Copyright 2015, American Chemical Society)

bimetal, and nonmetal catalysts (metal oxide and metal carbide). Selective growth methods corresponding to different catalysts would be discussed as follows.

3.1.1 Monometal Catalyst

Although precise control of catalyst structure may be the key issue for realizing selective growth, the preparation of uniform catalyst nanoparticles is still a big challenge. In addition, the catalyst nanoparticles tend to change their structure and dispersion state at the synthesis temperatures. However, Harutyunyan et al. were able to synthesize metallic-enriched SWNTs through manipulation of the morphology and coarsening behavior of Fe catalyst particles in different inert gases [74]. Although the relationship between catalyst structure and the electronic properties of the resulting nanotubes still remains unclear, faceted iron particles with sharp corners as shown in Fig. 5b, which are pre-annealed in He, are considered to be responsible for the selective growth. Since etching effects are mostly applicable for removing or hindering the growth of m-SWNTs, this method is of great significance for yielding sample with the fraction of metallic nanotubes being increased from one-third of the population to a maximum of 91% (Fig. 5c). Intriguingly, through manipulation of SWNT–catalyst interfacial formation energy, chirality controlled growth of SWNT has been proven in a new CVD process [75]. This specially designed growth system periodically changed temperature to vary SWNT chirality multiple times during elongation to finally reach the energetically preferred SWNT–catalyst interface. This method provided an innovative platform for achieving enrichment of any SWNT with low SWNT–catalyst interfacial

formation energy, including those with specific electronic properties by careful catalyst design and treatment.

3.1.2 Bimetal Catalyst

Other than the traditional catalytic metal such as Fe, Co, and Ni, more and more metal, oxide and carbide have been demonstrated as effective at catalyzing growth of SWNTs. Furthermore, the unique properties of the new catalytic materials enable them to preferentially catalyze the growth of SWNTs with special structures. For example, bimetal catalysts consisting of Ru or Pd have been proved capable of preferentially growing s-SWNTs (Fig. 5d) [20]. Ru or Pd metal was supposed to selectively scissor C–O and C–C bonds of ethanol molecules to produce absorbed oxygen (O_{ads}), which creates a feasible oxidative environment to eliminate the m-SWNTs during growth. Since the counterpart metal in the corresponding bimetallic metal such as Cu provided C_{ads} for the growth of SWNTs, the ratio between the two component metals needs to be tuned to balance the etching process and the carbon accumulation process and thus realize the highest s-SWNT purity, as shown in Fig. 5e. SWNT arrays on a ST-cut quartz surface with a s-SWNT ratio of about 93% and a high density of 4–8 tubes/ μm was obtained using Au/Pd (1:1) catalyst.

3.1.3 Nonmetal Catalyst

There is an argument that during high temperature growth, the metal catalyst particles are usually in a liquid or partial liquid state with fluctuating sizes and structures, which makes it difficult to obtain SWNT arrays with a predefined and precisely controlled structure. Therefore, catalysts remaining in a solid state during the CVD process are favorable for structure control of SWNTs. TiO_2 nanoparticles were chosen because of their high melting point and good stability against strong reduction under SWNT growth conditions [50]. More importantly, TiO_2 nanoparticles with a certain concentration of oxygen vacancies are theoretically predicted to have a lower formation energy between s-SWNT than m-SWNT. The interface between SWNT and TiO_2 nanoparticle with oxygen vacancies is as depicted in Fig. 5f. By varying the sintering atmosphere, the concentration of oxygen vacancies in nano-sized TiO_2 can be modulated to affect the SWNT– TiO_2 interface properties, to selectively grow s-SWNTs. In addition, with TiO_2 nanoparticles remaining solid and to reduce catalyst aggregation, and with no etching process for nanotubes involved, the growth efficiency is significantly increased, dense SWNT arrays with a density of ~10 tubes/ μm was obtained. Other semiconductor oxide nanoparticles (i.e., ZnO , ZrO_2 , and Cr_2O_3) with an appropriate amount of oxygen vacancies have also proved to be successful catalysts for the selective growth of s-SWNTs. There is an urgent demand for s-SWNT arrays with specific diameters for the applications in nanoelectronic devices. It is worth mentioning that solid Mo_2C nanoparticles were found able to selectively catalyze the scission of C–O bonds of ethanol molecules, and thus produce O_{ads} to preferentially etch m-SWNTs [76]. Moreover, by synthesizing Mo_2C nanoparticles with monodisperse sizes on a substrate, the

s-SWNT arrays obtained had very narrow diameter distribution ($\sim 85\%$ between 1.0 and 1.3 nm), which is believed to benefit their application in nanoelectronic devices.

3.2 Cap Engineering

Epitaxial growth of SWNTs, the use of a well-defined template molecule or high melting point metal nanoparticle to unambiguously dictate the diameter and helicities of the resulting SWNTs, appears to be a promising strategy for controlling the structure of SWNTs [77]. Using various nanocarbon segments as template is also known as cloning synthesis [78]. However, compared to the cap structures formed around the catalyst nanoparticles, which may remain liquid droplets and alter their original sizes and structures during growth, the structure of the cap formed at a nanotube-segment predetermines the chirality of the whole SWNT and remains stable if the growth conditions are maintained. The nanotube segments that have been used as template for the SWNT growth are summarized in Fig. 6a. In this section we will mainly review the progress in nanotube-segment-mediated SWNT synthesis and its efficiency for controlled growth.

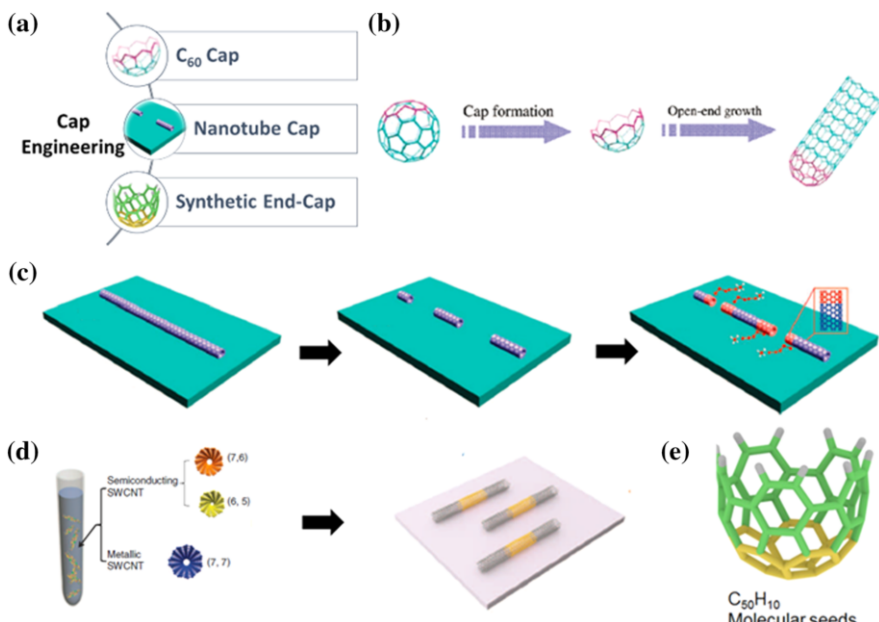


Fig. 6 Cap engineering for controlled growth of SWNT arrays on substrate surface. **a** Summary on the candidate materials that have been used for structure-controlled growth via cap engineering. **b** SWNT growth using fragmented C_{60} as an initiating cap (reproduced with permission [79], Copyright 2010, American Chemical Society). **c** Cloning growth via open-end growth mechanism (reproduced with permission [78], Copyright 2009, American Chemical Society). **d** Synthesis of SWNT with controlled chirality using VPE (reproduced with permission [21], Copyright 2012, Nature Publishing Group). **e** Growth of s-SWNTs from end-cap molecules (reproduced with permission [84], Copyright 2015, American Chemical Society)

A meaningful advance was made by Yu et al. who used opened C_{60} molecules with a desired size as the hemispherical caps to epitaxially control SWNT chirality (Fig. 6b) [79]. The importance of the size and edge structure of C_{60} caps on the structure of the grown nanotubes was emphasized and efficiently engineered by tuning the thermal treatment conditions. The diameter distributions of the as-grown SWNTs exhibited a step-like distribution, distinct from the SWNTs grown by traditional metallic catalysts. This indicates the possibility of growing nanotubes with specific diameters by treating the nano carbon segments in a controlled manner to get seeds with different sizes and edge states. Ibrahim et al. performed systematic investigations into the role of the dispersing media for C_{60} and oxygen-based groups during the development of nanotubes, which is believed to significantly advance our understanding of the growth mechanisms involved in all-carbon catalyst-free growth of SWNTs [80].

Predesigned nanotube segments may act as better seeds for the synthesis of SWNTs because SWNTs are expected to inherit chirality from the seed tubes. The concept of SWNT “amplification” was first proposed by Smalley and coworkers in 2005 [81]. They docked metal catalyst nanoparticles to the open ends of SWNTs and subsequently activated them to restart the SWNT growth epitaxially by introducing carbon feedstock. However, two obstacles need to be solved before this “amplification” method can efficiently yield chirality-controlled SWNTs. First, catalyst nanoparticles need to be attached to the open ends of nanotubes precisely, which is challenging; second, growth of newly nucleated nanotubes from the metal nanoparticles instead of the preexisting tube–particle interface should be suppressed. The “cloning” growth method developed by Zhang and coworkers in 2009 showed that open-ended SWNTs could be duplicated without the help of metal nanoparticles [78]. The experimental procedure for “cloning” growth is illustrated in Fig. 6c. Specifically, the chirality of the parent SWNT segment was retained by the elongated part, which was proved by the two parts giving identical Raman shifts. Moreover, without the catalyzing effect from the metal catalyst nanoparticles, the growth efficiency and rate were promoted by two means. One is introducing a C_2H_4 source to accelerate the decomposition of CH_4 ; the other is using single-crystal quartz as the substrate, which greatly improved the cloning yield from 9% on SiO_x to 40% on quartz.

Recently, the efficiency of such catalyst-free epitaxial growth was further improved by Zhou and coworkers (Fig. 6d) [21]. The starting SWNT segments were separated SWNTs with chirality purity of up to 90%. The vapor-phase epitaxy (VPE) cloning mechanism is to incorporate certain pyrolysis products into a graphitic carbon structure defined by the purified SWNT seed via Diels–Alder cycloaddition. The Diels–Alder reaction requires the presence of armchair sites on the SWNT edge, which consequently results in a chirality-dependent growth rate. The near-armchair (6, 5) nanotubes were found to grow noticeably faster than the near-zigzag (9, 1) nanotubes. Surprisingly, the conclusion of chirality-dependent SWNT growth rate for VPE agrees well with model proposed by Ding et al. for metal-catalyzed SWNT growth [82]. Another work by the same group discovered that the growth rates of nanotubes increased with their chiral angles while the active lifetimes of the growth showed the opposite trend [83]. For the first time, these

results correlated the cloning growth behaviors with the atomic arrangements of nanotube, providing new insight into the cloning growth of SWNTs.

Recent work by Zhou's group combines bottom-up organic chemistry synthesis with vapor phase epitaxy elongation to grow exclusively s-SWNT arrays [84]. This work shared the similar innovative constructing concept with the pioneer work to selectively synthesize (6, 6) SWNT on Pt (111) surface [85]. $C_{50}H_{10}$, an organic molecule with the hemispherical structure as shown in Fig. 6e, was used as the nanotube-end-cap molecule to initiate growth of the SWNT. The key to their success is the utilization of the strong correlation between the electronic properties of SWNTs and their diameters. Both theoretical and experimental studies revealed that metallic and semiconducting nanotubes have different stabilities, with the former ones generally less stable than semiconducting ones. By pretreating the seed molecules, it was guaranteed that most SWNTs grow from individual molecules or very small aggregates and thus have small diameter. The narrow diameter distribution is supposed to further help confine the electronic properties of the nanotubes. A chirality-changed growth model was proposed based on the theoretical calculation, and was believed to be one of the important origins for the selective growth.

Overall, the use of SWNT segments offers a straightforward pathway to directly obtain SWNTs with specific chirality. However, the improvement of the activity of nanocarbon seeds, which determines the growth rate and yield of SWNTs, is still a great challenge. An essential factor for an efficient cloning process is the annealing process in an oxidative atmosphere (air, water vapor, and oxygen plasma). The oxidation and subsequent hydrogen or water treatment are speculated to alter the functional groups on nanotube ends and expose more reactive hydrogen-terminated sp^2 carbon edges for growth. The thermal stability of the nanocarbon seeds and precision of the structure control will all be affected, potentially reducing the improvement efficiency. Another problem is the lack of a clear growth mechanism; this problem could be satisfactorily solved with *in situ* observation. Solutions to these limitations are still needed to pave the way to large-scale production of structure-controlled SWNTs via cloning growth.

3.3 In Situ Etching Method

Differences in the chemical reactivity and electronic properties of s-SWNTs and m-SWNTs are usually utilized to etch/remove away the kind of nanotubes that react/respond more strongly to the introduced reagents or applied field. Owing to the small energy band gap near the Fermi level in the density of states of s-SWNTs, m-SWNTs are more reactive than s-SWNTs when their diameters are similar [86]. Based on the environment in which the reaction occurs, the separation methods will be discussed from two aspects, *in situ* etching and *ex situ* etching/removing. For the *in situ* growth separation of s-/m- SWNTs, two approaches have been proposed, which are etching via weak oxidation and perturbation via an external field. As shown in Fig. 7a, a weak oxidation function could be offered either by using special carbon resource molecules or by the introduction of reagents with proper oxidative

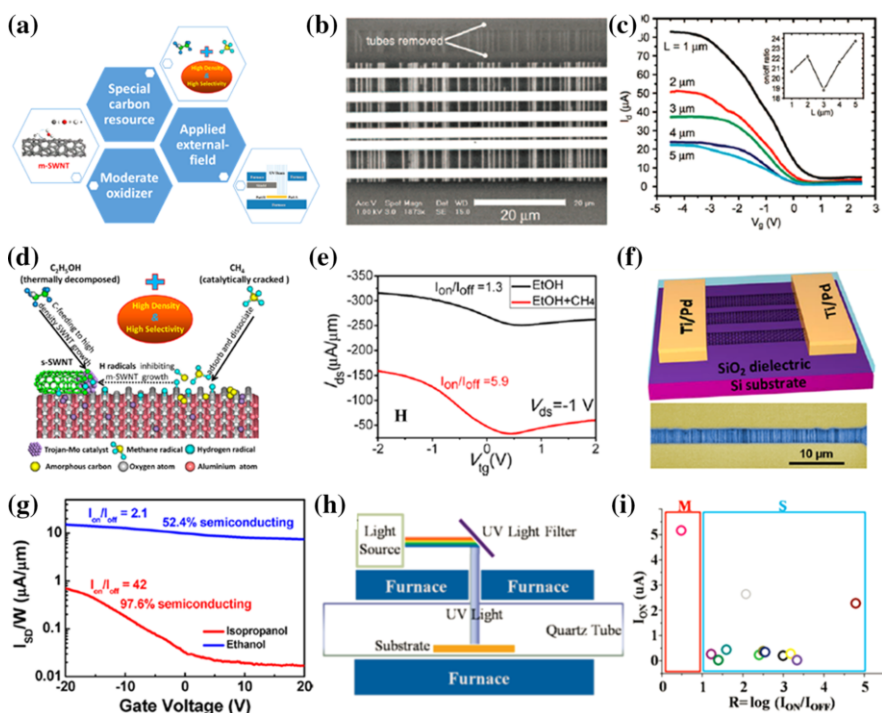


Fig. 7 In situ etching strategy for controlled growth of SWNT arrays on a substrate surface. **a** Scheme of selective growth methods based on in situ etching of m-SWNTs by etchant introduced in different ways. **b, c** Preferential growth of s-SWNTs arrays on quartz substrate using ethanol/methanol as the carbon feeds (reproduced with permission [87], Copyright 2009, American Chemical Society). **d, e** Selective growth of high-density s-SWNT array by ethanol/methane CVD (reproduced with permission [88], Copyright 2016, American Chemical Society). **f, g** Growth of nanotube arrays with enriched s-SWNTs by using IPA as carbon feed stock (reproduced with permission [89], Copyright 2012, American Chemical Society). **h, i** UV irradiation-assisted CVD growth of s-SWNT array (reproduced with permission [91], Copyright 2009, American Chemical Society)

activity, and applying an external field was demonstrated effective to produce reactive reagents such as radicals.

The production of a weakly oxidative atmosphere in the CVD system by adding special carbon resource during the growth of SWNTs has proven an efficient way to selectively synthesize s-SWNTs. In 2009, Ding et al. reported the preferential growth of s-SWNTs arrays on a quartz substrate using ethanol/methanol as the carbon feeds (Fig. 7b, c) [87]. The introduction of methanol is the key factor for the selective growth of s-SWNTs. It was proposed that the OH radical from methanol accounts for the selective etching of m-SWNTs because they have smaller ionization potential as compared to s-SWNTs with the same diameter. The growth selectivity could also be attributed to using ST-cut quartz as the substrate. Although not deeply discussed, the influence of the interaction between the catalyst/nanotube and the substrate is certainly of paramount importance.

A similar *in situ* etching approach was reported in recent work, using an ethanol–methane mixture carbon resource and Trojan-Mo catalyst to grow high-density s-SWNT arrays on a sapphire substrate (Fig. 7d, e) [88]. As schemed in Fig. 7d, in this approach, active H radicals provided by the incomplete pyrolysis of methane was suggested as the agents to inhibit growth of m-SWNT. These moderate and appropriate H radicals create a suitable etching environment for *in situ* inhibition of m-SWNT growth. The key role of the substrate was also emphasized in this work by suggesting that the selectivity originates from methane adsorbed and dissociated on the catalytic sapphire surface to generate H radicals. Meanwhile, due to milder reactivity and proper amount of H radicals, the density of the arrays had no obvious decrease.

By directly using special carbon feed stock such as isopropyl alcohol (IPA), a semiconducting nanotube purity of above 90% was achieved by Zhou's group [89]. The underlying chemical mechanism for the predominant growth was discussed based on mass spectrometric analysis. The presence of the right amount of water in the IPA CVD environment was shown to cause preferential growth of semiconducting SWNTs. The effective *in situ* enrichment of s-SWNTs was confirmed by the electronic property measurement (Fig. 7f, g). Previous work regarding the effect of water species on SWNT growth supported the same conclusion that m-SWNTs were preferentially etched by water vapor under certain conditions [90]. The work also showed that in addition to a suitable water vapor concentration, a low carbon feeding rate benefits the high selectivity of s-SWNTs over m-SWNTs.

UV irradiation has been tentatively introduced to assist the direct CVD growth of s-SWNTs (Fig. 7h, i) [91]. The wavelength of the UV light used ranged from 200 to 400 nm, which was effective in promoting the decomposition of reaction gases, leading to a concentration increase in oxidative chemicals such as free radicals. As shown in Fig. 7h, a specially manufactured furnace with a hole in the top of the furnace cover was used to allow light to irradiate the substrate. It was assumed that the selective etching of m-SWNTs under UV irradiation occurred at the stage of cap formation, so that the surviving s-SWNT arrays had chance to grow long and to maintain intrinsic structures. The irradiation time and light intensity are critical to the density of SWNTs. A shorter irradiation time was found to yield denser SWNT arrays.

The introduction of a weak oxidative gas during the process of growing SWNTs might be one of the most efficient methods to preferentially grow s-SWNTs. However, since the selectivity is based on removing the metallic nanotubes, this kind of method needs to compromise between a high density and semiconducting selectivity of SWNT arrays. The complexity of the CVD system including high temperature and coexistence of multiple reactive gases all challenge the efficiency and reproducibility of the etching reaction. Moreover, the compatibility between this technology and a normal CVD system should also be considered before the corresponding methods can be applied for large-scale selective production.

3.4 Ex Situ Removal/Etching Method

Although separating m-/s-SWNTs in the growth process is attractive for optimally maintaining the pristine properties, post-growth separation of SWNTs grown on the substrates has still attracted considerable research interest because it is easier to realize and more compatible with current semiconductor industry technology. Moreover, the knowledge and insight obtained from studying post-growth separation methods hold great significance for potentially transferring the technology into the CVD environment. The discussion in this section will focus on post-growth selective preparation of surface grown m-/s-SWNT arrays via selective etching or removal.

As illustrated in Fig. 8a, the methods can be mainly divided into two classes according to the principle of the separating process, depending on whether the dominant driving force is selective reaction or selective wrapping. The first one is selective etching. As is known, the conductivity of m-SWNTs is greater than s-SWNTs. Making use of this mechanism, Jin and coworkers selectively exposed m-SWNTs to reactive ion etching while keeping the s-SWNTs coated with a solid polymer layer [92]. The Joule heating induces thermal gradients that drive flow of thermocapillary resist away from the m-SWNT, leading to exposure and final removal of m-SWNTs (Fig. 8b). The electrical voltage was applied through removable electrode structures, producing arrays comprising only s-SWNTs. Later, the same group used a more convenient technology, microwave radiation, to selectively heat the m-SWNTs and initiate the thermocapillary flows [93]. As a noninvasive heating technique, microstrip dipole antennas of low work-function metals selectively couple microwaves to transfer the radiation energy into heating

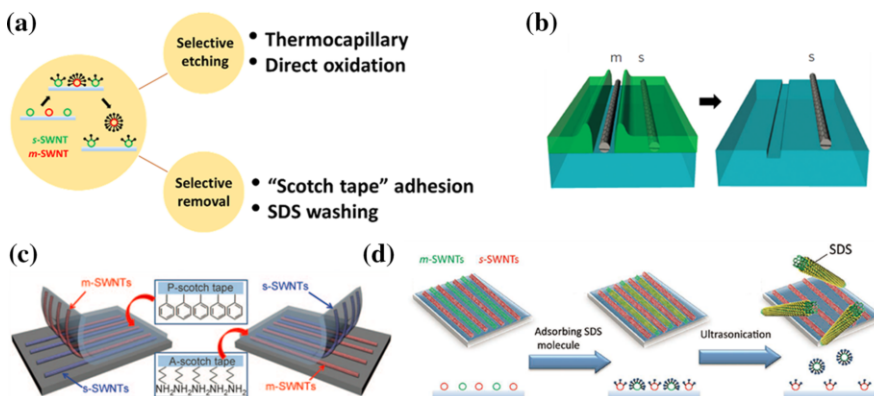


Fig. 8 Ex situ selective removal/etching strategy for controlled preparation of SWNT arrays on a substrate surface. **a** Scheme of preparation methods for s-SWNT arrays based on either selective etching or removal of m-SWNTs. **b** Utilization of nanoscale thermocapillary flows to create arrays of purely s-SWNTs (reproduced with permission [92], Copyright 2013, Nature Publishing Group). **c** Separation of m- and s-SWNT arrays by "Scotch Tape" (reproduced with permission [23], Copyright 2011, Wiley-VCH). **d** Separation of m-/s-SWNT arrays by washing off m-SWNTs using SDS aqueous solution (reproduced with permission [98], Copyright 2013, Wiley-VCH)

only the m-SWNTs. Although these two methods offer exceptional levels of efficiency, the procedures are cumbersome and require multiple processing steps. A simple, robust alternative that uses infrared laser irradiation to selectively heat the m-SWNTs was developed shortly afterwards [94]. The effectiveness of this simple thermocapillary flow induced purification process has been proven by complete and selective removal of m-SWNTs from arrays of SWNTs, including examples with very high density of SWNTs. One of the potential drawbacks could arise from formation of trenches around the m-SWNTs, which would probably affect the adjacent s-SWNTs or even destroy them.

Early work on the selective etching of m-SWNTs employed reactive gas phase plasma, providing high s-SWNT purity but a relatively low nanotube density [95]. UV light irradiation has also been tried as a means of separating m/s-SWNTs. In 2008, Zhang's group reported that long-arc xenon-lamp irradiation can be used to prepare densely packed, well-aligned individual s-SWNTs with the percentage estimated to be around 95% [96]. Selective etching of m-SWNTs was attributed to the decomposition of reaction gases under the UV light, which produced oxidative chemicals such as free radicals. In situ light treatment of FETs was performed to track the destructive process. It was shown that the off-state current dramatically decreased after 15 min of irradiation and the on/off ratio exceeded 2000, indicating the selective removal of m-SWNTs. Post-growth water vapor treatment was tried by the same group to prepare s-SWNT arrays [97]. They found that the oxidation temperature and the concentration of water vapor have a clear effect on the selectivity of etching of m-SWNTs. The influence of reaction temperature on the electronic structures of SWNTs and thus the etching reaction of SWNTs with water is discussed in detail. It was pointed out that relatively lower temperature is better for retaining the difference in reactive activities of s- and m-SWNTs, as well as a moderate oxidative potential of water, which were essential for effective sorting in the corresponding system.

The second kind of method is based on non-covalent selective interaction between SWNTs and other molecules. In 2011, Zhang's group designed a smart Scotch tape mechanism to extract s-SWNTs or m-SWNTs from the array mixture (Fig. 8c) [23]. They prepared soft polydimethylsiloxane (PDMS) thin films treated with phenyl functional terminal group and amino functional terminal groups for selective adsorption of m-SWNTs and s-SWNTs on the polymer surface, respectively. The PDMS-based "Scotch tapes" were applied to SWNT samples and then peeled off, selectively removing either s- or m-SWNTs and to leave their counterparts on the substrate. Furthermore, the researchers proposed another strategy to separate m-/s-SWNT arrays on ST-cut quartz surface by washing off m-SWNTs using sodium dodecyl sulfate (SDS) aqueous solution [98]. Washing means immersing the as-grown SWNT arrays on quartz into SDS aqueous solutions and then applying sonication. As seen from Fig. 8d, most SDS molecules prefer to adsorb onto the circumference of the m-SWNTs, which dramatically weakened their interaction with the substrate surface and made them easier to remove from the substrate surface (detergent action). The s-SWNT arrays remained on the substrate with their original aligned configurations.

Selective etching or wrapping that favors one kind of SWNTs have both proven effective for preparation of predominant s- or m-SWNT arrays. However, since this strategy produced arrays with the density strongly dependent on that of the starting materials, the development of this strategy relies on a high density being provided by the growth technology.

4 Self-Assembly from SWNT Solution

Among post-synthetic methods that have been developed to sort SWNTs by their electronic structure, the separation strategies performed in solutions/dispersions have produced samples with the best reproducibility and yield. While these approaches have achieved high purity of s-SWNTs, precise positioning, and ordered arrangements are urgently required for application of s-SWNTs in real devices. Surface chemical modification of the substrate was demonstrated to provide additional levels of control [91]. Electric fields, applied in an alternating current mode during solution deposition, can also yield alignment due to dielectrophoretic interaction [99]. In this review, dielectrophoresis, selective adsorption on patterned surface, and evaporation-driven assembly will be discussed. Methods such as Langmuir–Blodgett assembly will also be discussed.

4.1 Dielectrophoresis (DEP)

The earliest report on using alternating current dielectrophoresis to separate metallic from semiconducting SWNTs from suspension was in 2003 [99]. The method takes advantage of the difference of the relative dielectric constants of the two kinds of SWNTs with respect to the solvent, resulting in totally different movement of m- and s-SWNTs, with the former ones attracted toward a microelectrode array, and the latter ones left in the solvent. DEP technology utilizes an inhomogeneous electric field, typically formed between a pair of planar microelectrodes, to manipulate the placement of SWNTs via interaction with their induced dipole moment. The classic experimental setup for DEP technique is as that shown in Fig. 9a, c. It is important to note that DEP promotes the deposition of longer nanotubes in mixtures of different tube lengths, which is favorable for optimal device performance.

Later, this ac-DEP technique was extended for controlled deposition of SWNTs onto multiple submicrometer electrode pairs [100]. The capacitive coupling between the substrate and the electrodes was believed to limit the number of deposited tubes per contact. Using a novel aspect of nanotube DEP, the aligning process was scaled up by the same group [101]. By following an alternate and more universal mechanism that involves redistribution of the electric field around the deposited nanotube in the electrode gap, the researchers demonstrated the directed and precise assembly of single-nanotube devices with an integration density of several million devices per square centimeter (Fig. 9b, c). Through optimizing the frequency and trapping time of the DEP process, combined with nanotube concentration tuning in the solution, the linear density of the SWNT between

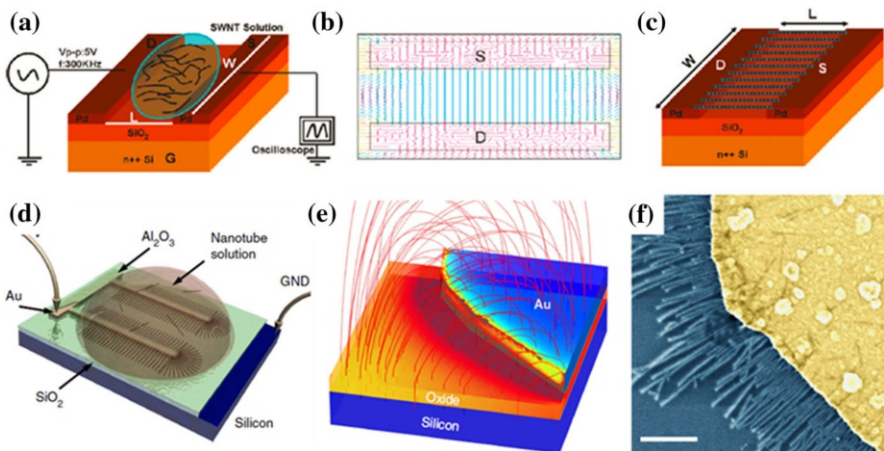


Fig. 9 Assembly of SWNT arrays by the DEP method. **a–c** Ultra-high-density alignment of SWNT arrays by DEP (reproduced with permission [102], Copyright 2011, American Chemical Society). **d–f** Fringing-field dielectrophoretic assembly of ultra-high-density s-SWNT arrays with a self-limited pitch (reproduced with permission [103], Copyright 2014, Nature Publishing Group)

prefabricated electrodes was increased from 0.5 SWNT/ μm to more than 30 SWNT/ μm [102].

In 2014, Cao et al. developed a method that utilized the alternating voltage-fringing electric field formed between surface microelectrodes and the substrate to assemble semiconducting nanotubes into highly aligned arrays with ultrahigh density of ~ 50 nanotubes per μm [103]. As illustrated in Fig. 9d–f, the fringing-field DEP aligned nanotubes into well-ordered arrays with a high degree of linearity, because its field-focusing effect led to very strong electro-orientation torque. Teslaphoresis, in which the directed motion and self-assembly of SWNTs by a Tesla coil, was introduced in a recent paper [104]. Compared with the conventional DEP technique, Teslaphoresis can create a gradient high-voltage force-field that projects into free space, making SWNTs self-assemble into wires that span from the nanoscale to the macroscale.

4.2 Surface Modification-Assisted Adsorption

The earliest representative technology of aligning separated SWNTs on a functionalized substrate was the one developed by Bao's group in 2008 [105]. They took SWNT solutions and spin-coated them onto SiO_2/Si surface modified with either amine- or phenyl-terminated silane monolayers, aiming at selectively adsorbing s-SWNTs and m-SWNTs, respectively. The advantage of this technology is that simultaneous control of density and alignment occur in one step during device fabrication. As is widely known, combining excellent selectivity with nanotube alignment at a high density is critical to enable the formation of single-nanotube devices. During the deposition process, the surface modification-assisted adsorption provides guidance for the nanotube alignment through selective

chemical/physical interaction and/or physical space confinement. Important progress was made by Park et al. in 2012 by placing individual SWNTs with a density of $1 \times 10^9 \text{ cm}^{-2}$ [106]. A new ion-exchange surface chemistry between the wrapping surfactant molecule and the decorated surface of the HfO_2 trenches ensures accurate positioning, as illustrated by Fig. 10a, b. Additionally, this work improved the alignment of nanotubes by reducing the trench width down to 70 nm.

Dai's group found that s-SWNTs dispersed in sodium cholate (SC) and SDS solutions could self-assemble into closely packed flat rafts, which was driven by depletion attraction during water evaporation on a 3-aminopropyltriethoxysilane (APTES)-modified SiO_2/Si substrate [107]. Further improvement was made later by combining top-down and bottom-up approaches [108]. Specifically, defined patterns of narrow pitch provided space confinement for the self-assembly of well-aligned raft-like structures. In such a way, densely packed SWNTs deposited into predefined polymer patterns were obtained. Recently, large ($>\text{cm}^2$) monodomain films of aligned single-walled carbon nanotubes could be prepared using slow vacuum filtration through filter membrane with 100-nm pore size (Fig. 10c) [25]. The formation of CNT alignment in a confined narrow layer region near the surface of the filter membrane was due to a potential well created by competition of the electrostatic repulsion force and an attraction force from the membrane surface. Other exciting progress is the placement of individual SWNT segments at predetermined locations with nanometer accuracy (Fig. 11) [109]. DNA-wrapped SWNT segments with uniform electronic properties were assembled onto lithographically patterned lines on a surface. Individual nanotube control was achieved with spacing as close as 100 nm. Such high-resolution placement is believed to benefit from the confinement effect of the physical space.

S-SWNT arrays have also been obtained by binding end-functionalized SWNT segments to lithographically defined nanoscale anchors [110]. However, the density of the array needs to be improved for the practical application of such a method. He et al. reported recently that wafer-scale monodomain films of aligned s-SWNTs can be prepared using slow vacuum filtration through a modified filtration film [25]. Although the film contained SWNTs with high density and good alignment, the

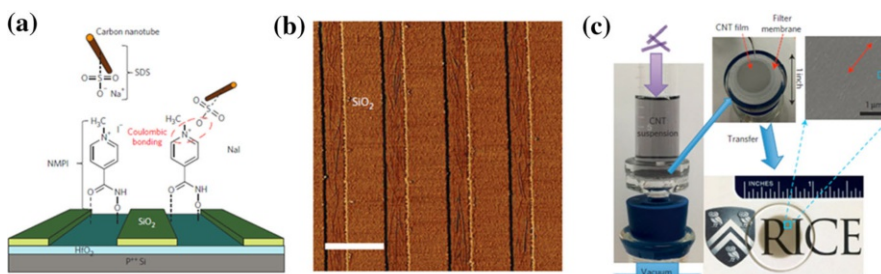


Fig. 10 Assembly of SWNT arrays by adsorption on lithographically patterned and/or chemically functionalized substrates. **a, b** High-density integration of s-SWNTs via chemical self-assembly through ion-exchange chemistry (reproduced with permission [106], Copyright 2012, Nature Publishing Group). **c** Wafer-scale monodomain films of spontaneously aligned s-SWNTs prepared by slow vacuum filtration (reproduced with permission [25], Copyright 2016, Nature Publishing Group)

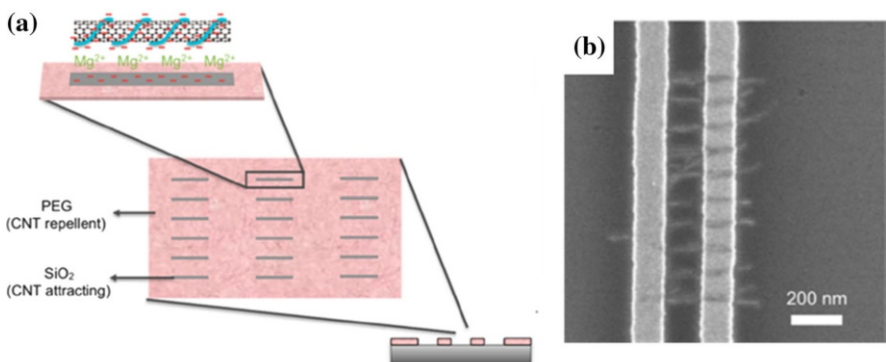


Fig. 11 Directed assembly of SWNT FETs with nanometer accuracy through elaborate design of surface modification (reproduced with permission [109], Copyright 2016, American Chemical Society)

thickness of the film was too thick to find more extensive applications, especially in the nanodevice field.

4.3 Langmuir–Blodgett and Langmuir–Schaefer Techniques

The best assembling results obtained by Langmuir–Blodgett analogue techniques were reported by Cao et al. [111]. The Langmuir–Schaefer-based method used a 1,2-dichloroethane (DCE) solution of s-SWNTs to disperse them on the water subphase, with the nanotubes spreading out to cover the whole surface as a result of the surface tension. Evaporation of the volatile organic solvent left the nanotubes to float on the two-dimensional air–water interface, forming an isotropic phase. Mobile barrier bars were used to apply a uniaxial compressive force that assembled the nanotubes into well-ordered arrays, which could then be horizontally transferred onto the receiving substrate. This Langmuir–Schaefer method produced films with better alignment and higher yield than the Langmuir–Blodgett method that uses vertical transfer technique [112], because of reduced disturbance to the rigid nanotube Langmuir film on water. The highly pure s-SWNT arrays could fully cover a surface with a nanotube density of more than 500 tubes/ μm . Nonetheless, performance of FET devices made from the aligned nanotubes was far from satisfying, which was believed to be hindered mainly by the bundling between the too closely packed nanotubes.

4.4 Evaporation-Driven Self-Assembly

As a simple approach, evaporation-driven self-assembly (EDSA) has been shown to be an effective and scalable technique to create thin films of aligned SWNTs within SWNT stripes. EDSA employs the well-known “coffee ring phenomenon”, where particles suspended in a droplet tend to aggregate at the edges of the drop, forming a ring-like structure [113]. The working mechanism of EDSA is as shown in Fig. 12a. When a target substrate is immersed vertically in the SWNT solution, a thin

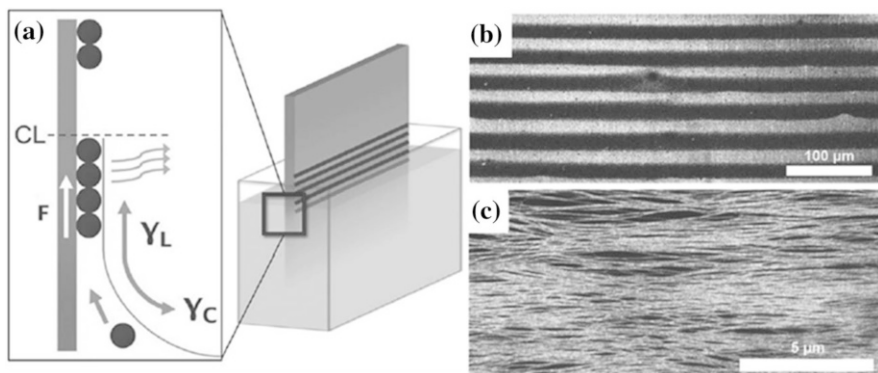


Fig. 12 Evaporation-driven self-assembly of SWNT array (reproduced with permission [115], Copyright 2013, Wiley–VCH)

meniscus forms at the solid–liquid–vapor interface (contact line). When the solvent evaporates, the aligned nanotubes in the liquid are brought by convective transport to the contact line and deposit on the substrate. A frictional force, F , together with the liquid surface tension, γ_L , pins the contact line. As evaporation proceeds, the buildup of the capillary force, γ_C , eventually leads to depinning of the contact line. The contact line thus jumps to a new position where it is subsequently pinned again by the deposition of a new row. The resulting repeated stick-slip motion of the liquid forms the super lattice of CNT stripes (Fig. 12b). Aligned geometries could be created through modulation of forces at the solid–liquid–air interface [114, 115]. Specifically, the width and spacing of the resulting SWNT stripes depend on the pinning probability, which in turn depends on the concentrations of SWNTs and surfactant in aqueous solution. Besides the evaporation of aqueous SWNT solution, diffusion of organic solvent on the water–air interface was shown to be able to deposit aligned s-SWNT on a partially submerged hydrophobic substrate [26]. EDSA contrasts with Langmuir–Blodgett analogue techniques [26, 116] in that the deposition is primarily driven by aligned self-assembly under evaporation rather than withdrawing the substrate at a certain velocity.

5 Conclusions

Recent years have seen great progress toward the ultimate goal of feasible production of SWNTs with high density and uniform electronic properties. If one compares the products of direct preparation methods to form SWNT arrays on a substrate with self-assembly methods of using pre-sorted SWNTs from solution, no definitive winning method has been demonstrated by either approach. Furthermore, the quality of SWNT products from solution-based sorting strategies has not matched that provided by in situ growth methods, mainly because of possible contamination by residual surfactant and the potential for degradation of nanotubes during the solubilization process. Meanwhile, for real device applications, in the

absence of a revolutionary breakthrough, it appears that the reproducibility of in situ sorting technology is still not as satisfying as the post-growth sorting techniques. The optimal solution is likely to include clever refinements of post-synthetic sorting approaches, or a deeper mechanistic understanding of selective growth methods.

Furthermore, for selective growth systems, a rapid and convenient analytical method for precisely establishing purity levels of large populations of SWNTs remains elusive. Developing selective growth methods based on the results of that kind of characterization is thus a high priority for SWNT researchers. In the meantime, in an effort to get SWNT arrays with higher density, attention should be paid to improving the length, quality, and dispersion state of SWNTs deposited from solution to attain high performance in the exciting new device.

Acknowledgements This work was supported by the NSFC (21233001, 51432002, and 51272006), MOST (2016YFA0200101 and 2016YFA0200104).

References

1. Nanot S, Hároz EH, Kim J-H, Hauge RH, Kono J (2012) Optoelectronic properties of single-wall carbon nanotubes. *Adv Mater* 24(36):4977–4994
2. Avouris P, Chen Z, Perebeinos V (2007) Carbon-based electronics. *Nat Nanotechnol* 2(10):605–615
3. Franklin AD (2013) Electronics: the road to carbon nanotube transistors. *Nature* 498(7455):443–444
4. Iijima S, Ichihashi T (1993) Single-shell carbon nanotubes of 1-nm diameter. *Nature* 363(6430):603–605
5. Dresselhaus MS, Dresselhaus G, Saito R (1995) Nanotubes physics of carbon nanotubes. *Carbon* 33(7):883–891
6. Druzhinina T, Hoeppener S, Schubert US (2011) Strategies for post-synthesis alignment and immobilization of carbon nanotubes. *Adv Mater* 23(8):953–970
7. Chen Y, Zhang Y, Hu Y, Kang L, Zhang S, Xie H, Liu D, Zhao Q, Li Q, Zhang J (2014) State of the art of single-walled carbon nanotube synthesis on surfaces. *Adv Mater* 26(34):5898–5922
8. Chen Y, Zhang J (2014) Chemical vapor deposition growth of single-walled carbon nanotubes with controlled structures for nanodevice applications. *Acc Chem Res* 47(8):2273–2281
9. Hersam MC (2008) Progress towards monodisperse single-walled carbon nanotubes. *Nat Nanotechnol* 3(7):387–394
10. Zhang H, Wu B, Hu W, Liu Y (2011) Separation and/or selective enrichment of single-walled carbon nanotubes based on their electronic properties. *Chem Soc Rev* 40(3):1324–1336
11. Pesetski AA, Baumgardner JE, Krishnaswamy SV, Zhang H, Adam JD, Kocabas C, Banks T, Rogers JA (2008) A 500-MHz carbon nanotube transistor oscillator. *Appl Phys Lett* 93(12):123506
12. Kocabas C, H-s Kim, Banks T, Rogers JA, Pesetski AA, Baumgardner JE, Krishnaswamy SV, Zhang H (2008) Radio frequency analog electronics based on carbon nanotube transistors. *Proc Natl Acad Sci USA* 105(5):1405–1409
13. Shulaker MM, Hills G, Patil N, Wei H, Chen H-Y, Wong HSP, Mitra S (2013) Carbon nanotube computer. *Nature* 501(7468):526–530
14. Shulaker MM, Van Rethy J, Wu TF, Suriyasena Liyanage L, Wei H, Li Z, Pop E, Gielen G, Wong HSP, Mitra S (2014) Carbon nanotube circuit integration up to sub-20 nm channel lengths. *ACS Nano* 8(4):3434–3443
15. Wen Q, Zhang R, Qian W, Wang Y, Tan P, Nie J, Wei F (2010) Growing 20 cm long DWNTs/TWNTs at a rapid growth rate of 80–90 $\mu\text{m}/\text{s}$. *Chem Mater* 22(4):1294–1296
16. Han S, Liu X, Zhou C (2005) Template-free directional growth of single-walled carbon nanotubes on α - and r -plane sapphire. *J Am Chem Soc* 127(15):5294–5295
17. Ismach A, Segev L, Wachtel E, Joselevich E (2004) Atomic-step-templated formation of single wall carbon nanotube patterns. *Angew Chem Int Ed* 43(45):6140–6143
18. Peng B, Jiang S, Zhang Y, Zhang J (2011) Enrichment of metallic carbon nanotubes by electric field-assisted chemical vapor deposition. *Carbon* 49(7):2555–2560

19. Hu Y, Kang L, Zhao Q, Zhong H, Zhang S, Yang L, Wang Z, Lin J, Li Q, Zhang Z, Peng L, Liu Z, Zhang J (2015) Growth of high-density horizontally aligned SWNT arrays using Trojan catalysts. *Nat Commun* 6:6099
20. Zhang S, Hu Y, Wu J, Liu D, Kang L, Zhao Q, Zhang J (2015) Selective scission of C–O and C–C bonds in ethanol using bimetal catalysts for the preferential growth of semiconducting SWNT arrays. *J Am Chem Soc* 137(3):1012–1015
21. Liu J, Wang C, Tu X, Liu B, Chen L, Zheng M, Zhou C (2012) Chirality-controlled synthesis of single-wall carbon nanotubes using vapour-phase epitaxy. *Nat Commun* 3:1199
22. Li J, Liu K, Liang S, Zhou W, Pierce M, Wang F, Peng L, Liu J (2014) Growth of high-density-aligned and semiconducting-enriched single-walled carbon nanotubes: decoupling the conflict between density and selectivity. *ACS Nano* 8(1):554–562
23. Hong G, Zhou M, Zhang R, Hou S, Choi W, Woo YS, Choi J-Y, Liu Z, Zhang J (2011) Separation of metallic and semiconducting single-walled carbon nanotube arrays by “scotch tape”. *Angew Chem Int Ed* 50(30):6819–6823
24. Sarker BK, Shekhar S, Khondaker SI (2011) Semiconducting enriched carbon nanotube aligned arrays of tunable density and their electrical transport properties. *ACS Nano* 5(8):6297–6305
25. He X, Gao W, Xie L, Li B, Zhang Q, Lei S, Robinson JM, Hároz EH, Doorn SK, Wang W, Vajtai R, Ajayan PM, Adams WW, Hauge RH, Kono J (2016) Wafer-scale monodomain films of spontaneously aligned single-walled carbon nanotubes. *Nat Nanotechnol* 11(7):633–638
26. Joo Y, Brady GJ, Arnold MS, Gopalan P (2014) Dose-controlled, floating evaporative self-assembly and alignment of semiconducting carbon nanotubes from organic solvents. *Langmuir* 30(12):3460–3466
27. Xiao J, Dunham S, Liu P, Zhang Y, Kocabas C, Moh L, Huang Y, Hwang K-C, Lu C, Huang W, Rogers JA (2009) Alignment controlled growth of single-walled carbon nanotubes on quartz substrates. *Nano Lett* 9(12):4311–4319
28. Kocabas C, Hur S-H, Gaur A, Meitl MA, Shim M, Rogers JA (2005) Guided growth of large-scale, horizontally aligned arrays of single-walled carbon nanotubes and their use in thin-film transistors. *Small* 1(11):1110–1116
29. Ibrahim I, Bachmatiuk A, Warner JH, Büchner B, Cuniberti G, Rümmeli MH (2012) CVD-grown horizontally aligned single-walled carbon nanotubes: synthesis routes and growth mechanisms. *Small* 8(13):1973–1992
30. Huang S, Maynor B, Cai X, Liu J (2003) Ultralong, well-aligned single-walled carbon nanotube architectures on surfaces. *Adv Mater* 15(19):1651–1655
31. Su M, Li Y, Maynor B, Buldum A, Lu JP, Liu J (2000) Lattice-oriented growth of single-walled carbon nanotubes. *J Phys Chem B* 104(28):6505–6508
32. Zhang Y, Chang A, Cao J, Wang Q, Kim W, Li Y, Morris N, Yenilmez E, Kong J, Dai H (2001) Electric-field-directed growth of aligned single-walled carbon nanotubes. *Appl Phys Lett* 79(19):3155–3157
33. Huang S, Woodson M, Smalley R, Liu J (2004) Growth mechanism of oriented long single walled carbon nanotubes using “fast-heating” chemical vapor deposition process. *Nano Lett* 4(6):1025–1028
34. Xie H, Zhang R, Zhang Y, Li P, Jin Y, Wei F (2013) Growth of high-density parallel arrays of ultralong carbon nanotubes with catalysts pinned by silica nanospheres. *Carbon* 52:535–540
35. Zhou W, Han Z, Wang J, Zhang Y, Jin Z, Sun X, Zhang Y, Yan C, Li Y (2006) Copper catalyzing growth of single-walled carbon nanotubes on substrates. *Nano Lett* 6(12):2987–2990
36. Zhang B, Hong G, Peng B, Zhang J, Choi W, Kim JM, Choi J-Y, Liu Z (2009) Grow single-walled carbon nanotubes cross-bar in one batch. *J Phys Chem C* 113(14):5341–5344
37. Jin Z, Chu H, Wang J, Hong J, Tan W, Li Y (2007) Ultralow feeding gas flow guiding growth of large-scale horizontally aligned single-walled carbon nanotube arrays. *Nano Lett* 7(7):2073–2079
38. Zheng LX, O’Connell MJ, Doorn SK, Liao XZ, Zhao YH, Akhadov EA, Hoffbauer MA, Roop BJ, Jia QX, Dye RC, Peterson DE, Huang SM, Liu J, Zhu YT (2004) Ultralong single-wall carbon nanotubes. *Nat Mater* 3(10):673–676
39. Hofmann M, Nezich D, Reina A, Kong J (2008) In-situ sample rotation as a tool to understand chemical vapor deposition growth of long aligned carbon nanotubes. *Nano Lett* 8(12):4122–4127
40. Ago H, Nakamura K, K-i Ikeda, Uehara N, Ishigami N, Tsuji M (2005) Aligned growth of isolated single-walled carbon nanotubes programmed by atomic arrangement of substrate surface. *Chem Phys Lett* 408(4–6):433–438

41. Ismach A, Kantorovich D, Joselevich E (2005) Carbon nanotube graphoepitaxy: highly oriented growth by faceted nanosteps. *J Am Chem Soc* 127(33):11554–11555
42. Orofeo CM, Ago H, Ikuta T, Takahasi K, Tsuji M (2010) Growth of horizontally aligned single-walled carbon nanotubes on anisotropically etched silicon substrate. *Nanoscale* 2(9):1708–1714
43. Chen Y, Hu Y, Fang Y, Li P, Feng C, Zhang J (2012) Lattice-directed growth of single-walled carbon nanotubes with controlled geometries on surface. *Carbon* 50(9):3295–3297
44. Chen Y, Shen Z, Xu Z, Hu Y, Xu H, Wang S, Guo X, Zhang Y, Peng L, Ding F, Liu Z, Zhang J (2013) Helicity-dependent single-walled carbon nanotube alignment on graphite for helical angle and handedness recognition. *Nat Commun* 4:2205
45. Joselevich E (2009) Self-organized growth of complex nanotube patterns on crystal surfaces. *Nano Res* 2(10):743–754
46. Ago H, Imamoto K, Ishigami N, Ohdo R, K-i Ikeda, Tsuji M (2007) Competition and cooperation between lattice-oriented growth and step-templated growth of aligned carbon nanotubes on sapphire. *Appl Phys Lett* 90(12):123112
47. Li P, Zhang X, Li J, Liu J (2015) Graphoepitaxial effect in the guided growth of SWNT arrays on quartz. *J Mater Chem C* 3(37):9678–9683
48. Wang B, Ma Y, Li N, Wu Y, Li F, Chen Y (2010) Facile and scalable fabrication of well-aligned and closely packed single-walled carbon nanotube films on various substrates. *Adv Mater* 22(28):3067–3070
49. Kang SJ, Kocabas C, Ozel T, Shim M, Pimparkar N, Alam MA, Rotkin SV, Rogers JA (2007) High-performance electronics using dense, perfectly aligned arrays of single-walled carbon nanotubes. *Nat Nanotechnol* 2(4):230–236
50. Kang L, Hu Y, Liu L, Wu J, Zhang S, Zhao Q, Ding F, Li Q, Zhang J (2015) Growth of close-packed semiconducting single-walled carbon nanotube arrays using oxygen-deficient TiO₂ nanoparticles as catalysts. *Nano Lett* 15(1):403–409
51. Kang L, Hu Y, Zhong H, Si J, Zhang S, Zhao Q, Lin J, Li Q, Zhang Z, Peng L, Zhang J (2015) Large-area growth of ultra-high-density single-walled carbon nanotube arrays on sapphire surface. *Nano Res* 8(11):3694–3703
52. Ago H, Uehara N, K-i Ikeda, Ohdo R, Nakamura K, Tsuji M (2006) Synthesis of horizontally-aligned single-walled carbon nanotubes with controllable density on sapphire surface and polarized Raman spectroscopy. *Chem Phys Lett* 421(4–6):399–403
53. Hong SW, Banks T, Rogers JA (2010) Improved density in aligned arrays of single-walled carbon nanotubes by sequential chemical vapor deposition on quartz. *Adv Mater* 22(16):1826–1830
54. Wang C, Ryu K, De Arco LG, Badmaev A, Zhang J, Lin X, Che Y, Zhou C (2010) Synthesis and device applications of high-density aligned carbon nanotubes using low-pressure chemical vapor deposition and stacked multiple transfer. *Nano Res* 3(12):831–842
55. Shulaker MM, Wei H, Patil N, Provine J, Chen H-Y, Wong HSP, Mitra S (2011) Linear increases in carbon nanotube density through multiple transfer technique. *Nano Lett* 11(5):1881–1886
56. Zhou W, Ding L, Yang S, Liu J (2011) Synthesis of high-density, large-diameter, and aligned single-walled carbon nanotubes by multiple-cycle growth methods. *ACS Nano* 5(5):3849–3857
57. Liu H, Takagi D, Chiashi S, Homma Y (2010) Transfer and alignment of random single-walled carbon nanotube films by contact printing. *ACS Nano* 4(2):933–938
58. Ago H, Nakamura Y, Ogawa Y, Tsuji M (2011) Combinatorial catalyst approach for high-density growth of horizontally aligned single-walled carbon nanotubes on sapphire. *Carbon* 49(1):176–186
59. Kocabas C, Kang SJ, Ozel T, Shim M, Rogers JA (2007) Improved synthesis of aligned arrays of single-walled carbon nanotubes and their implementation in thin film type transistors. *J Phys Chem C* 111(48):17879–17886
60. Ding L, Yuan D, Liu J (2008) Growth of high-density parallel arrays of long single-walled carbon nanotubes on quartz substrates. *J Am Chem Soc* 130(16):5428–5429
61. Zhou W, Rutherford C, Burke PJ (2008) Wafer scale synthesis of dense aligned arrays of single-walled carbon nanotubes. *Nano Res* 1(2):158–165
62. Yao Y, Li Q, Zhang J, Liu R, Jiao L, Zhu YT, Liu Z (2007) Temperature-mediated growth of single-walled carbon-nanotube intramolecular junctions. *Nat Mater* 6(4):283–286
63. Geblinger N, Ismach A, Joselevich E (2008) Self-organized nanotube serpentines. *Nat Nanotechnol* 3(4):195–200
64. Yao Y, Dai X, Feng C, Zhang J, Liang X, Ding L, Choi W, Choi J-Y, Kim JM, Liu Z (2009) Crinkling ultralong carbon nanotubes into serpentines by a controlled landing process. *Adv Mater* 21(41):4158–4162

65. Huang S, Cai X, Liu J (2003) Growth of millimeter-long and horizontally aligned single-walled carbon nanotubes on flat substrates. *J Am Chem Soc* 125(19):5636–5637
66. Ismach A, Joselevich E (2006) Orthogonal self-assembly of carbon nanotube crossbar architectures by simultaneous graphoepitaxy and field-directed growth. *Nano Lett* 6(8):1706–1710
67. Wagner RS, Ellis WC (1964) Vapor–liquid–solid mechanism of single crystal growth. *Appl Phys Lett* 4(5):89–90
68. Kong J, Soh HT, Cassell AM, Quate CF, Dai H (1998) Synthesis of individual single-walled carbon nanotubes on patterned silicon wafers. *Nature* 395(6705):878–881
69. Liu B, Ren W, Gao L, Li S, Pei S, Liu C, Jiang C, Cheng H-M (2009) Metal-catalyst-free growth of single-walled carbon nanotubes. *J Am Chem Soc* 131(6):2082–2083
70. Hofmann S, Csányi G, Ferrari AC, Payne MC, Robertson J (2005) Surface diffusion: the low activation energy path for nanotube growth. *Phys Rev Lett* 95(3):036101
71. Takagi D, Hibino H, Suzuki S, Kobayashi Y, Homma Y (2007) Carbon nanotube growth from semiconductor nanoparticles. *Nano Lett* 7(8):2272–2275
72. Yang F, Wang X, Li M, Liu X, Zhao X, Zhang D, Zhang Y, Yang J, Li Y (2016) Templated synthesis of single-walled carbon nanotubes with specific structure. *Acc Chem Res* 49(4):606–615
73. Yang F, Wang X, Zhang D, Yang J, LuoDa XuZ, Wei J, Wang J-Q, Xu Z, Peng F, Li X, Li R, Li Y, Li M, Bai X, Ding F, Li Y (2014) Chirality-specific growth of single-walled carbon nanotubes on solid alloy catalysts. *Nature* 510(7506):522–524
74. Harutyunyan AR, Chen G, Paronyan TM, Pigos EM, Kuznetsov OA, Hewaparakrama K, Kim SM, Zakharov D, Stachi EA, Sumanasekera GU (2009) Preferential growth of single-walled carbon nanotubes with metallic conductivity. *Science* 326(5949):116–120
75. Zhao Q, Xu Z, Hu Y, Ding F, Zhang J (2016) Chemical vapor deposition synthesis of near-zigzag single-walled carbon nanotubes with stable tube-catalyst interface. *Sci Adv* 2(5):1501729
76. Zhang S, Tong L, Hu Y, Kang L, Zhang J (2015) Diameter-specific growth of semiconducting SWNT arrays using uniform Mo₂C solid catalyst. *J Am Chem Soc* 137(28):8904–8907
77. Zhang F, Hou P-X, Liu C, Cheng H-M (2016) Epitaxial growth of single-wall carbon nanotubes. *Carbon* 102:181–197
78. Yao Y, Feng C, Zhang J, Liu Z (2009) “Cloning” of single-walled carbon nanotubes via open-end growth mechanism. *Nano Lett* 9(4):1673–1677
79. Yu X, Zhang J, Choi W, Choi J-Y, Kim JM, Gan L, Liu Z (2010) Cap formation engineering: from opened C₆₀ to single-walled carbon nanotubes. *Nano Lett* 10(9):3343–3349
80. Ibrahim I, Bachmatiuk A, Grimm D, Popov A, Makharza S, Knupfer M, Büchner B, Cuniberti G, Rümmeli MH (2012) Understanding high-yield catalyst-free growth of horizontally aligned single-walled carbon nanotubes nucleated by activated C₆₀ species. *ACS Nano* 6(12):10825–10834
81. Smalley RE, Li Y, Moore VC, Price BK, Colorado R, Schmidt HK, Hauge RH, Barron AR, Tour JM (2006) Single wall carbon nanotube amplification: en route to a type-specific growth mechanism. *J Am Chem Soc* 128(49):15824–15829
82. Ding F, Harutyunyan AR, Yakobson BI (2009) Dislocation theory of chirality-controlled nanotube growth. *Proc Natl Acad Sci USA* 106(8):2506–2509
83. Liu B, Liu J, Tu X, Zhang J, Zheng M, Zhou C (2013) Chirality-dependent vapor-phase epitaxial growth and termination of single-wall carbon nanotubes. *Nano Lett* 13(9):4416–4421
84. Liu B, Liu J, Li H-B, Bhola R, Jackson EA, Scott LT, Page A, Irle S, Morokuma K, Zhou C (2015) Nearly exclusive growth of small diameter semiconducting single-wall carbon nanotubes from organic chemistry synthetic end-cap molecules. *Nano Lett* 15(1):586–595
85. Sanchez-Valencia JR, Dienel T, Groning O, Shorubalko I, Mueller A, Jansen M, Amsharov K, Ruffieux P, Fasel R (2014) Controlled synthesis of single-chirality carbon nanotubes. *Nature* 512(7512):61–64
86. Strano MS, Dyke CA, Usrey ML, Barone PW, Allen MJ, Shan H, Kittrich C, Hauge RH, Tour JM, Smalley RE (2003) Electronic structure control of single-walled carbon nanotube functionalization. *Science* 301(5639):1519–1522
87. Ding L, Tselev A, Wang J, Yuan D, Chu H, McNicholas TP, Li Y, Liu J (2009) Selective growth of well-aligned semiconducting single-walled carbon nanotubes. *Nano Lett* 9(2):800–805
88. Kang L, Zhang S, Li Q, Zhang J (2016) Growth of horizontal semiconducting SWNT arrays with density higher than 100 tubes/ μm using ethanol/methane chemical vapor deposition. *J Am Chem Soc* 138(21):6727–6730

89. Che Y, Wang C, Liu J, Liu B, Lin X, Parker J, Beasley C, Wong HSP, Zhou C (2012) Selective synthesis and device applications of semiconducting single-walled carbon nanotubes using isopropyl alcohol as feedstock. *ACS Nano* 6(8):7454–7462
90. Zhou W, Zhan S, Ding L, Liu J (2012) General rules for selective growth of enriched semiconducting single walled carbon nanotubes with water vapor as in situ etchant. *J Am Chem Soc* 134(34):14019–14026
91. Hong G, Zhang B, Peng B, Zhang J, Choi WM, Choi J-Y, Kim JM, Liu Z (2009) Direct growth of semiconducting single-walled carbon nanotube array. *J Am Chem Soc* 131(41):14642–14643
92. Jin SH, Dunham SN, Song J, Xie X, Kim J-h LuC, Islam A, Du F, Kim J, Felts J, Li Y, Xiong F, Wahab MA, Menon M, Cho E, Grosse KL, Lee DJ, Chung HU, Pop E, Alam MA, King WP, Huang Y, Rogers JA (2013) Using nanoscale thermocapillary flows to create arrays of purely semiconducting single-walled carbon nanotubes. *Nat Nanotechnol* 8(5):347–355
93. Xie X, Jin SH, Wahab MA, Islam AE, Zhang C, Du F, Seabron E, Lu T, Dunham SN, Cheong HI, Tu Y-C, Guo Z, Chung HU, Li Y, Liu Y, Lee J-H, Song J, Huang Y, Alam MA, Wilson WL, Rogers JA (2014) Microwave purification of large-area horizontally aligned arrays of single-walled carbon nanotubes. *Nat Commun* 5:5332
94. Du F, Felts JR, Xie X, Song J, Li Y, Rosenberger MR, Islam AE, Jin SH, Dunham SN, Zhang C, Wilson WL, Huang Y, King WP, Rogers JA (2014) Laser-induced nanoscale thermocapillary flow for purification of aligned arrays of single-walled carbon nanotubes. *ACS Nano* 8(12):12641–12649
95. Zhang G, Qi P, Wang X, Lu Y, Li X, Tu R, Bangsaruntip S, Mann D, Zhang L, Dai H (2006) Selective etching of metallic carbon nanotubes by gas-phase reaction. *Science* 314(5801):974–977
96. Zhang Y, Zhang Y, Xian X, Zhang J, Liu Z (2008) Sorting out semiconducting single-walled carbon nanotube arrays by preferential destruction of metallic tubes using xenon-lamp irradiation. *J Phys Chem C* 112(10):3849–3856
97. Li P, Zhang J (2011) Sorting out semiconducting single-walled carbon nanotube arrays by preferential destruction of metallic tubes using water. *J Mater Chem* 21(32):11815–11821
98. Hu Y, Chen Y, Li P, Zhang J (2013) Sorting out semiconducting single-walled carbon nanotube arrays by washing off metallic tubes using SDS aqueous solution. *Small* 9(8):1306–1311
99. Krupke R, Hennrich F, Hv Löhneysen, Kappes MM (2003) Separation of metallic from semiconducting single-walled carbon nanotubes. *Science* 301(5631):344–347
100. Krupke R, Hennrich F, Weber HB, Kappes MM, v. Löhneysen H (2003) Simultaneous deposition of metallic bundles of single-walled carbon nanotubes using ac-dielectrophoresis. *Nano Lett* 3(8):1019–1023
101. Vijayaraghavan A, Blatt S, Weissenberger D, Oron-Carl M, Hennrich F, Gerthsen D, Hahn H, Krupke R (2007) Ultra-large-scale directed assembly of single-walled carbon nanotube devices. *Nano Lett* 7(6):1556–1560
102. Shekhar S, Stokes P, Khondaker SI (2011) Ultrahigh density alignment of carbon nanotube arrays by dielectrophoresis. *ACS Nano* 5(3):1739–1746
103. Cao Q, S-j Han, Tulevski GS (2014) Fringing-field dielectrophoretic assembly of ultrahigh-density semiconducting nanotube arrays with a self-limited pitch. *Nat Commun* 5:5071
104. Bornhoeft LR, Castillo AC, Smalley PR, Kittrell C, James DK, Brinson BE, Rybolt TR, Johnson BR, Cherukuri TK, Cherukuri P (2016) Teslaphoresis of carbon nanotubes. *ACS Nano* 10(4):4873–4881
105. LeMieux MC, Roberts M, Barman S, Jin YW, Kim JM, Bao Z (2008) Self-sorted, aligned nanotube networks for thin-film transistors. *Science* 321(5885):101–104
106. Park H, Afzali A, Han S-J, Tulevski GS, Franklin AD, Tersoff J, Hannon JB, Haensch W (2012) High-density integration of carbon nanotubes via chemical self-assembly. *Nat Nanotechnol* 7(12):787–791
107. Wu J, Jiao L, Antaris A, Choi CL, Xie L, Wu Y, Diao S, Chen C, Chen Y, Dai H (2013) Self-assembly of semiconducting single-walled carbon nanotubes into dense, aligned rafts. *Small* 9(24):4142–4148
108. Wu J, Antaris A, Gong M, Dai H (2014) Top-down patterning and self-assembly for regular arrays of semiconducting single-walled carbon nanotubes. *Adv Mater* 26(35):6151–6156
109. Penzo E, Palma M, Chenet DA, Ao G, Zheng M, Hone JC, Wind SJ (2016) Directed assembly of single wall carbon nanotube field effect transistors. *ACS Nano* 10(2):2975–2981
110. Penzo E, Palma M, Wang R, Cai H, Zheng M, Wind SJ (2015) Directed assembly of end-functionalized single wall carbon nanotube segments. *Nano Lett* 15(10):6547–6552

111. Cao Q, S-j Han, Tulevski GS, Zhu Y, Lu DD, Haensch W (2013) Arrays of single-walled carbon nanotubes with full surface coverage for high-performance electronics. *Nat Nanotechnol* 8(3):180–186
112. Li X, Zhang L, Wang X, Shimoyama I, Sun X, Seo W-S, Dai H (2007) Langmuir–Blodgett assembly of densely aligned single-walled carbon nanotubes from bulk materials. *J Am Chem Soc* 129(16):4890–4891
113. Deegan RD, Bakajin O, Dupont TF, Huber G, Nagel SR, Witten TA (1997) Capillary flow as the cause of ring stains from dried liquid drops. *Nature* 389(6653):827–829
114. Engel M, Small JP, Steiner M, Freitag M, Green AA, Hersam MC, Avouris P (2008) Thin film nanotube transistors based on self-assembled, aligned, semiconducting carbon nanotube arrays. *ACS Nano* 2(12):2445–2452
115. Shastry TA, Seo J-WT, Lopez JJ, Arnold HN, Kelter JZ, Sangwan VK, Lauhon LJ, Marks TJ, Hersam MC (2013) Large-area, electronically monodisperse, aligned single-walled carbon nanotube thin films fabricated by evaporation-driven self-assembly. *Small* 9(1):45–51
116. Brady GJ, Way AJ, Safron NS, Evensen HT, Gopalan P, Arnold MS (2016) Quasi-ballistic carbon nanotube array transistors with current density exceeding Si and GaAs. *Sci Adv* 2(9):1601240



REVIEW

Recent Developments in Single-Walled Carbon Nanotube Thin Films Fabricated by Dry Floating Catalyst Chemical Vapor Deposition

Qiang Zhang¹ · Nan Wei¹ · Patrik Laiho¹ · Esko I. Kauppinen¹

Received: 14 September 2017 / Accepted: 13 November 2017 / Published online: 27 November 2017
© Springer International Publishing AG, part of Springer Nature 2017

Abstract Transparent conducting films (TCFs) are critical components of many optoelectronic devices that pervade modern technology. Due to their excellent optoelectronic properties and flexibility, single-walled carbon nanotube (SWNT) films are regarded as an important alternative to doped metal oxides or brittle and expensive ceramic materials. Compared with liquid-phase processing, the dry floating catalyst chemical vapor deposition (FCCVD) method without dispersion of carbon nanotubes (CNTs) in solution is more direct and simpler. By overcoming the tradeoff between CNT length and solubility during film fabrication, the dry FCCVD method enables production of films that contain longer CNTs and offer excellent optoelectronic properties. This review focuses on fabrication of SWNT films using the dry FCCVD method, covering SWNT synthesis, thin-film fabrication and performance regulation, the morphology of SWNTs and bundles, transparency and conductivity characteristics, random bundle films, patterned films, individual CNT networks, and various applications, especially as TCFs in touch displays. Films based on SWNTs produced by the dry FCCVD method are already commercially available for application in touch display devices. Further research on the dry FCCVD method could advance development of not only industrial applications of CNTs but also the fundamental science of related nanostructured materials and nanodevices.

Chapter 4 was originally published as Zhang, Q., Wei, N., Laiho, P. & Kauppinen E. I. Top Curr Chem (Z) (2017) 375: 90. <https://doi.org/10.1007/s41061-017-0178-8>.

✉ Qiang Zhang
qiang.zhang@aalto.fi

¹ Department of Applied Physics, Aalto University School of Science, P.O. Box 15100, 00076 Aalto, Finland

Keywords Single-walled carbon nanotubes · Dry floating catalyst chemical vapor deposition · Transparent conducting film · Touch displays

1 Introduction

Since their discovery, carbon nanotubes (CNTs) have been the subject of intensive research [1–3]. CNTs can be thought of as graphene sheets rolled up in certain directions, designated by pairs of integers, existing as both single-walled nanotubes (SWNTs) and multiwalled nanotubes (MWNTs) [4, 5]. Compared with MWNTs, SWNTs have been shown to exhibit very distinct properties, providing greater potential for use of this outstanding structural material in nano- and macroscale applications [1, 6]. Depending on their chirality and diameter, SWNTs can be either semiconducting, metallic, or semimetallic in nature [7]. Both experiments and theory have confirmed that CNTs possess excellent and unique characters, which originate from their molecular structure [7]; For example, SWNTs possess high conductivity (up to 4×10^5 S cm $^{-1}$) [8], excellent current-carrying capacity (up to 10^9 A cm $^{-2}$) [9], excellent charge-carrier mobility (up to 10^5 cm 2 V $^{-1}$ s $^{-1}$ at room temperature) [10], excellent thermal conductivity (up to 3500 W m $^{-1}$ K $^{-1}$) [11], and excellent mechanical performance (Young's modulus in the range of 1–2 TPa) [12, 13].

Over recent decades, numerous academic and industrial groups have explored use of SWNTs in diverse potential applications [1, 14]. In particular, SWNTs with various types of architecture and different dimensions have been synthesized and investigated worldwide to fully utilize the excellent properties of individual SWNTs [15–18]. Thin films is an emerging research area, offering the advantage of statistical averaging for better reproducibility [14, 19–21]. The collective behavior of two-dimensional (2D) SWNT films can provide unique physical properties and enhanced device performance [22]. Their superior properties, including mechanical flexibility, optical transparency, unique electric properties, high surface area, etc., result in great potential for use of CNT films the applications in energy fields, electronic devices, displays, sensors, etc [19, 20]. However, some important challenges remain to be resolved: (1) controlled fabrication of SWNT films with good reproducibility, (2) utilization of the excellent properties of individual SWNTs at macroscopic level, and (3) prediction or exploration of new properties offered by macroscopic SWNT assemblies.

To date, several methods have been developed to fabricate CNT films. Specifically, two main types of process, i.e., liquid-phase and dry processing, have been used to assemble CNT films [19]. Liquid-phase processing involves deposition of tubes from surfactant solution or superacids to form CNT thin films, which is readily scalable. However, a practical challenge with such liquid-phase methods is that the low solubility and strong intertube interactions of SWNTs make it difficult to obtain submonolayer SWNT thin films with uniform, moderate to high coverage and without significant presence of bundles [23, 24]. Complete removal of residual surfactants and acids is also a difficult problem. Dry methods for fabrication of CNT

films mainly include three approaches: growth directly by on-substrate CVD, drawing from a vertically aligned CNT forest grown on a solid substrate, or deposition directly from a floating catalyst chemical vapor deposition (FCCVD) system. CNT networks can be grown directly on a substrate by CVD. The orientation, density, and even chiral distribution of the CNTs can be controlled by using selected and regulated catalysts on the substrate [25–27]. However, such on-substrate CVD normally requires multistep processing and has low yield. The aligned CNT films drawn from a CNT forest are anisotropic [28]. However, devices based on aligned CNT film components offer poor statistical reproducibility. SWNT films cannot be obtained from the CNT forest method. In addition, intricate treatment is needed to obtain MWNT films from a CNT forest for special applications; For example, laser trimming and metal deposition increase the transmittance and conductivity, respectively, when using MWNT films as transparent conductive films [29]. On the other hand, film fabrication by the FCCVD method is based on direct deposition of an SWNT aerosol synthesized by the FCCVD method [22, 30–32]. FCCVD is low-cost and readily scalable and offers good control over the morphology of the CNTs or bundles in the thin film, including their length, diameter, density, etc., which are critical parameters for film performance. In particular, films fabricated by the FCCVD method can contain individual SWNTs of theoretically unlimited length [33]. These characteristics will lead to many novel results and great improvements in CNT applications.

This review focuses on fabrication of films using the dry FCCVD method, as well as corresponding SWNT synthesis, thin-film fabrication and performance regulation, transparency and conductivity characteristics, random bundle films, patterned films, and individual CNT networks; in addition, various applications, especially as transparent conductive electrodes (TCEs), are highlighted. The final section concludes with some long-standing problems and identifies topics warranting further investigation in the near future.

2 CNT Synthesis Process and Mechanism

The research fields of CNT synthesis and CNT films are interdependent. Many key advances in CNT catalysts and synthesis lead immediately to new results in film fabrication, performance, and applications. There are three major methods of CNTs production: arc discharge, laser ablation, and chemical vapor deposition (CVD) [34]. Owing to its high yield and relatively mild synthesis conditions, CVD is the most common method used for CNT growth. However, most products synthesized by CVD are mainly powder like or supported on different substrates. FCCVD, as a special CVD method, has attracted tremendous attention. Since the catalyst particles and CNTs are suspended in gas phase as an aerosol throughout the entire CNT formation process, the FCCVD method is more flexible and controllable [29], not only being an effective approach to mass-produce CNTs of good quality [36] but also enabling direct synthesis of different SWNT architectures, such as continuous fibers [18, 37], transparent films [22, 31], and CNT sponges [38].

Many features of FCCVD can affect the morphology and properties of the resulting CNTs, with catalyst composition, catalyst size, carbon source, temperature, and gas-phase chemistry being the five principal parameters [39, 40]. The most effective catalysts for FCCVD are formed from pyrolysis of easily sublimed organometallic compounds, such as ferrocene, carbonyl iron, dimethoate, or metal nanoparticles generated using a hot-wire or spark system [35, 41, 42]. In 1998, Cheng et al. first applied the FCCVD method to synthesize SWNTs using ferrocene as catalyst [6, 43]. This result suggested that FCCVD is a potential method for high-yield production of CNTs. The catalyst size is slightly larger than the diameter of the resulting nucleated CNTs, a phenomenon also observed in on-substrate CVD and in situ growth in environmental transmission electron microscope [41]. Many excellent carbon sources for production of CNTs are known, including hydrocarbons and carbon monoxide (CO) [40]. Hydrocarbons thermally self-decompose into carbon clusters (C_xH_y), which are then absorbed by the catalyst. This process contributes to rapid and high-yield growth of CNTs [44]. However, high partial press of the hydrocarbon or temperature may result in production of surplus amorphous carbon [45]. CO as carbon source is significantly different from hydrocarbons; It decomposes only at the surface of the catalyst nanoparticles, liberating carbon atoms for CNT formation, since the disproportionation reaction $2CO(g) \leftrightarrow C(s) + CO_2(g)$ requires the presence of a catalyst surface [35, 36]. This reaction can greatly reduce byproduct generation. SWNT production based on CO disproportionation has been carried out at either high or atmospheric pressure (Fig. 1), and both methods are widely applied for commercial production of SWNTs and films. In 2001, Smalley's group [36] developed the high-pressure CO (HiPCO)

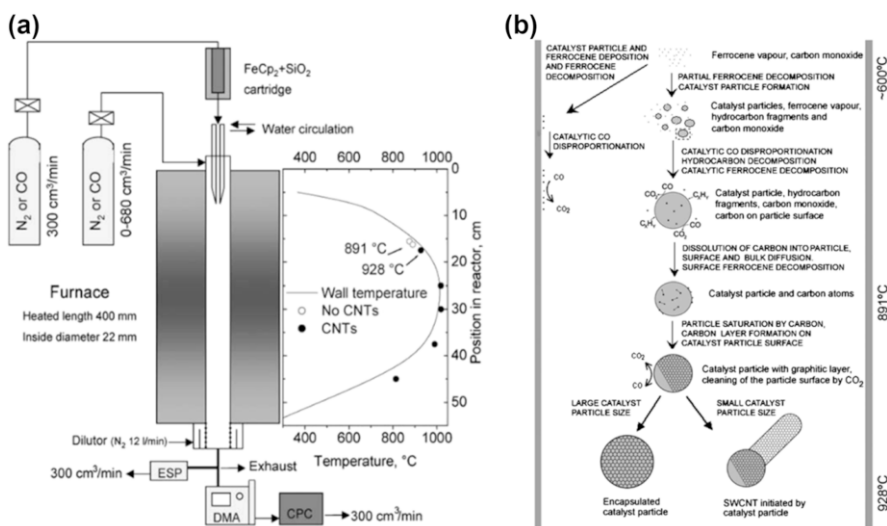


Fig. 1 High-quality SWCNTs synthesized with CO as carbon source at atmospheric pressure based on FCCVD [54]. Copyright 2006 Elsevier. **a** Schematic of experimental setup and wall temperature profile for FCCVD synthesis of SWCNTs with ferrocene as catalyst. Open circles indicate sampling locations where CNTs were not observed; solid circles indicate conditions for CNT sampling. **b** Schematic of SWCNT formation mechanism in FeCp₂-CO system at temperature of 1000 °C

approach to produce large quantities of SWNTs in presence of iron nanoparticles formed from decomposition of iron pentacarbonyl. More recently, He et al. [46] and Koziol et al. [40] examined the structural differences between tubes grown using CO, methane, ethanol, and toluene by electron diffraction methods. The optimal growth temperature appeared to range from 700 to 1200 °C, lying between the temperature for amorphous carbon formation and the graphitization temperature. Argon, helium, nitrogen, and hydrogen are commonly used as carrier gas for feedstock introduction and product carriage, although less research has been carried out on the difference between use of argon, helium, or nitrogen for CNT growth. It is reported that hydrogen can effectively suppress excessive decomposition of hydrocarbons and also reduce iron oxide during production of CNTs [47, 48]. In addition, hydrogen can etch amorphous carbon and CNTs. In 2014, Liu et al. reported production of 88% metallic SWNTs (m-SWNTs) when introducing H₂ as etchant to selectively etch semiconducting SWNTs (s-SWNTs) (Fig. 2) [49]. Based on the effect of tuning the growth parameters, it was proposed that small-diameter s-SWNTs and large-diameter m-SWNTs were first obtained, then introduction of hydrogen as etchant gas preferentially removed the smaller-diameter s-SWNTs. In the cited work, few-wavelength Raman was used to determine the fraction of metallic and semiconducting tubes. Due to the complexity of evaluation of such Raman spectra for assignment of CNT-type distributions, more accurate analysis methods are needed, e.g., electron diffraction, for determination of the metallic tube fraction [40, 50–52].

To obtain high-quality, high-yield SWNTs and films at atmospheric pressure, several crucial improvements have been made to the FCCVD method at Aalto University, including a well-designed FCCVD system and use of a CNT synthesis mechanism with CO as carbon source [35, 41, 53, 54]. As shown in Fig. 1a, the laminar reactor for SWNT production includes a water-cooled injector and a vertical furnace [35]. The injector probe reaches into the high-temperature zone of the vertical CVD reactor. Recirculation of the additional flow occurs only in the region close to the injector probe outlet. However, the flow containing the nanoparticles does not take part in the recirculation, and the total flow becomes fully developed and laminar as it moves towards the high-temperature zone of the furnace,

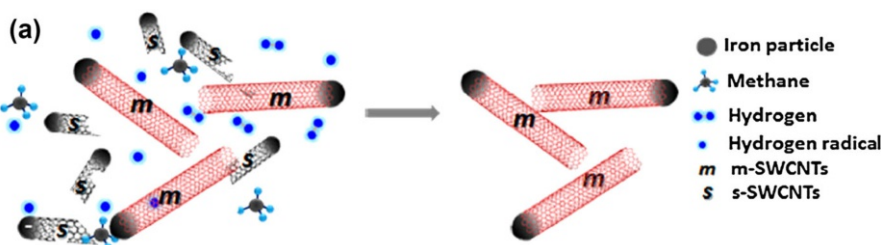


Fig. 2 Schematics proposing selective removal of small-diameter s-SWNTs from large-diameter m-SWNTs by hydrogen etching [49]. Copyright 2014 American Chemical Society

indicating laminar flow conditions for catalyst particle formation and SWNT growth. Use of this type of equipment can effectively reduce catalyst deposition on the reactor wall. The aerosol of catalyst or precursor, carbon source, and carrier gas are introduced through the injector probe into the high-temperature zone of the vertical CVD reactor. Floating CNTs and bundles can be directly and continuously obtained at the reactor end. The mechanism for SWNT formation in the FeCp₂-CO system is shown in Fig. 1b. Decomposition of FeCp₂ vapor results in catalyst particle formation and likely release of hydrocarbon fragments. Catalyst particles are formed by nucleation and continue to grow through collision processes. In addition, catalyst particle growth can continue as a result of ferrocene vapor decomposition on the particle surfaces. Depending on their size, the catalyst particles either nucleate growth of a SWNT or become inactive by growing too large (usually above 3 nm in diameter). In addition, through a series of CNT growth experiments, the growth window for temperature for the CO system was determined to be 891 to 928 °C [54]. In addition to high-quality SWNTs, a novel hybrid material, viz. nanobuds, in which fullerenes and SWNTs are combined into a single structure in which the fullerenes are covalently bonded onto the outer surface of the SWNTs, was invented at Aalto University. In 2007, based on the FeCp₂-CO system, carbon nanobuds (CNBs) were synthesized with increasing H₂O and CO₂ concentrations during the FCCVD process for synthesis of CNT [33, 55]. Due to their unique structure, CNBs possess advantageous properties compared with SWCNTs or fullerenes alone, including field-emission characteristics when in nonbonded configuration.

3 CNT Film Fabrication

Recently, the demand for TCFs has surged due to the expansion of the commercial market for optoelectronic devices such as liquid-crystal displays (LCDs), touch panels, photovoltaics, and organic light-emitting diodes (OLEDs) [56, 57]. In 2014, sales of TCFs in the LCD industry, which has led consumption for years, were approximately USD 1.5 billion [58]. In addition, the commercial market for TCFs in the solar industry is expected to exceed USD 16.3 billion by 2017 [59], and the market for TCFs in touch panels is anticipated to reach about USD 5 billion by 2019 [60].

Indium tin oxide (ITO) is the most widely used and current industry-standard transparent conductor material, offering excellent optoelectronic properties with low sheet resistance (R_s , from 10 to 100 Ω/sq) at high transmittance (> 85%) [57]. However, as a brittle ceramic, the limitations of its physical property have presented many challenges for development of flexible electronics [57, 61]. In addition, the high refractive index of ITO may result in images displayed on touch screens becoming washed out [61, 62]. Recently, various novel materials, including silver nanowires, metal mesh, graphene, and CNT films, have emerged as ITO replacement materials [56]. Owing to their low surface resistance due to the high conductivity of metal compared with ITO, silver nanowire films and metal mesh offer benefits for use in large-area touch displays [63]. However, there are also some severe problems with application of silver nanowires and metal meshes as TCFs,

such as performance stability and high ambient light reflectance [64]. The high cost and complex process of graphene synthesis seriously limit development of graphene for use as TCF [65]. Among these promising candidates, CNT TCFs exhibit great potential because of their high stretchability, mechanical flexibility, chemical stability, color neutrality, less haze, wider spectral range, etc. [56, 59, 66, 67].

4 2D Network Film

As mentioned above, FCCVD is a promising technique for SWNT film fabrication. It enables direct, single-step fabrication of clean, ready-to-use SWNT networks for use as high-performance TCFs. Currently, there are three main approaches for CNT film fabrication based on FCCVD, as shown in Fig. 3. The individual tubes or bundles produced by the FCCVD method are suspended in a carrier gas. Films can then be obtained by deposition of the CNTs or bundles onto a membrane filter [30, 31] or FCCVD chamber wall [22], or by direct transformation of the CNT aerosol into an aerogel [68]. The specific processes of film fabrication are discussed and compared below.

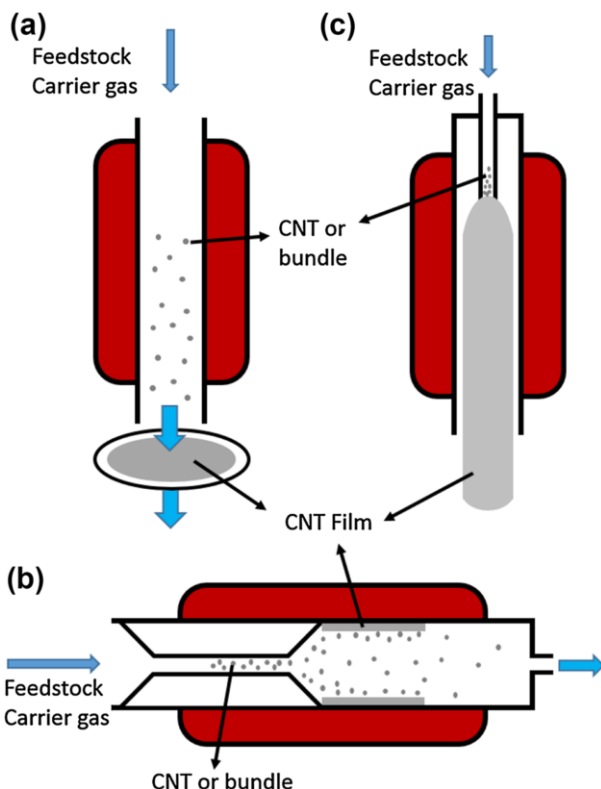


Fig. 3 Schematics of CNT film fabrication processes based on FCCVD, where CNTs and bundles are directly deposited onto a membrane filter (a) or FCCVD chamber wall (b), or c the CNT aerosol is transformed into an aerogel in the FCCVD reactor

CNT films can be prepared by dry deposition, combining the FCCVD method with an aerosol filtration system, as shown in Fig. 3a. The aerosol containing individual SWNTs and their small bundles is collected by a membrane filter at the outlet of the reactor to form a SWNT network. The sheet resistance and transmittance can be controlled by adjusting the network deposition time or reactor dimensions and conditions. In 2010, Kaskela et al. [31] integrated SWNTs collected on a nitrocellulose filter based on the laminar flow reactor with CO as carbon source and CO₂ as additive to enhance the catalyst particle activity (Fig. 4a). The micro-morphology of the SWNT film was a continuous 2D network, as shown in Fig. 4b. The sheet resistance of the SWNT films with bundle length of 9.4 μm ranged from 80 to 100 Ω/sq at a transmission of $T = 90\%$ after HNO₃ doping. Since such SWNT

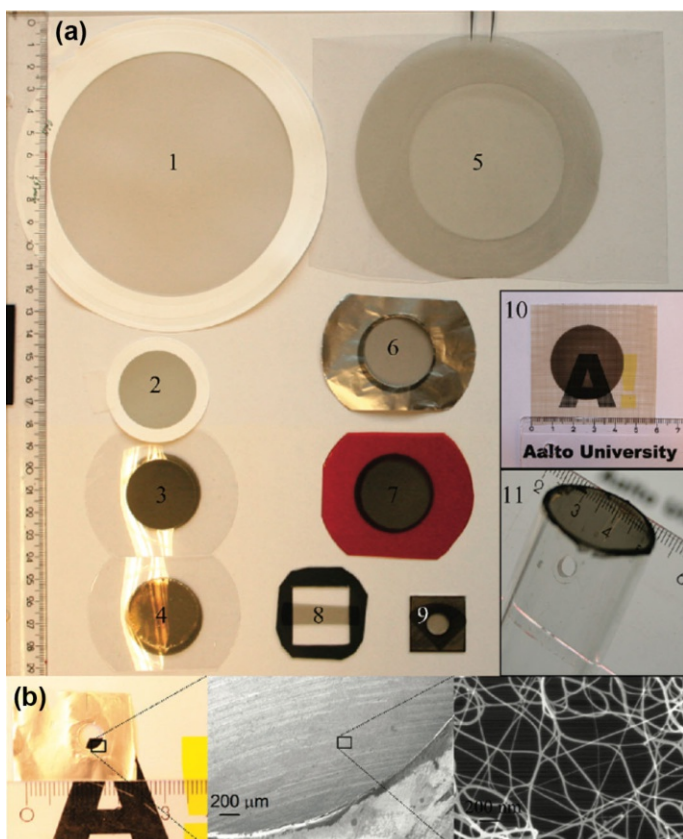


Fig. 4 Various SWNT films prepared by FCCVD [30] (Copyright 2011 American Chemical Society): **a** SWCNT films collected on nitrocellulose filters (1, 2), pristine (3) and ethanol-densified (4) films suspended over polyethylene terephthalate (PET), freestanding films (FSFs) on PET (5), aluminum foil (6), and Kapton (7), a strip film suspended over a rectangular hole (8), and on cold-rolled steel (9). Insets show semi-freestanding film on polyetheretherketone substrate (10) and a film suspended over the open end of a glass tube (11). **b** Set of images showing submonolayer FSF suspended over 5-mm openings in aluminum foil

films are collected on low-adhesion filters, they can be easily transferred to practically any substrate, including flexible polymers, glass, quartz, and various metals, using a simple press. SWNT films with various thicknesses and sizes on different substrates are shown in Fig. 4. This simple film fabrication method is also called direct dry transfer [31]. In addition, the CNT aerosol can also be deposited onto the substrate surface downstream of the FCCVD system by using an electric field thermophoretic technique for thin-film manufacture [69].

The press transfer method is compatible with roll-to-roll fabrication methods, thus opening up further upscaling potential for industrialized production. In particular, Carbon NanoBud (CNB) film, a special SWNT film from Canatu, is already in commercial production [62]. Homogeneous and patterned CNB films can be manufactured on large size sheets by combining the CNB aerosol synthesis method with room-temperature deposition. The film conductivity of CNB film at given transparency has doubled approximately every 12 months since 2007. In 2013, CNB films with properties of $100 \Omega/\text{sq}$ at 94% and $270 \Omega/\text{sq}$ at 98% were commercially available. The facility allowed capacity of up to $500,000 \text{ m}^2/\text{month}$ by Canatu. In addition, film performance of $100 \Omega/\text{sq}$ at >95% has been demonstrated [62].

Ma et al. [22] directly prepared SWNT films with methane as carbon source, argon as carrier gas, FeCp₂ as catalyst, and sulfur as promoter in 2007. During their preparation process, the CNTs are deposited on the FCCVD chamber wall in the high-temperature zone, then grow continuously to form CNT films (Fig. 3b) that can be easily peeled off after growth. The thickness of such freestanding and homogeneous SWNT films, with area up to several tens of square centimeters, can be regulated from 100 nm to 1 μm (Fig. 5a, b, c). These SWNT films are composed of highly entangled bundles about 30 nm in diameter and from tens to hundreds of micrometers in length (Fig. 5d, e). The diameter of the nanotubes in the bundles is about 1–2 nm. The bundles in the films are firmly connected with each other, as they grow to forming a continuous, preferentially 2D network at high temperature (Fig. 5e). Due to these good and long interbundle connections, such directly synthesized films offer good electrical and mechanical properties, with electrical conductivity of 2000 S/cm and strength of 360 MPa. Figure 5 f, g shows transmittance spectra from the ultraviolet to mid-infrared and the sheet resistance of freestanding SWNT films of different thicknesses. For 100-nm-thick film with sheet resistance of $50 \Omega/\text{sq}$, which was the thinnest intact film that could be peeled off the wall of the quartz tube, the transmittance in the visible region of the spectrum was above 70%.

In addition, freestanding CNT films can also be fabricated by transformation of the CNT aerosol into an aerogel using a well-designed FCCVD system. In 2013, Zhou et al. [68] introduced a blown aerosol technique into the process of CNT synthesis by FCCVD for continuous CNT film production (Fig. 3c). With injection of the feedstock for CNT synthesis and the carrier gas, transparent tubular films with diameter of ~100 mm were continuously blown out from the outlet of the FCCVD system at speed of ~120 m/h. The surface resistance of the as-synthesized SWNT films was ~200 Ω/sq at transmission of $T = 90\%$, for the optimized conditions. In

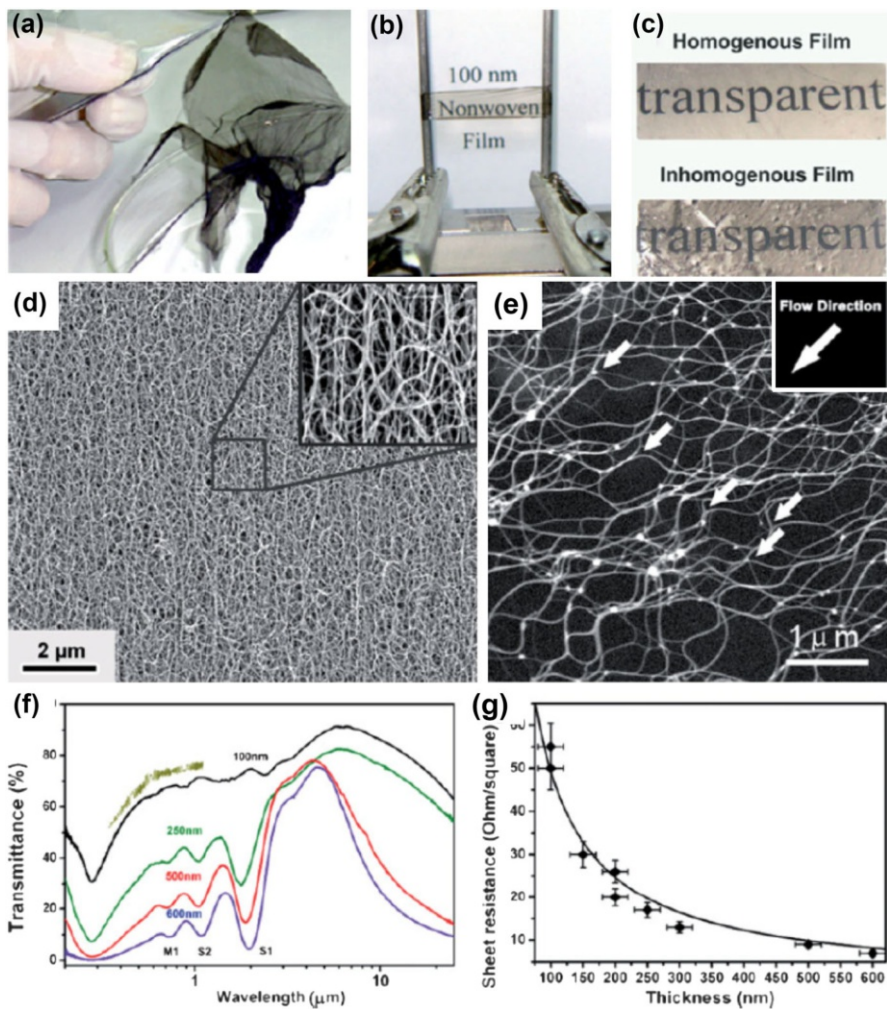


Fig. 5 **a** As-grown 250-nm-thick SWCNT nonwoven film. **b** Transparent 100-nm-thick film standing freely between metallic pillars. **c** 150-nm-thick homogeneous (upper) and inhomogeneous (lower) films. The importance of homogeneity is clear. **d** Large-scale scanning electron microscopy (SEM) image of 250-nm-thick film; inset shows higher magnification. **e** SEM image of SWCNT network in a single layer; white arrows indicate Y-type junctions and flow direction. **f** Transmittance spectra for as-grown films of different thicknesses. Numbers above curves indicate thickness, and the uppermost short curve corresponds to 100-nm-thick film on glass substrate. S1, S2 represent the electronic transitions for the semiconducting SWCNTs in the films, and M1 represents that of the metallic nanotubes. **g** Sheet resistance versus thickness of SWCNT films. The solid line is the best fit curve according to the definition of electrical conductivity [22]. Reprinted with permission from [22]. Copyright 2007 American Chemical Society

addition, the conductivity anisotropy could be regulated from 1 to 8 by increasing the film collection speed, resulting in more aligned bundles in the film.

5 Patterned Film Fabrication

Other than usual film manufacture, deposition of patterned films is another critical step for relevant final products such as touch panels and displays. Such patterning of CNT films can also overcome the tradeoff between transmittance and conductivity in TCFs. Patterned films are not uniformly transparent but may still meet many of the application requirements, as long as the features of the pattern are thin enough to not be recognized by the naked eye.

In the case of rectangular patterns, to a first-order approximation, the transmittance roughly equals the CNT coverage, while the conductance is proportional to the grid thickness:

$$R = \frac{\rho}{tf},$$

$$T = (1 - f) + fe^{-\alpha t},$$

where R is the sheet resistance, T is the film transmittance, ρ is the resistivity of the CNT grid, t is the grid thickness, α is the absorption coefficient of the CNT grid, and f is the duty cycle of the grid pattern, viz. $f = \frac{W}{A}$, where W is the CNT grid width and A is the grid pitch (Fig. 6d). Instead of vanishing, the transmittance approaches $1 - f$ as the pattern becomes thicker. Therefore, conductance and transmittance are

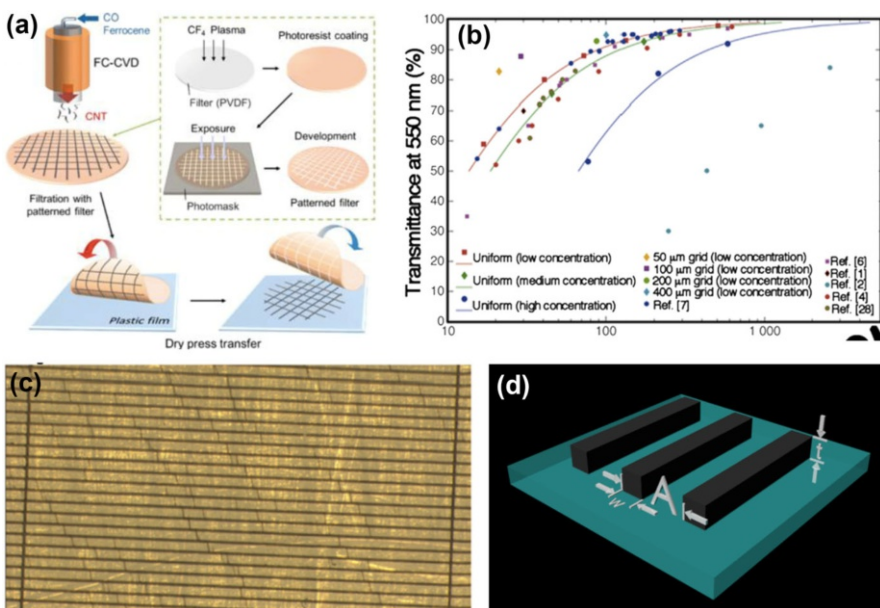


Fig. 6 Patterned carbon nanotube films: **a** Fabrication steps for patterned carbon nanotube film utilizing patterned filters [73]. Copyright 2014 American Chemical Society. **b** Comparison of sheet resistance between patterned and uniform carbon nanotube films and **c** optical image of patterned carbon nanotube films with rectangular geometry [33]. Copyright 2016 Elsevier. **d** Structural parameters of the rectangular pattern geometry

no longer strongly coupled. The factors limiting the conductivity are the quality of the CNTs and how thick the grid can be.

A few pioneering studies have been carried out on how to pattern carbon nanotube films. Inkjet printing is a facile method to make arbitrary patterns with linewidth above 50 microns [70]. On smaller scales, some specific patterns can be formed with the aid of polymer [71] or laser methods [72].

Among these methods, one approach is particularly well suited to the FCCVD method. This method utilizes dry transfer and photolithographically patterned filter membranes to achieve resolution down to microns, overcoming the tradeoff mentioned above. Fukaya et al. reported a 46% increase in conductivity for patterned compared with uniform film [73]. In a follow-up study, Kaskela et al. reported record-breaking performance of $69 \Omega/\text{sq}$ at 97% transmittance [33].

Improving the uniform film quality still matters in the patterned case, since it provides better base material, achieving the target conductance with lower thickness and material consumption. The conductivity versus transmittance characteristic can be further improved if the pattern can be made thicker; For example, a 40-nm-thick film can transmit 75% of light at 550 nm [30], corresponding to an absorption coefficient of $\alpha = 72,000/\text{cm}$. Improvement in the carbon nanotube quality results in little change in film density, so the absorption coefficient remains roughly unaltered. However, improvement in tube–tube contact and length will reduce the film resistivity, as shown in a recent report in which films of individual carbon nanotubes reached $89 \Omega/\text{sq}$ at 90% transmittance [33] with figure of merit of $\alpha\rho = 9.38$ and thus $\rho = 1.3 \times 10^{-6} \Omega \cdot \text{m}$ (*or* $7700 \text{ S} \cdot \text{cm}$). To achieve $10 \Omega/\text{sq}$ at 90% transmittance, the grid thickness required is 1.3 microns. This thickness could be reduced further by applying better CNTs or through use of doping techniques, which will have lower $\alpha\rho$.

The value of 1.3 microns is not very thick for TCFs. However, few attempts have been made to form patterned random carbon nanotube films of such thickness. In previous attempts, the thickness of the densified film was around 0.15 microns, being limited by the thickness of the photoresist [73]. It is reasonable to expect that increasing the thickness of the photoresist, or development of new patterning techniques for thicker CNT films, will help CNT TCFs to reach better performance and wider application scenarios.

6 Characterization, requirements, and performance of CNT films fabricated by FCCVD for use as TCFs

Low sheet resistance and high light transmission across the UV–Vis–NIR spectrum are pursued for ideal transparent conducting films. Practically, sheet resistance can be measured directly using the four-point probe, two-point conductivity probe, or two-line method, while transmission can be obtained by measuring the UV–Vis absorbance of the TCF. Because the transmittance of a film decreases through absorption as its thickness is increased, there is a tradeoff between these two parameters [74]. Therefore, a figure of merit (FOM) should be defined to compare

various TCFs, combining transmission and sheet resistance and being independent of thickness.

According to existing literature, two main FOMs are used for comparison of TCFs [75], i.e., $\alpha\rho$ and σ_{dc}/σ_{OP} , where α , ρ , σ_{dc} , and σ_{OP} are the absorption coefficient, resistivity, direct-current (dc) electrical conductivity, and optical conductivity of a uniform TCF, respectively. The sheet resistance of a uniform film is defined as $R_s = \rho/t$, where t is the film thickness. According to the Beer–Lambert law, the transmission of light (T) through a film of homogeneous material can be modeled as $T = \exp(-\alpha t)$. Combining these two equations yields

$$T = \exp\left(-\frac{\alpha\rho}{R_s}\right). \quad (1)$$

$\alpha\rho$ is a constant parameter for a uniform and homogeneous material. In addition to Eq. (1), the following is another formula commonly used to describe the relationship between R_s and T for TCFs [76]:

$$T = \left(1 + \frac{Z_0}{2R_s} \frac{\sigma_{OP}}{\sigma_{dc}}\right)^{-2}, \quad (2)$$

where Z_0 is the characteristic impedance of vacuum ($\sim 376.73 \Omega$). Both σ_{dc} and σ_{OP} are fundamental properties of the material, therefore σ_{dc}/σ_{OP} is also a useful FOM for TCF evaluation. It is worth noting that Eq. (2) is based on the assumption that the film thickness is much less than the wavelength of interest. In the case of CNT films as TCFs, their thickness is generally <50 nm. Therefore, σ_{dc}/σ_{OP} is valid as a FOM to evaluate their performance of CNT films as TCFs. Degiorgi et al. measured a σ_{OP} value of 200 S/cm at 550 nm for buckypaper composed of SWNTs [77]. This value applies for SWNT films obtained by FCCVD, because σ_{OP} is independent of doping level but varies with the number of walls in the CNTs.

Good candidates for use in TCFs will have higher FOM, $\alpha\rho$ and σ_{dc}/σ_{OP} , meaning a material with high conductivity and low optical absorption [78]. Based on Eqs. (1) and (2), $\alpha\rho = \frac{Z_0}{2} \frac{\sigma_{OP}}{\sigma_{dc}}$ can be obtained by performing a Taylor expansion in T/R_s to first order. Hence, $\alpha\rho$ and σ_{dc}/σ_{OP} are phenomenologically equivalent. Because σ_{dc}/σ_{OP} is dimensionless and simple, we use it to compare the properties required for practical applications of CNT TCFs in Table 1.

The requirements on the optoelectronic properties of TCFs vary depending on the application [19]. The minimal requirements for practical application of TCFs are presented in Table 1. CNT films offer various advantages in terms of physical flexibility, excellent optical properties, and chemical stability, compared with ITO or other candidate TCFs. However, the conductivity of even state-of-the-art SWNT films must still be improved to meet industrial requirements for certain applications in order to replace ITO (Table 1); For example, transparent electrodes for photovoltaic devices require high transmittance above 90% and conductivity of R_s below 10 Ω/sq for efficient energy harvesting, which means $\frac{\sigma_{OP}}{\sigma_{dc}} > 348.5$. Based on theoretical and experimental results, the optoelectronic properties of SWNT films depend on many parameters, including the morphology (length, diameter, and

Table 1 Minimal requirements for practical applications of TCFs and performance of SWNT films as TCFs

TCF or application	<i>T</i> (%)	<i>R</i> _s (Ω/sq)	σ_{dc}/σ_{op}	Comment	Refs.
Photovoltaic electrode	90	10	348.5		[19, 59]
ITO	90	10–100	348.5–34.8	Mature, low sheet resistance, high transparency; costly, brittle, high reflection	[19, 57]
Patterned SWNT film produced by FCCVD	97	69	178	Overcomes the tradeoff between <i>T</i> and <i>R</i> _s ; costly, time-consuming	[33, 66]
MWNT film from CNT forest	87	29	90		[29]
CNT film obtained by CNT forest	83	24	80.4	Efficient process, less impurities, anisotropic conductivity; aligned CNT forest required, laser ablation and metal deposition	
CNT film obtained by FCCVD	90	208	16.8		
OLED display electrode	90	50	69.7	Mature, efficient process, good control over thickness; residual catalyst, chemical doping	[62]
SWNT film obtained by liquid-phase processing	78–90	30–300	65.5	Fast and simple process, uniform films; chemical doping, high pollution	[19, 59]
SWNT film deposited on filter by FCCVD	90	80–100	43.6–34.8	Mature, efficient process, laser ablation and metal deposition; residual catalyst, chemical doping	[19, 59, 106]
Individual SWNT film obtained by FCCVD	90	89	39.2	Better performance for thin-film transistors; low yield, time-consuming, short CNTs	[31, 92, 126]
LCD screen electrode	85	100	22.3	88% M-SWNT, simple process; chemical doping, unclear mechanism	[33, 98]
Enriched metallic SWCNT film obtained by FCCVD	90	160	21.8		[19, 59]
SWNT film deposited on reactor wall by FCCVD	70	50	19.3	Without further chemical doping, without hydrogen; poor uniformity, large-scale production limited, little control over thickness,	[22]
Continuous tubular SWNT film obtained by FCCVD	90	200	17.4	High yield, without hydrogen, without further chemical doping; high synthesis temperature, poor uniformity	[68]
Touch panel electrode	85	500	4.5		[19, 62]

The requirements of various applications for TCFs are in bold

orientation) of the SWNTs and bundles, the quality, purity, and chirality of the SWNTs, doping, etc. [79–82].

Since the contact resistance between individual SWNTs or bundles is orders of magnitude higher than the resistance along a tube [31, 81, 83, 84], highly resistive junctions limit the electrical conductivity of SWNT films obtained from FCCVD as well as other methods. Recently, Znidarsic et al. [85] used conductive atomic force microscopy to analyze the contact resistance between tubes at isolated junctions of

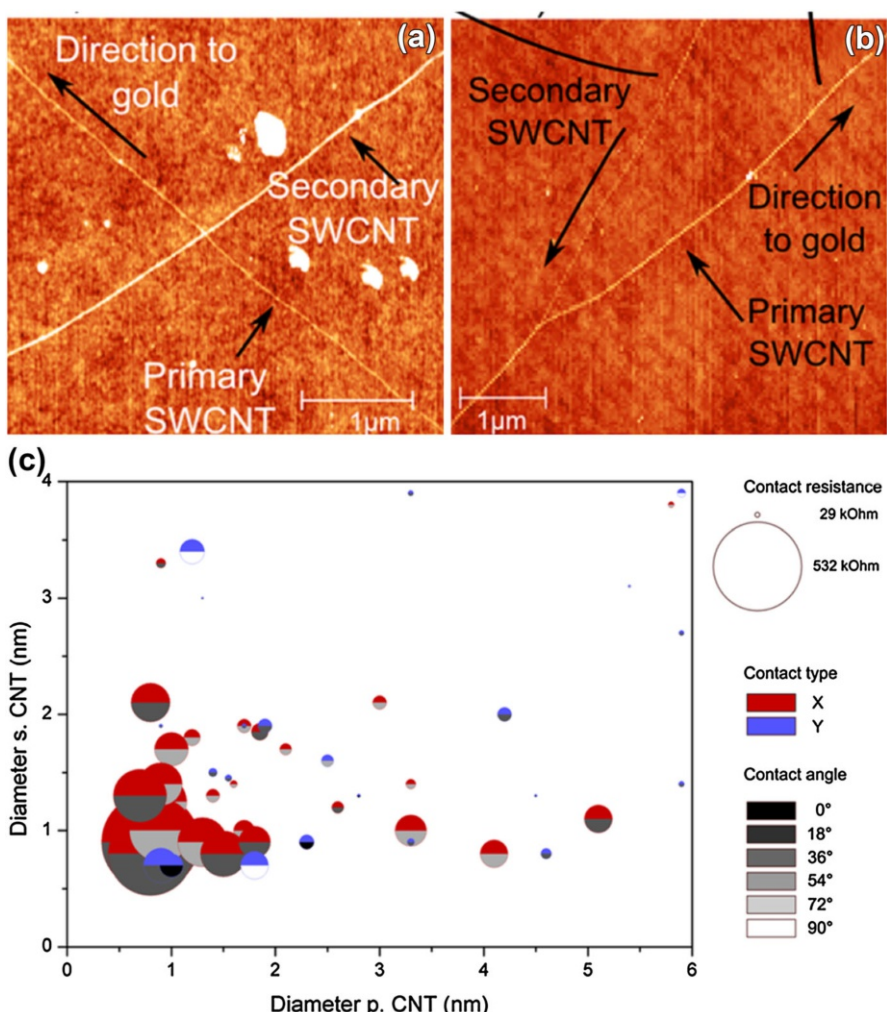


Fig. 7 Morphologies and contact resistances of SWCNT intermolecular junctions [85]. **a, b** AFM images of X and Y junctions, two main SWNT intermolecular junctions. **c** Contact resistance of X and Y junctions versus diameters of primary and secondary CNTs and their intersection angles. Y junctions have lower resistance than X junctions for given structural parameters, with minimum value of 29 kΩ. The contact resistance of both junctions is inversely proportional to the diameters of the CNT branches. Adapted with permission from [82]. Copyright 2014 American Chemical Society

pristine and nitric-acid-treated SWNT networks obtained by FCCVD, as shown in Fig. 7. At room temperature, the conductivity of a SWNT or bundle was found to be ohmic, with values close to 3–16 k Ω / μ m. The resistance of their junctions was much higher, ranging from 29 to 532 k Ω and decreasing with increasing SWCNT or bundle diameter. The contact resistance also depended on the contact morphology [86]. Compared with X junctions, the contact resistance of Y junctions is orders of magnitude lower [15], because they benefit from carrier transport via longer interbundle connections. The contact resistance of both types of junction is inversely proportional to the diameters of CNT branches. They also found that moderate nitric acid treatment reduced the sheet resistance by a factor of 4 by reducing the average junction resistance by a factor of 3, while the resistance of the nanotubes remained largely unaltered. These results suggest that the mechanism for resistance reduction on doping is related to contact modulation with no major impact on the conductance of the SWNTs themselves [87]. However, in the case of defective or substitutionally doped SWNTs, the resistance of the SWNTs or their bundles may be much larger due to scattering on lattice defects, dominating the total resistance of the thin film [88, 89].

As mentioned above, interbundle and intertube contacts dominate the overall resistance of typical SWNT networks. Therefore, increasing bundle length correlates with decreasing sheet resistance at constant optical transparency, as longer bundles reduce the amount of high-resistance interbundle contacts in the network [90]. An exponential relationship between conductance and average CNT bundle length has been found experimentally [91]. Although longer CNTs do benefit fabrication of more conducting films, they are more difficult to disperse, particularly at high concentration. This intrinsic contradiction complicates and compromises many liquid-phase methods for CNT film fabrication. For the dry FCCVD method, however, no such problem exists. The length of the SWNTs produced depends on the residence time and growth rate, since SWNT growth occurs in a certain region (growth zone) in the FCCVD method. Kaskela et al. [31] deposited TCFs containing SWNT bundles of various lengths, synthesized in different reactors of various sizes based on the FCCVD method. With bundle length improvement from 1.3 μ m to

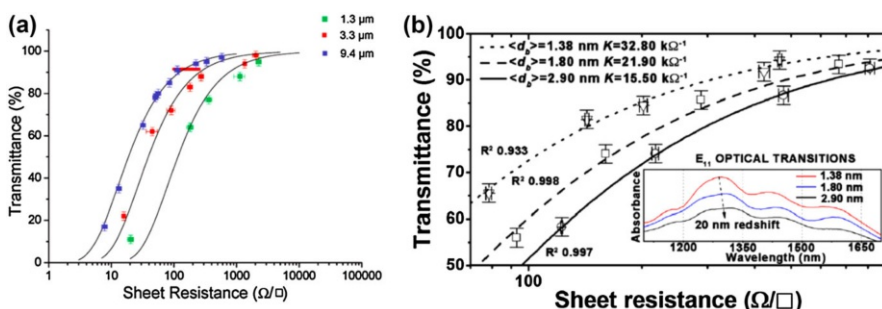


Fig. 8 Effect of bundle length and diameter on optoelectronic performance of SWNT films. With **a** increasing bundle length [31] or **b** decreasing bundle diameter [98], the performance of the SWNT films as TCFs was improved. Copyright 2010 American Chemical Society and Copyright 2009 AIP Publishing LLC

9.4 μm , the optoelectronic performance of the SWNT films was greatly improved, as shown in Fig. 8a. Moreover, a hybrid carbon source was applied to tune the bundle length based on different decomposition temperatures. Anoshkin et al. [92] fabricated SWNT films using a hybrid carbon source of CO and ethylene. SWNT film doped with gold chloride (AuCl_3) exhibited sheet resistance as low as 73 Ω/sq at transmittance of 90%. In addition, Reynaud et al. [93] obtained similar results when using toluene and ethylene as carbon sources. In general, use of a hydrocarbon carbon source leads to higher growth rate of CNTs compared with CO. For certain catalyst–carbon systems, use of appropriate additives including water, CO_2 , sulfur, etc. can improve the CNT growth rate [37, 53, 94].

In addition to the nanotube or bundle length, the mean bundle size is expected to have a large, but relatively little understood effect on the performance of the resulting thin film. Due to van der Waals interactions between them, SWNTs have a strong tendency to aggregate into bundles during synthesis and processing. At the individual SWNT level, dielectric screening caused by adjacent SWNTs modulates the electronic properties of an SWNT. Optically, this can be observed as a redshift caused by decreased exciton lifetime.

Some work has been carried out on the dependence of the performance of thin films based on liquid processing on the bundle diameter. However, the conclusions are inconsistent, owing to the complex processes and numerous influencing factors. Hecht et al. [91] and Shin et al. [95] studied the performance of films fabricated using vacuum filtration of SWNT dispersions, where the bundle length and diameter were controlled by using different sonication times. Hecht et al. could not reach reliable conclusions regarding the relation between bundle size and thin-film performance, because decreasing the bundle size also decreased the bundle length in their experimental procedure. However, Shin et al. claimed to be able to keep the bundle size and length more independent of each other, and concluded that the thin-film performance improved as the bundle size was decreased, for bundles of similar length. Lyons et al. [90] and Mustonen et al. [33] also considered the effect of bundling from a geometric viewpoint, using different commercially available SWNT dispersions and SWNTs synthesized using different floating catalyst CVD processes, respectively. They argued independently that decreasing the bundle diameter while keeping the optical density constant will increase the number of conductive pathways in the network and thereby the bulk electrical conductivity. However, this could be counteracted if the conductivity of bundles and especially the conductivity of junctions between them increases in proportion to the bundle size. Han et al. reported that conduction in large bundles can be constrained to the surface layer [96], meaning that the rest of the bundle contributes to optical absorption but not electrical conductivity. Likewise, contact resistances between bundles can be expected to be smaller than contact resistances between individual SWNTs due to their larger contact areas; this has been confirmed experimentally for nondoped tubes using conductive atomic force microscopy by Znidarsic et al. [85], although earlier study by Nirmalraj et al. [97] reached the opposite conclusion, possibly because their work used SWNTs deposited from a liquid dispersion and larger bundles could contain more contaminants. In the case of long rope-like structures, the intertube resistance inside the bundles themselves will also limit the

conductivity, although the contacts between them can be expected to be quite conductive due to the large contact areas between SWNTs arranged in this manner.

In contrast to liquid-phase processing, the bundle diameter can be controlled by regulating the catalyst and CNT concentration without affecting the length or chirality distribution when using FCCVD. Based on this fact, the aerosol CVD system can be used to reveal the essential relationship between film performance and bundle diameter. Mustonen et al. [98] studied the effect of bundle diameter (1.38, 1.80, and 2.90 nm) on TCE performance by deliberately aggregating aerosol-synthesized SWNTs in gas phase after synthesis [98], as shown in Fig. 8b. They concluded that films collected from a more bundled population of the same SWNTs performed worse and that the performance decrease could be described using a semiempirical model, assuming that the conductivity within the bundles is not higher compared with that in individual SWNTs, in accordance with Han et al. [96], and that the contact resistances between bundles are lower compared with those between individual SWNTs, in accordance with Znidarsic et al. [85]. Compared with earlier studies carried out using liquid dispersions, these experiments had the advantage that the properties of the individual SWNTs remained unchanged and the only variable was the amount of bundling. The conclusion that less bundled SWNTs are beneficial to improve the thin film conductivity is further supported by the studies of Mustonen et al. [42] and Kaskela et al. [33]. In these studies, the films fabricated from shorter (mean SWNT length 4 μm), nearly nonbundled SWNTs, displayed similar performance to earlier published films [31] consisting of longer SWNT bundles (mean bundle length 8–10 μm). The short SWNTs were synthesized at low concentration and thus undergoing almost no bundling during synthesis.

The ratio of metallic to semiconducting SWNTs in the network is also crucial to the film conductivity, based on two facts [99, 100]. Firstly, at room temperature, the resistance of an individual m-SWNT (10^{-4} – 10^{-3} $\Omega \text{ cm}$) is much lower than that of its semiconducting counterpart ($10 \Omega \text{ cm}$) [101, 102]. In addition, the contact resistance of metal–semiconducting (M–S) heterojunctions is $\sim 1 \text{ M}\Omega$ at ambient temperature, one order of magnitude higher than for metal–metal (M–M) or semiconducting–semiconducting (S–S) junctions ($\sim 20 \text{ k}\Omega$) [86, 103], although doping is likely to reduce this difference [85]. Because of the nature of CNT networks as a mixture of semiconducting and metallic objects, almost all of the junctions are heterojunctions. Simulation results for the conductance versus proportion of semiconducting tubes of a SWNT thin film are shown in Fig. 9 [4]. Because of the low resistance of M–M and S–S contacts, the conductance of films composed of pure metallic or semiconducting tubes is quite high (point A and E). With increasing proportion of semiconducting SWNTs (from point A to point B), the conductance becomes dominated by Schottky barriers (M–S junctions) rather than metallic tubes. When the proportion of semiconducting tubes approaches 80% (point B to D), the conductance is blocked. For small amounts of metallic tubes in the network (from point D to E), the film conductivity increases as charges pass along paths formed by semiconducting SWNTs, bypassing the Schottky barriers. In 2014, Hou et al. [49] used the FCCVD method to prepare enriched m-SWNT films by introducing hydrogen as etchant gas. With increasing m-SWNT content, the

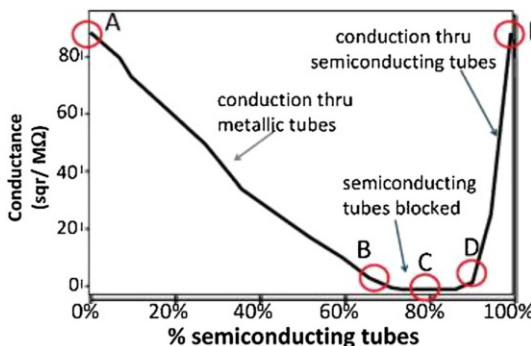


Fig. 9 Expected conductance as function of proportion of semiconducting tubes (assuming for simplicity that an unblocked semiconducting tube conducts as well as a metallic tube) [104]. Reprinted with permission from [101]. Copyright 2009 American Chemical Society. Conductance versus percentage of semiconducting CNTs in network, simulated for density three times the percolation threshold; CNT length, positions, and orientations are the same for different M/S ratios

sheet resistance at transmittance of 90% decreased from $500 \Omega/\text{sq}$ to $160 \Omega/\text{sq}$, as shown in Fig. 9b.

7 Applications of SWNT Films in Touch Sensors and Display Electrodes

Transparent conducting films based on SWNTs are vital components in a range of electronic devices, such as touch screens [61, 62], LCDs [105, 106], OLEDs [107, 108], and solar cells [109, 110]. Currently, touch displays are the most mature application of SWNT TCFs [62], whereas most other applications of CNTs remain at laboratory stage. Resistive and capacitive touch panels can already be manufactured in factories and purchased on the market, indicating that practical applications of SWNT films have already started.

In 2013, Anisimov et al. [62] discussed recent progress in achieving characteristics and applications of TCFs based on Canatu's CNB technology. The combination of aerosol synthesis and direct dry printing allows homogeneous or patterned deposition on any substrate at room temperature and pressure, resulting in a simple, scalable, one-step, low-cost, and environmentally friendly thin-film manufacturing process that improves the quality and performance of final products. Direct dry printing is applicable to both sheet and roll-to-roll implementations and can be combined with conventional screen, gravure, and flexo printing to enable production of continuous rolls of complex, multilayered components. These advances are significant because they will enable flexible and even three-dimensional (3D)-shaped touch sensors, high-optical-quality touch displays with almost no reflection and high outdoors contrast, and cost-effective manufacturing through dry roll-to-roll processing.

Deposition of homogeneous and patterned CNB films can be achieved by combining the aerosol synthesis method with room-temperature deposition based on a modification of the aforementioned filter transfer technique. The conductivity of

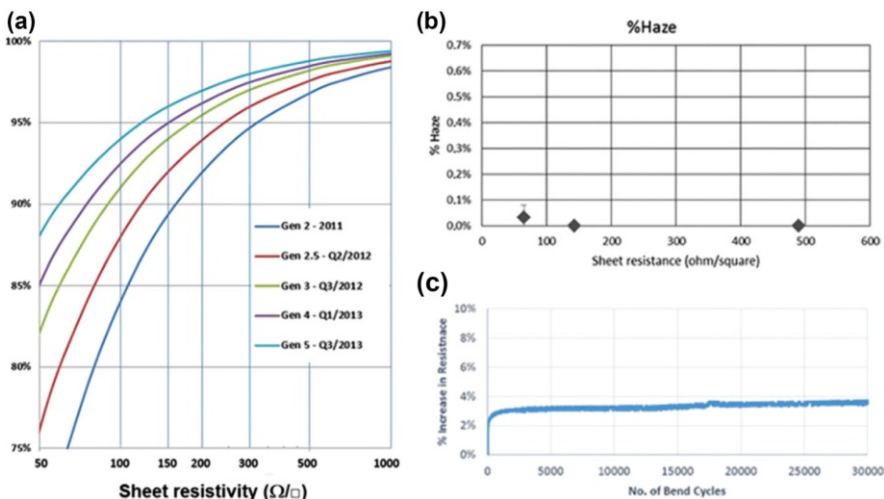


Fig. 10 **a** CNB film transmission versus sheet resistivity, comparing current Gen 5 with previous results from 2011 to 2013. Transmission is substrate-normalized. **b** Haze of substrate-normalized CNB films as function of sheet resistivity. Haze does not increase at low sheet resistivity as it does with AgNW and metal meshes. **c** Change in resistivity of CNB film on 130- μm PET substrate after repeated bends to radius of 2 mm [62]. Copyright 2014 Society for Information Display

CNB films of given transparency has doubled approximately every 12 months since 2007. Figure 10a shows CNB film releases since 2011. High transparency is needed to enable bright display images and pattern invisibility. In 2013, Gen 5 films with the following properties without substrate were reported: 100 Ω/sq at 94%, 150 Ω/sq at 96%, and 270 Ω/sq at 98%. In addition, film performance has reached up to 100 Ω/sq at > 95% in the laboratory [62].

CNT films have therefore been found to be low haze, neutrally colored, uniform, and both environmentally and mechanically stable.

Figure 10b shows the haze of substrate-normalized CNB films as a function of sheet resistivity. The haze of CNB film is negligible (< 0.1%) and does not increase at low sheet resistivity as it does with AgNW and metal meshes. The optical absorption of CNB film is uniform over the entire visible spectrum. The Commission Internationale de l'Éclairage (CIE) *Lab* color coordinates after normalization were measured as $L^* = 97.9 \pm 0.1$, $a^* = 0.0 \pm 0.1$, and $b^* = 0.6 \pm 0.1$, demonstrating that CNB films and sensors have very little color distortion. TCF stability is also critical in practical applications, because fabrication and operation of actual devices may involve various levels of temperature and humidity. CNB films have been evaluated using all typical consumer electronics environmental tests. As shown by the results in Table 2, they passed these standard tests when using both environmental and accelerated aging. Experiments on mechanical stability have also been carried out to evaluate the applicability of CNBs for flexible and foldable electronics. The results for CNB film on 130- μm -thick PET substrate exposed to severe (180°) bending to radius of 2 mm are shown in Fig. 10c. The sheet resistance remained nearly constant over 30,000 bending cycles, after an

Table 2 Test results on CNB films including both environmental and accelerated aging [62]. Copyright 2014 Society for Information Display

Specification						
Test	Standard	ΔR_s (sheet resistivity change)	$\Delta \%T$ (transmission change)	Δ Haze	ΔE (color change)	Adhesion (cross-cut and tape peel-off, JIS K5600)
Room-temperature storage	25 °C/60% RH	Passed	Passed	Passed	Passed	Passed
Constant-temperature/humidity storage	IEC 68-2-78 (IEC 68-2-3) 60 °C/90% RH	Passed	Passed	Passed	Passed	Passed
Thermal cycle storage	IEC 68-2-2, IEC 60068-2-14 Test N, IEC 60068-2-2 Na, 40 °C	Passed	Passed	Passed	Passed	Passed
High-temperature storage	IEC 68-2-2, IEC 60068-2-2 dry heat tests, 85 °C	Passed	Passed	Passed	Passed	Passed
Low-temperature storage	IEC 68-2-1–40 °C	Passed	Passed	Passed	Passed	Passed

initial change of a few percent. In another similar test with 140,000 bending cycles, the change in resistivity was less than 7%. The Canatu facility allows capacity of up to 500,000 m²/month. Together, these results indicate that CNB films can indeed be used as a substitute for ITO electrodes in consumer electronics.

Most touch sensors and displays require fine patterning with minimum feature sizes of 25–50 µm. For ITO, photolithography with eight steps is commonly used for such fine patterning. However, fine patterning of CNB films is achieved via laser ablation, which maintains the dry manufacturing process with no liquid handling and hence a lower environmental footprint. Because no masks and only one process step are required in laser ablation, the time and cost are competitive. In addition, the low incremental capital expenditure for laser equipment as opposed to a photolithography line makes it more flexible in the face of demand fluctuations and enables better line utilization. Ag traces are also fine-patterned to 30 µm/30 µm lines and gaps, either by laser ablation in the same process step as the CNB patterning or, for even better production efficiency, by direct screen printing. It is important to note that metal-mesh-based touch sensors require very high tolerance

and early design knowhow of display pixel geometry to reduce the moiré effect between the display and sensor. Metal mesh manufacture is also demanding, as the bonding equipment needs to be tightly controlled. CNB sensors are display design agnostic due to the pattern invisibility and random orientation of CNB deposition.

Based on the availability of flexible and cost-effective CNB films with excellent and stable performance, touch sensors (Fig. 11) and high-optical-quality touch displays (Fig. 12) have been manufactured. Specifically, a CNB-based two-layer glass-film-film (GFF) structure demonstrator was created, showing only 2.2% reflection and 40% better contrast in bright ambient light compared with a comparable structure using ITO. For 3D-shaped rigid touch sensing, formability with 1 mm radius edges and 120% stretching was achieved.

The 13.3-inch-diagonal CNB projected-capacitive touch sensors were manufactured (Fig. 12b) based on the process shown in Fig. 12a. The touch stack was of glass–film–film (GFF) type with sense and drive electrodes on separate PET sheets, laminated together and to the front glass using optically clear adhesive. The CNB film sheet resistivity was $220 \Omega/\text{sq}$. The sensors were bonded with a flexible circuit board to the driving electronics, and the touch module assembly was “plug and play” retrofitted to an existing Intel Ultrabook reference design for comparison with the existing standard commercial ITO One Glass Sensor (OGS). An Atmel mXT224 chip was used as touch controller. The CNB touch sensor passed Windows Hardware Certification Kit (WHCK) tests and is therefore fully certified for Windows 8. As characterized by Atmel, the touch performance was found to be equivalent to commercial ITO sensors. The reflectivity from the CNB GFF touch display was significantly lower than that from the comparison ITO OGS touch display. The optical characterization of various touch modules is presented in

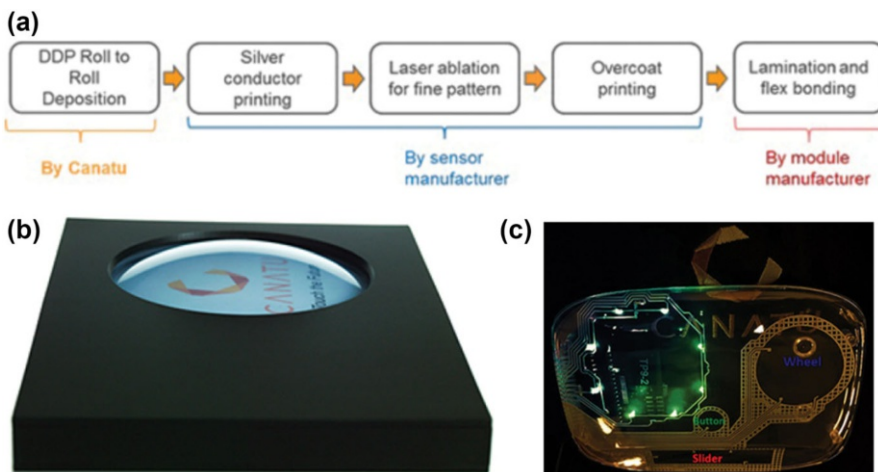


Fig. 11 Touch sensor based on CNB film [62]. Copyright 2014 Society for Information Display. **a** CNB touch sensor manufacturing process and business model for high-volume touch sensor sales. **b** Dome-shaped CNB projected-capacitive multitouch sensor. **c** 3D-shaped CNB FIM demonstrator with touch

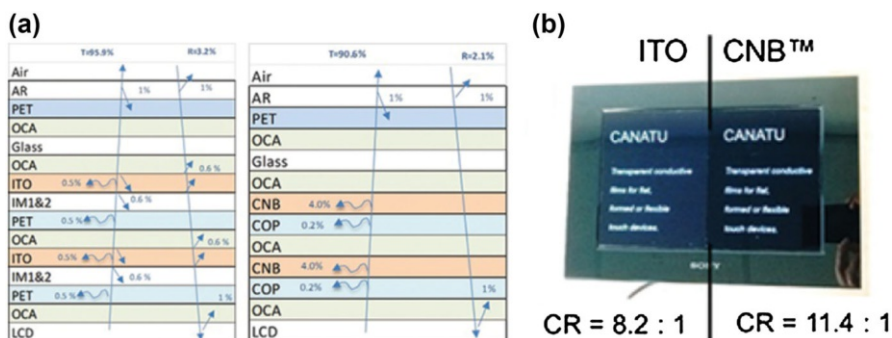


Fig. 12 **a** Stack diagram of touch display direct-bonded 150 Ω/sq ITO GFF (left) compared with CNB GFF (right). **b** ITO and CNB touch display [62]. The demonstrator is shown on the far right. Copyright 2014 Society for Information Display

Table 3 Optical characterization in terms of haze for touch modules with a variety of transparent conductors [62]. Copyright 2014 Society for Information Display

Touch module	Type	Sensor	Haze (%)
Carbon NanoBud	CNB	GFF	0.6
ITO OGS (no index matching)	ITO	OGS	3.3
Silver nanowire metal mesh	Mesh	GFF	1.4
Silver metal mesh #1	Mesh	GFF	2.0
Copper metal mesh #1	Mesh	GF2	1.6
Copper metal mesh #2	Mesh	GF2	2.0
Silver metal mesh #2	Mesh	GF2	1.3
iPAD 4 (air)	ITO	GF2	1.0

Table 3. Compared with ITO and metal mesh touch modules, CNB touch modules have the lowest haze.

A highly transparent 3D-shaped demonstrator with slider, wheel, and button touch was also created (Fig. 12c), based on the FIM process with CNB on thin polycarbonate substrate and clear poly(methyl methacrylate) overmold. The radius of curvature was 130 mm. For rigid 3D-shaped touch devices, film insert molding (FIM) as a standard industrial process was applied. The 120% stretching and 87° bending at 1 mm radius of the FIM device demonstrate the high stretchability of CNB films. Both one- and two-CNB-layer test devices for plastic-film (PF1)- and plastic-film-film (PFF)-type touch stack constructions were made. CNB layers, applied on polycarbonate Makrofol DE film, were 3D-shaped using a high-pressure forming process. The resulting inserts were injection back-molded with clear Makrolon polycarbonate resin. In all test devices, the CNB layers maintained their conductivity with linear response to stretching.

To demonstrate touch display contrast in a direct-bonded construction, 10-inch optical demonstrators of TFT LCD touch panels were also made (Fig. 12) with two types: an ITO-based 150 Ω/sq GFF stack and a 150 Ω/sq CNB GFF stack. As presented in Table 4, the CNB GFF device exhibited 2.2% total reflectance, whereas the total reflectance from the ITO GFF device was 3.4%. Table 4 presents a

Table 4 Specular and diffuse reflection results for CNB and ITO GFF optical demonstrators with AR coating [62]. Copyright 2014 Society for Information Display

Direct-bonded touch module	Specular reflection (%)	Diffuse reflection (%)	Total reflection (%)
CNB AR/GFF	1.85	0.36	2.21
ITO AR/GFF	2.91	0.47	3.38

breakdown of the reflection values in the touch display structure. The CNB sensor stack showed no inherent reflections, hence the 1.8% specular reflection for the GFF stack originated from the glass–antireflection (AR) coating–air interface and from the display (Fig. 8). For the ITO sensor stack, despite complex index-matching layers, 1% specular reflection from the ITO layers was still observed. By better optimizing the AR coating, using a less reflective display, and optimizing the direct bonding materials, < 1% specular reflection is feasible with CNB GFF sensors.

Demonstrators of touch and display devices have therefore been successfully produced, indicating that CNB films are now a commercially viable option for high-volume applications and for high-quality flat, flexible, and 3D-formed touch sensors for use in mobile phones, tablets, phablets, laptops, smart watches, digital cameras, automotive consoles, and white goods.

8 Summary and Outlook

This review has described recent developments in SWNT thin films fabricated by dry methods based on FCCVD, including SWNT synthesis and film fabrication, properties, and applications as TCFs. As an emerging class of materials, SWNT thin films possess unique optical transparency and superior electric properties and mechanical flexibility, resulting from not only the incorporation of individual SWNTs but also their collective behavior, with additional properties arising from tube–tube interactions. Among these promising candidate materials, CNT TCFs exhibit great potential because of their chemical stability, high stretchability, color neutrality and less haze, wider spectral range, etc. [56, 59, 67]. Compared with liquid-phase processing, which involves various time- and resource-consuming steps, dry FCCVD methods without dispersion in solution are more direct and simpler. By avoiding the tradeoff between CNT length and solubility during film fabrication, the dry FCCVD method enables production of films that contain longer CNTs and exhibit excellent optoelectronic properties. Films based on SWNTs produced by the dry FCCVD method are already commercially available for application in touch and display devices. However, the transparent and conductive properties of these CNT films must be further improved to expand their application scope, e.g., to include solar cells.

In the dry FCCVD method, control of the CNT morphology and chirality is critical to improve the film performance. Increasing the bundle length and reducing the diameter, down to individual tube level, can effectively improve the film conductivity. The length of the SWNTs or bundles depends on the growth time and

growth rate during the synthesis. Limiting the number concentration of CNTs in gas phase prevents nanotube collision and bundle formation. With increasing aspect ratio of CNTs and bundles, it becomes very important to maintain a stable laminar gas flow, to prevent formation of CNT and bundle loops, which would greatly reduce the effect of greater CNT length. Controlled synthesis of CNTs is still in the development stage, with further research efforts needed. Although there are some papers on direct or posttreatment methods to synthesize or separate pure metallic or semiconducting CNTs [31, 49, 52, 111, 112], scalable and reliable methods are still desired for further commercialization in CNT applications. Separation of tubes based on their electric conductivity would benefit applications in transparent conductors and thin-film transistors [113], another major application for CNT films. Considering the difficulty of obtaining high-purity semiconducting CNTs [112], CNT film transistor technology remains at an earlier stage compared with transparent conductors. In addition to the neat material, extensive investigations on numerous dopants for CNTs have been carried out. The effectiveness of doping for improving the conductance of CNT films has been demonstrated. However, stability issues and the effects of functional groups and residual dopant on device performance have been less well studied and evaluated [114, 115], being critical for actual device applications and commercial use.

Research on the dry FCCVD method for fabrication of SWNT films could advance the development of not only industrial applications but also the fundamental science of related nanostructured materials and nanodevices. Except for transparent electrodes and thin-film transistors, SWNT films produced by the dry FCCVD method also have great potential for use in several other high-impact applications, including sensors [116–118], ultrafast femtosecond lasers [30, 119–121], thermoacoustic loudspeakers [122], energy storage [123–125], etc. We believe that SWNT films produced by the dry FCCVD method will soon be an essential component in commercial device applications, because of not only their unique properties and low cost but also promising research results.

Acknowledgements We acknowledge financial support from the European Union Seventh Framework Programme (FP7/2007–2013) under Grant Agreement No. 604472 (IRENA project), the Aalto Energy Efficiency (AEF) Research Program through the MOPPI project, TEKES of Finland via CNT-PV project, and Academy of Finland via projects 286546 and 292600.

References

1. de Volder MFL, Tawfick SH, Baughman RH, Hart AJ (2013) Carbon nanotubes: present and future commercial applications. *Science* 339:535–539
2. Iijima S, Ichihashi T (1993) Single-shell carbon nanotubes of 1-nm diameter. *Nature* 363:603–605
3. Iijima S (1991) Helical microtubules of graphitic carbon. *Nature* 354:56–58
4. Dresselhaus MS, Dresselhaus G, Saito R (1995) Physics of carbon nanotubes. *Carbon N. Y.* 33:883–891
5. Saito R et al (2001) Chirality-dependent G-band Raman intensity of carbon nanotubes. *Phys Rev B* 64:853121–853127
6. Cheng HM, Li F, Sun X, Brown SDM, Pimenta MA, Marucci A, Dresselhaus G, Dresselhaus MS (1998) Bulk morphology and diameter distribution of single-walled carbon nanotubes synthesized by catalytic decomposition of hydrocarbons. *Chem Phys Lett* 289:602–610

7. Saito R, Fujita M, Dresselhaus G, Dresselhaus MS (1992) Electronic structure of graphene tubules based on C60. *Phys Rev B* 46:1804–1811
8. Kane CL, Mele EJ (1997) Size, shape, and low energy electronic structure of carbon nanotubes. *Phys Rev Lett* 78:1932
9. Yao Z, Kane CL, Dekker C (2000) High-field electrical transport in single-wall carbon nanotubes. *Phys Rev Lett* 84:2941–2944
10. Zhou X, Park JJY, Huang S, Liu J, McEuen PPL (2005) Band structure, phonon scattering, and the performance limit of single-walled carbon nanotube transistors. *Phys Rev Lett* 95:146805
11. Pop E, Mann D, Wang Q, Goodson K, Dai HJ (2006) Thermal conductance of an individual single-wall carbon nanotube above room temperature. *Nano Lett* 6:96–100
12. Pan ZW et al (1999) Tensile tests of ropes of very long aligned multiwall carbon nanotubes. *Appl Phys Lett* 74:3152–3154
13. Yu M (2000) Strength and breaking mechanism of multiwalled carbon nanotubes under tensile load. *Science* 287:637–640
14. Hu L, Hecht DS, Gru G (2010) Carbon nanotube thin films: fabrication, properties, and applications. *Chem Rev* 499:5790–5844
15. Ma W et al (2009) Monitoring a micromechanical process in macroscale carbon nanotube films and fibers. *Adv Mater* 21:603–608
16. Brieland-Shoultz A et al (2014) Scaling the stiffness, strength, and toughness of ceramic-coated nanotube foams into the structural regime. *Adv Funct Mater* 24:5728–5735
17. Zhou W, Bai X, Wang E, Xie S (2009) Synthesis, structure, and properties of single-walled carbon nanotubes. *Adv Mater* 21:4565–4583
18. Zhang Q et al (2017) Performance improvement of continuous carbon nanotube fibers by acid treatment. *Chin Phys B* 26:28802
19. Yu L, Shearer C, Shapter J (2016) Recent development of carbon nanotube transparent conductive films. *Chem Rev* 116:13413–13453
20. Cao Q, Rogers JA (2009) Ultrathin films of single-walled carbon nanotubes for electronics and sensors: a review of fundamental and applied aspects. *Adv Mater* 21:29–53
21. Zhou W, Ma W, Niu Z, Song L, Xie S (2012) Freestanding single-walled carbon nanotube bundle networks: fabrication, properties and composites. *Chin Sci Bull* 57:205–224
22. Ma W et al (2007) Directly synthesized strong, highly conducting, transparent single-walled carbon nanotube films. *Nano Lett* 7:2307–2311
23. Wu Z et al (2004) Transparent, conductive carbon nanotube films. *Science* 305:1273–1276
24. Mirri F et al (2012) High-performance carbon nanotube transparent conductive films by scalable dip coating. *ACS Nano* 6:9737–9744
25. Cao Q et al (2006) Highly bendable, transparent thin-film transistors that use carbon-nanotube-based conductors and semiconductors with elastomeric dielectrics. *Adv Mater* 18:304–309
26. Liu B et al (2009) Metal-catalyst-free growth of single-walled carbon nanotubes. *J Am Chem Soc* 131:2082–2083
27. Zhang L et al (2017) Selective growth of metal-free metallic and semiconducting single-wall carbon nanotubes. *Adv Mater*. <https://doi.org/10.1002/adma.201605719>
28. Zhang M (2005) Strong, transparent, multifunctional, carbon nanotube sheets. *Science* 309:1215–1219
29. Feng C et al (2010) Flexible, stretchable, transparent conducting films made from superaligned carbon nanotubes. *Adv Funct Mater* 20:885–891
30. Nasibulin AG et al (2011) Multifunctional free-standing single-walled carbon nanotube films. *ACS Nano* 5:3214–3221
31. Kaskela A et al (2010) Aerosol-synthesized SWCNT networks with tunable conductivity and transparency by a dry transfer technique. *Nano Lett* 10:4349–4355
32. Nasibulin AG et al (2008) Integration of single-walled carbon nanotubes into polymer films by thermo-compression. *Chem Eng J* 136:409–413
33. Kaskela A et al (2016) Highly individual SWCNTs for high performance thin film electronics. *Carbon N Y* 103:228–234
34. Baughman RH (2002) Carbon nanotubes—the route toward applications. *Science* 297:787–792
35. Nasibulin AG, Moisala A, Brown DP, Jiang H, Kauppinen EI (2005) A novel aerosol method for single walled carbon nanotube synthesis. *Chem Phys Lett* 402:227–232

36. Bronikowski MJ, Willis PA, Colbert DT, Smith KA, Smalley RE (2001) Gas-phase production of carbon single-walled nanotubes from carbon monoxide via the HiPco process: a parametric study. *J Vac Sci Technol* 19:1800–1805
37. Li Y-L (2004) Direct spinning of carbon nanotube fibers from chemical vapor deposition synthesis. *Science* 304:276–278
38. Gui X et al (2010) Soft, highly conductive nanotube sponges and composites with controlled compressibility. *ACS Nano* 4:2320–2326
39. Lamouroux E, Serp P, Kalck P (2007) Catalytic routes towards single wall carbon nanotubes. *Catal Rev* 49:341–405
40. Barnard JS, Paukner C, Koziol KK (2016) The role of carbon precursor on carbon nanotube chirality in floating catalyst chemical vapour deposition. *Nanoscale* 8:17262–17270
41. Moisala A, Nasibulin AG, Kauppinen EI (2003) The role of metal nanoparticles in the catalytic production of single-walled carbon nanotubes. *J Phys Condens Matter* 15(42):3011
42. Mustonen K et al (2015) Gas phase synthesis of non-bundled, small diameter single-walled carbon nanotubes with near-armchair chiralities. *Appl Phys Lett* 107:013106
43. Cheng HM et al (1998) Large-scale and low-cost synthesis of single-walled carbon nanotubes by the catalytic pyrolysis of hydrocarbons. *Appl Phys Lett* 72:3282–3284
44. Li Y-L, Zhang L-H, Zhong X-H, Windle AH (2007) Synthesis of high purity single-walled carbon nanotubes from ethanol by catalytic gas flow CVD reactions. *Nanotechnology* 18:225604
45. Chen Z et al (2004) An enhanced CVD approach to extensive nanotube networks with directionality. *Carbon N Y* 12:275504
46. He M, Jiang H, Kauppinen EI, Lehtonen J (2012) Diameter and chiral angle distribution dependencies on the carbon precursors in surface-grown single-walled carbon nanotubes. *Nanoscale* 4:7394
47. Harutyunyan AR et al (2009) Preferential growth of single-walled carbon nanotubes with metallic conductivity. *Science* 326:116–120
48. Vilatela JJ, Windle AH (2010) Yarn-like carbon nanotube fibers. *Adv Mater* 22:4959–4963
49. Hou PX et al (2014) Preparation of metallic single-wall carbon nanotubes by selective etching. *ACS Nano* 8:7156–7162
50. Piao Y et al (2016) Intensity ratio of resonant Raman modes for (n, m) enriched semiconducting carbon nanotubes. *ACS Nano* 10:5252–5259
51. Jiang H, Nasibulin AG, Brown DP, Kauppinen EI (2007) Unambiguous atomic structural determination of single-walled carbon nanotubes by electron diffraction. *Carbon N Y* 45:662–667
52. He M et al (2013) Chiral-selective growth of single-walled carbon nanotubes on lattice-mismatched epitaxial cobalt nanoparticles. *Sci Rep* 3:1460
53. Nasibulin AG et al (2006) An essential role of CO₂ and H₂O during single-walled CNT synthesis from carbon monoxide. *Chem Phys Lett* 417:179–184
54. Moisala A et al (2006) Single-walled carbon nanotube synthesis using ferrocene and iron pentacarbonyl in a laminar flow reactor. *Chem Eng Sci* 61:4393–4402
55. Nasibulin AG et al (2007) A novel hybrid carbon material. *Nat Nanotechnol* 2:156–161
56. Hecht DS, Hu L, Irvin G (2011) Emerging transparent electrodes based on thin films of carbon nanotubes, graphene, and metallic nanostructures. *Adv Mater* 23:1482–1513
57. Ellmer K (2012) Past achievements and future challenges in the development of optically transparent electrodes. *Nat Photon* 6:809–817
58. Chang DS, Lai ST (2015) Implementation of cross-generation automation transportation system in the TFT-LCD industry. *Int J Adv Manuf Technol* 78:753–763
59. Du J, Pei S, Ma L, Cheng HM (2014) 25th anniversary article: carbon nanotube- and graphene-based transparent conductive films for optoelectronic devices. *Adv Mater* 26:1958–1991
60. Feldman D et al. (2015) Shared solar: current landscape, market potential, and the impact of federal securities regulation (No. NREL/TP-6A20-63892). National Renewable Energy Lab.(NREL), Golden, CO (United States)
61. Hecht DS et al (2009) Carbon-nanotube film on plastic as transparent electrode for resistive touch screens. *J Soc Inf Disp* 17:941
62. Anisimov AS, Brown DP, Mikladal BF, Liam Ó (2014) Printed touch sensors using carbon NanoBud material. *Soc. Inf. Disp. Tech. Dig.* 1–8
63. Garnett EC et al (2012) Self-limited plasmonic welding of silver nanowire junctions. *Nat Mater* 11:241–249
64. Lee JY, Connor ST, Cui Y, Peumans P (2008) Solution-processed metal nanowire mesh transparent electrodes. *Nano Lett* 8:689–692

65. Li X et al (2009) Large-area synthesis of high quality and uniform graphene films on copper foils. *Science* 324:1312–1314
66. Fukaya N et al (2014) One-step sub-10 μm patterning of carbon-nanotube thin films for transparent conductor applications. *ACS Nano* 8:3285–3293
67. Sun D-M et al (2013) Mouldable all-carbon integrated circuits. *Nat Commun* 4:1–8
68. Zhou W, Zhang Q, Wang Y, Xie S (2014) Ultrathin carbon nanotube film and preparation method and device thereof. U.S. Patent Application No. 14/889,753
69. Gonzalez D et al (2005) A new thermophoretic precipitator for collection of nanometer-sized aerosol particles. *Aerosol Sci Technol* 39:1064–1071
70. Yu L, Shearer C, Shapter J (2016) Recent development of carbon nanotube transparent conductive films. *Chem Rev.* <https://doi.org/10.1021/acs.chemrev.6b00179>
71. Dionigi C et al (2007) Carbon nanotube networks patterned from aqueous solutions of latex bead carriers. *J Mater Chem* 17:3681
72. Castro MRS, Lasagni AF, Schmidt HK, Mücklich F (2008) Direct laser interference patterning of multi-walled carbon nanotube-based transparent conductive coatings. *Appl Surf Sci* 254:5874–5878
73. Fukaya N, Kim DY, Kishimoto S, Noda S, Ohno Y (2014) One-step sub-10 μm patterning of carbon-nanotube thin films for transparent conductor applications. *ACS Nano* 8:3285–3293
74. Zhou W et al (2004) Single wall carbon nanotube fibers extruded from super-acid suspensions: preferred orientation, electrical, and thermal transport. *J Appl Phys* 95:649–655
75. Dan B, Irvin GC, Pasquali M (2009) Continuous and scalable fabrication of transparent conducting carbon nanotube films. *ACS Nano* 3:835–843
76. Hu L, Hecht DS, Grüner G (2004) Percolation in transparent and conducting carbon nanotube networks. *Nano Lett* 4:2513–2517
77. Ruzicka B, Degiorgi L (2000) Optical and dc conductivity study of potassium-doped single-walled carbon nanotube films. *Phys Rev B* 61:R2468–R2471
78. Bergin SD et al (2008) Towards solutions of single-walled carbon nanotubes in common solvents. *Adv Mater* 20:1876–1881
79. Tian Y et al (2010) Analysis of the size distribution of single-walled carbon nanotubes using optical absorption spectroscopy. *J Phys Chem Lett* 1:1143–1148
80. King PJ, Higgins TM, De S, Nicoloso N, Coleman JN (2012) Percolation effects in supercapacitors with thin, transparent carbon nanotube electrodes. *ACS Nano* 6:1732–1741
81. De S, King PJ, Lyons PE, Khan U, Coleman JN (2010) Size effects and the problem with percolation in nanostructured transparent conductors. *ACS Nano* 4:7064–7072
82. De S, Coleman JN (2011) The effects of percolation in nanostructured transparent conductors. *MRS Bull* 36:774–781
83. Harris JM et al (2012) Electronic durability of flexible transparent films from type-specific single-wall carbon nanotubes. *ACS Nano* 6:881–887
84. Timmermans MY et al (2012) Effect of carbon nanotube network morphology on thin film transistor performance. *Nano Res* 5:307–319
85. Znidarsic A et al (2013) Spatially resolved transport properties of pristine and doped single-walled carbon nanotube networks. *J Phys Chem C* 117:13324–13330
86. Farajian AA, Esfarjani K, Kawazoe Y (1999) Nonlinear coherent transport through doped nanotube junctions. *Phys Rev Lett* 82:5084–5087
87. Shin D-W et al (2009) A role of HNO₃ on transparent conducting film with single-walled carbon nanotubes. *Nanotechnology* 20:475703
88. Susi T et al (2011) Nitrogen-doped single-walled carbon nanotube thin films exhibiting anomalous sheet resistances. *Chem Mater* 23:2201–2208
89. Geng H-Z et al (2007) Effect of acid treatment on carbon nanotube-based flexible transparent conducting films. *J Am Chem Soc* 129:7758–7759
90. Lyons PE et al (2008) The relationship between network morphology and conductivity in nanotube films. *J Appl Phys* 104:044302
91. Hecht D, Hu L, Grüner G (2006) Conductivity scaling with bundle length and diameter in single walled carbon nanotube networks. *Appl Phys Lett* 89:133112
92. Anoshkin IV et al (2014) Hybrid carbon source for single-walled carbon nanotube synthesis by aerosol CVD method. *Carbon N Y* 78:130–136
93. Reynaud O et al (2014) Aerosol feeding of catalyst precursor for CNT synthesis and highly conductive and transparent film fabrication. *Chem Eng J* 255:134–140

94. Hata K et al (2004) Water-assisted highly efficient synthesis of impurity-free single-walled carbon nanotubes. *Science* 306:1362–1364
95. Shin DH, Shim HC, Song JW, Kim S, Han CS (2009) Conductivity of films made from single-walled carbon nanotubes in terms of bundle diameter. *Scr Mater* 60:607–610
96. Han J-H, Strano MS (2014) Room temperature carrier transport through large diameter bundles of semiconducting single-walled carbon nanotube. *Mater Res Bull* 58:1–5
97. Nirmalraj PN, Lyons PE, De S, Coleman JN, Boland JJ (2009) Electrical connectivity in single-walled carbon nanotube networks. *Nano Lett* 9:3890–3895
98. Mustonen K et al (2015) Uncovering the ultimate performance of single-walled carbon nanotube films as transparent conductors. *Appl Phys Lett* 107:1–6
99. Blackburn JL et al (2008) Transparent conductive single-walled carbon nanotube networks with precisely tunable ratios of semiconducting and metallic nanotubes. *ACS Nano* 2:1266–1274
100. Rother M, Schießl SP, Zakharko Y, Gannott F, Zaumseil J (2016) Understanding charge transport in mixed networks of semiconducting carbon nanotubes. *ACS Appl Mater Interfaces* 8:5571–5579
101. Zhang WJ, Zhang QF, Chai Y, Shen X, Wu JL (2007) Carbon nanotube intramolecular junctions. *Nanotechnology* 18:395205
102. Ouyang M (2001) Atomically resolved single-walled carbon nanotube intramolecular junctions. *Science* 291:97–100
103. Stadermann M et al (2004) Nanoscale study of conduction through carbon nanotube networks. *Phys Rev B* 69:201402
104. Topinka MA, Rowell MW, Goldhaber-gordon D, Mcgehee MD, Gruner G (2009) Charge transport in interpenetrating networks of semiconducting and metallic carbon nanotubes. *Nano Lett* 9:2–4
105. Hayes RA, Feenstra BJ (2003) Video-speed electronic paper based on electrowetting. *Nature* 425:383–385
106. Park Y, Hu L, Gruner G, Irvin G, Drzaic P (2008) 37.4: late-news paper : integration of carbon nanotube transparent electrodes into display applications. *Sid Dig.* <https://doi.org/10.1889/1.3069721>
107. Zhang D et al (2006) Transparent, conductive, and flexible carbon nanotube films and their application in organic light-emitting diodes. *Nano Lett* 6:1880–1886
108. Li J et al (2006) Organic light-emitting diodes having carbon nanotube anodes. *Nano Lett* 6:2472–2477
109. Trancik JE, Barton SC, Hone J (2008) Transparent and catalytic carbon nanotube films. *Nano Lett* 8:982–987
110. Park J-U et al (2007) High-resolution electrohydrodynamic jet printing. *Nat Mater* 6:782–789
111. Yang F et al (2014) Chirality-specific growth of single-walled carbon nanotubes on solid alloy catalysts. *Nature* 510:522–524
112. Krupke R, Henrich F, Löhneysen HV, Kappes MM (2003) Separation of metallic from semiconducting single-walled carbon nanotubes. *Science* 301:344–347
113. Park S, Vosguerichian M, Bao Z (2013) A review of fabrication and applications of carbon nanotube film-based flexible electronics. *Nanoscale* 5:1727
114. Jackson R, Domercq B, Jain R, Kippelen B, Graham S (2008) Stability of doped transparent carbon nanotube electrodes. *Adv Funct Mater* 18:2548–2554
115. Doherty EM et al (2009) The spatial uniformity and electromechanical stability of transparent, conductive films of single walled nanotubes. *Carbon N Y* 47:2466–2473
116. Lipomi DJ et al (2011) Skin-like pressure and strain sensors based on transparent elastic films of carbon nanotubes. *Nat Nanotechnol* 6:788–792
117. Cai L et al (2012) Highly transparent and conductive stretchable conductors based on hierarchical reticular single-walled carbon nanotube architecture. *Adv Funct Mater* 22:5238–5244
118. Kim SN, Rusling JF, Papadimitrakopoulos F (2007) Carbon nanotubes for electronic and electrochemical detection of biomolecules. *Adv Mater* 19:3214–3228
119. Avouris P, Freitag M, Perebeinos V (2008) Carbon-nanotube photonics and optoelectronics. *Nat Photon* 2:341–350
120. Kivistö S et al (2009) Carbon nanotube films for ultrafast broadband technology. *Opt Express* 17:2358
121. Rotermund F et al (2012) Mode-locking of solid-state lasers by single-walled carbon-nanotube based saturable absorbers. *Quantum Electron* 42:663–670
122. Xiao L et al (2008) Flexible, stretchable, transparent carbon nanotube thin film loudspeakers. *Nano Lett* 8:4539–4545

123. Niu Z et al (2011) Compact-designed supercapacitors using free-standing single-walled carbon nanotube films. *Energy Environ Sci* 4:1440
124. Niu Z et al (2013) Highly stretchable, integrated supercapacitors based on single-walled carbon nanotube films with continuous reticulate architecture. *Adv Mater* 25:1058–1064
125. Liu C, Li F, Ma LP, Cheng HM (2010) Advanced materials for energy storage. *Adv Mater* 22:E28
126. Mustonen K et al (2012) Influence of the diameter of single-walled carbon nanotube bundles on the optoelectronic performance of dry-deposited thin films. *Beilstein J Nanotechnol* 3:692–702



Sorting Carbon Nanotubes

Ming Zheng¹

Received: 24 September 2016/Accepted: 19 December 2016/Published online: 12 January 2017
© Springer-Verlag Berlin Heidelberg (outside the USA) 2017

Abstract Sorting of single-wall carbon nanotubes by their electronic and atomic structures in liquid phases is reviewed in this chapter. We first introduce the sorting problem, and then provide an overview of several sorting methodologies, following roughly the chronological order of their development over the past 15 years or so. Major methods discussed include ion-exchange chromatography, density-gradient ultracentrifugation, selective extraction in organic solvents, gel chromatography, and aqueous two-phase extraction. A main focus of the review is on the common mechanisms underlining all sorting processes. We propose that differences in solvation among different nanotube species are the ultimate driving force of sorting, and we corroborate this proposal by presenting analysis on how the differences are realized in electronic-structure-based sorting and atomic-structure-based sorting. In the end, we offer some suggestions on future directions that may grow out of carbon nanotube sorting. In particular, the prospect of expanding the function of DNA/carbon nanotube hybrid to control inter-particle interactions both inside and outside the nanotube is discussed.

Keywords Chirality · DNA · Separation · Single-wall carbon nanotubes · Solvation energy

Chapter 5 was originally published as Zheng, M. Top Curr Chem (Z) (2017) 375: 13. DOI 10.1007/s41061-016-0098-z.

✉ Ming Zheng
ming.zheng@nist.gov

¹ Materials Science and Engineering Division, National Institute of Standards and Technology, 100 Bureau Drive, Gaithersburg, MD 20899, USA

1 Introduction

We humans, as a complex molecular assembly, have a peculiar obsession with structures that exhibit order and symmetry. From the ancient pyramids in Egypt to modern skyscrapers in cities around the globe, a long list of examples can be cited to illustrate this point. Carbon nanotube (CNT)—an ordered and symmetrical architecture at the molecular scale—is the latest addition to the list. Sorting CNTs to enable their practical applications is a motivation for those of us working on the subject. However, we are not honest without acknowledging the strong driving force stemming from our primal fascination by these geometrically perfect structures and our desire to follow them into new territories in molecular science. Elegant solutions to the CNT sorting problem have emerged as the result of over 15 years of effort by many researchers in the field. These can be found in a large body of published literature. This review is not going to be a collection of recipes for sorting, even though these have practical importance. Rather, we will give due attention to the physical mechanisms underlying CNT sorting and its broader implications.

The development of CNT sorting research is to a large extent a history of adopting separation methodologies previously developed by biochemists. Many CNT separation methods are copied directly from biochemical separation techniques. Furthermore, the most efficient CNT dispersants discovered so far, DNA and bile salts, are all biomolecules. There is a reason for the connection with biochemistry. Fundamentally, CNT separation is about manipulation of molecules. Biomolecules are evolved to do just that in water at a much more sophisticated level. Likewise, biochemical separation methods are developed for processing complex molecular mixtures. Exploiting biomolecules and biochemical separations for CNT sorting is not only a rational but also an inevitable choice. On the other hand, CNT sorting research may not always be on the receiving end. In the long run, it may enrich the phenomena as well as the understanding of molecular interactions in water. In comparison with biomacromolecules, CNT colloids have simpler geometries that can be easily identified and quantified by optical spectroscopy techniques. As such, they are ideally suited for studying molecular interactions. With this in mind, we try to write this review not just for CNT specialists but also for those who are interested in studying molecular interactions in water—a fundamental problem in biophysics.

Here is the outline of the review. We will begin by defining the CNT sorting problem. After a chronological review of several major sorting methodologies, we will delve into mechanisms of the sorting processes. The discussion is divided into two main parts according to two modes of sorting: electronic-structure-based sorting and atomic-structure-based sorting. You may find in this part many statements too speculative to swallow, but that is a reflection of limited understanding on the author's part, and his intention to provoke debate. In the end, we will provide some perspective on the future development that may grow out of CNT sorting. We view CNT sorting as the beginning of molecular manipulation of CNTs in particular, and many other tubular nanostructures in general. The enormous opportunities of macromolecular chemistry to control CNT's physical and chemical properties are

waiting to be explored. Throughout the review, we attempt to convey the point that DNA-based CNT sorting is an illustration of the power of sequence-controlled polymers, the emergence of which is probably the single greatest event in the evolution. For those of us working on CNT sorting, the exercise has rewarded us a unique opportunity to appreciate the central role of sequence-controlled polymers in a living cell.

1.1 Separation in Nature and in Human Technologies

Separation is a process by which a material/molecular mixture is transformed into a state with some spatial–temporal order in the distribution of the constituents, driven by interaction forces that obey fundamental laws of the universe. Separation thus is a disorder-to-order transition that runs in the face of the 2nd law of thermodynamics [1]. Separation processes can be identified everywhere within us and around us, at time and length scales short and long.

The importance of separation in the creation of the physical world around us has long been appreciated by our ancestors, as can be seen in creation myths from various cultures. In Chinese myth, the universe begins with Pangu (盘古)'s separation of the heaven and the earth from a wonton state of matter. In the Book of Genesis, the first three acts of God are to separate dark from light, waters above from waters below, and sea from land. Modern science confirms the role of separation in the creation of the universe, but replaces the act of supreme beings by the fundamental physical forces. The basic layer cake of earth—core, mantle, crust, hydrosphere, and atmosphere—is structured by the gravitational force acting on a grand scale. Inside a living cell, molecular sorting processes take place incessantly, driven by interactions that are electromagnetic in nature. If sorting molecules in cells is a spontaneous process perfected by natural selection, separation technologies invented by human are deliberate, designed processes taking advantage of various forms of interactions, to achieve certain technological goals. Behind any hardware-based technology, one can find many separation processes that provide building blocks for the technology. One has to do separation first, integration second.

1.2 The CNT Sorting Problem

New structural characteristics emerge when solid-state crystals are constructed in lower dimensions. This is exemplified by single-wall carbon nanotubes (SWCNT), which exhibit a degree of freedom in handedness, and a multitude of helicity (Figs. 1, 2) [2]. Conceptually, a SWCNT is formed by rolling a graphene sheet into a seamless cylinder. The resulting nanotube structure can be specified by a graphene lattice vector (n, m) along which the rolling-up operation is performed. To avoid confusion in terminology, in this review we define (n, m) and (m, n) tubes as having the same helicity, but different handedness. A chirality-defined tube is one with both defined handedness and helicity, corresponding to a unique set of (n, m) indices. For 2D and 3D crystals, translational symmetry actually imposes many constraints on the number of structures a periodic crystal can assume. Structural polydispersity of CNTs is thus associated with its quasi 1D nature. Other quasi 1D materials such as

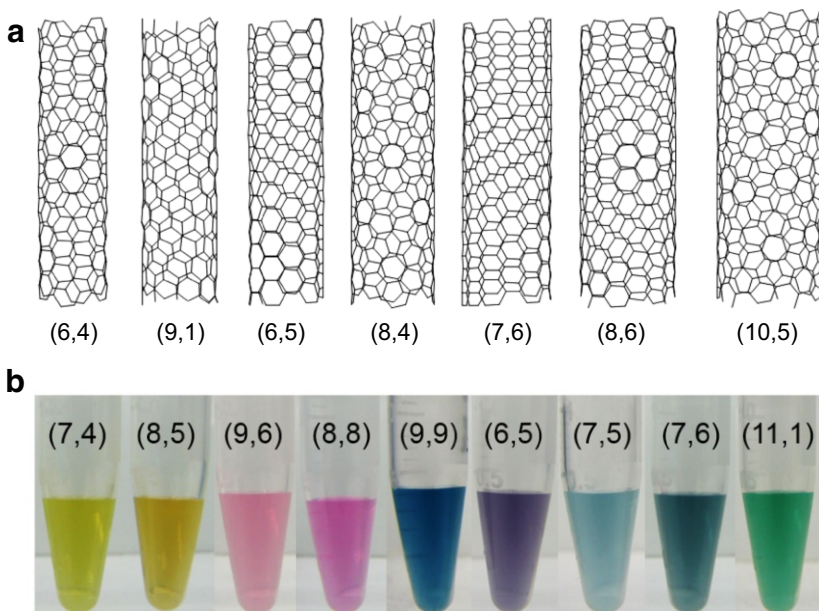


Fig. 1 **a** Structures of a few representative SWCNTs. **b** Photograph of a few purified DNA-dispersed single-chirality carbon nanotubes. Reproduced from Ref. [6] with permission

boron nitride nanotube (BNNT) also have the same issue. The problem we are concerned with is the following: for a given mixture of SWCNT species, can we find a process to extract each and every single species? The problem arises because no scalable synthesis solution is yet available for making SWCNTs of defined structure and property despite progress made in recent years [3–5]. For CNTs with two or more walls, the structure control problem becomes even more difficult to solve. We will focus mainly on SWCNTs in this review. Unless otherwise noted, CNTs in this review refers to single-wall nanotubes.

While the atomic-structure-based enumeration using (n, m) indices is a natural way to classify CNT species, it is not the only way to do so. An alternative is to view CNTs as solid-state crystals and classify them according to their electronic structures, or electronic bandgaps. CNTs are all made of carbon atoms locally bonded in the hexagon geometry of graphene, but variations in the helical twist angle (θ) of the hexagons and in tube diameter (d) result in a diverse set of electronic structures. On the basis of theoretical analysis [7–9] and experimental observation [10, 11], all CNTs can be ranked in an order according to the width of their electronic bandgap: armchair metallic tubes ($n = m$, $\theta = 30^\circ$) with zero bandgap; non-armchair quasi-metallic tubes ($n - m = \text{multiple of } 3$, and $n \neq m$) with small (< 100 meV) but nonvanishing bandgaps that scale as $\cos(3\theta)/d^2$; and semiconducting tubes ($n - m \neq \text{multiple of } 3$) with bandgaps that scale as $1/d$. For those who have a solid-state physics background, this classification is a very natural one. However, for those who are trained in molecular science, it may not be clear if such a classification offers any insight. It turns out that electronic-structure-based

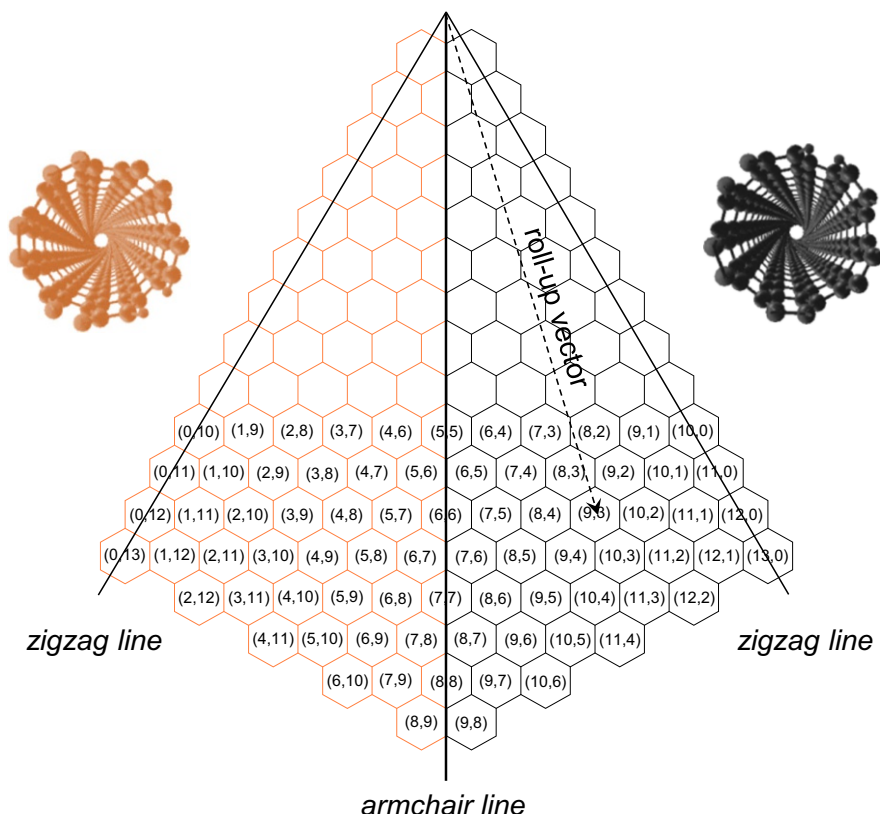


Fig. 2 A full chirality map of SWCNTs showing both left- and right-handed species

classification makes a lot of sense from chemistry point of view. Chemical reactivity correlates with electronic structure in general and with bandgap in particular. And because of this correlation, bandgap-based sorting of CNTs is made possible.

1.3 Special Challenges in CNT Sorting

If CNTs were readily soluble in either water or some organic solvents under mild conditions, then many existing separation techniques would be directly applicable to CNT sorting. Unfortunately, the strength of van der Waals interaction among CNTs is very high (\sim eV/nm), rivaling that of covalent bonds [12, 13]. This imposes a first challenge in CNT sorting. A prerequisite for CNT sorting is to disperse CNTs in a liquid medium. Many chemicals can disperse CNTs to some extent, but only a few are useful for separation. This is because there are stringent conditions a dispersion has to meet to enable separation: (1) CNTs have to be in singly dispersed state; (2) to enable atomic-structure-based sorting, the coating layer should not add any more degree of polydispersity. A dispersed CNT is covered by a surface assembly of dispersant molecules. If the structure or the conformation of such an assembly

adopts multiple forms at room temperature, it will create another level of polydispersity that impedes sorting. Therefore, an ordered coating structure is necessary for atomic-structure-based sorting. This is the reason why only a small number of surfactants, and a small percentage of single-stranded DNA (ssDNA) sequences can be used for atomic-structure-based sorting. For bandgap-based sorting, the demand on coating layer structure appears to be less stringent. We will elaborate on this point in later part of the review.

2 A Brief Account of the CNT Sorting Methodologies

Even though the discovery of SWCNTs were reported in 1993 [14], and the structure polydispersity problem recognized soon after, serious efforts on sorting did not take place until the turn of the 21st century. To feel the mood of the time, let us read a few lines from the foreword page of an edited book [15]:

“(Carbon nanotube) is a new species in organic chemistry, and possibly in molecular biology as well, a carbon molecule with the almost alien property of electrical conductivity, and super-steel strength.

Can it be sorted by diameter and chirality?

Can a single tube be cloned?

Can it be grown enzymatically?

Can it be assembled by the molecular machinery of living cells?

Can it be used to wire a brain?

There is no way of telling at this point.”—Richard Smalley (2001)

Evidently, Smalley was not sure at the moment if sorting could possibly be accomplished. Also easily discernible is his overwhelming anticipation of the interplay between carbon nanotube and biology. Smalley was certainly not alone in thinking about these issues. Around the same time in the now extinct DuPont Central Research and Development, a research project on bioelectronics was established, aiming at, among a few other things, adopting biomolecular recognition methods to solve the CNT sorting problem. Some of the team members explored peptide selection by phage display [16], whereas we (i.e., the author and his colleagues and associates) carried out *in vitro* selection of DNA sequences for CNT recognition [17].

2.1 Ion Exchange Chromatography (IEX) Separation of DNA- and Surfactant-Coated CNTs

In 2003, the DNA-based approach resulted in the first clear evidence that CNTs can indeed be separated by their electronic and atomic structures [17, 18]. Around the same time, a number of other reports appeared, showing some evidence of separation by centrifugation [19] and dielectrophoresis [20]. Looking back on these works, it's fair to say that evidence for separation was mostly tentative, and results were not that impressive by today's standards. Shown in Fig. 3 is what we first reported on using ion exchange chromatography (IEX) to separate DNA-wrapped

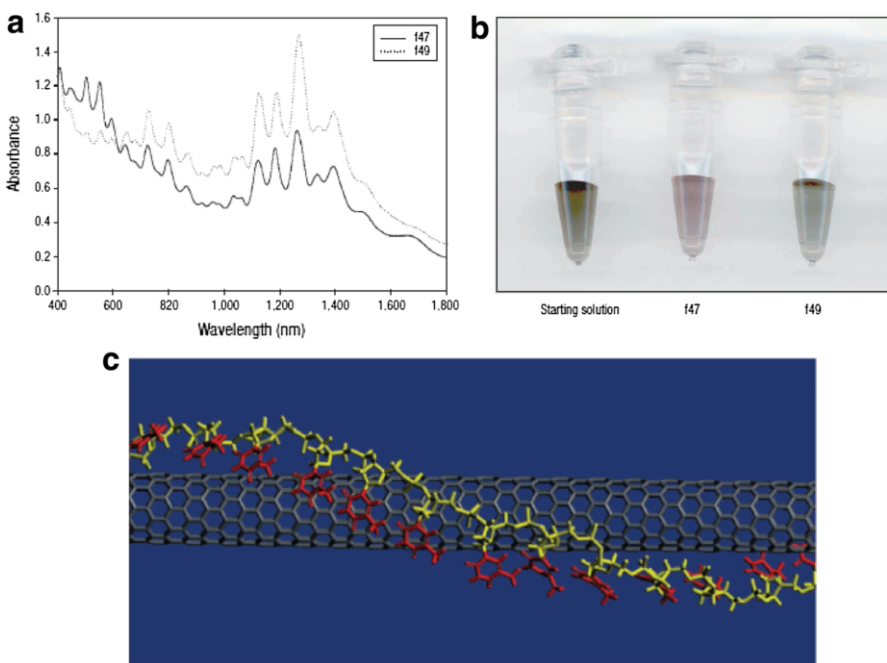


Fig. 3 Early evidence of sorting DNA-CNTs by the IEX method. Reproduced from Ref. [17] with permission. **a** Optical absorption spectra of two fractions collected. **b** Photograph showing the two collected fractions having different colors. **c** Molecular dynamics structure model of a polyT wrapped on a (10, 0) tube

CNTs (DNA-CNTs). Witnessing for the first time colorful CNT dispersion flowing out of the IEX column was a truly exciting experience. Admittedly, the degree of separation obtained was low. Nevertheless, the result indicated clearly that CNT sorting is a solvable problem.

In addition to CNT sorting, we also took advantage of the newly purified CNT materials to study redox property of CNTs [21], which turns out to be essential in semiconducting/metallic (S/M) CNT separation. To take advantage of the observed bandgap-dependent redox effect, we employed a charge-neutral surfactant Triton (TX)-405, and achieved S/M separation of the TX-405 dispersed HiPco high-pressure CO disproportionation synthesis material via IEX. This work was reported in a chapter in a monograph published in 2005 [22], but did not receive much attention at all. A very recent work by Wang et al. shows that IEX separation of TX-405 dispersed CNTs is indeed an effective way to obtain S/M separation [23].

In 2009, IEX-based separation of DNA-CNTs yielded many single-chirality semiconducting species (Fig. 4a) (unfortunately circular dichroism spectroscopy was not conducted to assess enantiomer enrichment, which is most likely the case in hindsight.) [24]. This was achieved by selecting from the vast ssDNA library specific sequences, each of which allows purification of a specific (n, m) species. In 2011, the approach was extended to the purification of armchair metallic tubes (Fig. 4c) [25].

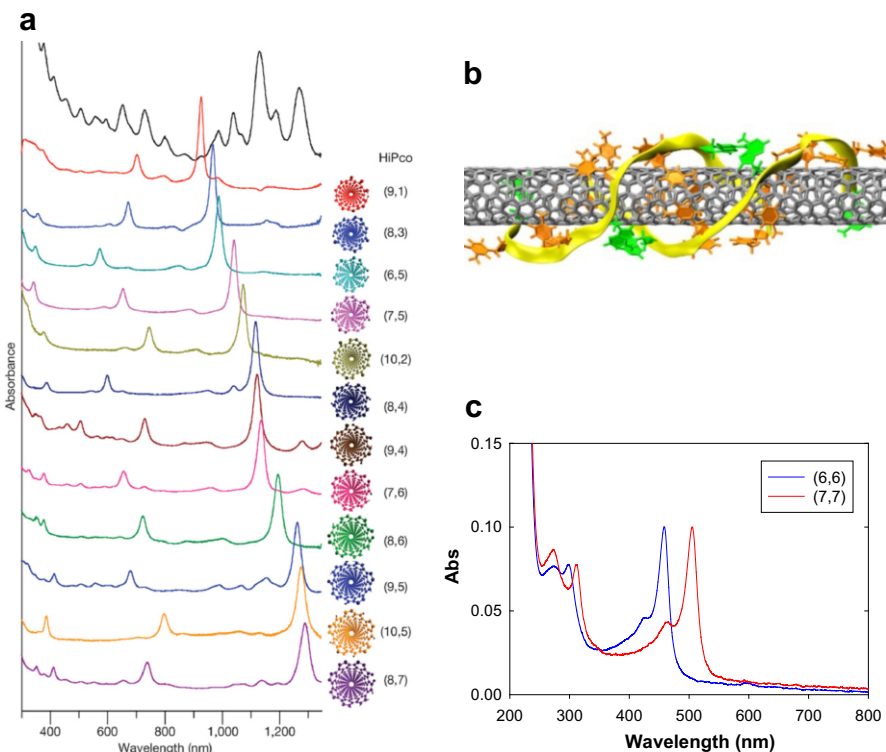


Fig. 4 Purification of CNTs with defined helicity with the aid of specific DNA sequences. **a** Absorption spectra of twelve purified semiconducting CNT species. **b** Molecular dynamics model of the recognition sequence ATTTTATTATTATT wrapped on a (8, 4) nanotube. Reproduced from Ref. [24] with permission. **c** Absorption spectra of two metallic armchair tubes purified by using specific DNA sequences evolved from those previously identified for semiconducting tubes. Reproduced from Ref. [25] with permission

IEX separates DNA-CNTs based on their differential adsorption and desorption onto chemically functionalized resins packed in an IEX column (Fig. 5). The choice of ssDNA sequence for CNT wrapping plays a key role in the separation process: the wrapping structure of ssDNA may be ordered or disordered depending on the ssDNA sequence and the SWCNT chirality, resulting in differential adsorption and retention of different types of CNTs when they are eluted by a salt gradient [17, 18, 24, 26, 27]. Initially, an electrostatic interaction-based separation mechanism was proposed for the low-resolution electronic-type and diameter separation observed in earlier work [28]. However, observations from purification of single-chirality nanotubes had led to the proposal that other factors, such as hydrophobic and van der Waals interactions between DNA-CNTs and IEX resin may be more important in the IEX separation of single-chirality CNTs when short ssDNA sequences are used [24, 27].

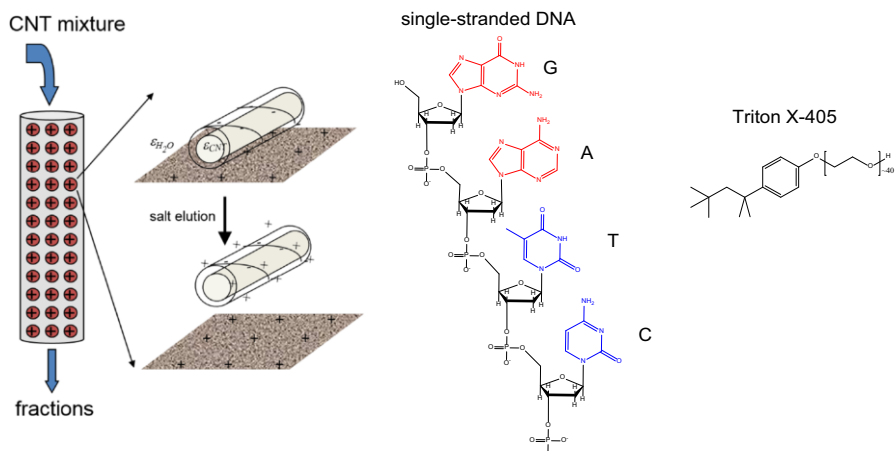


Fig. 5 Illustration of the IEX separation mechanism and dispersants used for IEX

2.2 Density Gradient Ultracentrifugation (DGU)

In 2005 and 2006, a big boost to the field of CNT sorting was provided by the Mark Hersam group. They found that DGU, a well-established biochemical separation method, can be adopted for the separation of CNTs. The first demonstration of the DGU method on CNT separation was performed on DNA-CNTs [29]. Shortly thereafter, Arnold et al. discovered that DGU can also separate sodium cholate (SC) and sodium deoxycholate (SDC)-dispersed CNTs [30] by their electronic structures and diameters (Fig. 6) [31]. This work stimulated many follow-up studies by many groups around the world [32–37]. A significant advancement was made by the Bruce Weisman group, showing separation of a number of single-chirality semiconducting tubes with simultaneous enantiomer enrichment [34]. Resolving the structure difference by gravitational force is conceptually simple and appealing. Probably the most significant finding of the DGU-based CNT sorting is the demonstration that surfactant coating and its hydration structure are dependent on the atomic and electronic structures of CNTs. This phenomenon, even though still not understood quantitatively, has been exploited successfully by CNT sorting methods developed later, including gel chromatography and aqueous two-phase (ATP) extraction.

DGU has captured the imagination of many researchers. Different structures ought to have different densities, and therefore using centrifugal force to separate them makes sense qualitatively. Quantitatively, however, the buoyant density of a colloidal particle is critically dependent on its surface coating, hydration layer and counter-ion distribution, in addition to the intrinsic density of the particle core [38, 39]. Interpreting the outcome of DGU separation is by no means straightforward. From an energy efficiency point of view, DGU may not be the best way for CNT separation, since centrifugal force is much weaker than the electromagnetic force underlying molecular interactions.

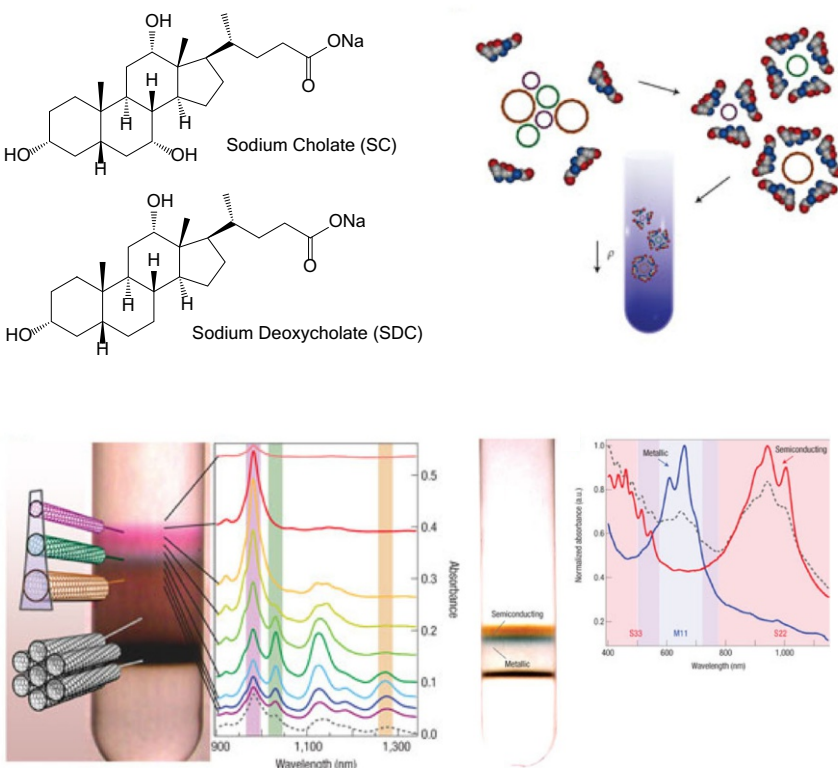


Fig. 6 DGU separation of surfactant-coated tubes by diameter and metallicity. Reproduced from Ref. [31] with permission

2.3 Selective Extraction in Organic Solvents by Conjugated Polymers and Small Molecules

In 2007, the Robin Nicolas group reported the use of polyfluorenes (PFO) to achieve selective dispersion of semiconducting CNTs in organic solvents [40]. This was another landmark advancement in CNT sorting. In the early report, the yield of the dispersed semiconducting tubes was very low, but the absorption spectrum showed remarkably low metallic features and sharp peaks from semiconducting tubes only observable with highly purified tubes (Fig. 7). This approach was quickly adopted and further developed by a number of groups [41–47]. Shown in Fig. 8 is the result reported by Mistry et al., demonstrating effective extraction of large-diameter semiconducting tubes by PFO derivatives [48]. Similar results were also reported by others. Recent studies show that selective extraction can be achieved by not only conjugated polymers but also small aromatic molecules (e.g., *N*-dodecyl isoalloxazine [49] and thiophene-substituted hexaazapentacene [50]). This finding opens up the possibility of designing and synthesizing many other small aromatic molecules for selective dispersion. The simplicity of the selective extraction process, and the

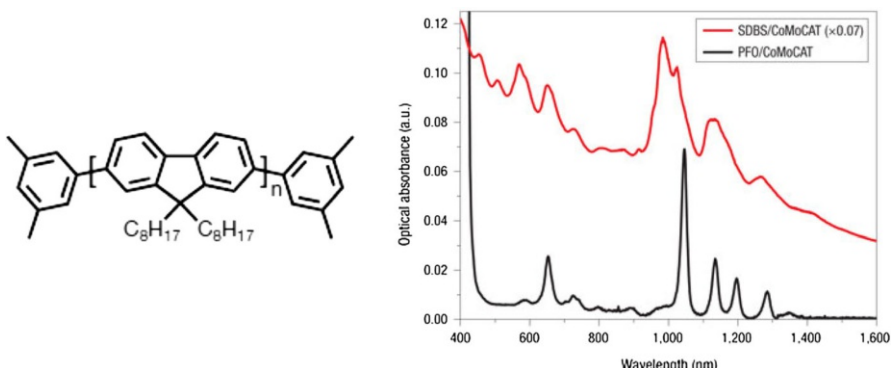
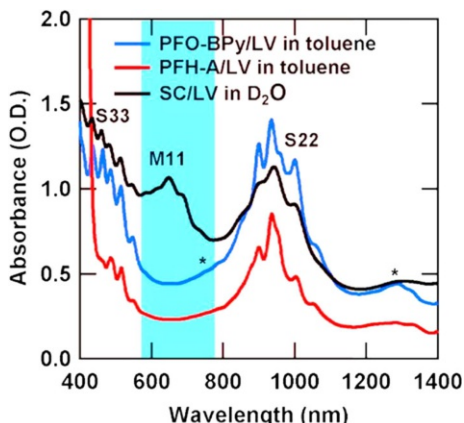


Fig. 7 PFO extraction of semiconducting tubes. Reproduced from Ref. [40] with permission. **a** PFO molecular structure used for the selective extraction. **b** Absorption spectra of the PFO dispersed CNTs (black trace), and that of the SDBS dispersed CNTs (red trace)

Fig. 8 Efficient selective extraction of large-diameter semiconducting tubes by PFO derivatives. LV: laser vaporization SWCNTs, PFO-BPy: poly[(9,9-diethylfluorenyl-2,7-diyl)-*alt*-co-(6,6'-{2,2'-bipyridine})] (PFO-BPy), PFH-A: poly[(9,9-diethylfluorenyl-2,7-diyl)-*co*-(9,10-anthracene)]. Reproduced from Ref. [48] with permission



high purity of extracted semiconducting tubes are all very impressive. These attributes make the selective extraction method arguably the most effective one to obtain electronic-grade semiconducting tubes for device applications. The mechanism of the selective extraction has long been elusive. In addition to the apparent importance of dispersants, solvent choice also affects the degree of selective dispersion. Our recent study shows that redox plays a key role in the selective extraction, suggesting a common mechanism governing both selective extraction in organic phase and S/M separation in aqueous phase [51]. We will present an in-depth discussion of the mechanism in later part of the review.

2.4 Gel Chromatography

In 2009, a chromatography-based separation approach different from IEX emerged. Polysaccharide gel is a common separation media used by biochemists. By exposing surfactant-coated CNTs to the gel media, Tanaka and his coworkers [52] observed

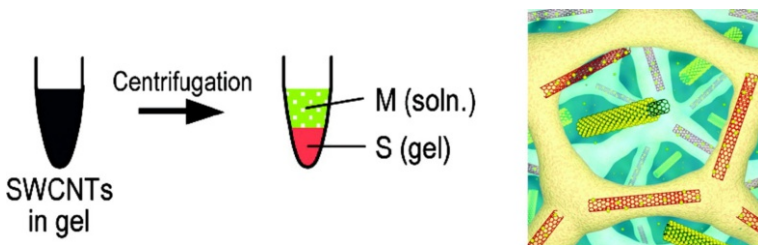


Fig. 9 Selective extraction of semiconducting CNTs from surfactant-coated CNTs by agarose gel. Reproduced from Ref. [52] with permission

an intriguing phenomenon: semiconducting tubes were found to be more strongly attracted by polysaccharide gels than metallic tubes. This allowed simple extraction of semiconducting tubes (Fig. 9). Around the same time, Moshammer et al. reported essentially the same phenomenon using gel chromatography column packed with polysaccharide gel beads [53]. Conceptually, gel chromatography is equivalent to multistep gel extraction. Later on, the Kataura group has carried out an extensive investigation to show that hydrogel/CNT binding can be influenced not only by metallicity but also by diameter and chirality, depending on the choice of surfactant composition. This allows helicity separation (Fig. 10) [54], and handedness separation [55]. Over the past several years, the Kataura group has made impressive demonstration of large-scale separation of single-chirality species via the gel chromatography method [54, 56, 57]. A challenge this method is currently facing is its inability to separate metallic tubes. This, however, can in principle be overcome by trying new stationary phase gel compositions or new mobile phase compositions.

2.5 Aqueous Two-Phase (ATP) Extraction

Applying the ATP extraction method to CNT sorting was first reported by us in 2013 (Fig. 11) [58]. The ATP extraction method, pioneered by Albertson [59], uses polymer–polymer phase separation to create two immiscible aqueous phases of slightly different physical properties. The formation of an ATP system itself represents an important mode of separation, driven by the homophilic character (i.e., like attracts like) of van der Waals force. In ATP extraction, any difference in solvation energy for a given analyte leads to its uneven distribution across the two phases. This provides a mechanism for sorting a complex mixture of analytes. The conceptual linkage between two-phase partition and chromatography is well known in separation science [1], but the way we arrived at the method was through the investigation of the effect of water-soluble polymers on the solubility of DNA-CNT colloids [60]. The ATP extraction method is scalable, and relies entirely on homogeneous molecular interactions to achieve separation. It is applicable to both surfactant-coated and DNA-CNTs. The appearance of the ATP method continues the trend of moving away from instrumentation-based, external field driven processes to spontaneous, molecular force driven CNT separation processes.

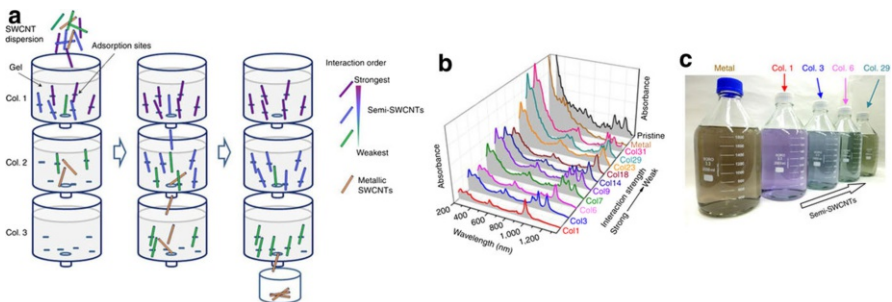


Fig. 10 Atomic-structure-based CNT sorting by gel chromatography. **a** Multigel overloading scheme for CNT sorting. **b** Optical spectra of some collected fractions and the starting material. **c** Photograph of large volumes of collected fractions. Reproduced from Ref. [54] with permission

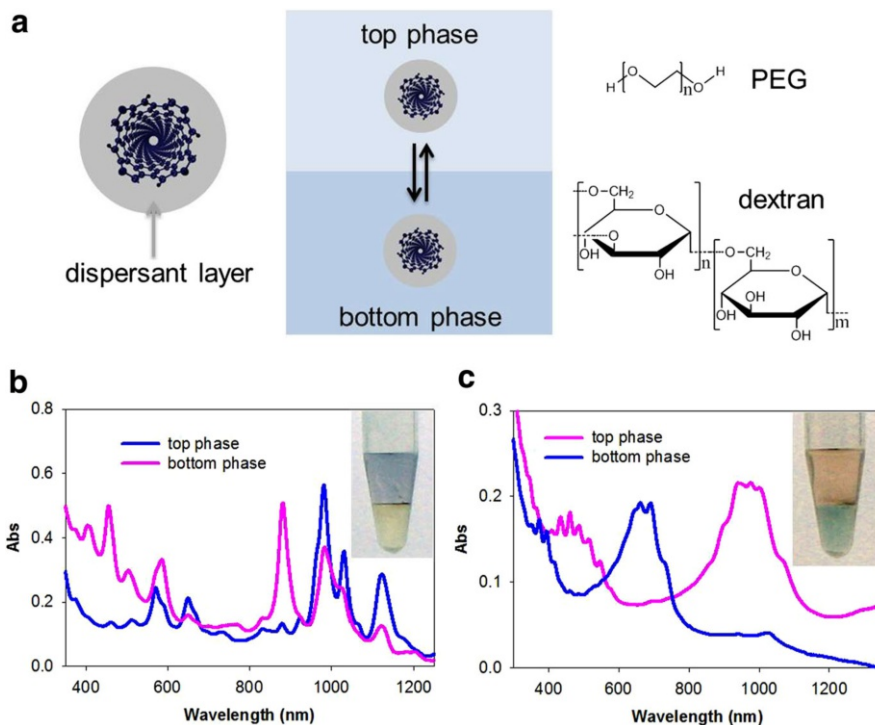


Fig. 11 ATP separation of surfactant-coated CNTs. **a** Schematic of ATP separation. **b** Optical absorption spectra of fractions obtained from ATP separation of small-diameter tubes. **c** Optical absorption spectra of metal- and semiconductor-enriched fractions obtained from ATP separation of large-diameter tubes. Reproduced from Ref. [58] with permission

A number of publications have demonstrated the versatility of the ATP separation approach and some of its unique advantages over other separation schemes [51, 58, 61–65]. These include robust chirality- and S/M separation for both small- and large-diameter CNTs (Fig. 12) [51, 62, 63, 65], and the possibility

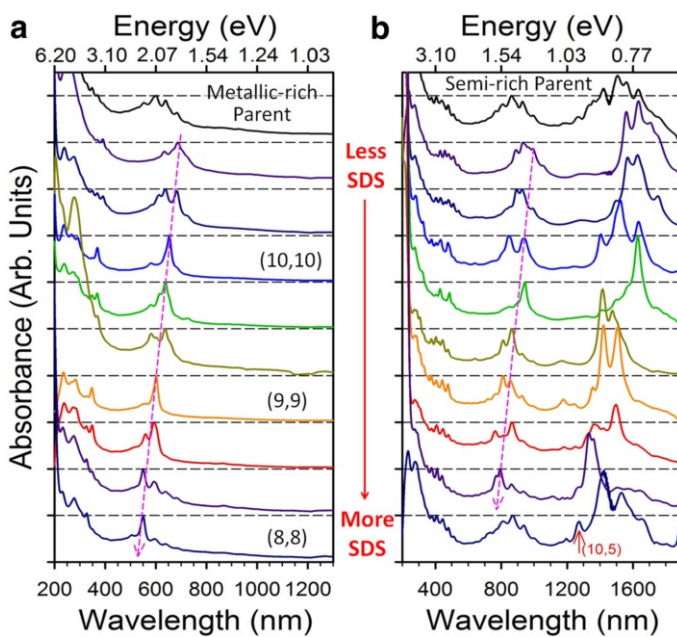


Fig. 12 Diameter separation of surfactant-coated large-diameter CNTs by ATP. **a** Absorption spectra of fractions obtained from metallic starting material. **b** Absorption spectra of fractions obtained from semiconducting starting material. Reproduced from Ref. [65] with permission

of automated multistage separation in the form of counter-current chromatography [64]. Recently, by applying ATP to the DNA-CNTs, we are able to purify CNTs of defined handedness and helicity from all three electronic types [6]. This marks a new milestone in the CNT sorting research.

ATP overcomes a number of issues faced by chromatography-based methods in general. First, the surface chemistry of the polymer beads that constitute the stationary phase is difficult to control, and as a result inhomogeneous broadening of the interaction between the stationary phase and CNT colloids is often unavoidable. Secondly, the polymer beads change over time due to irreversible adsorption of CNT colloids. In ATP, conceptually we replace the stationary and mobile phases with an aqueous two-phase (ATP) system, and achieve separation by using preferential affinity to one of the two aqueous phases. ATP confers a number of advantages: (1) both phases are homogeneous, leading to elimination of inhomogeneous broadening in molecular interactions and thus improvement in resolution; (2) partition depends on solvation energy difference between two similar phases of microscale volumes, resulting in cancellation of many extrinsic factors (e.g., length) and higher reproducibility. These improvements are critical for achieving simultaneous resolution of handedness and helicity via ATP selection. In addition to its technical utilities, the ATP method exposes the physical mechanisms of sorting more clearly than other approaches, enabling us to identify common factors underlying all sorting methodologies.

3 Sorting Mechanisms

Fifteen years of experimental exploration of CNT sorting has led to the discovery of an array of spectacular phenomena. From highly selective dispersion of semiconducting nanotubes by PFO and its derivatives, to highly efficient helicity and handedness selection by specific DNA sequences, these are remarkable observations that beg for a quantitative understanding. Our hope is that someday we will have the ability to design organic polymers or small molecules to extract nanotubes of a particular bandgap with high yield, and the ability to predict the right DNA sequence for the isolation of a specific (n, m) tube.

A quantitative understanding of the sorting mechanism presents many challenges at this moment. Solid-state physicists may be sympathetic to the difficulty we molecular scientists are facing: CNT sorting is a physical/chemical process occurring in liquid state involving many different types of molecules, with many more degrees of freedom than processes occurring in a crystalline lattice. The fundamental issue we are encountering is how to treat the triangular interactions among the nanotube, the solvent, and the dispersant molecules. In the case of DNA-based separation, we have to additionally deal with the macromolecular folding problem—one of the hardest in molecular science.

The place to start then is a qualitative understanding of the sorting mechanism. Even this is not a trivial task, otherwise someone as brilliant as Smalley should not fail to foresee the possibility of CNT sorting 15 years ago. On the other hand, the large body of experimental observations accumulated so far shows that CNT sorting can be accomplished via multiple routes, suggesting strongly that our success in sorting CNTs is guaranteed by certain robust and dominant physical and chemical interactions that override many other factors. Our task is to reveal this inevitability in terms of molecular interactions.

3.1 Solvation Structure, Solvation Energy and its Distribution

Some level of simplification is needed in order to proceed. Sorting is a complicated molecular process involving many factors. We divide them into intrinsic factors that are ultimately responsible for the structural and energetic difference among different CNT colloids, and extrinsic factors (e.g., centrifugal density gradient, stationary phases of chromatography, and polymer phases in ATP) that resolve the intrinsic differences. Our basic assumption is that the intrinsic difference in solvation energy, which originates from the structural difference of CNTs, is responsible for the outcome of sorting; and various separation techniques (e.g., chromatography, DGU, and ATP) are merely different ways to translate the solvation energy difference into spatial-temporal partition of different CNT species.

The intrinsic factors originate from the triangular affair among solvent molecules (e.g., water, toluene), dispersant molecules (e.g., bile salts, TX-405, DNA, PFO), and carbon nanotubes in the liquid state. Solvation energy measures the interaction between the solvent and an individual dispersant-CNT colloid. In this review, we define solvation energy as the amount of energy needed to transfer a solute from a

hypothetical vapor phase to a solvent. Let's examine the role of solvation in specific sorting methods one by one. Probably the simplest case is the PFO extraction method. Solvation energy in this case dictates the solubility of different CNT species. Selective extraction is achieved by tuning the redox condition (see next section for more details), such that the solubility of metallic species is reduced to zero, and only semiconducting tubes remain soluble in the solvent. By further tuning the redox condition to decrease solubility across the board, one can even achieve single-helicity enrichment [41, 66]. Gel chromatography and ATP are conceptually the same in the sense that two phases are used to bring out the intrinsic difference in solvation (or hydration) energy. In the case of ATP, many studies have shown that separation is driven by the difference in intrinsic hydrophobicity/hydrophilicity, or solvation (hydration) energy among different analytes [67, 68]. Modulators are needed to tune the relative solvation energy in the two phases so that differential partitions can be achieved. DGU differentiates species directly by their buoyant densities, which reflect their differences in hydration structure and hydration energy.

The intrinsic physical/chemical difference among different CNT structures ensures that there will be a difference in their solvation energies (see Fig. 13a for small molecule examples illustrating sensitive dependence of solvation energy on molecules structure). To make sorting possible, the difference has to be on the order of kT , where k is the Boltzmann constant and T temperature, to be experimentally detectable. We argue that the chance for this to happen is pretty high if a dispersant can successfully disperse CNTs into a solvent. Individual solvent/solvent, solvent/dispersant, and dispersant/CNT interactions are all non-covalent in nature and all fall conveniently in the range of $\approx kT$. Solvation of a CNT colloid involves $10^2\text{--}10^3$ molecular interactions. Thus, having a few kT difference in solvation energy between two different structures does not seem to be a low probability event. In other words, by conducting our sorting processes in a liquid state, we are guaranteed to have a high probability of success.

Another important issue to consider is the spread, or distribution of solvation energy for a given CNT species (Fig. 13b). A distribution instead of a sharply defined value for solvation energy arises because multiple copies of a dispersant molecule are needed to cover a single tube, and the coating structure may adopt many conformations if the adsorbed molecules lack coordination among themselves. This structural polydispersity inevitably creates a spread in the solvation energy and may overwhelm the intrinsic difference among different nanotube species. Selection of the right dispersants (DNA sequences and surfactants) to ensure their ordered assembly on the surface of CNTs thus becomes very important in atomic-structure-based sorting. It is also evident that if a species with a proper coating is at one of the two extreme ends of the solvation energy spectrum (Fig. 13), it will have lower probability to overlap with others and higher chance to be purified.

What about solvation energy variation caused by CNT length distribution? CNT dispersions made by sonication or by any other means inevitably have a broad tube length distribution. One would think that effect of length polydispersity might easily overwhelm that of chirality polydispersity, making it difficult to achieve atomic- or electronic-structure-based CNT sorting without first narrowing length distribution.

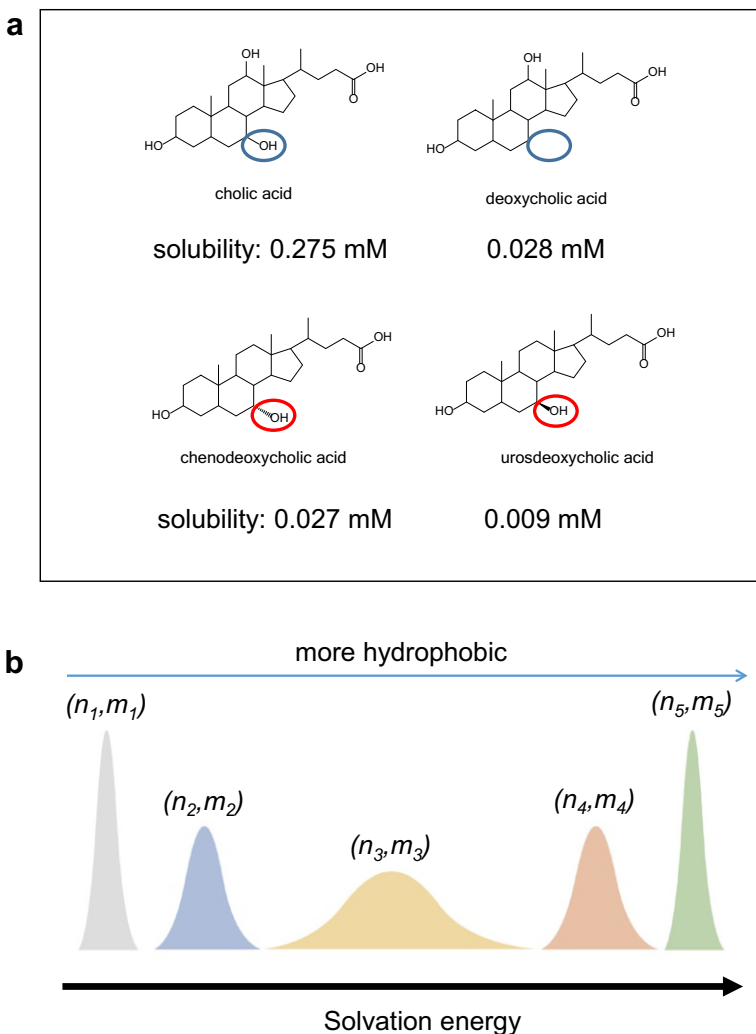


Fig. 13 Solvation energy and molecular structure. **a** Two pairs of bile acid molecules of very similar structures but drastically different solubilities in water [69]. **b** Schematic showing solvation energy (in aqueous phase) distribution of individual (n, m) species, and ranking of solvation energies in a mixture of CNTs

Indeed, the interaction energy between a CNT colloid and its solvent or an external field scales linearly with the tube length. But precisely because of this universal linear scaling, length effect largely cancels out in equilibrium-based CNT sorting. For instance, in DGU separation, the equilibrium position of a CNT in the density gradient is not dependent on its length. For other types of separation such as chromatography and ATP, sorting is achieved through equilibrium partition of CNTs in two different phases; the equal partition point, where the chemical potentials of a tube in the two phases are equal, is also independent of tube length.

Therefore, to a first approximation length variation does not affect the outcome of the CNT sorting. Nevertheless, length control through size-exclusion chromatography [70, 71] or polymer precipitation [60] does reduce higher-order length effects and improve the resolution in atomic- or electronic-structure-based CNT sorting [26, 72].

3.2 Electronic-Structure-Based Sorting via Redox Tuning

Perhaps the best understood separation process is electronic-structure-based sorting, or more specifically bandgap-based sorting with S/M sorting as a narrower case. In this section, we discuss the mechanism of bandgap-based sorting via redox tuning of solvation energies.

3.2.1 Redox Chemistry of CNTs

In Sect. 1.2, we have introduced electronic-structure-based nanotube classification. The bandgap-based nanotube ranking manifests itself in solution phase CNT redox chemistry, a research subject started over a decade ago with the emergence of effective nanotube dispersion and separation methods. Strano et al. first observed that dissolved oxygen at low pH suppresses CNT optical absorption and resonance Raman cross sections in a bandgap-dependent fashion: metallic tubes are more sensitive than semiconducting tubes, and among the latter, the smaller-bandgap/larger-diameter tubes are more sensitive than larger-bandgap/smaller-diameter tubes [73]. Shortly after, we showed that outer sphere electron transfer between CNTs and small-molecule oxidants also exhibits the same bandgap dependence, and we interpreted the oxygen- and pH-dependent optical response as the result of an outer-sphere electron transfer redox reaction between CNTs and oxygen [21]. Many ensuing studies have aimed at determining the redox potential of CNTs and its correlation with bandgap [74, 75]. To understand the role of CNT redox chemistry in sorting, it is useful to take a note from the classical coordination chemistry of transition metal ions, where ligand modulation of redox potential and ligand reorganization upon electron transfer are abundantly documented. If we view a dispersed CNT as a coordination complex, coupling is expected between the nanotube and the coordinating coating layer in electron transfer reactions (Fig. 14).

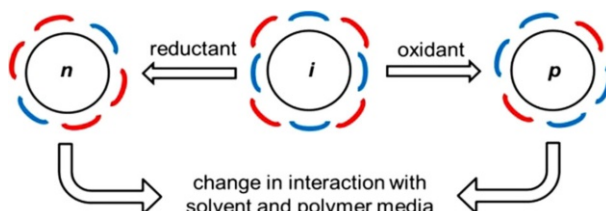


Fig. 14 Schematic illustration of coating layer structure change induced by electron transfer between a CNT and a redox reagent. Reproduced from Ref. [51] with permission

3.2.2 Evidence for the Role of Redox in Bandgap-Based Sorting

The role of redox in CNT sorting is best illustrated in the ATP separation of surfactant-dispersed CNTs. Figure 15 shows the redox modulation of CNT partition in a polyethylene glycol (PEG)/dextran (DX) system [51]. Arc-discharge CNTs were used in this particular experiment, but similar results were also observed for nanotubes with other diameter ranges. As shown in Fig. 15, five distinct partition regimes can be created under different redox conditions: (1) a “reduced” regime, where both metallic and semiconducting tubes are found in the bottom DX phase; (2) a “semi-reduced” regime, where metallic and semiconducting tubes are found in top PEG and bottom DX phase, respectively; (3) an “ambient” regime, where both metallic and semiconducting tubes are found in the top PEG phase; (4) a “semi-oxidized” regime, where metallic and semiconducting tubes are found in DX and PEG phase respectively, reversing the partition found in the “semi-reduced” regime; (5) an “oxidized” regime, where both semiconducting and metallic tubes are pushed to the bottom DX phase. By exploiting the redox modulation, one can obtain S/M separation with further bandgap-based fractionation of semiconducting tubes (Fig. 16).

In the same study, we have shown that bandgap-dependent sorting goes beyond semiconductor fractions. Figure 17 shows the absorption spectra of four successively extracted metallic fractions M3 to M6 from the metallic fraction. Raman radial breathing mode (RBM) profiles of M3 and M6 reveal that M6 has more RBM peak intensities from armchair or near-armchair tubes. This implies that M3 is enriched in smaller-diameter and non-armchair metallic tubes with higher $\cos(3\theta)/d^2$ values, whereas M6 is enriched in armchair or near-armchair and larger-diameter tubes with lower $\cos(3\theta)/d^2$ values. Taken together, our results demonstrate that the oxidative extraction process purifies CNTs in the order of large bandgap semiconducting tubes, small bandgap semiconducting tubes, semi-metals of non-zero bandgap, and armchair tubes of zero-bandgap.

The redox effect is not just operative in the ATP separation process. As a matter of fact, right after solution redox chemistry of CNTs was revealed [21], it was shown that redox can be exploited for S/M sorting of TX-405 dispersed CNTs [22]. A recent study by Wang et al. further illustrates the effectiveness of redox-controlled S/M separation of TX-405 dispersed CNTs via IEX [23]. Redox sorting has also been observed for double-wall carbon nanotubes via the ATP process [76],

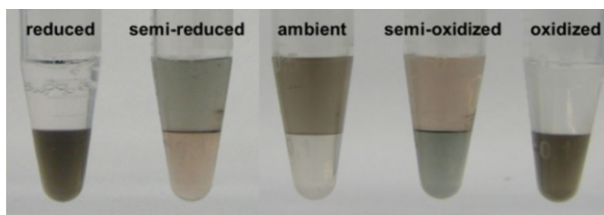


Fig. 15 Redox modulation of nanotube partition in a PEG/DX two-phase system. Reductant used in the experiment is NaBH_4 and oxidant used is NaClO . Reproduced from Ref. [51] with permission

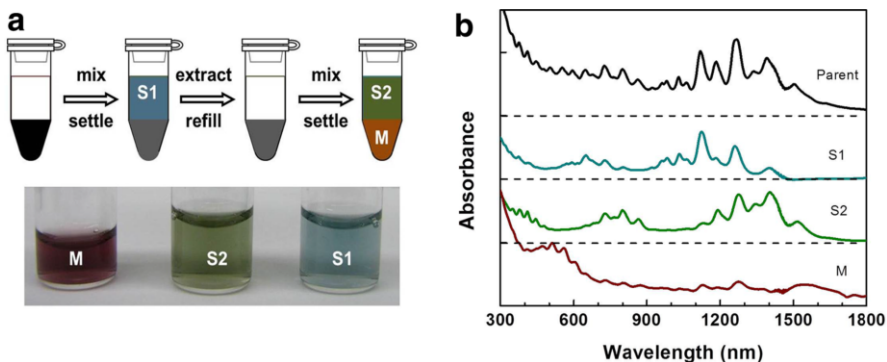


Fig. 16 Bandgap-based sorting of HiPco nanotubes by successive oxidative extraction. **a** Separation scheme and photographs of extracted fractions. **b** Optical absorption spectra of the parent HiPco material and fractions successively extracted from a PEG/DX ATP system with the aid of NaClO. “S1” and “S2” are two successive fractions extracted into the top PEG phase from the starting material, nanotubes remaining in the bottom DX phase are labeled “M” fraction. Reproduced from Ref. [51] with permission

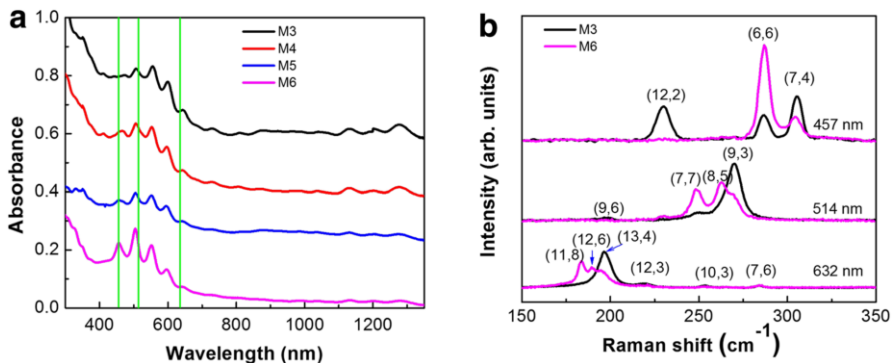


Fig. 17 Spectroscopic evidence for bandgap-based sorting of metallic fractions by redox modulation. **a** Absorption spectra of successive metallic fractions extracted by ATP. **b** Resonance Raman spectra of the M3 and M6 fractions. Reproduced from Ref. [51] with permission

again demonstrating the generality of the redox-based mechanism. A number of reported pH- and oxygen-dependent separation phenomena in DGU [77, 78] and gel chromatography [79, 80] are most likely due to redox-triggered coating layer reorganization. In the case of DGU, we have shown explicitly that redox conditions strongly modulate separation outcome [51].

We find that redox also affects selective CNT dispersion in organic solvents. PFO and its derivatives have been used for efficient extraction of semiconducting tubes in non-polar solvents [40]. The mechanism of the selective extraction remains elusive despite many investigations. We have examined a few commercially available PFO derivatives for the dispersion of various sources of CNTs. In all cases, we find that oxidizing condition enhances selective dispersion with a concomitant lowering of dispersion yield, whereas reducing condition does just the opposite (Fig. 18). Our findings show that solubility of polymer-wrapped CNTs in organic solvents is

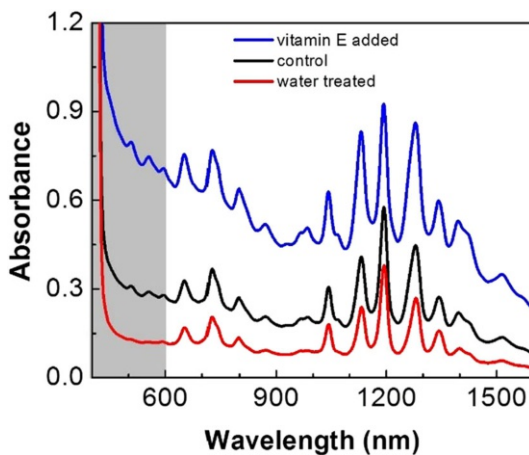


Fig. 18 Absorption spectra of HiPco SWCNT dispersions in toluene made with same amount of poly[(9,9-diethylfluorenyl-2,7-diyl)-alt-co-(6,6''-{2,2'-bipyridine})] (PFO-bipy) and CNT but under different redox conditions. Blue trace dispersion made with 10 mM vitamin E added to the PFO-bipy/CNT mixture; black trace control dispersion with no redox agent added; red trace dispersion made from the control by adding small volume of water, then bath sonication and centrifugation to remove the newly formed aggregates. Reproduced from Ref. [51] with permission

strongly dependent on the redox status of the solvent environment. Ambient redox condition fortuitously enables certain polymers to selectively extract semiconducting tubes under a narrow polymer/CNT mass ratio. Our findings also suggest that controlled oxidation may be used to enhance the semiconducting tube selectivity for those polymers [81] that lack the capability under ambient conditions.

3.2.3 Molecular Mechanism of Redox Sorting

Observations presented above suggest that oxidation somehow creates a ranking of solvation energy for CNT colloids according to their electronic bandgaps (Fig. 19). In each sub-population defined by similar bandgap, there are many CNT species of different atomic structures. A key question is, why the effect of atomic structure on

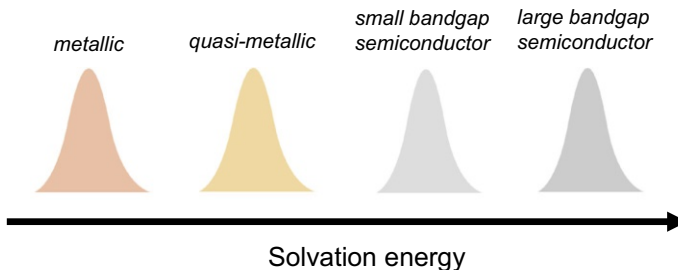


Fig. 19 Redox-induced solvation energy differentiation. Without redox modulation, solvation energy for different types of CNTs overlap. Upon oxidation, coating structure change results in differentiation of solvation energy

coating structure and solvation energy in this case becomes less important? What physical mechanism supersedes the atomic-structure-dependent interactions in this case? It appears that the long-range, strong electrostatic interaction is the dominant effect to consider. For CNTs coated by charge-neutral dispersants (PFO, TX-405), this ranking can be explained by the degree of charging upon removal of electrons from CNTs. This has been clearly demonstrated in the S/M sorting of TX-405 dispersed CNTs, where preferential charge accumulation in metallic tubes was exploited by IEX separation [23]. For PFO-dispersed CNTs in a non-polar solvent, metallic tubes are also preferentially charged via oxidation, which leads to an increase in solvation energy and decrease in solubility. The low dielectric constant of the non-polar solvent certainly enhances the electrostatic charging energy, creating a large enough solvation energy/solubility difference between metallic and semiconducting tubes so that they can be separated at the dispersion stage.

For CNTs coated by charged dispersants in water, we can model the resulting CNT colloids by a rigid rod of polyelectrolyte. We then consider the effect of redox-induced charge density change on the solvation energy of the polyelectrolyte. In general, the strong and long-range electrostatic interaction dominates the physics of polyelectrolytes in water [82, 83]. An important consequence is the counter ion condensation along a linear rod of polyelectrolyte [83]. This explains why a polyelectrolyte may have a very low level of ionization even if its constituent monomers are strong electrolytes themselves. In considering solvation of CNT colloids coated by charged dispersant molecules, one has to treat the condensed counter ions as an integral part of the coating layer. A number of experimental observations clearly demonstrate this. For instance, we have observed that crown ether, a metal ion chelator, greatly reduces the hydrophilicity of SDC- and DNA-coated CNTs. A recent study also shows that varying ionic strength can alter buoyant density of SDC-coated CNTs [39]. Based on these considerations, we suggest that CNT oxidation reduces the overall negative charge on a CNT, which leads to the release of condensed counter ions, which further leads to a decrease in its solvation energy. The situation is analogous to solubility increase of a weak electrolyte (e.g., acetic acid) when its degree of ionization is increased. Since the extent of CNT oxidation is bandgap-dependent, we expect solvation energy to be differentiated according to bandgap as shown in Fig. 19. Because of high dielectric constant of water, the magnitude of solvation energy change may be smaller than that seen in PFO-dispersed CNTs upon oxidation, but large enough to be detected.

What is the requirement on CNT dispersant for redox enabled bandgap sorting? On the one hand, the binding affinity of the dispersant to CNT should be strong enough to ensure CNT colloidal stability. On the other hand, the resulting coating layer should be relatively loose to allow the following events to take place: (1) the CNT atomic-structure-dependent solvation is diminished; and (2) redox molecules such as dissolved oxygen have access to nanotube surface for electron transfer reaction. Consistent with this analysis are a number of observations: (1) sodium dodecyl sulfate (SDS), a weak surfactant, enables S/M sorting; (2) the stronger surfactant SC by itself does not support S/M sorting, but a combination of SC/SDS does; (3) only specific DNA sequences allow S/M sorting, but DNA/sodium dodecylbenzenesulfonate (SDBS) combination enables S/M sorting almost

independent of sequence choice [84]; and (4) the strongest surfactant SDC does not seem to support S/M sorting.

3.3 Atomic-Structure-Based Sorting via Ordered Coating Structure Formation

It should be noted that the bandgap-based CNT sorting we have just discussed is not a complete solution to the CNT sorting problem. This is because there are structural degeneracies in bandgap-based classification: armchair metallic tubes of different diameters all have zero bandgap, semiconducting tubes of the same diameter but different chiralities have the same bandgap to first approximation, and an enantiomeric pair of CNTs have indistinguishable electronic structure. To achieve complete separation of CNTs, one has to resort to atomic-structure-based sorting, or chirality sorting as typically called. Experimental procedures for atomic-structure-based sorting have been developed for CNTs coated with either small-molecule surfactants or specific DNA sequences. To discuss the sorting mechanism, we again consider solvation energies of a mixture of CNT colloids dispersed by a small-molecule surfactant or a DNA sequence. For a given (n, m) tube, its solvation energy in general has a distribution that can be characterized by a mean value and a linewidth. The distribution originates from many possible molecular configurations of the adsorbed molecules. If the adsorbed molecules display a certain degree of coordination through their interactions with each other and with the CNT surface, then that will give the CNT species some degree of order in the coating structure, yielding narrower solvation energy distribution, less probability of overlap with other species, and a greater chance to be isolated. In addition, if a CNT species has an extreme solvation energy value among all the species, it will have an even better chance to be isolated. The key to atomic-structure-based sorting is to find the right dispersant that will form an ordered coating structure on at least a subgroup of CNT species.

In the case of surfactant-coated CNTs, we know that SC is good for S/M separation and the stronger surfactant SDC is good for chirality sorting. A weaker binding surfactant creates a fuzzy coating and a spread in solvation free energy. A stronger binding surfactant may produce better defined coating structure and sharper distribution of solvation free energy. Because surfactant molecules are small relative to the size of the CNT surface, many copies of surfactant molecules are needed to tile the CNT surface. A small change in CNT structure can be accommodated by a small change in the surfactant assembly without too much frustration. As a result, we expect the solvation energy of surfactant-coated CNTs to change as a smooth function of CNT chirality and diameter. The advantage of this is that a single surfactant may be used for the chirality sorting of many CNT species, the disadvantage is that overlapping in solvation energy may limit resolution and purity.

In the case of the DNA-coated CNTs, the importance of DNA sequence to obtain ordered structures is made abundantly clear by many observations [6, 17, 18, 24, 25, 61]. Certain special sequences can not only form an ordered structure on specific (n, m) , thus narrowing the solvation energy distribution, but

also make the mean solvation energy to be on one of the two extreme ends of the solvation energy ranking (Fig. 13). In contrast to the surfactant case, the coating structure and solvation energy of DNA-CNT colloids can change abruptly in the chirality space, since tiling a cylindrical surface by a set of molecules of comparable size is intrinsically difficult, and a well-folded structure is an exception rather than a rule. A number of molecular dynamics (MD) simulation studies have demonstrated this point. For instance, Roxbury et al. have compared the folding structure of $(TAT)_4$ on two CNT species (Fig. 20) [85]. It is evident that dramatic changes occur when we go from one CNT species to another. The ordered folding structure in $(TAT)_4$ -(6, 5) appears to be established by inter-strand interactions mediated by a hydrogen-bonding network.

Handedness resolved CNT separation is perhaps the best example to illustrate the mechanism of atomic-structure-based separation. Here, both left-handed and its mirror-image right-handed CNT have the same electronic structure, and mechanisms responsible for bandgap-based sorting cannot be operative. We have recently observed that DNA-based sorting by ATP almost always yields simultaneous control of both handedness and helicity when a proper sequence is chosen (Fig. 21). A DNA-CNT is selected when it is partitioned into either the top or bottom phase exclusively, and is well separated from other species (Fig. 21a). This implies that hydration energy of the selected species should have not only an extreme value [67, 68] but also be well separated from those of other DNA-CNT species. This, given the sensitivity of hydration energy to minute structure variations [58, 61], requires the selected species to have minimum structural variation, or minimum conformational entropy, to avoid overlapping partition with other species. Thus, minimum conformational entropy is an implicit selection criterion. Two sources of structure variation contribute to the conformational entropy of a DNA-CNT. First, a CNT may have either left- or right-handed configurations. Second, DNA folding may have a distribution of conformations populated at room temperature. Reducing ambiguity in CNT handedness is one way to minimize conformational entropy; another is to have a DNA sequence that adopts well-defined folding conformation and chiral character, commensurate with the encased CNT. We suggest that both need to happen in order to ensure selection of CNTs with defined handedness. This case is analogous to the folding of biopolymers where substrate stereo-selectivity is a natural outcome of a well-folded structure built by homochiral monomers.

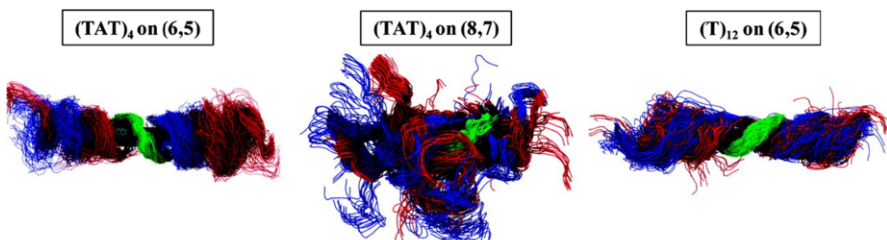


Fig. 20 MD simulation results demonstrating sequence-dependent wrapping of CNTs by DNA. Reproduced from Ref. [85] with permission

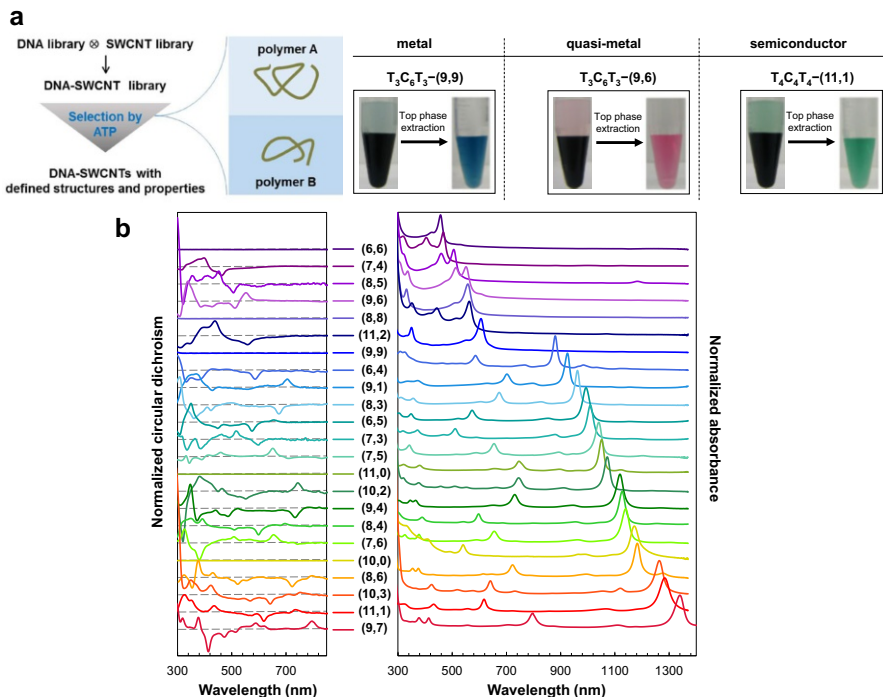


Fig. 21 Selection of CNTs of defined handedness and helicity. **a** ATP selection scheme and a few examples. **b** Circular dichroism and optical absorption spectra of selected CNT species. Reproduced from Ref. [6] with permission

Our current understanding of the chirality sorting mechanism discussed above is far from complete. To enable chirality sorting, the binding interaction between a dispersant and a CNT has to be sensitive to the chiral structure of the tube. Computational analyses currently available have not pinned down the source of the required chiral dependence. For instance, in the case of DNA, a quantum mechanical calculation shows that nucleobase binding is not sensitive to the chirality of the substrate CNT [86]. Perhaps it is the chiral sugar-moiety in the backbone that gives rise to chirality-dependent DNA binding affinity to a CNT. More studies on the chirality sorting mechanism are clearly needed.

3.4 Nanotube Length Effect on Atomic- and Electronic-Structure-Based Separation

CNT dispersions made by sonication or any other means inevitably have a broad range of tube length distribution. On first thought, one might think that length-related structural polydispersity may overwhelm chirality polydispersity, making it very difficult to achieve chirality sorting in samples with non-uniform length distribution. Indeed, any molecular interaction, especially solvation interaction that is believed to be the key differentiating factor, scales linearly with tube length.

However, it is precisely because of this universal scaling that length effect becomes secondary factor to consider in sorting. This is obvious for density-based separation, because the density of a colloidal CNT is independent of its length. For other types of separation such as chromatography and ATP, sorting is achieved through equilibrium partition of a tube in two different phases. The equal partition point at which the chemical potential of a tube in two phases are equal is independent of tube length. This is why length polydispersity does not affect atomic- and electronic-structure-based sorting to a first approximation. Nevertheless, a uniform length distribution is beneficial. Length sorting can be achieved by hydrodynamic radius-based sorting methods such as size-exclusion chromatography [36, 70, 87]. It has been shown that length sorting does improve the resolution of chirality sorting [26].

3.5 Resolution Limit of Atomic-Structure-Based Separation

From both a practical and theoretical point of view, it is important to know the limit of our ability to separate CNTs by their atomic structures. Currently, most chirality sorting methods are demonstrated for small-diameter tubes (≤ 1 nm), and for species with relatively high abundance. An increase in resolution is needed for atomic-structure-based separation of larger-diameter tubes, and for purification of species of very low abundance.

For simplicity, we consider single-stage separation. One can always use multi-stage separation techniques such as chromatography to further improve the resolution. As we discussed in the previous section, we rely on solvation energy difference among different chiralities for separation. In the simplest case where a mixture of two species of equal abundance is to be separated, we need a solvation energy difference of kT between the two species. In general, the amount of information needed for identifying a species of abundance a is $\log_2(1/a)$, and if we want to sort this species out of the mixture, we need a solvation energy difference between this species and the rest to be $kT \log_2(1/a)$ [88]. Currently, by choosing the right DNA sequences, we can purify a species with 0.1–1% abundance, corresponding to a solvation energy difference of $\approx 10 kT$. To be able to purify a species at 10^{-6} abundance, we would need a solvation energy difference of $\approx 20 kT$. This is equivalent to a difference of two to three hydrogen bonds in a solvation interaction that typically involves 10^2 – 10^3 hydrogen bonds. Given the practically unlimited choice of DNA sequences, it does not seem impossible to reach this level of differentiation by identifying the right DNA sequences.

A more reliable route for increasing the selectivity or resolution is to replace solvating water molecules by a macromolecule of defined structure. Liquid water has some structure, but not well defined. If there were a solvent medium that has a better-defined structure, then solvation energy difference among different CNT colloids could be increased. Here again, molecular recognition that is ubiquitous in biology may provide a real solution. The most relevant biological example is gene expression control. Living cells use special proteins called transcription factors to recognize specific double-stranded DNA fragments with a degree of selectivity easily exceeding 1 out of 10^6 [89]. Transcription factors achieve this feat via specific

interactions with major/minor grooves imbedded in the indistinguishable sugar-phosphate backbone of double-stranded (ds) DNA. To a first approximation, dsDNA is very much like DNA-CNTs, but the latter have more exposed and differentiable surfaces. If we can evolve proteins to recognize specific DNA-CNT complexes, we should be able to dramatically increase the selectivity. Synthetic mimics of transcription factors such as sequence-controlled pyrrole-imidazole oligomers [90–92] may provide an alternative path towards the same goal.

In summary, DNA-based separation may in the future be able to take advantage of molecular recognition by proteins to achieve 10^{-6} selectivity, or even higher. This should be useful for quantifying minute amount of metallic impurities in electronic-grade semiconducting tubes, and to enable biomedical applications that require specific targeting capability. Surfactant-based approaches may allow high-resolution purification with up to 10^{-4} selectivity using chromatography approach, but it is unlikely to compete with DNA–protein binding-based approach that employs two layers of molecular recognition.

3.6 Evolvability of DNA-Based Sorting

Commercial oligonucleotide synthesis currently can make ssDNA strands as long as 100 bases. The number of unique sequences available to us is thus on the order of 4^{100} or 10^{60} —an infinite number for all practical purposes. The physical essence of DNA-based CNT sorting is to control intermolecular interactions by the proper choice of sequence. In this regard, it resembles many processes occurring in a living cell, where intermolecular interactions are mediated by sequence-controlled polymers, i.e., DNA, RNA and proteins. In our case, DNA sequence strongly modulates intermolecular interactions during the CNT sorting processes. So far, only a limited number of sequences (<800) have been tested for CNT sorting [6, 24]. The overall rate of success, i.e., finding a recognition sequence, is around 5–10%. Once a recognition sequence is identified for certain (n, m) species, a bright spot in the vast DNA sequence space is located. One can mutate the sequence to explore the surrounding DNA sequence space for improvement, or for expansion in function. This strategy has been used successfully for the purification of metallic armchair tubes starting from known recognition sequences for semiconducting tube purification [25]. Another example is the (TAT)₄ sequence identified initially in the IEX purification [24] of (6, 5) and later used in ATP purification of the same species [61]. Recently, a mutation sequence—TTA TAT TAT ATT, was found to allow both left-handed and right-handed (6, 5) tubes to be purified in a PEG/polyacrylamide (PAM) two-phase system with very high yield [6]. In principle, this cycle of mutation-improvement can be repeated over and over again towards any desired level of purification. Thus, the DNA-based method provides not just a static solution but also a clear path for continued improvement. In this sense, we say it constitutes a complete solution to the CNT sorting problem.

The analysis presented above suggests a Mendelian/Darwinian way to look at DNA-CNT partition in an ATP system—a many-body molecular system with moderate complexity. We have called it a “single-gene molecular system” [61] to reflect its strong sequence-dependent behavior and its evolvability. Suppose in the

future we have gathered enough computing power and developed efficient algorithms to handle the folding of macromolecules and their interactions with water, it might be possible to perform a full-scale molecular dynamics and quantum chemical calculation to completely determine the behavior of such a system at every single spatial–temporal point—a Newtonian/Hamiltonian approach. How useful is such an approach and at what cost? Would the information obtained over-saturate our brain? Fortunately, our physical world is constructed in such a way that a sequence-controlled polymer like DNA can couple to a complex molecular assembly, and dictate to a large extent the behavior of the many-body system. The sequence information is much easier to handle than a large pile of computation output.

4 Future Directions

CNT sorting research has resulted in impressive progress in our ability to obtain CNTs of defined structures. Purified CNTs have enabled many fundamental studies and application developments. In CNT spectroscopy, this includes elucidation of phonon-assisted exciton relaxation channels, K -momentum dark excitons, non-Condon effect in resonance Raman excitation profiles, plasmon excitation, resonance Raman cross-section dependence on chirality, to name by a few [93–101]. Elsewhere, we find usage of purified tubes for redox [21] and photochemistry [102], for defect chemistry and related applications in single-photon sources and other photonic and optoelectronic devices [103–105], for FET devices [31, 72, 106–108], biosensing and imaging, and for CNT cloning [3, 109]. Future improvement in CNT sorting in terms of separation efficiency, yield, and resolution will undoubtedly take place driven by the growing demand for purified CNTs. What we would like to do here is to speculate some additional areas of research that may grow out of CNT sorting.

4.1 Sorting Other Types of Nanotubes

The rise of 2D materials raises the possibility of other types of nanotubes. Both graphene and single-layer boron nitride, two of the best-known 2D materials, have their tubular structure counterparts. This makes one to wonder how many of other 2D sheets can also be rolled up to form tubular structures. Indeed, there are a number of reports that indicate such a possibility. These include nanotubes from misfit layered compounds [110, 111], and transition-metal dichalcogenide (MoS_2 , WS_2) nanotubes [112, 113]. If future work does produce a large family of 1D tubular structures beyond CNTs and BNNTs, then for each member of this family with a distinct chemical composition, there is a structure polydispersity issue and a corresponding sorting problem that needs to be solved. At the dispersion level, we expect that many surfactants successfully used for CNT dispersion should be effective in dispersing other tubular structures. DNA should also be a good dispersant since it is capable of stacking interactions through nucleotide bases with many 2D materials. For instance, there are reports showing DNA base adsorption on

MoS₂ [114]. At the separation level, we expect both the bandgap-based and atomic structure-based sorting mechanisms we have discussed should be applicable to other tubular structures. As a matter of fact, none of the sorting mechanisms is specific to the chemical composition of CNTs.

4.2 Quantifying Solvation Interactions

We have attributed the ultimate driving force of CNT sorting to solvation interactions. Qualitatively, these interactions are electromagnetic in nature. Quantitatively, how to determine the solvation energy experimentally and computationally for a given object with defined geometry and surface coating is an unresolved problem. In general, macromolecular interaction with water is a fundamental problem in biophysics. What controls the hydrophobicity/hydrophilicity level of a macromolecule? How do different salts and polymers affect solvation in water? These are precisely the same questions we ask in the study of CNT sorting mechanism. As a new family of macromolecules, CNT colloids have a number of unique advantages over proteins and DNA: their structures can be varied systematically with atomic precision, they have optical signatures that allow us to easily identify and quantify them, and to monitor their movement. These are useful features for deriving scaling laws [115, 116], and for designing controlled and parallel experiments.

4.3 Expanding Functions of DNA-CNT Hybrids

CNT sorting is about the manipulation of molecular interactions, about using small and macro- organic molecules to control the behavior of inorganic materials in liquid phases. The atomic-structure-based CNT sorting is enabled by ordered coating structures that modulate interactions with solvent media. We can expand the utility of the ordered coating structures to the control of other interactions. Perhaps the most enticing future direction is to use specific DNA sequences to control CNT surface coating and many other properties associated with the nanotube. At the moment, we do not understand the DNA code for CNT recognition. Trial-and-error approaches have to be used to identify the right sequences. If someday we have acquired de novo design capability, or more likely, mastered sequence selection process, we basically know how to construct a hybrid of well-defined structure and property.

Can we select DNA sequences to confer CNT specificity to certain analyte? Can we select DNA sequences to control covalent modification of CNTs? Can we use DNA sequences to control electron transfer? Can we explore DNA photochemistry by using DNA-CNT hybrids [117]? Can we convert CNT into a catalyst with proper coating by DNA? Can we use DNA coating to enable stereochemistry of CNTs [6]? To answer these questions, we should be reminded of the broader role played by nucleic acids in the early stage of evolution, as revealed by the discovery of ribozymes, and further illustrated by the aptamer technology, where ssDNA and RNA sequences are identified to bind specifically to virtually any molecular target, and/or to even perform catalysis [118, 119]. Also conceivable, but not demonstrated, is the role of photochemistry of nucleic acids in early stage of evolution for

converting sunlight energy into chemically useful forms. The hope is that inclusion of a molecular-sized inorganic crystal with tunable electronic structure may greatly enrich the chemical functions of DNA. The challenge is to find sequences that have the dual function of differential CNT binding and specific response to certain molecular target, but conceptually there is no fundamental barrier to accomplishing this.

Can we improve the fluorescence quantum yield of semiconducting CNTs by proper DNA coating? Can we use DNA to control the spin state of electrons in transport [120, 121]? Can we use DNA sequences to control electron–electron interactions in order to create new phases of electronic state [122]? These questions deal with control of quasi-particle interactions inside a CNT. Here we are entering a territory with too much unknowns. How strong is electronic coupling between DNA and CNT? How much of modulation can we expect from sequence to sequence? Can we intercalate small-molecule species (e.g. dyes) between DNA and CNT to augment such interactions? Essentially we are trying to test if a proper choice of surface coating can alter the physical properties of CNT in a substantial way. Some relevant theoretical studies have been conducted [120, 123, 124], but more experimental and theoretical explorations are needed in this direction.

In general, inorganic electronic and optical materials are traditionally processed and investigated by the top down approach, relying heavily on man-made instrumentations. As the size of inorganic materials becomes comparable with that of macromolecules, molecular-based processing approaches will become more effective, resembling more and more biochemical processes occurring in a living cell. In this context, the use of DNA and proteins to manipulate CNT becomes an obvious choice. Our ability to sort CNTs by DNA illustrates its utility beyond the conventional domain of biology, and beyond current DNA nanotechnology that relies on canonical Watson–Crick base-pairing interactions. DNA is just a special example of sequence-controlled polymers. In the future, when more and more sequence-controlled polymers are made by synthetic chemists with different functional groups incorporated, there will be more and more options available for making polymer-CNT hybrids of desired physical and chemical properties. This may provide a seamless interface between inorganic nanomaterials and biology that Richard Smalley had anticipated, and shed some light on how we function as a complex molecular assembly.

Acknowledgments The author would like to express his gratitude to many of his colleagues and associates at DuPont CR&D, NIST and other institutions for their collaboration on the CNT sorting research. They are Anand Jagota, Bruce Diner, Xueying Huang, Scott Mclean, Ellen Semke, Xiaomin Tu, Constantine Khrapin, Jeffrey Fagan, Angela Hight-Walker, Geyou Ao, Jason Streit, Hui Gui, and Chongwu Zhou. Critical reading of the manuscript by Geyou Ao, Jeffrey Fagan, and Jason Streit is also greatly appreciated.

References

1. Giddings JC (1991) Unified separation science. Wiley-Interscience, New York
2. Saito R, Dresselhaus G, Dresselhaus MS (1998) Physical properties of carbon nanotubes. Imperial College Press, London

3. Liu J, Wang C, Tu X, Liu B, Chen L, Zheng M, Zhou C (2012) Chirality-controlled synthesis of single-wall carbon nanotubes using vapour-phase epitaxy. *Nat Commun* 3:1199. http://www.nature.com/ncomms/journal/v3/n11/suppinfo/ncomms2205_S1.html
4. Yang F, Wang X, Zhang D, Yang J, LuoDa, Xu Z, Wei J, Wang J-Q, Xu Z, Peng F, Li X, Li R, Li Y, Li M, Bai X, Ding F, Li Y (2014) Chirality-specific growth of single-walled carbon nanotubes on solid alloy catalysts. *Nature* 510(7506):522–524. doi:[10.1038/nature13434](https://doi.org/10.1038/nature13434). <http://www.nature.com/nature/journal/v510/n7506/abs/nature13434.html#supplementary-information>
5. Sanchez-Valencia JR, Dienel T, Groning O, Shorubalko I, Mueller A, Jansen M, Amsharov K, Ruffieux P, Fasel R (2014) Controlled synthesis of single-chirality carbon nanotubes. *Nature* 512(7512):61–64. doi:[10.1038/nature13607](https://doi.org/10.1038/nature13607)
6. Ao G, Streit J, Fagan J, Zheng M (2016) Differentiating left- and right-handed carbon nanotubes by DNA. *J Am Chem Soc*. doi:[10.1021/jacs.6b09135](https://doi.org/10.1021/jacs.6b09135)
7. Saito R, Fujita M, Dresselhaus G, Dresselhaus MS (1992) Electronic structure of chiral graphene tubules. *Appl Phys Lett* 60(18):2204–2206. doi:[10.1063/1.107080](https://doi.org/10.1063/1.107080)
8. Hamada N, S-i Sawada, Oshiyama A (1992) New one-dimensional conductors: graphitic micro-tubules. *Phys Rev Lett* 68(10):1579–1581
9. Kane CL, Mele EJ (1997) Size, shape, and low energy electronic structure of carbon nanotubes. *Phys Rev Lett* 78(10):1932–1935
10. Odom TW, Huang J-L, Kim P, Lieber CM (1998) Atomic structure and electronic properties of single-walled carbon nanotubes. *Nature* 391(6662):62–64
11. Ouyang M, Huang J-L, Cheung CL, Lieber CM (2001) Energy gaps in “metallic” single-walled carbon nanotubes. *Science* 292(5517):702–705
12. Thess A, Lee R, Nikolaev P, Dai H, Petit P, Robert J, Xu C, Lee YH, Kim SG, Rinzler AG, Colbert DT, Scuseria GE, Tománek D, Fischer JE, Smalley RE (1996) Crystalline ropes of metallic carbon nanotubes. *Science* 273(5274):483
13. Girifalco LA, Hodak M, Lee RS (2000) Carbon nanotubes, buckyballs, ropes, and a universal graphitic potential. *Phys Rev B* 62(19):13104–13110
14. Iijima S, Ichihashi T (1993) Single-shell carbon nanotubes of 1-nm diameter. *Nature* 363(6430):603–605
15. Dresselhaus MS, Dresselhaus G, Avouris P (eds) (2001) Carbon nanotubes: synthesis, structure, properties, and applications. Springer, Berlin
16. Wang S, Humphreys ES, Chung S-Y, Delduca DF, Lustig SR, Wang H, Parker KN, Rizzo NW, Subramoney S, Chiang Y-M, Jagota A (2003) Peptides with selective affinity for carbon nanotubes. *Nat Mater* 2(3):196–200
17. Zheng M, Jagota A, Semke ED, Diner BA, McLean RS, Lustig SR, Richardson RE, Tassi NG (2003) DNA-assisted dispersion and separation of carbon nanotubes. *Nat Mater* 2(5):338–342
18. Zheng M, Jagota A, Strano MS, Santos AP, Barone P, Chou SG, Diner BA, Dresselhaus MS, McLean RS, Onoa GB, Samsonidze GG, Semke ED, Usrey M, Walls DJ (2003) Structure-based carbon nanotube sorting by sequence-dependent DNA assembly. *Science* 302(5650):1545–1548
19. Chen Z, Du X, Du M-H, Rancken CD, Cheng H-P, Rinzler AG (2003) Bulk separative enrichment in metallic or semiconducting single-walled carbon nanotubes. *Nano Lett* 3(9):1245–1249. doi:[10.1021/nl0344763](https://doi.org/10.1021/nl0344763)
20. Krupke R, Hennrich F, Hv Löhneysen, Kappes MM (2003) Separation of metallic from semiconducting single-walled carbon nanotubes. *Science* 301(5631):344
21. Zheng M, Diner BA (2004) Solution redox chemistry of carbon nanotubes. *J Am Chem Soc* 126(47):15490–15494
22. Jagota A, Diner BA, Boussaad S, Zheng M (2005) Carbon nanotube -biomolecule interactions: applications in carbon nanotube separation and biosensing. In: Rotkin SV, Subramoney S (eds) Applied physics of carbon nanotubes—fundamentals of theory, optics and transport devices. Springer, New York
23. Wang J, Nguyen TD, Cao Q, Wang Y, Tan MYC, Chan-Park MB (2016) Selective surface charge sign reversal on metallic carbon nanotubes for facile ultrahigh purity nanotube sorting. *ACS Nano* 10(3):3222–3232. doi:[10.1021/acsnano.5b05795](https://doi.org/10.1021/acsnano.5b05795)
24. Tu X, Manohar S, Jagota A, Zheng M (2009) DNA sequence motifs for structure-specific recognition and separation of carbon nanotubes. *Nature* 460:250–253
25. Tu X, Hight Walker AR, Khripin CY, Zheng M (2011) Evolution of DNA sequences toward recognition of metallic armchair carbon nanotubes. *J Am Chem Soc* 133(33):12998–13001. doi:[10.1021/ja205407q](https://doi.org/10.1021/ja205407q)

26. Zheng M, Semke ED (2007) Enrichment of single chirality carbon nanotubes. *J Am Chem Soc* 129:6084–6085
27. Tu X, Zheng M (2008) A DNA-based approach to the carbon nanotube sorting problem. *Nano Research* 1:185–194
28. Lustig SR, Jagota A, Khrapin C, Zheng M (2005) Theory of structure-based carbon nanotube separations by ion-exchange chromatography of DNA/CNT hybrids. *J Phys Chem B* 109:2559–2566
29. Arnold MS, Stupp SI, Hersam MC (2005) Enrichment of single-walled carbon nanotubes by diameter in density gradients. *Nano Lett* 5(4):713–718. doi:[10.1021/nl050133o](https://doi.org/10.1021/nl050133o)
30. Wenseleers W, Vlasov II, Goovaerts E, Obraztsova ED, Lobach AS, Bouwen A (2004) Efficient isolation and solubilization of pristine single-walled nanotubes in bile salt micelles. *Adv Funct Mater* 14(11):1105–1112. doi:[10.1002/adfm.200400130](https://doi.org/10.1002/adfm.200400130)
31. Arnold MS, Green AA, Hulvat JF, Stupp SI, Hersam MC (2006) Sorting carbon nanotubes by electronic structure using density differentiation. *Nat Nano* 1(1):60–65. http://www.nature.com/nano/journal/v1/n1/supplinfo/nano.2006.52_S1.html
32. Niyogi S, Densmore CG, Doorn SK (2008) Electrolyte tuning of surfactant interfacial behavior for enhanced density-based separations of single-walled carbon nanotubes. *J Am Chem Soc* 131(3):1144–1153. doi:[10.1021/ja807785e](https://doi.org/10.1021/ja807785e)
33. Hároz EH, Rice WD, Lu BY, Ghosh S, Hauge RH, Weisman RB, Doorn SK, Kono J (2010) Enrichment of armchair carbon nanotubes via density gradient ultracentrifugation: Raman spectroscopy evidence. *ACS Nano* 4(4):1955–1962. doi:[10.1021/nn901908n](https://doi.org/10.1021/nn901908n)
34. Ghosh S, Bachilo SM, Weisman RB (2010) Advanced sorting of single-walled carbon nanotubes by nonlinear density-gradient ultracentrifugation. *Nat Nano* 5(6):443–450. <http://www.nature.com/nano/journal/v5/n6/abs/nano.2010.68.html#supplementary-information>
35. Yanagi K, Miyata Y, Kataura H (2008) Optical and conductive characteristics of metallic single-wall carbon nanotubes with three basic colors; cyan, magenta, and yellow. *Appl Phys Express* 1(3):034003
36. Fagan JA, Becker ML, Chun J, Hobbie EK (2008) Length fractionation of carbon nanotubes using centrifugation. *Adv Mater* 20(9):1609–1613. doi:[10.1002/adma.200702353](https://doi.org/10.1002/adma.200702353)
37. Kawai M, Kyakuno H, Suzuki T, Igarashi T, Suzuki H, Okazaki T, Kataura H, Maniwa Y, Yanagi K (2012) single chirality extraction of single-wall carbon nanotubes for the encapsulation of organic molecules. *J Am Chem Soc* 134(23):9545–9548. doi:[10.1021/ja3013853](https://doi.org/10.1021/ja3013853)
38. Fagan JA, Zheng M, Rastogi V, Simpson JR, Khrapin CY, Silvera Batista CA, Hight Walker AR (2013) Analyzing surfactant structures on length and chirality resolved (6, 5) single-wall carbon nanotubes by analytical ultracentrifugation. *ACS Nano* 7(4):3373–3387. doi:[10.1021/nn4002165](https://doi.org/10.1021/nn4002165)
39. Lam S, Zheng M, Fagan JA (2016) Characterizing the effect of salt and surfactant concentration on the counterion atmosphere around surfactant stabilized SWCNTs using analytical ultracentrifugation. *Langmuir* 32(16):3926–3936. doi:[10.1021/acs.langmuir.6b00605](https://doi.org/10.1021/acs.langmuir.6b00605)
40. Nish A, Hwang J-Y, Doig J, Nicholas RJ (2007) Highly selective dispersion of single-walled carbon nanotubes using aromatic polymers. *Nat Nano* 2(10):640–646. http://www.nature.com/nano/journal/v2/n10/supplinfo/nano.2007.290_S1.html
41. Chen F, Wang B, Chen Y, Li L-J (2007) Toward the extraction of single species of single-walled carbon nanotubes using fluorene-based polymers. *Nano Lett* 7(10):3013–3017. doi:[10.1021/nl071349o](https://doi.org/10.1021/nl071349o)
42. Lee HW, Yoon Y, Park S, Oh JH, Hong S, Liyanage LS, Wang H, Morishita S, Patil N, Park YJ, Park JJ, Spakowitz A, Galli G, Gygi F, Wong PHS, Tok JBH, Kim JM, Bao Z (2011) Selective dispersion of high purity semiconducting single-walled carbon nanotubes with regioregular poly(3-alkylthiophene)s. *Nat Commun* 2:541. doi:[10.1038/ncomms1545](https://doi.org/10.1038/ncomms1545). <http://www.nature.com/articles/ncomms1545#supplementary-information>
43. Ju S-Y, Doll J, Sharma I, Papadimitrakopoulos F (2008) Selection of carbon nanotubes with specific chiralities using helical assemblies of flavin mononucleotide. *Nat Nano* 3(6):356–362. http://www.nature.com/nano/journal/v3/n6/supplinfo/nano.2008.148_S1.html
44. Ozawa H, Fujigaya T, Niidome Y, Hotta N, Fujiki M, Nakashima N (2011) Rational concept to recognize/extract single-walled carbon nanotubes with a specific chirality. *J Am Chem Soc* 133(8):2651–2657. doi:[10.1021/ja109399f](https://doi.org/10.1021/ja109399f)
45. Lemasson FA, Strunk T, Gerstel P, Henrich F, Lebedkin S, Barner-Kowollik C, Wenzel W, Kappes MM, Mayor M (2011) Selective dispersion of single-walled carbon nanotubes with specific

- chiral indices by poly(*N*-decyl-2,7-carbazole). *J Am Chem Soc* 133(4):652–655. doi:[10.1021/ja105722u](https://doi.org/10.1021/ja105722u)
46. Stürzl N, Hennrich F, Lebedkin S, Kappes MM (2009) Near monochiral single-walled carbon nanotube dispersions in organic solvents. *J Phys Chem C* 113(33):14628–14632. doi:[10.1021/jp902788y](https://doi.org/10.1021/jp902788y)
 47. Tange M, Okazaki T, Iijima S (2011) Selective extraction of large-diameter single-wall carbon nanotubes with specific chiral indices by poly(9,9-diocetylfluorene-alt-benzothiadiazole). *J Am Chem Soc* 133(31):11908–11911. doi:[10.1021/ja204698d](https://doi.org/10.1021/ja204698d)
 48. Mistry KS, Larsen BA, Blackburn JL (2013) High-yield dispersions of large-diameter semiconducting single-walled carbon nanotubes with tunable narrow chirality distributions. *ACS Nano* 7(3):2231–2239. doi:[10.1021/nn305336x](https://doi.org/10.1021/nn305336x)
 49. Kato Y, Fukuzawa M, Toshimitsu F, Nakashima N (2015) Separation of semiconducting single-walled carbon nanotubes using a flavin compound. *Chem Lett* 44(4):566–567. doi:[10.1246/cl.141193](https://doi.org/10.1246/cl.141193)
 50. Han J, Ji Q, Li H, Li G, Qiu S, Li H-B, Zhang Q, Jin H, Li Q, Zhang J (2016) A photodegradable hexaaza-pentacene molecule for selective dispersion of large-diameter semiconducting carbon nanotubes. *Chem Commun* 52(49):7683–7686. doi:[10.1039/C6CC01558A](https://doi.org/10.1039/C6CC01558A)
 51. Gui H, Streit JK, Fagan JA, Hight Walker AR, Zhou C, Zheng M (2015) Redox sorting of carbon nanotubes. *Nano Lett* 15(3):1642–1646. doi:[10.1021/nl504189p](https://doi.org/10.1021/nl504189p)
 52. Tanaka T, Jin H, Miyata Y, Fujii S, Suga H, Naitoh Y, Minari T, Miyadera T, Tsukagoshi K, Kataura H (2009) Simple and scalable gel-based separation of metallic and semiconducting carbon nanotubes. *Nano Lett* 9(4):1497–1500. doi:[10.1021/nl8034866](https://doi.org/10.1021/nl8034866)
 53. Moshammer K, Hennrich F, Kappes M (2009) Selective suspension in aqueous sodium dodecyl sulfate according to electronic structure type allows simple separation of metallic from semiconducting single-walled carbon nanotubes. *Nano Res* 2(8):599–606. doi:[10.1007/s12274-009-9057-0](https://doi.org/10.1007/s12274-009-9057-0)
 54. Liu H, Nishide D, Tanaka T, Kataura H (2011) Large-scale single-chirality separation of single-wall carbon nanotubes by simple gel chromatography. *Nat Commun* 2:309. http://www.nature.com/ncomms/journal/v2/n5/supplinfo/ncomms1313_S1.html
 55. Liu H, Tanaka T, Kataura H (2014) Optical isomer separation of single-chirality carbon nanotubes using gel column chromatography. *Nano Lett* 14(11):6237–6243. doi:[10.1021/nl5025613](https://doi.org/10.1021/nl5025613)
 56. Yomogida Y, Tanaka T, Zhang M, Yudasaka M, Wei X, Kataura H (2016) Industrial-scale separation of high-purity single-chirality single-wall carbon nanotubes for biological imaging. *Nat Commun* 7:12056. doi:[10.1038/ncomms12056](https://doi.org/10.1038/ncomms12056). <http://www.nature.com/articles/ncomms12056#supplementary-information>
 57. Wei X, Tanaka T, Yomogida Y, Sato N, Saito R, Kataura H (2016) Experimental determination of excitonic band structures of single-walled carbon nanotubes using circular dichroism spectra. *Nat Commun* 7:12899. doi:[10.1038/ncomms12899](https://doi.org/10.1038/ncomms12899)
 58. Khrapin CY, Fagan JA, Zheng M (2013) Spontaneous partition of carbon nanotubes in polymer-modified aqueous phases. *J Am Chem Soc* 135(18):6822–6825. doi:[10.1021/ja402762e](https://doi.org/10.1021/ja402762e)
 59. Albertsson PA (1971) Partition of cell particles and macromolecules, 2nd edn. Wiley-Interscience, New York
 60. Khrapin CY, Arnold-Medabalimi N, Zheng M (2011) Molecular-crowding-induced clustering of DNA-wrapped carbon nanotubes for facile length fractionation. *ACS Nano* 5:8258–8266. doi:[10.1021/nn2029549](https://doi.org/10.1021/nn2029549)
 61. Ao G, Khrapin CY, Zheng M (2014) DNA-controlled partition of carbon nanotubes in polymer aqueous two-phase systems. *J Am Chem Soc* 136(29):10383–10392. doi:[10.1021/ja504078b](https://doi.org/10.1021/ja504078b)
 62. Fagan JA, Khrapin CY, Silvera Batista CA, Simpson JR, Hároz EH, Hight Walker AR, Zheng M (2014) Isolation of specific small-diameter single-wall carbon nanotube species via aqueous two-phase extraction. *Adv Mater* 26(18):2800–2804. doi:[10.1002/adma.201304873](https://doi.org/10.1002/adma.201304873)
 63. Subbaiyan NK, Cambré S, Parra-Vasquez ANG, Hároz EH, Doorn SK, Duque JG (2014) Role of surfactants and salt in aqueous two-phase separation of carbon nanotubes toward simple chirality isolation. *ACS Nano* 8(2):1619–1628. doi:[10.1021/nn405934y](https://doi.org/10.1021/nn405934y)
 64. Zhang M, Khrapin CY, Fagan JA, McPhie P, Ito Y, Zheng M (2014) Single-step total fractionation of single-wall carbon nanotubes by countercurrent chromatography. *Anal Chem* 86(8):3980–3984. doi:[10.1021/ac5003189](https://doi.org/10.1021/ac5003189)
 65. Fagan JA, Hároz EH, Ihly R, Gui H, Blackburn JL, Simpson JR, Lam S, Hight Walker AR, Doorn SK, Zheng M (2015) Isolation of >1 nm diameter single-wall carbon nanotube species using aqueous two-phase extraction. *ACS Nano* 9(5):5377–5390. doi:[10.1021/acsnano.5b01123](https://doi.org/10.1021/acsnano.5b01123)

66. Graf A, Zakharko Y, Schießl SP, Backes C, Pfohl M, Flavel BS, Zaumseil J (2016) Large scale, selective dispersion of long single-walled carbon nanotubes with high photoluminescence quantum yield by shear force mixing. *Carbon* 105:593–599. doi:[10.1016/j.carbon.2016.05.002](https://doi.org/10.1016/j.carbon.2016.05.002)
67. Albertsson P-A (1971) Partition of cell particles and macromolecules, 2nd edn. Wiley-Interscience, New York
68. Zaslavsky BY (1994) Aqueous two-phase partitioning. Marcel Dekker, New York
69. Hofmann AF, Roda A (1984) Physicochemical properties of bile acids and their relationship to biological properties: an overview of the problem. *J Lipid Res* 25(13):1477–1489
70. Huang X, Mclean RS, Zheng M (2005) High-resolution length sorting and purification of DNA-wrapped carbon nanotubes by size-exclusion chromatography. *Anal Chem* 77(19):6225–6228
71. Khrapin C, Tu X, Howarter JA, Fagan JA, Zheng M (2012) Concentration measurement of length-fractionated colloidal single-wall carbon nanotubes. *Anal Chem Artic ASAP*. doi:[10.1021/ac302023n](https://doi.org/10.1021/ac302023n)
72. Gui H, Chen H, Khrapin CY, Liu B, Fagan JA, Zhou C, Zheng M (2016) A facile and low-cost length sorting of single-wall carbon nanotubes by precipitation and applications for thin-film transistors. *Nanoscale* 8(6):3467–3473. doi:[10.1039/C5NR07329D](https://doi.org/10.1039/C5NR07329D)
73. Strano MS, Huffman CB, Moore VC, O'Connell MJ, Haroz EH, Hubbard J, Miller M, Rialon K, Kittrell C, Ramesh S, Hauge RH, Smalley RE (2003) Reversible, Band-gap-selective protonation of single-walled carbon nanotubes in solution. *J Phys Chem B* 107(29):6979–6985. doi:[10.1021/jp027664a](https://doi.org/10.1021/jp027664a)
74. Hirana Y, Juhasz G, Miyauchi Y, Mouri S, Matsuda K, Nakashima N (2013) Empirical prediction of electronic potentials of single-walled carbon nanotubes with a specific chirality (n, m). *Sci Rep* 3:2959. doi:[10.1038/srep02959](https://doi.org/10.1038/srep02959). <http://www.nature.com/srep/2013/131016/srep02959/abs/srep02959.html#supplementary-information>
75. Schäfer S, Cogan NMB, Krauss TD (2014) Spectroscopic investigation of electrochemically charged individual (6, 5) single-walled carbon nanotubes. *Nano Lett* 14(6):3138–3144. doi:[10.1021/nl5003729](https://doi.org/10.1021/nl5003729)
76. Streit J, Zheng M (2016) Redox sorting of double-wall carbon nanotubes (**unpublished results**)
77. Antaris AL, Seo J-WT, Brock RE, Herriman JE, Born MJ, Green AA, Hersam MC (2012) Probing and tailoring pH-dependent interactions between block copolymers and single-walled carbon nanotubes for density gradient sorting. *J Phys Chem C* 116(37):20103–20108. doi:[10.1021/jp3063564](https://doi.org/10.1021/jp3063564)
78. Homenick CM, Rousina-Webb A, Cheng F, Jakubinek MB, Malenfant PRL, Simard B (2014) High-Yield, single-step separation of metallic and semiconducting SWCNTs using block copolymers at low temperatures. *J Phys Chem C* 118(29):16156–16164. doi:[10.1021/jp5030476](https://doi.org/10.1021/jp5030476)
79. Flavel BS, Kappes MM, Krupke R, Henrich F (2013) Separation of single-walled carbon nanotubes by 1-dodecanol-mediated size-exclusion chromatography. *ACS Nano* 7(4):3557–3564. doi:[10.1021/nn4004956](https://doi.org/10.1021/nn4004956)
80. Hirano A, Tanaka T, Urabe Y, Kataura H (2013) pH- and solute-dependent adsorption of single-wall carbon nanotubes onto hydrogels: mechanistic insights into the metal/semiconductor separation. *ACS Nano* 7(11):10285–10295. doi:[10.1021/nn4046776](https://doi.org/10.1021/nn4046776)
81. Rice NA, Adronov A (2013) Supramolecular interactions of high molecular weight poly(2,7-carbazole)s with single-walled carbon nanotubes. *Macromolecules* 46(10):3850–3860. doi:[10.1021/ma400081d](https://doi.org/10.1021/ma400081d)
82. Gelbart WM, Bruinsma RF, Pincus PA, Parsegian VA (2000) DNA-inspired electrostatics. *Phys Today* 53(9):38–44
83. Manning GS (1978) The molecular theory of polyelectrolyte solutions with applications to the electrostatic properties of polynucleotides. *Quart Rev Biophys* 11(02):179–246
84. Ao G, Zheng M (2016) Metallicity-based carbon nanotube sorting by DNA and SDBS combination (**unpublished results**)
85. Roxbury D, Mittal J, Jagota A (2012) Molecular-basis of single-walled carbon nanotube recognition by single-stranded DNA. *Nano Lett* 12(3):1464–1469. doi:[10.1021/nl204182b](https://doi.org/10.1021/nl204182b)
86. Meng S, Wang WL, Maragakis P, Kaxiras E (2007) Determination of DNA-base orientation on carbon nanotubes through directional optical absorbance. *Nano Lett* 7(8):2312–2316. doi:[10.1021/nl070953w](https://doi.org/10.1021/nl070953w)
87. Khrapin CY, Tu X, Heddleston JM, Silvera-Batista C, Hight Walker AR, Fagan J, Zheng M (2012) High-resolution length fractionation of surfactant-dispersed carbon nanotubes. *Anal Chem* 85(3):1382–1388. doi:[10.1021/ac303349q](https://doi.org/10.1021/ac303349q)

88. Schneider TD (2010) 70% efficiency of bistate molecular machines explained by information theory, high dimensional geometry and evolutionary convergence. *Nucleic Acids Res.* doi:[10.1093/nar/gkq389](https://doi.org/10.1093/nar/gkq389)
89. Pabo CO, Sauer RT (1984) Protein-DNA recognition. *Annu Rev Biochem* 53(1):293–321. doi:[10.1146/annurev.bi.53.070184.001453](https://doi.org/10.1146/annurev.bi.53.070184.001453)
90. Dervan PB (1986) Design of sequence-specific DNA-binding molecules. *Science* 232(4749):464
91. White S, Szewczyk JW, Turner JM, Baird EE, Dervan PB (1998) Recognition of the four Watson-Crick base pairs in the DNA minor groove by synthetic ligands. *Nature* 391(6666):468–471. http://www.nature.com/nature/journal/v391/n6666/supplinfo/391468a0_S1.html
92. Kang JS, Meier JL, Dervan PB (2014) Design of sequence-specific DNA binding molecules for DNA methyltransferase inhibition. *J Am Chem Soc* 136(9):3687–3694. doi:[10.1021/ja500211z](https://doi.org/10.1021/ja500211z)
93. Chou SG, Plentz F, Jiang J, Saito R, Nezich D, Ribeiro HB, Jorio A, Pimenta MA, Samsonidze GG, Santos AP, Zheng M, Onoa GB, Semke ED, Dresselhaus G, Dresselhaus MS (2005) Phonon-assisted excitonic recombination channels observed in DNA-wrapped carbon nanotubes using photoluminescence spectroscopy. *Phys Rev Lett* 94(12):127402
94. Chou S, DeCamp MF, Jiang J, Samsonidze GG, Barros EB, Plentz F, Jorio A, Zheng M, Onoa GB, Semke ED, Tokmakoff A, Saito R, Dresselhaus G, Dresselhaus MS (2005) Phonon-assisted exciton relaxation dynamics for a (6, 5)-enriched DNA-wrapped single-walled carbon nanotube sample. *Phys Rev B* 72:195415
95. Carlson LJ, Maccagnano SE, Zheng M, Silcox J, Krauss TD (2007) Fluorescence efficiency of individual carbon nanotubes. *Nano Lett* 7:3698–3703
96. Torrens ON, Kikkawa JM, Zheng M (2008) Phonon sideband optical spectroscopy of carbon nanotubes: evidence for K'-momentum dark excitons. *Phys Rev Lett* 101:157401
97. Vora PM, Tu X, Mele EJ, Zheng M, Kikkawa JM (2010) Chirality dependence of the K-momentum dark excitons in carbon nanotubes. *Phys Rev B* 81:155123
98. Telg H, Duque JG, Staiger M, Tu X, Henrich F, Kappes MM, Zheng M, Maultzsch J, Thomsen C, Doorn SK (2011) Chiral index dependence of the G+ and G- Raman modes in semiconducting carbon nanotubes. *ACS Nano* 6(1):904–911. doi:[10.1021/nn2044356](https://doi.org/10.1021/nn2044356)
99. Duque JG, Telg H, Chen H, Swan AK, Shreve AP, Tu X, Zheng M, Doorn SK (2012) Quantum interference between the third and fourth exciton states in semiconducting carbon nanotubes using resonance Raman spectroscopy. *Phys Rev Lett* 108(11):117404
100. Duque JG, Chen H, Swan AK, Shreve AP, Kilina S, Tretiak S, Tu X, Zheng M, Doorn SK (2011) Violation of the Condon approximation in semiconducting carbon nanotubes. *ACS Nano* 5(6):5233–5241. doi:[10.1021/nn201430z](https://doi.org/10.1021/nn201430z)
101. Piao Y, Simpson JR, Streit JK, Ao G, Zheng M, Fagan JA, Hight Walker AR (2016) Intensity ratio of resonant Raman modes for (n, m) enriched semiconducting carbon nanotubes. *ACS Nano* 10(5):5252–5259. doi:[10.1021/acsnano.6b01031](https://doi.org/10.1021/acsnano.6b01031)
102. Zheng M, Rostovtsev VV (2006) Photoinduced charge transfer mediated by DNA-wrapped carbon nanotubes. *J Am Chem Soc* 128:7702–7703
103. Piao Y, Meany B, Powell LR, Valley N, Kwon H, Schatz GC, Wang Y (2013) Brightening of carbon nanotube photoluminescence through the incorporation of sp³ defects. *Nat Chem* 5(10):840–845. doi:[10.1038/nchem.1711](https://doi.org/10.1038/nchem.1711). <http://www.nature.com/nchem/journal/v5/n10/abs/nchem.1711.html#supplementary-information>
104. Hartmann NF, Velizhanin KA, Haroz EH, Kim M, Ma X, Wang Y, Htoon H, Doorn SK (2016) Photoluminescence dynamics of aryl sp³ defect states in single-walled carbon nanotubes. *ACS Nano*. doi:[10.1021/acsnano.6b02986](https://doi.org/10.1021/acsnano.6b02986)
105. Ma X, Hartmann NF, BaldwinJon KS, Doorn SK, Htoon H (2015) Room-temperature single-photon generation from solitary dopants of carbon nanotubes. *Nat Nano* 10(8):671–675. doi:[10.1038/nnano.2015.136](https://doi.org/10.1038/nnano.2015.136). <http://www.nature.com/nnano/journal/v10/n8/abs/nnano.2015.136.html#supplementary-information>
106. Zhang L, Tu X, Welsher K, Wang X, Zheng M, Dai H (2009) Optical characterizations and electronic devices of nearly pure (10, 5) single-walled carbon nanotubes. *J Am Chem Soc* 131:2454–2455
107. Wang C, Zhang J, Ryu K, Badmaev A, De Arco LG, Zhou C (2009) Wafer-scale fabrication of separated carbon nanotube thin-film transistors for display applications. *Nano Lett* 9(12):4285–4291. doi:[10.1021/nl902522f](https://doi.org/10.1021/nl902522f)

108. Tulevski GS, Franklin AD, Afzali A (2013) High purity isolation and quantification of semiconducting carbon nanotubes via column chromatography. *ACS Nano* 7(4):2971–2976. doi:[10.1021/nn400053k](https://doi.org/10.1021/nn400053k)
109. Liu B, Liu J, Tu X, Zhang J, Zheng M, Zhou C (2013) Chirality-dependent vapor-phase epitaxial growth and termination of single-wall carbon nanotubes. *Nano Lett* 13(9):4416–4421. doi:[10.1021/nl402259k](https://doi.org/10.1021/nl402259k)
110. Panchakarla LS, Radovsky G, Houben L, Popovitz-Biro R, Dunin-Borkowski RE, Tenne R (2014) Nanotubes from misfit layered compounds: a new family of materials with low dimensionality. *J Phys Chem Lett* 5(21):3724–3736. doi:[10.1021/jz5016845](https://doi.org/10.1021/jz5016845)
111. Lorenz T, Joswig J-O, Seifert G (2014) Two-dimensional and tubular structures of misfit compounds: structural and electronic properties. *Beilstein J Nanotechnol* 5:2171–2178. doi:[10.3762/bjnano.5.226](https://doi.org/10.3762/bjnano.5.226)
112. Seifert G, Terrones H, Terrones M, Jungnickel G, Frauenheim T (2000) Structure and electronic properties of MoS₂ nanotubes. *Phys Rev Lett* 85(1):146–149
113. Tenne R, Redlich M (2010) Recent progress in the research of inorganic fullerene-like nanoparticles and inorganic nanotubes. *Chem Soc Rev* 39(5):1423–1434. doi:[10.1039/B901466G](https://doi.org/10.1039/B901466G)
114. Heckl WM, Smith DP, Binnig G, Klagges H, Hänsch TW, Maddocks J (1991) Two-dimensional ordering of the DNA base guanine observed by scanning tunneling microscopy. *Proc Natl Acad Sci* 88(18):8003–8005
115. Chandler D (2005) Interfaces and the driving force of hydrophobic assembly. *Nature* 437(7059):640–647
116. Ashbaugh HS, Pratt LR (2006) Colloquium: scaled particle theory and the length scales of hydrophobicity. *Rev Mod Phys* 78(1):159
117. Ignatova T, Balaeff A, Blades M, Zheng M, Stoeckl P, Rotkin SV (2016) Two-color spectroscopy of UV excited ssDNA complex with a single-wall nanotube photoluminescence probe: fast relaxation by nucleobase autoionization mechanism. *Nano Res* 9(2):571–583. doi:[10.1007/s12274-015-0938-0](https://doi.org/10.1007/s12274-015-0938-0)
118. Ellington AD, Szostak JW (1990) In vitro selection of RNA molecules that bind specific ligands. *Nature* 346(6287):818–822
119. Tuerk C, Gold L (1990) Systematic evolution of ligands by exponential enrichment: RNA ligands to bacteriophage T4 DNA polymerase. *Science* 249(4968):505–510. doi:[10.1126/science.2200121](https://doi.org/10.1126/science.2200121)
120. Diniz GS, Latgé A, Ulloa SE (2012) Helicoidal fields and spin polarized currents in carbon nanotube–DNA Hybrids. *Phys Rev Lett* 108(12):126601
121. Alam KM, Pramanik S (2015) Spin filtering through single-wall carbon nanotubes functionalized with single-stranded DNA. *Adv Funct Mater* 25(21):3210–3218. doi:[10.1002/adfm.201500494](https://doi.org/10.1002/adfm.201500494)
122. Hamo A, Benyamin A, Shapir I, Khivrich I, Waissman J, Kaasbjerg K, Oreg Y, von Oppen F, Ilani S (2016) Electron attraction mediated by Coulomb repulsion. *Nature* 535(7612):395–400. doi:[10.1038/nature18639](https://doi.org/10.1038/nature18639). <http://www.nature.com/nature/journal/v535/n7612/abs/nature18639.html#supplementary-information>
123. Rotkin SV (2010) Electronic properties of nonideal nanotube materials: helical symmetry breaking in DNA hybrids. *Annu Rev Phys Chem* 61(1):241–261. doi:[10.1146/annurev.physchem.012809.103304](https://doi.org/10.1146/annurev.physchem.012809.103304)
124. Michalski PJ, Mele EJ (2008) Carbon nanotubes in helically modulated potentials. *Phys Rev B* 77(8):085429



REVIEW

Electronic and Optical Properties of Single Wall Carbon Nanotubes

R. Saito¹ · A. R. T. Nugraha¹ · E. H. Hasdeo¹ ·
N. T. Hung¹ · W. Izumida¹

Received: 21 September 2016/Accepted: 10 December 2016/Published online: 28 December 2016
© Springer International Publishing Switzerland 2016

Abstract In this article, we overview our recent theoretical works on electronic and optical properties of carbon nanotubes by going from the background to the perspectives. Electronic Raman spectra of metallic carbon nanotubes give a new picture of Raman processes. Thermoelectricity of semiconducting nanotubes gives a general concept of the confinement effect on the thermoelectric power factor. Selective excitation of only a single phonon mode is proposed by the pulsed train technique of coherent phonon spectroscopy. Occurrence of both two and four fold degeneracy in the carbon nanotube quantum dot is explained by difference group velocities and the intra/inter valley scattering near the hexagonal corner of the Brillouin zone.

Keywords Carbon nanotubes · Quantum dots · Coherent phonon · Electric Raman spectroscopy · Thermoelectric power · Intervalley scattering

1 Introduction

A single wall carbon nanotube (SWNT) is a graphene sheet rolled up into a cylinder. An SWNT is either metallic or semiconducting [1–3] depending on the geometrical structure that is specified by two integers, (n, m) , which is known as chirality. Since SWNTs were found in 1993, the experimental techniques of synthesis and purification have been improving for 25 years. Recently, SWNTs samples in mass production can be commercially obtained for general purposes, while in the

Chapter 6 was originally published as Saito, R., Nugraha, A. R. T., Hasdeo, E. H., Hung, N. T. & Izumida, W. Top Curr Chem (Z) 375: 7. DOI 10.1007/s41061-016-0095-2.

✉ R. Saito
rsaito@flex.phys.tohoku.ac.jp

¹ Department of Physics, Tohoku University, Sendai 980-8578, Japan

laboratory, the purified, single chirality samples are also available, which makes it possible to observe the physical properties of SWNTs as a function of (n, m). Then, selecting the optimum (n, m) for specific design of properties is now required in which we need supporting theoretical calculations that predict a perspective on the future of SWNT researches.

In this article, we present four subjects about physical properties of SWNTs as a function of (n, m): (1) electronic Raman spectra of metallic SWNTs (m-SWNTs), (2) thermoelectric power of semiconducting SWNTs (s-SWNTs), (3) single phonon generation of SWNT by fast optics, and (4) transport of quantum dots made of semiconducting SWNTs. Here, we briefly mention each problem of the four subjects discussed in this article.

It is known in metallic SWNTs that not only phonon Raman spectra but also electronic Raman spectra (ERS) appear at the energy position of the van Hove singularity E_{ii} [4]. The origin of ERS are the excitation of an electron–hole pair near the Fermi energy by an exciton through the Coulomb interaction [5]. The interference effect of phonon Raman and ERS can be explained by changing the Fermi energy, which is known as gated modulated Raman spectroscopy [6].

In thermoelectricity, many attempts for finding the optimum low-dimensional materials to get a high efficiency for thermoelectricity have been investigated, especially after the Hicks and Dresselhaus paper published in 1993 [7, 8]. They showed that the confinement effect of one- or two dimensional (1-D, 2-D) semiconductors is an important factor for obtaining high figure-of-merit (ZT) values. Since 1993, many new nanomaterials show the high ZT values [9]. However, it is also known that some materials with small confinement length do not show a large thermoelectric power factor [10]. We show that the thermoelectric power factor is enhanced only when the confinement length is smaller than the so-called thermal de Broglie length [11].

In nanomechanics, the selective excitation of a single vibrational mode in the THz region is useful for possible applications [12]. In coherent spectroscopy, it is known that the pulse train of laser selectively excites a RBM mode of the specified (n, m) SWNT if the pulse repetition rate is selected for the frequency of the RBM mode [13]. Using the same technique, we propose that other phonon modes such as the G band phonon mode can be excited while the other phonon modes are suppressed.

In the quantum dot of finite length SWNT, we can observe discrete energy levels with a two or four fold degeneracy as a function of the gate voltage [14]. The appearance of the two kinds of degeneracies is partially related to the anisotropic group velocity in the k space [15]. Another important fact is that the edge states affect the energy levels near the Fermi energy. However, since the edge states of a SWNT depend on the shape at the edge of a SWNT, it is not easy to discuss in general the number of edge states and their electronic structure as a function of the edge shape of SWNTs. In this article, we discuss that the topological nature of specific properties is essential to explain the number of the edge states [16].

In the following sections, we discuss each subject and a perspective for the SWNT research at the end of each section.

2 Electronic Raman Spectroscopy of Metallic Nanotubes

2.1 Breit–Wigner–Fano Lineshape and Continuous Spectra

One way to distinguish semiconducting carbon nanotubes (s-SWNTs) from metallic ones (m-SWNTs) is by observing the symmetric or asymmetric shape of Raman spectra at $\sim 1600\text{ cm}^{-1}$, which is known as the G band [17–21]. The G band originates from longitudinal optic (LO) and in-plane tangential optic (iTO) modes of phonons. In Fig. 1 we show the G band for a mixture of (a) semiconducting and (b) metallic SWNT bundles with nanotube diameters $d_t = 1.49 \pm 0.20\text{ nm}$ taken from the work by Brown et al. [17]. With a specified d_t , laser excitation energy $E_L = 2.19\text{ eV}$ in Fig. 1a is resonant to optical transition energy of s-SWNTs (S_{33}) while for $E_L = 1.58\text{ eV}$ in Fig. 1b, it is resonant to optical transition energy of m-SWNTs (M_{11}^-). Optical transition energies in s-SWNTs (S_{ii}) and m-SWNTs (M_{ii}) appear due to the Van Hove singularities (VHS) of joint density of states originating from maxima (minima) of the i th parabolic valence (conduction) band [3]. Indices M_{ii}^- and M_{ii}^+ come from the split of the M_{ii} due to the trigonal warping effect [22].

When we decompose the Raman spectra into subpeaks (dashed lines), the G band of s-SWNT bundles can be fitted to few Lorentzians (Fig. 1a) while the G band of m-SWNTs contains a broad spectrum with a long tail below the phonon energy $\sim 1545\text{ cm}^{-1}$ (Fig. 1b). It is suggested that a continuous spectrum appears due to the presence of linear energy band in m-SWNTs. The interference between the continuous spectrum and the discrete phonon spectra gives the asymmetric Breit–Wigner–Fano (BWF) lineshape. The BWF lineshape is expressed by

$$I(\omega) = I_0 \frac{[1 + (\omega - \omega_0)/(q_{\text{BWF}}\Gamma)]^2}{1 + [(\omega - \omega_0)/\Gamma]^2}, \quad (1)$$

where $1/q_{\text{BWF}}$, Γ , and ω_0 are, respectively, asymmetric factor, spectral width, and phonon frequency. According to Fano [23], $1/q_{\text{BWF}}$ is proportional to a coupling constant between the continuum spectrum and the discrete spectrum. In fact, this is when $1/q_{\text{BWF}} = 0$ in Eq. (1), $I(\omega)$ becomes a Lorentzian. Even though the BWF

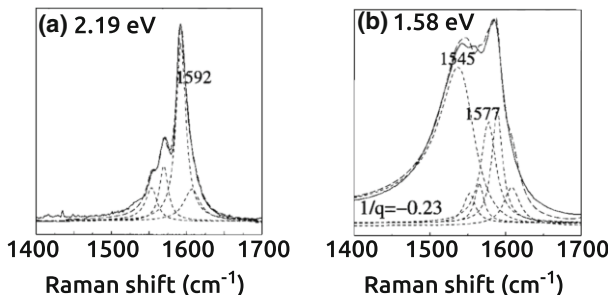


Fig. 1 The G band for a mixture of semiconducting and metallic SWNT bundles with $d_t = 1.49 \pm 0.20\text{ nm}$ excited by **a** $E_L = 2.19\text{ eV}$ resonant to S_{33} of semiconducting nanotubes and **b** $E_L = 1.58\text{ eV}$ resonant to M_{11}^- of metallic nanotubes [17]

lineshape appears in many metallic nanocarbon materials such as m-SWNTs [17, 20, 24], graphite intercalation compounds [25, 26], and graphene [27], origin of the continuous spectrum in m-SWNTs was not clear for 30 years. It was discussed that either single particle electron excitation [28, 29] or collective excitation (plasmon) [17, 30–32] were relevant to the continuous spectrum.

A breakthrough for understanding the origin of the continuous spectra has emerged by the observation of the electronic Raman spectra (ERS) in m-SWNTs by Farhat et al. [4]. In Fig. 2a, we can see the ERS with well-defined peak and broad spectral width ($\sim 500 \text{ cm}^{-1}$) between the radial breathing mode (RBM) and the G band for a (23,14) m-SWNT [4]. The ERS peak appears when scattered photon energy E_s matches to $M_{22}^- = 2.08 \text{ eV}$. With $E_L = 2.14 \text{ eV}$, the Raman shift of ERS at $M_{22}^- = 2.08 \text{ eV}$ corresponds to $E_L - M_{22}^- = 500 \text{ cm}^{-1}$ or 60 meV. Because of the broad spectral width of ERS, the G band and RBM lineshapes become asymmetric in m-SWNTs by interference between the ERS and phonon peaks. In Fig. 2b, on the other hand, no ERS appears in (25,8) s-SWNT indicating that the ERS originates from the linear energy band, which is absent in s-SWNTs. Farhat et al. can observe the ERS in m-SWNTs since the spectral width of ERS is smaller than that of the background spectra [4].

In order to study the origin of ERS, Farhat et al. further measured the ERS by changing the Fermi energy E_F [4]. In Fig. 2c, relative ERS intensity to the G band intensity is plotted as a function of E_F , which shows a maximum at $E_F = 0$ (Dirac

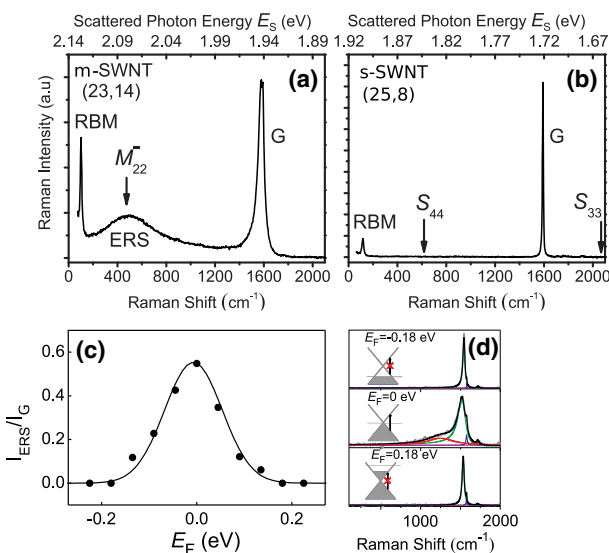


Fig. 2 **a** Raman spectra of (23,14) m-SWNTs excited by $E_L = 2.14 \text{ eV}$ showing the RBM, ERS and G bands. The ERS feature appears at $E_s = M_{22}^-$ indicated by an arrow. **b** Raman spectra of (25,8) s-SWNTs excited by $E_L = 1.92 \text{ eV}$ which showing only the RBM and G bands. No ERS is observed at S_{44} or S_{33} in the s-SWNT. **c** Relative ERS intensity to the G band intensity as a function of the Fermi energy E_F . **d** Raman spectra for $E_F = -0.18, 0, 0.18 \text{ eV}$ [4]

point). When $E_F < 0$, some parts of interband electron–hole excitation in the linear energy bands are suppressed due to no occupied, initial states above E_F (upper panel of Fig. 2d). When $E_F > 0$, interband electron–hole excitation are also suppressed because electrons in the final states already occupy the conduction band (lower panel of Fig. 2d). From this experiment, we can conclude that the ERS originates from electron–hole excitation near the Dirac point ($E_F = 0$) in the linear energy bands. We can rule out the contribution of plasmon in the ERS in m-SWNTs because the spectral function of plasmon would be proportional to charge density or $|E_F|$, while the experimental results show the opposite behavior. It is noted that the electro-magnetic wave (transverse wave) cannot excite a plasmon (longitudinal wave) except for the surface plasmon.

The electron–hole pair can be excited in the linear band by the electron–phonon interaction which gives rise to phonon softening or the Kohn anomaly effect in m-SWNTs [33]. In order to check that the ERS is free from the Kohn anomaly effect, Farhat et al. measured the E_L dependence of the Raman spectra [4]. Figure 3 shows the calculated and experimental results of E_L dependence of Raman spectra as a function of scattered photon energy E_s . Phonon spectra (RBM and G bands) have fixed Raman shifts so that their peak positions in E_s appear at $E_L - \hbar\omega_0$. However, the ERS peak always appears at $E_s = M_{22}^-$, which is independent of E_L . These results indicate that the ERS originates from electron–electron interaction between the photo-excited carrier at the M_{ii} state with the electron at the linear band. Hereafter, we will present the detailed analysis of the ERS spectra from the theoretical calculations.

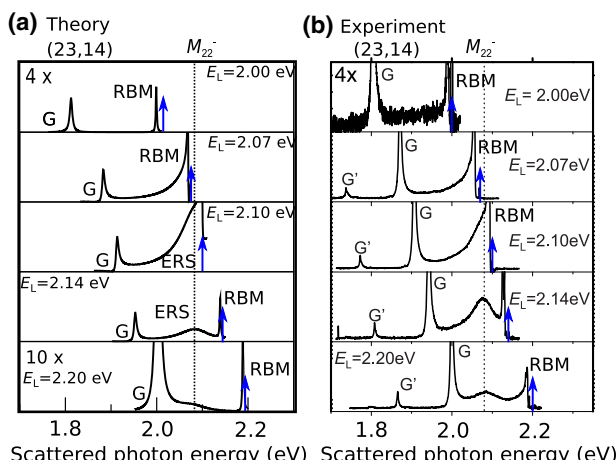


Fig. 3 **a** Calculated result [5] for (23,14) m-SWNT and **b** experimental results (adapted from Ref. [4]) of Raman intensity versus $\hbar\omega_s$ for a (23,14) m-SWNT where we have the calculated $M_{22}^- = 2.084$ eV and the experimental $M_{22}^- = 2.08$ eV. The laser excitation energies E_L are taken as 2.00, 2.07, 2.10, 2.14, and 2.20 eV [5]

2.2 Theory of Electronic Raman Spectra

In Fig. 4, optical processes of the ERS which consist of (1) an exciton generation via an exciton-photon interaction, (2) excitation of the linear energy band electron–hole pair(s) by the Coulomb interaction with the exciton, and (3) finally, the exciton goes back to the ground state by emitting a photon. The excitation of electron–hole pair(s) in (2) may occur in either a first-order or second-order process. For the first-order process, the exciton relaxes vertically ($\mathbf{q} = 0$) from a virtual state to the M_{ii} state after photo-absorption at a wave vector \mathbf{k} , while the electron–hole pair is created in the linear band at wave vector \mathbf{k}' by the Coulomb interaction with $\mathbf{q} = 0$ (see Fig. 4a). In the second-order process, two electron–hole pairs in the linear band are excited with nonzero momentum transfer \mathbf{q} and $-\mathbf{q}$. The existence of the two inequivalent K and K' valleys in the m-SWNTs Brillouin zone leads to either *intravalley* (AV) interaction or the *inter-valley* (EV) Coulomb interaction depends on the cases that the relaxation of the exciton and excitation of electron–hole pair in Fig. 4 occur in the same valley or different valley, respectively. After the electronic scattering processes, the scattered exciton then recombines to the ground state at \mathbf{k} by emitting a photon with an energy $E_s = M_{ii}$. This is the reason why the ERS peak position always appears at M_{ii} even though we change the laser energy E_L . It is important to note that the first-order ERS has negligibly small intensity compared with the second-order ERS because the direct Coulomb interaction vanishes at $\mathbf{q} = 0$ due to the symmetry of the wavefunction of graphene [5]. Thus, the ERS intensity is originated by the second-order process.

Total Raman intensity is calculated by taking the square of the sum of the amplitudes of inelastic scattering for RBM (A_{RBM}), G band ($A_G = A_{\text{iTO}} + A_{\text{LO}}$), and ERS (A_{ERS}) as follows,

$$I = \left| \sum_i (A_{\text{RBM}} + A_G + A_{\text{ERS}}) \right|^2. \quad (2)$$

In Fig. 5a, the calculated results of the Raman spectrum for (23,14) m-SWNT is shown by a solid line, in which the ERS overlaps with the RBM and G phonon modes, and, thus, the quantum interference gives rise to the asymmetric line shape, peak shifting, and the intensity enhancement of the G band relative to the $|A_{\text{RBM}}|^2$,

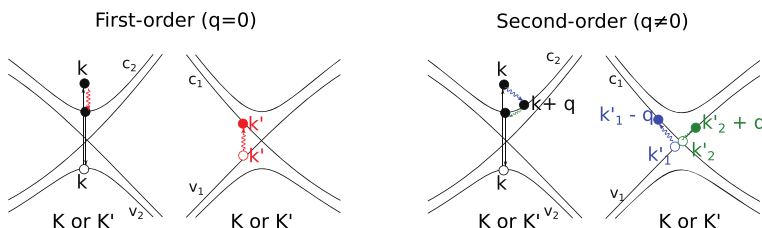


Fig. 4 **a** First-order and **b** second-order electronic Raman processes. In both processes, the interaction between electrons in the parabolic band and the linear band can take place in the same valley (AV) or in a different valley (EV)

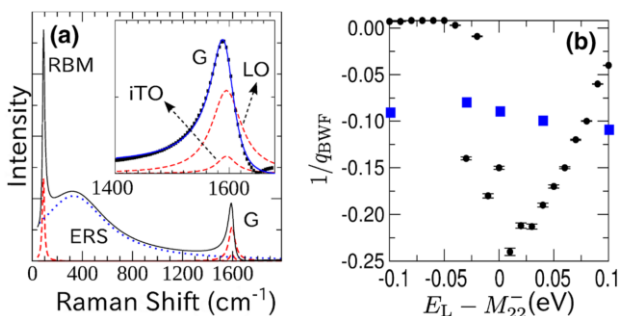


Fig. 5 **a** Calculated Raman spectra for a (23,14) SWNT with $E_L = 2.14$ eV. The total intensity shown is represented by the *solid line*. The *dashed lines* show contributions from the RBM and G modes, while the *dotted line* is the contribution from the ERS. Each *line shape* for the RBM, the G modes, and the ERS are Lorentzian. *Inset* shows the G band spectra after subtracted by the ERS spectrum. *Dots* are calculated results and the *solid line* shows the BWF fitting (Eq. (1)). **b** Asymmetric factor ($1/q_{\text{BWF}}$) as a function of resonance condition ($E_L - M_{22}^-$). The *circles* and *squares* denote calculated results and experimental results, respectively [4]

$|A_{\text{iTO}}|^2$ or $|A_{\text{LO}}|^2$ (dashed line). As shown in the inset of Fig. 5a, the asymmetric line shape of the G band is obtained after subtracting the ERS contribution which reproduce the experimental spectra (dots). In Fig. 5b, the asymmetric factor $1/q_{\text{BWF}}$ is plotted as a function of $E_L - M_{22}^-$ in which the calculated $1/q_{\text{BWF}}$ gives a “V” shape as a function of $E_L - M_{22}^-$. Though the calculated $1/q_{\text{BWF}}$ values are of the same order with the experimental result, the E_L dependence of $1/q_{\text{BWF}}$ does not explain the experimental results, which should be clarified in the future.

In order to understand the origin of asymmetric lineshape, we consider phase difference of amplitudes between the ERS and G (or RBM) phonon spectrum, which is given by

$$I = |A_{\text{ERS}}|^2 + |A_v|^2 + 2|A_{\text{ERS}}||A_v|\cos(\varphi_{\text{ERS}} - \varphi_v), \quad (v = \text{G, RBM}), \quad (3)$$

where φ_v is a phase for the v -th phonon mode ($v = \text{ERS}$, G band, and RBM). The phase difference between the ERS and phonon spectra in Eq. (3) gives the quantum interference effect.

In Fig. 6a, we show φ_v of the RBM, ERS, and G (LO and iTO) modes as a function of Raman shift for $E_L = M_{22}^- = 2.1$ eV. Phase shift at the phonon energies (RBM or G) or ERS energy from $-\pi/2 \rightarrow \pi/2$ appears at each peak of the Raman spectra. Since the phase of ERS keeps constant at the resonance frequency that phonon spectra exhibit phase shifts, the interference term in Eq. (3) changes their sign as shown in Fig. 6b, c which is the origin of asymmetric lineshape. In fact, the sign change from negative (positive) to positive (negative) correspond to positive (negative) $1/q_{\text{BWF}}$ because of the phase shift position of ERS is at the right (left) of the RBM (G mode). It is important to note that the $|1/q|$ value for the RBM is larger than that of the G band when $E_L = M_{22}^-$. The reason why we get the large value of $|1/q|$ for RBM is a strong resonant condition at $E_L = M_{22}^-$ which makes the ERS peak closer to the RBM peak than to the G band peak. However, since RBM spectra are too sharp ($\sim 5\text{cm}^{-1}$), it might be difficult for experimentalists to observe the

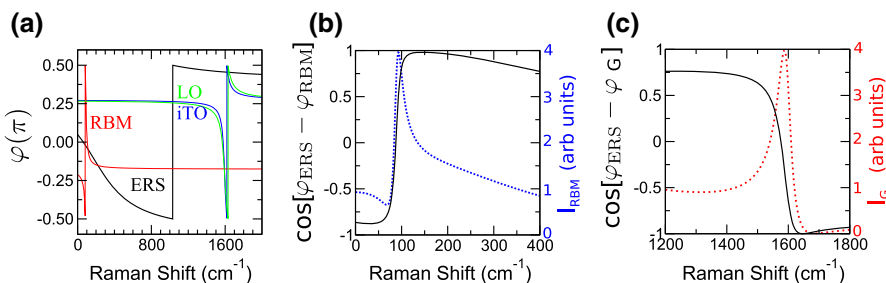


Fig. 6 **a** Raman phase of the RBM, ERS, and G (LO and iTO) mode at $E_L = M_{22}^- = 2.1$ eV for a (23,14) tube. **b, c** Cosine of phase difference $\varphi_{\text{ERS}} - \varphi_{\text{RBM}}$ and $\varphi_{\text{ERS}} - \varphi_G$, respectively. Dotted line in **b** and **c** shows the RBM and G mode total intensity form Eq. (2), respectively. Asymmetric factor $1/q_{\text{BWF}} = 0.65$ is for RBM and $1/q_{\text{BWF}} = -0.27$ for G mode

asymmetry of RBM. Theoretically, the BWF lineshape appears in any phonon modes as long as the ERS overlaps the phonon spectra, which should be observed by experiments in the future.

Recently, using single chirality SWNT samples, multiple ERS features originating from M_{ii}^- and M_{ii}^+ give either positive or negative values of $1/q_{\text{BWF}}$ depending on the position of ERS with respect to the phonon spectra [34]. Using many ERS spectra, they can do chirality assignment of m-SWNTs from M_{ii} within the accuracy of ~ 1 meV. The chirality assignment of m-SWNT was not possible by optical measurement due to the quenching of photoluminescence intensity in m-SWNTs [35]. This result is important for further characterization of m-SWNTs.

3 Thermoelectricity of SWNTs

3.1 Rediscovering Potential Applications of SWNTs in Thermoelectricity

In recent years, there has been significant interest in research on thermoelectric phenomena due to the increase in the demand for utilizing ubiquitous energy sources. It is important to find a good thermoelectric material with a high thermoelectric energy conversion efficiency, characterized by the so-called thermoelectric figure of merit, $ZT = S^2\sigma\kappa^{-1}T$, where S is the Seebeck coefficient (or thermopower), σ is the electrical conductivity, κ is the thermal conductivity, and T is the absolute temperature of the material. Other than ZT , it is also common to evaluate the power factor $\text{PF} = S^2\sigma$, which is the numerator of the ZT formula, to know the output electric power or thermoelectric performance of a material when we do not need to consider the efficiency.

As a one-dimensional material, SWNTs have been considered to be promising materials for thermoelectricity due to their electronic properties, in which the energy gaps depend on their geometrical structure [36–38]. However, it was difficult to obtain SWNTs with a specific (n, m) structure to design the thermoelectric devices

having the optimum performance. Most thermoelectric measurements were performed on bundled SWNT samples whose geometrical and electronic structures are mixed with one another [36–39], and, thus, most of the potential thermoelectric properties might be lost because of tube–tube interactions [36]. For the purpose of developing future thermoelectric devices based on SWNTs, we evaluate the thermopower of semiconducting SWNTs (s-SWNTs) as a function of (n, m). From our calculation, we will suggest the optimized (n, m) values to obtain a larger PF and ZT of SWNTs. We also explain the reason why s-SWNTs should be good candidates for thermoelectric materials based on our general theory related to the confinement effect in low-dimensional materials [11].

3.2 Methods for Calculating Thermoelectric Properties

When we adopt s-SWNTs in thermoelectric devices, we need two types of doping for s-SWNTs with the same (n, m), i.e., n-type and p-type s-SWNTs for making an electrical circuit as shown in Fig. 7. By having a temperature gradient ∇T from an edge of each type of s-SWNTs to another edge, charge carriers (electrons or holes) will flow with velocity v from the hot edge with temperature T_{hot} to the cold edge with T_{cold} . The Fermi distribution f as a function of electronic energy E and chemical potential μ is modified in the presence of ∇T , that satisfies the Boltzmann equation, from which the electric voltage ∇V is obtained. We adopt the relaxation time approximation (RTA) for solving the Boltzmann equation, and further we assume the relaxation time is a constant [40]. Within this assumption, Seebeck coefficient S is expressed [40] by

$$S = \frac{1}{qT} \frac{\int q\mathbf{v}\tau_c \frac{\partial f}{\partial E}(E - \mu)g(E)dE}{\int q\mathbf{v}\tau_c \frac{\partial f}{\partial E}g(E)dE}. \quad (4)$$

where $q = \pm e$ is the charge of the carrier, $T = (T_{\text{hot}} + T_{\text{cold}})/2$ is the averaged absolute temperature, \mathbf{v} is the carrier velocity, τ_c is the carrier relaxation time, and $g(E)$ is the density of state (DOS).

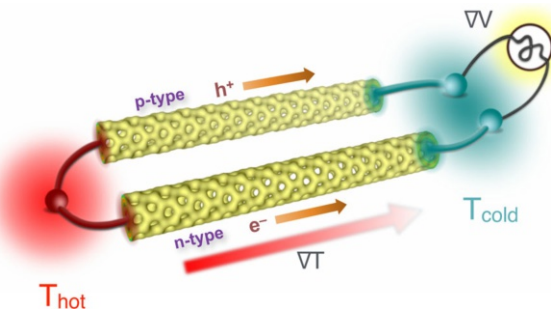


Fig. 7 Schematic model of a thermoelectric device using two s-SWNTs, one with p-type and the other with n-type doping. The temperature gradient between the two edges of each nanotube generates electricity

We employ both numerical and analytical methods to calculate S from Eq. (4). In the numerical calculation, we adopt the BoltzTraP code [41], which is a widely-used package to calculate thermoelectric properties, such as the S and electrical conductivity, σ . An input data for the BoltzTraP code is the electronic energy dispersion $E(\mathbf{k})$ for all energy bands. We calculate the energy dispersion $E(\mathbf{k})$ of SWNTs within the extended tight-binding (ETB) model [42]. The ETB model takes into account long-range interactions up to the 20th nearest neighbors, SWNT curvature effects, and geometrical structure optimization, which are sufficient to reproduce the experimentally observed energy band gaps of the SWNTs [42, 43]. In the BoltzTraP calculation, we use a $20\text{nm} \times 20\text{nm} \times |\mathbf{T}|$ supercell, where $|\mathbf{T}|$ (in nm) is the length of the translational vector of a SWNT [1]. A larger supercell length (20nm) in the x - and y -directions is chosen so as to guarantee the one-dimensionality of the SWNT. Although S in the BoltzTraP code is expressed in terms of a tensor [41], we only consider the zz component of S , S_{zz} , which is the thermopower along the tube axis direction z . Hereafter, we denote S for S_{zz} .

3.3 Chemical Potential Dependence of Thermopower

In Fig. 8, we plot the thermopower as a function of chemical potential for three different s-SWNT chiralities: (11, 0), (12, 4), and (15, 5), at $T = 300$ K [44]. The solid lines in Fig. 8 represent the numerical results, while dashed lines are analytical ones as shown below. For each chirality, the optimum value of the thermopower, indicated by a maximum (minimum) along the negative (positive) axis of the chemical potential, arises due to the p-type (n-type) s-SWNTs, which is consistent with a recent experimental observation [38]. The dependence of the thermopower on the chemical potential implies that it is possible to tune the thermoelectric properties of the s-SWNTs by applying gate voltages on the p-type and n-type s-SWNTs.

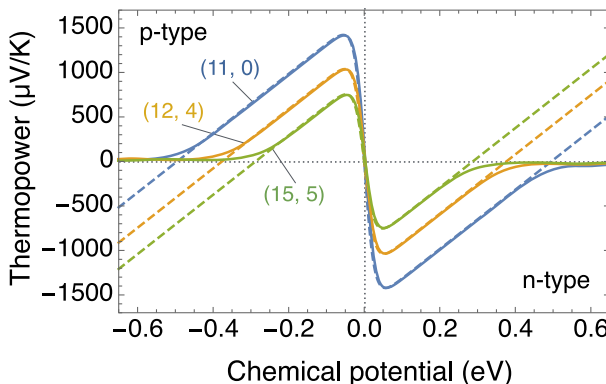


Fig. 8 Thermopower as a function of chemical potential for (11, 0), (12, 4), and (15, 5) at $T = 300$ K. Solid lines are obtained from the numerical calculation based on Eq. (4) while dashed lines are obtained from the analytical formula given in Eq. (5) [44]

In order to understand the numerical results of thermopower, we have derived an analytical formula for the thermopower from Eq. (4) for the valence and the conduction bands closest to the Fermi level, known as the two-band model [40, 45]. It is noted that the thermopower is a linear function with the chemical potential if we only consider only one band. Thus, the contribution of two bands (valence and conduction bands) is essential to get the optimum of the thermopower for the s-SWNTs. The thermopower for s-SWNTs, S_{CNT} , based on the two-band model and constant RTA, are given as a function of μ by [44]:

$$S_{\text{CNT}}(\mu) = \frac{k_{\text{B}}}{e} \left(\frac{\mu}{k_{\text{B}}T} - \frac{E_{\text{g}}}{2k_{\text{B}}T} - \frac{3}{2} + \frac{E_{\text{g}}/k_{\text{B}}T + 3}{e^{2\mu/k_{\text{B}}T} + 1} \right). \quad (5)$$

where E_{g} is the energy gap. In Fig. 8, we show analytical results of Eq. (5) in the dashed lines using the values of E_{g} from the ETB calculation. The analytical formula [Eq. (5)] reproduces the numerical results near $\mu = 0$. The analytical results deviate from the numerical results for larger $|\mu|$ because the two-band model is no longer valid at a higher doping level. It is clear that the two-band model is sufficient to describe the optimum thermopower of s-SWNTs which appear near $\mu = 0$.

We can determine a condition to obtain an optimized thermopower at the chemical potential μ_{opt} by taking $dS_{\text{CNT}}(\mu)/d\mu = 0$ for Eq. 5 as follows

$$\mu_{\text{opt}} = \frac{k_{\text{B}}T}{2} \ln \left(\frac{E_{\text{g}}}{k_{\text{B}}T} + 2 \pm \sqrt{\left(\frac{E_{\text{g}}}{k_{\text{B}}T} + 2 \right)^2 - 1} \right), \quad (6)$$

where the + and – signs correspond to the n-type and p-type SWNTs, respectively. From Eq. (6), we can say that the μ_{opt} values will move away from $\mu = 0$ as E_{g} becomes larger than $k_{\text{B}}T$. However, due to the presence of the logarithmic function, μ_{opt} is a slowly changing function of E_{g} when E_{g} is much larger than $k_{\text{B}}T$. For example, for the range of d_t of 0.5–1.5 nm, the s-SWNTs have E_{g} values 0.46–1.58 eV. In this case, the E_{g} 's are 17–61 times larger than $k_{\text{B}}T$ for $T = 300$ K. For those E_{g} values, we obtain $0.046 < |\mu_{\text{opt}}| < 0.062$ eV at a constant $T = 300$ K, which implies that the change in μ_{opt} (~ 16 meV) can be negligibly small compared with the width of $S(\mu)$ (~ 50 meV) as shown in Fig. 8. Thus at the room temperature, controlling the doping level or the chemical potential is important to obtain the optimum S for the even bundled s-SWNTs.

3.4 Chirality-Dependent Thermopower

Using both the numerical calculation by BoltzTraP and our analytical formula S_{CNT} , it is now possible for us to plot $S_{\text{CNT}}^{\text{opt}} \equiv S_{\text{CNT}}(\mu = \mu_{\text{opt}})$ as a function of d_t of s-SWNTs. In Fig. 9, we plot (a) $S_{\text{CNT}}^{\text{opt}}$ and (b) energy gap E_{g} as a function of d_t for $0.5 \leq d_t \leq 1.5$ nm. In Fig. 9a, we plot $S_{\text{CNT}}^{\text{opt}}$ calculated by both numerical BoltzTraP results (denoted by *circles*) and the analytical formula (*plus symbols*), from which we can see that the two methods give almost the same values of S . Thus, we will adopt the analytical formula for discussing the chirality dependence of S . By

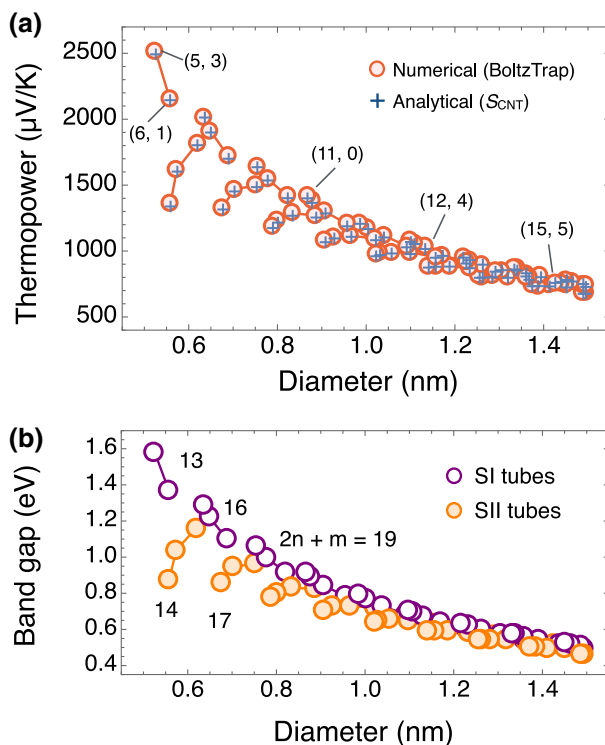


Fig. 9 **a** Optimum thermopower $S_{\text{CNT}}^{\text{opt}}$ values for all s-SWNTs within the diameter range of 0.5–1.5 nm plotted as a function of SWNT diameter. The temperature is set constant at 300 K. Numerical results from BoltzTrap are denoted by *circles*, while analytical results from Eqs. (5)–(6) are denoted by *plus symbols*. **b** The Kataura plot showing the family pattern of the SWNT band gap as a function of diameter. *Solid lines* are a guide for the eyes, connecting SWNTs with the same family number $2n + m$. The SI and SII tubes correspond to the SWNTs having $\text{mod}(2n + m, 3) = 1$ and 2, respectively

comparing Figs. 9a and 9b, $S_{\text{CNT}}^{\text{opt}}$ increases with decreasing d_t or with increasing E_g . For smaller diameter s-SWNTs with the family number [22] $2n + m = 13$, such as (5, 3) or (6, 1) s-SWNTs, the thermopower can reach a value more than $2000 \mu\text{V}/\text{K}$. The values of S are about 6–10 times larger than those found in other thermoelectric materials or in the SWNT bundles [46–49]. Thus, we have plenty of room to improve $S_{\text{CNT}}^{\text{opt}}$ of s-SWNTs experimentally.

The larger thermopower for smaller-diameter s-SWNTs can be explained by the relation of S_{CNT} with E_g as shown in Eq. (5) and by the fact that $E_g \propto 1/d_t$ [22]. The one-dimensional van Hove singularity of DOS in SWNTs also enhances the thermopower [7, 8]. Here, we should note that the thermopower of s-SWNTs as a function of diameter shows the nanotube family pattern, in which the different SWNTs with the same $2n + m$ can be connected, and they make a clearly distinct branch for $\text{mod}(2n + m, 3) = 1$ and $\text{mod}(2n + m, 3) = 2$, known as the nanotube SI and SII family branches, respectively as shown in Fig. 9a [22]. This behavior is

very similar to that found in the band gap as a function of diameter as shown in Fig. 9b, which is often referred to as the Kataura plot [20, 22, 50].

3.5 Quantum Confinement Effects in Thermoelectricity

It is important to discuss the reason why s-SWNTs have such large thermopower from the quantum confinement effect point of view. We recently found [11] that the quantum confinement effect [7, 8] occurs only when confinement length L_C is smaller than the thermal de Broglie wavelength Λ of any low dimensional (1-D, 2-D) semiconducting material. In the case of s-SWNTs, we may assume that the 1-D confinement length is characterized by the SWNT diameter and the thermal de Broglie wavelength Λ is defined by

$$\Lambda = \sqrt{\frac{2\pi\hbar^2}{k_B T m^*}}, \quad (7)$$

where \hbar is Planck's constant and m^* is the effective mass of s-SWNTs. The effective mass of electron and hole $m_{e,h}^*$ are expressed by

$$m^* = \hbar^2 \left(\frac{d^2 E}{dk^2} \right)^{-1}, \quad (8)$$

where $E(\mathbf{k})$ is the electronic energy dispersion obtained by the ETB model [42].

In Fig. 10 we plot Λ of s-SWNTs as a function of d_t for $0.5 < d_t < 1.5$ nm. It is clear that the d_t is much smaller than the Λ . Thus, 1-D s-SWNTs satisfy the condition of $L_C < \Lambda$, and, thus, the well-separated, small- d_t single (n, m) s-SWNTs should behave as excellent thermoelectric material. When we consider the case of the bundle SWNTs, we should redefine L_C as the diameter of the bundle, which should be investigated by experiment.

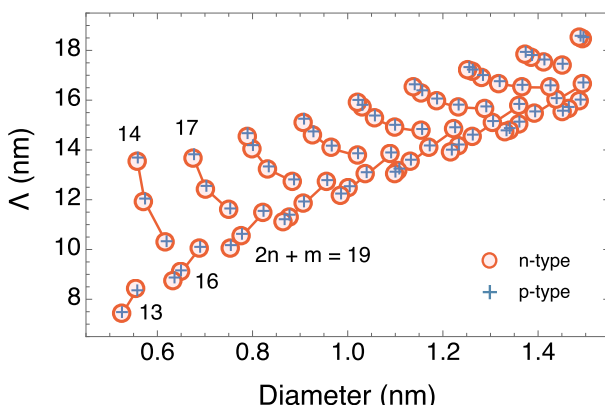


Fig. 10 Thermal de Broglie wavelength of several s-SWNTs as a function of SWNT diameter

4 Coherent Phonon Spectroscopy of SWNTs

Ultra-fast pump-probe spectroscopy is a useful tool for studying carrier and lattice dynamics in materials, since we can probe the physical properties on the same time scale as the relevant relaxation process. When ultra-short pump pulse of light is applied to a SWNT sample with a time duration less than a period of a phonon mode of the SWNT, all phonons start to oscillate with the same phase, which are known as the coherent phonon (CP) [51–55]. The CP is explained quantum mechanically in terms of coherent states, in which the amplitude-phase uncertainty reaches its minimum value [56–59]. Due to the coherent oscillations of phonons, macroscopic optical properties such as the reflectance R , transmittance T , or absorption coefficient α is modulated as a function of the time of the probe light, which is measured in CP spectroscopy.

Recently, by using sub-10-fs laser pulses, more than ten CP modes with frequency around 100–3000 cm⁻¹ could be observed in a (6, 5) enriched SWNT sample [60]. This measurement has opened up possibilities to utilize a particular CP mode of the SWNT for ultra-sensitive, mechanical detection [61], as well as quantum information science [62, 63] in the THz region. However, we have to excite a single phonon mode coherently while suppressing other phonon modes, which is not possible to achieve by using only a single laser pulse.

One possible technique to selectively excite a particular phonon mode is by using repeated pulses of pump light in pump-probe spectroscopy. Kim et al. have shown that multiple pulses with different repetition rates can be generated by a pulse shaping technique to excite a radial breathing mode (RBM) of a specific SWNT in a bundled SWNT sample [13]. The bundled SWNT sample consists of several (n, m) SWNTs with the different RBM frequencies that are inversely proportional to the SWNT diameter [64]. By applying the pulse train with a repetition frequency matched to the RBM frequency of a specified SWNT, it is possible to excite only the specified SWNT in the bundled sample [13], while all other RBM CP's can be suppressed. Thus, we expect that the pulse-train technique can be used to enhance other CP modes than the RBMs such as the G bands in the SWNTs, which we will discuss in this section.

4.1 Modeling Coherent Phonon Generation

In the pump-probe technique, (1) the pump light generates electron–hole pairs and (2) we measure either transient differential transmission ($\Delta T/T$) or differential reflection ($\Delta R/R$) spectra that oscillates at phonon frequencies. In Fig. 11a we show the photoexcitation process of a molecule for simplicity. An electron in the ground state is excited to the excited state for a potential minimum different from that for the ground states. Thus, the lattice starts to move to the minimum in the excited states at the same time, which is the origin of CP oscillation. In Fig. 11b a typical geometry of a CP phonon experiment is shown in which the probe pulse comes Δt after the pump light, and we detect either ($\Delta T/T$) or ($\Delta R/R$) of the probe light. In Fig. 11c, $\Delta T/T$ is shown as a function of Δt . By extracting the oscillating term in

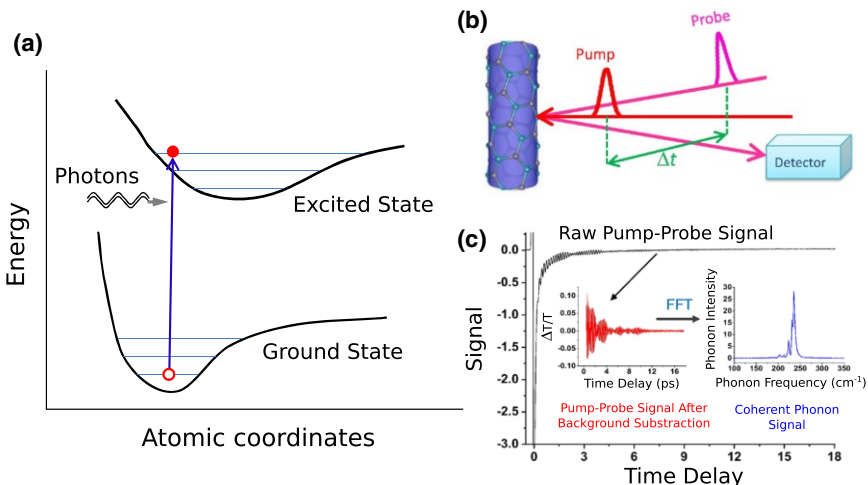


Fig. 11 Illustration of a typical coherent phonon experiment. **a** Schematic diagram showing the generation of coherent phonons in a molecular system, which is used as a simplified illustration for the SWNT case. The combined electronic and vibrational energy levels for the ground and excited states are shown. **b** Setup of ultra-fast pump-probe spectroscopy, which generates electron–hole pairs and triggers the coherent phonon oscillations. **c** The coherent phonon intensity is obtained from a Fourier transform of the pump-probe signal after background subtraction

$\Delta T/T$ from the monotonically changing term, we take the Fourier transform of $\Delta T/T$ to obtain the power spectrum, which is called the CP spectra.

In order to start all phonon oscillations at the same time with the same phase, it is necessary for the pulse width τ_p in time to be sufficiently short compared with a phonon period. For example, to generate coherent RBM phonons (5 THz), τ_p should be shorter than 200 fs. As for the G band (~ 47 THz), the τ_p should be shorter than 20 fs. It is the reason why they used a sub-10-fs pump to observe the G band and even the G' band (2700 cm^{-1}) [60].

The coherent phonons amplitude Q_m satisfies a driven oscillator equation defined by [12]

$$\frac{\partial^2 Q_v(t)}{\partial t^2} + \omega_v^2 Q_v(t) = S_m(t), \quad (9)$$

where v denotes the phonon mode and ω_v is frequency of the v -th phonon mode at phonon wavevector $q = 0$. The right hand side of Eq. 9 is the force generated by photoexcited carriers, which is given by

$$S_v(t) = -\frac{2\omega_v}{\hbar} \sum_{nk} \mathcal{M}_n^v(k) [f_n(k, t) - f_n^0(k)], \quad (10)$$

where $f_n(k, t)$ and $f_n^0(k)$ are, respectively, the time-dependent and the initial equilibrium Fermi distribution function for electrons. Here n labels an electronic state, and k gives the electron wavevector. $\mathcal{M}_n^v(k)$ denotes the electron–phonon matrix element within the ETB model [65]. When we consider the pulse train, the right

side of Eq. (9) becomes a sum of S_v of each pulse with the delays of the repetition time.

In the calculation of CP spectra, we calculate the absorption coefficient $\alpha(E_{\text{probe}}, \Delta t)$ as a function of the probe energy E_{probe} and Δt and the square of $\alpha(E_{\text{probe}}, \Delta t)$ is equivalent to $\Delta R/R$ or $\Delta T/T$ in the experiment. We can calculate $\alpha(E_{\text{L}}, \Delta t)$ using Fermi's golden rule [66] in which we take account of the time variation of the band structure within adiabatic approximation for given Q_m and carrier distribution functions in the ETB model [12, 67]. The modulation of absorption coefficient observed by the probe is given by

$$\Delta\alpha(E_{\text{probe}}, \Delta t) = -[\alpha(E_{\text{probe}}, \Delta t) - \alpha(E_{\text{probe}}, -\infty)], \quad (11)$$

where $t = -\infty$ denotes the condition when pump pulse is absent. Taking the Fourier transform of $\Delta\alpha(E_{\text{probe}}, \Delta t)$, we obtain CP spectra as a function of phonon frequency.

4.2 Single Phonon Mode Generation in Single Chirality SWNTs

Here, we discuss CP generation of a single phonon mode by repeated pulses of pump light, especially for the G band. In this case, we have to select a repetition period T_{rep} . The pulse repetition period, T_{rep} , is defined in the calculation by the time interval between two neighboring Gaussian pulses.

In the upper panel of Fig. 12a, we show six Gaussian pulses with $\tau_p = T_G$ and $1.5T_G$ where T_G is the period of the G band oscillation, and, in the lower panel, we plot the calculated coherent phonon amplitude $Q(t)$ for the G band for the two cases of pulse train. It can be seen that selection of T_{rep} which matches to integer multiples (half-integer multiples) of the G band period enhances (suppresses) the G band phonon amplitude. It is noted that monotonically increasing the term of $Q(t)$ does not contribute to the CP intensity as a function of the phonon frequency after the Fourier transformation.

In Fig. 12b, we show the CP spectra in which RBM CP spectra is very strong compared with G CP spectra for the six pulses even though we select $\tau_p = T_G$. It is important to point out that the integer multiple of T_G is *not always* sufficient to completely suppress the RBM amplitude although T_G is not an integer multiple of the period of the RBM. The reasons for the result are that (1) electron–phonon interaction of RBM is stronger than that of the G band [65] and that (2) $Q_m(t)$ is inversely proportional to ω_m when we solve the driven oscillator model. This means that the higher-frequency G phonon modes tend to have a smaller amplitude than the lower frequency RBM modes [67].

In order to suppress the Q_m for RBM, we propose to increase the number of pulses. In Fig. 12b we show the calculated results of 90 pulses with $T_{\text{rep}} = T_G$, in which the CP intensity of the RBM by 90 pulses is significantly suppressed compared with that of six pulses, while the CP intensity for the G band does not change. In the inset of Fig. 12b, we plot the intensity ratio of I_{RBM}/I_G as a function of the number of pulses. The intensity ratio exponentially decreases with increasing the number of pulses. It is noted that we cannot increase the number of pulses more

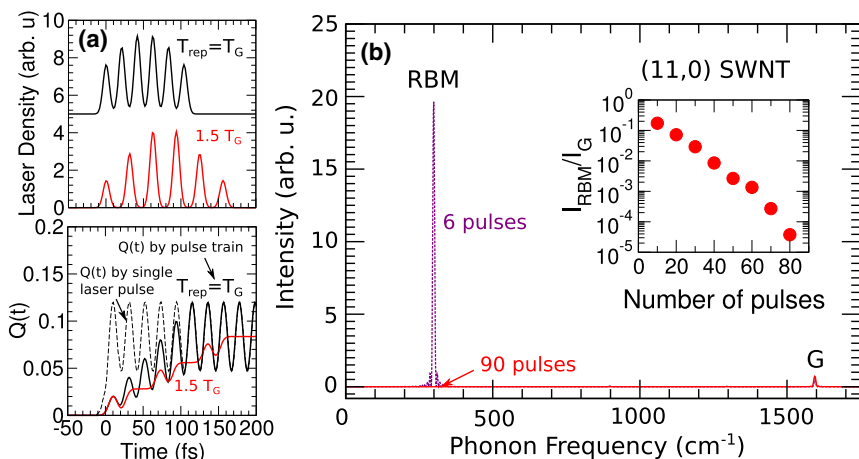


Fig. 12 Selective coherent G band excitation in (11,0) SWNT. **a** The laser density of the pulse train and the resulting coherent G band phonon amplitude with conditions of $T_{\text{rep}} = T_G$ and $T_{\text{rep}} = 1.5T_G$ for six laser pulses. For additional comparison, we show a *dashed line* that represents the G band amplitude generated by a single laser pulse. The pulse width τ_p is set to be 10 fs. **b** The coherent phonon intensity versus phonon frequency for a different number of laser pulses applied to a (11,0) SWNT. *Inset* shows the ratio between the G band intensity (I_G) and RBM intensity (I_{RBM}). The RBM intensity is drastically suppressed when we apply a larger number of pulses

than the recombination time of excited carriers on the order of 1 ps. If we increase the total duration time compared with the recombination time, the CP intensity monotonically decrease, which can be used for evaluating the recombination time by comparing with the theory. The single phonon mode excitation will be technically important, too, for extending the application of nanomechanics to higher frequencies of THz, which will be able to be coupled with specified molecules and nanomaterials.

5 Discrete Energy Levels in Finite-Length SWNT

Finally, we discuss the low energy properties of SWNTs, which are observed in the transport measurements of a finite length SWNT or a SWNT quantum dot. Since the nanotube surface has a cylindrical curvature, there appear curvature-induced effects of SWNTs, which are not described by the simple tight binding method in which electronic structure of SWNTs is calculated by that of 2-D graphene with a periodic boundary condition in the circumference direction. When we consider the curvature-induced effect, the small energy gap (~ 100 meV) for the m-SWNTs [2, 68–70] and the spin-orbit interaction [70–74] (~ 1 meV) are obtained and those properties are observed in the low temperature measurements [14]. Another important curvature effect for understanding the low energy properties is that the velocities of left- and right-going waves within the K (or K') valley are different [15]. The asymmetric velocities are chirality-dependent, which will be

important for understanding the alternating degeneracy of energy levels in a SWNT quantum dot, which is the subject of this subsection.

Figure 13a, b show the calculated energy bands near the K and K' valleys, respectively, for four different chiralities of m-SWNTs [15], in which the curvature induced energy gap are seen except for (4, 4) and (6, 6) armchair SWNTs. In particular, it is important to note that the absolute value of two slopes for linear energy bands (or the group velocities) for left- and right-going waves in the same valley are different from each other for the (4, 4) armchair nanotube, while the slopes are the same for the (9, 0) zigzag nanotube. The group velocities in the τ valley ($\tau = K, K'$) are defined by

$$v_L^{(\tau)} = -\frac{1}{\hbar} \frac{\partial \varepsilon_L^{(\tau)}}{\partial k} (> 0), \quad v_R^{(\tau)} = \frac{1}{\hbar} \frac{\partial \varepsilon_R^{(\tau)}}{\partial k} (> 0), \quad (12)$$

where $\varepsilon_L^{(\tau)}$ ($\varepsilon_R^{(\tau)}$) is the energy as a function of the wavenumber k of the left-going (right-going) wave in the τ valley, which has negative (positive) slope. It is noted that the relation $v_L^{(\tau)} = v_R^{(-\tau)}$ holds because of the time reversal symmetry. Hereafter, we put an integer value for $\tau = 1$ (-1) for K (K') for convenience. The velocities estimated in the linear dispersion region are plotted in Fig. 13c, d. The velocity difference between the left- and right-going waves becomes larger for the smaller diameter and near the armchair chirality. Using a perturbation theory with respect to the curvature, we fitted the group velocities to the following expressions [15],

$$v_L^{(\tau)} = v_{av} - \tau \Delta v, \quad v_R^{(\tau)} = v_{av} + \tau \Delta v, \quad (13)$$

where

$$v_{av} = v_0 + \frac{c_2 + c_4 \cos 6\theta}{d_t^2}, \quad \Delta v = \frac{c_6 \sin 3\theta}{d_t^2}, \quad (14)$$

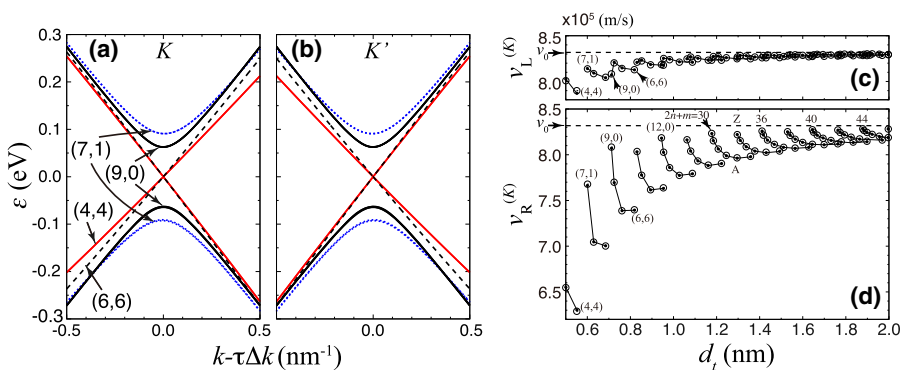


Fig. 13 **a, b** Energy bands for m-SWNTs around the Fermi energy, at the K and K' valleys. **c, d** Velocities of left-going wave ($v_L^{(K)}$) and right-going wave ($v_R^{(K)}$) in the K valley for the m-SWNTs. The values estimated from the numerical energy band calculation are shown with dots. The values of Eq. (13) for each (n, m) SWNT are also plotted as open circles. The numbers on the lines indicate the corresponding $2n + m$ family values. Z(A) denotes (n, m) value close to a zigzag (armchair) nanotube [15]

with $c_2 = -2.46$, $c_4 = 1.27$ and $c_6 = -2.45$ in units of $10^4 \text{ (m/s)} \cdot \text{nm}^2$ and $v_0 = 8.32 \times 10^5 \text{ m/s}$ for the diameter region of $0.6 < d_t < 2.0 \text{ nm}$.

Since the electrons are confined in the direction of the nanotube axis for a finite length SWNT (or simply called SWNT quantum dot), the discrete energy levels represent the standing wave consisting of left and right going waves. There are two possible couplings of left and right going waves, that is, left and right going waves within the same valley or in different valleys in the k space, which we call intravalley or intervalley coupling, respectively (see Fig. 14c). In the case of the intervalley coupling, in which the standing wave as the eigenstate are formed from the left-going wave at one valley and the right-going wave at *another valley*, there exist two inequivalent series of equispaced discrete energy levels, whose separations are given by $\hbar v_L^{(K)} \pi / L_{\text{NT}}$ and $\hbar v_R^{(K)} \pi / L_{\text{NT}}$, reflecting the asymmetric velocities (see Fig. 14a, c). However, the conventional picture only adopts the intravalley scattering, in which the standing wave is made of the left- and right-going waves in the *same valley* (see Fig. 14b, c) which gives two identical series of energy levels. The conventional picture explains the observation of the four fold degeneracy of the energy levels, reflecting the two valley states with two spin states, with a small lift of degeneracy by the spin-orbit interaction. However, recent experiments show oscillating behavior of the two fold and four fold degeneracies within the same SWNT [75–80] as a function of energy, which suggests that we must consider the intervalley scattering at both ends.

In order to consider the intervalley interaction, let us assume that both ends of a finite-length SWNT do not break the rotational symmetry C_d of SWNTs around the nanotube axis where d is the greatest common divisor, $d = \text{gcd}(n, m)$. Then we can use the conservation of angular momentum along the nanotube axis, L_μ . When the energy states belong to different L_μ 's, they are not coupled to each other, whereas the states with the same angular momentum are coupled with each other. It is known that a 1-D cutting line (or 1-D Brillouin zone) in the k -space corresponds to a L_μ [1, 81]. As far as we discuss the angular momentum from $L_\mu = 0$ to $d - 1$, it is convenient to adopt the long cutting lines [81], in which there are d ($L_\mu = 0, \dots, d - 1$) cutting lines, instead of the conventional N short cutting lines [1]. When we classified all (n, m) SWNTs, 80% of the SWNTs are classified

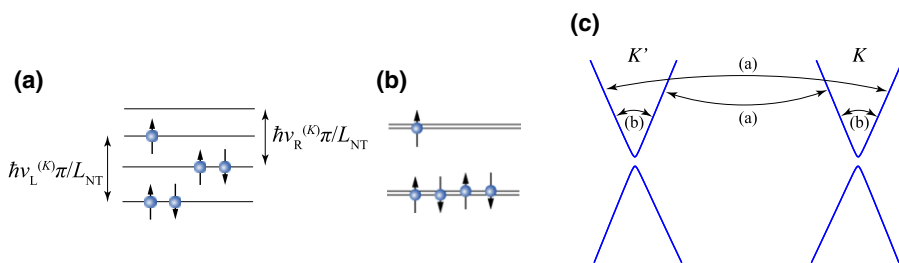


Fig. 14 Schematics of energy levels for two different cases, **a** strong coupling of two valleys (intervalley couplings), and **b** decoupling of two valleys (intravalley coupling). **c** Two different combinations of traveling waves in the standing waves for the cases of **a** intervalley and **b** intravalley couplings

into either metal-2 m-SWNT [82] or $d = 1$ and $d = 2$ s-SWNTs. The intervalley coupling occurs when the K and K' valley states belong to the same L_μ , which corresponds to the cases of (1) $L_\mu = 0$ for metal-2 and $d = 1$ s-SWNTs, and (2) $L_\mu = 1$ for $d = 2$ s-SWNTs [16, 83]. For other cases, the intervalley coupling does not occur, and, thus, the four fold degeneracy occurs. From the viewpoint of the rotational symmetry, intervalley coupling may occur for more than 80% of SWNTs with the diameter region of $0.5 < d_t < 3$ nm.

In Fig. 15 we plot calculated energy levels for $(n, m) = (7, 4)$, which is classified into metal-2, with the length $L_{\text{NT}} = 50$ nm [83] in order to study the valley coupling within a long cutting line that goes over both the K and K' points. The boundaries of Fig. 15 are defined by cutting the nanotube with the plane orthogonal to the nanotube axis. It is noted that both ends of the (7,4) SWNT have the same rotational symmetry with the bulk (7,4) SWNT. Figure 15a shows one of the boundary shapes, which contains a carbon atom with the Klein edge (an edge carbon atom that has only one nearest neighbor atom) at the foot of the z axis. In Fig. 15b, c we plot the energy levels, ε_l , and the energy level separation for the l -th energy level, $\varepsilon_{l+1} - \varepsilon_l$, respectively. The energy levels show the energy dependent degeneracy, nearly four fold degeneracy ($\varepsilon_{l+1} - \varepsilon_l$ becomes large for every 4 l 's) appears near $l \sim -25$ and $l \sim 13$ whereas two fold degeneracy appears near $l \sim -7$. The alternative behavior of the four fold and two fold degeneracies occurs by the intervalley coupling. That is, there exist two inequivalent series of equi-spaced discrete energy levels, $\hbar v_L^{(K)} \pi / L_{\text{NT}}$ and $\hbar v_R^{(K)} \pi / L_{\text{NT}}$, as shown by the solid and dashed arrows in Fig. 15b which are either close to (four fold degeneracy) or separated from (two fold degeneracy) one another. The alternative behavior of degeneracies is also observed in the experiments [75–80], which suggest that the intervalley coupling occurs.

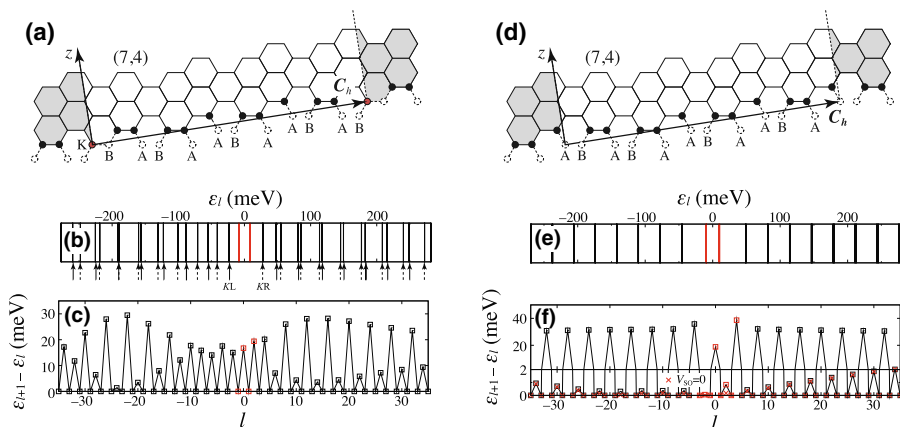


Fig. 15 Boundary shape, calculated energy levels and eigenstates for a (7, 4) nanotube of 50.17 nm length with two different boundaries. **a** Unfolded tube near the left boundary. **b** Energy levels ε_l in $-35 \leq l \leq 35$, and **c** level separation $\varepsilon_{l+1} - \varepsilon_l$ as a function of l , for the boundary in **a**. **d-f** show the unfolded tube, energy levels, and level separation, respectively, for the different boundary than **a**. The case of absence of spin-orbit interaction is shown by the red cross in the lower panel of **f** [83]

It should be mentioned that this behavior was considered as extrinsic factors such as impurities and defects, which might induce the intervalley valley coupling, too.

In Fig. 15d we show slightly modified the boundary shape from Fig. 15a, by removing the Klein edged carbon atom at the foot of z axis. The corresponding energy levels have nearly four fold degeneracy as shown in Fig. 15e, f, which is completely different behavior than (b) and (c) by removing just one atom. The four fold degeneracy occurs by the weakened intervalley coupling by the edge shape effect. Thus the shapes of edges are very sensitive to the occurrence of degeneracy, which makes the problem difficult.

In order to study the edge effect microscopically, it is useful to project total Hamiltonian to subHamiltonian with the angular momentum [83]. The Hamiltonian is decomposed into a projected Hamiltonian for L_μ -th angular momentum, L_μ , $H = \sum_{L_\mu} H_{L_\mu}$. By extracting a relevant H_{L_μ} , one gets an effective 1-D lattice model, whose detail is given in the reference [83]. The calculated results show that, in the low energy region near the Fermi energy, H_{L_μ} contains the evanescent modes of wavefunction for the edge state in which the wavefunctions of the edge state are localized at either the left or the right ends and either at the A sublattice or the B sublattice. The numbers of these modes are given as a function of (n, m) [16, 83, 84]. For example, the number of evanescent modes at the left boundary localized at either the A or B sublattice is given by $N_A^{\text{ev}} = 5$ and $N_B^{\text{ev}} = 4$ for (7, 4) nanotubes. Combining with the two delocalized states at K or K' valleys for each sublattice, there exist $N_A^{\text{ev}} + 2$ and $N_B^{\text{ev}} + 2$ independent modes for the A and B sublattices, respectively.

The eigenfunction of each sublattice is given by the linear combination of these modes. If the number of the boundary condition for $P = \text{A}$ or B sublattice, N_P^{bc} , is equal to or larger than that of the independent modes, all the coefficients in the eigenfunction should be zero. For this case, we have the fixed boundary condition for the envelope function $g_{P\tau}(\ell) \propto \sin(k\ell)$, which corresponds to the conventional standing wave. Since $1/kl$ is much longer than the lattice constant, the standing wave is formed within the same valley. Strictly speaking, the localized modes at the A sublattice have a non-zero amplitude at the B sublattice, which makes the weak intervalley coupling. This corresponds to the case of the Fig. 15d, in which the number of boundary conditions for A sublattice $N_A^{\text{bc}} = 7$, which is the number of empty site in A sublattice in Fig. 15d, is equal to that of the independent mode number, $N_A^{\text{ev}} + 2$. On the other hand, for the case of Fig. 15a, there is no fixed boundary condition for the envelope functions since $N_P^{\text{ev}} + 2 = N_P^{\text{bc}} + 1 > N_P^{\text{bc}}$. Furthermore, it is shown that the strong intervalley coupling occurs to construct the standing wave in the region of linear energy dispersion [16, 83].

Finally, let us briefly discuss the edge states in the energy gap region, which are indicated by the red lines in Fig. 15b, e. It is straightforward to apply the above analysis to count the number of edge states, by subtracting the number of boundary conditions from the number of independent evanescent modes [83]. For the case of Fig. 15a, as an example, the number of evanescent modes and that of the boundary conditions for the B sublattice are given by $N_B^{\text{ev}} = 6$ (in the energy gap region) and $N_B^{\text{bc}} = 5$, respectively. Therefore, the number of edge states per spin and per

boundary is given by $N_B^{\text{edge}} = 1$, which is consistent with the numerical result shown in Fig. 15b.

It is interesting and surprising for us to show that the winding number w_{L_μ} as a topological invariant defined in the bulk materials is equal to the number of edge states [16]. The winding number is an integer to count the phase integration divided by 2π in the k -space for the off-diagonal part of the Hamiltonian matrix defined by,

$$w_{L_\mu} = \frac{1}{2\pi} \int_0^{2\pi} dk \frac{\partial \arg \langle AkL_\mu | H_{L_\mu} | BkL_\mu \rangle}{\partial k}. \quad (15)$$

where $|PkL_\mu\rangle$ is the Bloch state of the P sublattice. By using the theorem known as Cauchy's argument principle in the complex analysis, the number of edge states is the same as the winding number, which is proven in our recent work [16]. The winding number in the bulk materials is redefined to consider the orthogonal boundary condition, which gives the number of edge states in the finite size [16]. The bulk-edge correspondence reveals another new concept of SWNTs as topological materials. In future experiments, it would be required to measure the electronic states not only by tunneling spectroscopy with contacting electrodes but also by the scanning tunneling spectroscopy for detecting the evanescent wave of the wavefunction without disturbing the edge shape of SWNT.

Acknowledgements R.S. acknowledges JSPS KAKENHI Grant Numbers JP25286005 and JP225107005. W.I. acknowledges JSPS KAKENHI Grant Numbers JP15K05118, JP16H01046 and JP15KK0147. A.R.T.N. and N.T.H. acknowledges the Interdepartmental Doctoral Degree Program for Material Science Leaders at Tohoku University. E.H.H. acknowledges the MEXT scholarship.

References

1. Saito R, Dresselhaus G, Dresselhaus MS (1998) Physical properties of carbon nanotubes. Imperial College Press, London
2. Saito R, Fujita M, Dresselhaus G, Dresselhaus MS (1992) Phys Rev B 46:1804
3. Saito R, Fujita M, Dresselhaus G, Dresselhaus MS (1992) Appl Phys Lett 60:2204
4. Farhat H, Berciaud S, Kalbac M, Saito R, Heinz TF, Dresselhaus MS, Kong J (2011) Phys Rev Lett 107:157401
5. Hasdeo EH, Nugraha ART, Sato K, Dresselhaus MS, Saito R (2013) Phys Rev B 88:115107
6. Saito R, Sato K, Araujo P, Mafrá D, Dresselhaus M (2013) Solid State Commun 175–176:18
7. Hicks LD, Dresselhaus MS (1993) Phys Rev B 47:12727
8. Hicks LD, Dresselhaus MS (1993) Phys Rev B 47:16631
9. Dresselhaus MS, Chen G, Tang MY, Yang RG, Lee H, Wang DZ, Ren ZF, Fleurial JP, Gogna P (2007) Adv Mater 19:1043
10. Boukai AI, Bunimovich Y, Tahir-Kheli J, Yu J, Goddard WA III, Heath JR (2008) Nature 451:168
11. Hung NT, Hasdeo EH, Nugraha ART, Dresselhaus MS, Saito R (2016) Phys Rev Lett 117:036602
12. Kim JH, Nugraha ART, Booshehri LG, Haroz EH, Sato K, Sanders GD, Yee KJ, Lim YS, Stanton CJ, Saito R, Kono J (2013) Chem Phys 413:55
13. Kim JH, Han KJ, Kim NJ, Yee KJ, Lim YS, Sanders GD, Stanton CJ, Booshehri LG, Hároz EH, Kono J (2009) Phys Rev Lett 102:037402
14. Laird EA, Kuemmeth F, Steele GA, Grove-Rasmussen K, Nygård J, Flensberg K, Kouwenhoven LP (2015) Rev Mod Phys 87:703
15. Izumida W, Vikström A, Saito R (2012) Phys Rev B 85:165430
16. Izumida W, Okuyama R, Yamakage A, Saito R (2016) Phys Rev B 93:195442

17. Brown SDM, Jorio A, Corio P, Dresselhaus MS, Dresselhaus G, Saito R, Kneipp K (2001) Phys Rev B 63:155414
18. Rao AM, Eklund PC, Bandow S, Thess A, Smalley RE (1997) Nature (London) 388:257
19. Pimenta MA, Marucci A, Empedocles S, Bawendi M, Hanlon EB, Rao AM, Eklund PC, Smalley RE, Dresselhaus G, Dresselhaus MS (1998) Phys Rev B Rapid 58:R16016
20. Kataura H, Kumazawa Y, Maniwa Y, Umezawa I, Suzuki S, Ohtsuka Y, Achiba Y (1999) Synth Metals 103:2555
21. Alvarez L, Righi A, Rols S, Anglaret E, Sauvajol JL (2000) Chem Phys Lett 320:441
22. Saito R, Dresselhaus G, Dresselhaus MS (2000) Phys Rev B 61:2981
23. Fano U (1961) Phys Rev 124:1866
24. Alvarez L, Righi A, Guillard T, Rols S, Anglaret E, Laplaze D, Sauvajol J (2000) Chem Phys Lett 316:186
25. Eklund PC, Dresselhaus G, Dresselhaus MS, Fischer JE (1977) Phys Rev B 16:3330
26. Solin S (1977) Mater Sci Eng 31:153
27. Yoon D, Jeong D, Lee H, Saito R, Son Y, Lee H, Cheong H (2013) Carbon 61:373
28. Lazzeri M, Piscanec S, Mauri F, Ferrari AC, Robertson J (2006) Phys Rev B 73:155426
29. Wu Y, Maultzsch J, Knoesel E, Chandra B, Huang M, Sfeir MY, Brus LE, Hone J, Heinz TF (2007) Phys Rev Lett 99:027402
30. Bose SM, Gayen S, Behera SN (2005) Phys Rev B 72:153402
31. Jiang C, Kempa K, Zhao J, Schlecht U, Kolb U, Basché T, Burghard M, Mews A (2002) Phys Rev B 66:161404
32. Kempa K (2002) Phys Rev B 66:195406
33. Ando T (2008) J Phys Soc Japan 77:014707
34. Zhang D, Yang J, Hasdeo EH, Liu C, Liu K, Saito R, Li Y (2016) Phys Rev B 93:245428
35. Zhang D, Yang J, Li M, Li Y (2016) ACS Nano 10(12):10789. doi:[10.1021/acsnano.6b04453](https://doi.org/10.1021/acsnano.6b04453)
36. Hone J, Ellwood I, Munro M, Mizel A, Cohen ML, Zettl A, Rinzler AG, Smalley RE (1998) Phys Rev Lett 80:1042
37. Hone J, Llaguno MC, Nemes NM, Johnson AT, Fischer JE, Walters DA, Casavant MJ, Schmidt J, Smalley RE (2000) Appl Phys Lett 77:666
38. Yanagi K, Kanda S, Oshima Y, Kitamura Y, Kawai H, Yamamoto T, Takenobu T, Nakai Y, Maniwa Y (2014) Nano Lett 14:6437
39. Romero HE, Sumanasekera GU, Mahan GD, Eklund PC (2002) Phys Rev B 65:205410
40. Goldsmid HJ, Sharp JW (1999) J Electron Mater 28:869
41. Madsen GK, Singh DJ (2006) Comput Phys Commun 175:67
42. Samsonidze GG, Saito R, Kobayashi N, Grüneis A, Jiang J, Jorio A, Chou SG, Dresselhaus G, Dresselhaus MS (2004) Appl Phys Lett 85:5703
43. Popov VN (2004) New J Phys 6:17
44. Hung NT, Nugraha ART, Hasdeo EH, Dresselhaus MS, Saito R (2015) Phys Rev B 92(16):165426
45. Goldsmid HJ (2010) Introduction to thermoelectricity. Springer, Berlin
46. Boukai AI, Bunimovich Y, Tahir-Kheli J, Yu JK, Goddard III WA, Heath JR (2008) Nature 451:168
47. Hochbaum AI, Chen R, Delgado RD, Liang W, Garnett EC, Najarian M, Majumdar A, Yang P (2008) Nature 451:163
48. Poudel B, Hao Q, Ma Y, Lan Y, Minnich A, Yu B, Yan X, Wang D, Muto A, Vashaei D, Chen X, Liu J, Dresselhaus MS, Chen G, Ren Z (2008) Science 320:634
49. Pei Y, Shi X, LaLonde A, Wang H, Chen L, Snyder GJ (2011) Nature 473:66
50. Weisman RB, Bachilo SM (2003) Nano Lett 3:1235
51. Dumitrićă T, Garcia ME, Jeschke HO, Yakobson BI (2004) Phys Rev Lett 92:117401
52. Gambetta A, Manzoni C, Menna E, Meneghetti M, Cerullo G, Lanzani G, Tretiak S, Piryatinski A, Saxena A, Martin RL, Bishop AR (2006) Nat Phys 2:515
53. Lim YS, Yee KJ, Kim JH, Haroz EH, Shaver J, Kono J, Doorn SK, Hauge RH, Smalley RE (2006) Nano Lett 6:2696
54. Lüer L, Gadermaier C, Crochet J, Hertel T, Brida D, Lanzani G (2009) Phys Rev Lett 102:127401
55. Makino K, Hirano A, Shiraki K, Maeda Y, Hase M (2009) Phys Rev B 80:245428
56. Zeiger HJ, Vidal J, Cheng TK, Ippen EP, Dresselhaus G, Dresselhaus MS (1992) Phys Rev B 45:768
57. Kuznetsov AV, Stanton CJ (1994) Phys Rev Lett 73:3243
58. Hu X, Nori F (1996) Phys Rev B 53:2419
59. Merlin R (1997) Solid State Commun 102:207

60. Lim YS, Nugraha ART, Cho SJ, Noh MY, Yoon EJ, Liu H, Kim JH, Telg H, Hroz EH, Sanders GD, Baik SH, Kataura H, Doorn SK, Stanton CJ, Saito R, Kono J, Joo T (2014) *Nano Lett* 14:1426
61. Eichler A, Moser J, Chaste J, Zdrojek M, Wilson-Rae I, Bachtold A (2011) *Nat Nanotechnol* 6:339
62. Ruskov R, Tahan C (2012) *JPCS* 398:012011
63. Li JJ, Zhu KD (2012) *Sci Rep* 2:903
64. Saito R, Takeya T, Kimura T, Dresselhaus G, Dresselhaus MS (1998) *Phys Rev B* 57:4145
65. Jiang J, Saito R, Samsonidze GG, Chou SG, Jorio A, Dresselhaus G, Dresselhaus MS (2005) *Phys Rev B* 72:235408
66. Chuang SL (1995) Physics of optoelectronic devices. Wiley, New York
67. Nugraha ART, Hasdeo EH, Sanders GD, Stanton CJ, Saito R (2015) *Phys Rev B* 91:045406
68. Hamada N, Sawada SI, Oshiyama A (1992) *Phys Rev Lett* 68:1579
69. Kane CL, Mele EJ (1997) *Phys Rev Lett* 78:1932
70. Ando T (2000) *J Phys Soc Japan* 69:1757
71. Chico L, Lopez-Sancho MP, Munoz MC (2004) *Phys Rev Lett* 93:176402
72. Izumida W, Sato K, Saito R (2009) *J Phys Soc Japan* 78:074707
73. Chico L, López-Sancho MP, Muñoz MC (2009) *Phys Rev B* 79(23):235423
74. Jeong JS, Lee HW (2009) *Phys Rev B* 80(7):075409
75. Maki H, Ishiwata Y, Suzuki M, Ishibashi K (2005) *Jpn J Appl Phys* 44:4269
76. Makarovski A, An L, Liu J, Finkelstein G (2006) *Phys Rev B* 74:155431
77. Moriyama S, Fuse T, Ishibashi K (2007) *Phys Stat Sol B* 244:2371
78. Holm JV, Jørgensen HI, Grove-Rasmussen K, Paaske J, Flensberg K, Lindelof PE (2008) *Phys Rev B* 77:161406(R)
79. Schmid DR, Smirnov S, Marganska M, Dirnachner A, Stiller PL, Grifoni M, Hüttel AK, Strunk C (2015) *Phys Rev B* 91:155435
80. Ferrier M, Arakawa T, Hata T, Fujiwara R, Delagrange R, Weil R, Deblock R, Sakano R, Oguri A, Kobayashi K (2016) *Nat Phys* 12(3):230
81. White CT, Robertson DH, Mintmire JW (1993) *Phys Rev B* 47:5485
82. Saito R, Sato K, Oyama Y, Jiang J, Samsonidze GG, Dresselhaus G, Dresselhaus MS (2005) *Phys Rev B* 72:153413
83. Izumida W, Okuyama R, Saito R (2015) *Phys Rev B* 91:235442
84. Akhmerov AR, Beenakker CWJ (2008) *Phys Rev B* 77:085423



REVIEW

Review of Electronics Based on Single-Walled Carbon Nanotubes

Yu Cao¹ · Sen Cong¹ · Xuan Cao² · Fanqi Wu² · Qingzhou Liu² · Moh. R. Amer^{3,4} · Chongwu Zhou¹

Received: 6 March 2017/Accepted: 11 July 2017/Published online: 14 August 2017
© Springer International Publishing AG 2017

Abstract Single-walled carbon nanotubes (SWNTs) are extremely promising materials for building next-generation electronics due to their unique physical and electronic properties. In this article, we will review the research efforts and achievements of SWNTs in three electronic fields, namely analog radio-frequency electronics, digital electronics, and macroelectronics. In each SWNT-based electronic field, we will present the major challenges, the evolutions of the methods to overcome these challenges, and the state-of-the-art of the achievements. At last, we will discuss future directions which could lead to the broad applications of SWNTs. We hope this review could inspire more research on SWNT-based electronics, and accelerate the applications of SWNTs.

Keywords Single-walled carbon nanotubes · Radio-frequency electronics · Digital electronics · Macroelectronics

Chapter 7 was originally published as Cao, Y., Cong, S., Cao, X., Wu, F., Liu, Q., Amer, M. R. & Zhou, C. Top Curr Chem (Z) (2017) 375: 75. DOI 10.1007/s41061-017-0160-5.

✉ Chongwu Zhou
chongwuz@usc.edu

¹ Department of Electrical Engineering, University of Southern California, Los Angeles, CA 90089, USA

² Department of Chemical Engineering and Materials Science, University of Southern California, Los Angeles, CA 90089, USA

³ Center of Excellence for Green Nanotechnologies, Joint Centers of Excellence Program, King Abdulaziz City for Science and Technology, P. O. Box 6086, Riyadh 11442, Saudi Arabia

⁴ Department of Electrical Engineering, University of California, Los Angeles, 420 Westwood Plaza, 5412 Boelter Hall, Los Angeles, CA 90095, USA

1 Introduction

In the past one and a half decades, continued downscaling of complementary metal–oxide–semiconductor (CMOS) technology toward nanoscale dimensions (e.g. sub-14-nm technology nodes) has been enabled by tremendous research breakthroughs and engineering innovations, such as the introduction of strained silicon channels, implementing high- κ /metal-gate dielectric stacks, and the use of non-planar transistor structures such as double-gate and fin field-effect transistors (FinFETs). Scaling beyond the silicon roadmap has generated much interest in the research of low-dimensional [i.e. one-dimensional (1D) and two-dimensional (2D)] electronic systems, the synthesis of nanomaterials, and the fabrication of nanoscale electronic devices. Low-dimensional nanomaterials have the desired scaling potential and also provide access to novel physical phenomena that results in unique electronic properties with exceptional transport characteristics that can enable future high-speed and low-power applications. In addition, low-dimensional materials bring new opportunities for flexible and portable electronics due to their ultrathin thickness. Single-walled carbon nanotubes (SWNTs) are the most prominent representatives of 1D nanomaterials. SWNTs, with diameters ranging between 1 and 3 nm, have chirality-dependent properties. Of particular interest, semiconducting SWNTs have shown to exhibit high mobility, high current-carrying capability, small intrinsic capacitance, and extraordinary thermal and mechanical properties [1–5]. Owing to their unique properties, SWNTs have been widely investigated as the channel materials for radio-frequency (RF) electronics, digital electronics, and macroelectronics.

In the application of RF electronics, researchers have devoted a majority of their efforts to improving the RF performance of SWNT transistors [6–18]. Different device structures, channel length scaling, and key SWNT parameters, such as diameter, semiconducting purity, and alignment, have all been investigated. The milestone came in 2016 when SWNT RF transistors with cut-off frequencies greater than 70 GHz were reported [11]. In addition, the linearity performance of these SWNT RF transistors has also been characterized [8, 11, 13, 14, 17–20]. Moreover, circuits (e.g. mixers and frequency doublers) [14, 16, 21] and systems (e.g. radio receivers) [4, 22, 23] based on SWNT RF transistors have also been demonstrated by several research groups.

In the application of digital electronics, significant progress has been achieved experimentally. SWNT-based digital systems are theoretically proven to have more than one order of magnitude higher energy-delay product in comparison with Si-based complementary metal–oxide–semiconductor (CMOS) technologies [24]. Field-effect transistors (FETs) based on a single nanotube [2, 5, 25–31] and aligned nanotube arrays [32–35] have all been fabricated and characterized, showing the tremendous potential for building future energy-efficient digital systems. SWNT FETs have also been further optimized in regard to nanotube alignment, dielectrics, and metal contact, and the channel length scaling of these transistors has been investigated systematically. Moreover, various methods to achieve n-type SWNT FETs have been developed, and complementary operations of SWNT FETs have

been demonstrated [36–43]. With the advancement in the transistor performance, both SWNT digital circuits and systems, e.g. central processing units (CPUs), have been demonstrated [35], and three-dimensional (3D) integration of SWNT digital electronics to achieve higher transistor density and more logic functions per area have been under active investigation [44–47].

In the application of macroelectronics, SWNT networks are considered as excellent materials for thin-film transistors (TFTs) due to their superior electrical performance, reliability, flexibility, and transparency [48–61]. A variety of methods to achieve pure, high-density, high-semiconducting, and highly uniform SWNT networks have been developed [48–50, 52, 54, 56, 62–73]. TFTs have been fabricated based on these SWNT networks on both rigid and flexible substrates and have been demonstrated to drive various displays and sensors [55–57, 74–76], and even to work as building blocks for digital circuits and systems [33, 48, 53, 68, 71, 77–82]. In addition, the application of SWNTs has extended into printed electronics due to their printability, and has generated great impacts in achieving large-scale and low-cost macroelectronics [49, 83–89].

In this review, we will discuss all the significant progress in the development of SWNT-based electronics, including SWNT-based RF electronics, SWNT-based digital electronics, and SWNT-based macroelectronics, including printed electronics. In the last part, further development of SWNT-based electronics will be discussed.

2 SWNT RF Electronics

The extraordinary properties of SWNTs, such as nanoscale size, high mobility, small intrinsic capacitance, and high current-carrying capability, make SWNTs one of the excellent materials for RF electronics [1–5]. In this research field, the majority of the efforts are devoted to improving the current gain cut-off frequency (f_t) and the maximum oscillation frequency (f_{max}) of SWNT RF transistors which are important for future circuit-level applications [6–18]. Recently, the RF performance of SWNT transistors has been advanced to 70 GHz which is ready for practical applications [11].

2.1 SWNT RF Transistors Based on CVD-Aligned Nanotubes

Arrays of aligned SWNTs are one existing form of the nanotubes used as the channel materials for RF transistors [10, 14–16]. Chemical vapor deposition (CVD) is a widely used method to produce aligned SWNT arrays [10, 90–92]. The density of such aligned nanotube arrays can be as high as 130 nanotubes/ μm by carefully engineering the catalyst and controlling the synthesis conditions [10]. The CVD-synthesized SWNT arrays are a mixture of semiconducting and metallic nanotubes, and the semiconducting purity of such CVD-aligned SWNT with high density is usually $\sim 60\%$. However, these nanotube arrays can be directly used for RF transistors. Unlike digital electronics which require an extremely high current on/off ratio, a high current on/off ratio is not a necessity for RF electronics.

Kocabas et al. are one group of pioneers who reported SWNT RF transistors based on CVD-aligned SWNTs [15]. Figure 1a presents their schematic cross-sectional illustration of the SWNT RF transistor layout. The density of the CVD-aligned SWNTs is 2–5 nanotubes/ μm , and the channel length (L) is 700 nm. Their device layout, which utilizes a double-channel configuration (two gate electrodes and two drain electrodes surrounding a drain electrode), is one of the two commonly used device structures for SWNT RF electronics. However, the drawback of this device structure is that there exist either un-gated channel regions or overlapped gate-to-source/drain regions which adversely affect the RF performance. Figure 1b

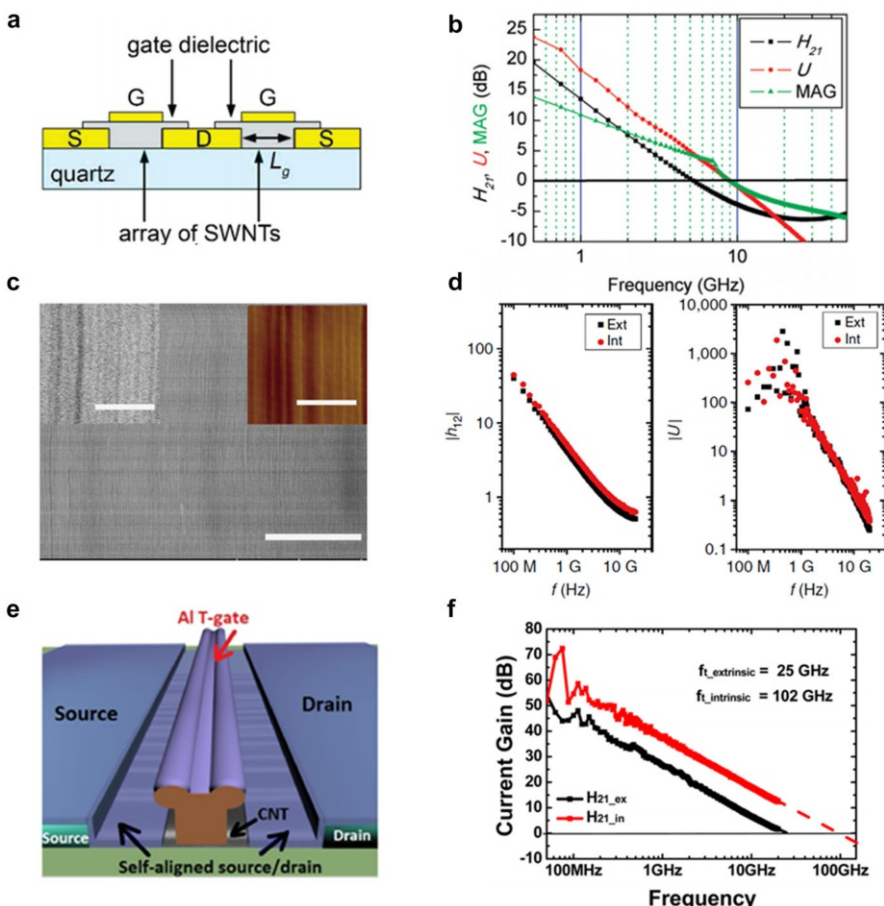


Fig. 1 **a, b** Schematic cross-sectional illustration of the SWNT RF transistors, and the corresponding frequency response, respectively. Adapted with permission from Ref. [15]. Copyright (2009) American Chemical Society. **c, d** SEM and AFM images of the high-density SWNT arrays on a sapphire surface, and the corresponding frequency response of the transistors based on these high-density aligned SWNTs, respectively. Adapted with permission from Ref. [10]. Copyright (2015) Nature Publishing Group. **e, f** Schematic of the CVD-aligned SWNT RF transistor with the self-aligned, self-oxidized, aluminum, T-shaped gate structure, and the corresponding frequency response, respectively. Adapted with permission from Ref. [14]. Copyright (2013) American Chemical Society

shows the RF performance of their SWNT RF transistor. According to the current gain (H_{21}), unilateral power gain (U), and maximum available gain (MAG) frequency response between 0.5 and 50 GHz, the f_t , which is the unity current gain frequency, and the f_{\max} , which is the unity power gain frequency, are ~ 5 and ~ 9 GHz, respectively.

One method to improve the RF transistors based on CVD-aligned SWNTs is to increase the SWNT density. Hu et al. successfully achieved SWNT arrays with a density of 130 nanotubes/ μm by using a Trojan catalyst [10]. Figure 1c shows SEM and AFM images of the as-grown high-density SWNT arrays on a sapphire surface. The RF performance of a typical SWNT transistor based on the high-density nanotube arrays with $L = 1200$ nm is shown in Fig. 1d. The extrinsic f_t and f_{\max} are 5 and 11 GHz, respectively. The intrinsic f_t and f_{\max} after device de-embedding, which would remove only the parasitics from the bonding pads without removing the capacitances associated with the gate, and reveal the performance of RF transistors achievable for practical applications, is 7 and 14 GHz, respectively. These RF transistors have similar device structure and RF performance as those reported by Kocabas et al. [15] but with a much larger channel length, indicating that one can achieve better RF performance by increasing the aligned nanotube density.

Another method to improve the RF transistors based on CVD-aligned SWNTs is to use a self-aligned gate structure. A self-aligned, self-oxidized, aluminum, T-shaped gate structure has been developed, as is shown in Fig. 1e [14]. This self-aligned, self-oxidized, aluminum, T-shaped gate structure has the advantages of reducing the gate parasitic capacitance, decreasing the gate resistance, scaling down the channel length, and offering optimized gate control. With this gate structure, the channel length of SWNT RF transistors has been scaled down to ~ 140 nm, and the thickness of the gate dielectric (self-oxidized Al_2O_3) has been reduced to 2–4 nm. The RF performance of these CVD-aligned SWNT transistors with a nanotube density of ~ 5 nanotubes/ μm is shown in Fig. 1f. The extrinsic f_t is as high as 25 GHz, and the intrinsic f_t after intrinsic de-embedding, which would remove the parasitics from both the bonding pads and the fringe capacitances associated with the gate, and reveal the upper-limit performance of the material's properties, is ~ 100 GHz. The f_{\max} is ~ 9 GHz. One can find that the f_t of these transistors with a self-aligned gate structure has been greatly improved compared with those without a self-aligned gate structure. The f_{\max} does not show significant improvement due to the low semiconducting purity of CVD-aligned SWNTs. Ding et al. also developed a similar self-aligned gate structure for single-nanotube transistors, and also demonstrated improved RF characteristics [93].

2.2 SWNT RF Transistors Based on Nanotube Networks

SWNT networks can also be used to make RF transistors. In comparison with CVD-aligned SWNT arrays, SWNT networks are usually formed by dispersing pre-separated SWNT solutions onto target substrate. The advantages of SWNT networks are that the SWNTs could be of much higher semiconducting purity than the CVD-aligned SWNTs, which helps the f_{\max} of the RF transistors. In addition, the

diameter distribution of SWNTs could also be engineered to achieve the optimal diameter range for RF transistors. However, unlike aligned SWNT arrays where the charge transport is electrically continuous and has an independent pathway, the charge transport in SWNT networks is based on percolation transportation. The tube-to-tube junctions will limit the maximum carrier mobility achievable, which limits both the f_t and f_{max} of RF transistors. However, SWNT networks still provide an important platform to investigate the RF performance of SWNTs, and researchers have demonstrated RF transistors based on SWNT networks [7, 8, 13, 17, 18].

The effects of SWNT semiconducting purity and diameter distribution on the performance of RF transistors based on SWNT networks have been investigated systematically [17, 18]. Cao et al. applied the excellent self-aligned, self-oxidized, aluminum, T-shaped gate structure to a variety of SWNT networks for the investigations, as schematically shown in Fig. 2a. Figure 2b, c shows the extrinsic and intrinsic current gain frequency response and power gain frequency response of RF transistors based on SWNTs with 99.99% semiconducting purity, respectively [17]. The extrinsic f_t and f_{max} are 22 and 19 GHz, respectively, and after device deembedding, the intrinsic f_t and f_{max} are 28 and 25 GHz, respectively. The RF performance is better than that based on SWNT networks with lower semiconducting purity, indicating the importance of achieving ultrahigh semiconducting purity separation of SWNTs for RF applications. In addition, Cao et al. also investigated the effects of diameter distribution [18]. Figure 2d shows the diameter-separated SWNT solution which has a tight diameter distribution and an average diameter of ~ 1.6 nm. The RF performance of these transistors based on the diameter-separated SWNTs are shown in Fig. 2e, f. The f_t and f_{max} are 23 and

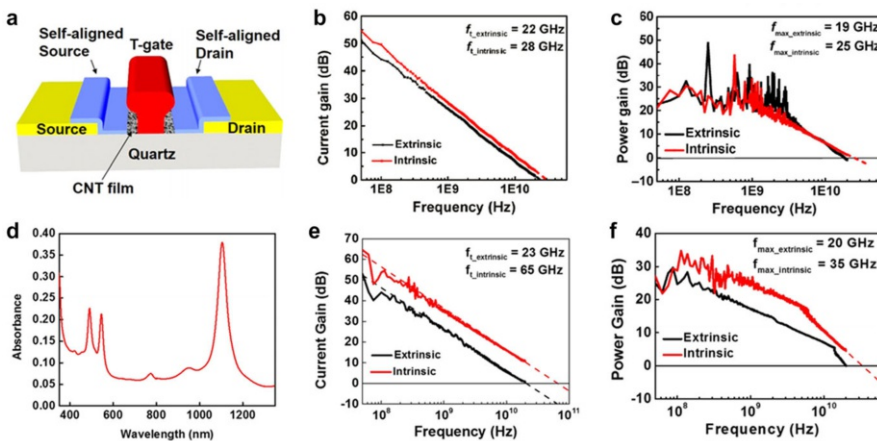


Fig. 2 **a** Schematic of the RF transistors based on SWNT networks. Adapted with permission from Ref. [18]. Copyright (2016) American Institute of Physics. **b, c** Current gain frequency response and power gain frequency response of RF transistors based on ultrahigh-purity semiconducting SWNTs, respectively. Adapted with permission from Ref. [17]. Copyright (2016) Springer. **d–f** Optical absorbance spectrum of the diameter-separated SWNTs, the current gain frequency response, and the power gain frequency response, respectively. Adapted with permission from Ref. [18]. Copyright (2016) American Institute of Physics

20 GHz before de-embedding, and are 65 and 35 GHz after intrinsic de-embedding, respectively. The RF performance is similar to that based on 99.99% ultrahigh-purity semiconducting SWNTs, indicating the necessity to achieve diameter separation for SWNT RF electronics.

We note that the superior RF performance achieved with SWNT networks even outperforms the best RF transistors based on CVD-aligned SWNTs, suggesting that SWNT networks are a valuable platform for nanotube RF electronics.

2.3 SWNT RF Transistors Based on Aligned Pre-separated SWNTs

Based on the discussions above, CVD-aligned SWNTs have the advantages of free tube-to-tube junctions and high-density while suffering from low semiconducting purity and degraded output resistance. In comparison, SWNT networks have the advantages of high semiconducting purity and engineered diameter distribution, while having the disadvantages of tube-to-tube junctions and low density. The best platform for SWNT RF transistors is to use SWNTs which go through the process of post-synthesis sorting and assembly, combining the advantages of CVD-aligned SWNTs and SWNT networks together.

Le Louarn et al. reported using a dielectrophoresis (DEP) assembly method to achieve aligned SWNTs for the RF transistors [12]. The transconductance increased by a factor of 2.5 compared with their previous work using SWNT networks, and the de-embedded f_t was 30 GHz. However, their SWNTs still suffered from a low semiconducting purity (~99.6%), and also achieved aligned SWNTs using the DEP assembly method [9]. Their RF transistors showed a big improvement for SWNT RF electronics. With a channel length of 100 nm, the extrinsic f_t and f_{max} were 7 and 15 GHz, respectively. The intrinsic f_t and f_{max} were 153 and 30 GHz, respectively, using an intrinsic de-embedding structure. However, the f_{max} of the RF transistors is still far below the f_t , which limits the highest frequency of their SWNT RF transistors in practical applications since a power gain is needed for real applications.

Recently, significantly improvement of the SWNT RF transistors has been achieved by the combined use of well-aligned, ultrahigh-purity semiconducting (>99.99%), high-density SWNTs and our self-aligned, self-oxidized, aluminum, T-shaped gate structure [11]. The well-aligned, ultrahigh-purity semiconducting, high-density SWNTs are achieved by dose-controlled, floating evaporative self-assembly (DFES) of poly[(9,9-diocetylfluorenyl-2,7-diyl)-*alt-co*-(6,60-(2,20-bipyridine))] (PFO-BPy) separated SWNTs. Figure 3a shows the SEM image of one channel region of a typical SWNT RF transistor. The T-shaped gate, self-aligned source and drain electrodes, and aligned PFO-BPy-sorted SWNTs underneath are clearly demonstrated. The RF performance of these SWNT RF transistors are shown in Fig. 3b, c. The extrinsic f_t and f_{max} of these transistors are both ~40 GHz. The intrinsic f_t and f_{max} are 80 GHz and 70 GHz with device de-embedding, and 100 GHz and 70 GHz with intrinsic de-embedding, respectively. The RF performance exceeds all previously reported SWNT RF transistors, especially for the f_{max} , which is at least twice that of the best previously reported results. The SWNT RF

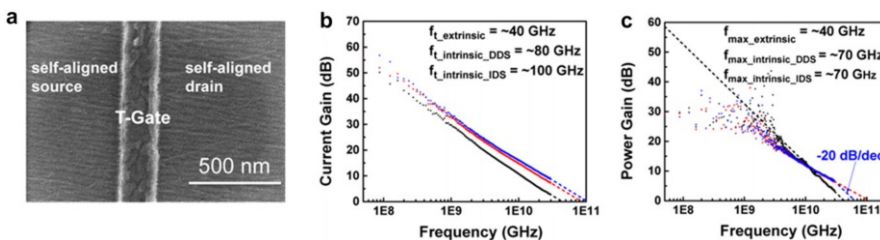


Fig. 3 **a** SEM image of a channel region of the RF transistor based on PFO-BPy-separated aligned SWNTs. The T-shape gate, self-aligned source and drain, and aligned polyfluorene-sorted SWNTs underneath are clearly demonstrated. **b, c** Current gain frequency response, and power gain frequency response, respectively. Adapted with permission from Ref. [11]. Copyright (2016) American Chemical Society

transistor advances the state-of-the-art of SWNT RF electronics, and may find broad applications for signal amplifications, wireless communications, and future flexible/wearable electronics.

2.4 Linearity Performance of SWNT RF Transistors

One great advantage of SWNT RF transistors is their linearity. Baumgardner et al. theoretically predicted that a carbon nanotube (CNT)-based field-effect transistor with ohmic contacts, quantum capacitance, and ballistic single-subband transport is inherently linear [19]. However, achieving the above conditions are difficult in realistic devices. Mothes et al. later used simulations to show that the requirements for high-linearity SWNT transistors could be relaxed with a moderate Schottky barrier at the source contact [20].

In addition to the simulation efforts, the linearity performance of SWNT RF transistors can be measured using single-tone and two-tone tests. Cao et al. have measured the linearity performance of the best SWNT RF transistors based on aligned PFO-BPy-separated SWNTs [11]. Figure 4a shows the schematic of the measurement setup commonly used for single-tone and two-tone tests [17]. In the single-tone test, they apply an RF single of a fixed frequency to one input of the measurement setup with various powers, and measure the power of the fixed frequency component at the output. A 1-dB gain compression point ($P_{1\text{ dB}}$), which defines the power level that causes the gain to drop by 1 dB from its small signal value, can be used to characterize the linearity. Figure 4b shows the results of the single-tone test. The $P_{1\text{ dB}}$ is 13–14 dBm. In the two-tone test, they apply two RF singles with a small frequency difference to the two inputs of the measurement setup, and measure the powers of the fundamental frequency term and the third-order frequency term at the output. Input third-order intercept point (IIP_3) is defined as the input power level which causes the fundamental frequency term and the third-order frequency term to have the same output power level. Figure 4c shows the results of the two-tone test. IIP_3 is ~ 22 dBm at a frequency of 8 GHz. Further improvement of the linearity performance of SWNT RF transistors can be achieved by carefully engineering the gate dielectric and source/drain contacts.

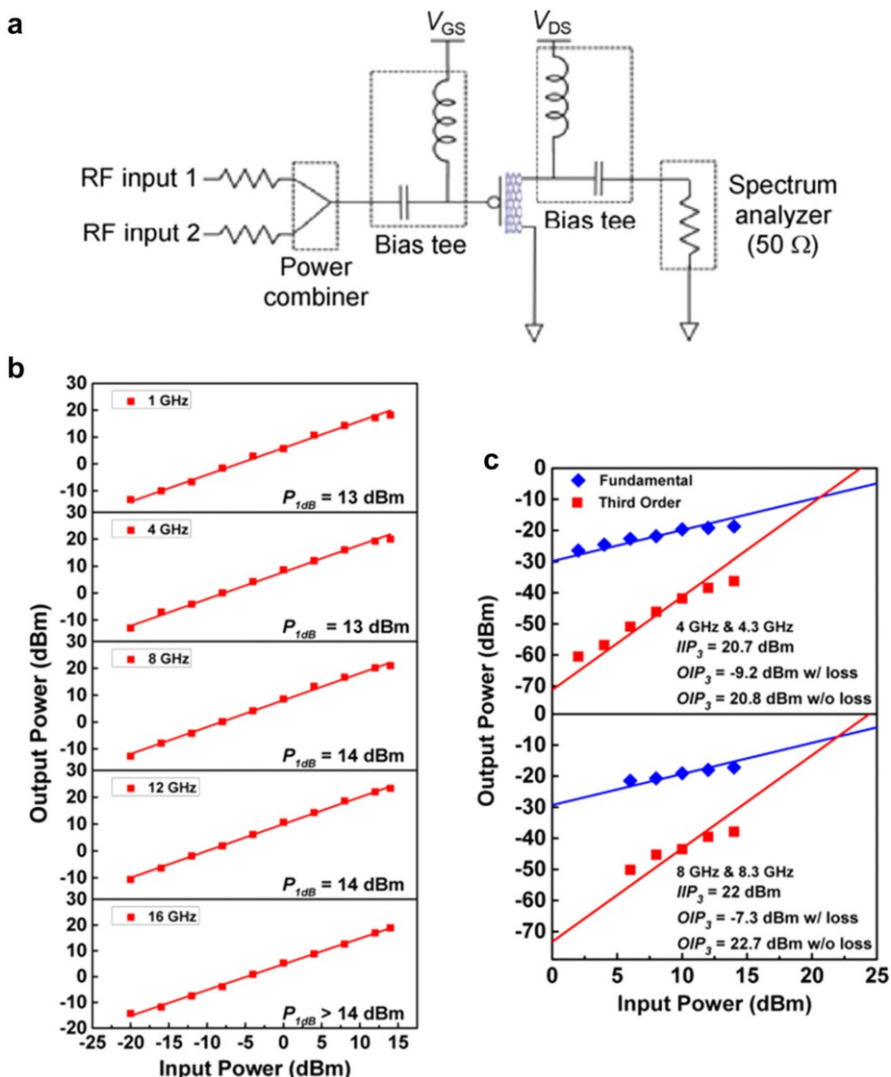


Fig. 4 **a** Schematic of the measurement setup for single-tone and two-tone tests. Adapted with permission from Ref. [17]. Copyright (2016) Springer. **b, c** Single-tone and two-tone test results for the RF transistors based on PFO-BPy-separated aligned SWNTs. Adapted with permission from Ref. [11]. Copyright (2016) American Chemical Society

2.5 Circuit Applications Based on SWNT RF Transistors

In addition to transistor-level investigation of SWNT RF transistors, research groups have integrated SWNT RF transistors into circuits for realistic applications [4, 14, 16, 21–23].

Kocabas et al. demonstrated a radio which utilized four SWNT RF transistors [22]. The circuit schematic, images, and frequency response are shown in Fig. 5a–c.

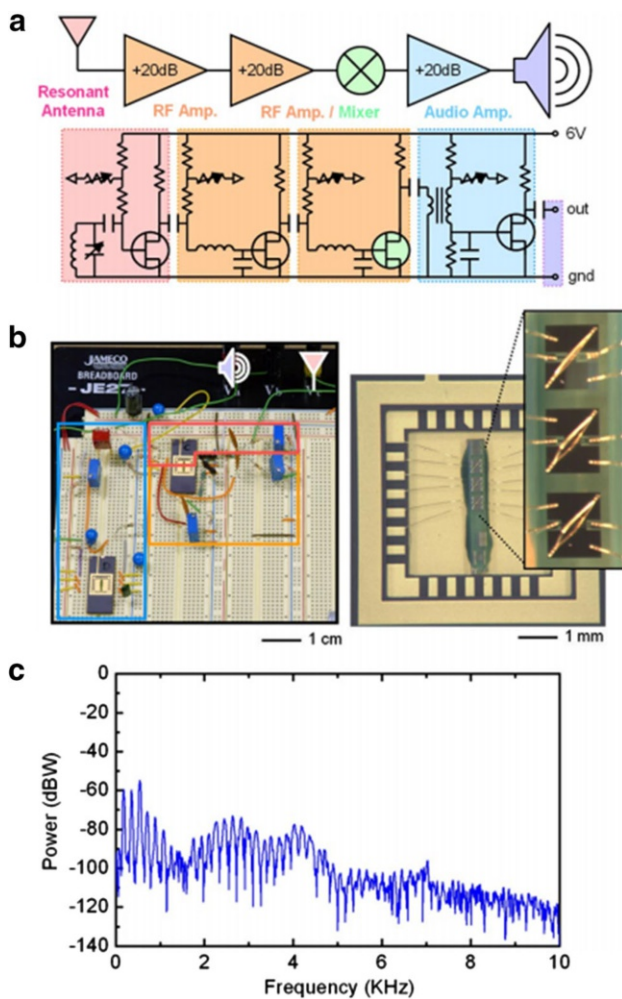


Fig. 5 **a** Block and circuit diagrams of a radio that uses SWNT transistors for the resonant antenna, two fixed RF amplifiers, an RF mixer, and an audio amplifier. **b** Image of the radio, with magnified views of SWNT transistor wire bonded into DIP packages. **c** Power spectrum of the radio output, recorded during a commercial broadcast of a traffic report. Adapted with permission from Ref. [22]. Copyright (2008) National Academy of Sciences of the United States of America

The radio could record a commercial broadcast of a traffic report. Rutherglen et al. and Jensen et al. also demonstrated components in a receiver built with SWNT RF transistors [4, 23]. These receivers represent the most complex circuits so far built with SWNT RF transistors. With the advancement of SWNT RF transistors, circuits and systems with more complex functions and higher operation frequencies are expected to be built. Considering that SWNTs have the inherent high linearity and could be made to be flexible, these circuits and systems may find broad applications for signal amplification, wireless communication, and wearable electronics.

3 SWNT Nanoelectronics

SWNTs, due to their exceptional intrinsic carrier mobility [5], high saturation velocity [94], and quasi-1D structure, may offer various advantages for future digital electronics. Furthermore, the quasi-ballistic transport property of SWNTs enables a lower energy delay product predicted to outperform silicon-based complementary metal–oxide–semiconductor (CMOS) technologies [24]. During the past few years, SWNT-based devices and circuits have been making progress in various aspects under intense research.

3.1 Single SWNT Transistor

With the progress in nanotube synthesis, researchers have the material platform and are making further steps to gain better comprehension of the electrical transport properties of the SWNT FETs. Due to the fact that the properties of individual nanotubes may vary strongly from one another, it is indispensable to fabricate a transistor with a single nanotube present in the channel to fully understand the transport properties of each nanotube. Since the report of the first individual SWNT FETs [25], the high current-carrying capacity in the quantum ballistic regime [2], the high carrier mobility in the diffusive regime [5], and the low leakage current [26] have all been investigated. Furthermore, researchers have also worked extensively to improve the device performance by carefully studying the ohmic contacts between SWNTs and the contact metal, optimizing the device structures, and scaling down the device dimensions.

Up to now, the superior intrinsic properties of SWNTs have been confirmed by single nanotube FETs. Javey and coworkers did pioneering work by demonstrating high-performance ballistic SWNT FETs using palladium (Pd) contacts, with the room-temperature conductance near the ballistic transport limit of $G_0 = 4e^2/h$ and the high current-carrying capability of 25 μA per tube [2]. Kim and co-workers developed a method to deduce the mean free path by studying the channel length dependence of the channel resistance, where they confirmed that the long mean free path of SWNTs is on the order of a millimeter [27]. To study the diffusive transport, Durkop et al. fabricated semiconducting SWNT FETs with ultralong channel lengths larger than 300 microns, and estimated the intrinsic SWNT mobility to be $10,000 \text{ cm}^2 \text{ V}^{-1} \text{ s}^{-1}$ at room temperature, which was the highest value for all known semiconductors at the time of study [5]. Weitz and coworkers demonstrated that transistors based on individual CNTs can achieve large transconductance (5 μS), small subthreshold swing (68 mV/dec), large on/off ratio (10^7), and good reliability of performance under ambient conditions simultaneously [28].

For future high-performance SWNT circuits, the scaling of SWNT FETs is inevitable to pack more transistors on the chip. Of all the scaling parameters, two dimensions are critical, i.e., the channel length (L_{ch}) and the contact length (L_c). Understanding the scaling behavior of both L_{ch} and L_c are crucial for the integration of SWNT FETs. The IBM group fabricated a series of transistors with channel length scaled from 3 mm to 15 nm on the same SWNT, and demonstrated that these

nanotube transistors maintained their performance without the presence of short-channel effects [29]. When L_{ch} is aggressively scaled, the on state performance improves significantly, potentially leading to a high-speed circuit. The SEM image, transfer (I_D - V_{LBG}), and output (I_D - V_{DS}) characteristics of these devices are shown in Fig. 6a–c. The 15-nm device has the shortest channel length and highest room-temperature conductance ($0.7 G_0$) and transconductance ($40 \mu\text{S}$). In a separate work, the same group further pushed the L_{ch} scaling, and demonstrated a sub-10-nm SWNT transistor [30]. The transistor outperforms the best competing silicon devices with more than four times the diameter-normalized current density ($2.41 \text{ mA}/\mu\text{m}$) at a low operating voltage of 0.5 V . In terms of contact length scaling, for large contact lengths ($>100 \text{ nm}$), some studies have suggested that sharp needle-like contacts are ideal, since transport between a metal and a nanotube occurs only at the contact edge [95, 96]. On the contrary, for contact length less than 100 nm , the IBM group applied the same strategy as in the L_{ch} scaling study, i.e., with multiple devices located on the same nanotube, to study the contact length scaling from 20 to 100 nm , and showed that L_c scaling affects the on state far more dramatically than the off state of a device [29]. Figure 6d–f shows the contact length dependence of the SWNT FET performance. To tackle the short contact length scaling effects, Cao et al. developed an end-bonded contact scheme that allows scaling the contacts to 10 nm and beyond without increasing contact resistance [31]. The molybdenum film acts as the source and drain for the FETs and reacts with the CNT to form a carbide contact. Figure 6g shows the schematic of such carbide contact. Figure 6h shows a false-colored SEM image of a set of transistors with such carbide contact, and Fig. 6i shows the corresponding transfer characteristics. The molybdenum nanotube end-bonded contact exhibited no Schottky barrier. Using the bonded contact method, a p-type SWNT transistor with sub-10-nanometer contact length was also fabricated, showing high performance of channel resistance below $36 \text{ k}\Omega$ and on current above $15 \mu\text{A}$ per tube. Recently, Qiu et al. at Peking University further scaled the gate length of single SWNT FETs down to $5\text{--}10 \text{ nm}$ [97]. Figure 6j, k shows the TEM images of the cross-sections of p-type and n-type transistors with a gate length of 10 nm , respectively. The transfer characteristics of the p-type and n-type transistors are shown in Fig. 6l. The p-type and n-type transistors exhibited nearly symmetric performance. In addition, the on-state current was as high as $17.5 \mu\text{A}$ for the p-type FET and $20 \mu\text{A}$ for the n-type FET at a relatively low bias of 0.4 V , demonstrating the potential of the SWNT FETs for low-power applications.

3.2 N-Type SWNT Transistors

In logic circuit applications, CMOS operation is highly preferable for the sake of various advantages including rail-to-rail swing, large noise immunity, and small static power consumption. Given the fact that SWNT transistors typically exhibit p-type behavior due to oxygen exposure [98], it is equally important to reliably convert nanotube devices into n types. One approach is to use low work function (Φ_M) metals as the contacts, in a way the Fermi level of the electrodes can be aligned with the conduction band edge of SWNTs, giving ohmic contacts for electron carrier transport. A variety of low work function metals have been

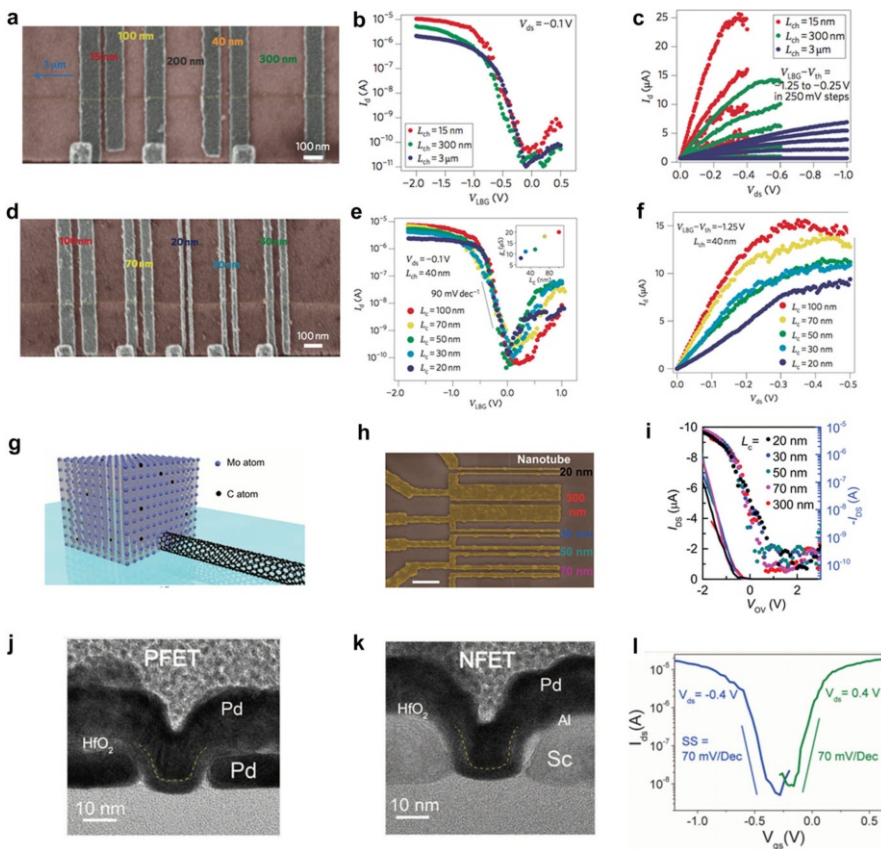
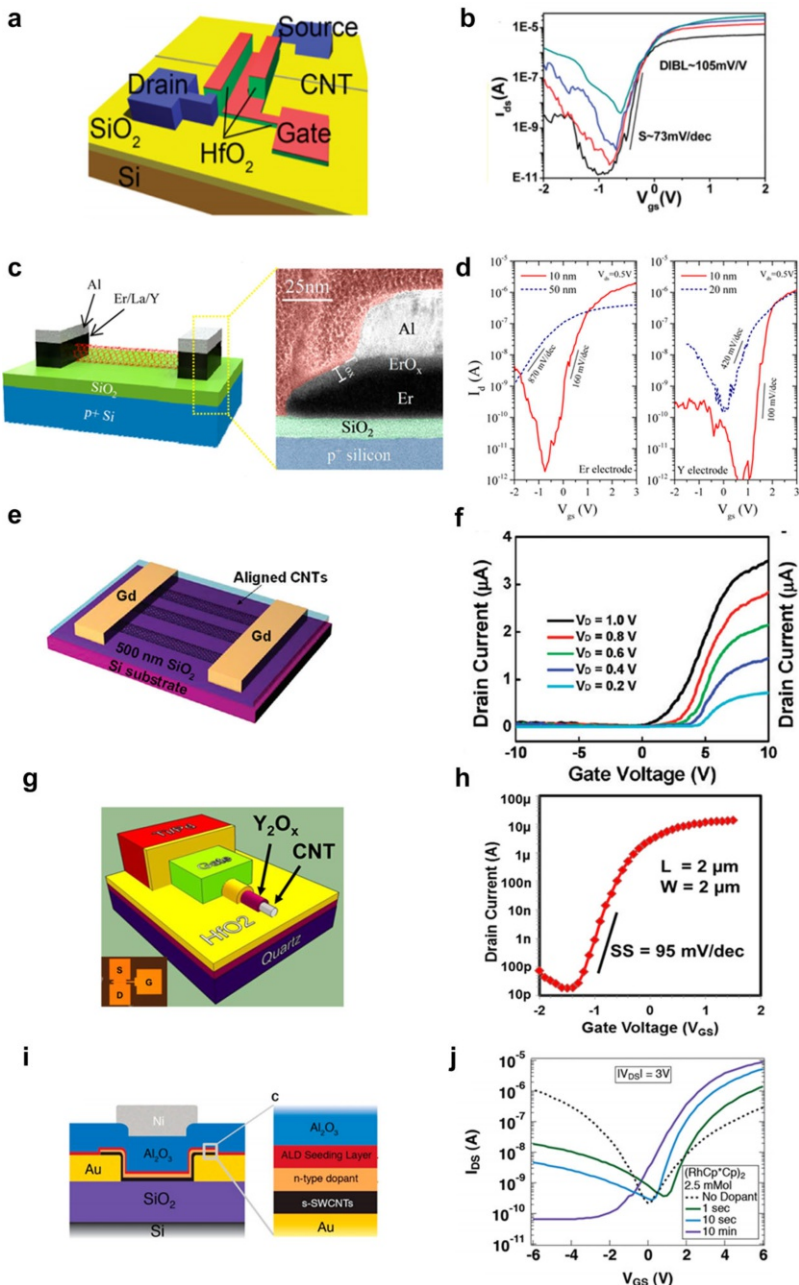


Fig. 6 Single nanotube transistor. **a–c** Effects of channel length scaling on nanotube transistor performance. **a** SEM image of a set of transistors on the same nanotube with different channel lengths. **b** Subthreshold $I_D - V_{LBG}$ curve from devices with channel lengths of ~ 15 nm, 300 nm, and 3 mm. **c** Output $I_D - V_{DS}$ characteristics of devices in (b). **d–f** Effects of contact length scaling on nanotube transistor performance. **d** SEM image of a set of transistors on the same nanotube with different contact lengths. **e** Subthreshold $I_D - V_{LBG}$ curve from devices with contact lengths of 100, 70, 50, 30, and 20 nm. Inset shows the dependence of g_m on L_c . **f** Output $I_D - V_{DS}$ characteristics of devices in (e). Adapted with permission from Ref. [29]. Copyright (2010) Nature Publishing Group. **g–i** Mo end-contacted SWNT transistors. **g** Schematics showing the SWNT is attached to the bulk Mo electrode through carbide bonds while the C atoms from the originally covered portion of the SWNT uniformly diffuse out into the Mo electrode. **h** False-colored SEM images of a set of transistors fabricated on the same nanotube, with L_c ranging from 20 to 300 nm. Scale bar 400 nm. **i** Collection of transfer characteristics from a set of Mo end-contacted single-nanotube transistors with different L_c plotted in both linear (lines, left axis) and logarithmic (symbols, right axis) scales with applied V_{DS} of -0.5 V. Adapted with permission from Ref. [31]. Copyright (2015) American Association for the Advancement of Science. **j, k** TEM images showing the cross-sections of a p-type FET and n-type FET; gate length 10 nm, channel length 20 nm. **l** Transfer characteristics (drain current I_{ds} versus gate voltage V_{gs}) of typical CMOS FETs fabricated on a single SWNT with a diameter of 1.3 nm at a drain bias $V_{ds} = \pm 0.4$ V. The solid blue and olive curves represent SWNT p-type and n-type FETs, respectively. **j–l** Adapted with permission from Ref. [97]. Copyright (2017) American Association for the Advancement of Science.

investigated, including gadolinium [36], yttrium [37], scandium [38], and erbium [39]. Ding et al. used yttrium as the source and drain contacts for top-gate FETs

with a single SWNT as the channel, and demonstrated n-type transistors with subthreshold swing (SS) of 73 mV/dec and drain-induced barrier lowering (DIBL) of 105 mV/V, as shown in Fig. 7a, b [37]. Shahjerdi et al. performed a thorough experimental study of n-type contacts for SWNT FETs based on erbium (Er,



◀ Fig. 7 N-type transistors from Ref. [37, 39–41, 43]. Schematic (**a**, **c**, **e**, **g**, **i**) and characteristics (**b**, **d**, **f**, **h**, **j**) of low work function metal, low work function metal aligned SWNT array, gate dielectric doping, and chemical doping N-type transistors, respectively. **a**, **b** Adapted with permission from Ref. [37]. Copyright (2009) American Chemical Society. **c**, **d** Adapted with permission from Ref. [39]. Copyright (2013) American Chemical Society. **e**, **f** Adapted with permission from Ref. [40]. Copyright (2011) American Chemical Society. **g**, **h** Adapted with permission from Ref. [41]. Copyright (2014) American Chemical Society. **i**, **j** Adapted with permission from Ref. [43]. Copyright (2016) American Chemical Society

$\Phi_M = 3.0$ eV), lanthanum (La, $\Phi_M = 3.5$ eV), and yttrium (Y, $\Phi_M = 3.1$ eV) [39]. Figure 7c shows the schematic of the bottom gate SWNT n-type FET (n-FET) and the corresponding high-resolution TEM image, which gives details of the Er contact with the oxidation layer and the Al encapsulation layer. The results suggest that by employing Er contacts, significant improvements in device characteristics can be achieved. Figure 7d shows the effect of partial oxidation of Er (left) and Y (right) electrodes on device performance. Due to rapid oxidation, the device performance degrades with increasing contact layer thickness. Controlling process parameters such as low base pressure and high deposition rate can help mitigate the oxidation effects. The electrical characteristics of n-FET devices with Er electrodes were shown to remain stable upon storage in air by employing a hydrophobic polymer deposited at 150°C. It is worthwhile to note that the technique of applying low work function metal to achieve n-type transistors can be applied to both a single nanotube and also an array of aligned tubes. A small work function metal gadolinium (Gd) with a work function of ~3.1 eV has been used by Wang et al. in aligned nanotube transistors [40]. Figure 7e shows the schematic of Gd used as n-type contact in air-stable, n-type, aligned nanotube transistors. The transistor transfer characteristics are shown in Fig. 7f, and the linear output characteristics indicate good ohmic contacts between SWNTs and the Gd contacts.

Another approach is to take advantage of the gate dielectric to give rise to n-type doping in SWNTs. Liyanage et al. applied low work function metal oxides (Y_2O_3) as the gate dielectrics to SWNT FETs [41]. This novel and very-large-scale-integrated (VLSI)-compatible doping technique enables wafer-scale fabrication of high performance n-type SWNT transistors. The partially oxidized yttrium gives rise to n-type doping in SWNTs. Figure 7g shows the schematic of the Y_2O_3 gate dielectric SWNT FETs. From Fig. 7h, we can see the transistors demonstrate good n-type behavior with high performance of a large on current, high on/off ratio, and small subthreshold voltage swing.

The third approach is to apply chemical and electrostatic doping methods to provide excess electrons to promote electron tunneling and conduction [42]. Recently, Geier et al. reported the controlled n-type doping of SWNT thin-film transistors with a solution-processed pentamethylrhodocene dimer [(RhCp*^{*}Cp)₂] [43]. Its molecular-scale thickness enables large-area arrays of top-gated, high-yield, n-type SWNT transistors, as shown in Fig. 7i. Figure 7j shows the transfer curves for the top-gated SWNT TFTs for different exposure times, which shows the conversion of the top-gated SWNT TFTs into n-types under 10-min dopant exposure. The air-stable n-type dopant study will thus facilitate ongoing efforts to realize high-density SWNT integrated circuits.

3.3 Transistors and Digital Circuits Based on Aligned SWNTs

In spite of the great potential of SWNTs demonstrated by single SWNT transistors, in terms of commercial applications, the device-to-device variation can undermine their benefits. Different factors can contribute to the variations, such as chirality, oxygen adsorption, and defects. Multiple aligned SWNTs within the same device channel can average out the SWNT properties and greatly reduce device variation. Another advantage of aligned nanotube arrays is the simultaneous contribution to the device current by multiple SWNTs, which can multiply the device conductance. CVD-grown SWNTs on crystalline substrates like quartz and sapphire can yield highly aligned nanotubes. Using the massive aligned nanotube arrays grown by CVD on sapphire, our group reported a high yield and registration-free nanotube-on-insulator approach, analogous to the silicon-on-insulator approach adopted by the semiconductor industry [32]. To overcome the drawbacks of small sample size, large millimeter-scale channel length, and unavailability of controlled doping, our group reported a full-wafer scale CMOS analogous fabrication with SWNT transistors feature size down to 0.5 μm [33]. After nanotube synthesis and transfer, the SWNT transistors employ the top-gate structure, and the metallic nanotubes inside the channel regions are removed by electrical breakdown to improve the current on/off ratio. P-type SWNT transistors are converted to n-type by potassium and electrostatic doping. Combining all the advantages, CMOS inverters, NAND, and NOR gates based on aligned SWNT array transistors are demonstrated in Fig. 8a. To demonstrate the feasibility of SWNT FET circuits at a highly scaled

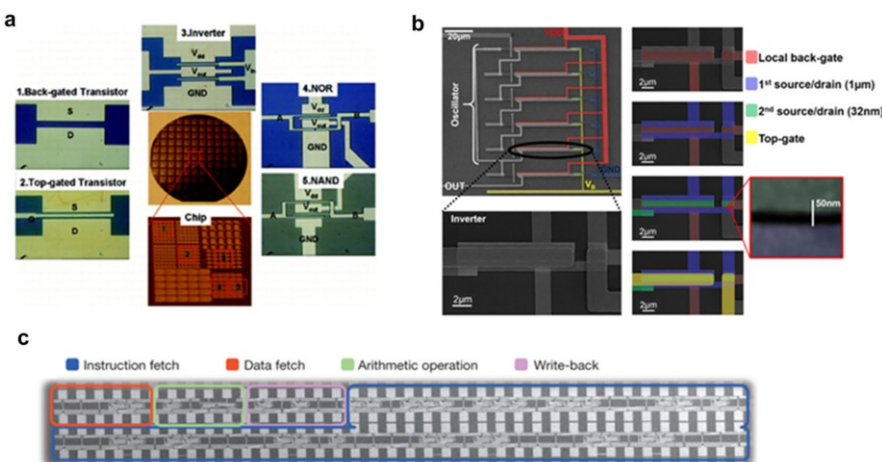


Fig. 8 Transistors and digital circuits based on aligned nanotubes. **a** Optical images of SWNT transistors and circuits built on a 4-inch Si/SiO₂ wafer: 1 back-gated transistor; 2 top-gated transistor; 3 CMOS inverter; 4 NOR logic gate; 5 NAND logic gate. Adapted with permission from Ref. [33]. Copyright (2009) American Chemical Society. **b** SEM of an integrated SWNT FET IR sensor and interface circuit (*left*), along with processing steps (*right*). Adapted with permission from Ref. [34]. Copyright (2014) American Chemical Society. **c** SEM of the SWNT computer. Adapted with permission from Ref. [35]. Copyright (2013) American Association for the Advancement of Science

technological node, Shulaker et al. at Stanford reported the first VLSI-compatible approach for SWNT FETs with devices as small as sub-20-nm channel lengths [34]. They demonstrated inverters functioning at 1 MHz and a fully integrated SWNT FET infrared (IR) light sensor and interface circuit at 32-nm channel length. The SEM images of the integrated SWNT FET IR sensor and interface circuit are shown in Fig. 8b. This demonstration is one step closer to highly scaled SWNT FET circuits as a digital VLSI technology.

In terms of the circuit complexity, the first SWNT computer has been demonstrated by the same Stanford group as an important milestone in the practical application of SWNT digital electronics [35]. The SWNT computer runs an operating system and achieves multitasking of counting and integer sorting simultaneously. The SEM of the computer comprising of instruction fetch, data fetch, arithmetic operation, and write back system is shown in Fig. 8c. Despite the fact that the first computer still has many aspects to improve, such as the PMOS-only logic and the low clock speed, the experimental demonstration of a SWNT computer is a breakthrough in the next generation of SWNT-based, highly energy-efficient electronic systems.

3.4 Large-scale Assembly of SWNTs

The materials challenges in the alignment and placement of SWNTs, as well as in the removal of metallic SWNTs, have prevented SWNTs from fully achieving their exceptional electronic properties. Joo et al. reported a novel yet simple method to deposit aligned semiconducting SWNTs on substrates via a dose-controlled, floating evaporative self-assembly (FESA) method [99]. The process starts from sorted SWNT solution with semiconducting purity of more than 99.9%. When dropping the solvent with semiconducting SWNT solution at a certain dose onto the water surface, the dose-covered air/water interface will spread out and reach the substrate. The solvent of the SWNT solution will evaporate, and SWNTs will stay on the substrate and align with the air/water interface. Repeatedly applying the solution dose and pulling out the receiving substrate at optimized speeds can give stripes of aligned nanotubes on the substrate. The FESA method can give high-density, aligned SWNTs with high semiconducting purity and few defects. The FESA steps are illustrated in Fig. 9a. The density of the assembled aligned tubes can be as high as 40–50 tubes/ μm . Based on the FESA platform, Grady et al. studied superior back-gated FET performance fabricated from these SWNT arrays, and achieved high on-conductance and a high on/off ratio simultaneously [100]. The schematic of the gate structure and the SEM image of the device channel area are shown in Fig. 9b, c, respectively. For a channel length (L_{ch}) of 240 nm, the on-conductance (G_{on}) per width and an on/off ratio ($G_{\text{on}}/G_{\text{off}}$) are as high as $261 \mu\text{S}/\mu\text{m}$ and 2×10^5 , respectively (Fig. 9d), and for an L_{ch} of 1 μm , the corresponding performances are $116 \mu\text{S}/\mu\text{m}$ and 1×10^6 , respectively (Fig. 9e).

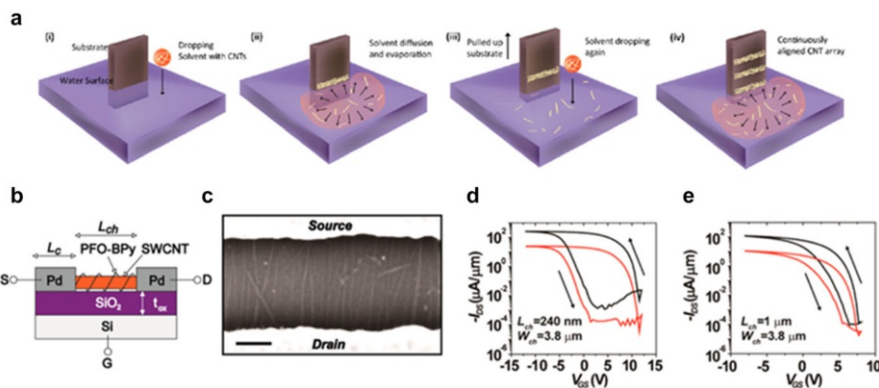


Fig. 9 Large-scale assembling of CNTs. **a** Schematic illustration of the iterative (FESA) process used to fabricate aligned nanotubes-SWNTs driven by the spreading and evaporation of controlled doses of organic solvent at the air/water interface. Adapted with permission from Ref. [99]. Copyright (2014) American Chemical Society. **b** Schematic of SWNT FET architecture. **c** Top-down SEM image of SWNT spanning Pd electrodes of a 240-nm L_{ch} SWNT FET (scale bar 100 nm). **d**, **e** Transfer characteristics at $V_{DS} = -1$ V (black) and -0.1 V (red) for a champion SWNT FET of $L_{ch} = 240$ nm and $W_{ch} = 3.8$ μ m in **d** and $L_{ch} = 1070$ nm and $W_{ch} = 3.8$ μ m in **e**. Adapted with permission from Ref. [100]. Copyright (2014) American Chemical Society

3.5 3D Integration and Novel Structures of SWNT Transistors

In order to increase the transistor density and/or improve the SWNT FET performance, different integration methods and gate structures have been proposed and demonstrated. Wei et al. reported a scalable integration process for monolithic 3D integrated circuits (3D ICs) using SWNT FETs [44]. In their approach, SWNT FETs with high I_{ON}/I_{OFF} can be flexibly placed on arbitrary layers of monolithic 3D ICs, and connected using conventional vias to build fully complementary monolithic 3D logic gates and multi-stage logic circuits. The monolithic 3D logic gates can operate correctly over a range of supply voltages from 3 to 0.2 V, which shows the robustness of the method.

Constructing ICs along a single SWNT is another novel idea to minimize the effect of variation in different nanotubes and shows SWNT FETs can be used as a building block for electronics [101–104]. In 2001, Derycke et al. reported both p- and n-type transistors on the same nanotube for the first complementary nanotube-based inverter logic gate [102]. In 2006, Chen et al. demonstrated a CMOS 5-stage ring oscillator built entirely on a single 18- μ m-long SWNT [103]. Later in 2014, Pei et al. reported an innovative modularized construction of ICs on individual CNTs [104]. In their work, pass-transistor-logic style 8-transistor (8-T) units were built and used as multifunctional function generators. The units have good tolerance to inhomogeneity in the CNTs and were used as building blocks for general ICs. An 8-bits BUS system used to transfer data between different systems in a computer was constructed.

Other possible novel SWNT gate structures with potential performance advantages at the circuit level including FinFETs [45] and gates all around [46]

have also been analyzed and studied. Furthermore, combining SWNT FETs with other semiconductors such as silicon to achieve CMOS integration [47] shows the promising future for high-performance digital logic applications.

4 SWNT Macroelectronics

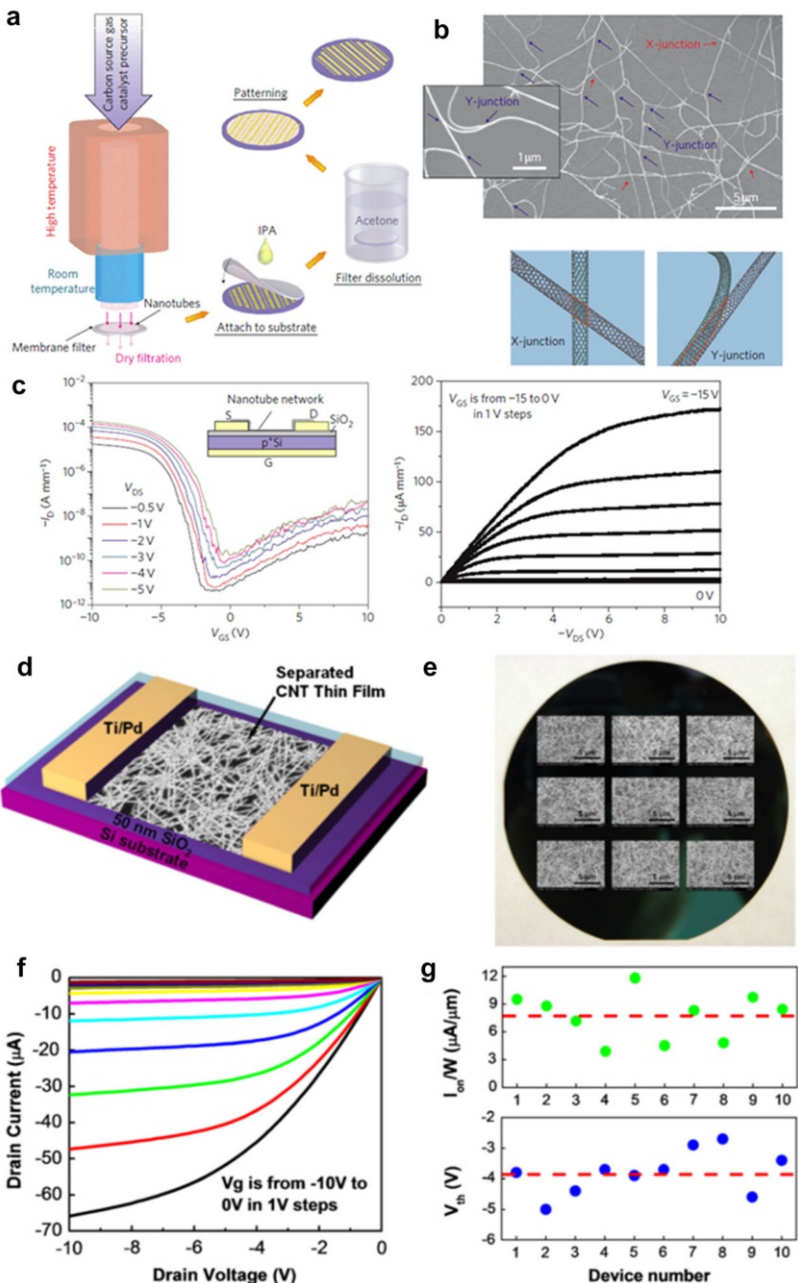
4.1 Fabricated SWNT TFTs

The use of SWNT networks present a highly promising path for the realization of high-performance TFTs for macro and flexible electronic applications. Using SWNT random networks for TFTs has many significant advantages: SWNT thin films are mechanically flexible, optically transparent, and can be prepared using solution-based room-temperature processing, all of which cannot be provided by amorphous and polysilicon technologies [48–61]. The most common assembly methods for random nanotube networks including direct CVD growth [48, 62], dry filtration [54], evaporation assembly [63], spin coating [64–66], drop coating [56, 67–71], and printing [49, 50, 52, 72, 73].

4.1.1 Gaseous Phase-Based SWNT TFTs

As-grown nanotube networks usually contain both metallic and semiconducting nanotubes [105, 106], which leads to a trade-off between charge carrier mobility (which increases with greater metallic tube content) and on/off ratio (which decreases with greater metallic tube content). Many research efforts have been devoted to the successful realization of high-performance FETs comprised of semiconducting-enriched SWNT random networks based on CVD synthesis [48, 53, 90, 107]. Medium-scale SWNT thin-film integrated circuits on flexible substrates have been demonstrated by Rogers' group [48]. For this method, growth substrates decorated with metal catalysts (Fe particles or ferritin) were placed in a furnace at elevated temperatures (>800 °C). Then, a precursor containing carbon feedstock, such as methane, ethylene, isopropyl alcohol, etc., was introduced into the growth chamber for the dissociation of hydrocarbon molecule from the feedstock. The hydrocarbon molecules then facilitated the growth of the CNTs on the catalysts [48, 90]. Although the flexible SWNT TFTs and circuits shows promising electrical performance, the existence of metallic nanotubes degrades the on/off ratio of the devices.

Ohno's group introduced a floating catalyst CVD technique with monoxide (CO) as the carbon source, and achieved high-performance flexible nanotube TFTs and D-flip-flop circuits [54]. In Fig. 10a, the nanotubes grown by plasma-enhanced CVD were collected through a simple gas phase filtration process [53, 54, 108]. The density of the nanotubes can be easily controlled by the collection time. The SWNTs were subsequently transferred onto the device substrate by dissolving the filter in acetone. The transferred CNT film has a network morphology consisting of rather straight and long nanotubes, ~ 10 μm in length, as shown in the SEM images in Fig. 10b. The advantage of utilizing as-grown SWNTs directly for fabrication of



devices is that there are more Y-type junctions between the nanotubes than the X-junctions, which can result in a higher mobility of the transistors [54]. Figure 10c shows the transfer and output characteristics of a bottom-gate TFT device. The device showed p-type characteristics with a high on/off ratio (6×10^6) and an

◀Fig. 10 **a** Schematic diagram showing CNT growth, collection by filter, transfer, and patterning. **b** SEM images of a CNT network on a Si/SiO₂ substrate after transfer. **c** Transfer and output characteristics of fabricated bottom-gate TFT based on the nanotube network shown in (b). **a–c** Adapted with permission from Ref. [54]. Copyright (2011) Nature Publishing Group. **d** Schematic diagram showing the configuration of a CNT TFT in which the CNT network is deposited using separated semiconducting nanotube solution. **e** SEM images of an SWNT random network captured at different regions of a wafer after SWNT deposition. **f** Output characteristics of an SWNT TFT. **g** Statistical study of on-state current density and threshold voltage of as-fabricated SWNT TFTs. **d–g** Adapted with permission from Ref. [56]. Copyright (2009) American Chemical Society

effective device mobility of $35 \text{ cm}^2 \text{ V}^{-1} \text{ s}^{-1}$. The transfer process of the CVD grown SWNTs is carried out at room temperature, which is desirable for the fabrication of flexible electronics.

4.1.2 Solution-Based SWNT TFTs

In addition to CVD-based SWNT random network electronics, there are many approaches in the area of solution-based SWNT electronics [55–57, 68, 70, 71, 109]. About one third of the as-grown SWNTs are metallic nanotubes [110], which can cause significant leakage of current when the transistors are in the off state and result in a low on/off ratio [111–114]. Thus, the metallic nanotubes should be selectively removed, and high-purity semiconducting nanotubes are desired for high-performance transistors. Separation between metallic and semiconducting tubes, and even separation of single chirality nanotubes have been achieved by a variety of methods, such as density gradient ultracentrifugation (DGU) [110, 113], gel chromatography [115], and DNA-based chromatographic purification [116].

SWNT networks can be obtained by spin coating/dropping the nanotube solution onto a spinning substrate [64]. The drawback with this method is scalability because the deposited SWNTs often align along different orientations depending on the location on the substrate, which leads to wafer-scale fabrication with low uniformity. Drop coating is found to be a more promising solution-based SWNT assembly method for large-scale applications of nanotube TFTs. In this method, the substrates are first functionalized with amine-containing molecules, which are effective adhesives for SWNTs. By simply immersing the substrate into the nanotube solution, highly uniform nanotube networks can be obtained throughout the wafer, enabling the fabrication of nanotube TFTs with high yield and small device-to-device variation [56, 68, 70, 71].

Many research groups have systematically studied electrical performance of SWNT TFTs based on the high-purity semiconducting SWNT solution [7, 56, 63, 68, 79, 109]. The device characteristics of SWNT TFTs are heavily dependent on the nanotube density [69, 70] and channel length [71, 117]. SWNT TFTs with mobility greater than $100 \text{ cm}^2 \text{ V}^{-1} \text{ s}^{-1}$ have been reported [117–119], which exceed the mobility of amorphous and organic FETs by at least two orders of magnitude. The fact that such high-mobility SWNT TFTs can be fabricated using a facile solution-based process and processed at room temperature makes the nanotube TFTs ideal for a wide range of applications.

We are among the first few research groups to demonstrate SWNT TFTs comprised of an enriched semiconducting SWNT random network. Figure 10d illustrates a common back-gated TFT based on a random network of separated SWNT solution [56]. The SWNT solution was uniformly deposited onto the device substrate by first functionalizing with aminopropyltriethoxy to terminate the surface of the substrate with a layer of amino groups, which enhances the attraction between the SWNTs and the surface [65]. As can be observed in Fig. 10e, the SWNT thin film can be deposited invariantly over the entire surface of a 3-inch Si/SiO₂ wafer, as shown by the SEM images captured at different regions of the wafer after SWNT deposition. This proves that the deposition process is scalable, and can be used in industrial-scale fabrication. The geometry of the channel of the transistors can be defined by standard photolithography, followed by O₂ plasma etching of the SWNT film in the region outside the channel. This technique eliminates the issue of assembly of the nanotubes. The transistors fabricated with the 98% enriched SWNT solution exhibited ideal p-type behavior with mobility as high as 52 cm² V⁻¹ s⁻¹, while maintaining a current on/off ratio of 10⁴. Although the mobility of the devices is not as high as that exhibited by silicon transistors, it is still an invaluable thin film material for applications such as drivers for display, or flexible electronics [120]. The output characteristic of the SWNT TFTs is exhibited in Fig. 10f. As can be observed in the plot, the output curves can be fully saturated. The uniformity of the devices is illustrated in Fig. 10g. The normalized on current (I_{on}/W) and threshold voltage (V_{th}) of 10 SWNT TFTs were delineated in the figure. The results provided evidence for the applicability to implement the separated CNT thin films in large-scale fabrication processes.

4.2 Printed SWNT TFTs

SWNTs, which are intrinsically printable at room temperature, show its great advantage over amorphous silicon and polysilicon for printed electronics [49, 83]. Compared with other printable organic materials, SWNTs have much higher mobility and are chemically stable in ambient [58, 86, 121]. Thanks to the great progress made in SWNT separation [122, 123], semiconducting SWNT-enriched solution has been realized, which leads to feasibility of printing high-performance SWNT TFTs for macro and display electronic applications [49, 84–89].

To realize fully printed high-performance SWNT TFTs, selection of materials for electrodes and gate dielectrics is critical. In terms of electrodes, silver and gold based nanoparticle inks are mostly selected for their system because of their high conductivity and the formation of Ohmic contact between electrodes and SWNTs [84, 124, 125]. Although nanomaterials such as metallic SWNTs have been used as electrodes [126], the performance was rather moderate and therefore hard to be applied for macro and display electronics. For printing gate dielectrics, mixtures composed of high-k metal oxide nanoparticles and organic binders are commonly used to achieve relatively high capacitance [86, 125], which can reduce the operation voltage of printed TFTs. Another group of dielectric materials is electrolyte, which have been reported by Frisbie and Hersam's groups [50, 88]. The most important advantage of employing electrolyte as the gate dielectric is the high

capacitance regardless of its rather large physical thickness. As a result, the performance of such printed electrolyte-gated SWNT TFT is superior in terms of on-state current density, on-off ratio and low operation voltage [127].

Multiple printing technologies reported for fabricating SWNT TFTs can be mainly divided into two groups [86]. The first one is of high registration accuracy represented by aerosol-jet printing and inkjet printing. The second one is of high scalability and throughput represented by gravure printing and flexographic printing. On one hand, for printing SWNTs as channel materials, ink-jet and aerosol-jet printing are main-stream technologies using relatively low viscosity inks to pattern an ultrathin and uniform film. On the other hand, ink-jet printing, aerosol-jet printing, screen printing, gravure printing and flexographic printing have all been employed for patterning gate dielectric and electrodes to achieve fully printed SWNT TFTs. Up until now, the fully-printed high-performance SWNT TFT has been used for macro, display, and sensor electronics. Our group made great efforts to developing fully printed SWNT TFTs for OLED driving using ink-jet printing (Fig. 11a) and screen printing (Fig. 11b) [49, 86]. Javey and Cho's groups pioneered in gravure printed SWNT electronics (Fig. 11c), realizing D flip-flop [52], full adder [51], and fully printed backplane for electronic skin [76]. Hersam's group reported high-performance printed ring oscillators using aerosol-jet printing [85, 128, 129]. Ohno's group made great efforts on developing fully flexographic printed SWNT TFTs with CVD grown nanotubes (Fig. 11d) [130]. Overall, such

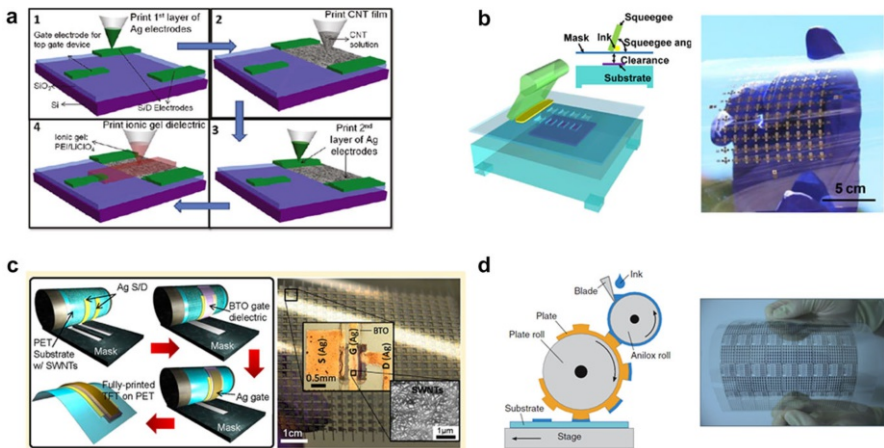


Fig. 11 **a** Schematic diagram showing the process of fully ink-jet printed SWNT TFTs **1** printing first silver electrodes. **2** Printing SWNT network. **3** Printing second layer of silver electrodes. **4** Printing ionic gel as dielectric material. Adapted with permission from Ref. [49]. Copyright (2011) American Chemical Society. **b** Schematic diagram of screen printer and an optical image of screen printed SWNT TFT array on a PET substrate. Adapted with permission from Ref. [86]. Copyright (2014) American Chemical Society. **c** Schematic diagram outlining gravure printing process of SWNT TFTs and images of printed TFT and nanotube network on a PET substrate. Adapted with permission from Ref. [125]. Copyright (2013) American Chemical Society. **d** Schematic diagram of flexographic printing and an optical image of flexographic printed CNT TFT electronics on a PET substrate. Adapted with permission from Ref. [130]. Copyright (2011) Japan Society of Applied Physics

cost-effective and solution-based printing technologies have been attracting more and more research interest and are promising for practical applications.

4.3 Applications Based on SWNT TFTs

SWNT TFTs show great potential in a wide range of applications, ranging from digital circuits, active-matrix backplanes for display electronics and sensors, to flexible electronics. Over the past years, tremendous efforts have been devoted into SWNT TFT research, trying to make it a real technology. Here, we will review the potential applications of SWNT TFTs, including (1) digital circuits, (2) active-matrix backplanes for display electronics and sensors, and (3) flexible electronics.

4.3.1 Digital Circuits

The extremely high intrinsic carrier mobility and current-carrying capacity make SWNTs a promising channel material for next-generation digital circuits. Many groups have made significant progress by successfully fabricating integrated circuits based on p-type SWNT TFT platforms [48, 53, 54, 68, 71, 131]. In 2008, Cao et al. successfully demonstrated the first medium-scale SWNT-based integrated digital circuits, a four-bit row decoder composed of 88 SWNT TFTs, on polyimide substrates [48]. Random SWNT networks were initially synthesized by CVD, and then transferred to polyimide substrate as the channel materials. Figure 12a shows the optical image of a flexible SWNT integrated circuit chip bonded to a curved surface and high-magnification photographic image of the fabricated four-bit row decoder consisting of 88 SWNT transistors. Moreover, Sun et al. successfully realized the fabrication of SWNT-based TFTs and logic circuits on flexible substrates, such as 21-stage ring oscillator and master-slave delay flip-flops, using a floating-catalyst CVD SWNT deposition method followed by gas phase filtration and a transfer process [54]. Based on the platform of gas phase-synthesized nanotube networks, they further demonstrated the first all-carbon XOR gates and 1-bit static random access memory (SRAM) [53]. Later on, instead of using CVD-synthesized SWNTs, Wang et al. used separated high-purity semiconducting-enriched SWNTs as the channel material for high-performance SWNT TFTs and demonstrated separated nanotube-based integrated logic gates, including an inverter, NAND, and NOR gates, serving as a good platform to bypass the issue of the coexistence of both metallic and semiconducting nanotubes in the as-synthesized SWNTs [68]. After that, solution-processed semiconducting SWNT thin films have drawn much more attention from researchers, because solution-processed separated SWNTs offer high electrical performance, good mechanical flexibility, relatively low cost, and ambient compatibility simultaneously. Wang et al. successfully demonstrated high-performance logic gates, including inverters, NAND, NOR gates, with superior bending stabilities [71]. A recent breakthrough was made by Chen et al. by realizing a 4-bit adder which consists of 140 p-type SWNT TFTs and a 2-bit multiplier for the first time [77]. Thanks to the high uniformity and desirable threshold voltage of the CNT TFTs, the integrated circuits based on these TFTs can be operated by a small voltage down to 2 V.

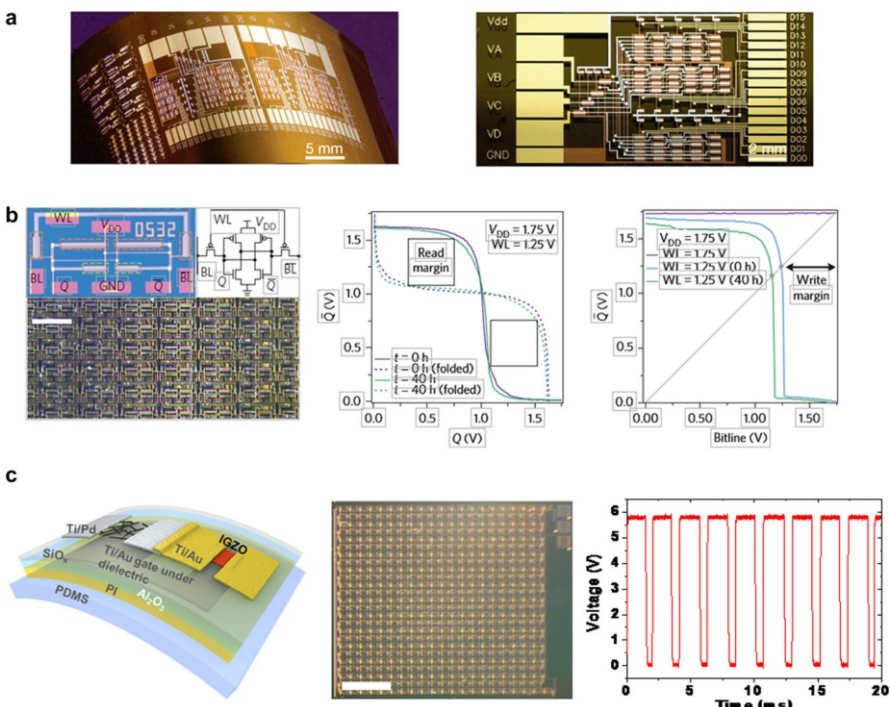


Fig. 12 **a** Optical image of a flexible SWNT integrated circuit chip bonded to a curved surface and high-magnification photographic image of the decoder consisting of 88 CNT transistors. Adapted with permission from Ref. [48]. Copyright (2008) Nature Publishing Group. **b** Optical micrograph, read margin measurement, folded read margin measurements, and hold operation of a fabricated SWNT CMOS SRAM cell. Adapted with permission from Ref. [81]. Copyright (2015) Nature Publishing Group. **c** Hybrid integration of IGZO TFT and SWNT TFT for a CMOS inverter. Adapted with permission from Ref. [82]. Copyright (2014) Nature Publishing Group

Large hysteresis, a commonly observed phenomenon in the transfer characteristics of SWNT TFTs, is highly undesired in the operation of transistors and integrated logic gates, because hysteresis often results in the shift of threshold voltage as the voltage sweeping direction and range changes. Multiple factors can cause hysteresis in a SWNT-based TFT, including interface-trapped charges and trapped charges induced by the absorption of water molecules inside the channel [78]. Therefore, hysteresis-free nanotube-based TFTs are highly desired for the stable operations of SWNT-based TFTs and digital circuits. Ha et al. developed a promising approach of using fluorocarbon polymer as the encapsulation layer for hysteresis-free SWNT devices, which showed great device stability in both air and water [78]. Thanks to the high hydrophobicity of this Teflon-like polymer, the water molecules absorbed in the nanotubes can be effectively removed, which yields hysteresis-free SWNT TFTs. Recently, Chen et al. discovered an alternative approach for hysteresis-free SWNT devices by using Y_2O_3 thin film as the gate dielectric layer, which was oxidized from e-beam-evaporated yttrium film [77]. Their results showed that Y_2O_3 can offer very high gate efficiency and high

uniformity for SWNT-based TFTs, which paves the way for large-scale integration of SWNT-based TFTs.

CMOS integrated circuits have many advantages, especially their low static power consumption. Over the past two decades, many groups including our group have devoted a lot of efforts into trying to convert p-type SWNT TFTs into air-stable n-type TFTs aiming for integrated CMOS logic gates. Here, we will review some recent progress in CMOS integrated circuits consisting of n-type and p-type SWNT TFTs as the NMOS and PMOS, respectively. Ryu et al. reported a fully integrated CMOS inverter and NAND and NOR gates by using chemical doping to convert p-type aligned nanotube transistors to n-types [33]. Later on, Zhang et al. developed a new approach of using a thin layer of high- κ oxide passivation layer, deposited by atomic layer deposition, to convert separated SWNT TFTs from p-type to air-stable n-type [79]. Interestingly, the converted n-type transistors and the p-type transistors show symmetric electrical performance, regarding device mobility, on-state current, and on/off ratio. They further demonstrated a CMOS inverter with rail-to-rail output, large noise margin, and symmetric input/output behavior. Recently, Ha et al. reported a novel strategy of achieving air-stable n-doping SWNTs with SiN_x thin films deposited by plasma-enhanced chemical vapor deposition [80]. The n-type nanotube transistors are highly air-stable and show very good uniformity over large areas, which is an important factor for integrated circuit applications. In 2015, a great breakthrough was achieved by Geier et al. whom demonstrated the first solution-processed SWNT thin film-complementary SRAM [81] (Fig. 12b). The uniform and stable electronic performance of the complementary p-type and n-type SWNT TFTs is attributed to the well-controlled adsorbed atmospheric dopants and robust encapsulation layers. Recently, Yang et al. reported CMOS ICs by using Sc or Pd as the source/drain contacts to selectively inject carriers into the CNT network channels for NMOS and PMOS, respectively [132]. They demonstrated a 4-bit full adders consisting of 132 CMOS TFTs with 100% yield, showing the potential of medium-scale CNT network film-based ICs.

Considering metal oxide semiconductors have gradually emerged as a mature technology platform for n-type TFTs, Chen et al. demonstrated the first large-scale hybrid integration of p-type CNT and n-type indium–gallium–zinc–oxide thin-film transistors to realize 501-stage ring oscillators, consisting of more than 1000 transistors, on both rigid and flexible substrates (Fig. 12c) [82]. In this hybrid integration approach, the strength of the p-type nanotube and n-type indium–gallium–zinc–oxide are successfully combined together to achieve high uniformity and high yield.

4.3.2 Active-Matrix Backplanes for Display Electronics and Sensors

Separated semiconducting-enriched SWNT thin films possess great potential for TFTs and active-matrix backplanes for display electronics and sensors, due to their high semiconducting purity, high mobility, and room-temperature processing compatibility. As early as 2009, Wang et al. made the first conceptual demonstration of an organic light-emitting diode (OLED) control circuit with a nanotube TFT,

with the output light intensity exceeding 10^4 , which paves the way for using nanotube TFTs for display electronics [56]. Active-matrix organic light-emitting diode (AMOLED) display exhibits great potential as a competitive candidate for next-generation display technologies due to its high light efficiency, light weight, high flexibility, and low-temperature processing compatibility. Later, Zhang et al. further successfully demonstrated monolithically integrated AMOLED display elements, consisting of 500 pixels driven by 1000 nanotube TFTs [57]. The optical image of an AMOLED substrate containing 7 AMOLED elements, each with 20×25 pixels, is shown in Fig. 13a. Figure 13b is a photograph showing the pixels on an integrated AMOLED. The electrical characteristics of the OLED controlled by a single pixel circuit is shown in Fig. 13c. Figure 13d shows the plot of the current through the OLED (I_{OLED} ; red line) and OLED light intensity (green line) versus V_{DATA} with $V_{\text{DD}} = 8$ V. This approach may serve as a critical foundation for using separated CNT thin-film transistors for display applications in the future. Later on, inkjet-printed [49] and screen-printed [86] OLED control circuits were demonstrated, showing a low-cost approach to realize OLED driving capability. Recently, Zou et al. reported first CVD-grown SWNT network-based TFT driver

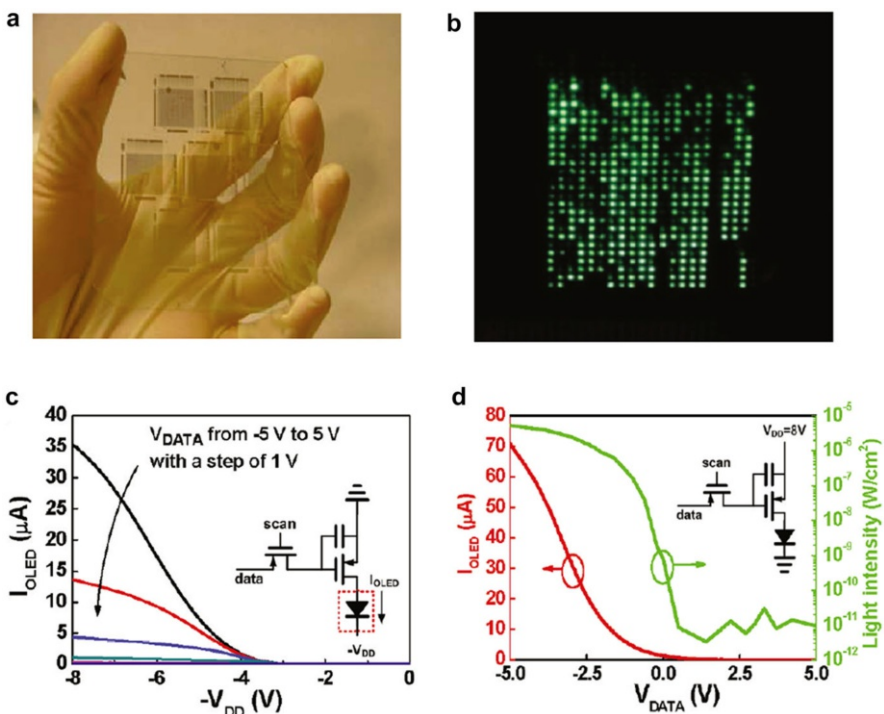


Fig. 13 AMOLED using SWNT TFTs. **a** Optical image of an AMOLED substrate containing 7 AMOLED elements, each with 20×25 pixels. **b** Photograph showing the pixels on an integrated AMOLED. **c** Characteristics of the OLED controlled by a single pixel circuit. **d** Plot of the current through the OLED (I_{OLED} ; red line) and OLED light intensity (green line) versus V_{DATA} with $V_{\text{DD}} = 8$ V. Adapted with permission from Ref. [57]. Copyright (2011) American Chemical Society

circuits for both static and dynamic 6×6 AMOLED displays, which further proved the suitability and capability of SWNT-TFTs for future OLED applications [74].

Additional great progress in this field was made by Wang et al. by demonstrating the first user-interactive electronic skin which can give simultaneously spatial-pressure mapping and visual response through a built-in AMOLED controlled by an SWNT-TFT-based active matrix (Fig. 14) [55]. In this system, the OLED arrays can be turned on locally at the location where there is pressure applied, and the intensity

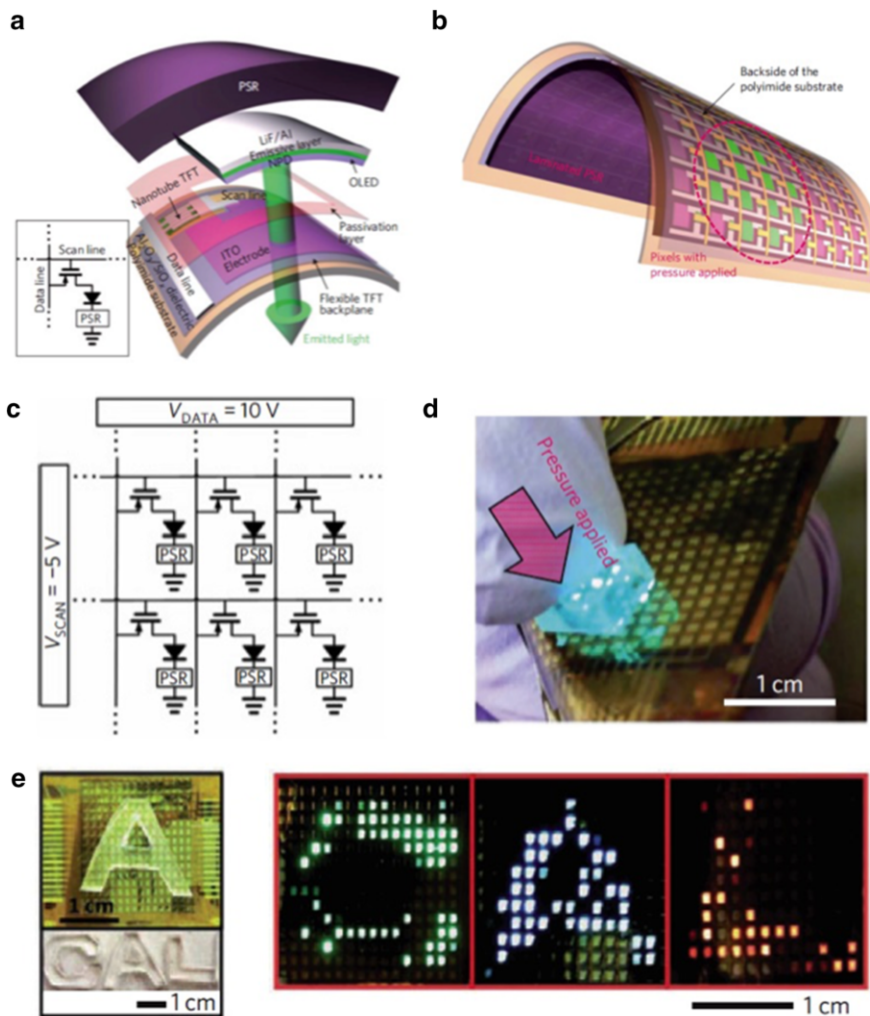


Fig. 14 User-interactive electronic skin based on SWNT TFTs. **a, b** Schematic diagrams showing the configuration of a pixel, consisting of a nanotube TFT, an OLED, and a pressure sensor (PSR) integrated vertically on a polyimide substrate. **c** Circuit schematic of the e-skin matrix. **d** Photograph of a fabricated device (16×16 pixels). **e** Green, blue, and red color interactive e-skins are used to spatially map and display the pressure applied with C- (left), A- (center), and L- (right) shaped PDMS slabs, respectively. Adapted with permission from Ref. [55]. Copyright (2013) Nature Publishing Group

of the emission light can be used to quantify the pressure applied to the surface. This work represents a successful large-scale demonstration of three different electronic components, including nanotube TFTs, pressure sensors, and OLED arrays, which are monolithically integrated over large areas on plastic substrates. This electronic skin has great potential to be used for a range of applications, such as medical monitoring devices, interactive input/output devices, etc.

As early as 2011, Takahashi et al. reported fabrication of SWNT thin-film-based 12×8 active-matrix backplanes for pressure mapping with a pressure sensitive rubber as the active sensor element [70]. After that, they further demonstrated a flexible nanotube active-matrix backplane for visible light and X-ray imagers [75]. Recently, they realized large-area pressure mapping by the large-scale integration of a printed SWNT active-matrix backplane with tactile sensor arrays, indicating a scalable, low-cost approach towards electronic skin applications using CNT TFTs [76].

4.3.3 Flexible Electronics

Recently, flexible electronics have been widely explored for new applications which are impossible to be realized using the conventional rigid substrates. Due to the intrinsic flexibility of SWNTs, nanotube TFTs have attracted many people's attention and emerged as a promising technology platform for flexible electronics. To achieve good flexibility, a very thin layer of high-quality dielectric on plastic substrate is highly desired. Here, we will review some recent progress achieved in nanotube-TFT-based flexible electronics.

As early as 2006, Cao et al. reported mechanically flexible, optically transparent "all-tube" TFT on flexible substrates fabricated using layer-by-layer transfer printing of CVD-grown SWNT networks as both electrodes and channel materials [133]. Elastomeric dielectrics and flexible substrates were used to achieve high flexibility. In 2012, Wang et al. demonstrated extremely bendable, high-performance integrated inverters, NAND, and NOR logic gates, analog, and radio frequency applications using semiconducting-enriched SWNTs [71]. Later, Lau et al. further reported fully printed SWNT-based TFTs on flexible substrates, and the devices showed no measurable change in electrical performance under a bending radius as small as 1 mm [125]. Afterwards, all-carbon integrated circuits were demonstrated by Sun et al. for the first time [53]. The devices were entirely composed of carbon-based materials with active channels and passive elements fabricated using stretchable and thermostable assemblies of SWNTs, plastic polymer dielectric layers, and plastic substrates. Surprisingly, functional integrated circuits have also been successfully made into a 3D dome. Another interesting progress was reported by Chae et al. demonstrating a highly stretchable and transparent FET which combined graphene/SWNT hybrid electrodes and an SWNT network channel with a wrinkled Al_2O_3 dielectric layer [134]. The authors claimed that the wrinkled Al_2O_3 layer contained effective built-in air gaps, offering a gate leakage current as small as 10^{-13} A. Thanks to the wrinkled dielectric layer, the devices retained their good performance under strains as large as 20% without noticeable leakage current increases or performance degradations. Furthermore, the

devices showed no significant degradation after over 1000 cycles of stretch-release process. Recently, Cao et al. successfully demonstrated ultraflexible and imperceptible p-type nanotube transistors and integrated circuits with a bending radius down to 40 μm [131]. The as-fabricated ultralight-weight ($<3 \text{ g/m}^2$) nanotube transistors showed high mechanical robustness which can accommodate severe crumpling and compressive strain of 67%. Moreover, the nanotube circuits remained properly functional under 33% compressive strain, showing great potential as indispensable components for ultraflexible complementary electronics.

5 Summary and Outlook

In summary, SWNTs are highly promising for future RF electronics, digital electronics, and macroelectronics applications due to their excellent electrical, mechanical, and thermal properties. In regard to RF electronics, RF performance of SWNT transistors ready for some practical applications have been achieved, and RF circuits and systems based on SWNTs have been demonstrated [11, 23]. For SWNT-based nanoelectronics, ballistic SWNT transistors provide a good platform for further pushing forward Moore's law [2]. For macroelectronics, SWNT random network TFTs have been demonstrated in various applications, including digital circuits, active-matrix backplanes for display electronics and sensors, as well as flexible electronics. In spite of the significant progress achieved, several further developments are needed before SWNTs can be adopted by industry. First, it is of key importance to achieve aligned SWNT arrays with both high density (150–200 tubes/ μm) and ultrahigh-purity semiconducting ($>99.9999\%$) for SWNT RF and digital electronics. With the advancement in the nanotube alignment technologies, multiple transfer of high-density and ultrahigh-purity semiconducting aligned SWNT arrays provides a promising way to reach the goal. Second, for all applications, hysteresis can be an issue compromising SWNT performance. Further optimization of dielectric materials for SWNT transistors to achieve hysteresis-free operations while maintaining excellent transistor performance is also necessary. In addition, passivation, integration, and stability of SWNT transistors require systematic investigations to cooperate with other functional parts. Moreover, developing reliable and small-area metal contacts for both p-type and n-type SWNT FETs in a sub-10-nm channel length also requires great research efforts to achieve energy-efficient digital electronics. With the advancement in the above developments, SWNT electronics will finally become an indispensable part of future electronics.

References

1. Saito R, Dresselhaus G, Dresselhaus MS (1998) Physical properties of carbon nanotubes. Imperial College Press, London, p 1 ([online resource](#))

2. Javey A, Guo J, Wang Q, Lundstrom M, Dai H (2003) Ballistic carbon nanotube field-effect transistors. *Nature* 424:654–657
3. Zhou X, Park JY, Huang S, Liu J, McEuen PL (2005) Band structure, phonon scattering, and the performance limit of single-walled carbon nanotube transistors. *Phys Rev Lett* 95:146805
4. Rutherford C, Jain D, Burke P (2009) Nanotube electronics for radiofrequency applications. *Nat Nanotechnol* 4:811–819
5. Durkop T, Getty SA, Cobas E, Fuhrer MS (2004) Extraordinary mobility in semiconducting carbon nanotubes. *Nano Lett* 4:35–39
6. Li SD, Yu Z, Yen SF, Tang WC, Burke PJ (2004) Carbon nanotube transistor operation at 2.6 GHz. *Nano Lett* 4:753–756
7. Nougaret L, Happy H, Dambrine G, Derycke V, Bourgoin JP, Green AA, Hersam MC (2009) 80 GHz field-effect transistors produced using high purity semiconducting single-walled carbon nanotubes. *Appl Phys Lett* 94:243505
8. Wang C, Badmaev A, Jooyaie A, Bao M, Wang KL, Galatsis K, Zhou C (2011) Radio frequency and linearity performance of transistors using high-purity semiconducting carbon nanotubes. *ACS Nano* 5:4169–4176
9. Steiner M, Engel M, Lin YM, Wu YQ, Jenkins K, Farmer DB, Humes JJ, Yoder NL, Seo JWT, Green AA, Hersam MC, Krupke R, Avouris P (2012) High-frequency performance of scaled carbon nanotube array field-effect transistors. *Appl Phys Lett* 101:053123
10. Hu Y, Kang L, Zhao Q, Zhong H, Zhang S, Yang L, Wang Z, Lin J, Li Q, Zhang Z, Peng L, Liu Z, Zhang J (2015) Growth of high-density horizontally aligned SWNT arrays using Trojan catalysts. *Nat Commun* 6:6099
11. Cao Y, Brady GJ, Gui H, Rutherford C, Arnold MS, Zhou C (2016) Radio frequency transistors using aligned semiconducting carbon nanotubes with current-gain cutoff frequency and maximum oscillation frequency simultaneously greater than 70 GHz. *ACS Nano* 10:6782–6790
12. Le Louarn A, Kapche F, Bethoux JM, Happy H, Dambrine G, Derycke V, Chenevier P, Izard N, Goffman MF, Bourgoin JP (2007) Intrinsic current gain cutoff frequency of 30 GHz with carbon nanotube transistors. *Appl Phys Lett* 90:233108
13. Che Y, Badmaev A, Jooyaie A, Wu T, Zhang J, Wang C, Galatsis K, Enaya HA, Zhou C (2012) Self-aligned T-gate high-purity semiconducting carbon nanotube RF transistors operated in quasi-ballistic transport and quantum capacitance regime. *ACS Nano* 6:6936–6943
14. Che Y, Lin YC, Kim P, Zhou C (2013) T-gate aligned nanotube radio frequency transistors and circuits with superior performance. *ACS Nano* 7:4343–4350
15. Kocabas C, Dunham S, Cao Q, Cimino K, Ho X, Kim HS, Dawson D, Payne J, Stuenkel M, Zhang H, Banks T, Feng M, Rotkin SV, Rogers JA (2009) High-frequency performance of submicrometer transistors that use aligned arrays of single-walled carbon nanotubes. *Nano Lett* 9:1937–1943
16. Wang Z, Liang S, Zhang Z, Liu H, Zhong H, Ye LH, Wang S, Zhou W, Liu J, Chen Y, Zhang J, Peng LM (2014) Scalable fabrication of ambipolar transistors and radio-frequency circuits using aligned carbon nanotube arrays. *Adv Mater* 26:645–652
17. Cao Y, Che YC, Gui H, Cao X, Zhou CW (2016) Radio frequency transistors based on ultra-high purity semiconducting carbon nanotubes with superior extrinsic maximum oscillation frequency. *Nano Res* 9:363–371
18. Cao Y, Che YC, Seo JWT, Gui H, Hersam MC, Zhou CW (2016) High-performance radio frequency transistors based on diameter-separated semiconducting carbon nanotubes. *Appl Phys Lett* 108:233105. doi:[10.1063/1.4953074](https://doi.org/10.1063/1.4953074)
19. Baumgardner JE, Pesetski AA, Murduck JM, Przybysz JX, Adam JD, Zhang H (2007) Inherent linearity in carbon nanotube field-effect transistors. *Appl Phys Lett* 91:052107. doi:[10.1063/1.2760159](https://doi.org/10.1063/1.2760159)
20. Mothes S, Claus M, Schrotter M (2015) Toward linearity in Schottky barrier CNTFETs. *IEEE Trans Nanotechnol* 14:372–378
21. Wang Z, Ding L, Pei T, Zhang Z, Wang S, Yu T, Ye X, Peng F, Li Y, Peng LM (2010) Large signal operation of small band-gap carbon nanotube-based ambipolar transistor: a high-performance frequency doubler. *Nano Lett* 10:3648–3655
22. Kocabas C, Kim HS, Banks T, Rogers JA, Pesetski AA, Baumgardner JE, Krishnaswamy SV, Zhang H (2008) Radio frequency analog electronics based on carbon nanotube transistors. *Proc Natl Acad Sci USA* 105:1405–1409
23. Jensen K, Weldon J, Garcia H, Zettl A (2007) Nanotube radio. *Nano Lett* 7:3508–3511

24. Nikonorov DE, Young IA (2012) Uniform methodology for benchmarking beyond-CMOS logic devices. In: 2012 IEEE international electron devices meeting (IEDM), San Francisco, CA, USA
25. Tans SJ, Verschueren ARM, Dekker C (1998) Room-temperature transistor based on a single carbon nanotube. *Nature* 393:49–52
26. Qiu C, Zhang Z, Zhong D, Si J, Yang Y, Peng LM (2015) Carbon nanotube feedback-gate field-effect transistor: suppressing current leakage and increasing on/off ratio. *ACS Nano* 9:969–977
27. Purewal MS, Hong BH, Ravi A, Chandra B, Hone J, Kim P (2007) Scaling of resistance and electron mean free path of single-walled carbon nanotubes. *Phys Rev Lett* 98:186808
28. Weitz RT, Zschieschang U, Forment-Aliaga A, Kalblein D, Burghard M, Kern K, Klauk H (2009) Highly reliable carbon nanotube transistors with patterned gates and molecular gate dielectric. *Nano Lett* 9:1335–1340
29. Franklin AD, Chen Z (2010) Length scaling of carbon nanotube transistors. *Nat Nanotechnol* 5:858–862
30. Franklin AD, Luisier M, Han SJ, Tulevski G, Breslin CM, Gignac L, Lundstrom MS, Haensch W (2012) Sub-10 nm carbon nanotube transistor. *Nano Lett* 12:758–762
31. Cao Q, Han SJ, Tersoff J, Franklin AD, Zhu Y, Zhang Z, Tulevski GS, Tang J, Haensch W (2015) End-bonded contacts for carbon nanotube transistors with low, size-independent resistance. *Science* 350:68–72
32. Liu X, Han S, Zhou C (2006) Novel nanotube-on-insulator (NOI) approach toward single-walled carbon nanotube devices. *Nano Lett* 6:34–39
33. Ryu K, Badmaev A, Wang C, Lin A, Patil N, Gomez L, Kumar A, Mitra S, Wong HS, Zhou C (2009) CMOS-analogous wafer-scale nanotube-on-insulator approach for submicrometer devices and integrated circuits using aligned nanotubes. *Nano Lett* 9:189–197
34. Shulaker MM, Van Rethy J, Wu TF, Liyanage LS, Wei H, Li Z, Pop E, Gielen G, Wong HS, Mitra S (2014) Carbon nanotube circuit integration up to sub-20 nm channel lengths. *ACS Nano* 8:3434–3443
35. Shulaker MM, Hills G, Patil N, Wei H, Chen HY, Wong HS, Mitra S (2013) Carbon nanotube computer. *Nature* 501:526–530
36. Kim HS, Jeon EK, Kim JJ, So HM, Chang H, Lee JO, Park N (2008) Air-stable n-type operation of Gd-contacted carbon nanotube field effect transistors. *Appl Phys Lett* 93:123106. doi:[10.1063/1.2990642](https://doi.org/10.1063/1.2990642)
37. Ding L, Wang S, Zhang Z, Zeng Q, Wang Z, Pei T, Yang L, Liang X, Shen J, Chen Q, Cui R, Li Y, Peng LM (2009) Y-contacted high-performance n-type single-walled carbon nanotube field-effect transistors: scaling and comparison with Sc-contacted devices. *Nano Lett* 9:4209–4214
38. Zhang ZY, Liang XL, Wang S, Yao K, Hu YF, Zhu YZ, Chen Q, Zhou WW, Li Y, Yao YG, Zhang J, Peng LM (2007) Doping-free fabrication of carbon nanotube based ballistic CMOS devices and circuits. *Nano Lett* 7:3603–3607
39. Shahjerdi D, Franklin AD, Oida S, Ott JA, Tulevski GS, Haensch W (2013) High-performance air-stable n-type carbon nanotube transistors with erbium contacts. *ACS Nano* 7:8303–8308
40. Wang C, Ryu K, Badmaev A, Zhang J, Zhou C (2011) Metal contact engineering and registration-free fabrication of complementary metal-oxide semiconductor integrated circuits using aligned carbon nanotubes. *ACS Nano* 5:1147–1153
41. Suriyasena Liyanage L, Xu X, Pitner G, Bao Z, Wong HS (2014) VLSI-compatible carbon nanotube doping technique with low work-function metal oxides. *Nano Lett* 14:1884–1890
42. Javey A, Tu R, Farmer DB, Guo J, Gordon RG, Dai H (2005) High performance n-type carbon nanotube field-effect transistors with chemically doped contacts. *Nano Lett* 5:345–348
43. Geier ML, Moudgil K, Barlow S, Marder SR, Hersam MC (2016) Controlled n-type doping of carbon nanotube transistors by an organoruthenium dimer. *Nano Lett* 16:4329–4334
44. Wei H, Shulaker M, Wong HSP, Mitra S (2013) Monolithic three-dimensional integration of carbon nanotube FET complementary logic circuits. 2013 IEEE international electron devices meeting (IEDM), San Francisco, CA, USA
45. Zhang PP, Qiu CG, Zhang ZY, Ding L, Chen BY, Peng LM (2016) Performance projections for ballistic carbon nanotube FinFET at circuit level. *Nano Res* 9:1785–1794
46. Franklin AD, Koswatta SO, Farmer DB, Smith JT, Gignac L, Breslin CM, Han SJ, Tulevski GS, Miyazoe H, Haensch W, Tersoff J (2013) Carbon nanotube complementary wrap-gate transistors. *Nano Lett* 13:2490–2495

47. Shulaker MM, Saraswat K, Wong HSP, Mitra S (2014) Monolithic three-dimensional integration of carbon nanotube FETs with silicon CMOS. In: VLSI technology (VLSI-technology): digest of technical papers, 2014 Symposium on VLSI Technology and Circuits, Honolulu, HI, USA
48. Cao Q, Kim HS, Pimparkar N, Kulkarni JP, Wang C, Shim M, Roy K, Alam MA, Rogers JA (2008) Medium-scale carbon nanotube thin-film integrated circuits on flexible plastic substrates. *Nature* 454:495–500
49. Chen P, Fu Y, Aminirad R, Wang C, Zhang J, Wang K, Galatsis K, Zhou C (2011) Fully printed separated carbon nanotube thin film transistor circuits and its application in organic light emitting diode control. *Nano Lett* 11:5301–5308
50. Ha M, Xia Y, Green AA, Zhang W, Renn MJ, Kim CH, Hersam MC, Frisbie CD (2010) Printed, sub-3 V digital circuits on plastic from aqueous carbon nanotube inks. *ACS Nano* 4:4388–4395
51. Noh J, Jung K, Kim J, Kim S, Cho S, Cho G (2012) Fully gravure-printed flexible full adder using SWNT-based TFTs. *IEEE Electron Device Lett* 33:1574–1576
52. Noh J, Jung M, Jung K, Lee G, Kim J, Lim S, Kim D, Choi Y, Kim Y, Subramanian V, Cho G (2011) Fully gravure-printed D flip-flop on plastic foils using single-walled carbon-nanotube-based TFTs. *IEEE Electron Device Lett* 32:638–640
53. Sun DM, Timmermans MY, Kaskela A, Nasibulin AG, Kishimoto S, Mizutani T, Kauppinen EI, Ohno Y (2013) Mouldable all-carbon integrated circuits. *Nat Commun* 4:2302
54. Sun DM, Timmermans MY, Tian Y, Nasibulin AG, Kauppinen EI, Kishimoto S, Mizutani T, Ohno Y (2011) Flexible high-performance carbon nanotube integrated circuits. *Nat Nanotechnol* 6:156–161
55. Wang C, Hwang D, Yu Z, Takei K, Park J, Chen T, Ma B, Javey A (2013) User-interactive electronic skin for instantaneous pressure visualization. *Nat Mater* 12:899–904
56. Wang C, Zhang J, Ryu K, Badmaev A, De Arco LG, Zhou C (2009) Wafer-scale fabrication of separated carbon nanotube thin-film transistors for display applications. *Nano Lett* 9:4285–4291
57. Zhang J, Fu Y, Wang C, Chen PC, Liu Z, Wei W, Wu C, Thompson ME, Zhou C (2011) Separated carbon nanotube macroelectronics for active matrix organic light-emitting diode displays. *Nano Lett* 11:4852–4858
58. Forrest SR (2004) The path to ubiquitous and low-cost organic electronic appliances on plastic. *Nature* 428:911–918
59. Sekitani T, Zschieschang U, Klauk H, Someya T (2010) Flexible organic transistors and circuits with extreme bending stability. *Nat Mater* 9:1015–1022
60. Cong S, Cao Y, Fang X, Wang YF, Liu QZ, Gui H, Shen CF, Cao X, Kim ES, Zhou CW (2016) Carbon nanotube macroelectronics for active matrix polymer-dispersed liquid crystal displays. *ACS Nano* 10:10068–10074
61. Street R (2000) Introduction. In: Street R (ed) Technology and applications of amorphous silicon. Springer, New York, pp 1–6
62. Snow ES, Novak JP, Campbell PM, Park D (2003) Random networks of carbon nanotubes as an electronic material. *Appl Phys Lett* 82:2145–2147
63. Engel M, Small JP, Steiner M, Freitag M, Green AA, Hersam MC, Avouris P (2008) Thin film nanotube transistors based on self-assembled, aligned, semiconducting carbon nanotube arrays. *ACS Nano* 2:2445–2452
64. Meitl MA, Zhou YX, Gaur A, Jeon S, Usrey ML, Strano MS, Rogers JA (2004) Solution casting and transfer printing single-walled carbon nanotube films. *Nano Lett* 4:1643–1647
65. LeMieux MC, Roberts M, Barman S, Jin YW, Kim JM, Bao Z (2008) Self-sorted, aligned nanotube networks for thin-film transistors. *Science* 321:101–104
66. Vosgueritchian M, LeMieux MC, Dodge D, Bao Z (2010) Effect of surface chemistry on electronic properties of carbon nanotube network thin film transistors. *ACS Nano* 4:6137–6145
67. Snow ES, Campbell PM, Ancona MG, Novak JP (2005) High-mobility carbon-nanotube thin-film transistors on a polymeric substrate. *Appl Phys Lett* 86:033105
68. Wang C, Zhang J, Zhou C (2010) Macroelectronic integrated circuits using high-performance separated carbon nanotube thin-film transistors. *ACS Nano* 4:7123–7132
69. Rouhi N, Jain D, Zand K, Burke PJ (2011) Fundamental limits on the mobility of nanotube-based semiconducting inks. *Adv Mater* 23:94–99
70. Takahashi T, Takei K, Gillies AG, Fearing RS, Javey A (2011) Carbon nanotube active-matrix backplanes for conformal electronics and sensors. *Nano Lett* 11:5408–5413

71. Wang C, Chien JC, Takei K, Takahashi T, Nah J, Niknejad AM, Javey A (2012) Extremely bendable, high-performance integrated circuits using semiconducting carbon nanotube networks for digital, analog, and radio-frequency applications. *Nano Lett* 12:1527–1533
72. Jung M, Kim J, Noh J, Lim N, Lim C, Lee G, Kim J, Kang H, Jung K, Leonard AD, Tour JM, Cho G (2010) All-printed and roll-to-roll-printable 13.56-MHz-operated 1-bit RF tag on plastic foils. *IEEE Trans Electron Devices* 57:571–580
73. Noh J, Kim S, Jung K, Kim J, Cho S, Cho G (2011) Fully gravure printed half adder on plastic foils. *IEEE Electron Device Lett* 32:1555–1557
74. Zou J, Zhang K, Li J, Zhao Y, Wang Y, Pillai SK, Volkan Demir H, Sun X, Chan-Park MB, Zhang Q (2015) Carbon nanotube driver circuit for 6×6 organic light emitting diode display. *Sci Rep* 5:11755
75. Takahashi T, Yu Z, Chen K, Kiriya D, Wang C, Takei K, Shiraki H, Chen T, Ma B, Javey A (2013) Carbon nanotube active-matrix backplanes for mechanically flexible visible light and X-ray imagers. *Nano Lett* 13:5425–5430
76. Yeom C, Chen K, Kiriya D, Yu Z, Cho G, Javey A (2015) Large-area compliant tactile sensors using printed carbon nanotube active-matrix backplanes. *Adv Mater* 27:1561–1566
77. Chen B, Zhang P, Ding L, Han J, Qiu S, Li Q, Zhang Z, Peng LM (2016) Highly uniform carbon nanotube field-effect transistors and medium scale integrated circuits. *Nano Lett* 16:5120–5128
78. Ha TJ, Kiriya D, Chen K, Javey A (2014) Highly stable hysteresis-free carbon nanotube thin-film transistors by fluorocarbon polymer encapsulation. *ACS Appl Mater Interfaces* 6:8441–8446
79. Zhang J, Wang C, Fu Y, Che Y, Zhou C (2011) Air-stable conversion of separated carbon nanotube thin-film transistors from p-type to n-type using atomic layer deposition of high-kappa oxide and its application in CMOS logic circuits. *ACS Nano* 5:3284–3292
80. Ha TJ, Chen K, Chuang S, Yu KM, Kiriya D, Javey A (2015) Highly uniform and stable n-type carbon nanotube transistors by using positively charged silicon nitride thin films. *Nano Lett* 15:392–397
81. Geier ML, McMorrow JJ, Xu W, Zhu J, Kim CH, Marks TJ, Hersam MC (2015) Solution-processed carbon nanotube thin-film complementary static random access memory. *Nat Nanotechnol* 10:944–948
82. Chen H, Cao Y, Zhang J, Zhou C (2014) Large-scale complementary macroelectronics using hybrid integration of carbon nanotubes and IGZO thin-film transistors. *Nat Commun* 5:4097
83. Chen K, Gao W, Emaminejad S, Kiriya D, Ota H, Nyein HY, Takei K, Javey A (2016) Printed carbon nanotube electronics and sensor systems. *Adv Mater* 28:4397–4414
84. Cai L, Zhang SM, Miao JS, Yu ZB, Wang C (2015) Fully printed foldable integrated logic gates with tunable performance using semiconducting carbon nanotubes. *Adv Funct Mater* 25:5698–5705
85. Kim B, Jang S, Geier ML, Prabhmirashi PL, Hersam MC, Dodabalapur A (2014) High-speed, inkjet-printed carbon nanotube/zinc tin oxide hybrid complementary ring oscillators. *Nano Lett* 14:3683–3687
86. Cao X, Chen H, Gu X, Liu B, Wang W, Cao Y, Wu F, Zhou C (2014) Screen printing as a scalable and low-cost approach for rigid and flexible thin-film transistors using separated carbon nanotubes. *ACS Nano* 8:12769–12776
87. Xu W, Dou J, Zhao J, Tan H, Ye J, Tange M, Gao W, Xu W, Zhang X, Guo W, Ma C, Okazaki T, Zhang K, Cui Z (2016) Printed thin film transistors and CMOS inverters based on semiconducting carbon nanotube ink purified by a nonlinear conjugated copolymer. *Nanoscale* 8:4588–4598
88. Ha M, Seo JW, Prabhmirashi PL, Zhang W, Geier ML, Renn MJ, Kim CH, Hersam MC, Frisbie CD (2013) Aerosol jet printed, low voltage, electrolyte gated carbon nanotube ring oscillators with sub-5 mus stage delays. *Nano Lett* 13:954–960
89. Vuttipittayamongkol P, Wu FQ, Chen HT, Cao X, Liu BL, Zhou CW (2015) Threshold voltage tuning and printed complementary transistors and inverters based on thin films of carbon nanotubes and indium zinc oxide. *Nano Res* 8:1159–1168
90. Che Y, Wang C, Liu J, Liu B, Lin X, Parker J, Beasley C, Wong HS, Zhou C (2012) Selective synthesis and device applications of semiconducting single-walled carbon nanotubes using isopropyl alcohol as feedstock. *ACS Nano* 6:7454–7462
91. Kocabas C, Hur SH, Gaur A, Meitl MA, Shim M, Rogers JA (2005) Guided growth of large-scale, horizontally aligned arrays of single-walled carbon nanotubes and their use in thin-film transistors. *Small* 1:1110–1116

92. Li J, Liu K, Liang S, Zhou W, Pierce M, Wang F, Peng L, Liu J (2014) Growth of high-density-aligned and semiconducting-enriched single-walled carbon nanotubes: decoupling the conflict between density and selectivity. *ACS Nano* 8:554–562
93. Ding L, Wang Z, Pei T, Zhang Z, Wang S, Xu H, Peng F, Li Y, Peng LM (2011) Self-aligned U-gate carbon nanotube field-effect transistor with extremely small parasitic capacitance and drain-induced barrier lowering. *ACS Nano* 5:2512–2519
94. Chen YF, Fuhrer MS (2005) Electric-field-dependent charge-carrier velocity in semiconducting carbon nanotubes. *Phys Rev Lett* 95:236803
95. Clifford JP, John DL, Castro LC, Pulfrey DL (2004) Electrostatics of partially gated carbon nanotube FETs. *IEEE Trans Nanotechnol* 3:281–286
96. Heinze S, Tersoff J, Martel R, Derycke V, Appenzeller J, Avouris P (2002) Carbon nanotubes as schottky barrier transistors. *Phys Rev Lett* 89:106801
97. Qiu CG, Zhang ZY, Xiao MM, Yang YJ, Zhong DL, Peng LM (2017) Scaling carbon nanotube complementary transistors to 5-nm gate lengths. *Science* 355:271–276
98. Kang D, Park N, Ko JH, Bae E, Park W (2005) Oxygen-induced p-type doping of a long individual single-walled carbon nanotube. *Nanotechnology* 16:1048–1052
99. Joo Y, Brady GJ, Arnold MS, Gopalan P (2014) Dose-controlled, floating evaporative self-assembly and alignment of semiconducting carbon nanotubes from organic solvents. *Langmuir ACS J Surf Colloids* 30:3460–3466
100. Brady GJ, Joo Y, Wu MY, Shea MJ, Gopalan P, Arnold MS (2014) Polyfluorene-sorted, carbon nanotube array field-effect transistors with increased current density and high on/off ratio. *ACS Nano* 8:11614–11621
101. Javey A, Kim H, Brink M, Wang Q, Ural A, Guo J, McIntyre P, McEuen P, Lundstrom M, Dai HJ (2002) High-kappa dielectrics for advanced carbon-nanotube transistors and logic gates. *Nat Mater* 1:241–246
102. Derycke V, Martel R, Appenzeller J, Avouris P (2001) Carbon nanotube inter- and intramolecular logic gates. *Nano Lett* 1:453–456
103. Chen ZH, Appenzeller J, Lin YM, Sippel-Oakley J, Rinzler AG, Tang JY, Wind SJ, Solomon PM, Avouris P (2006) An integrated logic circuit assembled on a single carbon nanotube. *Science* 311:1735
104. Pei T, Zhang PP, Zhang ZY, Qiu CG, Liang SB, Yang YJ, Wang S, Peng LM (2014) Modularized construction of general integrated circuits on individual carbon nanotubes. *Nano Lett* 14:3102–3109
105. Javey A, Kong J (2009) Carbon nanotube electronics. Springer Science & Business Media, New York
106. Odom TW, Huang J-L, Kim P, Lieber CM (1998) Atomic structure and electronic properties of single-walled carbon nanotubes. *Nature* 391:62–64
107. Zou Y, Li Q, Liu J, Jin Y, Qian Q, Jiang K, Fan S (2013) Fabrication of all-carbon nanotube electronic devices on flexible substrates through CVD and transfer methods. *Adv Mater* 25:6050–6056
108. Moisala A, Nasibulin AG, Brown DP, Jiang H, Khriachtchev L, Kauppinen EI (2006) Single-walled carbon nanotube synthesis using ferrocene and iron pentacarbonyl in a laminar flow reactor. *Chem Eng Sci* 61:4393–4402
109. Zhang JL, Wang C, Zhou CW (2012) Rigid/flexible transparent electronics based on separated carbon nanotube thin-film transistors and their application in display electronics. *ACS Nano* 6:7412–7419
110. Arnold MS, Green AA, Hulvat JF, Stupp SI, Hersam MC (2006) Sorting carbon nanotubes by electronic structure using density differentiation. *Nat Nanotechnol* 1:60–65
111. Cao Q, Rogers JA (2009) Ultrathin films of single-walled carbon nanotubes for electronics and sensors: a review of fundamental and applied aspects. *Adv Mater* 21:29–53
112. Rouhi N, Jain D, Burke PJ (2011) High-performance semiconducting nanotube inks: progress and prospects. *ACS Nano* 5:8471–8487
113. Arnold MS, Stupp SI, Hersam MC (2005) Enrichment of single-walled carbon nanotubes by diameter in density gradients. *Nano Lett* 5:713–718
114. Green AA, Hersam MC (2011) Nearly single-chirality single-walled carbon nanotubes produced via orthogonal iterative density gradient ultracentrifugation. *Adv Mater* 23:2185–2190
115. Liu H, Nishide D, Tanaka T, Kataura H (2011) Large-scale single-chirality separation of single-wall carbon nanotubes by simple gel chromatography. *Nat Commun* 2:309

116. Tu X, Manohar S, Jagota A, Zheng M (2009) DNA sequence motifs for structure-specific recognition and separation of carbon nanotubes. *Nature* 460:250–253
117. Sangwan VK, Ortiz RP, Alaboson JMP, Emery JD, Bedzyk MJ, Lauhon LJ, Marks TJ, Hersam MC (2012) Fundamental performance limits of carbon nanotube thin-film transistors achieved using hybrid molecular dielectrics. *ACS Nano* 6:7480–7488
118. Choi SJ, Wang C, Lo CC, Bennett P, Javey A, Bokor J (2012) Comparative study of solution-processed carbon nanotube network transistors. *Appl Phys Lett* 101:112104
119. Miyata Y, Shiozawa K, Asada Y, Ohno Y, Kitaura R, Mizutani T, Shinohara H (2011) Length-sorted semiconducting carbon nanotubes for high-mobility thin film transistors. *Nano Res* 4:963–970
120. Sze SM, Ng KK (2006) Physics of semiconductor devices. Wiley, Hoboken
121. Che YC, Chen HT, Gui H, Liu J, Liu BL, Zhou CW (2014) Review of carbon nanotube nanoelectronics and macroelectronics. *Semicond Sci Technol* 29:073001
122. Ding J, Li Z, Lefebvre J, Cheng F, Dubey G, Zou S, Finnie P, Hrdina A, Scoles L, Lopinski GP, Kingston CT, Simard B, Malenfant PR (2014) Enrichment of large-diameter semiconducting SWCNTs by polyfluorene extraction for high network density thin film transistors. *Nanoscale* 6:2328–2339
123. Xu W, Zhao J, Qian L, Han X, Wu L, Wu W, Song M, Zhou L, Su W, Wang C, Nie S, Cui Z (2014) Sorting of large-diameter semiconducting carbon nanotube and printed flexible driving circuit for organic light emitting diode (OLED). *Nanoscale* 6:1589–1595
124. Cao C, Andrews JB, Kumar A, Franklin AD (2016) Improving contact interfaces in fully printed carbon nanotube thin-film transistors. *ACS Nano* 10:5221–5229
125. Lau PH, Takei K, Wang C, Ju Y, Kim J, Yu Z, Takahashi T, Cho G, Javey A (2013) Fully printed, high performance carbon nanotube thin-film transistors on flexible substrates. *Nano Lett* 13:3864–3869
126. Sajed F, Rutherford C (2013) All-printed and transparent single walled carbon nanotube thin film transistor devices. *Appl Phys Lett* 103:143303. doi:[10.1063/1.4824475](https://doi.org/10.1063/1.4824475)
127. Kim SH, Hong K, Xie W, Lee KH, Zhang S, Lodge TP, Frisbie CD (2013) Electrolyte-gated transistors for organic and printed electronics. *Adv Mater* 25:1822–1846
128. Kim B, Park J, Geier ML, Hersam MC, Dodabalapur A (2015) Voltage-controlled ring oscillators based on inkjet printed carbon nanotubes and zinc tin oxide. *ACS Appl Mater Interfaces* 7:12009–12014
129. Kim B, Geier ML, Hersam MC, Dodabalapur A (2014) Complementary D flip-flops based on inkjet printed single-walled carbon nanotubes and zinc tin oxide. *IEEE Electron Device Lett* 35:1245–1247
130. Higuchi K, Kishimoto S, Nakajima Y, Tomura T, Takesue M, Hata K, Kauppinen EI, Ohno Y (2013) High-mobility, flexible carbon nanotube thin-film transistors fabricated by transfer and high-speed flexographic printing techniques. *Appl Phys Express* 6:085101
131. Cao X, Cao Y, Zhou C (2016) Imperceptible and ultraflexible p-type transistors and macroelectronics based on carbon nanotubes. *ACS Nano* 10:199–206
132. Yang YJ, Ding L, Han J, Zhang ZY, Peng LM (2017) High-performance complementary transistors and medium-scale integrated circuits based on carbon nanotube thin films. *ACS Nano* 11:4124–4132
133. Cao Q, Hur SH, Zhu ZT, Sun YG, Wang CJ, Meitl MA, Shim M, Rogers JA (2006) Highly bendable, transparent thin-film transistors that use carbon-nanotube-based conductors and semiconductors with elastomeric dielectrics. *Adv Mater* 18:304–309
134. Chae SH, Yu WJ, Bae JJ, Duong DL, Perello D, Jeong HY, Ta QH, Ly TH, Vu QA, Yun M, Duan X, Lee YH (2013) Transferred wrinkled Al₂O₃ for highly stretchable and transparent graphene-carbon nanotube transistors. *Nat Mater* 12:403–409



REVIEW

Carbon Nanotube Thin Film Transistors for Flat Panel Display Application

Xuelei Liang¹ · Jiye Xia¹ · Guodong Dong¹ ·
Boyuan Tian¹ · lianmao Peng¹

Received: 22 August 2016 / Accepted: 5 November 2016 / Published online: 21 November 2016
© Springer International Publishing Switzerland 2016

Abstract Carbon nanotubes (CNTs) are promising materials for both high performance transistors for high speed computing and thin film transistors for macroelectronics, which can provide more functions at low cost. Among macroelectronics applications, carbon nanotube thin film transistors (CNT-TFT) are expected to be used soon for backplanes in flat panel displays (FPDs) due to their superior performance. In this paper, we review the challenges of CNT-TFT technology for FPD applications. The device performance of state-of-the-art CNT-TFTs are compared with the requirements of TFTs for FPDs. Compatibility of the fabrication processes of CNT-TFTs and current TFT technologies are critically examined. Though CNT-TFT technology is not yet ready for backplane production line of FPDs, the challenges can be overcome by close collaboration between research institutes and FPD manufacturers in the short term.

Keywords Carbon nanotube · Thin film transistors · Backplane · Flat panel display

Chapter 8 was originally published as Liang, X., Xia, J., Dong, G., Tian, B. & Peng, l. Top Curr Chem (Z) (2016) 374: 80. DOI 10.1007/s41061-016-0083-6.

-
- ✉ Xuelei Liang
liangx1@pku.edu.cn
 - ✉ lianmao Peng
lpmpeng@pku.edu.cn

¹ Key Laboratory for the Physics and Chemistry of Nanodevices and Department of Electronics, Peking University, Beijing 100871, China

1 Introduction

Since its discovery nearly two-and-a-half decades ago, the carbon nanotube (CNT) remains of great interest as an emerging material in nano-science and technology [1, 2]. Because of its unique structure and superb electronic properties [3], single-walled CNTs (SWCNTs) are envisioned as the most promising candidate for information processing technologies beyond CMOS [4]. To compete with Si-based high performance transistors for computational devices, ideal carbon nanotube field-effect transistors (CNT-FETs) should be fabricated on well-aligned high-density semiconducting CNTs with controllable location, inter-tube spacing, and chirality on a 300-mm wafer scale [5, 6]. However, it is still a great challenge for such high standard SWCNT material production. In addition to the material challenge, the device fabrication technology is also far from ready for manufacturing, though some complicated CNT-FET circuits have been demonstrated [7–10]. The fabrication processes should be compatible or can be integrated with the highly developed Si-based chip fabrication technology, and the performance of the devices must be uniform around the wafer scale. Therefore, it is hard to predict whether the CNT-based high performance transistor technology will be ready at the time node around 2020, when the Si-based CMOS will reach its absolute performance limits [11].

In parallel to the high performance transistors for computational devices, such as microprocessor, thin film transistors (TFTs) are widely used for macroelectronics. The performance of the transistors required for the macroelectronics are not as high as those for the computational devices, while the costs and functions are critical concerns for the macroelectronics [11]. The channel materials for the thin film transistor are, therefore, not necessarily single crystal semiconductor material. Amorphous and polycrystalline semiconductors can be employed as the channel material, such as amorphous Si (a-Si), poly-Si, metal oxide, and organic semiconductors [12]. Nevertheless, performance uniformity is still strictly required for TFTs on large area substrates up to meters scale and even larger. The channel size of TFTs are usually several to hundreds of micrometers. Thus, the non-uniformity due to the channel material may be smoothed out in the large channel area and uniform performance on large area substrates is obtainable.

In recent years carbon nanotube thin film transistors (CNT-TFTs) have drawn more and more attentions. In CNT-TFTs, the channel layer is random network or partially aligned CNT films composed of numerous SWCNTs. Many methods have been reported for producing SWCNT thin film at low cost on large area substrates. In some aspects the reported performances of the CNT-TFTs are superior to those fabricated by the current TFT manufacturing technologies [13–25]. These make CNT-TFTs strong competitors in the field of macroelectronics [17–19] for products such as displays, flexible electronics, bio-chemical sensors, and solar cells.

Flat panel display (FPD), an industry with a total value of hundreds of billions of U.S. dollars [26], is undoubtedly one of the most important macroelectronic products. A backplane with TFT array is a necessary component of each FPD, which is used for pixel addressing. Actually, the development of FPDs burgeoned only when a-Si TFTs became available [12]. As FPDs develop to larger size, ultra-

high resolution, low power, high frame rate, and flexibility, the current TFT technologies are difficult to meet all these demands. Therefore, new materials and technologies for TFTs are demanded to keep the FPD industry growing.

As an emerging TFT technology, CNT-TFTs have shown high mobility, high on/off ratio, and high on-current [27, 28], the performance of which can surpass the current TFT technologies potentially. Moreover, the fabrication process is regarded as facile, reliable, scalable to large area, and compatible with the current TFT manufacturing process [29]. Therefore, CNT-TFT technology is very promising for the future FPD industry. Research on using CNT-TFTs for pixel-driving circuits for displays has been performed in many groups [24, 30, 31]. Active matrix organic light-emitting diode (AMOLED) displays driven by CNT-TFTs have been demonstrated in the laboratory [13, 32], though with limited yields.

Much of the effort on the application of CNT-TFTs for backplane FPD electronics has been in research laboratories previously, and now it is at a critical status of being transferred from lab to industry. Two-and-a-half decades have passed since the discovery of CNT; however, almost no electronic products of CNT-FETs have been commercialized. Since research on CNT-TFTs is progressing rapidly in recent years, we have good reasons to believe that FPD products integrated with CNT-TFT technology are possible in the near future.

In this paper, we review the progress on CNT-TFTs from the point of FPD manufacturing. This review is organized as follows. In Sect. 2, we briefly introduce the structure of the FPD. Herein, we show how to address pixels using a TFT array. In Sect. 3, we discuss the trends of the FPD products and their requirements for TFT technologies, and elucidate why CNT-TFTs are promising for future FPDs. In Sect. 4, we discuss the challenges of the CNT-TFT technology for display applications. The challenges are discussed from the aspects of materials, fabrication process, device performance, stability, and uniformity. Finally, in Sect. 5, we conclude the review and future prospect of CNT-TFT technology.

2 Flat Panel Displays and TFTs

A flat panel display comprises many pixels arranged in arrays, which compose an image. There is an element in each pixel that has an electro-optical effect, and this effect can be switched on and off for displaying an image. It is not an easy task to deliver picture data to each pixel of a FPD with millions of pixels. To deliver image data to the electro-optical element in each pixel correctly, an addressing circuit is needed for a FPD so that each pixel can be addressed individually. All of today's high quality displays use active matrix addressing, where there is at least one TFT in each pixel. The TFTs in each pixel are used as switching devices to set image data of the pixel in a short addressing time and to store it until the next refresh signal is obtained.

For a principle demo, as illustrated in Fig. 1, the TFT matrix is connected in rows and columns, with a common connection to the gate electrodes in each row, and a common connection to the drain terminals in each column (n-type FET). The source of each TFT is connected to the element for electro-optical effect. The image signal

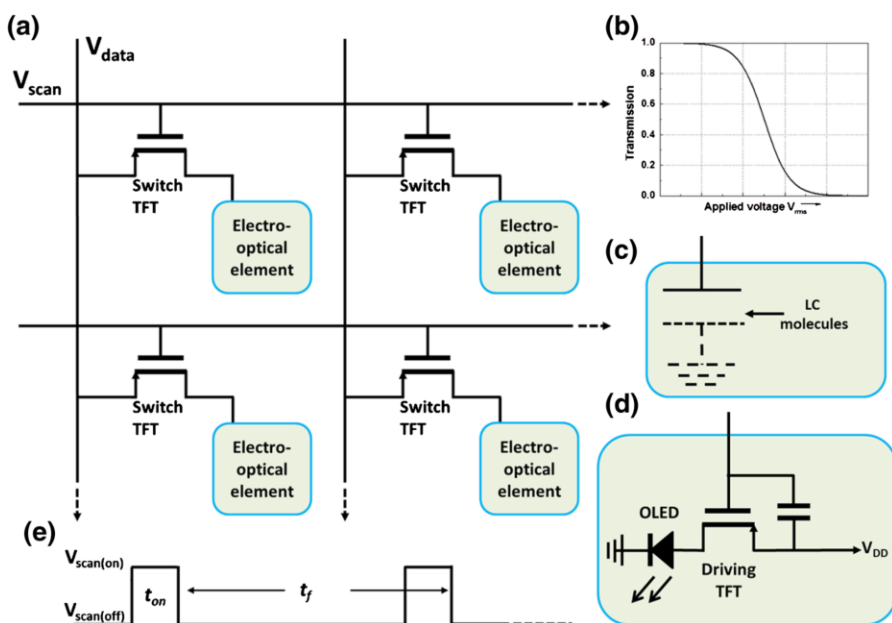


Fig. 1 **a** Active matrix layout. **b** Illustration of typical transmission versus voltage curve of LC. **c** Diagram of the electro-optical element based on LC and **d** OLED. **e** Row timing signal wave form

is fed into the pixel array in a serial row-by-row mode, by sequentially switching on each row of TFTs ($V_{\text{scan}} = V_{\text{on}}$), whilst holding the others in the off-state ($V_{\text{scan}} = V_{\text{off}}$). During the time interval of a row was switching on (t_{on}), the signal voltages (V_{data}) on the column electrodes of the display are applied in parallel to the common drains of TFTs. However, the signal will be sent to only the one row of the electro-optical effect elements connected to the row of TFTs, which has been turned on. At the end of t_{on} , that row is deselected (by switching the gate bias to V_{off}), and the adjacent row is switched on, and the process described above is repeated. In this way, the image information is loaded row by row during a frame time (t_f), and signals need to be maintained. Then the whole process is repeated with the next frame of image information.

The representatives of the electro-optical elements are realized using liquid crystal (LC) molecules or organic light emission diodes (OLED). In the liquid crystal display (LCD), the LC molecules work as the dielectrics of the capacitor in each pixel (Fig. 1c). When the capacitor is charged by V_{data} , the LC molecule will turn in the electric field, and the transmission of the ambient illumination is modulated in this way (shown in Fig. 1b). In the active matrix OLED (AMOLED) display, an OLED in the pixel gives emission of light when switched on. In addition to the addressing TFT, another driving TFT and a capacitor are needed, composing the 2T1C driving circuits for AMOLED (Fig. 1d). When the addressing TFT (switch transistor) is switched on by V_{scan} , V_{data} is sent to the pixel. Then the driving TFT is turned on and current flow through the OLED, which emits light. During the

time period of t_{on} , the capacitor is also charged, which can supply a voltage to keep the driving TFT on during t_f when the addressing TFT is off.

From the above discussion, we know the TFTs are crucial for a FPD. Actually, the growth of this industry has been facilitated by the manufacturability of high quality TFTs for display addressing, and, equally, the development of the industry has stimulated worldwide interest and research into TFTs.

Currently, there are three types of commercialized TFT technologies, amorphous Si (a-Si), metal oxide (MO or MOx), and low temperature poly-silicon (LTPS). We will compare them with CNT-TFTs in the next section.

3 Why Is CNT-TFT Technology Promising for FPDs?

As mentioned before, the development of FPDs burgeoned only when a-Si TFTs became available. Nowadays, a-Si is still the dominant TFT technology for the display industry. However, the mobility of the a-Si TFTs is usually $<1 \text{ cm}^2/\text{Vs}$ [12]. It has been reported that the a-Si TFTs cannot drive larger LCDs (e.g. 55 inches) operating at a high frame rate above 120 Hz [33, 34] due to its low mobility (shown in Fig. 2). The required mobility is even higher for displays with larger panel size, higher frame rate, and higher resolution.

Two materials with higher mobility, LTPS and MO, are beginning to replace a-Si in TFTs for display. Table 1 compares these three TFT technologies, and CNT-TFT as well. Though LTPS and MO are superior to a-Si in some aspects, they have their own disadvantages. Each of the three materials is well suited to the requirements of specific commercial FPD products.

Typical mobility of LTPS TFTs is in the range of 30–100 cm^2/Vs [34], which is almost 100 times better than a-Si. LTPS is applicable for CMOS architecture that

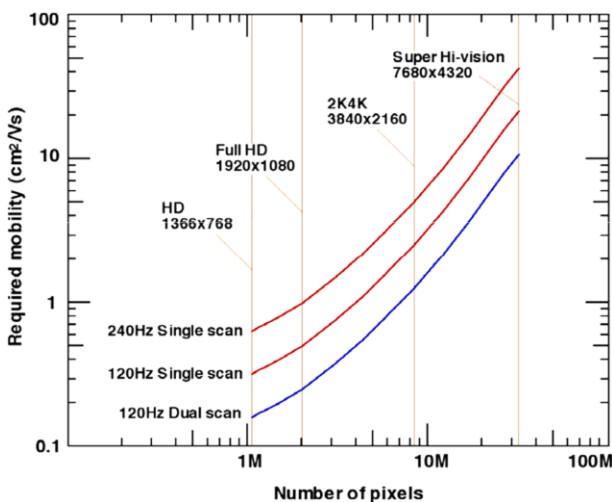


Fig. 2 Required carrier mobility for future displays [34] (Copyright 2010 Taylor & Francis)

Table 1 Comparison of the TFT technologies

	a-Si	LTPS	a-IGZO	CNT-TFT
Generation	>10G	4G/8G?	8G	
TFT masks for LCD/OLED	(3)4–5/6–7	5–9/7–11	4–5/6–7	Compatible with a-Si
Mobility (cm^2/Vs)	0.1 ~ 1	50 typical, ~ 250 possible	5–15 currently, ~ 50 possible	>250 reported
TFT uniformity	Good	Poor/better	Good	
TFT polarity	n-channel	CMOS	n-channel	p/n, CMOS
Pixel circuit for OLED		Complex (ex. 6T2C)	Simple (3T + 1C)	2T + 1C demonstrated
Cost/yield	Low/high	High/medium	Low/medium	Can be low
Reliability	Medium	Good	Medium	
Max. process temperature (°C)	330	Depo. 200, anneal 450	depo. 350	<300
Circuit integration	No	Yes	No	Yes
Display mode	LCD	LCD, OLED	LCD, OLED	LCD, OLED
Solution process, printing	No	Laser annealed	270–400 °C	Yes
Production status	Mass production	Mass production	Mass production	R & D
Semiconductor deposition	PECVD	PECVD + crystallization	PVD	Solution process, room temp.
I_{on}	Low	High	Medium	High
I_{off}	Medium	High	Low	High/low, depends on tube diameter
On/off	Low	High/medium	High	Low ~ medium
SS	High	Medium	Low	Low ~ medium
Substrate	Glass, metal (plastic)	Glass, metal (plastic)	Glass, metal, plastic	Glass, metal, plastic

uses complementary pairs of p-type and n-type transistors for circuitry design [35]. However, the fabrication processes are very complicated, e.g. usually 5–11 photo masks are used [36], and the process temperature is high (400–500 °C). Consequently, the manufacturing cost of LTPS TFTs is very high. Furthermore, the uniformity of LTPS TFTs is relatively poor [34], which hinders its scales up to large size panels. Currently, LTPS are mainly used in high-end small-size FPD products, e.g. smart phones with high pixel density.

Among the reported MO TFTs, the most researched is amorphous In–Ga–Zn–O (a-IGZO) [34, 36], which has typical mobility in the range of 5–15 cm^2/Vs . The a-IGZO TFTs have extremely low off-current and high on/off ratio. These advantages enable FPDs with faster frame rate and lower power consumption than

a-Si. Also, the fabrication cost of IGZO TFTs is lower than LTPS. Though the mobility of a-IGZO is higher than a-Si, it is lower than that for LTPS [37], which limits its application in ultra-high resolution FPDs. More importantly, the narrow process window and poor long term stability are still challenges for the MO TFTs [36].

The current trends of FPDs products are large panel size, ultra-high resolution, low power, high frame rate, flexibility, and transparency. New materials and technologies for high performance TFTs are in high demand to keep the FPD industry growing. There are continuous efforts in searching for new types of TFTs to improve performance or to lower the production cost of TFTs. CNT-TFTs are promising candidates, which may comply with the requirements of the above trends.

Single-wall CNT (SWCNT) can be regarded as a seamless cylinder rolled by graphene. Though it is only one atomic thick, there are no dangling bonds in the surface. Owing to its perfect structure and quasi-one-dimensional quantum confinement effects, the carrier scattering in SWCNT was greatly reduced. The mean free path of carriers in SWCNT is up to micrometer, thus ballistic transport is easily obtained. The mobility of SWCNT can be high up to $100,000\text{ cm}^2/\text{Vs}$ [11]. High performance CNT-TFTs with mobility ranging from tens to hundreds of cm^2/Vs have been reported by many research groups [15, 16, 38–41]. These results make CNT-TFTs very attractive for pixel driving circuits of display. The atomic thin body results in excellent gate control of the channel even in extremely scaled CNT-FETs. The strong carbon–carbon bond and the high thermal conductance allow it to carry high current up to 10^9 A/cm^2 . SWCNT is one of the most strong and flexible known materials. CNT thin film is transparent, making it suitable for transparent and flexible electronics. Moreover, CNT thin film can be fabricated at room temperature in air and is compatible with printing technology, which we will discuss later. These relieve the requirements for high vacuum instruments and high temperature tolerant glass substrates, and hence the production cost of CNT-TFT backplane may be lowered greatly. The low temperature process also enables CNT-TFTs for the flexible display. These advantages make CNT-TFT technology a strong competitor for TFT backplanes in FPDs.

The potential application of CNT-TFTs for backplanes in FPD has been demonstrated in laboratory-scale experiments, as shown in Fig. 3. Chongwu Zhou's group fabricated AMOLED display elements with 500 pixels driven by 1000 CNT-TFTs. Three hundred and forty-eight out of the 500 pixels are turned on, corresponding to a yield of 70% [13]. They also fabricated CNT-TFTs by fully printed process with resulting mobility of $9\text{--}30\text{ cm}^2/\text{Vs}$ [24]. An OLED was successfully driven by circuits composed of two such fully printed CNT-TFTs [24]. These works show potential for low cost fabrication of CNT-TFT backplanes. Fully transparent [31] and printed flexible pixel [30] circuits driven by CNT-TFT are also demonstrated. CNT-TFT driver circuits for both static and dynamic AMOLED displays with 6×6 pixels [32] was reported by Qing Zhang's group recently.

All these progresses demonstrated the possibility of CNT-TFT technology for backplane in FPDs. However, there are still many challenges to overcome before it reach to the manufacturing of FPD products. We discuss the main challenges in the following section.

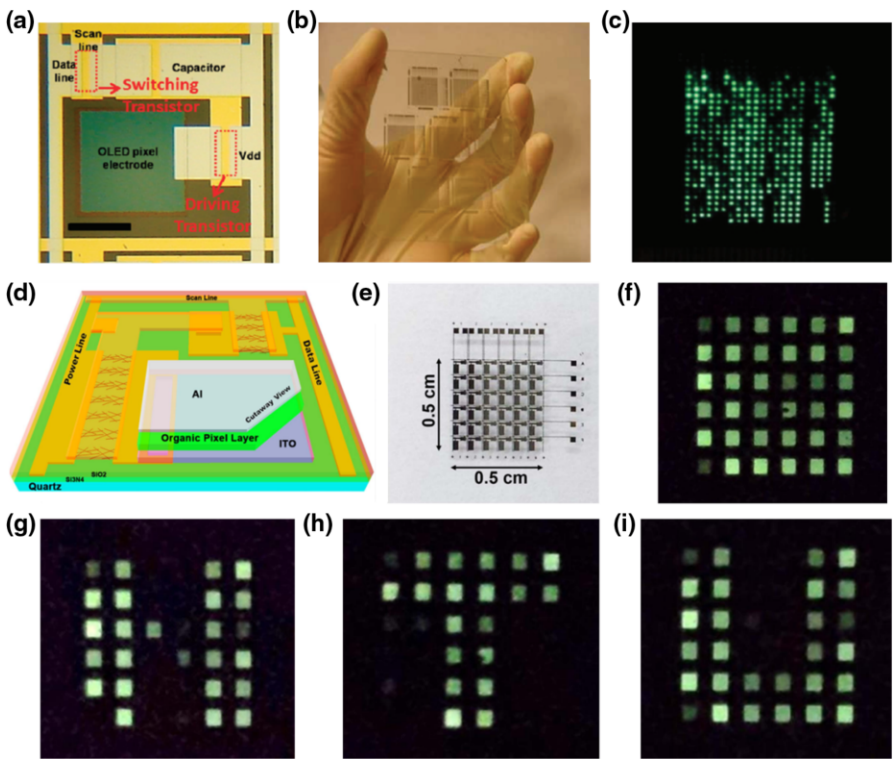


Fig. 3 Demonstration of AMOLED display driven by CNT-TFTs. Optical microscope images of the single pixel circuit (**a**) and **b** 7 AMOLED arrays, each with 20×25 pixels. **c** Photograph showing the AMOLED array was turned on. Reprinted with permission from [13] (Copyright 2011 American Chemical Society). **d** A schematic cross-sectional perspective view of the single AMOLED pixel. **e** Photograph of the 6×6 pixel array. **f–i** Turn on image of the AMOLED array. Reprinted with permission from [32] (Copyright 2015 Nature Publishing Group)

4 Challenges of CNT-TFT Technology for Display

The components of a CNT-TFT includes a CNT thin film channel, electrodes (source, drain, and gate), and an insulating layer for gate dielectrics. For display application, the CNT-TFTs are fabricated in arrays on the backplane glass. The performance of the CNT-TFTs must comply with those requirements for pixel addressing and picture quality. The fabrication process must be facile, reliable, and scalable to large area. Low cost and compatibility to current TFT fabrication processes are also required. In the following, we discuss the challenges of the materials for CNT-TFTs (including the CNT thin film, the electrodes, and gate dielectrics), the device fabrication process, and the device performance.

4.1 SWCNT Materials and Thin Film Fabrication

The channel of CNT-TFTs is a two-dimensional film composed of numerous SWCNTs. Undoubtedly, high quality CNT thin film is critical to the performance of CNT-TFTs. The techniques for SWCNT thin films production can be divided into three categories, direct growth on target substrates, growth and transfer to target substrates, and solution process.

In the direct growth method, a catalyst was first coated on the target substrate. Then the substrate was loaded into a reaction chamber, usually a furnace, and SWCNTs were grown by chemical vapor deposition (CVD) process. Random network [31] or aligned [42] SWCNT film are obtained and the CNT-TFTs are, therefore, fabricated by conventional lithography processes. Though such SWCNTs are very high quality, many metallic SWCNTs exist, which is undesirable for CNT-TFTs. Moreover, the growth temperatures of the CVD processes are very high, usually above 800–1000 °C [43]. These limit the substrate choice only to quartz glass [44], which can tolerate such high temperature for the CNT direct growth method for display application.

To avoid the high growth temperature, transfer techniques are introduced. The CNT films are grown on high temperature tolerable substrates first, e.g. Si or quartz, using the usual CVD processes, as discussed above. Then they are transferred to the target substrates through a low temperature process. To transfer the CNT film, a layer of gold film was deposited onto the growth substrate to cover the CNT thin film in Chongwu Zhou's group [14]. Then the gold/CNT film was peeled off from the growth substrate by thermal release tape and released to the target substrate at relatively low temperature (~130 °C). After etching of the gold layer, the CNT film was ready for device fabrication on the target substrate. Similar transfer processes were developed by Kang et al. [45] by using PDMS instead of thermal release tape. Sun et al. [41] used a different type of transfer technique. The CNTs were grown using a floating-catalyst CVD technique and the CNT film was collected by filtering through membrane filters at room temperature. The CNT film was transferred to the target substrate by placing the membrane filter on the substrate and dissolved the filter in acetone. Since the target substrates do not experience the high growth temperature, there are no limits for substrate choices, and hence flexible CNT-TFTs can be fabricated.

However, the fatal weakness of the above two categories of SWCNT thin film production techniques is that considerable SWCNTs (nearly one third) in the film are metallic. These metallic CNTs degrade the on/off current ratio of the CNT-TFTs greatly. To improve the on/off ratio, further engineering of the CNT film must be done. For the random CNT network, the geometries of the TFT channel are engineered according to the percolating transport theory [25, 46, 47]. The number of the percolating metallic pathways from the source to drain can be reduced by either stripping [20, 31, 32] (Fig. 4a) the CNT film or lowering the tube density and enlarge the channel length (~100 μm) [41] at the same time (Fig. 4b). For the aligned CNTs, an electrical breakdown strategy is used to remove the metallic CNTs [42]. Stripping or electrical breakdown complicate the fabrication process of CNT-TFTs and increases the manufacturing costs. Using lower density CNT films

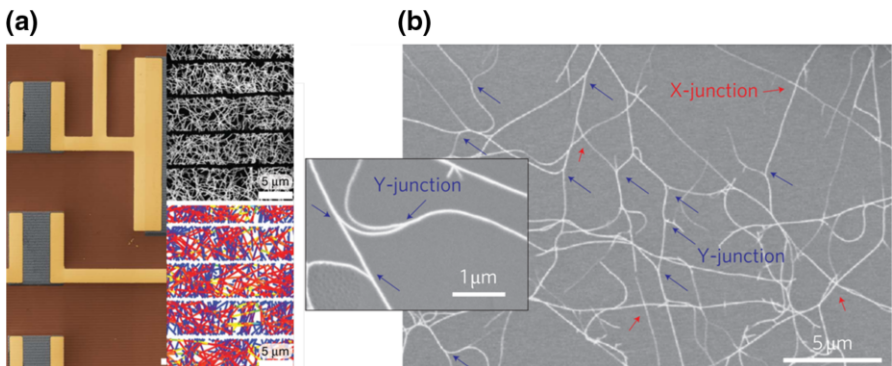


Fig. 4 Increasing the on/off ratio of the CNT-TFT. **a** Stripping high density SWCNT film. Reprinted with permission from [20] (Copyright 2008 Nature Publishing Group). **b** Using low density SWCNT film. Reprinted with permission from [41] (Copyright 2011 Nature Publishing Group)

with longer channel lengths results in very low on-current density [41]. To obtain high enough current for pixel driving, the channel width of the CNT-TFT has to be enlarged meanwhile. Thus, the size of such CNT-TFT is pretty large, which limits the application of this strategy for high pixel density displays. Moreover, CVD growth on substrates is included in both of the two CNT film fabrication techniques, which is a relatively low productivity process. Whether the CVD growth of CNT is scalable to large area substrates, e.g. the size of backplane glasses, is not known. Therefore, neither the direct growth on target substrates method and the growth and transfer to target substrates method are suitable for mass production of CNT-TFT backplanes.

SWCNTs can be generated in powder form by several methods, and the products can be dissolved in solutions [29]. Then CNT thin films can be produced by solution deposition. The high temperature CNT growth processes are separated by the thin film fabrication processes in this route, which enables the thin film to be fabricated at room temperature on arbitrary substrates. Although the as-produced CNTs are a mixture of both semiconducting and metallic types, a variety of post-production sorting techniques have been developed to enrich semiconducting SWCNTs in the solution. Some of these techniques include DNA-assisted sorting [48, 49], conjugated polymer-assisted sorting [50, 51], porphyrin-assisted sorting [52], sorting using copolymers [53], gel chromatography [54, 55], aqueous two-phase extraction [56], and density gradient ultracentrifugation (DGU) [57]. A high purity of separated semiconducting SWCNTs up to 99.9%, measured by electrical testing, has been reported [58]. Although still not meeting the purity requirement of 99.9999% [5] for high performance FETs, it does satisfy CNT-TFTs. A benefit of these research progresses is that SWCNT solutions with semiconducting purity above 99% are now commercially available [59, 60]. Currently the sorted SWCNT solution is pretty expensive, e.g., several hundreds of U.S. dollars per milligram, which is an obstacle for mass production of CNT-TFT backplanes. However, this is mostly due to the relatively small quantity of market demand presently. If production of the sorted SWCNT material is scaled up, the cost will be reduced greatly.

Once high purity semiconducting SWCNT solutions are obtained, industrially well-established solution deposition methods such as ink-jet/aerosol printing [24, 61, 62] can be used to deposit SCWNTs onto the large size backplane glasses or flexible substrates with high throughput and low cost. More importantly, fabrication of the SWCNT films is compatible with the existing TFT backplane manufacturing process. Therefore, solution processed SWCNTs are the best choice for CNT-TFT backplane electronics. Hereafter, we focus our discussions on the solution processed SWCNTs.

Many methods have been reported for SWCNT thin film fabrication from SWCNT solutions. Among these methods, the most used is direct solution deposition [15, 21, 38]. In this method, a piece of substrate is immersed into the SWCNT solution for certain time, and then the SWCNTs are deposited onto the substrate, which forms a thin film. The film density can be controlled by the solution concentration and soaking time. This method is very simple; however, the throughput is low because the deposition usually takes hours to even several days to obtain a film with the desired density [21, 38]. To improve the SWCNT deposition, the surface of the substrate is commonly functionalized with a self-assembling monolayer by using aminopropyltriethoxysilane (APTES) [15], poly-L-lysine (PLL) [63–65], or HMDS [16, 39, 66]. Thus, pretty uniform SWCNT films are obtained in relatively short time. However, the short range uniformity of the film is usually worse than long range [13, 15, 67], which leads to higher performance fluctuation when the TFTs are scaled down for high pixel density displays.

In addition to the direct deposition method, the well-established ink-jet or aerosol printing methods amenable to solution processed SWCNTs [24, 30, 61], as mentioned before. These thin film fabrication technologies are high throughput and scalable to large area. Printing is also an “additive” lithographic technique, which can avoid the wasting of material and the use of photolithography or other expensive lithographic tools, potentially reducing the fabrication cost. An OLED driving circuit composed of fully printed CNT-TFTs on Si wafers controlled the OLED successfully and was demonstrated by Chen et al. [24]. Similar circuits for OLED driving on flexible substrate was reported by Xu et al. [30]. These works demonstrate the significant potential of printed CNT-TFTs for display backplane applications.

The uniformity of the printed CNT films is usually worse than those of direct solution deposited, especially at the rim of the printed patterns, due to the coffee ring effect. Many more contaminants are easily observed in the as-fabricated SWCNT films by printing methods than solution deposition. There are usually excessive surfactants and or other species in the CNT solution, which are used for CNT dispersion and sorting. In the printing process, all of these species are left on the substrate, which contaminates the CNT thin film. Therefore, a thorough washing step is needed to clean these contaminants [24, 30, 68, 69]. Meanwhile, in the solution deposition processes, the deposition is assisted by the electrostatic interaction between the functionalized substrate and the SWCNTs in solution [70, 71] so that less contaminants were observed.

SWCNT thin films, generated by either solution deposition or printing, are random networks, which include numerous inter-tube junctions. These junctions

limit the charge transport through the film. The number of the junctions can be reduced by aligning the tubes, thus improving the mobility of the film. Densely aligned SWCNT films can be obtained in self-assembly processes by tuning the interaction at the interface of the three phases, i.e. CNT solution, air, and the solid substrate [66, 72–74]. Figure 5 depicts some self-assembled SWCNT stripes with aligned tubes. However, the critical disadvantages of the self-assembly processes are the low throughput and difficult to scale up to large area. Otherwise, the self-assembly process is not easy to control, e.g. the positions (or the starting position of the first stripe) and the spacing between these self-assembled stripes shown in Fig. 5 are not strictly controlled. Therefore, such films are not suitable for TFT array fabrication.

External forces can also be employed to align SWCNTs. A notable alignment method is ac-dielectrophoresis (DEP), where ac-voltage is applied between two

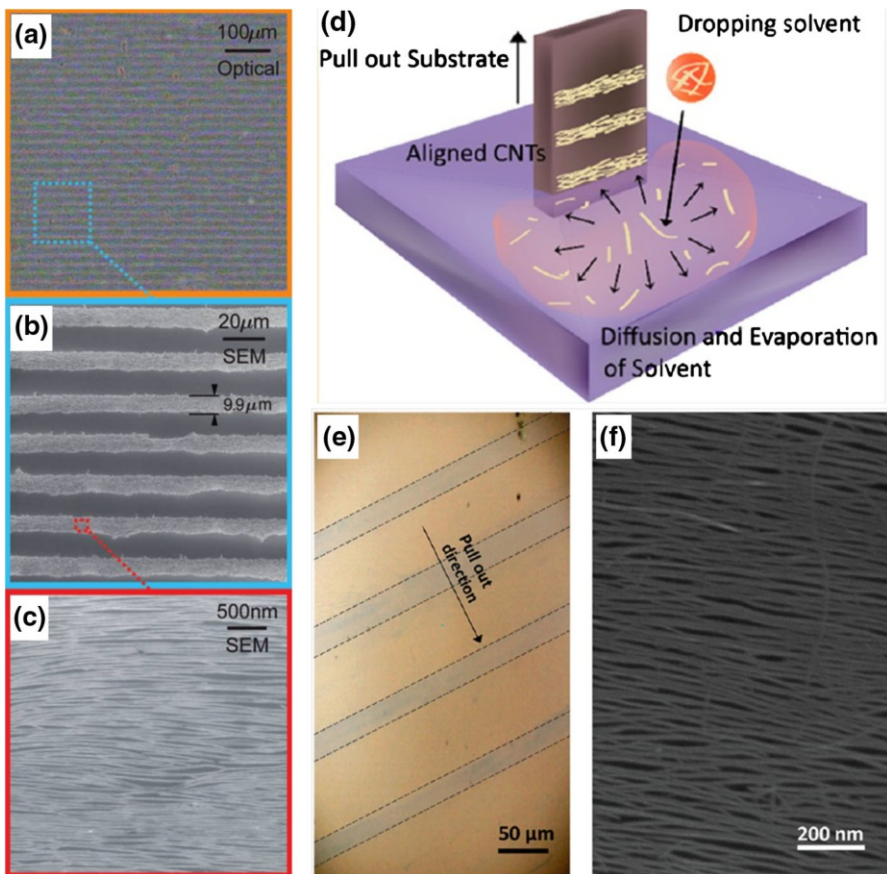


Fig. 5 Densely aligned SWCNT thin film obtained by self-assembly method. **a–c** Evaporation self-assembly. Reprinted with permission from [72] (Copyright 2008 American Chemical Society). **d–f** Dose-controlled floating evaporation method. Reprinted with permission from [66] (Copyright 2014 American Chemical Society)

electrodes to align SWCNTs, as shown in Fig. 6 [75, 76]. Highly aligned SWNTs with controllable density can be obtained by tuning the solution concentration or the ac-voltage frequency. The advantages of DEP are scalable, location selective and high efficiency, wherein the CNT assembly can be finished in several minutes or even seconds [77]. However, DEP preferentially assemble metallic SWCNT, which results in low on/off ratios of the TFTs unless extremely high purity semiconducting SWCNT solution was used [78].

Table 2 compared the above methods for SWCNT film fabrication using solution processed materials. The direct solution deposition and printing methods are more promising; however, they are still under-developed for mass production of CNT-TFT backplanes. More efforts are needed to develop the techniques of CNT thin film fabrication. It should be noted that CNT-TFTs fabricated on glass substrates that are being used for current TFT backplanes are seldom reported (as shown in Table 3). Though might be a trivial issue, it should be confirmed before the CNT-TFTs go out of the laboratory to manufacturing.

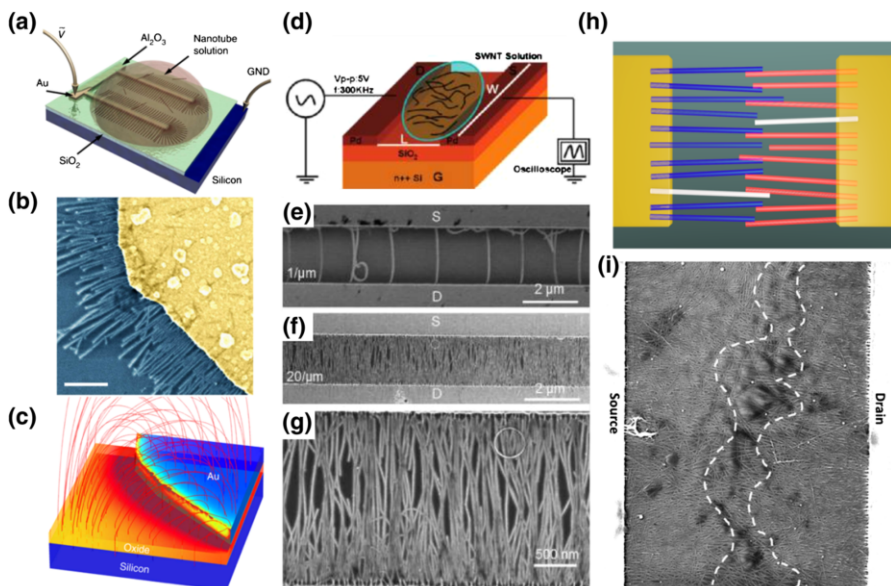


Fig. 6 SWCNTs assembled by DEP. **a–c** Fringing field DEP method Reprinted with permission from [76] (Copyright 2014 Nature Publishing Group). **d–g** Normal co-planar DEP method. Reprinted with permission from [75] (Copyright 2011 American Chemical Society). **h–i** Two step fringing field DEP method. Reprinted with permission from [99] (Copyright 2016 Science China Press). **a** shows the experimental set-up for fringing field DEP, while **d** for normal co-planar DEP. **c** Simulated space distribution of the fringing electric field. **e–d** Control the assembled SWCNT density by simply tuning the concentration of the solution while keeping all other DEP parameters fixed. **h** Two SWCNT arrays were assembled at the source and drain electrodes sequentially which form a cascade structure for reducing the possibility of percolating metallic pathways and the inter-tube junctions in each path

Table 2 Comparison of the SWCNT thin film fabrication methods

	Direct solution deposition	Printing (ink jet/aerosol)	Self-assembly	DEP
CNT geometry	Random network	Random network	Aligned	Aligned
Contamination	Low	High (cleaning needed)	Low	Low
Throughput	High	High	Low	High
Scalability	Good	Good	Poor	Good
Cost	Low	Low	Low	High (pattern electrodes for DEP)
Uniformity	Good	Poor	Medium	Medium
Compatibility to current TFTs manufacturing process	Good	To be determined	Poor	Poor
Process complexity	Low	Medium	High	High

4.2 The Fabrication Process of CNT-TFTs

The investment of a display production line is huge, e.g. billions of U.S. dollars for a line of generation 8 (G8). If the fabrication process of CNT-TFTs can accommodate the existing backplane manufacturing process, the production cost will be greatly reduced. In this section, we discuss the reported CNT-TFT fabrication processes in the laboratory and the requirements for mass production flow in industry.

We have discussed the CNT thin film fabrication in the previous section. After depositing the CNT film on substrates, photolithography is used to pattern the channel of the CNT-TFTs. The channel area is protected by a photoresist and the unwanted areas are removed by oxygen plasma reactive ion etching (RIE). For the fully printed fabrication processes, the photolithography patterning step can be avoided [24, 79]. However, the performances of fully printed CNT-TFTs are relatively low, and the device sizes are relatively big. In those non-fully printed fabrication processes, photolithography is needed for patterning the gate insulator, the source/drain and gate electrodes [61, 80].

Almost all of the reported photolithography processes for CNT-TFT fabrication are lift-off (shown in Fig. 7). In the lift-off process, the photoresist was first patterned, and then the targeted material was deposited over the whole surface of the substrate, and the unwanted area was lifted off using solvents. On the contrary, in the industry of TFT backplane manufacturing, almost every pattern transfer step was combined photolithography and etching processes, either dry or wet. In lift-off process, the un-wanted area of the deposited film was lifted off into the solvents. However, debris may be left on the substrate, which results in device or circuit failure. This problem can be more easily controlled in the etching process. Thus, etching processes are preferred due to production control. Furthermore, there are photoresist patterns on the substrates in the thin film deposition steps in the lift-off process (as shown in Fig. 7). However, the photoresist is not allowed to enter

Table 3 Performance metrics of reported solution processed CNT-TFTs

Ref	CNT separation	Thin film fabrication	L (μm)	W (μm)	Ion ($\mu\text{A}/\mu\text{m}$)	I_{off} (A)	On/off	Mobility (cm^2/Vs)	SS (V/dec)	Hysteresis	Substrate
[123]	No	Spray coating	100	2000	0.15 @ 2 V			6.7	0.26		(PEI-TiO _x) ₁₅ /SiO ₂ /Si
[124]	No	Self-sorting/ aligned	50	1000	~0.001 @ 0.1–1 V	$>10^{-10}$	10^2 – 10^5	0.01–3			SiO ₂ /S, APTES
[125]	Yes	Drop-casting	20	500	~0.02 @ -1 V		10^3 – 10^5	0.4–1.3			SiO ₂ /Si, APTES
[126]	Yes	Drop-casting	25	25	<0.1 @ 1 V		10^3 – 10^7	0.3–10			SiO ₂ /Si
[127]	No	Self-sorting/ spin coating	50	1000	<0.01 @ -1 V	10^{-11}	10^5	<2			SiO ₂ /Si, APTES
[128]	No	Self-sorting/ spin coating	50	1000	<0.05 @ -0.5 V		10^4	<5			Yes
[129]	Yes	Ink-jet printing	125	13	<0.001 @ 1 V			10^2	0.327		SiO ₂ /Si
[130]	Yes	Direct deposition	50–200	500	<0.03		10^{-11}	10^5 – 10^6	<5		
[131]	Yes	Direct deposition	50	500	<0.03 @ 10 V		10^{-13}	10^6 – 10^7	<1		
[132]	Yes	Drop and blow	40	200	~2 @ -1 V		10^{-10}	10^6	164		
[133]	Yes	Direct deposition	5–100	10–200	<0.1 @ 1 V		10^{-11}	10^6	<15		
[134]	Yes	Direct deposition	4–100	10–200	<1 @ 1 V		10^{-11}	10^4 – 10^5	20–30		
[135]	Yes	Spray coating	60–180	50	<0.2 @ 2 V		10^{-10}	10^5	4–23	Yes	SiO ₂

Table 3 continued

Ref	CNT separation	Thin film fabrication	L (μm)	W (μm)	Ion (μA/μm)	I _{off} (A)	On/off	Mobility (cm ² /Vs)	SS (V/dec)	Hysteresis	Substrate
[136]	Yes	Inkjet printing	140	60	<0.1 @0.5 V	10^4 - 10^5	~40		Yes (0.5-2.5 V)	HfO ₂ /PET	
[137]	Yes	Direct deposition	0.8-3	2-30	~1.2 @-0.5 V	10^{-13} - 10^5	73			SiO ₂ /Si, PLL	
[79]	Yes	Direct deposition	~85	~1250	<0.03 @-5 V	10^{-10}	10^4 - 10^5 @-	~2-8		BTO/PET, PLL	
[138]	Yes	DEP	8	22-80	<3 @-1 V	10^3 - 10^5	0.1-20		Yes (>30 V)	Al ₂ O ₃ /glass	
[139]	Yes	Direct deposition	25	100	<1 @1 V	10^5 - 10^7	5-25		Yes	SiO ₂ /Si, PLL	
[140]	Yes	Direct deposition	40	500	~0.02 @-1 V	10^{-12}	10^5 - 10^7	1-10		SiO ₂ /Si, APTES	
[141]	Yes	Drop casting	300-900	500	<0.01 @1 V	10^{-12}	10^5 - 10^6	~1		Al ₂ O ₃ /paper	
[142]	Yes	Direct deposition	40	40	<0.03 @2 V	10^{-13}	10^5	10-20		PET/SiO ₂ , APTES, MgO + Al ₂ O ₃	
[106]	Yes	Direct deposition	5	80	0.01-0. @1 V	10^4 - 10^5	16-20	0.2 (avg.), 0.09 (min.)		HfO, PLL	
[143]	Yes	Direct deposition	4-100	200-2000	<0.01 @0.5 V	10^{-11}	10^4 - 10^7	1-27		SiO ₂ /Si	
[144]	Yes	Aerosol jet printing	100	160	0.1 @-2 V	10^{-12}	10^6	5.3		SiO ₂ /Si, PLL	
[145]	Yes	Direct deposition	4	400	<3 @-5 V	10^5 - 10^7	15-20		Yes	SiO ₂ /Si, PLL	
[15]	Yes		4-100	10-200	~10 @1 V	$>10^4$	~52			SiO ₂ /Si, APTES	

Table 3 continued

Ref	CNT separation	Thin film fabrication	L (μm)	W (μm)	Ion ($\mu\text{A}/\mu\text{m}$)	I _{off} (A)	On/off	Mobility (cm^2/Vs)	SS (V/dec)	Hysteresis	Substrate
[65]	Yes	Direct deposition	105	1000	<0.01 @ -1 V	10^{-10}	$10^4\text{-}10^5$	7.67	Yes (minimal)	SiO ₂ , PET + PLL	
[24]	Yes	Printing	10–200	100–500	<0.1 @ 1 V ~0.8 @ 1 V	$10^4\text{-}10^7$	9–30 $>10^4$	31.65		SiO ₂ /Si	
[13]	Yes	Direct deposition	20	100	<0.1 @ 1 V	10^{-10}	$10^3\text{-}10^4$	4.47		Glass: Al ₂ O ₃ / SiO ₂ /APTES;	
[67]	Yes	Direct deposition	100	100	<0.1 @ 1 V	10^{-10}	$10^3\text{-}10^4$	0.8		Glass, flexible, Al ₂ O ₃ , APTES	
[105]	Yes	Drop cast	50	1000	~0.1 @ -5 V	10^{-12} @ - 5 V	~ 10^5	17.26 ± 4.77	0.28 ± 0.04	0 ± 0.09 V	SiO ₂ /Si, PLL

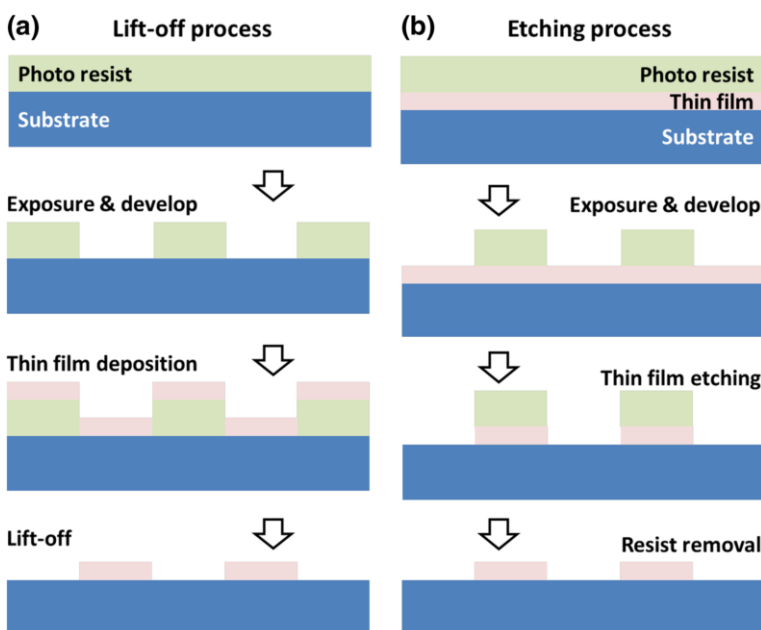


Fig. 7 Diagram depiction of the lift-off and etching processes

industrial vacuum instruments with plasma process, e.g. PVD or PECVD, otherwise the instruments may be damaged by discharge generated by the photoresist.

In the etching process, the fabrication of metal contact to the CNTs is more complicated than lift-off. Source/drain metal electrodes may be fabricated through wet etching and then depositing the SWCNT film and pattern the channel by RIE. In the RIE step, the metal leads unprotected by the photoresist are exposed to the oxygen plasma, which may be oxidized. Moreover, the CNTs lie on the electrode, and the contact is built on van de Waals interaction between the CNTs and the metal in this way. Such contacts are high resistance, and the geometry of metal deposited on CNTs is preferred for lowering the contact resistance according to the experiences of FETs on individual CNT [28, 81]. For this geometry, the metal is deposited over the substrate, and then the source/drain electrodes are defined by photolithography and wet etching. In this way, the SWCNT film channel area is covered by the metal film first and then exposed by wet etching of the metal. In manufacturing, the metal films are usually deposited by PVD process due to its high throughput, instead of thermal or e-beam evaporation used in the literature [15]. The atomic thin SWCNTs in the channel area are bombarded by the high energy particles in the PVD process, which may damage the SWCNTs. In the following metal wet etching, the SWCNT film is exposed to the metal etchants. How the metal etching residues and the contamination of the wet chemical etchants affect the devices performance are not known. In the metal PVD deposition step, an insulating layer may be used to protect the SWCNT film from being bombarded, just as the etching stop layer in the fabrication of a-IGZO TFTs [36, 82]. However, windows

for metal contacts must be opened in this layer by photo lithography and wet etch only, otherwise the SWCNTs below will be damaged by dry etch. Then the metal is deposited and the source/drain patterned by another photo lithography step. Thus, one more photolithography step is needed, which increases the fabrication cost. Also, how insulator etchant contamination and insulating residues on the SWCNTs affect the contact is waiting for study [83, 84].

4.3 The Electrodes and Dielectric Materials

It is known that the Fermi level pinning effect in SWCNT is negligible due to its quasi-one-dimensional structure [85]. Thus, one can choose a metal with an appropriate work function to obtain Ohmic contact with the semiconducting SWCNTs [27, 28, 86]. In addition to the work function, the wettability between the metal and the SWCNT also affects the contact properties significantly [87]. Among the many existing metal materials, p-type Ohmic contact is obtained by using Pd [28], while n-type by using Sc [27] or Y [86]. Pd, Sc, and Y are the mostly used contact metals for high performance carbon-based nanoelectronics, including CNT and graphene in the literature. Also, the deposition method is mainly e-beam evaporation, instead of the widely used PVD method in industry. These metals have never been used in the TFT backplane manufacturing. The currently used metal is Al due to its high chemical stability, low resistivity, and low cost. Though Schottky barriers form at the contact of these metals to SWCNTs [27, 28, 88], the corresponding etching processes of these metals are well-established for mass production. If changing the metals to Pd or Sc in the production line, PVD deposition and the corresponding wet etching processes should be developed and verified, which are nontrivial matters. For example, the hillock formation problems of the metal films are resolvable for the metals in manufacturing [36, 89, 90]. However, Pd is found not stick to the substrate well, so that a very thin layer of Ti was employed to improve the adhesion to substrates [91]. Moreover, the cost of Pd and Sc are much higher than those currently used metals for TFTs.

Besides the metal electrodes, the gate dielectrics also impact the performance of the TFT greatly. CNT-TFTs fabricated on Si substrates with the thermally grown SiO_2 as gate dielectrics have been reported. In addition to the thermally grown SiO_2 , other materials such as HfO_2 and Al_2O_3 grown by atomic layer deposition (ALD) have been employed as gate dielectrics. Though high quality dielectrics are easily obtained by ALD, the cost is high. In the backplane manufacturing, the mostly used gate dielectric materials are Si_3N_4 or SiO_2 , which are grown by using PECVD. There are a few reports on CNT-TFT using PECVD grown gate dielectrics [32, 92]. However, fixed charges exist in the PECVD grown Si_3N_4 will dope the SWCNT channel to n-type [32]. This is unfavorable for the Pd contacted devices because a barrier forms between the p-type contact and the n-type doped channel. Other types of dielectrics have been reported for CNT-TFTs; however, the fabrication processes are pretty complicated [93, 94]. Therefore, the choice and the fabrication of the electrodes metal and gate dielectrics for CNT-TFTs need to be optimized according to the backplane manufacturing process.

4.4 Performance of CNT-TFTs

The key device metrics for evaluating the performance of a TFT include on-state current (I_{on}), off-state current (I_{off}), the on/off current ratio (I_{on}/I_{off}), mobility (μ), sub-threshold swing (SS), and threshold voltage (V_{th}). In addition to these metrics, the devices uniformity in large area and stability are also critical concerns. Table 3 summarized these metrics reported on solution processed CNT-TFTs. Some of the metrics concerned in backplane electronics application are not paid enough attention in previous studies, as evident by the missing data in the table. In this section, we will discuss the requirements of these metrics for backplane of displays and the status of the CNT-TFTs research.

4.4.1 I_{on} , I_{off} , and I_{on}/I_{off}

LCDs hold the largest market share of FPDs, so we focus on the requirements for TFTs based on LCD. From Sect. 2, the pixels of a FPD are addressed by scanning the TFT array on the backplane row-by-row. The addressing TFT is switched on during the interval of t_{on} , and the capacitor in the pixel is charged by V_{data} in the column to turn the pixel on. I_{on} of the TFT must be high enough to charge the capacitor within one line time, i.e.,

$$I_{on}t_{on} > C_{pixel_charge}V_{charge} \quad (1)$$

where V_{charge} is the voltage of the capacitor to be set, and C_{pixel_charge} is the pixel capacitance during charging. Typical I_{on} value of a-Si TFT in backplane is about 1 μ A. For a 1024 lines image with 60 Hz frame rate, t_{on} for each line is about $(1/60)/1024 \sim 16.3 \mu$ s and t_f is ~ 16.67 ms. At the end of t_{on} , this row of TFTs is switched off by remove V_{scan} , until next frame. It is important to maintain the original signal voltage across the LC capacitor during this interval. However, the de-selected TFTs will experience a variety of different voltages between their source and drain during t_f . This voltage can be high up to $2V_{data}$, because alternative voltages, $-V_{data}$ to $+V_{data}$ are applied to prevent the orientation layer DC blocking effect and mobile ions DC residue effect in LCD [95]. A leakage current (I_{off}) exist even when the TFT is switched off. This leakage lowers the V_{charge} on the capacitor, which changes the status of the LC molecules and hence the brightness of the pixel. The leakage should be small enough to keep the brightness change less than one gray scale, i.e.

$$I_{off}t_f < C_{pixel_leak}V_{hold} \quad (2)$$

where V_{hold} is the voltage change for one gray scale and C_{pixel_leak} is the pixel capacitance during leakage. Thus, the requirement for the on/off ratio of the switching TFTs is

$$\frac{I_{on}}{I_{off}} > \frac{C_{pixel_charge}}{C_{pixel_leak}} \frac{V_{charge}}{V_{hold}} \frac{t_f}{t_{on}} \quad (3)$$

Figure 1b shows an illustration of typical transmission versus voltage curve of LC molecule. About 2 V is needed for the transparency of the LC molecule changes from 10 to 90% [95]. If these 2 V are divided into a 256 gray scale (8 bit), then ~ 8 mV is needed for one gray scale change. $C_{\text{pixel_charge}}$ is usually about 1 \sim 4 times of $C_{\text{pixel_leak}}$ [95], thus the required $I_{\text{on}}/I_{\text{off}} \sim 10^6$ for a 1024 line image with 60 Hz frame rate. If the frame rate is higher than 60 Hz, the on/off ratio is required to be higher than 10^6 . Moreover, higher on/off ratio makes easier design for the driving circuits and better control of picture quality.

I_{on} is not a problem for CNT-TFTs. Because of the excellent electrical properties of SWCNT, the current of an individual SWCNT can be higher than $20 \mu\text{A}$ [27, 28]. Though there are many inter-tube junctions, high I_{on} is easily obtained in the network type CNT-TFTs. The current density in the range of $1\text{--}10 \mu\text{A}/\mu\text{m}$ is commonly reported for solution processed CNT-TFTs (as shown in Table 3). These current densities are much higher than that of the a-Si TFTs [12], and even higher than some of those reported a-IGZO [34] and LTPS TFTs [96]. The current density is greatly improved when the tubes in the channel are aligned [16, 39, 72]. The high I_{on} of CNT-TFTs not only meet the requirement of high resolution displays, but is also benefit for improving the aperture ratio.

Lower I_{off} and higher $I_{\text{on}}/I_{\text{off}}$ are preferred for low power consumption and better picture quality of FPDs. Both the semiconducting purity of the SWCNTs in the channel and the diameter (or band gap) affect the I_{off} and $I_{\text{on}}/I_{\text{off}}$ of the CNT-TFTs. In early studies, considerable metallic SWCNTs exist in the channel of the CNT-TFTs. Though high I_{on} and high mobility are easily obtained, the I_{off} is relatively high and the $I_{\text{on}}/I_{\text{off}}$ is very low [15]. To improve the $I_{\text{on}}/I_{\text{off}}$ and lower I_{off} , the CNT film was stripped to suppress the possibility of the percolated metallic conducting paths that directly bridge the source to the drain [20, 31]. By tuning the ratio of the width and length of the CNT film stripe, high $I_{\text{on}}/I_{\text{off}}$ up to 10^5 can be obtained. However, it is very difficult to obtain $I_{\text{on}}/I_{\text{off}}$ higher than 10^6 .

Bao's group developed a self-sorted technique for solution processed SWCNTs which can obtain high $I_{\text{on}}/I_{\text{off}}$ [70, 97]. The un-separated SWCNT solution was spin-coated to surface functionalized substrates, and semiconducting SWCNTs are preferred to be absorbed onto the substrates and partially aligned. In this way, $I_{\text{on}}/I_{\text{off}}$ of the fabricated CNT-TFTs can be high up to $10^5\text{--}10^6$ due to the high semiconducting purity. Unfortunately, the tube density of the SWCNT film is very low, which results in too low I_{on} .

As the development of the solution-based sorting techniques of semiconducting SWCNTs, high purity (>99%) semiconducting SWCNT solutions are commercialized, and even with certain chirality [59, 60]. By using the separated SWCNT solutions, the metallic percolation paths was suppressed greatly and the obtained $I_{\text{on}}/I_{\text{off}}$ of the CNT-TFTs can be up to $10^5\text{--}10^7$, which meet the requirements for display application.

It should be noted that the reported high $I_{\text{on}}/I_{\text{off}}$ values are mostly obtained in relatively long channel CNT-TFTs (usually $>10 \mu\text{m}$) and at low source/drain bias (usually <1 V as shown in Table 3). The reason is large channel length to tube length ratio is benefit to suppress the metallic percolating paths, and hence high $I_{\text{on}}/I_{\text{off}}$ is obtainable according to the percolation theory [46, 47]. However, to maintain

high I_{on} , the channel width should be increased meanwhile for long channel length devices. Thus, the size of the CNT-TFTs increases, which lowers the aperture ratio, and limits their application in high pixel density (e.g. ~ 1000 ppi) FPDs.

To obtain high $I_{\text{on}}/I_{\text{off}}$ in CNT-TFTs with relatively short channel length (or small size device), the purity of the SWCNT material should be further enhanced and/or decreasing the average length of the SWCNTs. Usually, high power sonication is used to shorten the SWCNTs in solution, which also introduces more defects [98] and degrades the mobility of the fabricated CNT-TFTs. Thus, we need to balance the $I_{\text{on}}/I_{\text{off}}$ and the mobility. Recently, Liang et al. [99] used a two-step fringing field dielectrophoretic method to fabricate short channel CNT-TFTs with high $I_{\text{on}}/I_{\text{off}}$ (shown in Fig. 6h, i). Densely aligned SWCNT arrays were assembled at the source and drain electrodes sequentially which form a cascade structure of the aligned SWCNT arrays. The cascade structure reduces the possibility of percolating metallic pathways in the channel. In this way, both high $I_{\text{on}}/I_{\text{off}}$ (up to 10^7) and high I_{on} ($8.5 \mu\text{A}/\mu\text{m}$) were obtained in CNT-TFTs with short channel length ($1\text{--}2.5 \mu\text{m}$). This work promises the application of CNT-TFTs in high pixel density FPDs.

The band gap of the SWCNT also impacts the I_{off} , and hence the on/off ratio critically. Ambipolar transport is more likely observed in small band gap (large diameter) SWCNTs [100]. The pronounced ambipolar behavior results in higher leakage current, and hence lower $I_{\text{on}}/I_{\text{off}}$, especially at high source/drain bias. The reported high $I_{\text{on}}/I_{\text{off}}$ values are mostly obtained at relatively low bias ($< 1 \text{ V}$). However, the bias on the TFTs can be as high as $2V_{\text{data}}$ ($\sim 10 \text{ V}$ for LCD) during t_{f} , as mentioned before. Therefore, the $I_{\text{on}}/I_{\text{off}}$ of the CNT-TFTs should be $\sim 10^6$ even at such high bias. In industrial backplane manufacturing, the I_{off} and $I_{\text{on}}/I_{\text{off}}$ of a TFT is measured at pretty high bias (\sim up to over 10 V) and wide gate voltage sweep range (can be up to $-30 \text{ V} \sim +30 \text{ V}$). However, high $I_{\text{on}}/I_{\text{off}}$ at such high bias of CNT-TFTs is seldom reported.

To suppress the ambipolar transport, larger band gap (small diameter) SWCNTs are preferred. The diameter distribution of the SWCNT depends on the production methods. For solution based sorting, the SWCNT source materials are mainly produced by arc-discharge, HiPCO, plasma, and CoMoCAT. The corresponding diameter distributions are listed in Table 4. Obviously, the HiPCO and CoMoCAT SWCNTs are more preferred for low I_{off} and high $I_{\text{on}}/I_{\text{off}}$ [101]. However, the cost of the HiPCO CNT is much higher than other methods, which is an obstacle for its application in TFT backplanes.

In addition to choosing smaller diameter SWCNTs, the ambipolar transport can be suppressed by engineering the device structure. Lin et al. [100] used an asymmetric gate structure with respect to the source and drain electrodes (Fig. 8a,

Table 4 Diameter distribution of SWCNTs produced by various methods

	Diameter (nm)	Ref.
Arc-discharge	1.55 ± 0.1	[146]
HiPCO	0.8–1.2	[59]
CoMoCAT	0.7–1.4	[147]
Plasma	0.9–1.9	[59]

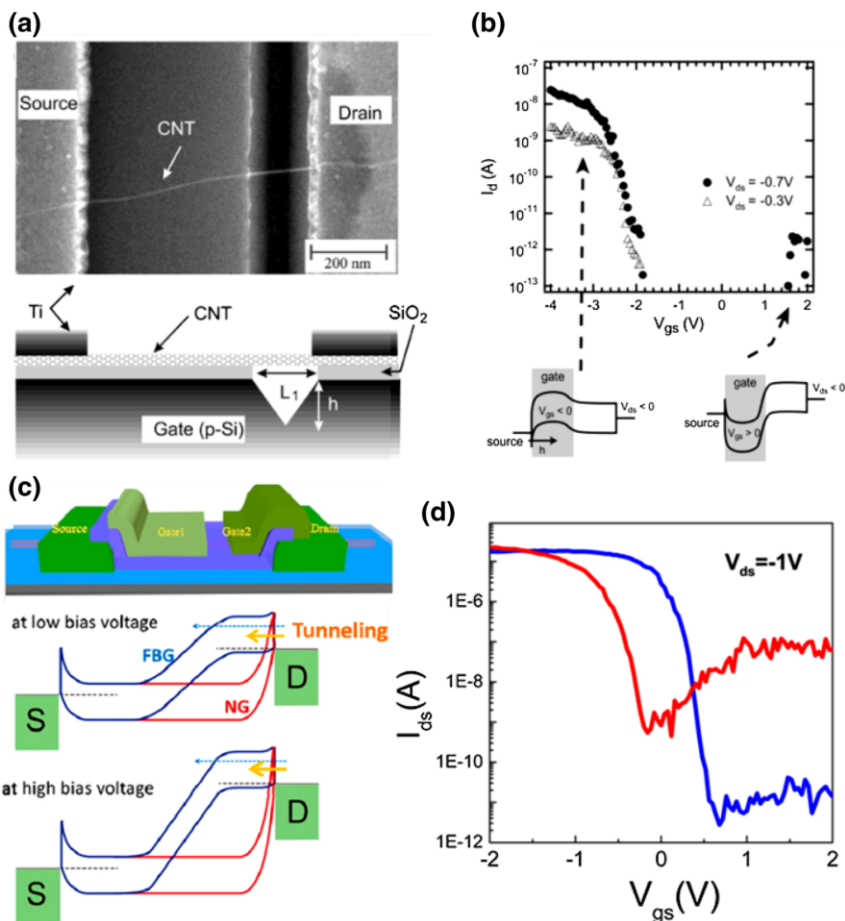


Fig. 8 Suppress the ambipolar transport behavior of SWCNT by device structure engineering. **a** Partially gated structure by Lin et al. and their results (**b**). Reprinted with permission from [100] (Copyright 2011 American Chemical Society) **c** Feedback gate structure by Qiu et al. and **d** comparison of the transfer curves of normal (red) and feedback gate CNT-FETs. Reprinted with permission from [102] (Copyright 2015 American Chemical Society)

b). Qiu et al. [102] proposed a feedback gate structure FET, where an additional gate was introduced at the drain end of the FETs (Fig. 8c, d). Both strategies suppressed the ambipolar behavior of the SWCNT effectively; however, the feedback gate structure is more facile for fabrication. It should be noted those strategies are proposed in individual CNT devices. Whether it can be generalized to the CNT-TFTs should be verified, though it is very possible in principle.

4.4.2 Sub-threshold Swing (SS)

Lower SS value indicates the TFT can be switched from off- to on-state quickly, which is required for high resolution FPDs due to the short t_{on} . Typical SS value for

a-Si TFT is ~ 1 V/dec, while those for LTPS and a-IGZO TFTs are $0.3 \sim 0.5$ V/dec. The SS value nearly 60 mV/dec has been reported in CNT-FETs [103], and values lower than 0.1 V/dec are routinely obtained [102, 104]. For CNT-TFTs, the SS down to 0.15 V/dec was reported by Sangwan et al. [93] by using the hybrid molecular dielectrics (V-sand). These low SS values are obtained in devices, either CNT-FETs or CNT-TFTs, with high quality and relatively thin gate dielectrics. The gate dielectrics of the CNT-TFTs for backplane electronics cannot be very thin. It must be thick enough to minimize the gate leakage current at high bias and wide gate voltage range. Thicker dielectrics will degrade the gate control of the channel and hence increase the SS values of the CNT-TFTs. SS of CNT-TFTs is seldom measured at high bias [105]; however, typical values of $0.1 \sim 0.3$ V/dec were reported [105, 106]. Owing to its thin body, it is expected that the SS value of CNT-TFTs can be further optimized to surpass those of LTPS and oxide TFTs.

4.4.3 Threshold Voltage (V_{th})

The V_{th} of the TFTs in backplanes are required to be near 0 V stably. The reported V_{th} values of the CNT-TFTs are somewhat deviated [38]. Furthermore, large hysteresis is usually observed in CNT-TFTs [15, 24, 69], which is believed to be due to the charge trapping induced by the absorbed water and hydroxyl groups at the substrate surface and mobile charges in the gate dielectrics [105, 107, 108]. It is meaningless to talk about tuning V_{th} before fully suppressing the hysteresis. The hysteresis in CNT-FETs can be suppressed by many methods, such as passivation by using PMMA [107], HMDS [109], or suspending the SWCNTs [107, 110]. These methods work pretty well at relatively low bias and/or small gate sweep ranges. However, the situation is more complicated in CNT-TFTs. In addition to the absorbed water molecules and surface hydroxyl groups, many dangling bonds at the tube ends and splices binding to the tube surface which are used for sorting the SWCNTs exist in the channel. These results in more trap centers, which makes fully suppressing the hysteresis of CNT-TFTs more difficult. Lefebvre et al. [111] used hydrophobic dielectrics for CNT-TFTs, and the hysteresis was suppressed effectively (Fig. 9a, b). However, the device fabrication process needs to be optimized to be compatible with the TFT backplane fabrication process. Ha et al. [105] encapsulated the CNT-TFTs by using a fluorocarbon polymer. The hydrophobic fluoropolymers remove the absorbed water molecules from the vicinity of CNTs efficiently and provide effective screening of the charge carriers in nanotubes from various trap states in the substrate. The hysteresis is suppressed even when the device is biased at 5 V and gate voltage sweep from -10 V to $+10$ V, as shown in Fig. 9c, d. More importantly, the device fabrication is compatible with the TFT backplane production. Once the hysteresis is suppressed, consistent V_{th} is obtainable, and it can be tuned to targeted values, e.g. by doping [112, 113], engineering the work function of the gate [114], or dual gate device structure [105].

When the above problems are solved, the gate bias stress (GBS) stability would be a critical concern for CNT-TFTs. It has been reported that a variation in V_{th} of only ± 0.1 V leads to the luminance of OLED changes by 16% [34]. Poor GBS stability results in V_{th} shift subject to prolonged gate-source bias, and hence device malfunction. In conventional TFTs, the GBS instability usually correlates with the

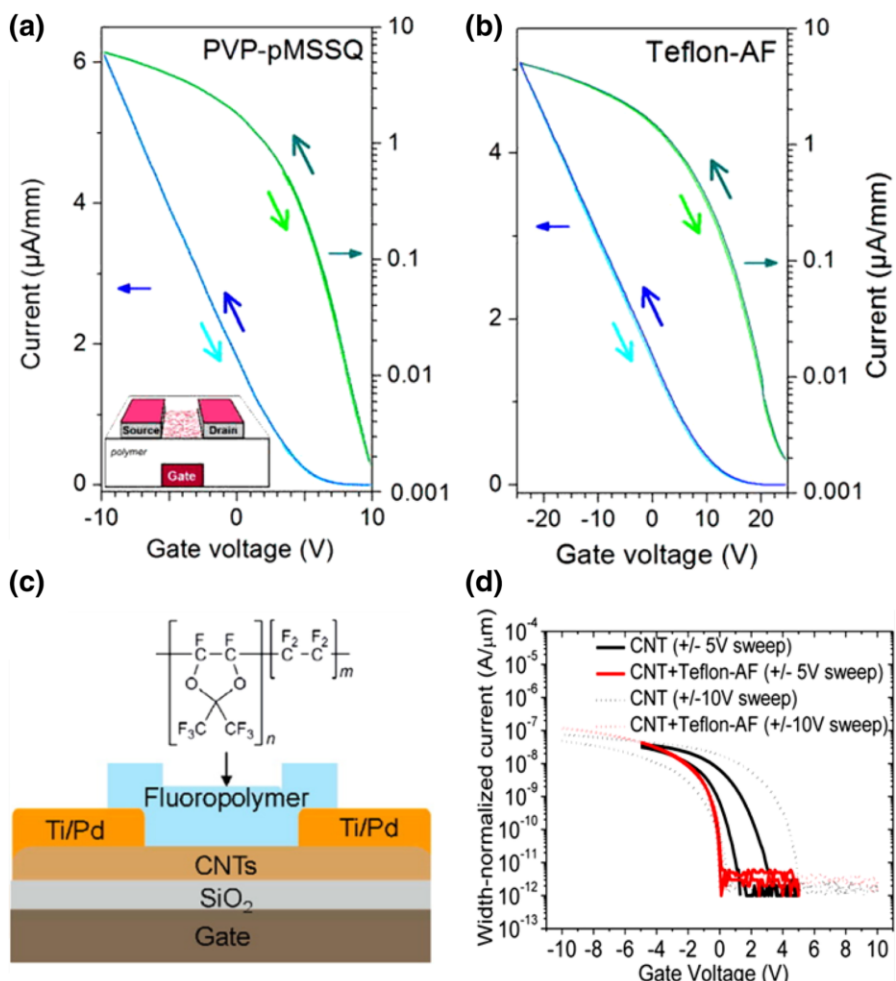


Fig. 9 Hysteresis-free CNT-TFTs using hydrophobic dielectrics of PVP-pMSSQ **(a)** and Teflon-AF **(b)**. Reprinted with permission from [111] (Copyright 2015 AIP Publishing LLC). Fluorocarbon polymer encapsulation of CNT-TFTs **(c)** and the resulting hysteresis-free transfer curves **(d)**. Reprinted with permission from [105] (Copyright 2014 American Chemical Society)

hysteresis problem. Factors that lead to hysteresis may also contribute to GBS instability. However, not enough attentions have been paid to the GBS stability of the CNT-TFTs. Lee et al. studied GBS stabilities of solution processed CNT-TFTs [115, 116], as shown in Fig. 10. Obviously, the GBS stabilities of CNT-TFTs need to be further improved.

4.4.4 Mobility

As discussed in Sect. 3, high mobility is one of the biggest advantages of the CNT-TFTs over other TFT technologies. The mobility is closely related to the quality of

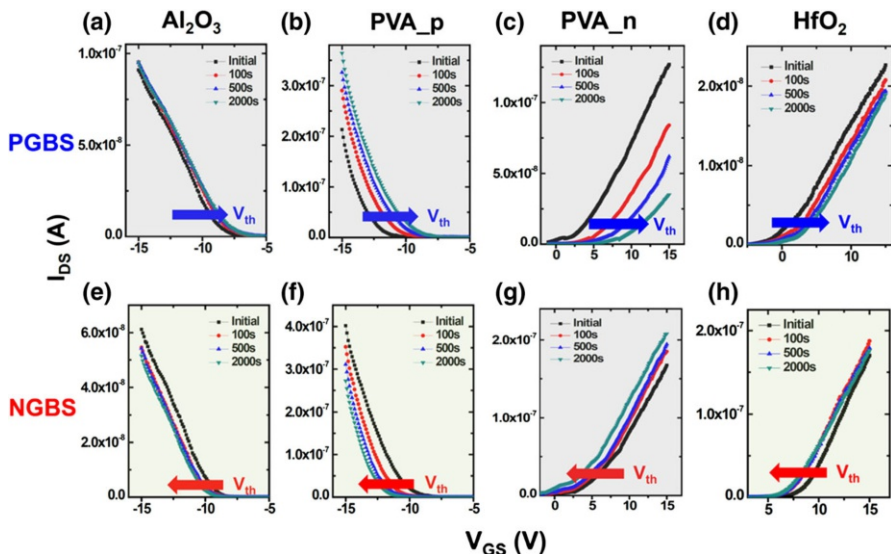


Fig. 10 Positive GBS (a)–(d) and negative GBS (e)–(h) measurements of CNT-TFTs, which were fabricated on SiO_2/Si substrates with (a, e) Al_2O_3 , (b, c, f, g) PVA, (d, h) HfO_2 passivation layer. Reprinted with permission from [115] (Copyright 2014 AIP Publishing LLC)

the channel material. For CNT-TFTs, electrons are scattered within the individual tubes and at the inter-tube junctions as well. Lower structural defect density in the individual tubes and less inter-tube junctions are preferred to obtain higher mobility. The structural defect density in the solution processed SWCNTs are relatively high due to additional defects introduced during the solution processing. Cao et al. [98] have evaluated the mobility of the solution processed SWCNTs. The mobility of an individual SWCNT was measured in the range of 200–600 cm^2/Vs . We believe the mobility can be further improved by optimizing the solution processing, and higher values up to $\sim 1000 \text{ cm}^2/\text{Vs}$ of an individual tube are expected. Since inter-tube scattering at the junctions deteriorate the mobility, the mobility of the CNT-TFTs would be much lower than those of the individual solution processed SWCNTs intuitively. However, the situation may not be that bad. The mobility of a material depends on the scattering rate of the electrons. If there is no scattering at the inter-tube junctions, the mobility of the CNT film will be almost equal to that of the average value of the individual SWCNTs, which is expected to be several hundred to a thousand cm^2/Vs . When considering the inter-tube junctions, the junctions between two semiconducting tubes are overwhelming in the channel due to the high purity semiconducting SWCNT solution used. The junction conductance between two semiconducting tubes is very high, as reported experimentally [117]. Theoretical studies predicted that the transmission coefficient between two CNTs can be very high [118]. These results indicate the scattering at the junction can be very low if intimate contact between these tubes is realized [119]. Considering the density of the inter-tube junction in the film is much lower than that of the structural defects, the mobility of the CNT films may be expected close to those of the

individual tubes. Mobility higher than $100\text{ cm}^2/\text{Vs}$ in the CNT-network has been reported by several groups [16, 120, 121]. When the tubes are aligned, the number of inter-tube junctions are further reduced, which is a benefit for mobility enhancing, and mobility in the range $200\text{--}380\text{ cm}^2/\text{Vs}$ has been reported in aligned SWCNT films [16]. These results indicate that even higher mobility for CNT-TFTs is very possible.

4.4.5 Stability and Uniformity

Stability and uniformity are prior requirements of any developed TFT technologies for real production. For the backplane electronics application, the stability of environment, temperature, UV irradiation, and GBS for CNT-TFTs should be investigated thoroughly. However, such investigations are still lacking, just as the GBS stability, which was discussed in the Sect 4.4.3.

There are some reports on the device uniformity statistics [38, 79]. However, most results are obtained from devices on relatively small pieces of substrate. Although a few results on 4-inch wafer scale are reported, the device performance uniformity does not meet the requirements for practical production [21, 22, 38]. These substrate sizes are much smaller than the backplane glass, even those of the generation 2.5 ($370\text{ mm} \times 470\text{ mm}$). Much effort is needed to improve the uniformity of the SWCNT thin film over a large area, hence improving the device performance uniformity.

5 Conclusions and Outlook

So far, we have discussed the application of the CNT-TFTs in FPD products from the viewpoint of backplane manufacturing. We reviewed the progress of CNT-TFTs, which were fabricated by solution processed SWCNT materials, which is the most promising route for mass production. When examining the key performance metrics of the individual CNT-TFTs, we found that they meet the requirements for pixel addressing in backplanes of a FPD, and strategies for improving each metric exist. Some prototype displays have been demonstrated in laboratories. These progresses give us more confidence of the CNT-TFTs technology for future FPD industry. However, there is not yet a report on CNT-TFTs for which performance metrics comply with all those required for displays. The fabrication process is also needed to be optimized to integrate with the existing TFT manufacturing technologies. The current research on CNT-TFTs for display is mainly carried out in research institutes. Now it is time for close collaboration between the research institutes and FPD manufacturers. In this way, the challenges for CNT-TFTs we discussed in this paper will be overcome earlier. Although we focus on our discussion on using CNT-TFTs for the pixel addressing array, we must point out that CNT-TFTs are capable of much more than that. For example, high performance CNT-TFT CMOS circuits are demonstrated [122], providing more possibility for the application of CNT-TFTs in future high-end FPDs, such as the peripheral circuits on the backplane. Owing to the rapid development of the FPD industry,

nowadays lifestyle has been changed greatly. After two-and-a-half decades of the discovery of CNT, a FPD with CNT-TFT backplane is now expectable in the near term. Low power consumption, light-weight, fully transparent, and flexible displays are also enabled by CNT-TFTs, and the CNT-TFTs technology will impact the FPD industry profoundly.

Acknowledgements This work was supported by the National Natural Science Foundation of China (Grant No. 61321001), National Key Research and Development program (Grant No. 2016YFA0201902), and BOE Technology Group, Co., Ltd.

References

1. Iijima S (1991) Nature 354:56. doi:[10.1038/354056a0](https://doi.org/10.1038/354056a0)
2. Iijima S, Ichihashi T (1993) Nature 363:603. doi:[10.1038/363603a0](https://doi.org/10.1038/363603a0)
3. Saito R, Dresselhaus G, Dresselhaus MS (1998) Physical properties of carbon nanotubes. Imperial College Press, UK
4. International technology roadmap for semiconductors www.itrs.net
5. Franklin AD (2013) Nature 498:443. doi:[10.1038/498443a](https://doi.org/10.1038/498443a)
6. Tulevski GS, Franklin AD, Frank D, Lobež JM, Cao Q, Park H, Afzali A, Han S-J, Hannon JB, Haensch W (2014) ACS Nano 8:8730. doi:[10.1021/nn503627h](https://doi.org/10.1021/nn503627h)
7. Pei T, Zhang PP, Zhang ZY, Qiu CG, Liang SB, Yang YJ, Wang S, Peng LM (2014) Nano Lett 14:3102. doi:[10.1021/nl5001604](https://doi.org/10.1021/nl5001604)
8. Ding L, Zhang ZY, Liang SB, Pei T, Wang S, Li Y, Zhou WW, Liu J, Peng LM (2012) Nature Communications 3. doi:[10.1038/ncomms1682](https://doi.org/10.1038/ncomms1682)
9. Shukla MM, Hills G, Patil N, Wei H, Chen HY, Philip Wong HS, Mitra S (2013) Nature 501:526. doi:[10.1038/nature12502](https://doi.org/10.1038/nature12502)
10. Chen B, Zhang P, Ding L, Han J, Qiu S, Li Q, Zhang Z, Peng L-M (2016) Nano Lett 16:5120. doi:[10.1021/acs.nanolett.6b02046](https://doi.org/10.1021/acs.nanolett.6b02046)
11. Waldrop MM (2016) Nature 530:144. doi:[10.1038/530144a](https://doi.org/10.1038/530144a)
12. Brotherton SD (2013) Introduction to thin film transistors—physics and technology of TFTs. Springer, New York
13. Zhang J, Fu Y, Wang C, Chen PC, Liu Z, Wei W, Wu C, Thompson ME, Zhou C (2011) Nano Lett 11:4852. doi:[10.1021/nl202695v](https://doi.org/10.1021/nl202695v)
14. Ishikawa FN, Chang HK, Ryu K, Chen PC, Badmaev A, De Arco LG, Shen GZ, Zhou CW (2009) ACS Nano 3:73. doi:[10.1021/nn800434d](https://doi.org/10.1021/nn800434d)
15. Wang C, Zhang JL, Ryu KM, Badmaev A, De Arco LG, Zhou CW (2009) Nano Lett 9:4285. doi:[10.1021/nl902522f](https://doi.org/10.1021/nl902522f)
16. Brady GJ, Joo Y, Wu MY, Shea MJ, Gopalan P, Arnold MS (2014) ACS Nano 8:11614. doi:[10.1021/nn5048734](https://doi.org/10.1021/nn5048734)
17. Sun DM, Liu C, Ren WC, Cheng HM (2013) Small 9:1188. doi:[10.1002/smll.201203154](https://doi.org/10.1002/smll.201203154)
18. Wang C, Takei K, Takahashi T, Javey A (2013) Chem Soc Rev 42:2592. doi:[10.1039/c2cs35325c](https://doi.org/10.1039/c2cs35325c)
19. Park S, Vosguerichian M, Bao Z (2013) Nanoscale 5:1727. doi:[10.1039/c3nr33560g](https://doi.org/10.1039/c3nr33560g)
20. Cao Q, Kim HS, Pimparkar N, Kulkarni JP, Wang CJ, Shim M, Roy K, Alam MA, Rogers JA (2008) Nature 454:495. doi:[10.1038/nature07110](https://doi.org/10.1038/nature07110)
21. Liyanage LS, Lee H, Patil N, Park S, Mitra S, Bao Z, Wong HS (2012) ACS Nano 6:451. doi:[10.1021/nn203771u](https://doi.org/10.1021/nn203771u)
22. Kim J, Hong D, Lee H, Shin Y, Park S, Khang Y, Lee M, Hong S (2013) The Journal of Physical Chemistry C 117
23. Lau PH, Takei K, Wang C, Ju Y, Kim J, Yu ZB, Takahashi T, Cho G, Javey A (2013) Nano Lett 13:3864. doi:[10.1021/nl401934a](https://doi.org/10.1021/nl401934a)
24. Chen P, Fu Y, Aminirad R, Wang C, Zhang J, Wang K, Galatsis K, Zhou C (2011) Nano Lett 11:5301. doi:[10.1021/nl202765b](https://doi.org/10.1021/nl202765b)
25. Kocabas C, Pimparkar N, Yesilyurt O, Kang SJ, Alam MA, Rogers JA (2007) Nano Lett 7:1195. doi:[10.1021/nl062907m](https://doi.org/10.1021/nl062907m)
26. Ohshima H (2014) Solid-state circuits conference (A-SSCC), 2014 IEEE Asian p 1

27. Zhang ZY, Liang XL, Wang S, Yao K, Hu YF, Zhu YZ, Chen Q, Zhou WW, Li Y, Yao YG, Zhang J, Peng LM (2007) *Nano Lett* 7:3603. doi:[10.1021/nl0717107](https://doi.org/10.1021/nl0717107)
28. Javey A, Guo J, Wang Q, Lundstrom M, Dai H (2003) *Nature* 424. doi:[10.1038/nature01797](https://doi.org/10.1038/nature01797)
29. Park S, Vosguerichian M, Bao Z (2013) *Nanoscale* 5:1727. doi:[10.1039/c3nr33560g](https://doi.org/10.1039/c3nr33560g)
30. Xu W, Zhao J, Qian L, Han X, Wu L, Wu W, Song M, Zhou L, Su W, Wang C, Nie S, Cui Z (2014) *Nanoscale* 6:1589. doi:[10.1039/c3nr04870e](https://doi.org/10.1039/c3nr04870e)
31. Kim S, Kim S, Park J, Ju S, Mohammadi S (2010) *ACS Nano* 4:2994. doi:[10.1021/nn1006094](https://doi.org/10.1021/nn1006094)
32. Zou J, Zhang K, Li J, Zhao Y, Wang Y, Pillai SKR, Volkan Demir H, Sun X, Chan-Park MB, Zhang Q (2015) *Sci Rep* 5:11755. doi:[10.1038/srep11755](https://doi.org/10.1038/srep11755)
33. Matsueda Y (2010) Digest of Int. Transistor Conf. 2010 Hyogo, Japan p 314
34. Toshio K, Kenji N, Hideo H (2010) *Sci Technol Adv Mater* 11:044305
35. Ohshima H (2014) SID Symp Digest Techn Pap 45:75. doi:[10.1002/j.2168-0159.2014.tb00021.x](https://doi.org/10.1002/j.2168-0159.2014.tb00021.x)
36. Wang L, Xu M, Lan L, Zou J, Tao H, Xu H, Li M, Luo D, Peng J (2013) *Sci Sin Chim* 43:1383. doi:[10.1360/032013-293](https://doi.org/10.1360/032013-293)
37. Cunningham KL (2014) *Nanochip Fab Solut* 9:24
38. Tian B, Liang X, Yan Q, Zhang H, Xia J, Dong G, Peng L, Xie S (2016) *J Appl Phys* 120:034501. doi:[10.1063/1.4958850](https://doi.org/10.1063/1.4958850)
39. Brady GJ, Joo Y, Singha Roy S, Gopalan P, Arnold MS (2014) *Appl Phys Lett* 104:083107. doi:[10.1063/1.4866577](https://doi.org/10.1063/1.4866577)
40. Sun DM, Timmermans MY, Kaskela A, Nasibulin AG, Kishimoto S, Mizutani T, Kauppinen EI, Ohno Y (2013) *Nat Commun* 4:2302. doi:[10.1038/ncomms3302](https://doi.org/10.1038/ncomms3302)
41. Sun DM, Timmermans MY, Tian Y, Nasibulin AG, Kauppinen EI, Kishimoto S, Mizutani T, Ohno Y (2011) *Nat Nanotechnol* 6:156. doi:[10.1038/nnano.2011.1](https://doi.org/10.1038/nnano.2011.1)
42. Kang SJ, Kocabas C, Ozel T, Shim M, Pimparkar N, Alam MA, Rotkin SV, Rogers JA (2007) *Nat Nanotechnol* 2:230. doi:[10.1038/nnano.2007.77](https://doi.org/10.1038/nnano.2007.77)
43. Dresselhaus MS, Dresselhaus G, Avouris P (eds) (2001) Carbon nanotubes: synthesis, structure, properties, and applications. Springer, Heidelberg
44. Choi YS, Yun JU, Park SE (2016) *J Non Cryst Solids* 431:2. doi:[10.1016/j.jnoncrysol.2015.05.007](https://doi.org/10.1016/j.jnoncrysol.2015.05.007)
45. Kang SJ, Kocabas C, Kim HS, Cao Q, Meitl MA, Khang DY, Rogers JA (2007) *Nano Lett* 7:3343. doi:[10.1021/nl071596s](https://doi.org/10.1021/nl071596s)
46. Kumar S, Murthy JY, Alam MA (2005) *Phys Rev Lett* 95:066802. doi:[10.1103/Physrevlett.95.066802](https://doi.org/10.1103/Physrevlett.95.066802)
47. Alam MA, Pimparkar N, Kumar S, Murthy J (2006) *MRS Bull* 31:466. doi:[10.1557/Mrs2006.120](https://doi.org/10.1557/Mrs2006.120)
48. Tu XM, Manohar S, Jagota A, Zheng M (2009) *Nature* 460:250. doi:[10.1038/nature08116](https://doi.org/10.1038/nature08116)
49. Zheng M, Jagota A, Semke ED, Diner BA, Mclean RS, Lustig SR, Richardson RE, Tassi NG (2003) *Nat Mater* 2:338. doi:[10.1038/nmat877](https://doi.org/10.1038/nmat877)
50. Nish A, Hwang J-Y, Doig J, Nicholas RJ (2007) *Nat Nano* 2:640. doi:[10.1038/nnano.2007.290](https://doi.org/10.1038/nnano.2007.290)
51. Lee HW, Yoon Y, Park S, Oh JH, Hong S, Liyanage LS, Wang H, Morishita S, Patil N, Park YJ, Park JJ, Spakowitz A, Galli G, Gygi F, Wong PHS, Tok JBH, Kim JM, Bao Z (2011) *Nat Commun* 2:541. doi:[10.1038/ncomms1545](https://doi.org/10.1038/ncomms1545)
52. Li H, Zhou B, Lin Y, Gu L, Wang W, Fernando KAS, Kumar S, Allard LF, Sun Y-P (2004) *J Am Chem Soc* 126:1014. doi:[10.1021/ja037142o](https://doi.org/10.1021/ja037142o)
53. Wang WZ, Li WF, Pan XY, Li CM, Li L-J, Mu YG, Rogers JA, Chan-Park MB (2011) *Adv Funct Mater* 21:1643. doi:[10.1002/adfm.201002278](https://doi.org/10.1002/adfm.201002278)
54. Liu H, Tanaka T, Urabe Y, Kataura H (2013) *Nano Lett* 13:1996. doi:[10.1021/nl400128m](https://doi.org/10.1021/nl400128m)
55. Liu H, Nishida D, Tanaka T, Kataura H (2011) *Nat Commun* 2:309. doi:[10.1038/ncomms1313](https://doi.org/10.1038/ncomms1313)
56. Khrapin CY, Fagan JA, Zheng M (2013) *J Am Chem Soc* 135:6822. doi:[10.1021/ja402762e](https://doi.org/10.1021/ja402762e)
57. Arnold MS, Green AA, Hulvat JF, Stupp SI, Hersam MC (2006) *Nat Nano* 1:60. doi:[10.1038/nnano.2006.52](https://doi.org/10.1038/nnano.2006.52)
58. Tulevski GS, Franklin AD, Afzali A (2013) *ACS Nano* 7:2971. doi:[10.1021/nn400053k](https://doi.org/10.1021/nn400053k)
59. <http://www.nanointegrис.com>
60. <http://www.atommanoelectronics.com>
61. Ha M, Xia Y, Green AA, Zhang W, Renn MJ, Kim CH, Hersam MC, Frisbie CD (2010) *ACS Nano* 4:4388. doi:[10.1021/nn100966s](https://doi.org/10.1021/nn100966s)
62. Abdellahim A, Abdellah A, Scarpa G, Lugli P (2014) *Nanotechnology* 25:055208. doi:[10.1088/0957-4484/25/5/055208](https://doi.org/10.1088/0957-4484/25/5/055208)
63. Takahashi T, Takei K, Gillies AG, Fearing RS, Javey A (2011) *Nano Lett* 11:5408. doi:[10.1021/nl203117h](https://doi.org/10.1021/nl203117h)

64. Wang C, Chien JC, Takei K, Takahashi T, Nah J, Niknejad AM, Javey A (2012) *Nano Lett* 12:1527. doi:[10.1021/nl2043375](https://doi.org/10.1021/nl2043375)
65. Cao X, Chen H, Gu X, Liu B, Wang W, Cao Y, Wu F, Zhou C (2014) *ACS Nano* 8:12769. doi:[10.1021/nn505979j](https://doi.org/10.1021/nn505979j)
66. Joo Y, Brady GJ, Arnold MS, Gopalan P (2014) *Langmuir* 30:3460. doi:[10.1021/la500162x](https://doi.org/10.1021/la500162x)
67. Zhang J, Wang C, Zhou C (2012) *ACS Nano* 6:7412. doi:[10.1021/nm3026172](https://doi.org/10.1021/nm3026172)
68. Qian L, Xu WY, Fan XF, Wang C, Zhang JH, Zhao JW, Cui Z (2013) *J Phys Chem C* 117:18243. doi:[10.1021/jp4055022](https://doi.org/10.1021/jp4055022)
69. Wang C, Qian L, Xu WY, Nie SH, Gu WB, Zhang JH, Zhao JW, Lin J, Chen Z, Cui Z (2013) *Nanoscale* 5:4156. doi:[10.1039/c3nr34304a](https://doi.org/10.1039/c3nr34304a)
70. LeMieux MC, Roberts M, Barman S, Jin YW, Kim JM, Bao Z (2008) *Science* 321:101. doi:[10.1126/science.1156588](https://doi.org/10.1126/science.1156588)
71. Opatkiewicz JP, LeMieux MC, Bao Z (2010) *ACS Nano* 4:1167. doi:[10.1021/nn901388v](https://doi.org/10.1021/nn901388v)
72. Engel M, Small JP, Steiner M, Freitag M, Green AA, Hersam MC, Avouris P (2008) *ACS Nano* 2:2445. doi:[10.1021/nn800708w](https://doi.org/10.1021/nn800708w)
73. Li X, Zhang L, Wang X, Shimoyama I, Sun X, Seo W-S, Dai H (2007) *J Am Chem Soc* 129:4890. doi:[10.1021/ja071114e](https://doi.org/10.1021/ja071114e)
74. Cao Q, Han SJ, Tulevski GS, Zhu Y, Lu DD, Haensch W (2013) *Nat Nanotechnol* 8:180. doi:[10.1038/nnano.2012.257](https://doi.org/10.1038/nnano.2012.257)
75. Shekhar S, Stokes P, Khondaker SI (2011) *ACS Nano* 5:1739. doi:[10.1021/nn102305z](https://doi.org/10.1021/nn102305z)
76. Cao Q, Han SJ, Tulevski GS (2014) *Nat Commun* 5:5071. doi:[10.1038/ncomms6071](https://doi.org/10.1038/ncomms6071)
77. Monica AH, Papadakis SJ, Osiander R, Paranjape M (2008) *Nanotechnology* 19:085303. doi:[10.1088/0957-4484/19/8/085303](https://doi.org/10.1088/0957-4484/19/8/085303)
78. Krupke R, Hennrich F, Löhneysen HV, Kappes MM (2003) *Science* 301: 344
79. Lau PH, Takei K, Wang C, Ju Y, Kim J, Yu Z, Takahashi T, Cho G, Javey A (2013) *Nano Lett* 13:3864. doi:[10.1021/nl401934a](https://doi.org/10.1021/nl401934a)
80. Xu W, Dou J, Zhao J, Tan H, Ye J, Tange M, Gao W, Xu W, Zhang X, Guo W, Ma C, Okazaki T, Zhang K, Cui Z (2016) *Nanoscale* 8:4588. doi:[10.1039/c6nr00015k](https://doi.org/10.1039/c6nr00015k)
81. Tans SJ, Verschueren ARM, Dekker C (1998) *Nature* 393:49
82. Zhu XM, Jiang CS, Yuan GC, Liu W, Li XY, Xin LB, Wang ML, Wang G (2015) SID symposium digest of technical papers, vol 46, p 1198. doi:[10.1002/sdtp.10057](https://doi.org/10.1002/sdtp.10057)
83. Li W, Liang YR, Yu DM, Peng LM, Pernstich KP, Shen T, Walker ARH, Cheng GJ, Hacker CA, Richter CA, Li QL, Gundlach DJ, Liang XL (2013) *Appl Phys Lett* 102. doi:[10.1063/1.4804643](https://doi.org/10.1063/1.4804643)
84. Li W, Hacker CA, Cheng GJ, Liang YR, Tian BY, Walker ARH, Richter CA, Gundlach DJ, Liang XL, Peng LM (2014) *J Appl Phys* 115. doi:[10.1063/1.4868897](https://doi.org/10.1063/1.4868897)
85. Leonard F, Tersoff J (2000) *Phys Rev Lett* 84:4693. doi:[10.1103/PhysRevLett.84.4693](https://doi.org/10.1103/PhysRevLett.84.4693)
86. Ding L, Wang S, Zhang ZY, Zeng QS, Wang ZX, Pei T, Yang LJ, Liang XL, Shen J, Chen Q, Cui RL, Li Y, Peng LM (2009) *Nano Lett* 9:4209. doi:[10.1021/nl9024243](https://doi.org/10.1021/nl9024243)
87. Zhang Y, Franklin NW, Chen RJ, Dai HJ (2000) *Chem Phys Lett* 331:35. doi:[10.1016/S0009-2614\(00\)01162-3](https://doi.org/10.1016/S0009-2614(00)01162-3)
88. Chen ZH, Appenzeller J, Knoch J, Lin YM, Avouris P (2005) *Nano Lett* 5:1497. doi:[10.1021/NI0508624](https://doi.org/10.1021/NI0508624)
89. Morrison NA, Stolley T, Hermanns U, Reus A, Deppisch T, Bolandi H, Melnik Y, Singh V, Griffith Cruz J (2015) *Proc IEEE* 103:518. doi:[10.1109/jproc.2015.2408052](https://doi.org/10.1109/jproc.2015.2408052)
90. Wang P, Hwang J, Chuang A, Huang F-S (2000) *Thin Solid Films* 358:292. doi:[10.1016/S0040-6090\(99\)00674-4](https://doi.org/10.1016/S0040-6090(99)00674-4)
91. Franklin AD, Farmer DB, Haensch W (2014) *ACS Nano* 8:7333. doi:[10.1021/nn5024363](https://doi.org/10.1021/nn5024363)
92. Wind SJ, Appenzeller J, Martel R, Derycke V, Avouris P (2002) *Appl Phys Lett* 80:3817. doi:[10.1063/1.1480877](https://doi.org/10.1063/1.1480877)
93. Sangwan VK, Ortiz RP, Alaboson JMP, Emery JD, Bedzyk MJ, Lauhon LJ, Marks TJ, Hersam MC (2012) *ACS Nano* 6:7480. doi:[10.1021/nn302768h](https://doi.org/10.1021/nn302768h)
94. Hur S-H, Yoon M-H, Gaur A, Shim M, Facchetti A, Marks TJ, Rogers JA (2005) *J Am Chem Soc* 127:13808. doi:[10.1021/ja0553203](https://doi.org/10.1021/ja0553203)
95. Dai YX (2010) Design and operation of TFT LCD panels. Tsinghua University Press, Beijing
96. Brotherton SD, Ayres JR, Young ND (1991) *Solid State Electron* 34:671. doi:[10.1016/0038-1101\(91\)90002-G](https://doi.org/10.1016/0038-1101(91)90002-G)
97. Opatkiewicz JP, LeMieux MC, Liu D, Vosgueritchian M, Barman SN, Elkins CM, Hedrick J, Bao Z (2012) *ACS Nano* 6:4845. doi:[10.1021/nn300124y](https://doi.org/10.1021/nn300124y)

98. Cao Q, Han SJ, Tulevski GS, Franklin AD, Haensch W (2012) ACS Nano 6:6471. doi:[10.1021/nm302185d](https://doi.org/10.1021/nm302185d)
99. Liang Y, Xia J, Liang X (2016) Sci Bull 61:794. doi:[10.1007/s11434-016-1075-1](https://doi.org/10.1007/s11434-016-1075-1)
100. Lin YM, Appenzeller J, Avouris P (2004) Nano Lett 4:947. doi:[10.1021/nl049745j](https://doi.org/10.1021/nl049745j)
101. Zhang J, Gui H, Liu B, Liu J, Zhou C (2013) Nano Res 6:906. doi:[10.1007/s12274-013-0368-9](https://doi.org/10.1007/s12274-013-0368-9)
102. Qiu C, Zhang Z, Zhong D, Si J, Yang Y, Peng L-M (2015) ACS Nano 9:969. doi:[10.1021/nm506806b](https://doi.org/10.1021/nm506806b)
103. Wang ZX, Xu HL, Zhang ZY, Wang S, Ding L, Zeng QS, Yang LJ, Pei TA, Liang XL, Gao M, Peng LM (2010) Nano Lett 10:2024. doi:[10.1021/nl100022u](https://doi.org/10.1021/nl100022u)
104. Javey A, Tu R, Farmer DB, Guo J, Gordon RG, Dai HJ (2005) Nano Lett 5:345. doi:[10.1021/nl047931j](https://doi.org/10.1021/nl047931j)
105. Ha TJ, Kiriya D, Chen K, Javey A (2014) Acs Appl Mater Interfaces 6:8441. doi:[10.1021/am5013326](https://doi.org/10.1021/am5013326)
106. Kim B, Franklin A, Nuckolls C, Haensch W, Tulevski GS (2014) Appl Phys Lett 105:063111. doi:[10.1063/1.4891335](https://doi.org/10.1063/1.4891335)
107. Kim W, Javey A, Vermesh O, Wang O, Li YM, Dai HJ (2003) Nano Lett 3:193. doi:[10.1021/nl0259232](https://doi.org/10.1021/nl0259232)
108. Park RS, Shulaker MM, Hills G, Suriyasena Liyanage L, Lee S, Tang A, Mitra S, Wong HSP (2016) ACS Nano 10:4599. doi:[10.1021/acsnano.6b00792](https://doi.org/10.1021/acsnano.6b00792)
109. Franklin AD, Tulevski GS, Han SJ, Shahjerdi D, Cao Q, Chen HY, Wong HSP, Haensch W (2012) ACS Nano 6:1109. doi:[10.1021/nm203516z](https://doi.org/10.1021/nm203516z)
110. Shlafman M, Tabachnik T, Shtempluk O, Razin A, Kochetkov V, Yaish YE (2016) Appl Phys Lett 108:163104. doi:[10.1063/1.4947099](https://doi.org/10.1063/1.4947099)
111. Lefebvre J, Ding J, Li Z, Cheng F, Du N, Malenfant PRL (2015) Appl Phys Lett 107:243301. doi:[10.1063/1.4937223](https://doi.org/10.1063/1.4937223)
112. Ha TJ, Chen K, Chuang S, Yu KM, Kiriya D, Javey A (2015) Nano Lett 15:392. doi:[10.1021/nl5037098](https://doi.org/10.1021/nl5037098)
113. Seong N, Kim T, Kim H, Ha T-J, Hong Y (2015) Curr Appl Phys 15:S8. doi:[10.1016/j.cap.2015.03.009](https://doi.org/10.1016/j.cap.2015.03.009)
114. Zhang ZY, Wang S, Ding L, Liang XL, Pei T, Shen J, Xu HL, Chen O, Cui RL, Li Y, Peng LM (2008) Nano Lett 8:3696. doi:[10.1021/nl8018802](https://doi.org/10.1021/nl8018802)
115. Lee SW, Suh D, Lee SY, Lee YH (2014) Appl Phys Lett 104. doi:[10.1063/1.4873316](https://doi.org/10.1063/1.4873316)
116. Lee SW, Lee SY, Lim SC, Kwon Y-d, Yoon J-S, Uh K, Lee YH (2012) Appl Phys Lett 101:053504. doi:[10.1063/1.4740084](https://doi.org/10.1063/1.4740084)
117. Fuhrer MS, Nygard J, Shih L, Forero M, Yoon YG, Mazzoni MSC, Choi HJ, Ihm J, Louie SG, Zettl A, McEuen PL (2000) Science 288:494. doi:[10.1126/science.288.5465.494](https://doi.org/10.1126/science.288.5465.494)
118. Liu Q, Luo G, Qin R, Li H, Yan X, Xu C, Lai L, Zhou J, Hou S, Wang E, Gao Z, Lu J (2011) Phys Rev B 83:155442. doi:[10.1103/PhysRevB.83.155442](https://doi.org/10.1103/PhysRevB.83.155442)
119. Pimparkar N, Alam MA (2008) Electron Device Lett IEEE 29:1037. doi:[10.1109/led.2008.2001259](https://doi.org/10.1109/led.2008.2001259)
120. Xia J, Dong G, Tian B, Yan Q, Zhang H, Liang X, Peng L (2016) Nanoscale 8:9988. doi:[10.1039/c6nr00876c](https://doi.org/10.1039/c6nr00876c)
121. Choi SJ, Bennett P, Takei K, Wang C, Lo CC, Javey A, Bokor J (2013) ACS Nano 7:798. doi:[10.1021/nm305277d](https://doi.org/10.1021/nm305277d)
122. Yang YJ, Ding L, Zhang ZY, Peng LM (2016) 4th carbon nanotube thin film electronics and applications satellite. In: Seventeenth international conference of the scienceand applications of nanotubes and low-dimensional materials, University of Vienna, Austria
123. Shin K, Jeon H, Park CE, Kim Y, Cho H, Lee G, Han JH (2010) Org Electron 11:1403. doi:[10.1016/j.orgel.2010.05.012](https://doi.org/10.1016/j.orgel.2010.05.012)
124. Barman SN, LeMieux MC, Baek J, Rivera R, Bao Z (2010) Acs Appl Mater Interfaces 2:2672. doi:[10.1021/am1005223](https://doi.org/10.1021/am1005223)
125. Asada Y, Miyata Y, Ohno Y, Kitaura R, Sugai T, Mizutani T, Shinohara H (2010) Adv Mater 22:2698. doi:[10.1002/adma.200904006](https://doi.org/10.1002/adma.200904006)
126. Lee CW, Han X, Chen F, Wei J, Chen Y, Chan-Park MB, Li L-J (2010) Adv Mater 22:1278. doi:[10.1002/adma.200902461](https://doi.org/10.1002/adma.200902461)
127. LeMieux MC, Sok S, Roberts ME, Opatkiewicz JP, Liu D, Barman SN, Patil N, Mitra S, Bao Z (2009) ACS Nano 3:4089. doi:[10.1021/nm900827v](https://doi.org/10.1021/nm900827v)
128. Vosgeritchian M, LeMieux MC, Dodge D, Bao Z (2010) Acs Nano 4:6137. doi:[10.1021/nm1012226](https://doi.org/10.1021/nm1012226)

129. Yuki N, Yuki T, Shota G, Satoki M, Kazuhiro Y, Taishi T (2012) Jpn J Appl Phys 51:06FD15
130. Ohmori S, Ihara K, Nihey F, Kuwahara Y, Saito T (2012) Rsc Adv 2:12408. doi:[10.1039/c2ra22272h](https://doi.org/10.1039/c2ra22272h)
131. Asada Y, Nihey F, Ohmori S, Shinohara H, Saito T (2011) Adv Mater 23:4631. doi:[10.1002/adma.201102806](https://doi.org/10.1002/adma.201102806)
132. Miyata Y, Shiozawa K, Asada Y, Ohno Y, Kitaura R, Mizutani T, Shinohara H (2011) Nano Res 4:963. doi:[10.1007/s12274-011-0152-7](https://doi.org/10.1007/s12274-011-0152-7)
133. Zhang J, Wang C, Fu Y, Che Y, Zhou C (2011) Acs Nano 5:3284. doi:[10.1021/nn2004298](https://doi.org/10.1021/nn2004298)
134. Wang C, Zhang J, Zhou C (2010) Acs Nano 4:7123. doi:[10.1021/nn1021378](https://doi.org/10.1021/nn1021378)
135. Raman Pillai SK, Chan-Park MB (2012) Acs Applied Mater Interfaces 4:7047. doi:[10.1021/am302431e](https://doi.org/10.1021/am302431e)
136. Lee CW, Raman Pillai SK, Luan X, Wang Y, Li CM, Chan-Park MB (2012) Small 8:2941. doi:[10.1002/smll.201200041](https://doi.org/10.1002/smll.201200041)
137. Lee D, Seol M-L, Moon D-I, Bennett P, Yoder N, Humes J, Bokor J, Choi Y-K, Choi S-J (2014) Appl Phys Lett 104:143508. doi:[10.1063/1.4871100](https://doi.org/10.1063/1.4871100)
138. Tatsuya T, Hiroshi F, Mamoru F (2013) Jpn J Appl Phys 52:03BB09
139. Li Z, Ding J, Lefebvre J, Malenfant PRL (2015) Org Electron 26:15. doi:[10.1016/j.orgel.2015.07.006](https://doi.org/10.1016/j.orgel.2015.07.006)
140. Yuki K, Fumiayuki N, Shigekazu O, Takeshi S (2015) Appl Phys Express 8:105101
141. Liu N, Yun KN, Yu H-Y, Shim JH, Lee CJ (2015) Appl Phys Lett 106:103106. doi:[10.1063/1.4914400](https://doi.org/10.1063/1.4914400)
142. Li G, Li Q, Jin Y, Zhao Y, Xiao X, Jiang K, Wang J, Fan S (2015) Nanoscale 7:17693. doi:[10.1039/c5nr05036g](https://doi.org/10.1039/c5nr05036g)
143. Wei L, Liu B, Wang X, Gui H, Yuan Y, Zhai S, Ng AK, Zhou C, Chen Y (2015) Adv Electron Mater 1:1500151. doi:[10.1002/aelm.201500151](https://doi.org/10.1002/aelm.201500151)
144. Cao C, Andrews JB, Kumar A, Franklin AD (2016) Acs Nano 10:5221. doi:[10.1021/acsnano.6b00877](https://doi.org/10.1021/acsnano.6b00877)
145. Gui H, Chen H, Khripin CY, Liu B, Fagan JA, Zhou C, Zheng M (2016) Nanoscale 8:3467. doi:[10.1039/c5nr07329d](https://doi.org/10.1039/c5nr07329d)
146. <http://www.carbonsolution.com/>
147. <http://www.sigmaaldrich.com/>



REVIEW

Carbon Nanotube Thin Films for High-Performance Flexible Electronics Applications

Jun Hirotani¹ · Yutaka Ohno^{1,2}

Received: 18 September 2018 / Accepted: 11 December 2018
© Springer Nature Switzerland AG 2019

Abstract

Carbon nanotube thin films have attracted considerable attention because of their potential use in flexible/stretchable electronics applications, such as flexible displays and wearable health monitoring devices. Due to recent progress in the post-purification processes of carbon nanotubes, high-purity semiconducting carbon nanotubes can be obtained for thin-film transistor applications. One of the key challenges for the practical use of carbon nanotube thin-film transistors is the thin-film formation technology, which is required for achieving not only high performance but also uniform device characteristics. In this paper, after describing the fundamental thin-film formation techniques, we review the recent progress of thin-film formation technologies for carbon nanotube-based flexible electronics.

Keywords Carbon nanotube · Thin film · Flexible electronics

1 Introduction

Carbon nanotube (CNT) thin films are promising materials for flexible electronics applications because of their multi-functionalities, extraordinary electronic and mechanical properties, optical transparencies, biocompatibilities, and chemical stabilities [1–6]. In particular, the multi-functionalities are quite a unique property of CNT thin films. Various active and passive components of flexible devices, such as transistors [1, 7], integrated circuits [2, 4], and sensors [8], including gas sensors [9–11], ion sensors [12–14], biosensors [15–17], interconnections [18], and

Chapter 9 was originally published as Hirotani, J. & Ohno, Y. Topics in Current Chemistry (2019) 377: 3. https://doi.org/10.1007/s41061-018-0227-y.

✉ Yutaka Ohno
yohno@nagoya-u.jp

¹ Department of Electronics, Nagoya University, Furo-cho, Chikusa-ku, Nagoya 464-8603, Japan

² Institute of Materials and Systems for Sustainability, Nagoya University, Furo-cho, Chikusa-ku, Nagoya 464-8603, Japan

Published online: 02 January 2019

Reprinted from the journal

transparent conductors [19, 20], can be realized with CNT thin films. It should be emphasized that these functionalities can be achieved simultaneously with CNTs. The multi-functionalities and high performances are especially important properties for wearable devices, where various functional devices must be integrated on a stretchable ultra-thin substrate. Another advantage of CNT thin films is processability. Simple room-temperature and nonvacuum processes can be adopted to form CNT thin films, such as the solution-based coating [21, 22], printing [23–27], and dry transfer [20, 28] processes. High-performance flexible devices can be manufactured by low-cost processes.

The greatest challenge for CNT electronics is the control of the structures of CNTs, i.e., the bandgap [29]. Recent progress on chirality-controlled growth and post-growth separation [30–33] will create new possibilities for the practical use of CNT devices. In particular, post-growth separation processes, such as density-gradient ultracentrifugation [30] and gel-column chromatography [34], have enabled the use of high-purity semiconducting CNTs in transistor applications. The formation of ultra-high-purity semiconducting CNTs with a purity of > 99.9% was reported [35, 36].

However, to achieve the performance potentials of CNT materials, the formation of CNT thin films is a key issue. The current flows through multiple CNTs in the thin film. The conductivity of a CNT thin film is governed by the junctions between the CNTs, where a high junction resistance may exist. The junction resistances between the CNTs range from 100 k Ω to 10 M Ω , depending on the type of CNTs and the junction structure [37–39], which are much higher than the quantum resistances of one-dimensional ballistic conductors. Therefore, to obtain highly conductive CNT thin films, it is essential to reduce the number of tube-to-tube junctions in the current path by using long CNTs as well as maintaining clean tube surfaces to prevent increases in the junction resistance during the film formation process.

The alignment of the CNTs can also enhance the performance of thin film devices, especially for short channel field-effect transistors (FETs), in which the channel length is shorter than the length of the CNTs and each CNT is connected to electrodes directly. Highly aligned CNTs were grown on single-crystal oxide substrates, such as quartz and sapphire [40–43]. However, as-grown CNT arrays inevitably contain metallic CNTs, which significantly degrade the device performance.

The variability control in the device properties is also one of the most challenging issues to be addressed for CNT thin-film electronics. The variability is intrinsically caused by the randomness of the network structure of a CNT thin film, especially in the case of ultra-thin films for FET channels. The variability of the CNT thin film directly impacts the variability of the thin-film transistor (TFT) electrical performance, especially the current driving ability and gate capacitance. For logic circuits, the operation speed is limited by devices with low current driving abilities. Higher operation voltages are needed to secure a margin of error to account for the worst-case scenario, resulting in increased power consumption. For analogue circuits, such as amplifiers and analogue-to-digital converters for sensor applications, the transistor variability directly affects the circuit variability and performance. The accuracy of an analogue-to-digital converter is degraded by this variability, and a dedicated circuit design is necessary to compensate for the variability.

However, the experimentally observed variability is much larger than the intrinsic variability [44]. To date, the extrinsic origins of the characteristic variation are still unclear. There have been several numerical [45, 46] and experimental studies [44, 47] in which the characteristic variations of TFTs based on randomly dispersed CNT film were investigated. In the numerical simulations, two-dimensional percolation theory predicted that the characteristic variation would be reduced by increasing the number of CNTs in the channel, thereby increasing (averaging) the number of current paths [45]. This was observed experimentally by increasing the CNT number density with shortened CNTs [47]. The averaging method would be effective for solving the variability issue. However, other problems would arise, such as overlaying and bundling of CNTs, resulting in a degradation of the gate field effect due to the screening effect. For a bundle of CNTs, the gate field is screened by the outer CNTs, and the carrier densities of the inner CNTs are not significantly modified by the gate field. This results in a drain leakage current in the off state. For the variability issue, a film formation technique that provides a uniform monolayer film of individualized CNTs needs to be developed.

In this paper, we review the recent progress on the above-mentioned issues of film formation technologies for CNT-based flexible electronics after overviewing the fundamental film formation processes.

2 Fundamental Film Formation Processes

CNTs are not typically grown directly on plastic substrates because of the large gap between the growth temperature of the CNTs and the glass transition point of the plastic substrate, and thus, the growth and deposition processes are separately carried out. There are two types of process for depositing a CNT thin film on a plastic substrate: solution and dry processes, as illustrated in Fig. 1. In the solution process, the raw soot of CNTs grown by chemical vapor deposition or other techniques is dispersed in a liquid, such as water or an organic solvent, to make an ink. Subsequently, a thin film is formed on a plastic substrate by printing or coating techniques. As a feature of the solution method, a separation process that yields high-purity semiconducting or metal CNTs by the previously mentioned method can be used after the dispersion process, based on the requirements of the application.

The key challenge of the solution process is the mono-dispersion of CNTs in the ink without damaging the CNTs. The degree of mono-dispersion directly impacts the purity and yield in the metal/semiconductor separation process. To achieve this, ultrasonication is applied in the dispersion process to de-bundle the CNTs in the raw soot. However, the CNTs are damaged and cut to shorter lengths by the sonication. This increases the number of junctions in the current path and degrades the carrier mobility and conductivity. In addition, a dispersant, such as a surfactant, and a polymer are added to the liquid to stabilize the dispersion of CNTs. The residual dispersant in the CNT film increases the contact resistance between the CNTs. Furthermore, some surfactants also cause unintentional carrier doping of the CNTs, making it difficult to control the threshold voltage of the transistors. A cleaning process

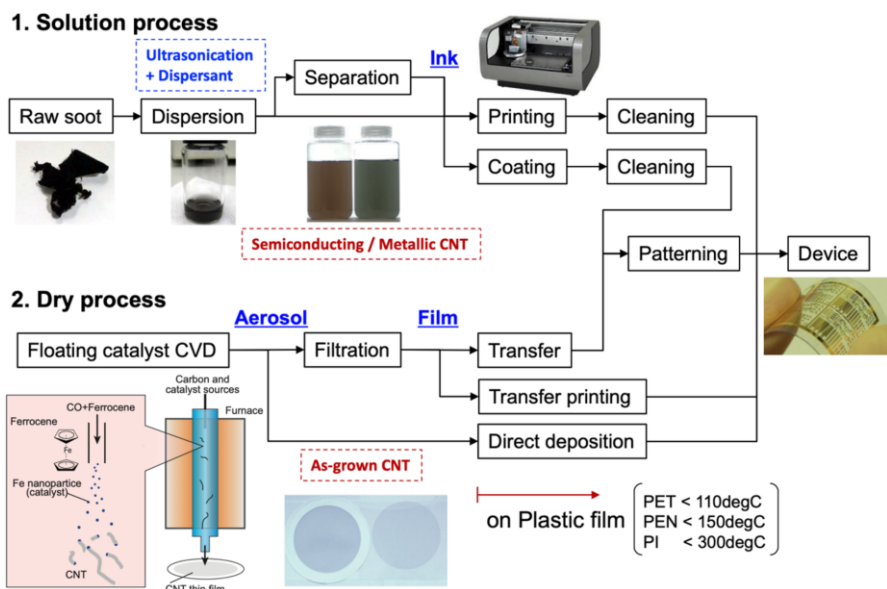


Fig. 1 Process flow chart from CNT thin film formation to device fabrication for solution and dry processes

must be developed to completely remove the surfactants and polymers used as the dispersant.

CNT thin films produced by the solution method exhibit much poorer performance than expected from the conductivity of individual CNTs in many cases. The typical lengths of CNTs range from 0.1 to 1.5 μm , depending on the sonication power and time [22, 48]. Recently, some efforts have been made to address these issues. Shirae et al. developed a repetitive dispersion–extraction process to overcome the trade-off between achieving sufficient dispersion and the lengths of the dispersed CNTs and obtained a highly conductive transparent conductive film based on the solution process [49]. This technique also overcomes the quality–quantity trade-off in the dispersion process, yielding long CNTs (10–20 μm) and short CNTs that were a few μm long for few-wall CNTs. The length-sorting technique based on gel-column chromatography developed by Miyata et al. is also effective for obtaining high-performance CNT thin films, though the yield is low [50]. The mean length of the length-sorted semiconducting CNTs was $\sim 1.5 \mu\text{m}$. A high carrier mobility of $164 \text{ cm}^2 \text{ V}^{-1} \text{ s}^{-1}$ was achieved in a CNT TFT. Toshimitsu et al. struggled with the residual dispersant issue and developed a removable solubilizer based on dynamic supramolecular coordination chemistry [51].

Another difficult issue to be addressed is the uniformity and bundling control of the CNT thin film in the deposition process. CNTs tend to agglomerate due to the surface tension of the liquid when the ink dries on the substrate, resulting in a non-uniform film. For transistor applications, the bundling of the CNTs should also be controlled. Recent progress regarding this issue will be presented further in the next section.

The main dry process for CNT film formation is a transfer process based on the floating-catalyst chemical vapor deposition technique [52]. In floating-catalyst chemical vapor deposition, the catalyst nanoparticles for CNT growth are not supported on a substrate but float in the carrier gas, and thus, individualized or bundled CNTs are obtained in aerosol form. A thin film can be easily obtained from the CNT aerosol by filtration [20] or direct deposition [53] methods. By the filtration method, the CNTs are collected by a membrane filter and a fairly uniform thin film of CNTs is obtained on the filter. The CNT thin film on the filter is transferable to various kinds of target substrates, such as plastic, glass, silicon, and metals [20]. For very thin CNT films for transistor applications, the thin films can be transferred by dissolving the nitrocellulose-based membrane filter with acetone after attaching the filter onto the target substrate [4]. Micro-patterning necessary for device applications is also possible in the filtration process by using a micro-patterned filter [28]. In the direct deposition techniques, the CNTs are directly deposited on the plastic film by utilizing electrostatic forces [53] or temperature-gradient-induced thermophoresis [54–56] to attract the CNTs to the substrate. Alignment of the CNTs would also be possible by utilizing gas flow.

In dry processes, a thin film is directly formed by as-grown CNTs without dispersion in the liquid, unlike the solution process. Therefore, it is possible to obtain a uniform and high-performance thin film with long and contamination-free CNTs. The length of the single-walled CNTs ranges from 2 to 6 μm [57]. Aggregation of CNTs does not occur in the dry process. High-performance, transparent, conductive films with sheet resistances of $78 \Omega \text{ sq}^{-1}$ and optical transmittances of 90% were achieved [58]. The trade-off between the sheet resistance and optical transmittance can be overcome by applying a microscale grid structure [28]. A roll-to-roll process for producing meter-scale transparent conductive films on a plastic film was recently developed by Wang et al. [59]. CNT TFTs with high-carrier mobilities of more than $1000 \text{ cm}^2 \text{ V}^{-1} \text{ s}^{-1}$ were also fabricated using the semi-dry process based on floating-catalyst chemical vapor deposition, where a CNT thin film was formed on a membrane filter and was subsequently transferred to a plastic substrate by dissolving the filter with acetone [4, 5.] The unique morphology of the long CNT network with Y-type tube-to-tube junctions rather than X-type junctions also contributed to the low contact resistance and high carrier mobility [4].

However, it is difficult to introduce a semiconductor/metal separation process, which is normally a solution-based process. The conduction property is controlled by the density and ratio of semiconducting/metallic CNTs. Semiconducting behavior can be obtained by using a network-like CNT thin film with a very low density near the percolation threshold. However, a short-circuit issue is likely to occur if it is a mixture of semiconducting and metallic CNTs. The probability of the short-circuit issue occurring increases with an increase in the density of the CNTs, and thus, there is a trade-off between uniformity and performance of the CNT TFTs. To overcome the trade-off, preferential growth of semiconducting CNTs and chirality-controlled growth of particular CNT species may be possible solutions [60–62]. An alternate route is the selective removal of the metallic or semiconducting CNTs after the growth. The electrical breakdown technique by Joule heating is often used to selectively cut the metallic CNTs without damaging the other CNTs, exploiting the

Fig. 2 Effect of surfactant type on morphologies of CNT thin films formed by solution process. **a** AFM images and height profiles (the green line in the AFM image) of the typical CNT networks formed using (i) SDS, (ii) SDBS, (iii) SC, and (iv) DOC. Scale bar 1 μm. Inset in panels (iii) and (iv): magnified views of the thin film. Scale bar 400 nm. **b** Schematic images of the network with different attractive interactions in the solution just before removing it. More CNTs are aligned in a parallel fashion as the attractive interaction increases. (i) Aligned short bundles (SDS). (ii) Continuously connected bundles (SDBS). (iii) Locally aligned CNTs (SC). (iv) Random network of CNTs (DOC). (v, vi) Side-view images of the lateral capillary force, which is present when the substrate is dried. (v) The CNTs form bundles due to inhomogeneous lateral capillary forces (SDS, SDBS). (vi) The networks maintain a random network (SC, DOC) because the capillary forces cancel each other. Copyright 2013 American Chemical Society [78]

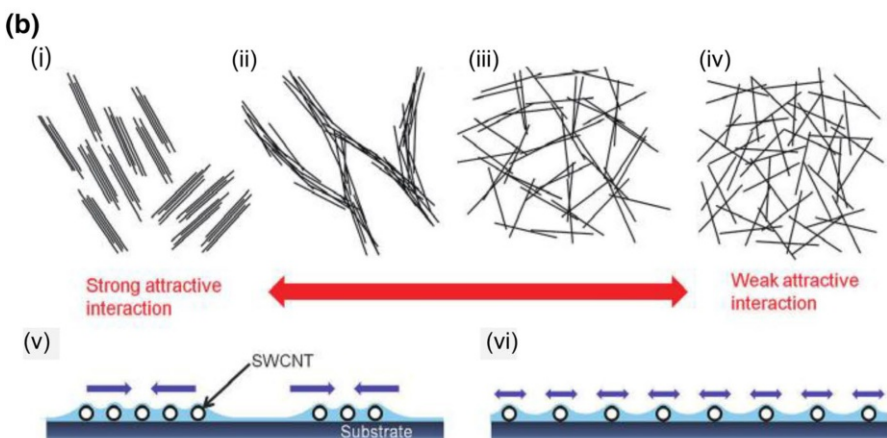
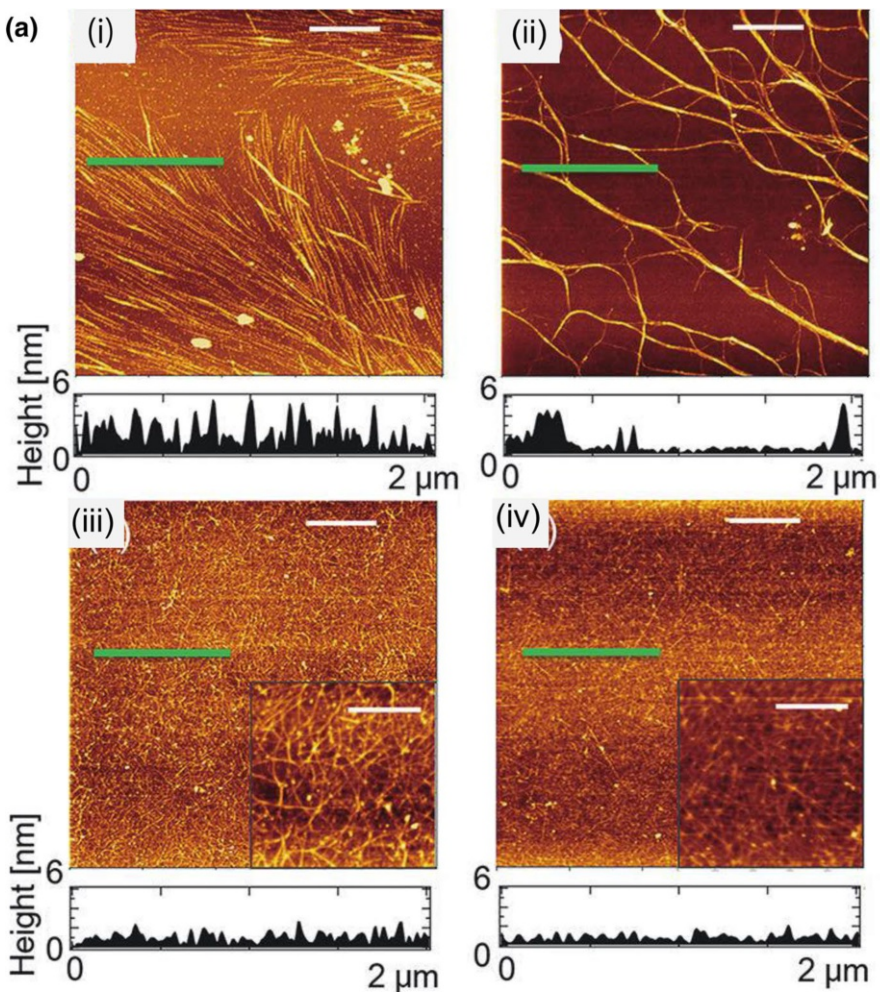
difference in the electrical transport properties of the two types of CNTs [63–66]. Polymer- and water-assisted electrical breakdown have been developed to burn metallic CNTs with large lengths [64, 67]. Chemical and electrochemical approaches [68–70] are scalable batch process for the removal of metallic CNTs.

3 Thin-Film Formation for Semiconductor Applications

Solution-processed semiconducting CNTs can potentially be used to realize high-performance flexible transistors with high uniformity and yield. In this section, we focus on the recent progress in the deposition of semiconducting CNTs from suspensions onto substrates. By utilizing specific interactions between CNTs and functionalized surfaces [71, 72], the controlled deposition of CNT thin films, e.g., alignment, desired density, and micro-patterning, has been enabled.

Solution-based wet processes for random CNT network formation are mainly categorized as drop-casting [73], immersion-coating [74], spray-coating [75], filtration/transfer methods [19, 76], and dielectrophoretic assembly [77]. With a drop-casting technique, Shimizu et al. indicated that the surfactant type affects the morphology of CNT thin film and the TFT performance [78]. The network morphologies were highly dependent on the surfactant type, even though the CNT thin-films were fabricated from the same CNTs using the same process, as shown in Fig. 2. Sodium deoxycholate produced structures with the finest mesh sizes that comprised mostly individual CNTs. The performance of the TFTs was highly correlated with the morphology of the CNT network. The highest on/off ratio and mobility of 1×10^6 and $42 \text{ cm}^2 \text{ V}^{-1} \text{ s}^{-1}$ were obtained, respectively, for the TFT produced from sodium deoxycholate, due to the fine mesh structure. Designing surfactant–substrate interactions is important for assembling CNT networks. However, the mechanisms involved have not been clarified well.

Kiriya et al. investigated a CNT assembly with steroid- and alkyl-based surfactants [79]. They found that the steroid-based surfactants yielded highly dense CNT films. However, the alkyl surfactants prohibited CNT assembly due to formation of packed alkyl layers of residual surfactants on the substrate surface that repel surfactant-encapsulated CNTs, as illustrated in Fig. 3. Using this method, roll-to-roll assembly of CNTs on plastic substrates with high densities was achieved. Large-scale 4-in.-area CNT film formation was also reported by Tian et al. by covering the Si/SiO₂ surface with a CNT suspension, and wafer-scale



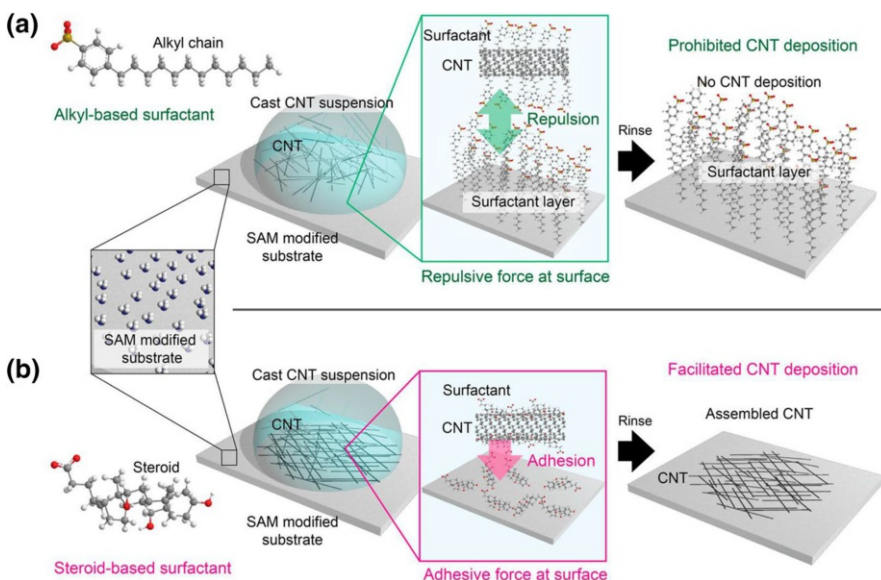


Fig. 3 Schematic illustration of adhesion of CNTs on a substrate modified with amine self-assembled monolayer (SAM). *Top*: CNT dispersion with an alkyl-type surfactant (AS). The illustrated chemical is SDBS. The residual AS is assembled onto the surface of the amine-modified substrate, which induced a repulsive force against the CNTs surrounded by the same surfactant. Thus, CNTs are not deposited, and only surfactants remain on the surface of the substrate. *Bottom*: CNT dispersion with a steroid type surfactant (SS). Because of the rigid structure of the steroid surfactants, the dense blocking layer formed in the AS case is not formed on the substrate, facilitating adhesion of the CNTs. Copyright 2014 American Chemical Society [79]

fabrication of TFTs was achieved with high yield on the entire surface of a Si substrate [80]. Using various geometries, 25,200 devices were fabricated on rigid and flexible substrates, and the structures exhibited relatively uniform characteristics. A similar technique was used to obtain TFTs that showed small threshold voltage distributions. Consequently, logic gates were able to achieve voltages as low as 2 V [81, 82].

Wet-filtration processes using a vacuum [76, 83] are also good candidates for obtaining large-scale and relatively uniform CNT films. The density of CNTs is easily controlled by the amount of installed CNT suspension. The CNT film deposited on the filter was easily transferred onto rigid/flexible substrates. Geier et al. fabricated a large number of TFTs for CNT thin-film complementary static random-access memory using the filtration method [83].

Aligned CNT assemblies with high-purity semiconducting CNTs are a potential way to enhance device performances. One of the earliest reports on the Langmuir–Blodgett assembly of aligned CNTs was reported by Li et al. They fabricated TFTs with high current driving abilities of $\sim 300 \text{ mA mm}^{-1}$ normalized by the channel width [84]. Cao et al. reported arrays of high-purity semiconducting CNTs with full surface coverage using the Langmuir–Schaefer method [85], as

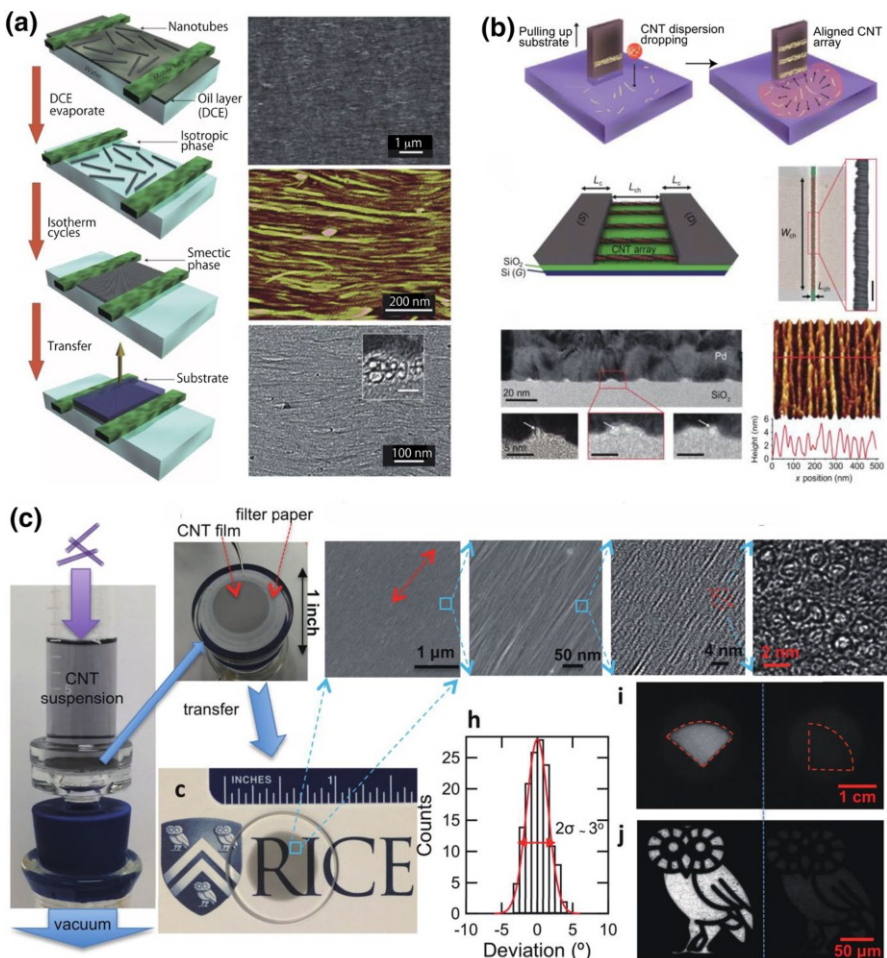


Fig. 4 Assembly of aligned CNT thin films. **a** Langmuir–Schaefer assembly process. SEM, AFM, and TEM images of the aligned CNT thin film. Inset of TEM image is the high-resolution cross-sectional TEM image (*scale bar* 5 nm). Copyright 2013 Macmillan Publishers Limited [85]. **b** The iterative process used to fabricate aligned CNTs driven by the spreading and evaporation of controlled doses of organic solvent at the air/water interface. Copyright 2014 American Chemical Society [86]. FETs constructed from densely packed aligned semiconducting CNT arrays. Schematic of CNT array resting on a SiO_2/Si back gate with top Pd source and drain electrodes. False-colored SEM image of a representative FET with channel width W_{ch} of 4.1 μm and channel length L_{ch} of 150 nm. Inset SEM image (*scale bar* 200 nm) shows the CNT array, with 47 CNTs μm^{-1} and a high degree of alignment. Cross-sectional TEM image of Pd/CNT/SiO₂ electrode stack where the “humps” in the Pd correspond to CNTs in the array. High-resolution TEM images reveal individual CNTs beneath the Pd “humps” with diameters of 1.3–1.9 nm. AFM image of 30 nm of Pd coating a CNT array, showing the Pd conforming to the individual CNTs. Copyright 2016 American Association for the Advancement of Science [87]. **d** Slow filtration method for wafer-scale monodomain films of aligned CNTs. A CNT suspension passes slowly through a vacuum filtration system. A wafer-scale, uniform CNT film is formed on the filter membrane. The SEM and top-view TEM images show the strong alignment and high density of the film. A cross-sectional TEM image shows a high cross-sectional areal density of $\sim 10^6 \mu\text{m}^{-2}$. The angular distribution of CNTs with a standard deviation of 1.5° shows the high degree of alignment. The film is opaque to light polarized parallel to the CNT alignment direction and transparent to light polarized perpendicular to the alignment direction on a macroscopic scale. Copyright 2016 Springer Nature [90]

shown in Fig. 4a. Their method achieved semiconducting CNT arrays with high densities of more than 500 tubes μm^{-1} , and the transistor exhibited a high current density of 120 mA mm^{-1} and a transconductance greater than 40 mS mm^{-1} .

Floating evaporative self-assembly and alignment of semiconducting CNTs from organic solvents was achieved by Joo et al. The CNTs were highly aligned (within $\pm 14^\circ$), packed at a density of ~ 50 tubes μm^{-1} , and formed a well-ordered monolayer, as shown in Fig. 4b [86]. Their TFTs showed high performances with mobilities of $38 \text{ cm}^2 \text{ V}^{-1} \text{ s}^{-1}$ and on/off ratios of 2.2×10^6 for a channel size of $9 \mu\text{m}$. The CNT FET with a channel length of 140 nm exhibited a current driving ability of 350 mA mm^{-1} , which exceeded that of the 90-nm Si MOSFET [87]. Radio-frequency FETs were fabricated using aligned semiconducting CNTs, and current-gain cut-off and maximum oscillation frequencies greater than 70 GHz were simultaneously achieved [88].

The other approach for aligning CNTs is top-down patterning and self-assembly for regular arrays of semiconducting CNTs, producing a density of $80 \text{ CNTs } \mu\text{m}^{-1}$ and large-scale homogeneity of the patterned areas [89]. This method is advantageous in terms of arbitral direction of CNT alignment.

Large-area assembly of aligned CNTs is also an important challenge for practical applications. A wafer-scale monodomain film of aligned single-walled CNTs was realized by slow vacuum filtration by He et al. as shown in Fig. 4c [90]. They performed vacuum filtration of a CNT suspension at a low speed, forming a large area ($> \text{cm}^2$) film of aligned CNTs with a thickness of a few to 100 nm. In this method, CNTs accumulated, interacted with each other, and formed an ordered two-dimensional phase on the hydrophilic surface of the membrane filter. The authors demonstrated the improved responsivity in an optical detector using the aligned CNT film. This method would also be applicable for transistors. However, monolayer-thick film formation is a key issue to avoid the screening of the gate field.

4 Conclusions and Prospects

Recent development of post-growth purification processes has enabled the fabrication of high-purity semiconducting CNT materials for electronics applications. Various film formation techniques have been developed to realize CNT TFTs. Simple solution-based dip-coating and filtration/transfer methods are useful for achieving large-area, uniform thin films from a dispersion of semiconducting CNTs for low-cost flexible devices. These processes are scalable and reproducible. Further improvement is needed to minimize the variability of the device characteristics and power consumption of the integrated circuits.

Aligned and high-density assembly techniques are also emerging for high-performance semiconductor applications. CNT FETs have been fabricated that outperformed Si MOSFETs. Scaleup of the alignment assembly technique will open new paths for achieving the ultimate goal of a “CNT wafer”.

For practical use of CNT thin film devices, complete removal of the residual surfactants and polymers used for the ink is needed to ensure the controllability of the device properties and reliability. Computer-aided design tools for CNT integrated

circuits are indispensable for designing functional circuits, such as analogue–digital converters for wearable sensor applications.

References

1. Snow ES, Novak JP, Campbell PM, Park D (2003) Random networks of carbon nanotubes as an electronic material. *Appl Phys Lett* 82:2145–2147
2. Cao Q et al (2008) Medium-scale carbon nanotube thin-film integrated circuits on flexible plastic substrates. *Nature* 454:495–502
3. Hu LB, Hecht DS, Gruner G (2010) Carbon nanotube thin films: fabrication, properties, and applications. *Chem Rev* 110:5790–5844
4. Sun DM et al (2011) Flexible high-performance carbon nanotube integrated circuits. *Nat Nanotechnol* 6:156–161
5. Sun DM et al (2013) Mouldable all-carbon integrated circuits. *Nat. Commun.* 4:2302
6. Wu ZC et al (2004) Transparent, conductive carbon nanotube films. *Science* 305:1273–1276
7. Bradley K, Gabriel JCP, Gruner G (2003) Flexible nanotube electronics. *Nano Lett* 3:1353–1355
8. McCreery RL (2008) Advanced carbon electrode materials for molecular electrochemistry. *Chem Rev* 108:2646–2687
9. Chopra S, McGuire K, Gothard N, Rao AM, Pham A (2003) Selective gas detection using a carbon nanotube sensor. *Appl Phys Lett* 83:2280–2282
10. Woo CS et al (2007) Fabrication of flexible and transparent single-wall carbon nanotube gas sensors by vacuum filtration and poly(dimethyl siloxane) mold transfer. *Microelectron Eng* 84:1610–1613
11. Kim J, Yoo H, Ba VAP, Shin N, Hong S (2018) Dye-functionalized sol–gel matrix on carbon nanotubes for refreshable and flexible gas sensors. *Sci Rep* 8:11958
12. Ly SY (2008) Diagnosis of copper ions in vascular tracts using a fluorine-doped carbon nanotube sensor. *Talanta* 74:1635–1641
13. Melzer K et al (2015) Flexible electrolyte-gated ion-selective sensors based on carbon nanotube networks. *IEEE Sens J* 15:3127–3134
14. Xuan X, Park JY (2018) A miniaturized and flexible cadmium and lead ion detection sensor based on micro-patterned reduced graphene oxide/carbon nanotube/bismuth composite electrodes. *Sensor Actuators B* 255:1220–1227
15. Cai H, Cao XN, Jiang Y, He PG, Fang YZ (2003) Carbon nanotube-enhanced electrochemical DNA biosensor for DNA hybridization detection. *Anal Bioanal Chem* 375:287–293
16. Besteman K, Lee JO, Wiertz FGM, Heering HA, Dekker C (2003) Enzyme-coated carbon nanotubes as single-molecule biosensors. *Nano Lett* 3:727–730
17. Laurila T, Sainio S, Caro MA (2017) Hybrid carbon based nanomaterials for electrochemical detection of biomolecules. *Prog Mater Sci* 88:499–594
18. Sekitani T et al (2008) A rubberlike stretchable active matrix using elastic conductors. *Science* 321:1468–1472
19. Hu L, Hecht DS, Gruner G (2004) Percolation in transparent and conducting carbon nanotube networks. *Nano Lett* 4:2513–2517
20. Kaskela A et al (2010) Aerosol-synthesized SWCNT networks with tunable conductivity and transparency by a dry transfer technique. *Nano Lett* 10:4349–4355
21. Wang HL et al (2010) High-performance field effect transistors from solution processed carbon nanotubes. *ACS Nano* 4:6659–6664
22. Asada Y et al (2010) High-performance thin-film transistors with DNA-assisted solution processing of isolated single-walled carbon nanotubes. *Adv Mater* 22:2698–2701
23. Lin YH, Lu F, Wang J (2004) Disposable carbon nanotube modified screen-printed biosensor for amperometric detection of organophosphorus pesticides and nerve agents. *Electroanal.* 16:145–149
24. Hur SH et al (2005) Printed thin-film transistors and complementary logic gates that use polymer-coated single-walled carbon nanotube networks. *J Appl Phys* 98:114302
25. Takenobu T et al (2009) Ink-jet printing of carbon nanotube thin-film transistors on flexible plastic substrates. *Appl Phys Express* 2:025005
26. Ha MJ et al (2010) Printed, sub-3 V digital circuits on plastic from aqueous carbon nanotube inks. *ACS Nano* 4:4388–4395

27. Cao X et al (2016) Fully screen-printed, large-area, and flexible active-matrix electrochromic displays using carbon nanotube thin-film transistors. *ACS Nano* 10:9816–9822
28. Fukaya N, Kim DY, Kishimoto S, Noda S, Ohno Y (2014) One-step sub-10 μm patterning of carbon-nanotube thin films for transparent conductor applications. *ACS Nano* 8:3285–3293
29. Saito R, Dresselhaus G, Dresselhaus MS (1998) Physical properties of carbon nanotubes. World Scientific Publishing Co. Pte. Ltd., Singapore
30. Arnold MS, Green AA, Hulvat JF, Stupp SI, Hersam MC (2006) Sorting carbon nanotubes by electronic structure using density differentiation. *Nat Nanotechnol* 1:60–65
31. Tanaka T et al (2009) Simple and scalable gel-based separation of metallic and semiconducting carbon nanotubes. *Nano Lett* 9:1497–1500
32. Liu HP, Tanaka T, Urabe Y, Kataura H (2013) High-efficiency single-chirality separation of carbon nanotubes using temperature-controlled gel chromatography. *Nano Lett* 13:1996–2003
33. Wu J et al (2012) Short channel field-effect transistors from highly enriched semiconducting carbon nanotubes. *Nano Res* 5:388–394
34. Tanaka T, Jin HH, Miyata Y, Kataura H (2008) High-yield separation of metallic and semiconducting single-wall carbon nanotubes by agarose gel electrophoresis. *Appl Phys Express* 1:114001
35. Qiu S et al (2018) Solution-processing of high-purity semiconducting single-walled carbon nanotubes for electronics devices. *Adv Mater* 30:1800750
36. Lefebvre J et al (2017) High-purity semiconducting single-walled carbon nanotubes: a key enabling material in emerging electronics. *Acc Chem Res* 50:2479–2486
37. Fuhrer MS et al (2000) Crossed nanotube junctions. *Science* 288:494–497
38. Nirmalraj PN, Lyons PE, De S, Coleman JN, Boland JJ (2009) Electrical connectivity in single-walled carbon nanotube networks. *Nano Lett* 9:3890–3895
39. Znidarsic A et al (2013) Spatially resolved transport properties of pristine and doped single-walled carbon nanotube networks. *J Phys Chem C* 117:13324–13330
40. Kocabas C et al (2007) Experimental and theoretical studies of transport through large scale, partially aligned arrays of single-walled carbon nanotubes in thin film type transistors. *Nano Lett* 7:1195–1202
41. Kang SJ et al (2007) High-performance electronics using dense, perfectly aligned arrays of single-walled carbon nanotubes. *Nat Nanotechnol* 2:230–236
42. Ago H et al (2005) Aligned growth of isolated single-walled carbon nanotubes programmed by atomic arrangement of substrate surface. *Chem Phys Lett* 408:433–438
43. Han S, Liu XL, Zhou CW (2005) Template-free directional growth of single-walled carbon nanotubes on a- and r-plane sapphire. *J Am Chem Soc* 127:5294–5295
44. Hirotani J, Kishimoto S, Ohno Y (2018) Origins of the variability of the electrical characteristics of solution-processed carbon nanotube thin-film transistors and integrated circuits. *Nanoscale Adv.* <https://doi.org/10.1039/c1038na00184g>
45. Ishida M, Nihey F (2008) Estimating the yield and characteristics of random network carbon nanotube transistors. *Appl Phys Lett* 92:163507
46. Islam AE et al (2012) Effect of variations in diameter and density on the statistics of aligned array carbon-nanotube field effect transistors. *J Appl Phys* 111:054511
47. Ohmori S, Ihara K, Nihey F, Kuwahara Y, Saito T (2012) Low variability with high performance in thin-film transistors of semiconducting carbon nanotubes achieved by shortening tube lengths. *RSC Adv* 2:12408
48. Asada Y et al (2011) Thin-film transistors with length-sorted DNA-wrapped single-wall carbon nanotubes. *J Phys Chem C* 115:270–273
49. Shirae H et al (2015) Overcoming the quality–quantity tradeoff in dispersion and printing of carbon nanotubes by a repetitive dispersion–extraction process. *Carbon* 91:20–29
50. Miyata Y et al (2011) Length-sorted semiconducting carbon nanotubes for high-mobility thin film transistors. *Nano Res* 4:963–970
51. Toshimitsu F, Nakashima N (2014) Semiconducting single-walled carbon nanotubes sorting with a removable solubilizer based on dynamic supramolecular coordination chemistry. *Nat Commun* 5:5041
52. Moisala A et al (2006) Single-walled carbon nanotube synthesis using ferrocene and iron pentacarbonyl in a laminar flow reactor. *Chem Eng Sci* 61:4393–4402
53. Zavodchikova MY et al (2009) Carbon nanotube thin film transistors based on aerosol methods. *Nanotechnology* 20:085201

54. Lefebvre J, Ding J (2017) Carbon nanotube thin film transistors by droplet electrophoresis. *Mater Today Commun* 10:72–79
55. Laiho P, Mustonen K, Ohno Y, Maruyama S, Kauppinen EI (2017) Dry and direct deposition of aerosol-synthesized single-walled carbon nanotubes by thermophoresis. *ACS Appl Mater Interfaces* 9:20738–20747
56. Laiho P et al (2018) Wafer-scale thermophoretic dry deposition of single-walled carbon nanotube thin films. *ACS Omega* 3:1322–1328
57. Kaskela A et al (2016) Highly individual SWCNTs for high performance thin film electronics. *Carbon* 103:228–234
58. Ding EX, Zhang Q, Wei N, Khan A, Kauppinen EI (2018) High-performance single-walled carbon nanotube transparent conducting film fabricated by using low feeding rate of ethanol solution. *R Soc Open Sci* 5:180392
59. Wang BW et al (2018) Continuous fabrication of meter-scale single-wall carbon nanotube films and their use in flexible and transparent integrated circuits. *Adv Mater* 30:e1802057
60. Zhou WW, Zhan ST, Ding L, Liu J (2012) General rules for selective growth of enriched semiconducting single walled carbon nanotubes with water vapor as in situ etchant. *J Am Chem Soc* 134:14019–14026
61. Yang F et al (2016) Templated synthesis of single-walled carbon nanotubes with specific structure. *Acc Chem Res* 49:606–615
62. Yang F et al (2014) Chirality-specific growth of single-walled carbon nanotubes on solid alloy catalysts. *Nature* 510:522–524
63. Li JH, Franklin AD, Liu J (2015) Gate-free electrical breakdown of metallic pathways in single-walled carbon nanotube crossbar networks. *Nano Lett* 15:6058–6065
64. Otsuka K, Inoue T, Chiashi S, Maruyama S (2014) Selective removal of metallic single-walled carbon nanotubes in full length by organic film-assisted electrical breakdown. *Nanoscale* 6:8831–8835
65. Collins PC, Arnold MS, Avouris P (2001) Engineering carbon nanotubes and nanotube circuits using electrical breakdown. *Science* 292:706–709
66. Otsuka K, Inoue T, Shimomura Y, Chiashi S, Maruyama S (2016) Field emission and anode etching during formation of length-controlled nanogaps in electrical breakdown of horizontally aligned single-walled carbon nanotubes. *Nanoscale* 8:16363–16370
67. Otsuka K, Inoue T, Shimomura Y, Chiashi S, Maruyama S (2017) Water-assisted self-sustained burning of metallic single-walled carbon nanotubes for scalable transistor fabrication. *Nano Res* 10:3248–3260
68. Yang CM et al (2005) Selective removal of metallic single-walled carbon nanotubes with small diameters by using nitric and sulfuric acids. *J Phys Chem B* 109:19242–19248
69. Zhang GY et al (2006) Selective etching of metallic carbon nanotubes by gas-phase reaction. *Science* 314:974–977
70. Wei DC et al (2009) Selective electrochemical etching of single-walled carbon nanotubes. *Adv Funct Mater* 19:3618–3624
71. LeMieux MC et al (2008) Self-sorted, aligned nanotube networks for thin-film transistors. *Science* 321:101–104
72. LeMieux MC et al (2009) Solution assembly of organized carbon nanotube networks for thin-film transistors. *ACS Nano* 3:4089–4097
73. Bardecker JA et al (2008) Directed assembly of single-walled carbon nanotubes via drop-casting onto a UV-patterned photosensitive monolayer. *J Am Chem Soc* 130:7226–7227
74. Shimizu M, Fujii S, Asano S, Tanaka T, Kataura H (2013) Fabrication of homogeneous thin films of semiconductor-enriched single-wall carbon nanotubes for uniform-quality transistors by using immersion coating. *Appl Phys Express* 6:105103
75. Jeong M, Lee K, Choi E, Kim A, Lee SB (2012) Spray-coated carbon nanotube thin-film transistors with striped transport channels. *Nanotechnology* 23:505203
76. Maeda M et al (2015) Printed, short-channel, top-gate carbon nanotube thin-film transistors on flexible plastic film. *Appl Phys Express* 8:045102
77. Liang YR, Xia JY, Liang XL (2016) Short channel carbon nanotube thin film transistors with high on/off ratio fabricated by two-step fringing field dielectrophoresis. *Sci Bull* 61:794–800
78. Shimizu M, Fujii S, Tanaka T, Kataura H (2013) Effects of surfactants on the electronic transport properties of thin-film transistors of single-wall carbon nanotubes. *J Phys Chem C* 117:11744–11749
79. Kiriya D et al (2014) Design of surfactant-substrate interactions for roll-to-roll assembly of carbon nanotubes for thin-film transistors. *J Am Chem Soc* 136:11188–11194

80. Tian B et al (2016) Wafer scale fabrication of carbon nanotube thin film transistors with high yield. *J Appl Phys* 120:034501
81. Chen BY et al (2016) Highly uniform carbon nanotube field-effect transistors and medium scale integrated circuits. *Nano Lett* 16:5120–5128
82. Xiang L et al (2018) Low-power carbon nanotube-based integrated circuits that can be transferred to biological surfaces. *Nat Electron* 1:237–245
83. Geier ML et al (2015) Solution-processed carbon nanotube thin-film complementary static random access memory. *Nat Nanotechnol* 10:944–948
84. Li XL et al (2007) Langmuir–Blodgett assembly of densely aligned single-walled carbon nanotubes from bulk materials. *J Am Chem Soc* 129:4890–4891
85. Cao Q et al (2013) Arrays of single-walled carbon nanotubes with full surface coverage for high-performance electronics. *Nat Nanotechnol* 8:180–186
86. Joo Y, Brady GJ, Arnold MS, Gopalan P (2014) Dose-controlled, floating evaporative self-assembly and alignment of semiconducting carbon nanotubes from organic solvents. *Langmuir* 30:3460–3466
87. Brady GJ et al (2016) Quasi-ballistic carbon nanotube array transistors with current density exceeding Si and GaAs. *Sci Adv* 2:e1601240
88. Cao Y et al (2016) Radio frequency transistors using aligned semiconducting carbon nanotubes with current-gain cutoff frequency and maximum oscillation frequency simultaneously greater than 70 GHz. *ACS Nano* 10:6782–6790
89. Wu J, Antaris A, Gong M, Dai H (2014) Top-down patterning and self-assembly for regular arrays of semiconducting single-walled carbon nanotubes. *Adv Mater* 26:6151–6156
90. He XW et al (2016) Wafer-scale monodomain films of spontaneously aligned single-walled carbon nanotubes. *Nat Nanotechnol* 11:633–638

Publisher's Note Springer Nature remains neutral with regard to jurisdictional claims in published maps and institutional affiliations.



REVIEW

Single-Walled Carbon Nanotubes in Solar Cells

I¹ Jeon¹ · Yutaka Matsuo^{1,2} · Shigeo Maruyama^{1,3}

Received: 28 January 2017 / Accepted: 23 December 2017 / Published online: 22 January 2018
© Springer International Publishing AG, part of Springer Nature 2018

Abstract Photovoltaics, more generally known as solar cells, are made from semiconducting materials that convert light into electricity. Solar cells have received much attention in recent years due to their promise as clean and efficient light-harvesting devices. Single-walled carbon nanotubes (SWNTs) could play a crucial role in these devices and have been the subject of much research, which continues to this day. SWNTs are known to outperform multi-walled carbon nanotubes (MWNTs) at low densities, because of the difference in their optical transmittance for the same current density, which is the most important parameter in comparing SWNTs and MWNTs. SWNT films show semiconducting features, which make SWNTs function as active or charge-transporting materials. This chapter, consisting of two sections, focuses on the use of SWNTs in solar cells. In the first section, we discuss SWNTs as a light harvester and charge transporter in the photoactive layer, which are reviewed chronologically to show the history of the research progress. In the second section, we discuss SWNTs as a transparent conductive layer outside of the photoactive layer, which is relatively more actively researched. This section introduces SWNT applications in silicon solar cells, organic solar cells, and perovskite solar cells each, from their prototypes to recent results. As we go along, the science and prospects of the application of solar cells will be discussed.

Chapter 10 was originally published as Jeon, I., Matsuo, Y. & Maruyama, S. Top Curr Chem (Z) (2018) 376: 4. https://doi.org/10.1007/s41061-017-0181-0.

✉ Shigeo Maruyama
maruyama@photon.t.u-tokyo.ac.jp

¹ Department of Mechanical Engineering, The University of Tokyo, Tokyo 113-8656, Japan

² Hefei National Laboratory for Physical Sciences at Microscale, University of Science and Technology of China, Anhui 230026, China

³ Energy Nano Engineering Laboratory, National Institute of Advanced Industrial Science and Technology (AIST), Ibaraki 305-8564, Japan

Keywords Carbon nanotube · Silicon solar cells · Organic solar cells · Perovskite solar cells

1 Single-Walled Carbon Nanotubes as the Photoactive Material in Solar Cells

SWNTs provide an ideal light-harvesting medium that has a wide range of direct band gaps [1], strong absorptions within the solar spectrum [2–4], and high carrier mobility [5, 6] with excellent chemical stability. Compared with carbon nanotubes (CNTs), organic compounds have inherently low carrier mobility and low stability. Organic semiconductors have carrier mobility that is a hundredth that of inorganic materials. This creates a bottleneck in the performance of organic solar cells (OSCs) [7–11]. Therefore, incorporating CNTs in OSCs can improve device performance greatly. In this section, we discuss the use of SWNTs in the photoactive layer of photovoltaics, and review demonstrations of this technology in literature.

An individual SWNT can form a p–n junction diode, giving rise to the photovoltaic effect [12, 13]. Thus, SWNTs exhibit high power conversion efficiency (PCE) under illumination. SWNTs comprise semiconducting and metallic forms, generally in a 2:1 ratio. Semiconducting SWNTs form Schottky contacts with metallic objects, which are responsible for the ideal diode behavior, whereas metallic SWNTs easily recombine electrons and holes [14]. It is therefore important that SWNTs be purified according to their use. The difference in electronic structure between semiconducting and metallic SWNTs originates from their chirality, and they can be chiral-specifically synthesized [15, 16] or sorted by various methods based on their diameters and electronic properties (Fig. 1). Well-known sorting methods are density gradient ultracentrifugation [17, 18], gel-chromatography [19], and aqueous two-phase separation [20]. These methods exploit differences in diameter, chirality, and electronic properties of CNTs to precisely collect multiple chiralities of semiconducting SWNTs. Since each chirality absorbs a specific light wavelength, the semiconducting SWNTs obtained by this method can be used as a photoactive material. Because CNTs have high conductivity along the tube axis, SWNTs can act effectively, not

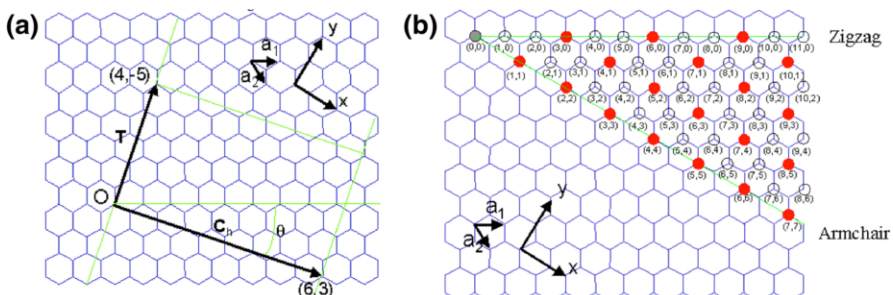


Fig. 1 **a** Definition of chiral vectors in a hexagonal lattice. **b** For a SWNT chirality of (n,m) , if the value of $(n - m)/3$ is an integer, the SWNT is metallic. The red dots represent metallic SWNTs

only as a light harvester, but also as a charge transporter in the photoactive layer. This means that SWNTs possess the dual functionality of a light absorber and a charge-selective material.

Solar cell devices, in general, are mainly composed of an active layer, a charge selective layer, and a charge conductive layer. The active layer absorbs light and generates excitons. The charge selective layers are placed above and below the active layer to filter out any unwanted charges, preventing recombination after excitation. These are then followed by the conductive layers, which extract the filtered charges. A polymer matrix composed of conductive polymer, and SWNTs allows exciton dissociation in a strong electric field, with the CNTs functioning as the electron transporter [21]. An interpenetrating donor–acceptor heterojunction achieves efficient charge separation and charge collection such that electrons and holes can travel toward their respective contacts through the polymer donors and CNT acceptors. Poly(3-hexylthiophene), or P3HT, and poly(3-octylthiophene), P3OT, are the most commonly used polymer donors and are generally mixed with SWNTs in solution [22, 23].

1.1 CNT as Electron Acceptors/Transporters

In this line of research, CNTs started out as electron acceptors. Prof. Sir. Richard Friend reported polymer- and CNT-based OSCs using poly(*p*-phenylene vinylene), PPV, and MWNTs (Table 1: report A for the first time to the best of our knowledge) [24]. Despite effective charge transfer from PPV to the CNTs, charge recombination within the CNT networks limited the device performance. Moreover, poor dispersion of CNTs in PPV resulted in severe aggregation of the CNTs. Kymakis and Amaralunga reported the OSCs using SWNTs, which were mixed with P3OT (Table 1: report B) [21, 25]. Although the PCE was low (0.04%), they successfully demonstrated the electron acceptor behavior of the SWNTs with an open-circuit voltage (V_{OC}) of 0.9 V and fill factor (FF) of 0.4. The results revealed that photoinduced electron transfer occurred at the polymer/nanotube interface and showed the promise of conjugated polymer-SWNT composites. C_{60} -modified SWNTs were mixed with P3HT to give a much improved PCE of 0.57% (Table 1: report C) [26, 27]. SWNTs and C_{60} were mixed in toluene and irradiated with microwaves, followed by addition of P3HT. Improved short-circuit current density (J_{SC}) was a direct result of higher electron mobility owing to the SWNTs. Furthermore, a change of morphology increased FF as well.

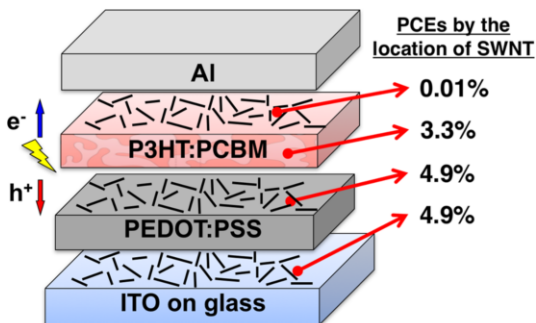
Thermal post-treatment was discovered at this point, which entails heating devices beyond the glass transition temperature of the polymer donor. This treatment caused beneficial phase separation of the blend and improved the ordering of the polymeric chains, which improved charge transfer, transport, and collection. It was also reported that this treatment substantially increased the hole mobility of the polymer–CNT composites [28]. Jousselme and colleagues reported SWNT, P3HT, and 1-(3-methoxycarbonyl)-propyl-1-phenyl[6]C₆₁ (PCBM) nanocomposites that were prepared by a method using high dissolution followed by concentration to control the ratio of CNTs-to-P3HT/PCBM in the mixture and disperse the CNTs

Table 1 Photovoltaic data of representative devices from literature, in which SWNTs have been used as either a light harvester or charge transporter

	Structures	PCE (%)	Note
A	MWNT/PPV/AI	1.8	The very first OSC using CNTs in the active layer
B	ITO/P3OT:SWNT/AI	0.04	The first OSC using SWNTs in the active layer
C	ITO/PEDOT/P3HT:C ₆₀ -SWNT/Au	0.57	C ₆₀ -SWNT composites were used
D	ITO/PEDOT/CNT:P3HT:PCBM/LiF/AI	2.0	Studied the effect of CNT content in composites
E	ITO/PEDOT:SWNT/P3HT:PCBM/AI	4.9	Investigated positional effect of SWNTs on PCE
F	ITO/PEDOT/SWNT:P3HT:BCP/AI	0.72	Using semiconducting SWNTs coated with P3HT
G	ITO/SWNT:PCBM/C60/BCP/Ag	1.3	SWNTs as electron donor and infrared absorber
H	ITO/PEDOT/SWNT:r-GO:C ₇₀ /C ₇₀ /AI	0.85	Incorporated reduced graphene oxide
I	ITO/PEDOT/TFB/PC ₇₁ BM:r-GO:SWNT/AI	1.3	Further improved PCE by using PC ₇₁ BM
J	ITO/PEDOT/SWNT/C ₆₀ /Ag	0.46	No SWNT composite, attempt at full-carbon SC
K	ITO/ZnO NW/SWNT:PC ₇₁ BM/MoO _x /Ag	3.1	Application of ZnO NW
L	ITO/PEDOT/P3HT:PCBM:B-CNT/TiO _x /AI	4.1	B-, N-doped MWNTs were used to enhance PCE
M	ITO/PEDOT/P3HT:ICBA:QD:N-CNT/TiO _x /AI	6.1	QDs were used to enhance doping and dispersion
N	ITO/PEDOT/PTB7:PC ₇₁ BM:N-CNT/Ca/AI	8.6	Low-band gap polymer, PTB7 was used
O	ITO/ZnO/P3HT:SWNT/MoS ₂ /PEDOT/Au	0.46	SWNTs enabled a mixture of MoS ₂ and P3HT

homogeneously throughout the matrix (Table 1: report D) [5]. A P3HT/PCBM (1:1) mixture with 0.1 wt% MWNTs gave the highest PCE of 2.0%. Ozkan and colleagues realized controlled placement of an SWNT monolayer network at four different positions in polymer–fullerene solar cells and found that SWNTs on the hole-collecting side of the active layer gave a high PCE of 4.9% (Table 1: report E; Fig. 2) [6]. They also demonstrated that SWNTs on top of the active layer led to an increased fluorescence lifetime of P3HT. Dip coating from a hydrophilic suspension was used for this experiment. Gradecak and co-workers researched SWNTs as electron acceptors and demonstrated a PCE of 0.72% for SWNT/P3HT bulk heterojunction solar cells (Table 1: report F) [29]. A key point in this research was using purely semiconducting SWNTs coated with well-ordered P3HT by π – π interactions to enhance charge separation and transport. They found that the electrical characteristics of the devices were strongly dependent on the SWNT loading. Modeling of the V_{OC} suggested that despite the large carrier mobility in SWNTs, PCE was limited by carrier recombination.

Fig. 2 Illustration of a work reported in reference [6]. SWNTs located either above or below the hole-transporting layer of OSCs perform the best (the numbers indicate PCEs obtained with different positions of the SWNT layer)



1.2 CNT as Light Absorber and Electron Donor

Arnold and colleagues went further and showed that semiconducting SWNTs can be used not only as an electron acceptors but as light-harvesting electron donors as well [30–32]. They formed a semiconducting SWNT/PCBM bulk heterojunction with a layer of bathocuproine (BCP) and overcame the limited diffusion of semiconducting SWNTs to produce near-infrared efficiency of 1.3% (Table 1: report G) [33]. A follow-up work [34] provided some mechanistic insights but did not produce a higher efficiency, particularly in the visible region of the solar spectrum. Higher efficiency was not realized until reduced graphene oxide (r-GO) was introduced as a cascade material connecting SWNTs and fullerene acceptors. Both pristine CNTs and graphene have low surface energy arising from neutral C–C bonding [35, 36]. In contrast, chemically modified graphene, such as r-GO and nitrogen-doped GO, have higher surface energy due to their surface functional groups and doped heteroatoms with differing electronegativity [37–39]. With atomic-scale flatness and sufficiently high surface energy, chemically modified graphene adds a robust additional layer to be built upon in further nanoscale processing. The high thermal and chemical stability of chemically modified graphene is advantageous for direct nanoscale processing. Huang and colleagues achieved PCEs of 0.21 and 0.85% using C₆₀ and C₇₀, respectively, in a system with semiconducting SWNTs as the donor, fullerenes as the acceptor, and r-GO as an energetically mediating species (Table 1: report H) [40, 41]. Ren and colleagues followed suit, but this time they used r-GO and SWNTs with [6]-phenyl C71-butyric acid methyl ester (PC₇₁BM). Also, poly[(9,9-diocetylfluorenyl-2,7-diyl)-co-(4,40-(N-(4-sec-butylphenyl)) diphenylamine)] (TFB) was used as a hole-blocking layer, which is rather unusual. They achieved a PCE of 1.3% using a composition of PC₇₁BM (88–97%)/semiconducting-SWNT (1–10%)/r-GO (~ 2%; Table 1: report I) [42]. Bao and colleagues reported an attempt at an all-carbon OSC, in which the anode, the active layer, and the cathode were all made up of carbon materials. As a first step, they optimized the active layer composed of a bilayer film of solution-sorted semiconducting SWNTs as the light absorber and donor and C₆₀ as the acceptor between indium tin oxide (ITO) and metal electrodes. By optimizing the semiconducting SWNT dispersion and deposition conditions and the C₆₀ layer thickness, they produced a PCE of 0.46% (Table 1: report J) [43, 44]. As a next

step, they replaced the ITO anode with r-GO layers and the metallic cathode with an *n*-type SWNT film to achieve an all-carbon OSC. However, PCEs were on the order of 0.1%. In 2014, Hersam and colleagues reported a National Renewable Energy Laboratory-certified PCE of 2.5% and a highest PCE of 3.1% using semiconducting SWNTs of various chiralities as the hole-transporting and light-harvesting materials (Table 1: report K) [45]. Compared with single-chirality semiconducting SWNTs, multi-chirality semiconducting SWNTs enabled a wider range of absorption from visible to near-infrared. Normal and inverted architectures were also fabricated and compared. An inverted architecture gave a higher efficiency owing to ZnO nanowires (NWs) penetrating the active layer (Fig. 3).

1.3 CNT as Charge Transporter and Others

Despite considerable research effort, the use of CNTs as a charge transporter did not yield a substantial leap in PCE without the use of dopants and the introduction of inorganic materials, such as quantum dots (QDs). Kim and co-workers addressed the intrinsic limitation imposed by the recombination effect and improved PCE by more than 30% through B and N doping (Table 1: report L) [46]. B- and N-doped CNTs functioned as effective charge-selective transport materials without a quenching effect. The low work function of N-doped CNTs aligned well with the electron transport energy level, while the high work function of B-doped CNTs aligned well with the hole transport level. Kamat and colleagues studied the interaction between SWNTs and light-harvesting CdS [47, 48]. Since then, Raffaele and colleagues [49] demonstrated the first incorporation of QDs into SWNT composites in 2005 and colloidal QD-decorated N-doped CNTs were developed for synergistic charge separation and transport enhancement. Positively charged QDs could directly attach at N-doped sites of CNTs via electrostatic interactions. Such an ideal hybrid structure without an adhesive layer showed a synergistic effect, combining effective electron and hole separation. Efficiency soared, reaching 4.7–6.11% (Table 1: report M) when using indene-C60 bisadduct (ICBA) as the electron acceptor [50], and climbed to 7.5–8.6% upon further development using different organic photoactive materials (Table 1: report N) [51]. With QDs as an acceptor and doped CNTs as an efficient

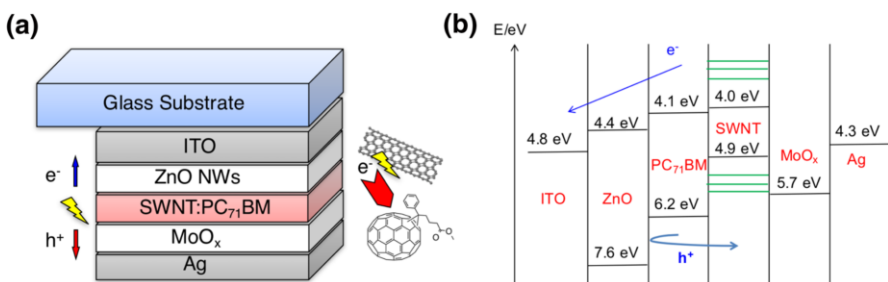


Fig. 3 Illustration of **a** an inverted solar cell where ZnO NW and SWNT:PC₇₁BM were used and **b** the energy level diagram

charge transporter, these studies demonstrate that work function-tunable chemically modified CNTs have the potential to improve charge separation, transport, and recombination in SWNT-based OSCs, which generally suffer from trapping and slow transport of charge carriers in their organic active layers and energy level mismatch at interfaces.

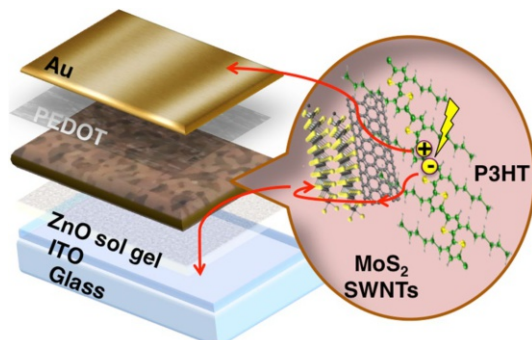
Other approaches have been taken to apply SWNTs in the active layer. We reported the use of multilayered MoS₂ on low-cost metallic/semiconducting SWNTs as the electron acceptor in a bulk heterojunction with P3HT in inverted OSCs (Fig. 4) [52]. MoS₂ is an inorganic material that is intrinsically immiscible with organic compounds. However, we were able to disperse it in organic matrix by exploiting the tendency of SWNTs to intercalate with P3HT through π–π interactions. The successful binding of MoS₂ onto SWNT bundles and its photovoltaic effect was clearly evidenced by a PCE of 0.46% (Table 1: report O).

We have briefly reviewed the use of SWNTs as the light harvester or charge transporter in the photoactive layer of solar cells. Chirality, chemical doping, and dispersibility in solution were crucial factors in achieving high performance. Various approaches have been introduced to improve SWNT applications and these findings expanded the possibilities of CNT technology in solar cells. Yet, this is still just the tip of the iceberg. Uniform blending of the electron-donating conjugated polymer and the electron-accepting CNT is one of the most challenging as well as crucial aspects in creating efficient photocurrent collection in CNT-based OSC devices. Therefore, research on using CNTs in the photoactive layer of OSC devices is still in the early stages and room remains for novel methods to take better advantage of the advantageous properties of CNTs.

2 Single-Walled Carbon Nanotubes as a Transparent Electrode in Solar Cells

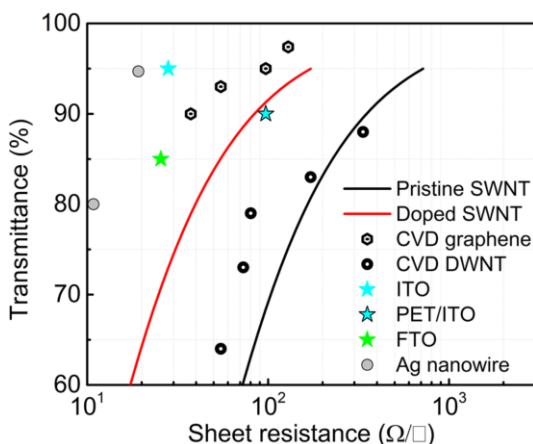
Many types of solar cells have been developed over the years: silicon solar cells, followed by OSCs [53–55], and most recently perovskite solar cells (PSCs), which have emerged as a focus of research. A critical aspect common to these devices is their transparent electrode through which light travels before causing

Fig. 4 Illustration of MoS₂:SWNT:P3HT-based solar cells



excitation in the active layer. Conventionally, ITO has been used as the transparent electrode, and is an essential component in almost all the devices discussed in the first section. The high conductivity and transmittance of ITO are unparalleled thus far. There have been many attempts to replace ITO because of its high cost and limited earth-abundance. Other downsides include its brittleness, which makes it unable to withstand cyclic flexibility tests without breaking. An additional drawback is ITO's vulnerability to high temperature. Therefore, fluorine-doped tin oxide (FTO), which can withstand higher temperatures than ITO, is sometimes used instead. Avoiding these limitations by using alternative transparent electrode materials has therefore been the subject of intense research for many years [56, 57]. The difficulty has been the finding an alternative electrode that is not only robust and cheap, but also optically transparent and electrically conductive [58–60]. CNTs have good optical transparency over a broad range from the visible to the near-infrared as well as high electrical conductivity [61–64]. In addition to this, the outstanding mechanical resilience of CNTs not only exceeds that of ITO but also affords flexibility to solar cell devices. SWNTs are effective for hole collection because their work function is in the range 4.8–5.0 eV, which is higher than that of ITO (usually less than 4.8 eV) [64]. The cost of CNT fabrication has also been reported to be the same or lower than that of ITO [65]. Good performance of sheet resistance versus optical transmittance can be obtained by metal based electrodes such as metal grid transparent electrode [66] or silver (Ag) nanowires [67]. Comprehensive review of transparent electrode for devices are available [68]. In Fig. 5, the sheet resistance versus optical transmittance at 550 nm wavelength of the dry-deposited SWNT film [63] are compared with CVD graphene [69], DWNT [70], typical ITO, PET/ITO, FTO, and Ag nanowires [67]. Performance of SWNT film can be further enhanced by adequate doping [71]. In this section, we discuss the feasibility of SWNTs as a transparent flexible electrode in solar cells by reviewing applications reported to date.

Fig. 5 Sheet resistance vs. transmittance plot for various transparent conductors (Pristine SWNT [63], Doped SWNT [63], CVD graphene [69], CVD DWNT [70], ITO from Kuramoto Co., Ltd., PET/ITO from Nitto Denko Co., Ltd., FTO from Nippon Sheet Glass Co., Ltd., and Ag nanowires [67])



2.1 Single-Walled Carbon Nanotubes as a Transparent Electrode in Silicon Solar Cells

The high cost of silicon led scientists to look for alternative viable semiconductors. It was found that CNTs can serve as both photogeneration sites and the charge transport layer. A semi-transparent CNT film next to an *n*-type crystalline silicon substrate creates high-density *p–n* heterojunctions inducing charge separation in which electrons are extracted through *n*-Si and holes are extracted through CNTs. Although the mechanism is not fully understood, there are two prevailing theories. In the first theory, the CNT film is the *p*-type semiconductor material (Fig. 6a) [72–74] and silicon absorbs the photons dominantly as normal silicon solar cells [75]. Although CNT films can absorb photons, this is limited when the film is transparent to the passage of incident light. The photons generate excitons, and then the excitons are separated into free charge carriers by the built-in potential between the *p*-type CNT and *n*-type Si. The second theory is that a Schottky junction is formed when metallic CNT is in contact with semiconductor Si, and typically it is believed that a thin insulator, SiO_2 , exists (Fig. 6b) [76, 77] again as normal silicon solar cells [78, 79]. Excitons are produced by silicon-absorbing photons and diffuse into SiO_2 which is formed by the built-in potential of the Fermi level difference, and minority carriers are transported by tunneling thorough the thin layer of SiO_2 . Taking the chirality of CNTs into account can further complicate the mechanism. Many individual nanotubes are present in a device, and each forms a heterojunction with the *n*-type silicon. As CNTs exhibit semiconducting or metallic behavior depending on their chirality, a *p–n* junction can be expected for the former and a Schottky junction for the latter.

The very first CNT-based silicon solar cell was reported by Jia et al., in which they used double-walled CNTs. The CNTs performed multiple functions, such as charge separation, charge transport, and charge collection [80]. In the same year,

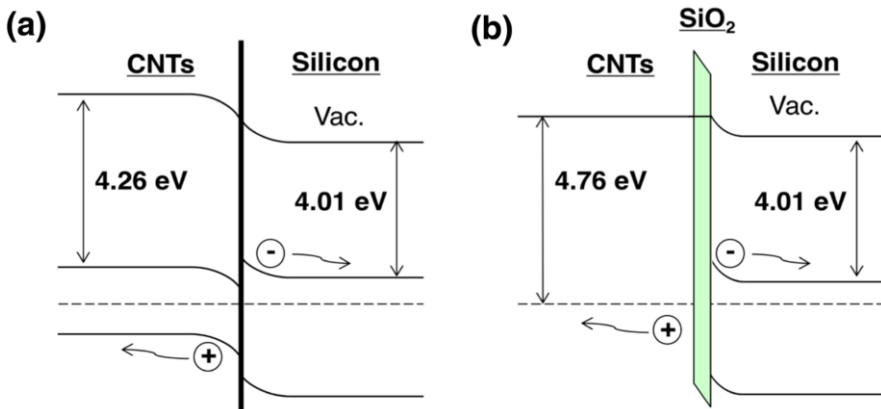


Fig. 6 Illustration of **a** the CNT film functioning as a *p*-type emitter material and **b** a Schottky junction is formed by an insulator, SiO_2 . (Work functions taken from references [72, 77])

Biris and colleagues showed a PCE of 1.3% (Table 2: report A) using SWNTs [81]. They formed this SWNT film by spray-coating from a dimethylformamide suspension. They also tested post-treatment with SOCl_2 for the first time, which led to mobility and carrier density being increased by more than 60% according to Hall effect measurements. In the following year, Biris and co-workers reported a PCE of 4.5% (Table 2: report B) [82]. Again, they used the same SOCl_2 treatment, but transferred as-grown SWNTs onto silicon [83]. More detailed studies of acid doping were subsequently conducted. They identified SOCl_2 as a *p*-type dopant that shifts the Fermi level of SWNTs below ν_1 , thus increasing the mobility and carrier density (Fig. 7a) [84]. This results in suppression of the S_{11} transition in the semiconducting SWNTs and stronger doping would suppress the S_{22} transition as well (Fig. 7b), as observed by near-infrared absorption spectroscopy. It is argued by some researchers that after the acid treatment, CNTs and silicon switched from acting as a *p–n* junction to acting as a Schottky junction, giving the CNTs more metallic character. In other words, the mechanism acting in the interface network changed from variable range hopping to tunneling. The correlation between suppression of the transitions and CNT chirality was analyzed in greater detail by Levitsky and colleagues (Table 2: report C) [85]. They used the photocurrent with a high-resolution absorption spectrum to identify the S_{11} band at around 1100 nm, corresponding to the (7,6) and (8,6) chiralities of SWNTs. They also discovered that metallic SWNTs function as a light absorber in a Schottky junction, though their device showed a PCE of only 1.7%. In the same year, Rinzler and colleagues reported an impressive PCE of 10.9% (Table 2: device D) [86]. The devices initially had a PCE of 8.5%, but by using electrolyte junction control of gate potential, they controlled the Fermi level to strengthen the interface dipole at the electronic junction. Jia et al. further improved PCE by treating SWNTs with dilute nitric acid (Table 2: device E) [87]. The HNO_3 treatment increased FF greatly by reducing series resistance (R_S) as a result of *p* doping lowering the Fermi level of the SWNTs. They also demonstrated enhanced the doping effect by employing porous CNTs. According to them, the contact between CNTs and silicon was significantly improved through formation of a semiconductor/electrolyte interface by the exposed silicon surface in the empty areas without CNTs. They further demonstrated NaCl doping to show that any wet state of CNT doping works as an electrolyte bridge. Subsequently, encapsulating the active area with polydimethylsiloxane (PDMS) further improved PCE and stability (Table 2: report F) [88]. They discussed that the improvement in PCE came from the anti-reflective function of the PDMS film and SiO_2 layer increasing V_{OC} by reducing charge recombination. Stability was improved by the PDMS protecting *n*-Si from oxidation. In a follow-up study, Rinzler and colleagues achieved a PCE of 12% using grid lines of SWNTs etched to cover only a fraction of the silicon surface (Table 2: report G) [89]. The addition of electrolyte immediately improved the device performance. The mechanism at play is said to be similar to that of nitric acid doping, where improvement in performance came partly from the accumulation of NO_3^- at the junction, which has electron-blocking functionality in addition to that of SiO_2 . Likewise, the surface dipole of the accumulated negative ions in the electrolyte is supposed to block electrons, preventing charge recombination [90]. Matsuda and colleagues reported a PCE of 2.4% by optimizing the thickness

Table 2 Photovoltaic data of representative silicon solar cells using SWNTs, from literature

	CNT treatment	Si treatment	Structures	PCE (%)	Note
A	SOCl ₂	n/a	Si/SWNT	1.3	The first SWNT-based silicon solar cells
B	SOCl ₂	n/a	Ag/Si/SWNT/Ag	4.5	Transferring as grown SWNT onto silicon
C	n/a	HF	Ag/Si/SWNT/Cr/Au	1.7	Studied CNT chirality and transition reduction
D	n/a	Oxide etch	—	10.9	Electrolyte junction control of gate potential
E	HNO ₃ /NaCl	HF	Ti/Si/SWNT/Au	13.8	<i>p</i> doping of HNO ₃
F	HNO ₃	HF	Ti/Si/SWNT/Au	10.0	Encapsulating the active area by PDMS
G	n/a	Oxide etch	—	12.0	Grid lines of SWNTs to cover small area of Si
H	—	—	—	2.4	(6.5) SWNTs with optimized thickness
I	HNO ₃	HF	Al/Si/SiO ₂ /SWNT/Cr/Au	11.3	Keeping acid inside the void space of CNTs
J	HNO ₃	HF	Al/Si/SiO ₂ /SWNT/Cr/Au(Al)	11.5	Superacid slide casting method
K	HNO ₃	—	Pt/Ti/n-Si/SWNT/Pt	10.0	Micro-honeycomb network CNTs
L	—	—	—	14.9	SWNTs and graphene comparison next to Si
M	—	—	Pt/Ti/n-Si/SWNT/Pt	11	Application of aerosol SWNTs
N	MoO _x	HF	In/Si/SWNT/MoO _x /Au	17.0	Application of MoO _x doping.

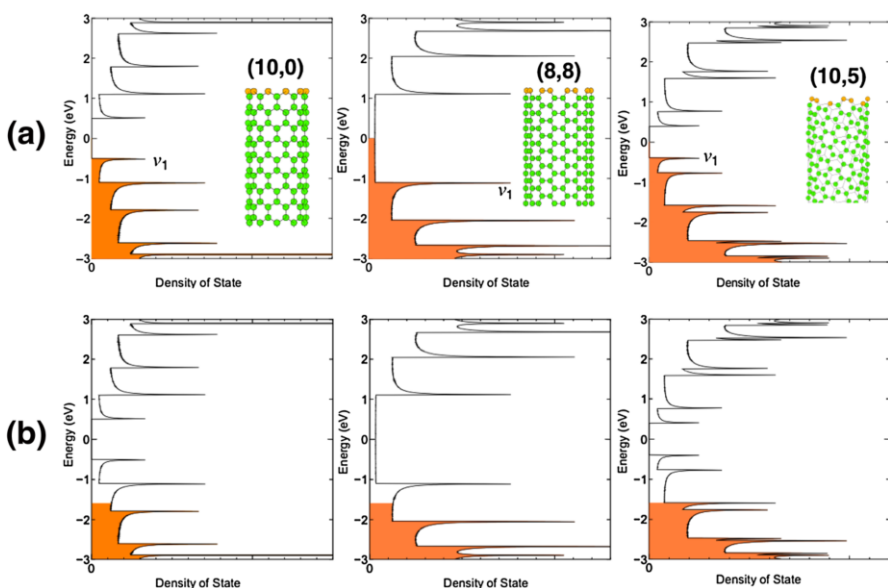


Fig. 7 **a** Density of states and v_1 of an armchair SWNT, a zig-zag SWNT, and a chiral SWNT. **b** Density of states after *p* doping

of (6,5) SWNTs (Table 2: report H) [91]. Returning to acid doping, an even higher PCE greater than 11.2% was achieved by Taylor and colleagues via keeping the acid inside the void space of CNTs (Table 2: report I) [73]. They discussed the characteristics of dark forward current density with varying temperature and found that temperature-dependent current rectification originates from thermally activated band-to-band transitions of carriers in silicon and that the SWNT thin films established a built-in potential for carrier separation/collection. In the same year, Taylor published another paper with a marginally improved PCE of 11.5%. A new super acid slide casting method was used for the CNT fabrication (Table 2: report J) [92]. A PCE of 10.0% was also achieved by us using micro-honeycomb CNT network in silicon SCs (Table 2: report K) [93]. We reported vertically aligned SWNTs treated with water to form a honeycomb network on *n*-Si substrate. CNTs and graphene were combined with crystalline silicon wafers to fabricate silicon solar cells. Solar cells with direct graphene-to-silicon contact exhibited better characteristics than did those with CNT-to-silicon contact, owing to improved junction quality and increased contact area. Using the composite films, the obtained SWNT/graphene/Si solar cells reached a PCE of 14.9% (Table 2: report L) [94]. A problem with wet acid doping is a high exciton quenching rate, but they resolved this issue by employing aligned CNTs, which shortened the transport distance. Moreover, the aligned CNTs were in better contact with the silicon as evidenced by an increase in J_{SC} . Cui et al. used pristine aerosol SWNTs with long bundle lengths to fabricate SWNT/Si solar cells [95]. A PCE approaching 11% was achieved using a pristine SWNT without any chemical treatment (Table 2: report M). More importantly, the solar cells were stable for

at least 10 months in air without any passivation. In fact, a slight increase in PCE was observed after storing in air, in contrast to previous results in the literature. Li et al. [96] demonstrated an *n*-SWNT/*p*-Si photovoltaic system by tuning SWNTs from *p*-type to *n*-type through polyethylene imine functionalization. Recently, Matsuda and colleagues used metal oxide layers to prepare both *p*-SWNT/*n*-Si and *n*-SWNT/*p*-Si with significantly improved PCEs [97]. The metal oxides also serve as both an antireflective layer and an efficient carrier dopant, leading to reduced loss of incident solar light and increased photocurrent, respectively. As a consequence, the photovoltaic performance of both *p*-SWNT/*n*-Si and *n*-SWNT/*p*-Si heterojunction solar cells using MoO_x and ZnO layers was improved, resulting in very high PCEs of 17.0 and 4.0%, respectively (Table 2: report N).

Since the early reports of a PCE around 1%, CNT/Si solar cells have seen rapid performance gains up to around 17%. However, the mechanism is still not clear, as the Schottky metal oxide junction theory established by Jia et al. contradicts the *p–n* junction theory of Ong et al. [85]. However, the Schottky metal oxide junction theory seems to be more dominant for the time being. Although the polychirality of CNTs further obscures this issue, pure CNTs are becoming increasingly available, so we can anticipate a clearer understanding in the near future. Considering the decades of wide-ranging research into silicon solar cells, this is still a relatively small area of research and it is worthwhile to investigate these devices further. The apparent ease with which high PCEs have been rapidly achieved by a limited number of research groups, is both exciting and sure to prompt further research.

2.2 Single-Walled Carbon Nanotubes as a Transparent Electrode in Organic Solar Cells

OSCs have received focused attention in recent academic research [98–100] due to OSCs providing flexibility and a lower cost that silicon solar cells cannot match. OSCs utilize conductive organic compounds as electron donors and electron-rich fullerene derivatives as electron acceptors [55, 101]. Owing to their high absorption coefficient, low cost, and mechanical flexibility, OSCs have been established as one of the important categories of solar cell research. Nevertheless, despite laudable achievements in recent years, OSCs are still faced with limitations including the fixed light absorption range of organic compounds, restricted hole mobility, and intrinsic instability [102]. Above all, the maximum PCEs of OSCs (ca. 10%) are lagging behind those of silicon solar cells (ca. 20%).

Early on, many studies were conducted that used CNTs as a light harvester in OSCs, as discussed in the first section of this chapter [21]. Nowadays, however, CNTs in OSCs are typically not responsible for exciton generation upon light absorption. Instead, a more promising approach is to use CNTs on either side of the device as a charge-collecting transparent electrode. In this section, we focus mainly on the use of SWNTs as electrodes in OSCs. SWNTs have been used mostly as the anode. For example, Gruner and colleagues reported the use of SWNTs as a transparent anode and demonstrated efficient, flexible OSCs with a structure of poly-ethylene terephthalate (PET)/SWNT/poly(3,4-ethylenedioxythiophene) (PEDOT)/

P3HT:PCBM/AI. SWNTs were deposited using a filtration method, and PEDOT was used to coat the rough CNT surface and lower R_s through its acidic nature functioning as a weak dopant (Table 3: report A) [103]. The resulting flexible device showed a PCE of 2.5%, which was close to that of the ITO glass-based control device. Moreover, PET-based devices demonstrated outstanding flexibility, with good performance even at large bending angles, where the ITO-based devices cracked at a bending angle of 60° [104]. In another study, SWNTs were used as a transparent cathode, which requires a lower Fermi level (Table 3: report B) [105]. Chhowalla and co-workers fabricated inverted OSCs with a configuration of PET/SWNT/ZnO NW/P3HT/Au, which achieved a maximum PCE of 0.6%. The resulting OSCs showed good long-term stability, but the PCE was extremely low, presumably because of an intrinsic energy level mismatch and a lack of doping effect. Thus, researchers have focused on applying SWNTs. Franghiadakis and colleagues reported hybridization of PEDOT and SWNTs to replace both ITO and PEDOT as a hole-transporting electrode (Table 3: report C) [106]. A PCE of 1.3% was achieved and the only drawback was low FF (0.4), which arose from high resistance between the polymer and SWNT film. Four years later, DeMello and colleagues investigated two SWNT film fabrication methods: spin coating from dichloroethane solvent and spray coating from deionized water containing sodium dodecyl sulfate or sodium dodecyl benzene sulfonate as a surfactant (Table 3: report D) [107]. Films produced by both of the methods were mechanically robust. HNO_3 -treated SWNT films yielded sheet resistances of around $100 \Omega \text{sq}^{-1}$ with an average transmittance of 90%. Spin-coated SWNT films provided better performance and a PCE of 2.3%. In the following year, Hersam and colleagues focused on reducing the roughness of SWNTs in order to increase performance via improved morphology (Table 3: report E) [108]. In addition, they investigated the change in PCE according to the ratio of metallic and semiconducting SWNTs, and found that a purely metallic (99.9% metallic) SWNT film gave the best performance as the transparent electrode. The device using a purely metallic SWNT film exhibited a PCE of 2.035%, in stark contrast to the value of 0.038% for the device using a purely semiconducting SWNT film. Zarbin and colleagues used interfacial synthesis of CNTs to produce a transparent conductive film for ITO-free OSCs (Table 3: report F) [109]. The interfacial synthesis produced a mixture of SWNTs and MWNTs, and very high CNT loadings could be achieved using these films without a significant effect on transparency. Secondary polyaniline was used for doping to achieve a PCE of 2.27% in a flexible device. The PCE of SWNT-based OSCs reached a new peak of 6.04% in 2015, when our laboratory reported OSCs based on aerosol-synthesized SWNTs (Table 3: report G; Figs. 8 and 9) [110]. Anaerobic thermal annealing of CNTs next to MoO_3 increased their conductivity greatly [111]. This doping effect lasted much longer than that of HNO_3 [112]. Using this approach, we thermally annealed an SWNT film sandwiched between MoO_3 layers at around 300 °C in nitrogen for longer than 2 h. The composition of MoO_3 changed to MoO_x where x is between 2 and 3 (Fig. 10) [113]. The same SWNT films were used as the top electrode in an inverted structure, which was reported in Scientific Reports [114]. These semi-transparent OSCs with a top electrode consisting of laminated transparent SWNTs are highly promising when used in tandem or power-generating windows (Table 3: report H; Fig. 11).

Table 3 Photovoltaic data of representative SWNT OSCs from literature

	Structures	PCE (%)	Note
A	SWNT/PEDOT/P3HT:PCBM/Al	2.5	Filtration-transferred CNTs as anode on PET
B	PET/SWNT/ZnO NW//P3HT/Au	0.6	Filtration-transferred SWNTs as cathode on PET
C	SWNT/PEDOT/P3HT:PCBM/LiF/Al	2.3	Spin-coated SWNTs as anode
D	PEDOT-SWNTs/P3HT:PCBM/Al	1.3	SWNTs and PEDOT hybrid as anode
E	SWNT/PEDOT/P3HT:PCBM/LiF/Al	2.0	Purely metallic SWNTs as anode
F	CNT/PEDOT/R8T2/C ₆₀ /Al	2.27	CNT was generated by interfacial synthesis
G	MoOx/SWNT/MoOx/PEDOT/PTB7:PC ₇₁ BM/LiF/Al	6.04	Aerosol-synthesized SWNT film
H	ITO/ZnO/PTB7/PTB7:PC ₇₁ BM/MoO ₃ /SWNT	4.1	p-doped SWNT film as top electrode

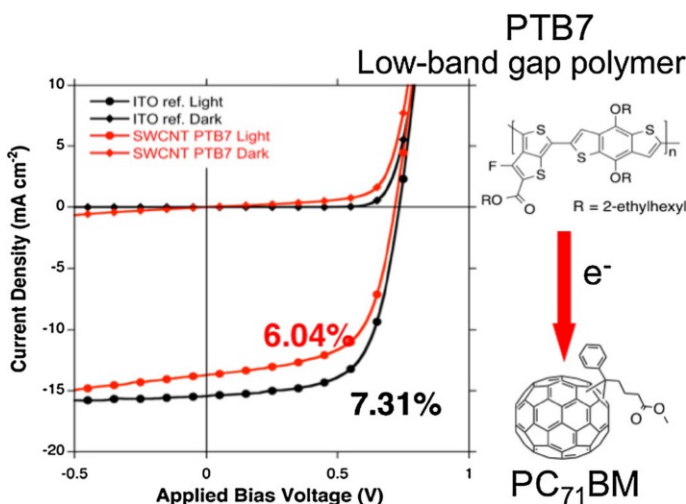


Fig. 8 Current density–voltage curves of the devices from the report G

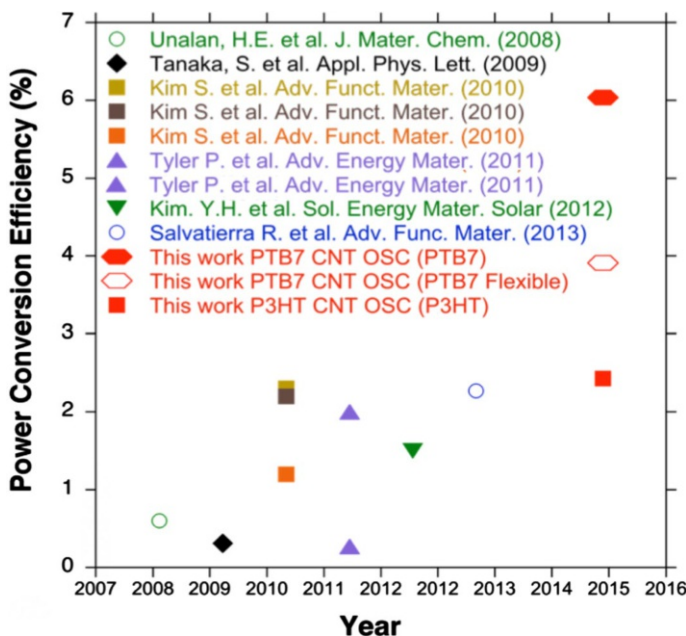


Fig. 9 Literature PCE values of SWNT-based OSCs as compared to the work presented in reference [110]

From the results discussed above, we can see that SWNTs have shown tremendous potential for use in OSCs. They can replace not only ITO but also metal electrodes. Nevertheless, further study is needed, as these results do not completely

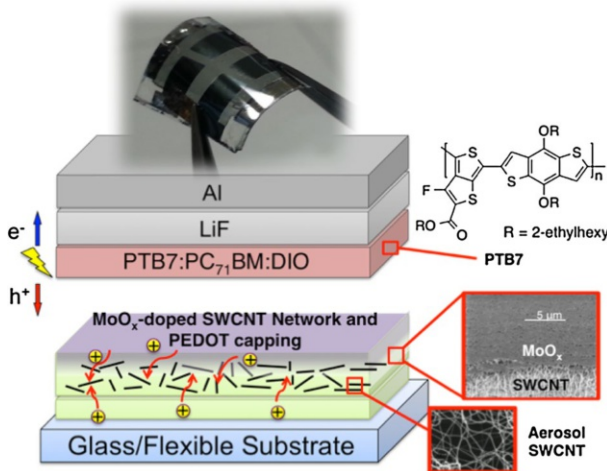


Fig. 10 Schematic of the device from the report G

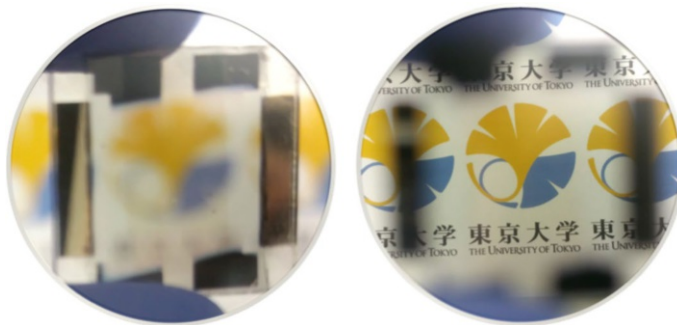


Fig. 11 Transparent OSCs for window application

equal the performance of ITO. We will discuss how to go about addressing this issue at the conclusion of this chapter.

2.3 Single-Walled Carbon Nanotubes as a Transparent Electrode in Perovskite Solar Cells

2.3.1 DSSCs

To discuss PSCs, let us first review dye-sensitized solar cells (DSSCs). Due to their simple fabrication and high efficiency, DSSCs have attracted considerable interest from researchers around the world. Titanium dioxide nanoparticles have been widely used as the working electrode in DSSCs because they provide higher efficiency and more robustness than any other metal oxide semiconductor investigated [115].

To search for an effective counter-electrode in DSSCs, Yanagida and co-workers examined different kinds of carbon materials [116]. A PCE of 4.5% was obtained when SWNTs were used (Table 4: report A). This value was comparable to that of platinum-sputtered fluorine-doped tin oxide-based DSSCs. There had been several attempts at fabricating DSSCs using a carbon material as the counter-electrode, but this work was the first to produce a fair PCE [117]. Later, Kim and colleagues investigated the effects of acid treatment of SWNTs in a TiO₂ film with the dyes anchored. Compared with an unmodified cell, DSSCs using acid-treated SWNTs at the TiO₂/electrolyte interface had significantly improved photocurrent–voltage characteristics [118]. The modified cell showed a 25% increase in J_{SC} , which resulted from improved contact between the acid-treated SWNTs and the TiO₂ particles and enhanced light scattering by TiO₂ clusters. For dye-linked, acid-treated SWNTs anchored to the TiO₂/electrolyte interface, V_{OC} increased by around 0.1 V, mainly due to the basicity of the TiO₂ surface from the NH groups of ethylenediamine moieties in the anchored dye linked to the SWNTs. Kamat and co-workers reported use of SWNTs not only as an electrode but also as a charge transporter [119]. SWNTs utilized as conducting scaffolds in TiO₂-based DSSCs boosted PCE by a factor of 2 (Table 4: report B). Titanium dioxide nanoparticles were scattered on an SWNT film to improve photo-induced charge separation and transport of carriers to the collecting electrode surface. An approximately 100-mV shift in the Fermi level of the SWNTs/TiO₂ system compared with the pristine TiO₂ indicated equilibration of the Fermi level between the two systems. The interplay between the TiO₂ and SWNTs for achieving charge equilibrium was an important factor in improving solar cell performance. Yoo and colleagues used the sol–gel method to prepare TiO₂-coated MWNTs for use a DSSC electrode (Table 4: report C) [120]. CNTs coated with TiO₂ achieved better solar cell performance through a reduction in R_S . Compared with the conventional device, the TiO₂-CNT (0.1 wt%) cell showed a ~ 50% increase in PCE from 3.32 to 4.97%, which is attributed to the increase in J_{SC} due to improved interconnectivity between the TiO₂ particles and the TiO₂-CNTs in the porous TiO₂ film.

Table 4 Photovoltaic data of representative SWNT-DSSCs and SWNT-PSCs from literature

	Structure or research impact	PCE (%)
A	Membrane filter/SWNT/electrolyte/reflection layer/TiO ₂ /dye/FTO	4.5
B	TiO ₂ particles were scattered on SWNTs to improve charge separation and transport	0.6
C	DSSCs using the sol–gel method to obtain TiO ₂ -coated MWNTs	4.97
D	SWNT/PEDOT/CH ₃ NH ₃ PbI ₃ /PCBM/Al	6.32
E	FTO/TiO ₂ /mesoporous TiO ₂ /CH ₃ NH ₃ PbI ₃ /SWNT/spiro-MeOTAD	9.90
F	FTO/TiO ₂ /mesoporous TiO ₂ /(FAPbI ₃) _{3-x} (MAPbBr ₃) _x /SWNT/spiro-MeOTAD	15.5
G	FTO/TiO ₂ /Al ₂ O ₃ /CH ₃ NH ₃ PbI _x Cl _{3-x} /P3HT/SWNT/PMMA/Ag	15.3
H	SWNT/MoO ₃ /PEDOT/CH ₃ NH ₃ PbI ₃ /C ₆₀ /BCP/Al	12.8
J	SWNT/P3HT/CH ₃ NH ₃ PbI ₃ /PCBM/SWNT	7.32

2.3.2 PSCs

The emergence of organic/inorganic halide PSCs, which have PCEs of approximately 20%, has caused a paradigm shift from DSSCs to PSCs (Fig. 12) [121, 122], just within the 5 years that PSCs have been at the forefront of photovoltaics research. This entailed some of the researchers from the OSC field to join the PSC research. Initially there was a confusion in coinage of the PSC structural types as to which is “normal” and which is “inverted”. A broad range of fabrication approaches and device concepts are being constantly developed and this diversity suggests that performance is still far from being fully optimized [123].

The first application of an SWNT film as an ITO replacement in PSCs was demonstrated by our laboratory in 2015 [124]. Specifically, we examined the use of SWNTs subjected to acid treatment, wettability control, and MoO_x doping. Diverse methods were employed to overcome the hydrophobicity of SWNTs and doping issues in solar cell devices, including modification of the wettability of PEDOT, MoO_3 thermal doping, and HNO_3 (aq) doping with various dilutions from 15 to 70% (v/v) to minimize the instability and toxicity of the SWNTs. We discovered that isopropanol-modified PEDOT worked better than surfactant-modified PEDOT as an electron-blocking layer on SWNTs in PSCs because of superior wettability, whereas MoO_3 was incompatible due to energy level mismatch. A diluted HNO_3 (35% v/v)-doped SWNT-based device produced the highest PCE of 6.32% among the SWNT-based PSCs tested—70% of the PCE of an ITO-based device (9.05%). Furthermore, a flexible cell was prepared using a PET film and a PCE of 5.38% was realized (Table 4: report D; Fig. 13). By inverting the structure, the SWNT film could be deposited from above to replace the metal electrode. Mhaisalkar and co-workers reported transparent PSCs made by laminating aerosol-synthesized SWNT

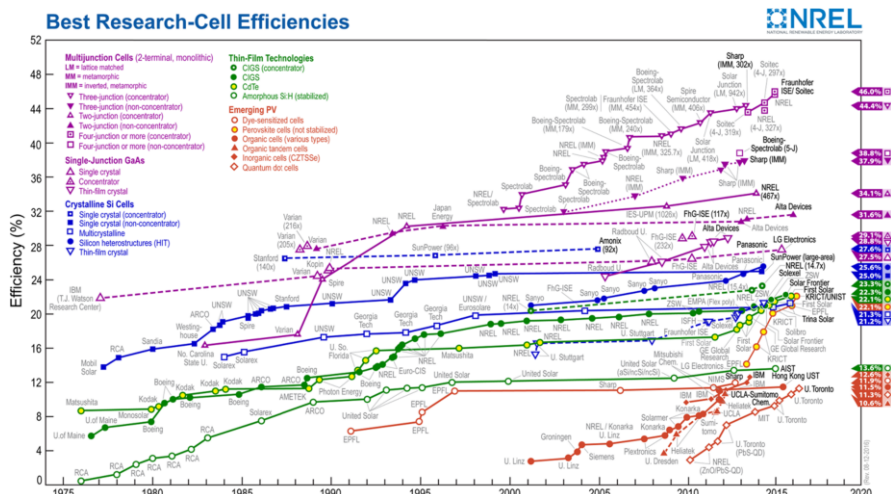


Fig. 12 Certified solar cell PCE charts of all types of solar cells. We can see the PCEs of PSCs in orange (<https://www.nrel.gov/pv>)

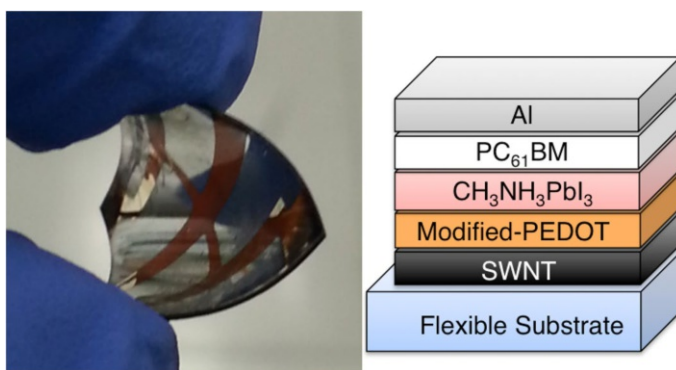


Fig. 13 Flexible SWNT-PSC structure (*right*) and its picture (*left*)

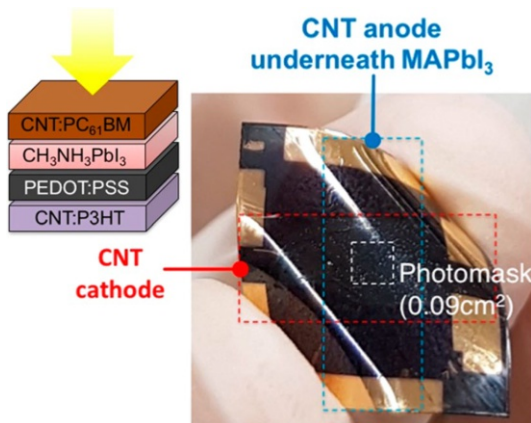
films onto a $\text{CH}_3\text{NH}_3\text{PbI}_3$ layer, with the SWNT films functioning as both a hole collector and electrode [125]. This enabled metal deposition, an energy-consuming vacuum process, to be bypassed. In the absence of an organic hole-transporting material and metal contact, $\text{CH}_3\text{NH}_3\text{PbI}_3$ and CNTs formed a solar cell with an efficiency up to 6.87% (Table 4: report E). The $\text{CH}_3\text{NH}_3\text{PbI}_3$ /CNTs solar cells were semi-transparent and produced photovoltaic output under dual-side illumination because of the transparency of the CNT electrode. Interfacial charge transfer in solar cells was investigated through photoluminescence and impedance measurements. The flexible and transparent CNT network film showed great potential for realizing flexible and semitransparent PSCs. With the addition of 2,2,7,7-tetrakis(*N,N*-di-*p*-methoxyphenylamine)-9,9,9-spirobifluorene (spiro-MeOTAD) to the CNT network, PCE improved from 6.87 to 9.90% as a result of enhanced hole extraction and reduced charge recombination. A similar approach was demonstrated by Wong and colleagues [126]. Ti foil-TiO₂ nanotubes with an organic-inorganic halide perovskite absorber and transparent CNTs was adopted in PSC fabrication. Ti foil-TiO₂ nanotubes were formed by one-step anodization. The composition served as a deposition scaffold and electron conductor for the perovskite absorber. Later, a transparent conductive CNT film was laminated on top of perovskite and served as a hole transporter as well as a transparent electrode for light illumination. A PCE of 8.31% was achieved, which is the highest among TiO₂ nanotube-based flexible solar cells. These kinds of PSCs, in which CNTs were used to replace the top metal electrode, reached their current peak in a study by Boschloo and co-workers [127]. They demonstrated highly efficient PSCs with a hybrid hole-transporting counter-electrode based on aerosol-synthesized SWNT films and drop-cast spiro-MeOTAD. An average PCE of 13.6% with a maximum of 15.5% was recorded, while the reference solar cell with spiro-MeOTAD and a gold electrode showed an average of 17.7% (Table 4: report F). The results revealed the feasibility of high-efficiency PSCs with carbon-based hole-transporting materials. The SWNTs function not only as a charge conductor or transporter, but also as an encapsulating layer that protects the device from water infiltration. The stability of PSCs using SWNTs was addressed by Snaith and colleagues (Table 4: report G) [128]. They demonstrated a method for

mitigating thermal degradation by replacing the organic hole-transporting material with polymer-functionalized SWNTs as in an insulating polymer matrix. With this sort of composite structure, a PCE of 15.3% was accomplished, along with strong retardation of thermal degradation and good resistance to water infiltration. Going back to the bottom transparent electrode, our group compared SWNT with graphene in the viewpoint of photovoltaic and mechanical performance (Table 4: report H) [129]. With the demonstration of a 12.8% PCE, we discovered that using graphene electrode as the bottom electrode results in slightly higher photovoltaic performance than that of SWNTs, yet SWNTs had the upper hand in terms of mechanical resilience and reproducibility. The use of a SWNT electrode expanded to replacing both the metal and transparent metal oxide conductor. As shown in Fig. 14, a flexible PSC using SWNTs both as cathode and as anode was recently demonstrated by our group [130]. Although the achieved efficiency was 7.32%, a possibility of roll-to-product processability was demonstrated.

Up to this point, We have looked at the applications of SWNTs in solar cells. There is no doubt that the excellent properties of SWNTs make them promising candidates for incorporation into future low-cost, multifunctional photovoltaic devices. Their application initially started as the photoactive materials in solar cells due to their semiconducting properties. However, difficulties in purification slowed the progress. In silicon solar cells, SWNTs began to be used as both electrode and photoactive materials, boosting their potential as a solar cell component. With the emergence of thin-film solar cells, namely OSCs and PSCs, the number of reports on application of SWNTs increased rapidly as they could replace ITO, generating flexible and low-cost photovoltaics. There have been intermittent reports on their usage as photovoltaic materials; again, the progress was limited by the challenging nature of the separation of the semiconducting SWNTs. Overall, many challenges still remain. Below, we outline five key points that are crucial for further improvement:

1. Conductivity and transparency: The performance of photovoltaic devices is strongly dependent on CNT properties. The sheet resistance and transparency

Fig. 14 Flexible PSC using SWNTs both as cathode and as anode. structure (*left*) and its picture (*right*). (Table 4: report J)



- of CNTs are not yet comparable to those of ITO, which has sheet resistance of around $5 \Omega \text{ sq}^{-1}$ and a transparency of more than 90%. Therefore, it is imperative that more stable and effect dopants be investigated.
2. Fermi level: To achieve high performance, especially as the cathode in OSCs, CNT electrodes must have a proper Fermi level to minimize energy barriers for charge transfer. Normally, carbon materials have a Fermi level of 4.5–5 eV, similar to that of an ITO film with a work function of 4.6–4.8 eV. The Fermi level can be tuned for various electrode uses [121–133]. Materials like PEDOT are commonly used to increase the Fermi level for charge injection at the anode, whereas materials like Cs_2CO_3 are used to reduce the Fermi level for electron collection at the cathode.
 3. Wettability: CNTs are hydrophobic, so either they need to be made of hydrophilic or the materials being deposited on top need to be hydrophobic. Even better would be deposition of the material by a method that is independent of the wettability, such as thermal evaporation. Many chemical treatments to increase hydrophilicity decrease conductivity by introducing oxygen-containing groups or defects. Thus, other methods are needed that do not undermine the properties of CNTs while improving the wettability.
 4. Surface roughness: A rough surface of CNTs creates shunt pathways within the device, which results in reduced performance. The reproducibility of SWNT-based OSCs mainly hinges on their surface roughness. Therefore, much more attention should be paid to keeping the surface smooth and clean during the fabrication and processing of SWCNTs.
 5. Encapsulation: Device stability under ambient conditions is a crucial issue for practical applications, especially for OSCs and PSCs. The photoactive materials of these types of cells are rather unstable in air, and the barrier properties of plastic encapsulation are simply not good enough. Therefore, it is necessary to develop a flexible barrier that can passivate the device effectively. CNTs have shown some promise in this regard, yet not much research has been conducted. Further study will help open a path to more industrially viable CNT-based solar cells.

References

1. Avouris P, Freitag M, Perebeinos V (2008) Carbon–nanotube photonics and optoelectronics. *Nat Photon* 2(6):341–350
2. O’Connell MJ, Bachilo SM, Huffman CB, Moore VC, Strano MS, Haroz EH, Rialon KL, Boul PJ, Noon WH, Kittrell C, Ma J, Hauge RH, Weisman RB, Smalley RE (2002) Band gap fluorescence from individual single-walled carbon nanotubes. *Science* 297(5581):593–596
3. Lebedkin S, Hennrich F, Kiowski O, Kappes MM (2008) Photophysics of carbon nanotubes in organic polymer–toluene dispersions: emission and excitation satellites and relaxation pathways. *Phys Rev B* 77(16):165429
4. Kataura H, Kumazawa Y, Maniwa Y, Umezu I, Suzuki S, Ohtsuka Y, Achiba Y (1999) Optical properties of single-wall carbon nanotubes. *Synth Met* 103(1–3):2555–2558
5. Berson S, de Bettignies R, Bailly S, Guillerez S, Jousselme B (2007) Elaboration of P3HT/CNT/PCBM composites for organic photovoltaic cells. *Adv Funct Mater* 17(16):3363–3370

6. Chaudhary S, Lu H, Müller AM, Bardeen CJ, Ozkan M (2007) Hierarchical placement and associated optoelectronic impact of carbon nanotubes in polymer–fullerene solar cells. *Nano Lett* 7(7):1973–1979
7. Ma BH, Yip H, Huang F, Jen AK-Y, Ma H, Yip H, Huang F, Jen AK-Y (2010) Interface engineering for organic electronics. *Adv Funct Mater* 20(9):1371–1388
8. Steim R, Kogler FR, Brabec CJ (2010) Interface materials for organic solar cells. *J Mater Chem* 20(13):2499–2512
9. Li G, Shrotriya V, Huang J, Yao Y, Moriarty T, Emery K, Yang Y (2005) High-efficiency solution processable polymer photovoltaic cells by self-organization of polymer blends. *Nat Mater* 4(11):864–868
10. Park SH, Roy A, Beaupré S, Cho S, Coates N, Moon JS, Moses D, Leclerc M, Lee K, Heeger AJ (2009) Bulk heterojunction solar cells with internal quantum efficiency approaching 100%. *Nat Photon* 3(5):297–302
11. Huynh WU (2002) Hybrid nanorod-polymer solar cells. *Science* 295(5564):2425–2427
12. Lee JU (2005) Photovoltaic effect in ideal carbon nanotube diodes. *Appl Phys Lett* 87(7):073101
13. Avouris P, Freitag M, Perebeinos V (2008) Carbon-nanotube photonics and optoelectronics. *Nat Photon* 2(6):341–350
14. Fuhrer MS (2000) Crossed nanotube junctions. *Science* 288(5465):494–497
15. Yang F, Wang X, Zhang D, Yang J, Luo D, Xu Z, Wei J, Wang JQ, Xu Z, Peng F, Li X, Li R, Li Y, Li M, Bai X, Ding F, Li Y (2014) Chirality-specific growth of single-walled carbon nanotubes on solid alloy catalysts. *Nature* 510(7506):522–524
16. Yuan Y, Karahan HE, Yıldırım C, Wei L, Bırer Ö, Zhai S, Laua R, Chen Y (2016) “Smart poisoning” of Co/SiO₂ catalysts by sulfidation for chirality-selective synthesis of (9,8) single-walled carbon nanotubes. *Nanoscale* 8:17705–17713
17. Arnold MS, Stupp SI, Hersam MC (2005) Enrichment of single-walled carbon nanotubes by diameter in density gradients. *Nano Lett* 5(4):713–718
18. Arnold MS, Green AA, Hulvat JF, Stupp SI, Hersam MC (2006) Sorting carbon nanotubes by electronic structure using density differentiation. *Nat Nanotechnol* 1(1):60–65
19. Liu H, Nishide D, Tanaka T, Kataura H (2011) Large-scale single-chirality separation of single-wall carbon nanotubes by simple gel chromatography. *Nat Commun* 2:309
20. Fagan JA, Khripin CY, Silvera Batista CA, Simpson JR, Hároz EH, Hight Walker AR, Zheng M (2014) Isolation of specific small-diameter single-wall carbon nanotube species via aqueous two-phase extraction. *Adv Mater* 26(18):2800–2804
21. Kymakis E, Alexandrou I, Amaralunga GAJ (2003) High open-circuit voltage photovoltaic devices from carbon–nanotube–polymer composites. *J Appl Phys* 93(3):1764
22. Landi BJ, Raffaelle RP, Castro SL, Bailey SG (2005) Single-wall carbon nanotube-polymer solar cells. *Prog Photovolt Res Appl* 13(2):165–172
23. Kazaoui S, Minami N, Nalini B, Kim Y, Hara K (2005) Near-infrared photoconductive and photovoltaic devices using single-wall carbon nanotubes in conductive polymer films. *J Appl Phys* 98(8):084314
24. Ago H, Petritsch K, Shaffer MSP, Windle AH, Friend RH (1999) Composites of carbon nanotubes and conjugated polymers for photovoltaic devices. *Adv Mater* 11(15):1281–1285
25. Kymakis E, Amaralunga GAJ (2002) Single-wall carbon nanotube/conjugated polymer photovoltaic devices. *Appl Phys Lett* 80(1):112
26. Pradhan B, Batabyal SK, Pal AJ (2006) Functionalized carbon nanotubes in donor/acceptor-type photovoltaic devices. *Appl Phys Lett* 88(9):093106
27. Li C, Chen Y, Wang Y, Iqbal Z, Chhowalla M, Mitra S (2007) A fullerene–single wall carbon nanotube complex for polymer bulk heterojunction Photovoltaic cells. *J Mater Chem* 17(23):2406–2411
28. Chirvase D, Parisi J, Hummelen JC, Dyakonov V (2004) Influence of nanomorphology on the photovoltaic action of polymer–fullerene composites. *Nanotechnology* 15(9):1317–1323
29. Ren S, Bernardi M, Lunt RR, Bulovic V, Grossman JC, Gradečák S (2011) Toward efficient carbon nanotube/P3HT solar cells: active layer morphology, electrical, and optical properties. *Nano Lett* 11(12):5316–5321
30. Bindl DJ, Safron NS, Arnold MS (2010) Dissociating excitons photogenerated in semiconducting carbon nanotubes at polymeric photovoltaic heterojunction interfaces. *ACS Nano* 4(10):5657–5664
31. Arnold MS, Zimmerman JD, Renshaw CK, Xu X, Lunt RR, Austin CM, Forrest SR (2009) Broad spectral response using carbon nanotube/organic semiconductor/c 60 photodetectors. *Nano Lett* 9(9):3354–3358

32. Bindl DJ, Wu MY, Prehn FC, Arnold MS (2011) Efficiently harvesting excitons from electronic type-controlled semiconducting carbon nanotube films. *Nano Lett* 11(2):455–460
33. Bindl DJ, Brewer AS, Arnold MS (2011) Semiconducting carbon nanotube/fullerene blended heterojunctions for photovoltaic near-infrared photon harvesting. *Nano Res.* 4(11):1174–1179
34. Jain RM, Howden R, Tvrdy K, Shimizu S, Hilmer AJ, McNicholas TP, Gleason KK, Strano MS (2012) Polymer-free near-infrared photovoltaics with single chirality (6,5) semiconducting carbon nanotube active layers. *Adv Mater* 24(32):4436–4439
35. Raj R, Maroo SC, Wang EN (2013) Wettability of graphene. *Nano Lett* 13(4):1509–1515
36. Rafiee J, Mi X, Gullapalli H, Thomas AV, Yavari F, Shi Y, Ajayan PM, Koratkar NA (2012) Wetting transparency of graphene. *Nat Mater* 11(3):217–222
37. Wang SR, Zhang Y, Abidi N, Cabrales L (2009) Wettability and surface free energy of graphene films. *Langmuir* 25(18):11078–11081
38. Kim BH, Kim JY, Jeong SJ, Hwang JO, Lee DH, Shin DO, Choi SY, Kim SO (2010) Surface energy modification by spin-cast, large-area graphene film for block copolymer lithography. *ACS Nano* 4(9):5464–5470
39. Shin YJ, Wang Y, Huang H, Kalon G, Wee ATS, Shen Z, Bhatia CS, Yang H (2010) Surface-energy engineering of graphene. *Langmuir* 26(6):3798–3802
40. Tung VC, Huang J-HJ, Kim J, Smith AJ, Chu C-W, Huang J-HJ (2012) Towards solution processed all-carbon solar cells: a perspective. *Energy Environ Sci* 5(7):7810
41. Tung VC, Huang JH, Tevis I, Kim F, Kim J, Chu CW, Stupp SI, Huang J (2011) Surfactant-free water-processable photoconductive all-carbon composite. *J Am Chem Soc* 133(13):4940–4947
42. Bernardi M, Lohrman J, Kumar PV, Kirkeminde A, Ferralis N, Grossman JC, Ren S (2012) Nano-carbon-based photovoltaics. *ACS Nano* 6(10):8896–8903
43. Ramuz MP, Vosgueritchian M, Wei P, Wang C, Gao Y, Wu Y, Chen Y, Bao Z (2012) Evaluation of solution-processable carbon-based electrodes for all-carbon solar cells. *ACS Nano* 6(11):10384–10395
44. Wang H, Koleilat GI, Liu P, Jiménez-Osés G, Lai Y-C, Vosgueritchian M, Fang Y, Park S, Houk KN, Bao Z (2014) High-yield sorting of small-diameter carbon nanotubes for solar cells and transistors. *ACS Nano* 8(3):2609–2617
45. Gong M, Shastry TA, Xie Y, Bernardi M, Jasion D, Luck KA, Marks TJ, Grossman JC, Ren S, Hersam MC (2014) Polychiral semiconducting carbon nanotube-fullerene solar cells. *Nano Lett* 14(9):5308–5314
46. Lee JM, Park JS, Lee SH, Kim H, Yoo S, Kim SO (2011) Selective electron- or hole-transport enhancement in bulk-heterojunction organic solar cells with N- or B-doped carbon nanotubes. *Adv Mater* 23(5):629–633
47. Robel I, Bunker BA, Kamat PV (2005) Single-walled carbon nanotube-CdS nanocomposites as light-harvesting assemblies: photoinduced charge-transfer interactions. *Adv Mater* 17(20):2458–2463
48. Barazzouk S, Hotchandani S, Vinodgopal K, Kamat PV (2004) Single-wall carbon nanotube films for photocurrent generation. A prompt response to visible-light irradiation. *J Phys Chem B* 108(44):17015–17018
49. Landi BJ, Castro SL, Ruf HJ, Evans CM, Bailey SG, Raffaelle RP (2005) CdSe quantum dot-single wall carbon nanotube complexes for polymeric solar cells. *Sol Energy Mater Sol Cells* 87(1–4):733–746
50. Lee JM, Kwon B-HH, Park H, Kim H, Kim MG, Park JS, Kim ES, Yoo S, Jeon DY, Kim SO (2013) Exciton dissociation and charge-transport enhancement in organic solar cells with quantum-dot/N-doped CNT hybrid nanomaterials. *Adv Mater* 25(14):2011–2017
51. Lu L, Xu T, Chen W, Lee JM, Luo Z, Jung IH, Park H, Kim SO, Yu L (2013) The role of N-doped multiwall carbon nanotubes in achieving highly efficient polymer bulk heterojunction solar cells. *Nano Lett* 13(6):2365–2369
52. Jeon I, Kutsuzawa D, Hashimoto Y, Yanase T, Nagahama T, Shimada T, Matsuo Y (2015) Multi-layered MoS₂ nanoflakes bound to carbon nanotubes as electron acceptors in bulk heterojunction inverted organic solar cells. *Org Electron* 17:275–280
53. Thompson BC, Fréchet JMJ (2008) Polymer-fullerene composite solar cells. *Angew Chemie Int Ed* 47(1):58–77
54. Nelson J (2011) Polymer:fullerene bulk heterojunction solar cells. *Mater Today* 14(10):462–470
55. Denner G, Scharber MC, Brabec CJ (2009) Polymer-fullerene bulk-heterojunction solar cells. *Adv Mater* 21(13):1323–1338

56. Zilberberg K, Gasse F, Pagui R, Polywka A, Behrendt A, Trost S, Heiderhoff R, Görnr P, Riedl T (2014) Highly robust indium-free transparent conductive electrodes based on composites of silver nanowires and conductive metal oxides. *Adv Funct Mater* 24(12):1671–1678
57. Inganäs O (2011) Organic photovoltaics: avoiding indium. *Nat Photon* 5(4):201–202
58. Yang M, Kim D, Jha H, Lee K, Paul J, Schmuki P (2011) Nb doping of TiO₂ nanotubes for an enhanced efficiency of dye-sensitized solar cells. *Chem Commun* 47(7):2032–2034
59. Delacou C, Jeon I, Seo S, Nakagawa T, Kauppinen EI, Maruyama S, Matsuo Y (2017) Indium tin oxide-free small molecule organic solar cells using single-walled carbon nanotube electrodes. *ECS J. Solid State Sci. Technol.* 6(6):M3181–M3184
60. Sakaguchi T, Jeon I, Chiba T, Shawky A, Xiang R, Chiashi S, Kauppinen EI, Park N-G, Matsuo Y, Maruyama S (2017) Single-walled carbon nanotube-based metal-free perovskite solar cells with improved stability and efficiency. *J Mater Chem A* (Submitted)
61. Wu Z, Chen Z, Du X, Logan JM, Sippel J, Nikolou M, Kamaras K, Reynolds JR, Tanner DB, Hebard AF, Rinzler AG (2004) Transparent, conductive carbon nanotube Films. *Science* 305(5688):1273–1276
62. Lee YH, Kim SG, Tománek D (1997) Catalytic growth of single-wall carbon nanotubes: an ab initio study. *Phys Rev Lett* 78(12):2393–2396
63. Nasibulin AG, Kaskela A, Mustonen K, Anisimov AS, Ruiz V, Kivistö S, Rackauskas S, Timmermans MY, Pudas M, Aitchison B, Kauppinen M, Brown DP, Okhotnikov OG, Kauppinen EI (2011) Multifunctional free-standing single-walled carbon nanotube films. *ACS Nano* 5(4):3214–3221
64. van de Lagemaat J, Barnes TM, Rumbles G, Shaheen SE, Coutts TJ, Weeks C, Levitsky I, Peltonen J, Glatkowski P (2006) Organic solar cells with carbon nanotubes replacing In₂O₃: Sn as the transparent electrode. *Appl Phys Lett* 88(23):233503
65. Ahn N, Jeon I, Yoon J, Kauppinen EI, Yutaka M, Maruyama S, Choi M (2018) Carbon-sandwiched perovskite solar cell. *J Mater Chem A*. <https://doi.org/10.1039/C7TA09174E>
66. Schneider J, Rohner P, Thureja D, Schmid M, Galliker P, Poulikakos D (2016) Electrohydrodynamic nanodrip printing of high aspect ratio metal grid transparent electrodes. *Adv Funct Mater* 26:833–840
67. Langley D, Giusti G, Mayousse C, Celle C, Bellet D, Simonato JP (2013) Flexible transparent conductive materials based on silver nanowire networks: a review. *Nanotechnology* 24(45):452001
68. Cao W, Li J, Chen H, Xue J (2014) Transparent electrodes for organic optoelectronic devices: a review. *J Photonics Energy* 4:040990
69. Bae S, Kim H, Lee Y, Xu X, Park JS, Zheng Y, Balakrishnan J, Lei T, Kim HR, Song YI, Kim YJ, Kim KS, Ozylilmaz B, Ahn JH, Hong BH, Iijima S (2010) Roll-to-roll production of 30-inch graphene films for transparent electrodes. *Nat Nanotechnol* 5:574–578
70. Hou PX, Yu B, Su Y, Shi C, Zhang LL, Liu C, Li SS, Du JH, Cheng HM (2014) Double-wall carbon nanotube transparent conductive films with excellent performance. *J Mater Chem A* 2:1159–1164
71. Hecht DS, Heintz AM, Lee R, Hu L, Moore B, Cucksey C, Risser S (2011) High conductivity transparent carbon nanotube films deposited from superacid. *Nanotechnology* 22:075201
72. Tune DD, Flavel BS, Krupke R, Shapter JG (2012) Carbon nanotube-silicon solar cells. *Adv Energy Mater* 2(9):1043–1055
73. Jung Y, Li X, Rajan NK, Taylor AD, Reed MA (2013) Record high efficiency single-walled carbon nanotube/silicon p–n junction solar cells. *Nano Lett* 13(1):95–99
74. Wei J, Jia Y, Shu Q, Gu Z, Wang K, Zhuang D, Zhang G, Wang Z, Luo J, Cao A, Wu D (2007) Double-walled carbon nanotube solar cells. *Nano Lett* 7(8):2317–2321
75. Wenham SR, Green MA (1996) Silicon solar cells. *Prog Photovolt Res Appl* 4(1):3–33
76. Song Y, Li X, Mackin C, Zhang X, Fang W, Palacios T, Zhu H, Kong J (2015) Role of interfacial oxide in high-efficiency graphene-silicon schottky barrier solar cells. *Nano Lett* 15(3):2104–2110
77. Shi E, Zhang L, Li Z, Li P, Shang Y, Jia Y, Wei J, Wang K, Zhu H, Wu D, Zhang S, Cao A (2012) TiO₂-coated carbon nanotube-silicon solar cells with efficiency of 15%. *Sci Rep* 2:884
78. Anderson WA (1974) An 8% efficient layered Schottky-barrier solar cell. *J Appl Phys* 45(9):3913
79. Tung RT (2001) Recent advances in Schottky barrier concepts. *Mater Sci Eng R Rep* 35(1–3):1–138
80. Jia Y, Wei J, Wang K, Cao A, Shu Q, Gui X, Zhu Y, Zhuang D, Zhang G, Ma B, Wang L, Liu W, Wang Z, Luo J, Wu D (2008) Nanotube-silicon heterojunction solar cells. *Adv Mater* 20(23):4594

81. Li Z, Kunets VP, Saini V, Xu Y, Dervishi E, Salamo GJ, Biris AR, Biris AS (2008) SOCl₂ enhanced photovoltaic conversion of single wall carbon nanotube/n-silicon heterojunctions. *Appl Phys Lett* 93(24):243117
82. Li Z, Kunets VP, Saini V, Xu Y, Dervishi E, Salamo GJ, Biris AR, Biris AS (2009) Light-harvesting using high density *p*-type single wall carbon nanotube/*n*-type silicon heterojunctions. *ACS Nano* 3(6):1407–1414
83. Li Z, Jia Y, Wei J, Wang K, Shu Q, Gui X, Zhu H, Cao A, Wu D (2010) Large area, highly transparent carbon nanotube spiderwebs for energy harvesting. *J Mater Chem* 20(34):7236
84. Blackburn JL, Barnes TM, Beard MC, Kim Y-H, Tenent RC, McDonald TJ, To B, Coutts TJ, Heben MJ (2008) Transparent conductive single-walled carbon nanotube networks with precisely tunable ratios of semiconducting and metallic nanotubes. *ACS Nano* 2(6):1266–1274
85. Ong P-L, Euler WB, Levitsky IA (2010) Hybrid solar cells based on single-walled carbon nanotubes/Si heterojunctions. *Nanotechnology* 21(10):105203
86. Wadhwa P, Liu B, McCarthy MA, Wu Z, Rinzler AG (2010) Electronic junction control in a nanotube-semiconductor Schottky junction solar cell. *Nano Lett* 10(12):5001–5005
87. Jia Y, Cao A, Bai X, Li Z, Zhang L, Guo N, Wei J, Wang K, Zhu H, Wu D, Ajayan PM (2011) Achieving high efficiency silicon-carbon nanotube heterojunction solar cells by acid doping. *Nano Lett* 11(5):1901–1905
88. Jia Y, Li P, Gui X, Wei J, Wang K, Zhu H, Wu D, Zhang L, Cao A, Xu Y (2011) Encapsulated carbon nanotube-oxide-silicon solar cells with stable 10% efficiency. *Appl Phys Lett* 98(13):133115
89. Wadhwa P, Seol G, Petterson MK, Guo J, Rinzler AG (2011) Electrolyte-induced inversion layer Schottky junction solar cells. *Nano Lett* 11(6):2419–2423
90. Chen W, Seol G, Rinzler AG, Guo J (2012) Carrier dynamics and design optimization of electrolyte-induced inversion layer carbon nanotube-silicon Schottky junction solar cell. *Appl Phys Lett* 100(10):103503
91. Kozawa D, Hiraoka K, Miyauchi Y, Mouri S, Matsuda K (2012) Analysis of the photovoltaic properties of single-walled carbon nanotube/silicon heterojunction solar cells. *Appl Phys Express* 5(4):042304
92. Li X, Jung Y, Sakimoto K, Goh TH, Reed MA, Taylor AD (2013) Improved efficiency of smooth and aligned single walled carbon nanotube/silicon hybrid solar cells. *Energy Environ Sci* 6(3):879–887
93. Cui K, Chiba T, Omiya S, Thurakitseree T, Zhao P, Fujii S, Kataura H, Einarsson E, Chiashi S, Maruyama S (2013) Self-Assembled microhoneycomb network of single-walled carbon nanotubes for solar cells. *J Phys Chem Lett* 4(15):2571–2576
94. Xu W, Deng B, Shi E, Wu S, Zou M, Yang L, Wei J, Peng H, Cao A (2015) Comparison of nano-carbon-silicon solar cells with nanotube-Si or graphene-Si contact. *ACS Appl Mater Interfaces* 7(31):17088–17094
95. Cui K, Anisimov AS, Chiba T, Fujii S, Kataura H, Nasibulin AG, Chiashi S, Kauppinen EI, Maruyama S (2014) Air-stable high-efficiency solar cells with dry-transferred single-walled carbon nanotube films. *J Mater Chem A* 2(29):11311–11318
96. Li Z, Saini V, Dervishi E, Kunets VP, Zhang J, Xu Y, Biris AR, Salamo GJ, Biris AS (2010) Polymer functionalized *n*-type single wall carbon nanotube photovoltaic devices. *Appl Phys Lett* 96(3):033110
97. Wang F, Kozawa D, Miyauchi Y, Hiraoka K, Mouri S, Ohno Y, Matsuda K (2015) Considerably improved photovoltaic performance of carbon nanotube-based solar cells using metal oxide layers. *Nat Commun* 6:6305
98. Dou L, You J, Yang J, Chen C, He Y, Murase S, Moriarty T, Emery K, Li G, Yang Y (2012) Tandem polymer solar cells featuring a spectrally matched low-bandgap polymer. *Nat Photon* 6(3):180–185
99. Angono D, Krebs FC (2013) Flexible ITO-free polymer solar cells. *J Appl Polym Sci* 129(1):1–14
100. Jariwala D, Sangwan VK, Lauhon LJ, Marks TJ, Hersam MC (2013) Carbon nanomaterials for electronics, optoelectronics, photovoltaics, and sensing. *Chem Soc Rev* 42(7):2824–2860
101. Liu Y, Wan X, Wang F, Zhou J, Long G, Tian J, You J, Yang Y, Chen Y (2011) Spin-coated small molecules for high performance solar cells. *Adv Energy Mater* 1(5):771–775
102. Li S-S, Chen C-W (2013) Polymer–metal-oxide hybrid solar cells. *J Mater Chem A* 1(36):10574
103. Rowell MW, Topinka MA, McGehee MD, Prall H-J, Dennler G, Sariciftci NS, Hu L, Gruner G (2006) Organic solar cells with carbon nanotube network electrodes. *Appl Phys Lett* 88(23):233506

104. De Gomez Arco L, Zhang Y, Schlenker CW, Ryu K, Thompson ME, Zhou C (2010) Continuous, highly flexible, and transparent graphene films by chemical vapor deposition for organic photovoltaics. *ACS Nano* 4(5):2865–2873
105. Unalan HE, Hiralal P, Kuo D, Parekh B, Amarantunga G, Chhowalla M (2008) Flexible organic photovoltaics from zinc oxide nanowires grown on transparent and conducting single walled carbon nanotube thin films. *J Mater Chem* 18(48):5909
106. Kymakis E, Klapas G, Koudoumas E, Stratakis E, Kornilios N, Vidakis N, Franghiadakis Y (2006) Carbon nanotube/PEDOT:PSS electrodes for organic photovoltaics. *Eur Phys J Appl Phys* 36(3):257–259
107. Kim S, Yim J, Wang X, Bradley DDC, Lee S, DeMello JC (2010) Spin- and spray-deposited single-walled carbon-nanotube electrodes for organic solar cells. *Adv Funct Mater* 20(14):2310–2316
108. Tyler TP, Brock RE, Karmel HJ, Marks TJ, Hersam MC (2011) Electronically monodisperse single-walled carbon nanotube thin films as transparent conducting anodes in organic photovoltaic devices. *Adv Energy Mater* 1(5):785–791
109. Salvatierra RV, Cava CE, Roman LS, Zarbin AJG (2013) ITO-free and flexible organic photovoltaic device based on high transparent and conductive polyaniline/carbon nanotube thin films. *Adv Funct Mater* 23(12):1490–1499
110. Jeon I, Cui K, Chiba T, Anisimov A, Nasibulin AG, Kauppinen EI, Maruyama S, Matsuo Y (2015) Direct and dry deposited single-walled carbon nanotube films doped with MoO_x as electron-blocking transparent electrodes for flexible organic solar cells. *J Am Chem Soc* 137(25):7982–7985
111. Hellstrom SL, Vosgueritchian M, Stoltzberg RM, Irfan I, Hammock M, Wang YB, Jia C, Guo X, Gao Y, Bao Z (2012) Strong and stable doping of carbon nanotubes and graphene by MoO_x for transparent electrodes. *Nano Lett* 12(7):3574–3580
112. Shin D-W, Lee JH, Kim Y-H, Yu SM, Park S-Y, Yoo J-B (2009) A role of HNO_3 on transparent conducting film with single-walled carbon nanotubes. *Nanotechnology* 20(47):475703
113. Deb SK (1966) Optical properties and color-center formation in thin films of molybdenum trioxide. *J Appl Phys* 37(13):4818
114. Jeon I, Delacou C, Kaskela A, Kauppinen IE, Maruyama S, Matsuo Y (2016) Metal-electrode-free window-like organic solar cells with p-doped carbon nanotube thin-film electrodes. *Sci Rep* 6:31348
115. Chappel S, Chen S-G, Zaban A (2002) TiO_2 -coated nanoporous SnO_2 electrodes for dye-sensitized solar cells. *Langmuir* 18(8):3336–3342
116. Suzuki K, Yamaguchi M, Kumagai M, Yanagida S (2003) Application of carbon nanotubes to counter electrodes of dye-sensitized solar cells. *Chem Lett* 32(1):28–29
117. Kay A, Grätzel M (1996) Low cost photovoltaic modules based on dye sensitized nanocrystalline titanium dioxide and carbon powder. *Sol Energy Mater Sol Cells* 44(1):99–117
118. Jang S-R, Vittal R, Kim K-J (2004) Incorporation of functionalized single-wall carbon nanotubes in dye-sensitized TiO_2 solar cells. *Langmuir* 20(22):9807–9810
119. Kongkanand A, Martínez Domínguez R, Kamat PV (2007) Single wall carbon nanotube scaffolds for photoelectrochemical solar cells. capture and transport of photogenerated electrons. *Nano Lett* 7(3):676–680
120. Lee TY, Alegaonkar PS, Yoo J-B (2007) Fabrication of dye sensitized solar cell using TiO_2 coated carbon nanotubes. *Thin Solid Films* 515(12):5131–5135
121. Snaith HJ (2013) Perovskites: the emergence of a new era for low-cost, high-efficiency solar cells. *J Phys Chem Lett* 4(21):3623–3630
122. Green MA, Ho-Baillie A, Snaith HJ (2014) The emergence of perovskite solar cells. *Nat Photon* 8(7):506–514
123. McGehee MD (2014) Perovskite solar cells: continuing to soar. *Nat Mater* 13(9):845–846
124. Jeon I, Chiba T, Delacou C, Guo Y, Kaskela A, Reynaud O, Kauppinen EI, Maruyama S, Matsuo Y (2015) Single-walled carbon nanotube film as electrode in indium-free planar heterojunction perovskite solar cells: investigation of electron-blocking layers and dopants. *Nano Lett* 15(10):6665–6671
125. Li Z, Kulkarni SA, Boix PP, Shi E, Cao A, Fu K, Batabyal SK, Zhang J, Xiong Q, Wong LH, Mathews N, Mhaisalkar SG (2014) Laminated carbon nanotube networks for metal electrode-free efficient perovskite solar cells. *ACS Nano* 8(7):6797–6804
126. Wang X, Li Z, Xu W, Kulkarni SA, Batabyal SK, Zhang S, Cao A, Wong LH (2015) TiO_2 nanotube arrays based flexible perovskite solar cells with transparent carbon nanotube electrode. *Nano Energy* 11:728–735

127. Aitola K, Sveinbjörnsson K, Correa-Baena J-P, Kaskela A, Abate A, Tian Y, Johansson EMJ, Grätzel M, Kauppinen EI, Hagfeldt A, Boschloo G (2016) Carbon nanotube-based hybrid hole-transporting material and selective contact for high efficiency perovskite solar cells. *Energy Environ Sci* 9(2):461–466
128. Habisreutinger SN, Leijtens T, Eperon GE, Stranks SD, Nicholas RJ, Snaith HJ (2014) Carbon nanotube/polymer composites as a highly stable hole collection layer in perovskite solar cells. *Nano Lett* 14(10):5561–5568
129. Jeon I, Yoon J, Ahn N, Atwa M, Delacou C, Sota M, Kauppinen EI, Choi M, Maruyama S, Matsuo Y (2017) Carbon nanotubes versus graphene as flexible transparent electrodes in perovskite solar cells. *J Phys Chem Lett* 8:5395–5401
130. Jeon I, Seo S, Sato Y, Delacou C, Suenaga K, Kauppinen EI, Maruyama S, Matsuo Y (2017) Perovskite solar cells using carbon nanotubes as both cathode and anode electrodes'. *J Phys Chem C* 21(46):25743–25749
131. Choe M, Lee BH, Jo G, Park J, Park W, Lee S, Hong WK, Seong MJ, Kahng YH, Lee K, Lee T (2010) Efficient bulk-heterojunction photovoltaic cells with transparent multi-layer graphene electrodes. *Org Electron Phys Mater Appl* 11(11):1864–1869
132. Du J, Pei S, Ma L, Cheng H-M (2014) 25th anniversary article: carbon nanotube- and graphene-based transparent conductive films for optoelectronic devices. *Adv Mater* 26(13):1958–1991
133. Jo G, Choe M, Lee S, Park W, Kahng YH, Lee T (2012) The application of graphene as electrodes in electrical and optical devices. *Nanotechnology* 23(11):112001



REVIEW

Advances in Production and Applications of Carbon Nanotubes

Xilai Jia¹ · Fei Wei²

Received: 31 August 2016 / Accepted: 2 January 2017 / Published online: 30 January 2017
© Springer International Publishing Switzerland 2017

Abstract Recent decades have witnessed many breakthroughs in research on carbon nanotubes (CNTs), particularly regarding controllable synthesis, production scale-up, and application advances for this material. This sp^2 -bonded nanocarbon uniquely combines extreme mechanical strength, exceptionally high electrical conductivity, as well as many other superior properties, making it highly attractive for fundamental research and industrial applications. Synthesis and mass production form the solid basis for high-volume applications of CNTs. During recent decades, CNT production capacity has reached more than thousands of tons per year, greatly decreasing the price of CNTs. Although the unique physiochemical properties of an individual CNT are stated repeatedly, manifestation of such unique properties in a macroscopic material, e.g., realization of high-strength CNT fibers, remains a great challenge. If such challenges are solved, many critical applications will be enabled. Herein we review the critical progress in the development of synthesis and scaled-up production methods for CNTs, and discuss advances in their applications. Scientific problems and technological challenges are discussed together.

Keywords Carbon nanotube · Mass production · Application advances

Chapter 11 was originally published as Jia, X. & Wei, F. Top Curr Chem (Z) (2017) 375: 18. DOI 10.1007/s41061-017-0102-2.

✉ Fei Wei
wf-dce@tsinghua.edu.cn

¹ School of Materials Science and Engineering, University of Science and Technology Beijing, Beijing 100083, People's Republic of China

² Beijing Key Laboratory of Green Chemical Reaction Engineering and Technology, Department of Chemical Engineering, Tsinghua University, Beijing 100084, People's Republic of China

1 Introduction

Since being reported in 1991 by Sumio Iijima [1], carbon nanotubes (CNTs) have attracted great attention from researchers and industry. CNTs can be classified into single-walled CNTs (SWNTs), double-walled CNTs (DWNTs), and multiwalled CNTs (MWNTs) based on the number of graphitic layers. They are composed of sp^2 -bonded carbon atoms assembled into a cylindrical tube with length ranging from less than 100 nm to several centimeters. The diameter of SWNTs is typically 0.4–2 nm, while the diameter of MWNTs ranges from ~1.4 nm to nearly 100 nm, depending on the synthesis conditions.

CNTs are well known for their unique physicochemical properties, including extremely high tensile strength, high electrical conductivity, high ductility, and relative chemical inactivity. All these properties make CNT-based products attractive. Moreover, due to their low dimensionality, CNTs are also favored for use in nanocomposite engineering. In this context, CNTs open a new avenue in materials science and nanotechnology [2]. CNTs can be found in a wide range of applications, e.g., in electronics, polymer composites, energy storage materials, catalysis, gas storage materials, and sensors.

Since its discovery, there have been thousands of publications and patents aiming to explore the synthesis and applications of this material, and encouraging progress has been made by academic researchers and industry. Mass production of CNTs has become possible, offering more than thousands of tons of CNTs per year worldwide. In fact, production capacity could reach much higher than this if high-volume applications of CNTs could be found. Along with improved mass production, the cost of CNTs has been greatly reduced. The price of MWNTs has reached below US \$100 kg⁻¹ and that of SWNTs below US \$2000 kg⁻¹ in recent years [3].

A wide range of applications for CNTs have been reported in literature [4–6]. Rather than a detailed survey on CNTs, herein we pay more attention to the critical progress in terms of production scale-up and high-volume applications of CNTs, as well as technological challenges. We start with controllable synthesis of CNTs and scale-up techniques, then posttreatments such as purification, dispersion, and doping are also briefly introduced, since they are important for the following applications. Then, recent advances in critical applications, including macroscopic assembly of CNTs, composite materials, energy storage, catalysis materials, and environmental applications, are reviewed and analyzed. We hope this review will offer readers valuable opinions on advances in terms of CNT production and practical applications.

2 Synthesis and Production Scale-Up

2.1 Basic Principles of CNT Synthesis

For the wide range of applications of CNTs, synthesis and mass production with controlled structures is the first and critical step. Before the well-known report of CNTs in 1991 by Iijima, Endo reported synthesis of “vapor-grown carbon fiber,”

which actually contained MWNTs with diameter of tens of nanometers [7]. During development in recent years, a number of laboratory and scaled-up synthesis methods for CNTs have been reported, e.g., arc discharge, laser ablation, chemical vapor deposition (CVD), gas-phase pyrolysis, template methods, etc. [8], among which the CVD route has become dominant for mass production of CNTs. In particular, fluidized bed reactor-based CVD can produce CNTs with capacity of thousands of tons per year worldwide.

Before scale-up of CNT synthesis, their growth mechanism was widely studied in recent years. In a typical CVD process, hydrocarbon gas (e.g., methane, CH_4) is cracked into carbon atoms and hydrogen atoms on transition-metal (e.g., iron) catalysts. During growth, the catalyst nanoparticles can either sit on top of the CNTs (Fig. 1a) or remain at their base (Fig. 1b) [9], depending on the competition between the gas flow and the interactions between catalyst and substrate. It is widely believed that the catalyst size plays a key role in the formation of SWNTs or MWNTs. A small and narrow catalyst size of around a few nanometers (nm) favors formation of SWNTs, while MWNTs are more likely to form for catalyst size above 10 nm [9].

2.2 Synthesis of SWNTs

Based on the understanding of the CVD process, synthesis of SWNTs can be tuned with preferential control. The selectivity of metallic or semiconducting SWNTs can

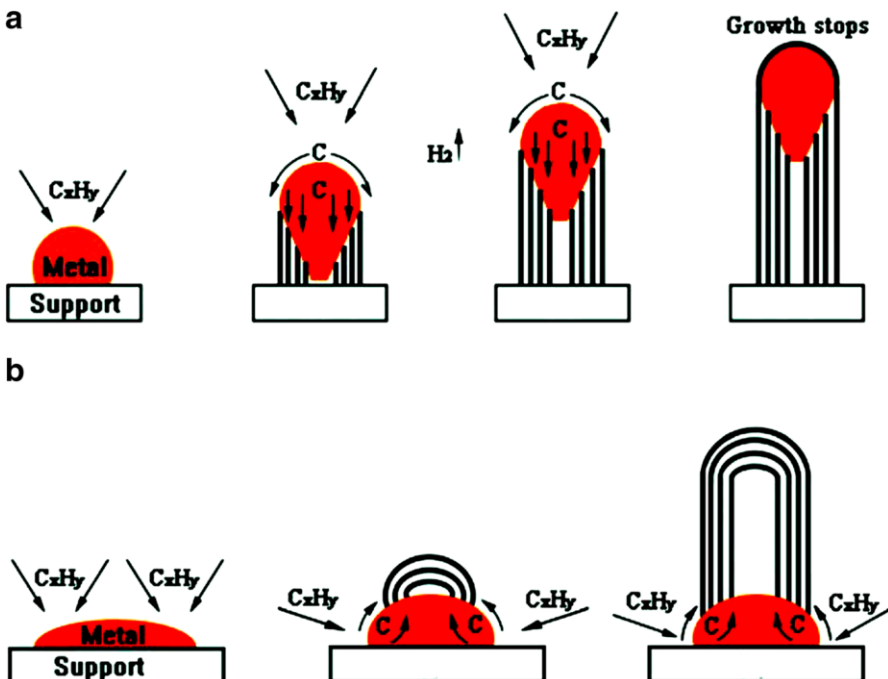


Fig. 1 Growth mechanisms for CNTs: **a** tip-growth mechanism and **b** base-growth mechanism Modified from Ref. [8], Royal Society of Chemistry, copyright 2015

reach 90–95% at optimized conditions [10, 11]. However, synthesis of SWNTs with controlled structure still faces challenges. Understanding of catalyst composition and growth conditions for SWNTs therefore remains an important theme. Recently, Li and coworkers proposed use of high-melting-point alloys as catalysts for controlled growth of SWNTs [12]. Due to their high melting point, such alloy catalyst nanoparticles remain in solid state, ensuring crystalline structure during CVD growth. As a result, the selectivity of metallic SWNTs has reached more than 99%.

Regarding macroscopic SWNT structures, Maruyama's group provided a breakthrough in synthesis of SWNT arrays [13] by uniformly depositing a dense layer of metal catalyst on a quartz plate to achieve vertical growth of SWNT arrays using alcohol as carbon source. Thereafter, a trace amount of water is introduced as a weak oxidant in the CNT growth process, strongly promoting the growth rate by maintaining the activity of the catalyst [14, 15]. Some other strategies for higher-quality SWNT arrays have also been studied, including feedstock optimization [16] among others. At present, scale-up techniques for reduced cost of SWNTs are required for their large-scale application. A high-pressure CO disproportionation (HiPco) process is one successful development to meet increasing demands for SWNTs [17]. CVD processes using a supported catalyst, e.g., the CoMoCAT® -process, which uses a fluidized bed reactor, also offer an effective approach to manufacture larger quantities of SWNTs [18]. The supported catalyst approach also offers the unique ability to provide a substantial degree of chirality control during synthesis.

2.3 Synthesis of MWNTs

In synthesis of CNTs, one important theme is growth of defect-free long CNTs. Wei's group pioneered growth of superlong defect-free CNTs [19, 20]. In this synthesis method, the catalyst nanoparticle is at the floating end of the CNT and keeps moving forward with its growth (Fig. 2a). By tuning the growth conditions to promote the activity of the iron catalyst nanoparticles, CNTs can grow up to 55 cm long (Fig. 2b). Raman and transmission electron microscopy (TEM) (Fig. 2c) characterization confirmed the perfect structure of such CNTs. The tensile strength of this kind of CNTs reaches ~140 GPa at strain of ~15% (Fig. 2d), which is nearly the theoretical value for MWNTs. Also, such defect-free CNTs were found to show superlubricity phenomena [21].

For vertically aligned MWNT arrays, one important method is to deposit catalyst nanoparticles on specially treated substrates (e.g., silicon wafer), which are then placed in a horizontal furnace [22]. Generally, a dense catalyst on the substrates is important for formation of CNT arrays. Such arrays represent an important platform material for subsequent CNT assembly, especially CNT fibers and films [23].

On the other hand, for large-scale and continuous production of aligned CNT arrays, millimeter-diameter spheres have been used as growth substrates by Wei's group [24], a method further developed by Noda's group by using ceramic beads in a fluidized bed reactor [25] and Bai's group by using alumina particles [26]. In most cases, the operation temperature of the CVD process ranges from 500 to 1200 °C.

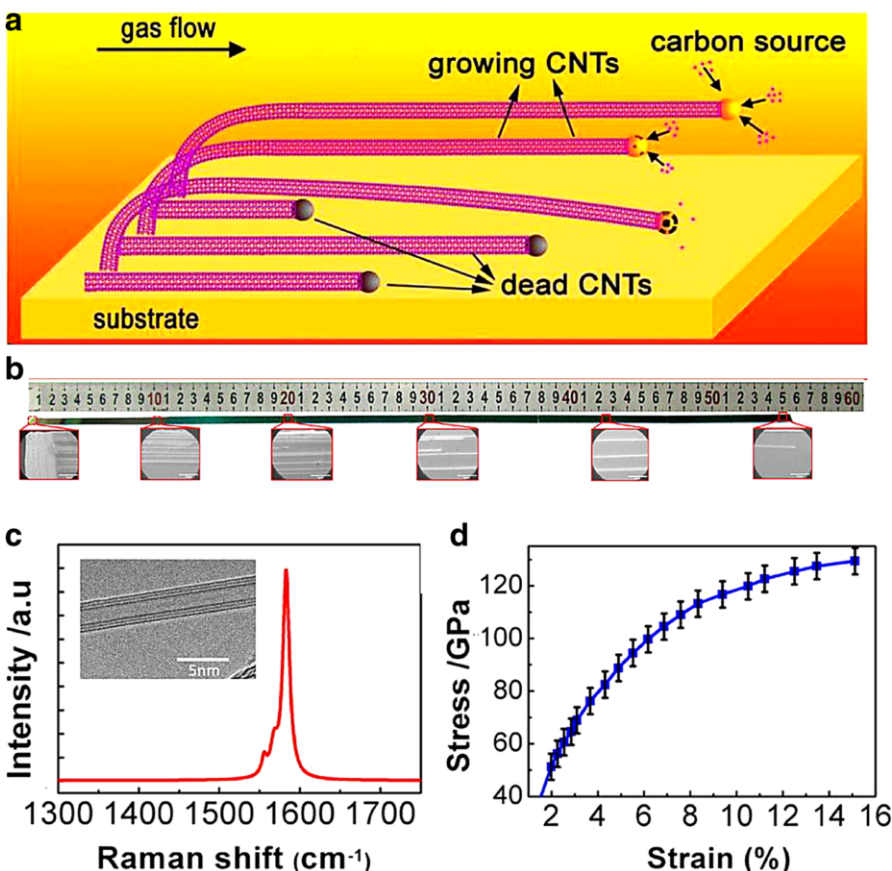


Fig. 2 **a** Tip growth of ultralong CNTs. The catalyst nanoparticle is at the floating end of the CNT and keeps moving forward with its growth in the synthesis process. **b** Mosaic scanning electron microscopy (SEM) images of as-grown ultralong CNTs with length approaching 55 cm. **c** Raman spectrum and transmission electron microscopy (TEM) morphology (*inset*) of as-grown CNT, displaying no D-band peak. **d** Mechanical properties of as-grown CNTs Reprinted from Ref. [20]. Permitted by American Chemical Society, copyright 2013

The catalyst nanoparticles may easily aggregated if they are not well controlled. Wei's group developed use of layered vermiculite to stabilize the catalyst nanoparticles (Fig. 3a) [27]. Vertically aligned MWNTs approaching tens of microns can be produced in such vermiculite flakes (Fig. 3b). Moreover, layered double hydroxides (LDHs) have been developed as a catalyst for CNT growth [28]. As shown in Fig. 3c, d, calcination and reduction of LDHs give rise to corresponding metal oxides or metal nanoparticles with good dispersion [29]. At controlled conditions, S/DWCNTs are grown on both sides of FeMgAl LDHs (Fig. 3e) [30]. Moreover, the density of these catalyst nanoparticles can be tuned from 10^{14} to 10^{16} m^{-2} . When the catalyst nanoparticles are distributed on the flakes at high density, CNT arrays rather than randomly entangled nanotubes can be grown (Fig. 3f, g) [29].

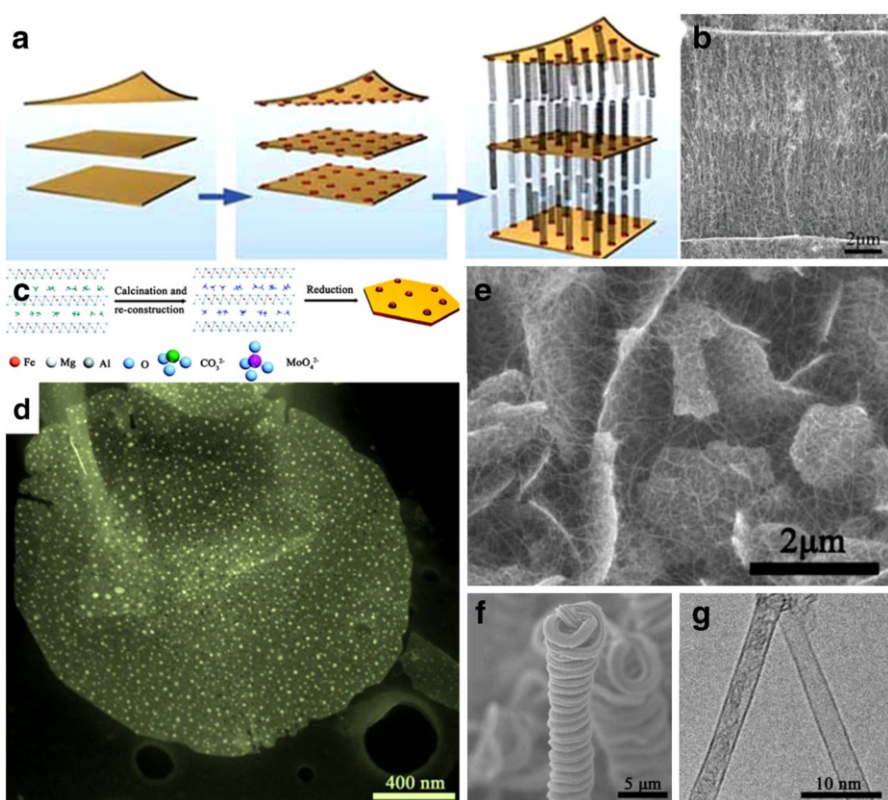


Fig. 3 **a** Formation of hybrid composites by intercalating vertically aligned CNT films into layered inorganic compounds. **b** Morphology of vermiculite–CNT composite after intercalation. Reprinted from Ref. [27]. Copyright 2009, Wiley–VCH, Weilheim, Germany. **c** Concept of chemical precursor-mediated catalyst synthesis. **d** Morphology of Fe NPs distributed on reduced Fe/Mg/Al layered double oxide (LDO) flake. Reproduced from Ref. [29]. Copyright 2010, American Chemical Society. **e** Agglomerated S/DWCNTs grown on LDO with low catalyst density. Reproduced from Ref. [30]. Copyright 2010, Wiley–VCH, Weilheim, Germany. **f** SEM and **g** TEM image of SWNT arrays grown on LDH with high catalyst density Reproduced from Ref. [29]

2.4 Production Scale-Up of CNTs Using Fluidized-Bed CVD

CNTs are typically synthesized in a fixed horizontal furnace. For large-scale production, fluidized-bed CVD has been developed as an important technique for production of CNT powder worldwide, considering its advantages of uniform mass and heat transfer, sufficient growth space, and continuous operation [3, 31]. As shown in Fig. 4, this process operates with an input gas to achieve fluidization of catalyst particles. Although it is difficult to fluidize individual CNTs in such a reactor, the strong interactions between CNTs lead to formation of large-size aggregates in the gas, which can then be fluidized [32]. The growth ratio can reach more than 40-fold, resulting in product purity above 98%. Aligned CNTs can also be produced using fluidized CVD by tuning the catalyst structure; For example,

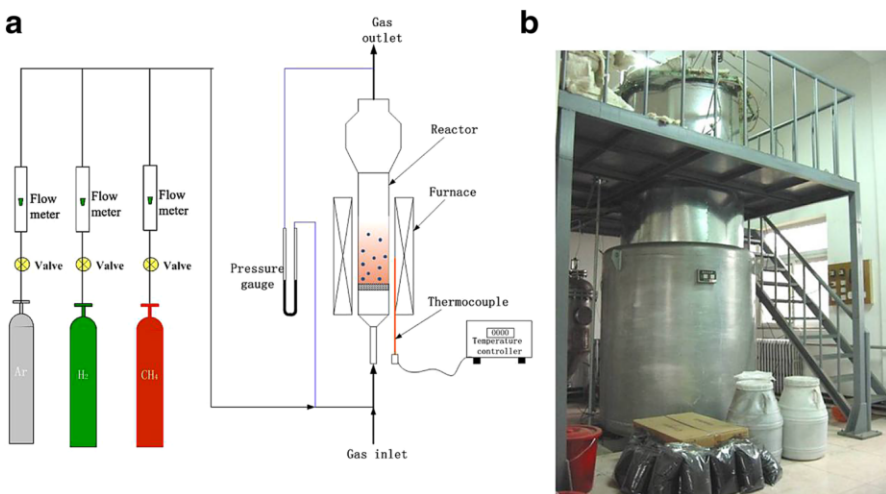


Fig. 4 **a** Scheme of typical fluidized-bed reactor system: a cylindrical fluidized-bed reactor is fixed inside a furnace with appropriate temperature, pressure, and gas flow controls. **b** A factory fluidized-bed reactor for producing CNT powder (images courtesy of Cnano Ltd.)

CNT arrays can be grown among the layers of vermiculite in a fluidized bed reactor [33]. By using LDHs as catalyst, SWNTs can be prepared in a fluidized bed reactor [34]. After further purification, the purity of such SWNTs can reach 99.5 wt%, offering high-quantity material for high-end applications [35]. This method can offer SWNT capacity of 1000 kg per year with price lower than US \$2000 kg⁻¹.

Note that scientific research and production scale-up of CNTs has also promoted development of other nanocarbons [36], such as graphene (G). The combination of CNTs and graphene may extend the applications of both [37–42]. As shown in Fig. 5a, by incorporating the catalysts of CNT and graphene together, SWNT/G hybrids or composites can be prepared based on catalytic growth on LDHs [37]. The morphology of the resulting structure (Fig. 5b, c) reveals a robust connection between the SWNTs and graphene, facilitating construction of a high-electrical-conductivity nanocarbon architecture. Moreover, catalyst residuals can be removed using a CO₂-oxidation-assisted purification method (Fig. 5d), leading to high carbon purity of 98.4 wt% [43]. Such nanocarbon architectures can combine high conductivity and high surface area, with important applications in energy storage and electrocatalysis [37, 38].

3 Postprocessing of CNTs

3.1 CNT Purification and Dispersion

As discussed in “[Synthesis of MWNTs](#)” section, many as-produced MWNT materials are aggregated powders with a certain content of impurities and catalyst residue. For SWNTs, the problem of impurities is more serious. In some

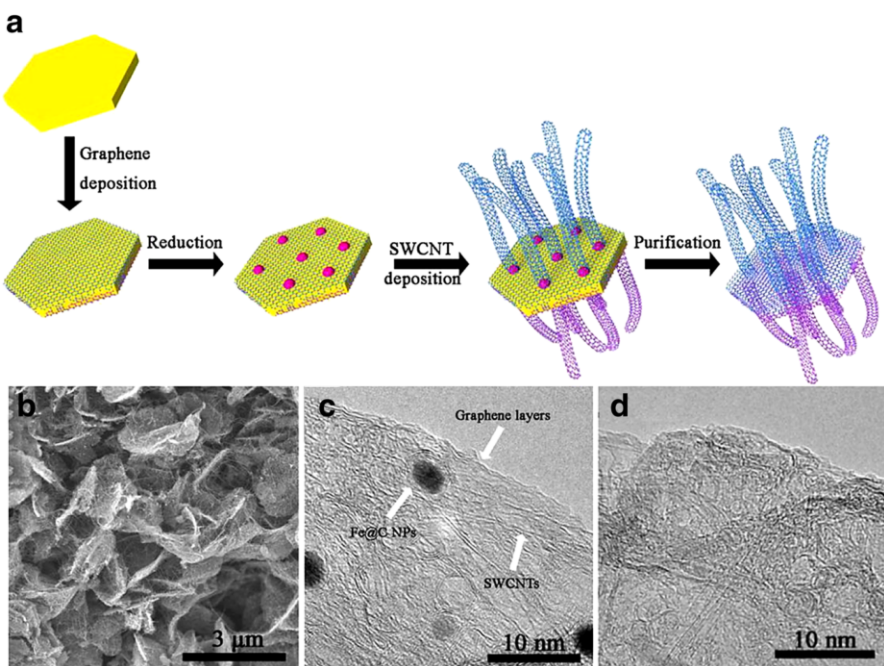


Fig. 5 **a** Schematic illustration of catalytic CVD of G/SWNT hybrids on LDH flakes. **b** SEM and **c** TEM images of as-fabricated G/SWNT hybrids. Reprinted from Ref. [37]. American Chemical Society, copyright 2012. **d** G/SWNT hybrids after removal of residual impurities. Reprinted from Ref. [43]. Elsevier, copyright 2013

applications, such as polymer composites, the problem of impurities and catalyst residues may be less critical; for example, MWNT powders with catalyst residues can still be directly mixed with polymer matrix [44]. Nevertheless, in most cases, catalyst residues and impurities must be removed, and CNT aggregates need to be dispersed before use. Therefore, purification and dispersion are important steps before CNT application. It is necessary to develop cost-effective and reliable processes for dispersion of CNTs for various applications.

As is well known, for CNT powders, the strong $\pi-\pi$ interactions between CNTs and their structural entanglement make them difficult to disperse for applications. One direct method to disperse MWNTs is through mechanical treatment such as high-energy sand milling, high-speed liquid-phase shearing, etc. in industrial units. The solvent is typically nonaqueous. Aqueous solutions with a certain surfactant can also be used. Figure 6a shows that MWNTs made from fluidized-bed CVD can be uniformly dispersed into *N*-methyl-2-pyrrolidone by high-speed liquid-phase shearing. The dispersed CNTs easily form network structures due to their maintained lengths (Fig. 6b). Currently, manufacturers can produce MWNT dispersion, slurry, or paste, which may find a broad range of applications, e.g., in lithium (Li)-ion batteries, supercapacitors, printed electronics, electromagnetic shielding, coating materials, heat dissipation, etc. The largest application in China is as a conductive additive on the cathode side of Li-ion batteries to replace conductive

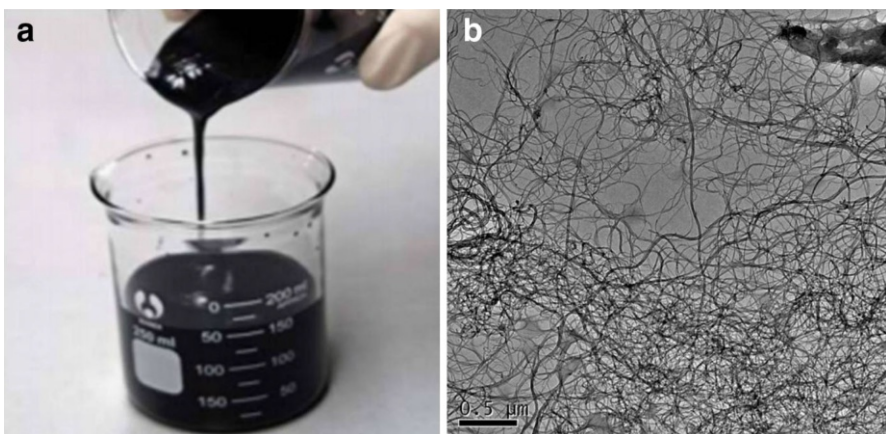


Fig. 6 **a** MWNTs dispersed in *N*-methyl-2-pyrrolidone at concentration of 1.0 mg mL^{-1} by high-speed liquid-phase shearing, displaying excellent dispersion. **b** Network structure of dispersed CNTs under TEM observation

carbon black for increased conductivity as well as cyclability. More than 10,000 t/a of CNT slurry have been used in Li-ion batteries for electric vehicles (EVs) and smartphones in China. It should be pointed out that high-energy mechanical treatments may destroy the structure of CNTs and decrease their length, thereby compromising their properties [45]. Also, the toxicity of the organic solvents used should be considered in manufacturing.

Alternatively, surface modifications, including noncovalent or covalent treatments, have been intensively investigated throughout the development of CNTs; progress in this regard has been summarized in many literature reports [46, 47]. Such strategies are still widely used for CNT treatments and applications. We only briefly introduce them here.

To preserve the structure and properties of CNTs, noncovalent treatment has been applied by adding a guest molecule for interfacial interaction. Typically, aromatic molecules can be appended to outer surfaces of CNTs by $\pi-\pi$ interactions [48]. Groups emanating from these molecules interact with the surrounding solvent or matrix, making CNTs easier to disperse in a solvent or polymer matrix. Also, a certain structured polymer can be wrapped around CNTs via noncovalent interactions. This strategy has been utilized to harvest ultrahigh-purity SWNTs [49, 50], since separation of semiconducting and metallic SWNTs is challenging [51].

On the other hand, chemical modifications are also used to treat CNTs. Surface treatments of CNTs by acid oxidation seem to be a direct and powerful method [52] that can introduce carboxyl, hydroxyl, and ketone groups onto their surface. After such treatment, CNTs are much easier to disperse in solvents. In addition, CNTs can be grafted with other functional groups on their surface for various applications [53]. Unfortunately, chemical modifications create defects in the CNT structure, which may lower the electrical conductivity or compromise the mechanical properties to a certain degree.

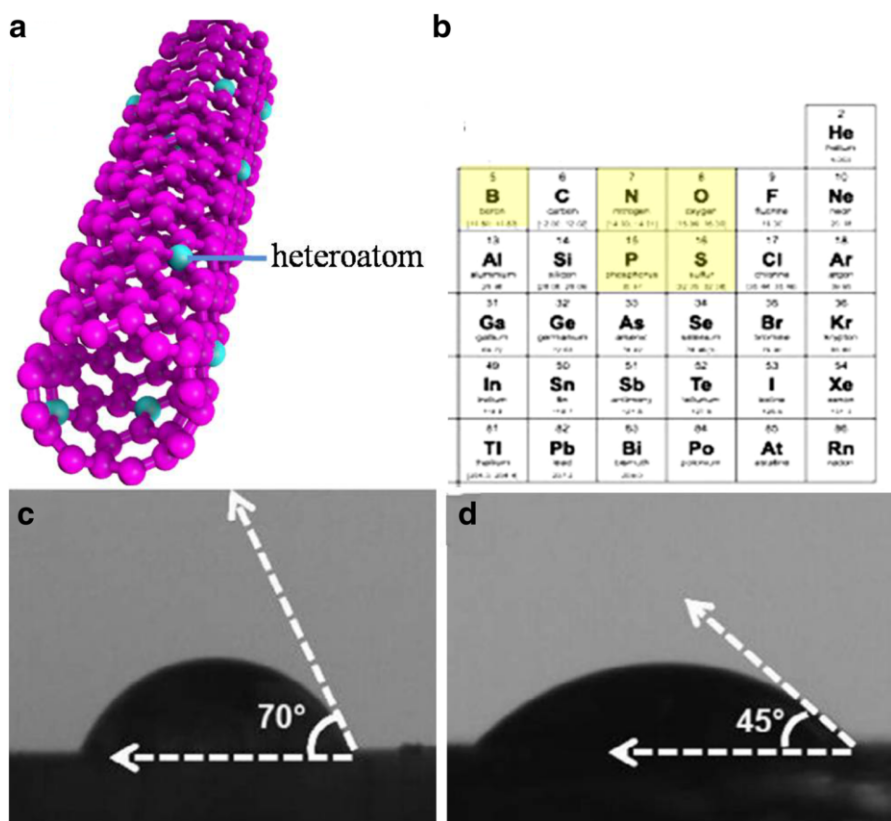


Fig. 7 **a** Doping of CNTs by introducing heteroatoms into the carbon framework. **b** Elements reported to be suitable for heteroatom doping of CNTs, mainly including B, N, P, O, S, etc. Contact angles of CNTs **c** before and **d** after S doping Reprinted from Ref. [62]. Elsevier, copyright 2015

3.2 Heteroatom Doping

Introduction of heteroatoms into the carbon framework (Fig. 7a) of CNTs has been used to tailor the electronic and interfacial properties of this material. Figure 7b shows the most widely used elements for doping into the carbon skeleton. Boron (B), nitrogen (N), phosphorus (P), oxygen (O), sulfur (S), etc. have been solely or jointly utilized to dope CNTs and tune their structural properties [54–57]. Heteroatom doping strategies greatly change the properties of CNTs, extending their potential applications.

To date, much progress on heteroatom doping of CNTs has been made. The methods can mostly be categorized into in situ and posttreatment approaches. As their name implies, in situ approaches rely on introduction of heteroatom sources during the CNT synthesis process [58]. Posttreatment methods including wet chemical methods, thermal annealing of CNTs with heteroatom precursors, and plasma approaches have been developed in literature [59]. Precisely controlled heteroatom doping techniques are currently being developed for applications.

It is well known that pristine CNTs are quite chemically inert. Introduction of heteroatoms tailors the physicochemical properties of CNTs, which can result in catalyst activity; For example, N-doped CNTs can be used as electrode materials for fuel cells, with performance comparable to that of current platinum (Pt)-based catalyst [60, 61]. Theoretical and experimental investigations are being combined for more targeted doping of CNTs to achieve higher activity.

Additionally, CNTs display highly hydrophobic properties. Doping strategies may change this. Heteroatom doping enables CNTs to be much more easily dispersed, which is important for polymer composite and energy storage applications; For example, S-doped CNTs can be obtained by thermal annealing of pristine CNTs with sulfur compounds. Due to the sulfur doping, the contact angle of the CNTs is greatly reduced compared with pristine CNTs (Fig. 7c, d), suggesting effective modification of the CNT surfaces. The obtained S-doped CNTs can be stably dispersed in water [62]. When used in battery electrodes, higher capacity and rate performance can be achieved due to the improved dispersion due to construction of conductive networks.

4 Application Advances

4.1 Macroscopic Assemblies and Their Applications

The unique properties of CNTs have been measured for individual nanotubes. An important theme is to produce large-scale CNT architectures which also offer such properties [63, 64], although this still remains a big challenge. Generally, macroscopic CNT architectures can be fabricated by direct growth methods or by postprocessing of dispersed CNTs.

CNT arrays made by CVD are typical assemblies where CNTs are aligned on the substrate [23]. Many groups have reported synthesis of such structured CNTs for various applications. CNT films can be made by spinning aligned CNT arrays (Fig. 8a). Also, the CNT arrays can be continuously spun into macroscopic fibers (Fig. 8b). CNT films are believed to represent an alternative to indium tin oxide, since CNTs can make flexible displays [65]. Based on the CVD technique, Xie's group prepared nonwoven SWNT films (Fig. 8c, d) [66]. The SWNTs created Y-type junctions during synthesis, leading to the formation of a network structure. This unique structure can be easily handled for further study and use, e.g., in tough polymer composites [67], electrodes for flexible supercapacitors [68], etc. Recently, Kauppinen et al. developed an aerosol CVD method for fabrication of highly conductive and transparent free-standing SWNT films, where the products can be directly and continuously collected [69, 70]. For reduced formation of SWNT bundles, a spark generator-based floating catalyst CVD method was developed to produce nonbundled, small-diameter single-walled carbon nanotubes by feeding catalyst nanoparticles into a laminar flow chemical vapor deposition reactor [71, 72]. The resulting films exhibited outstanding properties that are desirable for touch panels, etc.

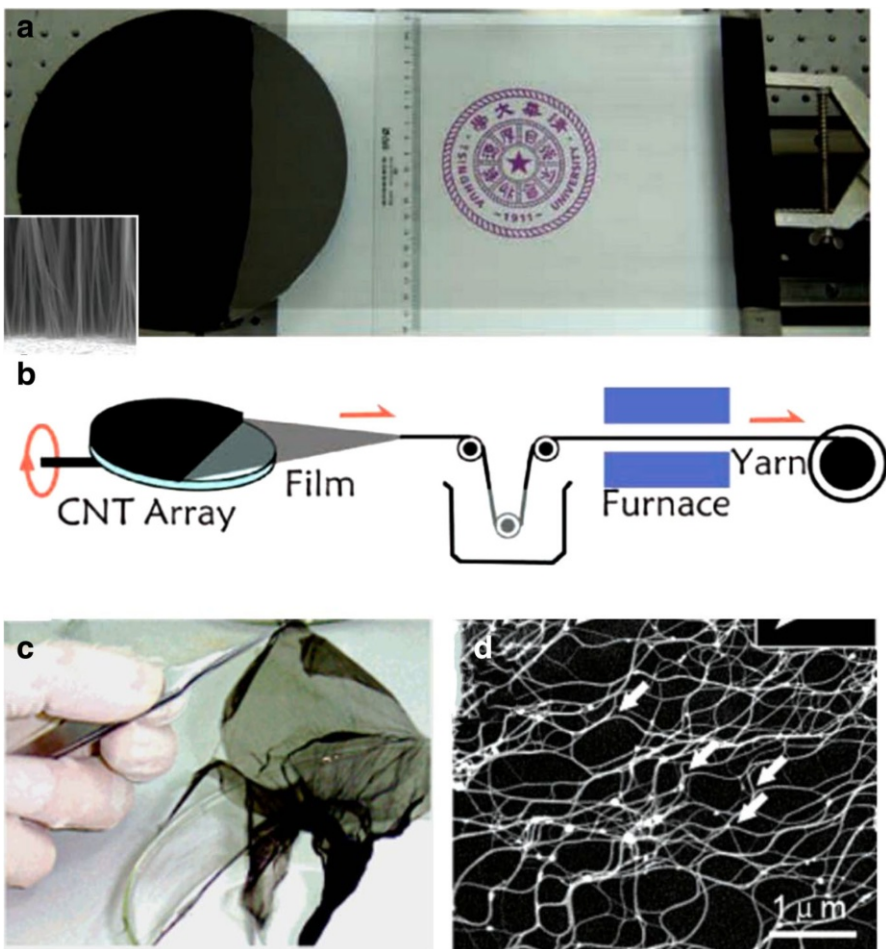


Fig. 8 **a** Drawing of a transparent conducting film of 8-inch superaligned CNT arrays (*inset* SEM structure). **b** Schematic illustration of process from superaligned CNT array to films and then shrunk yarns. Reprinted from Ref. [23]. Copyright 2011, Wiley–VCH, Weinheim, Germany. **c** As-grown 250-nm-thick SWNT film. **d** SEM image of SWNT network in a single layer; *white arrows* indicate Y-type junctions and flow direction Reprinted from Ref. [66]. American Chemical Society, copyright 2007

In terms of mechanical properties, most CNT fibers are reported to show tensile strength of 0.2–8.8 GPa [73]. To date, this strength value is still not competitive with that of traditional carbon fibers for actual applications. The critical factors affecting this need to be investigated. Commonly, condensation and alignment of CNTs, as well as interface engineering between CNTs, are important to increase the fiber strength. Recently, Wang's group continuously produced CNT macroscopic assemblies in the form of a hollow cylinder based on a floating catalyst approach (Fig. 9a) [74]. The hollow cylinder assembly was aligned, condensed, and deposited on a winding drum to form a CNT film (Fig. 9b). The prepared film displayed

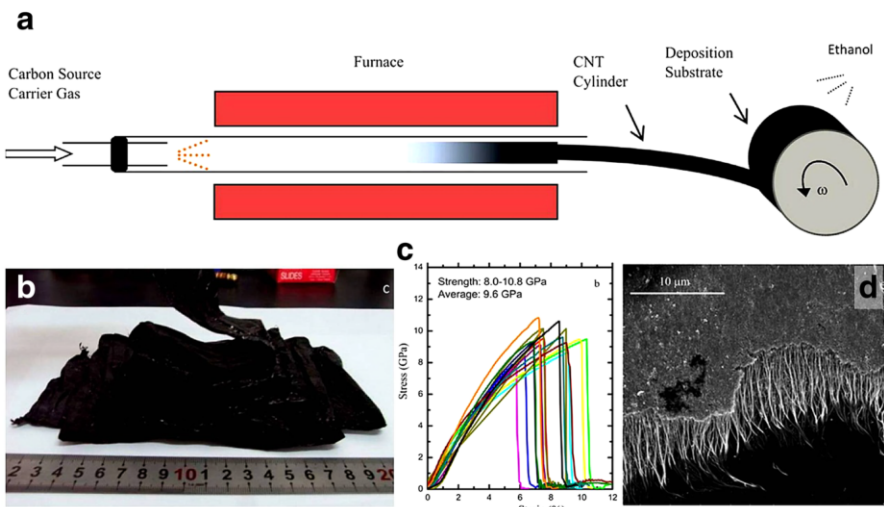


Fig. 9 **a** Schematic illustration of fabrication of CNT film. Reaction solution is sprayed into a tube reactor and pyrolyzed to form a hollow CNT cylinder, which is then condensed and deposited on a winding drum. **b** Film removed from the substrate. **c** Stress versus strain curves, showing averaged tensile strength of 9.6 GPa. **d** Fracture surface visualized under SEM, displaying the aligned structure Reprinted from Ref. [74]. American Chemical Society, copyright 2016

tensile strength of 9.6 GPa (Fig. 9c, d), well above that of all other manmade films or fibers.

CNT foams/sponges with interconnected network structure can also be produced by the CVD method [75]. In this case, CNTs are randomly distributed in the sponge, rather than having aligned morphology. Such foams/sponges have been explored for energy and environmental applications. Moreover, Hata and coworkers developed a viscoelastic material from CNTs that is similar to silicone rubber, but maintains temperature-invariant viscoelasticity from -196 to $1000\text{ }^{\circ}\text{C}$ in an oxygen-free environment [76]. This CNT material could find applications in extremely hot or cold environments.

On the other hand, stable CNT dispersions can be obtained based on gradually maturing dispersion techniques. As a one-dimensional nanocarbon material, CNT is attractive for engineering of large-scale architectures, including fibers, films, and aerogels/foams [63]. Similar to the important process used to produce industrial fibers, wet spinning of dispersions has enabled fabrication of SWNT and MWNT fibers [77–79]; For example, SWNTs dissolved in chlorosulfonic acid at weight concentrations of 0.5 wt% could be readily processed into macroscopic fibers or sheets to obtain functional materials [77]. Such functional fibers have conductivity comparable to copper wire but 1/8 of the density and several times the strength, enabling important engineering applications in the aerospace industry. In addition, three-dimensional aerogels/foams can be assembled from dispersed CNTs, showing highly porous structure. The high aspect ratio and strong interactions between CNTs are important for such porous structures. Gao's group described that CNTs can be

used as “ribs” to reinforce the framework of CNT/G aerogel [80]. The porous structure has porosity above 99.9%, yet structural flexibility and robustness.

4.2 Composite Materials

The elastic modulus of an individual MWNT is measured to approach 1 TPa, while the tensile strength exceeds 100 GPa [81]. This strength is over tenfold higher than any other fiber, even the well-known carbon fibers. Considering this high strength, it is believed that CNTs can be incorporated into another matrix for enhanced mechanical properties, including strength, toughness, and stiffness. Such polymer composites have been successfully prepared by adding CNTs and indeed offer excellent properties [82, 83]. These polymer composites have found a diverse range of applications such as automotive, tires, sports goods, aerospace, packaging, and even household goods.

Although individual CNTs show very good mechanical properties, transferring these unique properties to macroscopic composite materials remains a great challenge. If this issue is solved, many key applications will be enabled. When engineering polymer composites for load-bearing applications, the alignment, dispersion, diameter, and aspect ratio of the CNTs and their interfacial interactions with the matrix are critical for the final composite. Most CNTs obtained today are entangled powders. Commonly, when making CNT-based composites, the first question is how and which CNT structure to disperse in the matrix.

For cost-effective and large-scale applications, melt blending is one of the most widely used methods to achieve CNT-containing composites [84], since it offers easy and continuous operation. Manufacturers have used this technique to make composite rubbers containing CNTs. Figure 10 shows a high-performance tire tread produced using only 0.7% weight fraction of MWNTs; TEM results confirmed that the CNTs were uniformly dispersed in the rubber matrix. The prepared tires showed optimal comprehensive performance with practical applications [85]. As-prepared CNT–polymer composites can be engineered for various applications, such as spinning of conductive fibers [86]. In addition, ongoing interest in three-dimensional (3D) printing also offers opportunities for use of CNT-based composite resins. Adding CNTs to the raw polymers results in feedstocks with improved properties for this technique. This method can produce polymer composites with CNTs randomly distributed in the matrix. The CNT loading is mostly below 10 wt%, as higher contents of CNTs are difficult to process due to the high viscosity resulting from the CNTs. Zheng et al. demonstrated preparation of MWNT–rubber composites with high CNT concentration of ca. 37 wt%. The results showed that the persistence length and reorientation of MWNTs during stretching have a significant impact on the mechanical properties [87]. Addition of CNTs into polymers can indeed enhance the tensile strength and toughness. However, note that current dispersion processes still face undesirable problems, as well as damage to CNTs, which may compromise the mechanical properties of the final composites. To circumvent this problem, various other techniques such as *in situ* polymerization with CNTs have also been developed [88].

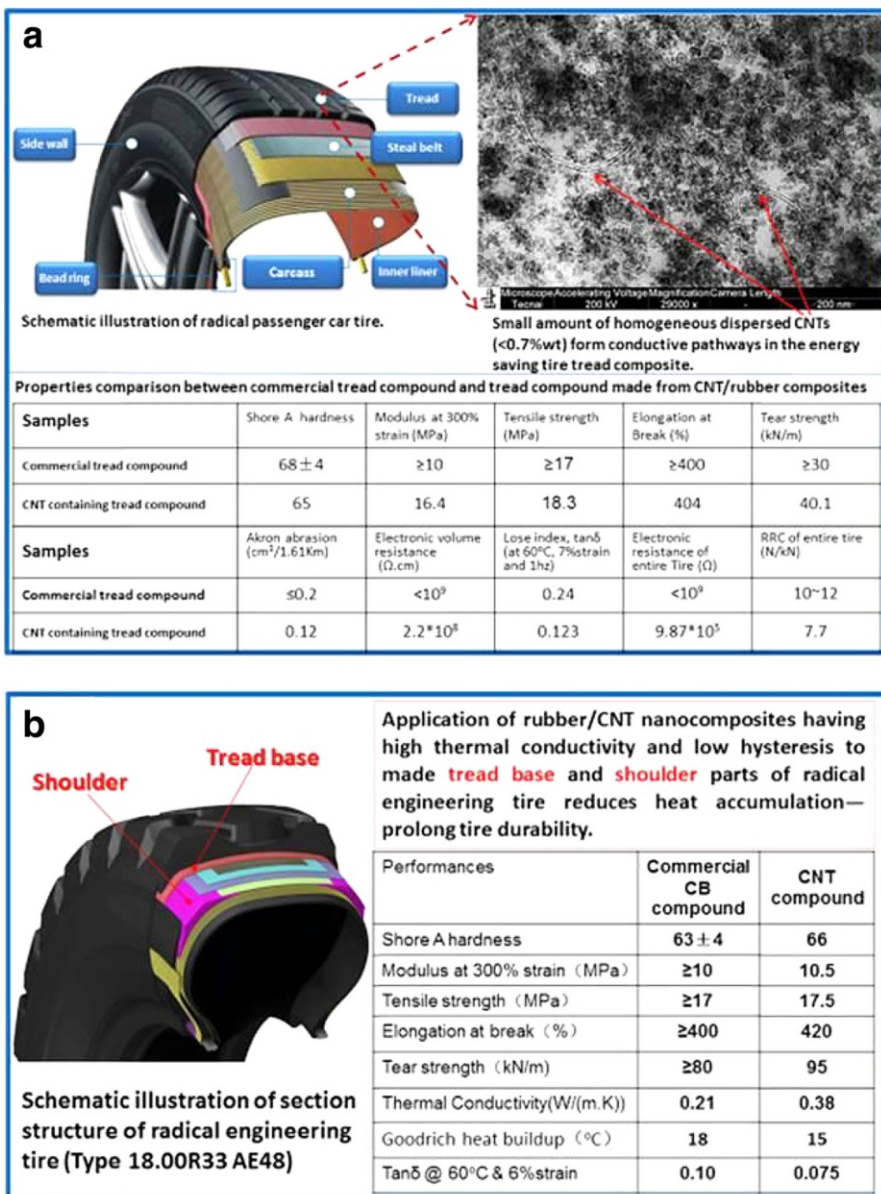
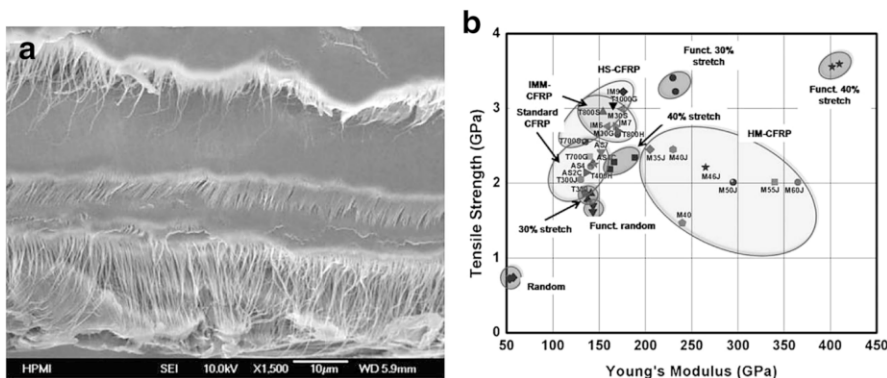


Fig. 10 Application of rubber–CNT nanocomposites in high-performance tires: **a** use of CNTs in highly filled rubber/nanosilica tread composite to solve the problem of electrical charge release from energy-saving passenger tires; **b** application of rubber–CNT nanocomposite in high-performance engineering tires for reduced heat accumulation Reprinted from Ref. [85]. Copyright 2016, Elsevier

Instead of directly mixing CNTs with a resin matrix, another strategy to make CNT–polymer composites based on a special resin infiltration process has been described. Various CNT structures, including films, foams, fibers, and arrays, can be incorporated

into polymers based on this method; For example, well-dispersed SWNT papers can be prepared by filtration for subsequent impregnation with precursors and polymers [89]. Although these SWNTs are well dispersed, their random entanglement still limits the strength. More importantly, CNTs can be grown or deposited on traditional fibers (e.g., carbon fiber [90], glass fiber [91], and quartz fiber [92], etc.) to improve the mechanical properties of the composite due to improved load transfer between interfaces.

For mechanical applications, current CNTs are usually considered to be short fibers. Polymer composites with CNT fillers are always analogs of random, short-fiber composites. By comparison, traditional carbon fibers have long-fiber features. Organizing CNTs into aligned continuous fibers is very effective to increase the content of CNTs and obtain high-strength fibers. In most cases, the enhancements achieved in polymer composites including randomly distributed CNTs are limited. The actual strength of CNTs is therefore not fully utilized in such composites containing random short CNTs. However, reorganizing the dispersed CNTs into an aligned architecture is challenging. Cheng et al. reported that CNT carpets with high aspect ratio can be aligned based on well-controlled strategies. The aligned CNTs are treated with epoxidation functionalization, and further incorporated into bismaleimide (BMI) resin to form a high-strength bulk composite with 60 vol% CNT concentration [93, 94] (Fig. 11a). The tensile strength and Young's modulus of these composites reached 3081 MPa and 350 GPa, respectively, exceeding those of state-of-the-art unidirectional carbon-fiber-reinforced composites (Fig. 11b). Another method to achieve aligned CNTs is growth of vertically aligned CNTs on substrates, as discussed above. Continuous yarns or sheets can be produced from such aligned CNTs; however, their mechanical properties still require further improvement. The anisotropic characteristics of such aligned CNT fibers also make them valuable for multifunctional applications.



CNTs are highly conductive. As a result, conductive polymer composites, and increasing their value, have been applied for certain commercial applications. A certain type of CNT-based conductive composite is already used for dissipating electrostatic discharge, in conductive plastics, and other applications. Benefiting from the high conductivity, together with high aspect ratio (i.e., length-to-diameter ratio of 10^2 to 10^7), nonconductive polymers become conductive on addition of as little as 0.1 wt%, without compromising other properties [88, 95, 96]. On the other hand, use of CNTs also enhances the mechanical properties of conductive composites, whereas use of much higher content of carbon black or metal nanoparticles in conductive polymers may decrease the tensile strength of the composites. Low CNT content is desirable for conductive polymers, considering manufacturing and cost issues. The conductivity largely depends on the processing method, type of CNT, and polymer matrix applied [97]. Adding CNTs to polymers also results in other, multifunctional properties, e.g., thermal conductivity [98], electromagnetic interference shielding [99], etc.

Besides polymer composites, other composites have also received much attention, such as metal [100, 101], ceramic [102], and other composite materials [103]. Although these composites are designed for various aims, they face similar problems regarding production of CNT-based polymer composites. Indeed, if the challenges discussed above are solved, many techniques will benefit, enabling many high-volume CNT applications.

4.3 Energy Storage

4.3.1 Lithium-Ion Batteries

Lithium-ion batteries are widely used in electronics and laptops, and their applications are now extending to include electric vehicles and large-scale energy storage applications. Currently, battery charging takes more than 10 h due to the low conductivity of the electrode materials. Based on their reduced cost, CNTs are now being used in lithium-ion batteries. MWNT powders are ground into slurry to improve the conductivity of the electrode. A small amount of MWNTs can be added simply into the electrode by mechanical blending. Benefiting from this improvement, LIBs in electric vehicles can be charged in less than 1 h. Compared with traditional carbon black, CNTs offer long-range conductivity, resilient network structures for electrodes, better interfacial contacts, and thermally conductive networks, representing prominent advantages over traditional carbon black materials for improved Li-ion batteries [104–106].

Most cathode materials (e.g., LiFePO_4) face problems of low conductivity and limited ion transport in several current classes of cathode material. Obviously, CNTs are becoming important additives for cathodes of Li-ion batteries. By partially replacing carbon black (CB), it was reported that addition of CNTs to electrodes could result in formation of three-dimensional conductive scaffolds with effective charge transport (Fig. 12a, b) [107]. As a result, introduction of CNTs greatly improves the charging rate and stability of such battery electrodes (Fig. 12c). This strategy is now starting to be used to improve the power

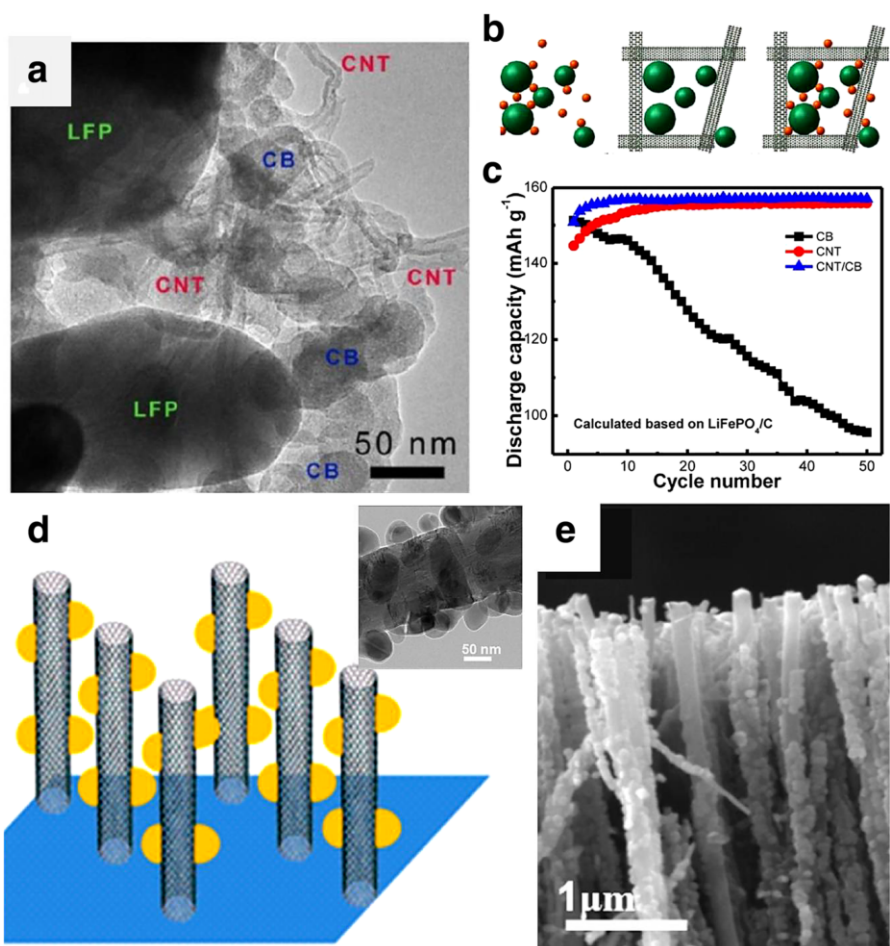


Fig. 12 **a** SEM image of CNT/CB-modified LiFePO₄/C cathodes, as well as **b** structural illustration. **c** Cycling stability of LiFePO₄/C cathode with CNT/CB as conductive scaffold, compared with that made from CBs or CNTs. Reprinted from Ref. [107]. American Chemical Society, copyright 2014. **d** Schematic diagram showing the Si/CNT hybrid nanostructures; **e** SEM image of the CNT array covered with Si nanoclusters Reproduced from Ref. [117]. Copyright 2010, American Chemical Society

performance of batteries. For industrial applications, a uniform dispersion of CNTs in the cathode material is vitally important. Cnano technology limited has developed a method to disperse MWNTs by sand milling to form CNT slurry, with production of more than 10,000 t/a. CNT slurries are being used as conductive additives for Li-ion battery cathodes for EVs and smartphones, representing the largest application of CNTs in China.

For higher energy density, Li–S cathodes are being explored for use in next-generation Li-ion batteries. CNTs are used as effective scaffolds to improve the electrode performance of S [108–110]. By direct thermal treatment of SWNTs with S powder, S/SWNT composites can be prepared with tight adhesion of S on CNT

surfaces [111]. However, the capacity decay is still critical for actual applications of Li–S batteries. Interfacial modifications and porous structure engineering of CNTs, as well as rational combination of CNTs with other kinds of nanocarbon, are underway to achieve further improvements of Li–S batteries [112, 113].

CNTs can also be used for anode materials because they are composed of curved graphitic layers [114]. However, they usually display highly irreversible capacity during the initial cycles, which may be due to their high interfacial activity. Some posttreatments of CNTs are therefore necessary for use in battery anodes.

Instead of direct use as anode materials, it seems that making composite materials of CNTs and other active materials is an effective strategy for use of CNTs in batteries. Silicon (Si) is a promising anode material with theoretical capacity of 4200 mAh g⁻¹ and low voltage plateau [115]. However, Si anodes suffer from large changes in volume during charge/discharge cycles and low electron conductivity, resulting in poor cycling stability and rate capacity. CNT/Si hybrids with entangled structure can be prepared by simple mechanical mixing [116], displaying improved rate capacity and cycling stability. Ordered nanostructured composites as battery electrodes are expected to minimize ion/electron transport resistances, thereby offering much better performance. Aligned CNTs have therefore been used to form ordered nanostructured composites. Wang et al. reported deposition of Si on aligned CNTs by a CVD technique [117] (Fig. 12d, e), achieving reversible stable capacity and good rate capability. Gleb Yushin's group also reported that aligned CNTs coated with Si can be used to form thick (~1 mm) electrodes [118]. Such ordered nanostructured composite materials have great potential if they become readily available. Some other anode composites containing CNTs have also been prepared, including metal alloys, metal oxides, etc. [105], showing greatly improved performance.

It must be pointed out that the spray drying process is a versatile and simple method to produce CNT-based nanostructured electrode materials [109, 119]. A large variety of micro/nanostructured energy storage particles containing CNTs have been reported based on this method. In this process (Fig. 13a), precursor solution/dispersion is sprayed into droplets, which then condense into solid particles for conversion into active composite materials after further treatment [119]. As a typical example, using CNTs in oxide nanocrystal dispersion, resilient CNT/oxide composite granules have been prepared based on self-assembly in such a spray process (Fig. 13b) [120]. This kind of composite material offers good resilience due to the introduction of CNTs (Fig. 13c). Moreover, by dispersing CNTs into the precursor solution of cathode/anode materials [121, 122], the CNTs are directly condensed into the active material in the final composite. Such nanostructured cathode materials may be developed for use in high-power batteries.

A unique feature of the structure of CNTs is their high aspect ratio, making such materials highly flexible. Moreover, the high surface area, as well as the interconnected network, enable them to accommodate almost all types of electrode material. In principle, electrode materials with efficient conductive and transport properties could work as battery electrodes. Therefore, electrodes consisting of only

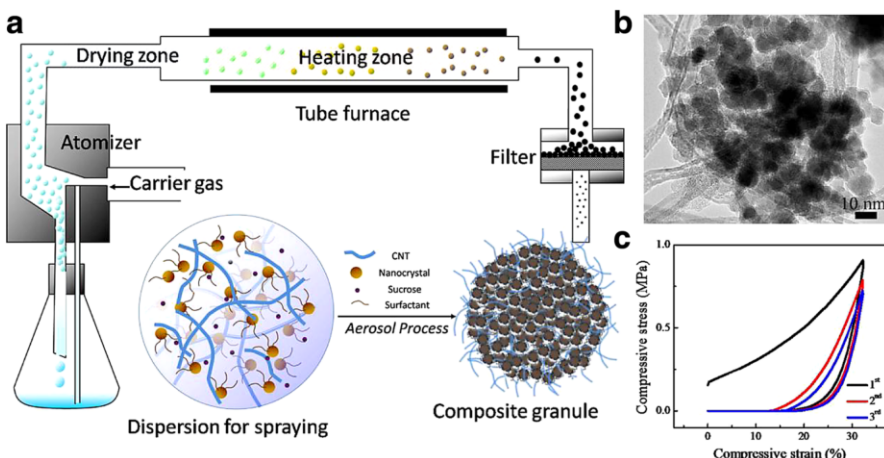


Fig. 13 **a** Schematic process of aerosol-assisted heteroassembly of oxide nanocrystals and CNTs into hierarchically structured mesoporous composite particles. Modified from Ref. [119], Copyright 2015, Wiley–VCH, Weinheim, Germany. **b** SEM image of CNT/Fe₃O₄ composites, showing interwoven networks. **c** Compressive stress–strain curves of CNT/Fe₃O₄ composites, suggesting high structural durability Reprinted from Ref. [120]. American Chemical Society, copyright 2014

CNTs and active materials can be prepared and work well. CNTs are being considered for use as both a current-collector support for active materials and as free-standing electrodes without any binder. Jia et al. reported fabrication of binder-free electrodes based on a simple vacuum filtration method (Fig. 14a, b) [123]. In such structures, the particles of active material are tightly trapped in CNT networks (Fig. 14c), forming effective conductive pathways. Based on their tight entanglement, as-formed entangled electrodes show tensile strength approaching 1.2 MPa (Fig. 14d). By comparison, traditional carbon black–polyvinylidene fluoride bound electrodes show limited flexibility. For high-capacity electrode materials (e.g., V₂O₅, Fig. 14e, f) [124], binder-free electrodes represent a highly flexible architecture that can accommodate the volume change while retaining the conductive network. Although no binders were added, these electrodes worked well and showed high rate capacity and improved stability. Moreover, Peng's group incorporated lithium-based nanoparticles into CNT fibers to make a lithium-ion battery, which also performed stably after being stretched [125]. Such devices could be used in smart clothing and other applications.

Besides flexible electrodes, CNT paper may be produced from dispersions for use in the papermaking industry. This may enable lightweight and highly conductive current collectors for use in batteries with higher energy and power density. Interestingly, ground CNT paste, as well as other conductive pastes, can be incorporated onto metal substrates to form more effective collectors to load active materials. Construction of such mechanically flexible and deformable substrates to load active materials for battery electrodes enables facile fabrication of lightweight flexible energy-storage devices [126].

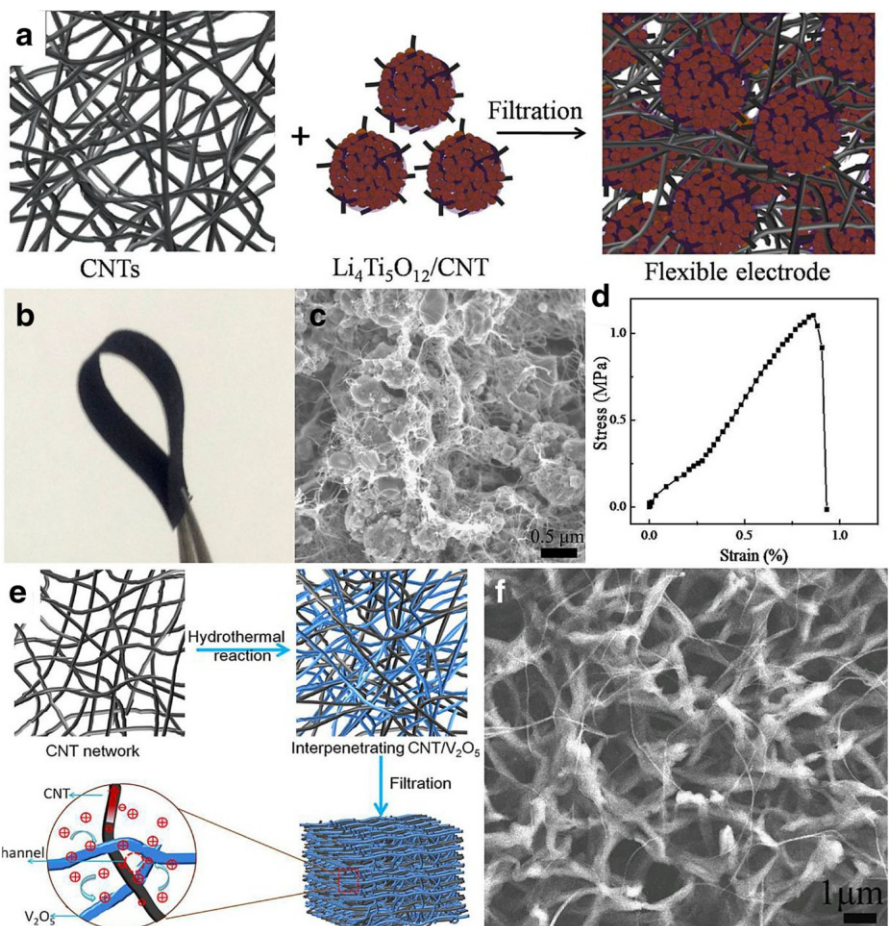


Fig. 14 **a** Fabrication of binder-free flexible Li₄Ti₅O₁₂/CNT electrode based on simple vacuum filtration process. **b** Flexible electrode and **c** its cross-sectional morphology, showing intimate entanglement. **d** Stress–strain curve of flexible electrodes. Reprinted from Ref. [123]. Copyright 2013, Elsevier. **e** Schematic of synthesis of composites of ultralong CNTs and V₂O₅ nanowires with interpenetrating network structure. **f** SEM image of V₂O₅ nanowire networks and CNTs penetrating through the networks. Reproduced from Ref. [124]. Copyright 2012, Royal Society of Chemistry

4.3.2 Supercapacitors

Another promising energy storage device is the supercapacitor, which is known for its high power density, fast charging time, and long lifetime. The storage mechanism of this kind of device is based on storage of opposite charges between two closely spaced surfaces [127]. Based on this storage mechanism, it is expected that large specific surface area (typically over 1500 m² g⁻¹) will be key to achieve supercapacitors with high specific capacitance by providing effective charge storage sites in the double layer. Activated carbons (AC) are currently the most common electrode materials for supercapacitors, due to their low cost. However, the

defective microstructure and disordered small pore structure of ACs limit performance.

Due to their high electrical conductivity and high specific surface area, CNTs (including both SWNTs and MWNTs) are being extensively studied for use in electrode materials for supercapacitors with both aqueous and nonaqueous electrolytes. In aqueous devices, KOH or H₂SO₄ are the most widely used electrolytes. The size of the ions is very small, around 0.5 nm, so nearly no diffusion limitation exists within the electrode. In this case, the capacitance of the electrode is mainly determined by its specific surface area. For MWNTs with specific surface area of 470 m² g⁻¹, the capacitance ranges from 5 to 200 F/g. It seems that there are no obvious advantages of MWNTs over AC. SWNTs could offer comparable surface area to AC in aqueous electrolyte. However, the high current cost of production and purification of SWNTs hampers their high-volume use.

One way to increase the capacitance of CNT electrodes is to modify the surface of the CNTs by acid or base treatment. Functional groups including OH, COOH, or C=O exhibit pseudofaradaic capacitance in the range of 4–135 F g⁻¹. Therefore, MWNTs with moderate surface area of 470 m² g⁻¹ exhibit capacitance comparable to commercial AC after such modifications [128]. This surface modification makes the CNTs hydrophilic, allowing quick access of ions from the aqueous electrolyte. In addition, it must be pointed out that heteroatom doping of CNTs represents an important strategy to enhance the pseudofaradaic capacitance [129].

Making CNT-based hybrid/composite materials for supercapacitors is another method to increase the pseudofaradaic capacitance. Many publications have reported CNT/metal oxides and CNT/conductive polymers for use in supercapacitors [130]. Faradaic reaction (or pseudocapacitance) is obtained in these nanostructures by tuning their structure and interfaces. The designed three-dimensional architectures can offer facile kinetics, thereby enabling production of energy storage devices with high energy and power and long lifetime. However, CNT/oxide materials suffer from low specific surface area (mostly <50 m² g⁻¹) and poor electrical conductance, greatly compromising the power performance. Moreover, metal oxides also face problems of structure fading during the charge-discharge process.

For higher energy density, electrolytes included organic electrolytes and pure ionic liquids (ILs) can be operated at high voltage (>3 V). This could enable energy densities six to nine times that of aqueous electrolyte. The size of the ions of organic electrolyte and ILs is typically 1.1–1.5 and 1.5–2.5 nm, respectively. Because of the increased size of the electrolyte, the true ion-accessible surface area of AC is estimated to decrease from the original value of 1000–2000 to 200–300 m² g⁻¹ [131]. By comparison, aligned SWNTs can be condensed into the electrode (Fig. 15a) [132]. Such electrodes with unique channels allow simultaneous adsorption of ions and rapid transport of electrons along the *c*-axis (Fig. 15b). The energy density of such an aligned SWNT array membrane reached 94 W h kg⁻¹ in Et₄NBF₄/propylene carbonate electrolyte at 4 V. This exceeds the operating voltage limit of activated carbon electrodes (3 V), thereby delivering significantly improved energy and power performance (Fig. 15c). When high-purity SWNTs were used for the electrode, excellent capacitance retention was achieved. Overall,

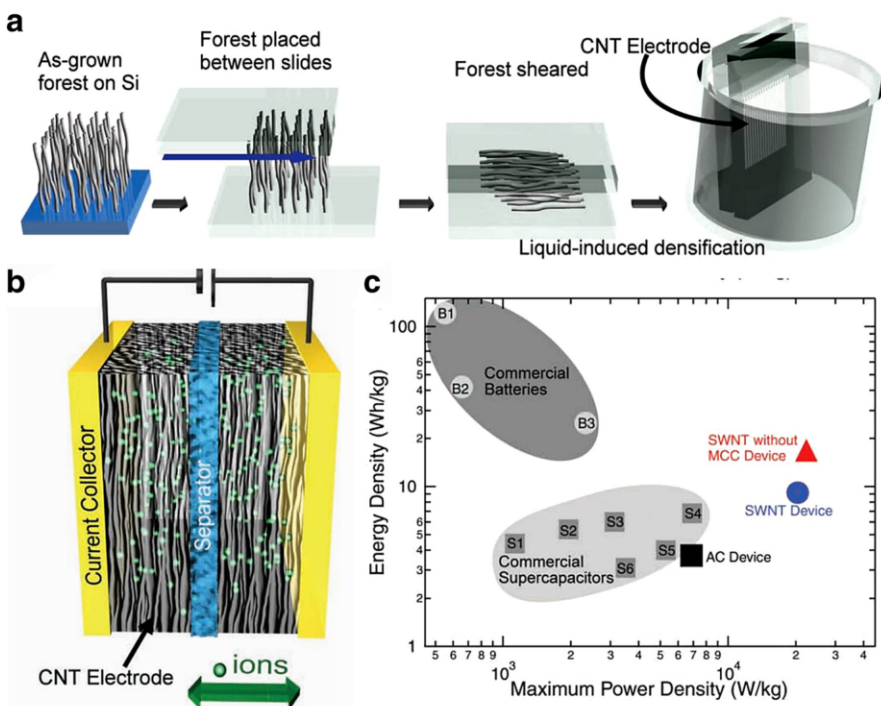


Fig. 15 **a** Electrode fabrication from SWNT arrays. **b** Typical cell assembly based on SWNT electrode in 1 M Et_4NBF_4 /propylene carbonate electrolyte. **c** Ragone plot of SWNT device at the cusp of bridging the energy gap between commercial supercapacitors and batteries. (*S1* Panasonic 2000F, *S2* Superfarad 250F, *S3* Saft Gen2, *S4* Saft Gen3, *S5* Maxwell 2700F, *S6* Panasonic 800F; *B1* Li-ion, *B2* NiHD, *B3* Pb-acid) Reprinted from Ref. [132]. Copyright 2010, Wiley–VCH, Weilheim, Germany

CNTs with high surface area, large bulk density, and ultrahigh purity offer a good platform to demonstrate the application of CNTs in high-voltage supercapacitors. Thus, several SWNT companies such as Gnnano in China, Zeon in Japan, and OCSiAl in Russia have tonnage capacity of SWNT production to focus on this market.

Although SWNTs are attractive for use in supercapacitors, they normally form nanotube bundles, so that the available surface area of the nanotubes is usually reduced. In addition, the current cost of SWNTs is still a major obstacle to their wide application. For MWNTs, the rise of graphene may remedy the disadvantages of each material. Composites combining CNTs and graphene have been proposed to prepare high-power high-energy supercapacitors (Fig. 16a, b) [133, 134]. Recently, three-dimensional porous graphene fibers were reported for use in supercapacitor applications (Fig. 16c) [135]. The capacitance can be even better than with SWNTs, particularly at increasing current densities (Fig. 16d). In addition, similar to lithium-ion batteries, a great advantage is that CNTs enable fabrication of electrodes without binders or current collectors, which are attractive for use in flexible, stretchable, compressible, and fiber supercapacitors [136, 137].

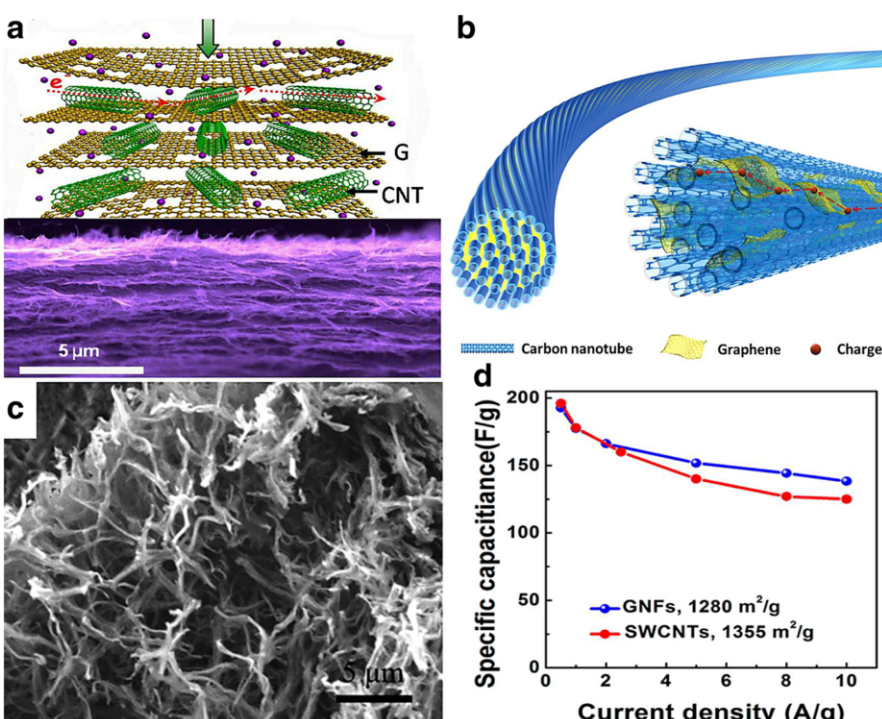


Fig. 16 **a** Schematic illustration of ion diffusion behavior for porous CNT–graphene film. Reprinted from Ref. [133]. Elsevier, copyright 2010. **b** Schematic illustration of structure of graphene–CNT composite fiber. Reproduced from Ref. [134]. Copyright John Wiley and Sons 2014. **c** Morphology of mesoporous graphene nanofibers (GNFs). **d** Comparison of specific capacitance of GNFs and SWNTs. Reproduced from Ref. [135]. Copyright 2014, American Chemical Society

4.4 Catalysis Applications

CNTs themselves as well as their composites can be engineered into efficient catalysts for use in sustainable energy applications. Different from traditional inorganic catalysts, CNTs can easily form a unique network structure that enables facile mass transport. They have inert properties, making them stable in strong acid and alkali solutions. Moreover, CNTs can also be used as catalyst supports for development of other candidate catalysts. These features make CNTs promising for application in catalysis. CNTs are therefore playing an increasingly important role in this research field [8].

As is well known, oxygen reduction reaction (ORR) catalysts are mostly based on platinum (Pt) and its alloys. However, Pt metal suffers from high cost and instability in actual applications. It is therefore very important to identify alternatives. At present, nanocarbon materials such as CNTs and graphene [138] have been developed as effective electrocatalysts or electrocatalyst supports. However, pristine CNTs usually show very limited performance for ORR due to their inactive surface.

To obtain the desired catalyst performance, introduction of heteroatoms into the CNT framework has been found to endow them with excellent activity. A breakthrough in this regard was the synthesis and use of vertically aligned N-doped CNTs as a metal-free electrode for ORR [61]. The performance of this electrocatalyst for oxygen reduction in alkaline cells revealed much better electrocatalytic activity, long-term operation stability, and tolerance to crossover effect compared with Pt. The reason for the ORR activity may be mostly ascribed to the carbon atoms with Lewis basicity next to pyridinic N, as confirmed in N-doped graphene [139]. To date, use of N-doped CNTs for ORR in alkaline electrolytes has been confirmed by many groups, and this work is being extended to other nanocarbon materials. However, the catalyst performance of N-doped CNTs is highly compromised in acidic media. CNTs offering excellent performance in both alkaline and acidic media are therefore desirable.

On the other hand, based on composite engineering, the surface of CNTs can be loaded with various catalysts with good dispersion, offering excellent electrocatalyst supports. One effective Pt-free ORR catalyst is the complex of MN_x , where M is one metal of Fe, Co, and Ni, coordinated by N-containing ligands such as phthalocyanine [140]. However, phthalocyanines have low conductivity and must be mixed with conductive carbon black to form electrodes. CNTs seem to be a better alternative. If well engineered, use of CNTs could significantly improve the activity of the catalyst for ORR. In this case, carbon ring nitrogen coordination of transition-metal catalysts can be achieved. Dai's group has reported the design and synthesis of many efficient CNT-based electrocatalysts. As a typical example, by unzipping CNTs by oxidation and ammonia treatment, a highly efficient NT-G-Fe electrocatalyst was prepared (Fig. 17a, b) [141]. The NT-G catalysts showed ORR activity comparable to that of state-of-the-art Pt/C in 0.1 M KOH (Fig. 17c), also offering promising performance in acid 0.1 M $HClO_4$ medium cells (Fig. 17d).

The development of high-performance catalysts for the hydrogen evolution reaction (HER) and oxygen evolution reaction (OER) also holds great promise for clean energy technologies. One of the typical reactions is water splitting. Making cost-effective electrocatalysts to replace precious iridium (Ir)- or Pt-based catalysts is an important theme. MWNTs modified by surface oxidation treatment, hydrothermal annealing, and electrochemical activation displayed unprecedented OER activity in alkaline media (Fig. 18a) [142]. Oxygen-containing functional groups such as ketonic $C=O$ on the outer wall of MWNTs are found to play crucial roles in catalyzing OER by altering the electronic structures of the adjacent carbon atoms and facilitating adsorption of OER intermediates. On the other hand, to further improve the activity, an effective approach is to make composite electrocatalysts by introducing CNTs. As shown in Fig. 18b, application of a multilayer covalent cobalt porphyrin framework on MWNTs resulted in a highly active electrocatalyst for water oxidation [143]. Nickel–iron layered double hydroxide (NiFe-LDH) nanoplates can also be loaded on MWNTs to form a composite OER electrocatalyst (Fig. 18c–e). The resulting NiFe-LDH/CNT complex exhibits higher electrocatalytic activity and stability for oxygen evolution compared with commercial precious-metal (Ir) catalysts [144]. In addition, such

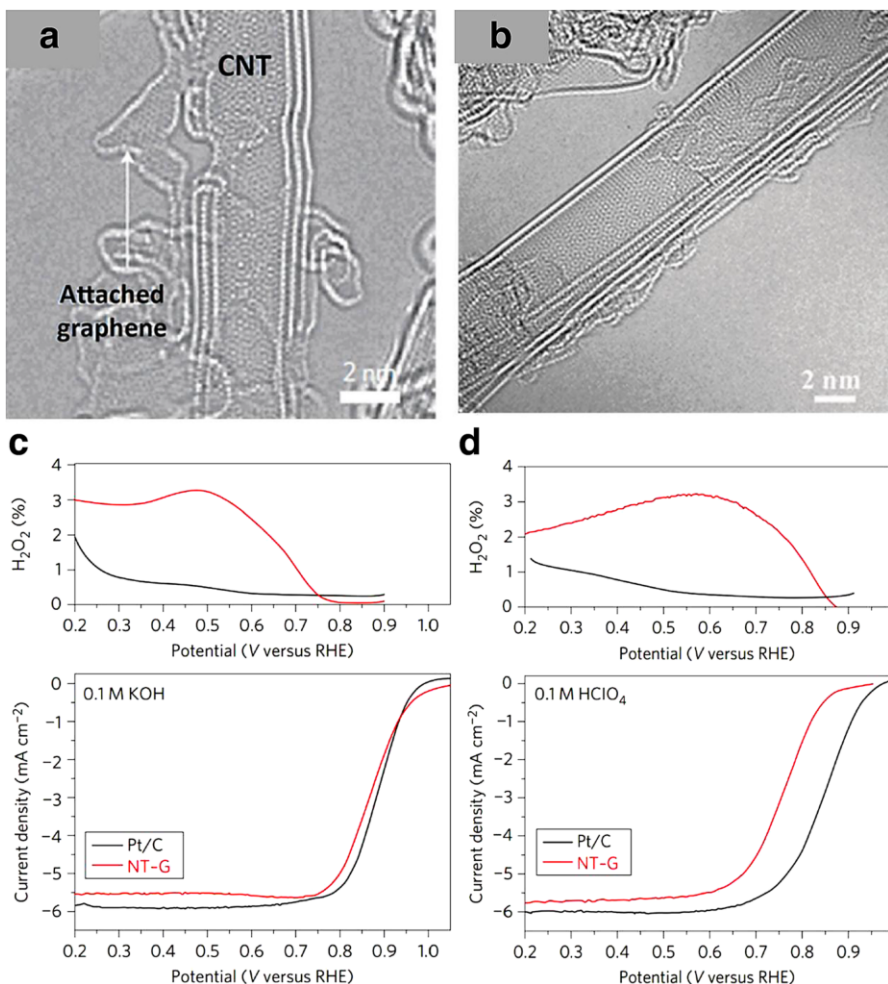


Fig. 17 **a, b** TEM images of NT-G catalysts showing exfoliated graphene pieces attached to CNTs. Rotating-ring disk electrode polarization curves and peroxide yield of NT-G in **c** 0.1 M KOH and **d** 0.1 M HClO₄ Adapted from Ref. [141]. Copyright 2012, Macmillan

composite electrocatalysts may also find applications in photocatalytic and photoelectrochemical water splitting cells [8].

In the field of heterogeneous catalysis, porous carbon materials (e.g., mesoporous carbons) have been used to disperse and stabilize metal particles. As a catalyst support, the external surface area and interconnected pores of CNTs greatly improve diffusion of reactants and products, thereby increasing the catalytic activity and selectivity. A variety of inorganic metal catalysts, including molecular catalysts, metal nanoparticles, metal oxides or even more complex hierarchical hybrids, have been loaded onto CNTs for improved reaction performance [145]. Apart from the aforementioned applications, CNTs have also been utilized for desulfurization of

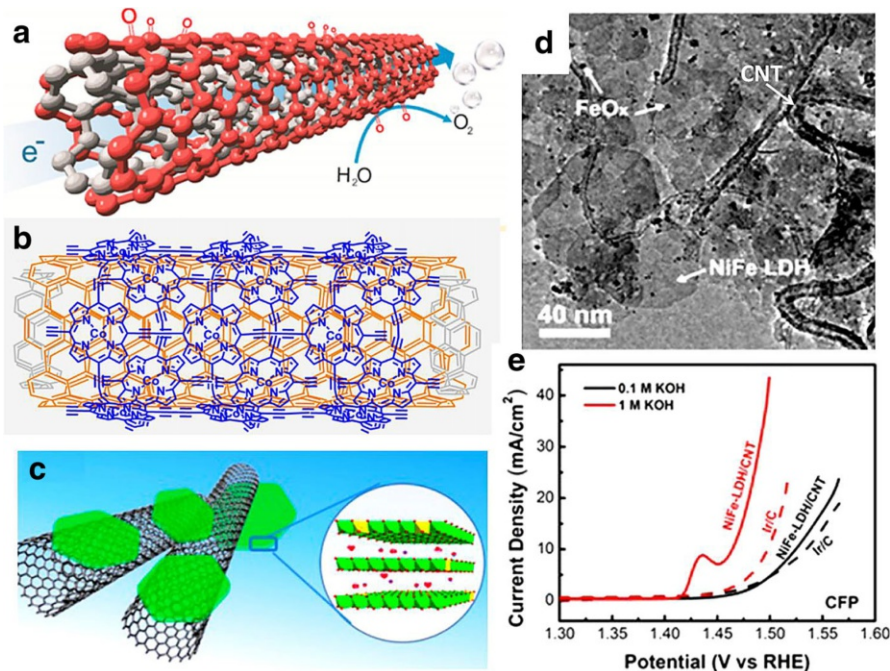


Fig. 18 **a** As-prepared surface-oxidized and electrochemically activated MWNTs for use as OER electrocatalyst. Reproduced from Ref. [142]. Copyright 2015, American Chemical Society. **b** Cobalt porphyrin loaded on MWNTs for efficient OER catalysis. Reproduced from Ref. [143]. Copyright 2015, American Chemical Society. **c** Schematic showing hybrid architecture and LDH crystal structure. **d** Morphology of NiFe-LDH/CNT hybrid. **e** iR-corrected polarization curves of NiFe-LDH/CNT hybrid and Ir/C catalysts on carbon fiber paper, measured in 0.1 and 1 M KOH. Reproduced from Ref. [144]. Copyright 2013, American Chemical Society

diesel fuel, oil hydrocarbon aerobic oxidation, hydrodesulfurization processes, etc. [146]. Overall, direct use of CNTs as catalysts has been shown to be viable for several processes. The scope of such reactions has expanded considerably over the past year. Moreover, inspired by research on CNTs, interest in preparation of CNT-like materials for catalyst applications has been increasing [138].

4.5 Environmental Applications

4.5.1 Gas Filtration

In most cases, traditional fiber mats can achieve efficient filtration of megascopic particles, meeting application requirements. However, it is difficult to remove particles smaller than 1 μm from a gas flow. High filtration efficiency for such particles is important in many critical applications, such as release of nuclear-active materials, semiconductor manufacture, aerospace environments, pharmaceutical processing, and bioengineering.

It has been widely reported that introduction of nanofibers into macrofiber mats can significantly increase their filtration efficiency and improve the pressure drop of pristine macrofiber filters. CNTs with diameter around the nanoscale may enable highly efficient filtration [147]. CNTs themselves can be interwoven into a mat for filtration. However, this will lead to a large pressure drop, which leads to low efficiency. Alternatively, the combination of CNTs with traditional fiber mats to fabricate CNT-based filters may result in highly efficient air filtration. The challenge lies in control of the structure between the CNTs and filter fibers to avoid a large pressure drop.

As shown in Fig. 19a-f, Li et al. proposed a “gradient nanostructure filtration” concept to eliminate clogging of nanofiber filters [148]. When grown with only a small amount of 1.17 wt% CNTs, the efficiency was greatly improved. The filters displayed the combination of high efficiency, low pressure drop, and long service lifetime at the same time. They fabricated hierarchical CNT/QF filters with gradient nanostructures where the content of the CNTs decreased exponentially along the axial direction of the filter, resulting in higher filtration efficiency and lower pressure drop [149]. Moreover, a high-efficiency particulate air filter based on an agglomerated CNT fluidized bed has been developed [150]. Indeed, based on its high efficiency, aerosols and peculiar smells in the air could also be removed using this filter. Recently, Yang et al. found that the CNT/QF filter also has very strong ability to remove O₃ from air in comparison with activated carbon. Such environmental applications represent a new field for CNTs [151].

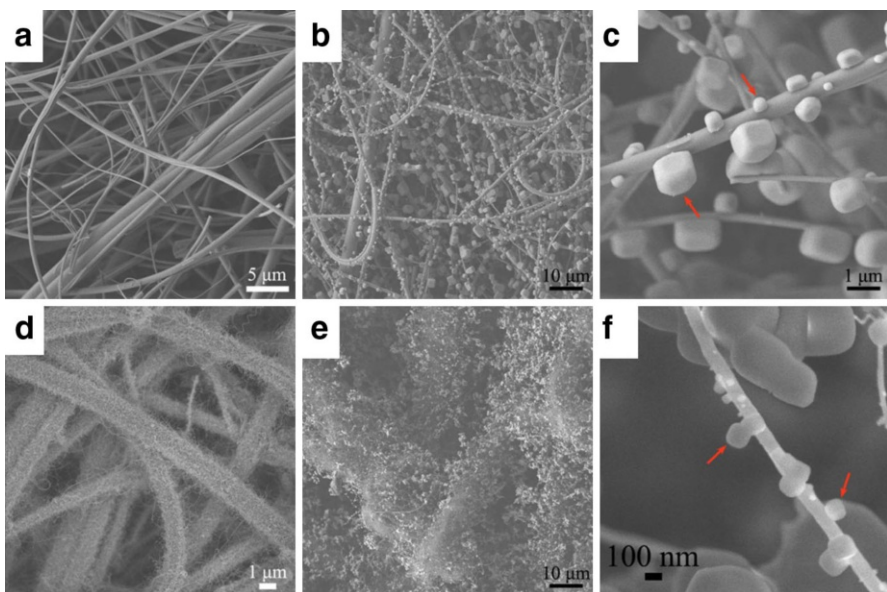


Fig. 19 SEM images of filters before and after filtration process. **a** Pristine quartz fiber (QF) filter; **b** NaCl aerosol particles deposited on QF filter; **c** NaCl aerosol particles deposited on single quartz fiber; **d** CNT/QF filter; **e** NaCl aerosol particles deposited on CNT/QF filter; **f** NaCl aerosol particles deposited on single CNT Reproduced from Ref. [148]. Copyright 2013, Royal Society of Chemistry

4.5.2 Water Absorption and Filtration

Another upcoming application domain for CNTs is water purification. Serious water pollution results in a great deal of damage to the environment, also affecting human health and animal and plant survival. Water pollution includes heavy metals, inorganic nonmetals, organic matter, etc., from both domestic and industrial wastewater. CNTs represent a special fiber material with many advantages. They are entangled into robust networks and offer mechanical strength and stability. CNTs have good performance for adsorption of contaminants from water due to their high affinity and selective adsorption capacity for contaminants, particularly organic pollutants, bacteria, and heavy metals. Production of portable filters containing CNT meshes has been reported for purification of contaminated drinking water [2]. In addition, by adding a suitable amount of MWNTs to polyamide (e.g., 15.5 wt%), a high-performance reverse osmosis composite thin membrane can be obtained, which not only improves the membrane performance in terms of flow and antifouling, but also inhibits chlorine degradation of the membrane [152].

More importantly, an interesting issue discussed by researchers is water transport in the internal tubes of small-diameter CNTs. It has been found that transport of fluids using CNTs is orders of magnitude faster than for other nanoporous materials due to the unprecedented smoothness and regularity of CNT pores [153, 154]. In this case, aligned CNT membranes are being evaluated for use in desalination technology (Fig. 20) [155]. They can be embedded into a resin or ceramic matrix and then engineered with open ends for water purification. The results show that this kind of CNT filter has a water flux approximately three times higher than

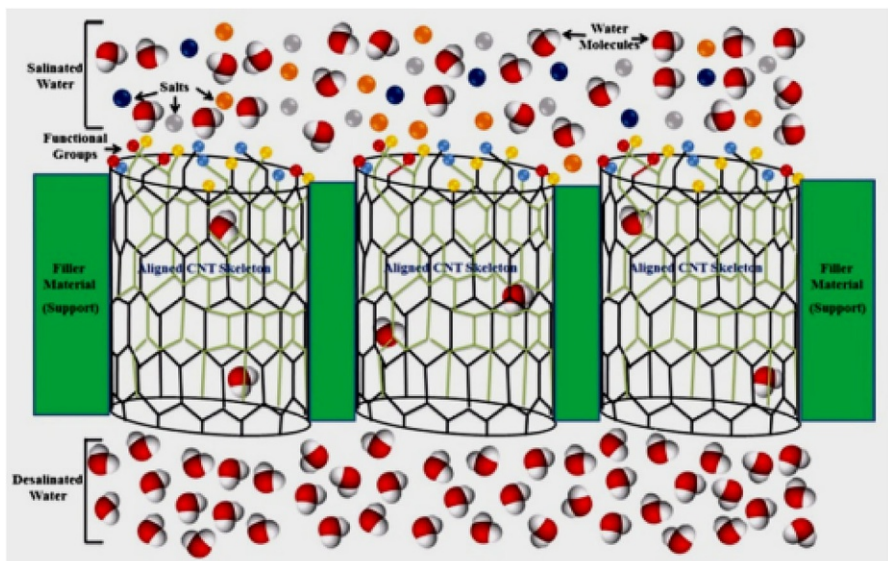


Fig. 20 Carbon nanotube (CNT) membranes for water purification. The membrane facilitates water influx, rejects salts, and removes most pollutants Reprinted from Ref. [155]. Elsevier, copyright 2013

commercial ultrafiltration membranes and water transport approximately 70,000 times faster than conventional no-slip flow [156]. Moreover, by engineering the ends of CNTs using different functionalization strategies, such filters also display enhanced ability to gate molecular transport through the CNT cores [157]. These studies indicate that CNTs have potential to overcome the inherent limitations resulting from the trade-off between flux and selectivity of any membrane process. In this regard, CNT membranes are considered to have a bright future for use in next-generation water desalination. If this technique is scaled up, water desalination and purification may rapidly become promising [158].

Studies have shown that CNTs have good performance for adsorption of contaminants from water. Compared with traditional adsorbents, CNTs offer advantages of large adsorptive capacity and short adsorption equilibrium time. However, there are still some problems including high production cost, poor cycle stability, etc. Another major concern regarding CNTs for air and water filtration is environmental and human exposure to CNTs, since there are some reports that CNTs may damage human health [159]. Mechanical stability is very important for the safety of CNT-based filters. The structure of CNT-based filters should be designed to prevent CNT detachment from the filter under the force of fluid flow or other external forces. Such health and environmental concerns are also important for CNT production and their subsequent processing, application, recycling, etc. [160].

5 Summary and Outlook

CNTs display many extreme properties, such as superior mechanical strength, semiconducting properties, etc. However, these properties are only achieved when they have perfect structure. It is very important to control or even completely avoid defects at the atomic to macro level during CNT synthesis, as well as to achieve production scale-up. This is an engineering problem and currently represent the most challenging issue in the field of CNTs. Although this challenge seems difficult, such ultrahigh-strength materials and ultra-high-performance semiconductor materials are in great demand for future society.

Large-scale production of MWNTs has become available, now offering production capacity of more than thousands of tons per year. The processing techniques used are critical for their application. It is important to develop cost-effective and reliable processes for CNT processing depending on the application. Now, MWNT powders are milled into pastes, which are widely used in lithium-ion batteries. However, dispersion techniques and extended applications of this kind of material need to be further explored, especially to solve the dispersion problems of high-aspect-ratio and high-purity CNTs, and to identify applications.

Synthesis and scaled-up production of SWNTs with high aspect ratio and purity remain key issues for future development and applications of CNTs. Addressing these problems will benefit many critical applications.

Meanwhile, the development of CNTs has promoted research into other nanocarbons, currently including graphene. The combination of CNTs with other nanocarbons will open up new horizons for development of CNTs. Such rational

combinations will further enhance the potential applications of CNTs and other materials.

Looking ahead, CNTs have made great breakthroughs in energy storage applications. Considering the rapid development of EVs and other practical devices, it is very possible that CNTs will be used in industrial applications at levels up to several million tons per year in the next decade. In the field of CNT catalysis, the superior performance of doped Dirac carbon materials compared with Pt/C in ORR, OER, HER, etc., may enable rapid development in the chloralkali industry and fuel cells. Also, due to the significant advantages of SWNTs in load-bearing materials and conductive materials, it is believed that they will become key materials for use in high-end applications, e.g., in the aviation, aerospace, and military fields.

Acknowledgements We greatly appreciate the reviewers' constructive comments. This work was supported by the National Natural Science Foundation of China (Nos. 21306102 and 21422604, Prof. F. Wei), and partially by the National Natural Science Foundation of China (Nos. 51502347, Dr. X. Jia).

References

- Iijima S (1991) Nature 354:56
- De Volder MFL, Tawfick SH, Baughman RH, Hart AJ (2013) Science 339:535
- Zhang Q, Huang J-Q, Qian W-Z, Zhang Y-Y, Wei F (2013) Small 9:1237
- Endo M, Strano MS, Ajayan PM (2007) Potential applications of carbon nanotubes, Springer, Berlin Heidelberg, p 13
- Liu C, Cheng H-M (2013) Mater Today 16:19
- Baughman RH, Zakhidov AA, de Heer WA (2002) Science 297:787
- Endo M (1988) ChemTech 18:568
- Yan Y, Miao J, Yang Z, Xiao F-X, Yang HB, Liu B, Yang Y (2015) Chem Soc Rev 44:3295
- Sinnott SB, Andrews R, Qian D, Rao AM, Mao Z, Dickey EC, Derbyshire F (1999) Chem Phys Lett 315:25
- Liu C, Cheng H-M (2016) J Am Chem Soc 138:6690
- Chen Y, Zhang Y, Hu Y, Kang L, Zhang S, Xie H, Liu D, Zhao Q, Li Q, Zhang J (2014) Adv Mater 26:5898
- Yang F, Wang X, Zhang D, Yang J, Luo D, Xu Z, Wei J, Wang J-Q, Xu Z, Peng F, Li X, Li R, Li Y, Li M, Bai X, Ding F, Li Y (2014) Nature 510:522
- Murakami Y, Chiashi S, Miyauchi Y, Hu M, Ogura M, Okubo T, Maruyama S (2004) Chem Phys Lett 385:298
- Hata K, Futaba DN, Mizuno K, Namai T, Yumura M, Iijima S (2004) Science 306:1362
- Amama PB, Pint CL, McJilton L, Kim SM, Stach EA, Murray PT, Hauge RH, Maruyama B (2009) Nano Lett 9:44
- Chen Z, Kim DY, Hasegawa K, Noda S (2013) ACS Nano 7:6719
- Nikolaev P, Bronikowski MJ, Bradley RK, Rohmund F, Colbert DT, Smith KA, Smalley RE (1999) Chem Phys Lett 313:91
- Resasco DE, Alvarez WE, Pompeo F, Balzano L, Herrera JE, Kitayanan B, Borgna A (2002) J Nanopart Res 4:131
- Zhang R, Wen Q, Qian W, Su DS, Zhang Q, Wei F (2011) Adv Mater 23:3387
- Zhang R, Zhang Y, Zhang Q, Xie H, Qian W, Wei F (2013) ACS Nano 7:6156
- Zhang R, Ning Z, Zhang Y, Zheng Q, Chen Q, Xie H, Zhang Q, Qian W, Wei F (2013) Nat Nanotech 8:912
- Jiang K, Li Q, Fan S (2002) Nature 419:801
- Jiang K, Wang J, Li Q, Liu L, Liu C, Fan S (2011) Adv Mater 23:1154
- Xiang R, Luo GH, Qian WZ, Wang Y, Wei F, Li Q (2007) Chem Vapor Depos 13:533
- Kim DY, Sugime H, Hasegawa K, Osawa T, Noda S (2011) Carbon 49:1972

26. Dichiara A, Bai J (2012) *Diam Rel Mater* 29:52
27. Zhang Q, Zhao M, Liu Y, Cao A, Qian W, Lu Y, Wei F (2009) *Adv Mater* 21:2876
28. Zhao M-Q, Zhang Q, Huang J-Q, Wei F (2012) *Adv Funct Mater* 22:675
29. Zhao M-Q, Zhang Q, Zhang W, Huang J-Q, Zhang Y, Su DS, Wei F (2010) *J Am Chem Soc* 132:14739
30. Zhao M-Q, Zhang Q, Jia X-L, Huang J-Q, Zhang Y-H, Wei F (2010) *Adv Funct Mater* 20:677
31. Zhang Q, Huang J-Q, Zhao M-Q, Qian W-Z, Wei F (2011) *ChemSusChem* 4:864
32. Wei F, Zhang Q, Qian W-Z, Yu H, Wang Y, Luo G-H, Xu G-H, Wang D-Z (2008) *Powder Technol* 183:10
33. Zhang Q, Zhao M-Q, Huang J-Q, Liu Y, Wang Y, Qian W-Z, Wei F (2009) *Carbon* 47:2600
34. Zhao M-Q, Zhang Q, Huang J-Q, Nie J-Q, Wei F (2010) *Carbon* 48:3260
35. Chen T-C, Zhao M-Q, Zhang Q, Tian G-L, Huang J-Q, Wei F (2013) *Adv Funct Mater* 23:5066
36. Zhang J, Terrones M, Park CR, Mukherjee R, Monthioux M, Koratkar N, Kim YS, Hurt R, Frackowiak E, Enoki T, Chen Y, Chen Y, Bianco A (2016) *Carbon* 98:708
37. Zhao M-Q, Liu X-F, Zhang Q, Tian G-L, Huang J-Q, Zhu W, Wei F (2012) *ACS Nano* 6:10759
38. Tian G-L, Zhao M-Q, Yu D, Kong X-Y, Huang J-Q, Zhang Q, Wei F (2014) *Small* 10:2251
39. Tang C, Zhang Q, Zhao MQ, Huang JQ, Cheng XB, Tian GL, Peng HJ, Wei F (2014) *Adv Mater* 26:6100
40. Zhu Y, Li L, Zhang C, Casillas G, Sun Z, Yan Z, Ruan G, Peng Z, Raji A-RO, Kittrell C, Hauge RH, Tour JM (2012) *Nat Commun* 3:1225
41. Lv R, Cui T, Jun M-S, Zhang Q, Cao A, Su DS, Zhang Z, Yoon S-H, Miyawaki J, Mochida I, Kang F (2011) *Adv Funct Mater* 21:999
42. Fan Z, Yan J, Zhi L, Zhang Q, Wei T, Feng J, Zhang M, Qian W, Wei F (2010) *Adv Mater* 22:3723
43. Zhao M-Q, Zhang Q, Huang J-Q, Tian G-L, Chen T-C, Qian W-Z, Wei F (2013) *Carbon* 54:403
44. Zhang WD, Phang IY, Liu TX (2006) *Adv Mater* 18:73
45. Wang Y, Wu J, Wei F (2003) *Carbon* 41:2939
46. Karousis N, Tagmatarchis N, Tasis D (2010) *Chem Rev* 110:5366
47. Premkumar T, Mezzenga R, Geckeler KE (2012) *Small* 8:1299
48. Ajayan PM, Tour JM (2007) *Nature* 447:1066
49. Nish A, Hwang J-Y, Doig J, Nicholas RJ (2007) *Nat Nano* 2:640
50. Gu J, Han J, Liu D, Yu X, Kang L, Qiu S, Jin H, Li H, Li Q, Zhang J (2016) *Small* 12:4993
51. Hersam MC (2008) *Nat Nano* 3:387
52. Preston C, Song D, Dai J, Tsinas Z, Bavier J, Cumings J, Ballarotto V, Hu L (2015) *Nano Res* 8:2242
53. Georgakilas V, Bourlinos A, Gournis D, Tsoufis T, Trapalis C, Mateo-Alonso A, Prato M (2008) *J Am Chem Soc* 130:8733
54. Zhao Y, Yang L, Chen S, Wang X, Ma Y, Wu Q, Jiang Y, Qian W, Hu Z (2013) *J Am Chem Soc* 135:1201
55. Yu D, Xue Y, Dai L (2012) *J Phys Chem Lett* 3:2863
56. Ma X, Baldwin JKS, Hartmann NF, Doorn SK, Htoon H (2015) *Adv Funct Mater* 25:6157
57. Yang L, Jiang S, Zhao Y, Zhu L, Chen S, Wang X, Wu Q, Ma J, Ma Y, Hu Z (2011) *Angew Chem Int Ed* 123:7270
58. Thurakitseret T, Kramberger C, Zhao P, Aikawa S, Harish S, Chiashi S, Einarsson E, Maruyama S (2012) *Carbon* 50:2635
59. Wang X, Sun G, Routh P, Kim D-H, Huang W, Chen P (2014) *Chem Soc Rev* 43:7067
60. Shui J, Wang M, Du F, Dai L (2015) *Sci Adv* 1:e1400129
61. Gong K, Du F, Xia Z, Durstock M, Dai L (2009) *Science* 323:760
62. Qi C, Ma X, Ning G, Song X, Chen B, Lan X, Li Y, Zhang X, Gao J (2015) *Carbon* 92:245
63. Liu L, Ma W, Zhang Z (2011) *Small* 7:1504
64. Li Z, Liu Z, Sun H, Gao C (2015) *Chem Rev* 115:7046
65. Feng C, Liu K, Wu J-S, Liu L, Cheng J-S, Zhang Y, Sun Y, Li Q, Fan S, Jiang K (2010) *Adv Funct Mater* 20:885
66. Ma W, Song L, Yang R, Zhang T, Zhao Y, Sun L, Ren Y, Liu D, Liu L, Shen J, Zhang Z, Xiang Y, Zhou W, Xie S (2007) *Nano Lett* 7:2307
67. Ma W, Liu L, Zhang Z, Yang R, Liu G, Zhang T, An X, Yi X, Ren Y, Niu Z, Li J, Dong H, Zhou W, Ajayan PM, Xie S (2009) *Nano Lett* 9:2855
68. Niu Z, Zhou W, Chen J, Feng G, Li H, Ma W, Li J, Dong H, Ren Y, Zhao D, Xie S (2011) *Energy Environ Sci* 4:1440

69. Nasibulin AG, Kaskela A, Mustonen K, Anisimov AS, Ruiz V, Kivistö S, Rackauskas S, Timmermans MY, Pudas M, Aitchison B, Kauppinen M, Brown DP, Okhotnikov OG, Kauppinen EI (2011) ACS Nano 5:3214
70. Reynaud O, Nasibulin AG, Anisimov AS, Anoshkin IV, Jiang H, Kauppinen EI (2014) Chem Eng J 255:134
71. Mustonen K, Laiho P, Kaskela A, Zhu Z, Reynaud O, Houbenov N, Tian Y, Susi T, Jiang H, Nasibulin AG, Kauppinen EI (2015) Appl Phys Lett 107:013106
72. Kaskela A, Mustonen K, Laiho P, Ohno Y, Kauppinen EI (2015) ACS Appl Mater Interfaces 7:28134
73. Lu W, Zu M, Byun J-H, Kim B-S, Chou T-W (2012) Adv Mater 24:1805
74. Xu W, Chen Y, Zhan H, Wang JN (2016) Nano Lett 16:946
75. Gui X, Wei J, Wang K, Cao A, Zhu H, Jia Y, Shu Q, Wu D (2010) Adv Mater 22:617
76. Xu M, Futaba DN, Yamada T, Yumura M, Hata K (2010) Science 330:1364
77. Davis VA, Parra-Vasquez ANG, Green MJ, Rai PK, Behabtu N, Prieto V, Booker RD, Schmidt J, Kesselman E, Zhou W, Fan H, Adams WW, Hauge RH, Fischer JE, Cohen Y, Talmon Y, Smalley RE, Pasquale M (2009) Nat Nano 4:830
78. Zhang S, Koziol KKK, Kinloch IA, Windle AH (2008) Small 4:1217
79. Behabtu N, Young CC, Tsentalovich DE, Kleinerman O, Wang X, Ma AWK, Bengio EA, ter Waarbeek RF, de Jong JJ, Hoogerwerf RE, Fairchild SB, Ferguson JB, Maruyama B, Kono J, Talmon Y, Cohen Y, Otto MJ, Pasquale M (2013) Science 339:182
80. Sun H, Xu Z, Gao C (2013) Adv Mater 25:2554
81. Peng B, Locascio M, Zapol P, Li S, Mielke SL, Schatz GC, Espinosa HD (2008) Nat Nano 3:626
82. Spitalsky Z, Tasis D, Papagelis K, Galiotis C (2010) Prog Polym Sci 35:357
83. Xie X-L, Mai Y-W, Zhou X-P (2005) Mater Sci Eng R 49:89
84. Tang W, Santare MH, Advani SG (2003) Carbon 41:2779
85. Lu Y, Liu J, Hou G, Ma J, Wang W, Wei F, Zhang L (2016) Compos Sci Technol 137:94
86. Johannsen I, Jakšík K, Wirch N, Pötschke P, Fiedler B, Schulte K (2016) Polymer 97:80
87. Deng F, Ito M, Noguchi T, Wang L, Ueki H, Niihara KI, Kim YA, Endo M, Zheng QS (2011) ACS Nano 5:3858
88. Jia X, Zhang Q, Zhao M-Q, Xu G-H, Huang J-Q, Qian W, Lu Y, Wei F (2012) J Mater Chem 22:7050
89. Wang Z, Liang Z, Wang B, Zhang C, Kramer L (2004) Compos Part A Appl Sci Manuf 35:1225
90. Belyarova E, Thostenson ET, Yu A, Kim H, Gao J, Tang J, Hahn HT, Chou TW, Itkis ME, Haddon RC (2007) Langmuir 23:3970
91. An Q, Rider AN, Thostenson ET (2013) ACS Appl Mater Interfaces 5:2022
92. Jin L, Zhang L, Su D, Li C (2012) Ind Eng Chem Res 51:4927
93. Cheng Q, Wang B, Zhang C, Liang Z (2010) Small 6:763
94. Cheng Q, Bao J, Park J, Liang Z, Zhang C, Wang B (2009) Adv Funct Mater 19:3219
95. Sandler JKW, Kirk JE, Kinloch IA, Shaffer MSP, Windle AH (2003) Polymer 44:5893
96. Huang J, Mao C, Zhu Y, Jiang W, Yang X (2014) Carbon 73:267
97. Bauhofer W, Kovacs JZ (2009) Compos Sci Technol 69:1486
98. Han Z, Fina A (2011) Prog Polym Sci 36:914
99. Arjmand M, Apperley T, Okoniewski M, Sundararaj U (2012) Carbon 50:5126
100. Bakshi S, Lahiri D, Agarwal A (2010) Int Mater Rev 55:41
101. Chen B, Li S, Imai H, Jia L, Umeda J, Takahashi M, Kondoh K (2015) Mater Des 72:1
102. Cho J, Boccaccini AR, Shaffer MS (2009) J Mater Sci 44:1934
103. Chae HG, Choi YH, Minus ML, Kumar S (2009) Compos Sci Technol 69:406
104. Landi BJ, Ganter MJ, Cress CD, DiLeo RA, Raffaelli RP (2009) Energy Environ Sci 2:638
105. Liu X-M, Huang ZD, Oh SW, Zhang B, Ma P-C, Yuen MM, Kim J-K (2012) Compos Sci Technol 72:121
106. Sehrwat P, Julien C, Islam SS (2016) Mater Sci Eng B 213:12
107. Liu X-Y, Peng H-J, Zhang Q, Huang J-Q, Liu X-F, Wang L, He X, Zhu W, Wei F (2014) ACS Sustain Chem Eng 2:200
108. Xin S, Gu L, Zhao N-H, Yin Y-X, Zhou L-J, Guo Y-G, Wan L-J (2012) J Am Chem Soc 134:18510
109. Ma J, Fang Z, Yan Y, Yang Z, Gu L, Hu Y-S, Li H, Wang Z, Huang X (2015) Adv Energy Mater 5:1500046
110. Cheng X-B, Huang J-Q, Zhang Q, Peng H-J, Zhao M-Q, Wei F (2014) Nano Energy 4:65

111. Zhang SM, Zhang Q, Huang JQ, Liu XF, Zhu W, Zhao MQ, Qian WZ, Wei F (2013) Part Part Syst Charact 30:158
112. Song J, Gordin ML, Xu T, Chen S, Yu Z, Sohn H, Lu J, Ren Y, Duan Y, Wang D (2015) Angew Chem Int Ed 54:4325
113. Zhou G, Wang D-W, Li F, Hou P-X, Yin L, Liu C, Lu GQ, Gentle IR, Cheng H-M (2012) Energy Environ Sci 5:8901
114. Li X, Liu J, Zhang Y, Li Y, Liu H, Meng X, Yang J, Geng D, Wang D, Li R, Sun X (2012) J Power Sources 197:238
115. Magasinski A, Dixon P, Hertzberg B, Kvit A, Ayala J, Yushin G (2010) Nat Mater 9:353
116. Xue L, Xu G, Li Y, Li S, Fu K, Shi Q, Zhang X (2013) ACS Appl Mater Interfaces 5:21
117. Wang W, Kumta PN (2010) ACS Nano 4:2233
118. Evanoff K, Khan J, Balandin AA, Magasinski A, Ready WJ, Fuller TF, Yushin G (2012) Adv Mater 24:533
119. Jia X, Zhu X, Cheng Y, Chen Z, Ning G, Lu Y, Wei F (2015) Small 11:3135
120. Jia X, Cheng Y, Lu Y, Wei F (2014) ACS Nano 8:9265
121. Jia X, Zhang L, Zhang R, Lu Y, Wei F (2014) RSC Adv 4:21018
122. Choi SH, Lee J-H, Kang YC (2015) ACS Nano 9:10173
123. Jia X, Kan Y, Zhu X, Ning G, Lu Y, Wei F (2014) Nano Energy 10:344
124. Jia X, Chen Z, Suwarnasarn A, Rice L, Wang X, Sohn H, Zhang Q, Wu BM, Wei F, Lu Y (2012) Energy Environ Sci 5:6845
125. Zhang Y, Bai W, Cheng X, Ren J, Weng W, Chen P, Fang X, Zhang Z, Peng H (2014) Angew Chem Int Ed 53:14564
126. Zhou G, Li F, Cheng H-M (2014) Energy Environ Sci 7:1307
127. Pandolfo AG, Hollenkamp AF (2006) J Power Sources 157:11
128. Niu C, Sichel EK, Hoch R, Moy D, Tennent H (1997) Appl Phys Lett 70:1480
129. Hao L, Li X, Zhi L (2013) Adv Mater 25:3899
130. Wang G, Zhang L, Zhang J (2012) Chem Soc Rev 41:797
131. Lazzari M, Mastragostino M, Pandolfo A, Ruiz V, Soavi F (2011) J Electrochem Soc 158:A22
132. Izadi-Najafabadi A, Yasuda S, Kobashi K, Yamada T, Futaba DN, Hatori H, Yumura M, Iijima S, Hata K (2010) Adv Mater 22:E235
133. Jiang L, Sheng L, Long C, Fan Z (2015) Nano Energy 11: 471
134. Sun H, You X, Deng J, Chen X, Yang Z, Ren J, Peng H (2014) Adv Mater 26:2868
135. Cui C, Qian W, Yu Y, Kong C, Yu B, Xiang L, Wei F (2014) J Am Chem Soc 136:2256
136. Liu L, Niu Z, Chen J (2016) Chem Soc Rev 45:4340
137. Dong L, Xu C, Li Y, Huang Z-H, Kang F, Yang Q-H, Zhao X (2016) J Mater Chem A 4:4659
138. Xu Y, Kraft M, Xu R (2016) Chem Soc Rev 45:3039
139. Guo D, Shibuya R, Akiba C, Saji S, Kondo T, Nakamura J (2016) Science 351:361
140. Wu G, More KL, Johnston CM, Zelenay P (2011) Science 332:443
141. Li Y, Zhou W, Wang H, Xie L, Liang Y, Wei F, Idrobo J-C, Pennycook SJ, Dai H (2012) Nat Nano 7:394
142. Lu X, Yim W-L, Suryanto BHR, Zhao C (2015) J Am Chem Soc 137:2901
143. Jia H, Sun Z, Jiang D, Du P (2015) Chem Mater 27:4586
144. Gong M, Li Y, Wang H, Liang Y, Wu JZ, Zhou J, Wang J, Regier T, Wei F, Dai H (2013) J Am Chem Soc 135:8452
145. Melchionna M, Marchesan S, Prato M, Fornasiero P (2015) Catal Sci Technol 5:3859
146. Zhang W, Zhang H, Xiao J, Zhao Z, Yu M, Li Z (2014) Green Chem 16:211
147. Li P, Wang C, Zhang Y, Wei F (2014) Small 10:4543
148. Li P, Zong Y, Zhang Y, Yang M, Zhang R, Li S, Wei F (2013) Nanoscale 5:3367
149. Li P, Wang C, Li Z, Zong Y, Zhang Y, Yang X, Li S, Wei F (2014) RSC Adv 4:54115
150. Wang C, Li P, Zong Y, Zhang Y, Li S, Wei F (2014) Carbon 79:424
151. Yang S, Nie J, Wei F, Yang X (2016) Environ Sci Technol 50:9592
152. Inukai S, Cruz-Silva R, Ortiz-Medina J, Morelos-Gomez A, Takeuchi K, Hayashi T, Tanioka A, Araki T, Tejima S, Noguchi T, Terrones M, Endo M (2015) Sci Rep 5:13562
153. Holt JK, Park HG, Wang Y, Stadermann M, Artyukhin AB, Grigoropoulos CP, Noy A, Bakajin O (2006) Science 312:1034
154. Majumder M, Chopra N, Andrews R, Hinds BJ (2005) Nature 438:44
155. Das R, Ali ME, Hamid SBA, Ramakrishna S, Chowdhury ZZ (2014) Desalination 336:97

156. Baek Y, Kim C, Seo DK, Kim T, Lee JS, Kim YH, Ahn KH, Bae SS, Lee SC, Lim J, Lee K, Yoon J (2014) *J Membr Sci* 460:171
157. Hinds BJ, Chopra N, Rantell T, Andrews R, Gavalas V, Bachas LG (2004) *Science* 303:62
158. Kar S, Bindal RC, Tewari PK (2012) *Nano Today* 7:385
159. Nakanishi J, Morimoto Y, Ogura I, Kobayashi N, Naya M, Ema M, Endoh S, Shimada M, Ogami A, Myojyo T, Oyabu T, Gamo M, Kishimoto A, Igarashi T, Hanai S (2015) *Risk Anal* 35:1940
160. Nowack B, David RM, Fissan H, Morris H, Shatkin JA, Stintz M, Zepplin R, Brouwer D (2013) *Environ Int* 59:1